



## Sorption of Cobalt and Nickel on *Narcissus tazetta L.* Leaf Powder

Süleyman İnan , Bekir Özkan 

Ege University, Institute of Nuclear Sciences, İzmir, Turkey.

**Abstract:** *Narcissus tazetta Linnaeus* are grown in the Karaburun district of the Aegean Region in Turkey in large quantities. The flower has an economic value; however, the leaves of the plant are of no use. Within this study's scope, sorption behaviors of *Narcissus tazetta L.* leaf powder against cobalt and nickel ions were investigated by batch experiments. The effects of initial pH, contact time, initial metal concentration, temperature, and biosorbent dosage were examined using one-factor-at-a-time method. Maximum sorption capacities for Co(II) and Ni(II) were 43.48 and 35.97 mg g<sup>-1</sup>, respectively. The biosorption process is fast, and the equilibrium was attained in 15 min. for Co(II) and Ni(II). Data fit the pseudo-second-order kinetic model well for both metal ions. Thermodynamic parameters reveal that the biosorption is exothermic and spontaneous. *Narcissus tazetta L.* Leaf powder is a readily available, costless, and promising biomaterial that can be used to separate Co(II) and Ni(II) ions from an aqueous solution.

**Keywords:** Biosorption, cobalt, nickel, *Narcissus tazetta*, separation.

**Submitted:** February 17, 2021. **Accepted:** May 25, 2021.

**Cite this:** İnan S, Özkan B. Sorption of Cobalt and Nickel on *Narcissus tazetta L.* Leaf Powder. JOTCSA. 2021;8(3):705-14.

**DOI:** <https://doi.org/10.18596/jotcsa.881291>.

**\*Corresponding author. E-mail:** [inansuleyman@gmail.com](mailto:inansuleyman@gmail.com).

### INTRODUCTION

Industrial effluents contain a wide range of hazardous metals, including Co and Ni. Among these metals, cobalt is arising from metallurgical, chloro-alkali, paint, dye, petroleum, battery industries, and coal-fired power plants and penetrates water sources (1). On the other hand, nickel-containing wastes are generated due to nickel mining, nickel plating, and battery production (2). Apart from this, <sup>63</sup>Ni and <sup>60</sup>Co are radionuclides with long half-lives formed during the nuclear energy generation, and also accumulate in the metallic parts of the core and the reactor vessel. Due to its long half-life (100 years), <sup>63</sup>Ni will remain a significant radioactivity source for 20 years after decommissioning a nuclear reactor (3). Hazardous metals have destructive effects and therefore their removal from wastewaters and the aqueous stream is vital for preserving humanity and the environment. For this reason, inexpensive, eco-friendly, and effective materials have always been the focus of attention in removing hazardous metal ions from dilute solutions (1 - 100 mg L<sup>-1</sup>) and for

the mitigation of heavy metal ion concentration to acceptable levels.

Separation techniques such as solvent extraction, chemical precipitation, and reverse osmosis can be inefficient or very expensive (4). Biosorption is an intriguing technique often used to remove hazardous metals from various types of contaminated waste solutions. It has been reported that a significant number of biomass are used as biosorbent in removing metal ions from liquid waste. Proteins, lipids, and polysaccharides are the constituents of biomass cell walls containing hydroxyl, phosphate sulfate, carboxylate, and amino groups that can adsorb metal ions (4).

Seaweeds (5), brown algae (2,6), fungi (7), rice bran (4), crab shell particles (8), plants (9), tree leaves (1,10) were utilized for cobalt and nickel biosorption studies. Biosorption behaviors of six different seaweed species for Co(II) and Ni(II) were examined by Vijayaraghavan et al. They reported that sorption capacity of *Sargassum wightii* was 18.58 mg g<sup>-1</sup> for Ni(II) at pH 4 and 20.63 mg g<sup>-1</sup> for

Co(II) at pH 4.5 (5). Biosorption studies of Ni(II) ions were carried out using 4 types of brown algae by Pahlavanzadeh et al. Ni(II) biosorption was optimized at pH 6 for all types of algae. The maximum Ni(II) uptake was found as 55.56 mg g<sup>-1</sup> for *Sargassum glaucescens* (2). Zafar et al. analyzed the influence of pH, biosorbent size and dosage, initial concentration, and time on Ni(II) sorption using protonated rice bran. It was reported that the Ni(II) removal was rapid, and 57% of sorption took place between 15-30 min. Ni(II) uptake was 102 mg g<sup>-1</sup> at pH 6 (4).

*Narcissus* is the common name of the plant species from the *Amaryllidaceae* family of the *Narcissus* genus. The homeland of these plants is Europe, and the richest species is found in Spain and Portugal (11). *Narcissus tazetta* is the name of the genus particularly grown in the Karaburun district of the Aegean Region in Turkey. Flowers are harvested in the winter period, and afterward, leaves coming out of bulbs starts to dry. During the summer period, they become totally dry. Dried leaves have no use, and they are considered as biowaste. The utilization of *Narcissus tazetta L.* leaf powder for the biosorption of Eu(III) ions has been reported by İnan and Özkan (12). It is noteworthy to investigate the separation and removal potential of this novel biomaterial for hazardous ions.

In this study, we aimed to examine *Narcissus tazetta L.* leaf powder's biosorption behaviors for cobalt and nickel removal from aqueous media. The biosorbent was characterized, and batch tests were performed to assess the parameters affecting Co(II) and Ni(II) sorption.

## EXPERIMENTAL SECTION

### Materials

Co(NO<sub>3</sub>)<sub>2</sub>·6H<sub>2</sub>O, Ni(NO<sub>3</sub>)<sub>2</sub>·6H<sub>2</sub>O, Co and Ni calibration standards for Inductively Coupled Plasma-Optical Emission Spectrometer (ICP-OES) (1000 mg L<sup>-1</sup>), nitric acid and ammonia solution were supplied from Sigma-Aldrich, Germany. 1000 mg L<sup>-1</sup> stock solutions of cobalt and nickel were

prepared with dissolving 4.94 g and 4.95 g of cobalt nitrate hexahydrate and nickel nitrate hexahydrate in 1 L distilled water, respectively.

### Preparation of Biosorbent

Dry *Narcissus tazetta L.* leaves were collected from a flower garden in Karaburun district (38°40'9.97"N, 26°26'24.61"E), İzmir province (Turkey) in June 2018. The leaves were kept in the oven at 50 °C for 72 h and ground in a mortar. The ground leaf powders were sieved, and the fraction between 0.125 mm and 0.250 mm were used in batch experiments.

### Characterization Studies

The infrared spectrum of *Narcissus tazetta L.* leaf powder was acquired before and after biosorption by Fourier Transform Infrared-Attenuated Total Reflectance (FTIR-ATR) spectrometer (Perkin Elmer Spectrum Two) between 550 and 4000 cm<sup>-1</sup>. Brunauer-Emmett-Teller (BET) surface area and porosity measurements of leaf powders were taken at 77 K by a surface area analyzer (Micromeritics ASAP 2020). Before measurements, powders were degassed at 323 K under vacuum for 72 h. BET and Barrett-Joyner-Halenda (BJH) methods were employed to calculate surface area and pore characteristics of *Narcissus tazetta L.* leaf powder, respectively.

### Batch Experiments

Batch tests were employed to find out the effects of sorption parameters on Co(II) and Ni(II) biosorption. The stock solutions were diluted and the desired concentrations of test solutions (25 – 600 mg L<sup>-1</sup>) were obtained. The pH adjustments of solutions were done by using nitric acid and ammonia.

For each run, liquid and solid phases were contacted in a temperature controlled shaker (GFL 1086) at 130 rpm. Each parameter's effect was determined by alteration of one variable at a time while others were kept constant. The experimental conditions under investigation were provided in Table 1.

**Table 1:** Experimental conditions under investigation.

Parameter	Value
Initial pH	2, 3, 4, 5, 6, 7
Contact time ( <i>t</i> ), min	1, 5, 15, 30, 60, 120
Initial metal concentration ( <i>C</i> <sub>0</sub> ), mg L <sup>-1</sup>	25, 50, 100, 200, 400, 600
Temperature ( <i>T</i> ), K	303, 313, 323
Biosorbent dosage ( <i>w</i> ), g L <sup>-1</sup>	0.4, 1, 2, 4, 8

At the equilibrium, the liquid phase was separated from the biosorbent using quantitative filter paper.

Co(II) and Ni(II) concentrations were determined by ICP-OES (Perkin Elmer Optima 2000DV). Uptake

capacity ( $\text{mg g}^{-1}$ ) and biosorption efficiency (%) were calculated as given in Eqs. (1) and (2), respectively.

$$\text{Uptake capacity } (Q) = (C_0 - C_e) \times \frac{V}{m} \quad (\text{Eq. 1})$$

$$\text{Biosorption efficiency } (\%) = \frac{C_0 - C_e}{C_0} \times 100 \quad (\text{Eq. 2})$$

where  $C_0$  and  $C_e$  are the initial and equilibrium concentrations of Co(II) and Ni(II) ions ( $\text{mg L}^{-1}$ ),  $V$  is the solution volume (mL) and  $m$  is the mass of the biosorbent (g).

## RESULTS AND DISCUSSION

### Surface Analyses

Data on surface area and pore properties were collected for 0.125 - 0.250 mm particle size. BET surface area and BJH adsorption cumulative pore volume of leaf powders were measured as  $1.725 \pm 0.0988 \text{ m}^2 \text{ g}^{-1}$  and  $0.00252 \text{ cm}^3 \text{ g}^{-1}$ , respectively.

The majority of pores have an average diameter of 1.75 nm; however, there are few pores with an average diameter between 5 and 100 nm.

### FT-IR Analysis

FTIR curves as shown in Figure 1 of the raw and metal sorbed form of the biosorbent are almost similar except for a slight alteration in some peaks' intensity. The peak around  $3337 \text{ cm}^{-1}$  indicates -OH stretching vibrations of hydroxyl containing functional groups (13), and two peaks at 2917 and  $2849 \text{ cm}^{-1}$  refer to -CH stretching vibrations (14). A peak at  $1732 \text{ cm}^{-1}$  shows the C=O stretching of ketones and carboxylic acids whereas the peak at  $1608 \text{ cm}^{-1}$  demonstrates the asymmetrical C=O stretching of COO- groups (15). The peaks at  $1245 \text{ cm}^{-1}$  and  $1020 \text{ cm}^{-1}$  can be the indicator of O-H stretching in phenol group and C-O stretching, respectively.

### The Effect of Initial pH

Co(II) and Ni(II) uptake capacity with the change in initial pH was assessed in the pH range 2 - 7 (Figure 2). Experiments above pH 7 were not conducted due to the risk of metal hydrolysis.

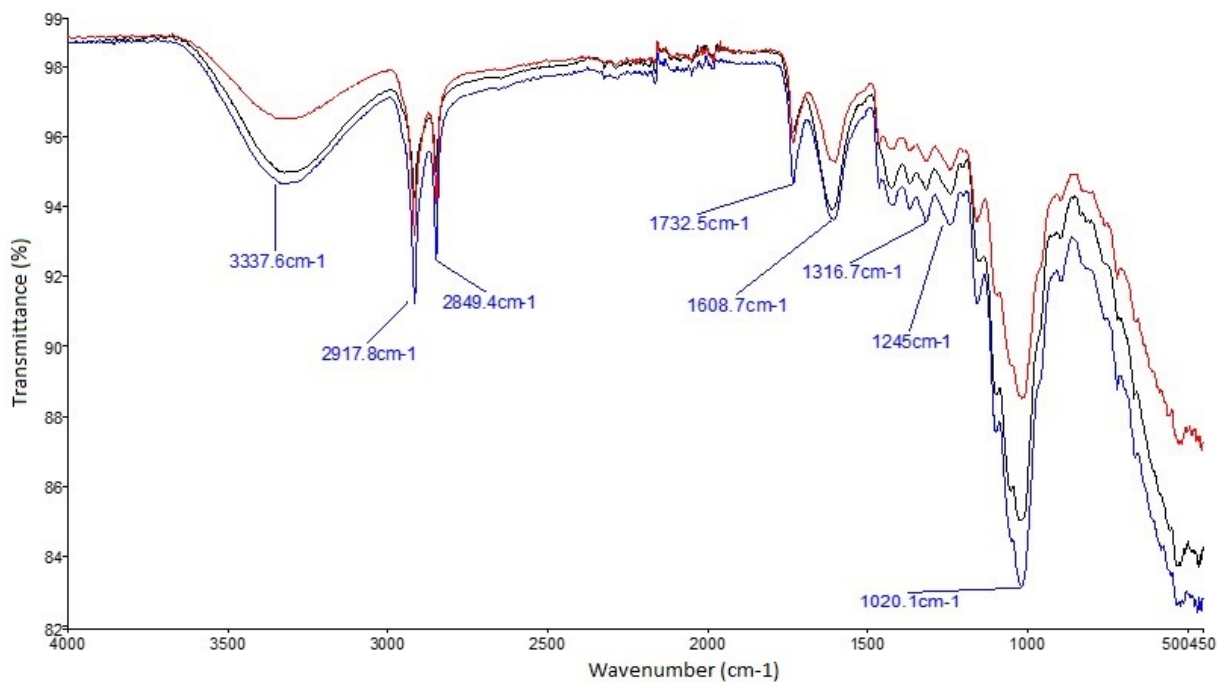


**Figure 1:** Infrared spectra of *Narcissus tazetta L.* leaf powder before and after biosorption: before sorption (black), after Co(II) sorption (red), after Ni(II) sorption (blue).

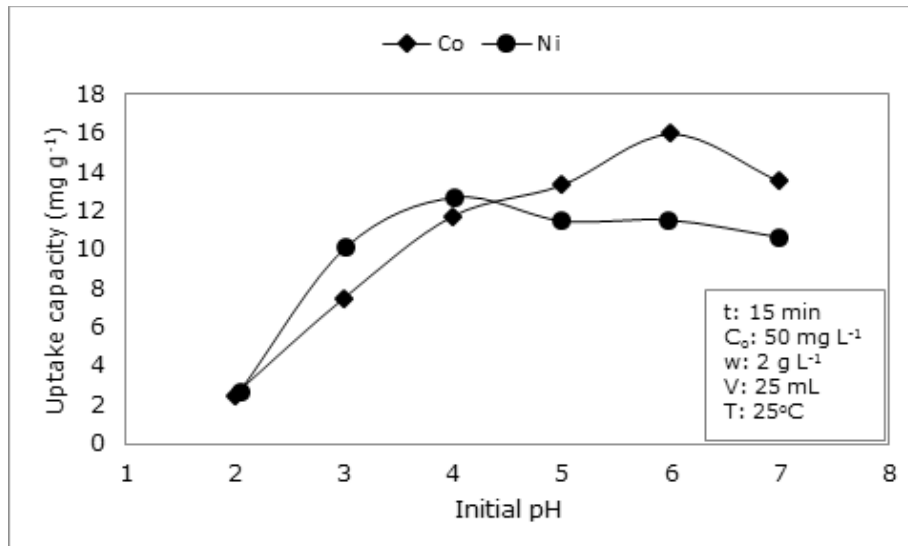


**Figure 2:** Change in Co(II) and Ni(II) uptake capacity with initial pH.

A gradual increase in Co(II) uptake capacity up to pH 6 is seen. Maximum Co(II) uptake capacity of  $15.98 \text{ mg g}^{-1}$  was reached. After pH 6, Co(II) uptake capacity tends to decrease. Biosorption of cobalt using *Sargassum glaucescens* nanoparticles was investigated by Esmaeili and Beni. The optimum Co(II) sorption capacity was found at pH 6 (6).

On the other hand, Ni(II) uptake follows an increasing trend up to pH 4, and at this point, Ni(II) uptake was  $12.71 \text{ mg g}^{-1}$ . Between pH 4 and 7, Ni(II) uptake capacity decreases slightly. Vijayaraghavan et al. reported that *Sargassum wightii* had a Ni(II) uptake of  $18.58 \text{ mg g}^{-1}$  at pH 4 (5).

### The Effect of Contact Time

Figure 3 represents the variation of metal uptake on *Narcissus tazetta L.* leaf powder depending on contact time. It is clearly seen that the sorption was fast, and the sorption equilibrium was established in 15 min for both Co(II) and Ni(II). At the end of 15 min, uptake capacities were obtained as  $11.43$  and  $10.15 \text{ mg g}^{-1}$  for Co(II) and Ni(II), respectively. No significant change was determined after 15 min of contact. Similar data were reported by Akar et al. (16) where nickel(II) uptake on silica-gel-immobilized waste biomass increased up to 20 min, and no considerable change was observed after this time. Fast biosorption kinetics of Co(II) and Ni(II) on *Narcissus tazetta L.* leaf powder could be interpreted by the abrupt filling of the easily accessible sites on the cell wall of the biosorbent.

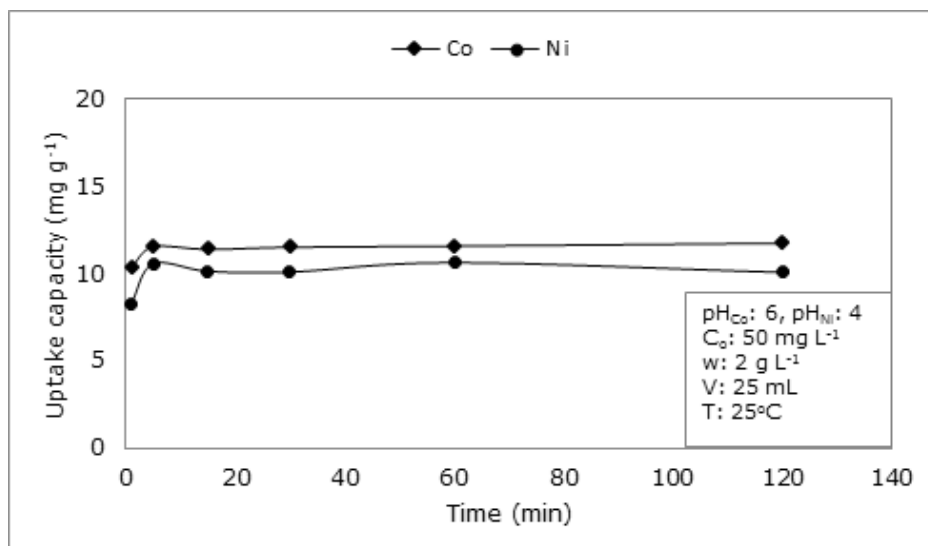


**Figure 3:** Influence of contact time on Co(II) and Ni(II) uptake capacity.

Experimental kinetic data were interpreted by empirical models. Pseudo-first order model (Eq.(3)) and its linear form (Eq.(4)) are presented below:

$$\frac{dq_t}{dt} = k_1(q_e - q_t) \quad (\text{Eq. 3})$$

$$\ln(q_e - q_t) = \ln q_e - k_1 t \quad (\text{Eq. 4})$$

where  $k_1$  is the rate constant ( $\text{min}^{-1}$ ),  $q_e$  and  $q_t$  are the quantity of metal uptake per unit mass of sorbent ( $\text{mg g}^{-1}$ ) at equilibrium and at time  $t$ , respectively (17–19). Using the slope and intercept values of the graph,  $k_1$  and  $q_e$  were obtained. The experimental data can not, however, be explained well with the pseudo-first order model due to the relatively low  $R^2$  values and the fact that calculated  $q_e$  values are not in accordance with the experimental data.

The pseudo-second order model (20) is associated with the capacity of sorbent. The model (Eq. (5)) and its linear form (Eq. (6)) are given below:

$$\frac{dq_t}{dt} = k_2(q_e - q_t) \quad (\text{Eq. 5})$$

$$\frac{t}{q_t} = \frac{1}{k_2 q_e^2} + \frac{t}{q_e} \quad (\text{Eq. 6})$$

where  $k_2$  is the second order rate constant ( $\text{g mg}^{-1} \text{min}^{-1}$ ). The second-order model parameters were provided in Table 2. Correlation coefficient ( $R^2$ ) values point out that Co(II) and Ni(II) biosorption can be explained well with second-order equation.

### The Effect of Initial Concentration

The effect of initial concentration was presented in Figure 4. Co(II) uptake increased from 5.88 to 35.80  $\text{mg g}^{-1}$  with an increase in the initial Co(II) concentration from 25 to 200  $\text{mg L}^{-1}$ . After 200  $\text{mg L}^{-1}$  of initial concentration, Co(II) uptake capacity of biosorbent reached a plateau and was almost constant. For Ni(II) uptake, a gradual increase can be seen up to 400  $\text{mg L}^{-1}$ . After 400  $\text{mg L}^{-1}$ , the rate of increase slowed down, and it can be interpreted that the filling of active zones on the biosorbent has started.

**Table 2:** Second-order kinetic data.

Metal ion	$q_e$ ( $\text{mg g}^{-1}$ )	$k_2$ ( $\text{g mg}^{-1} \text{min}^{-1}$ )	$R^2$
Co(II)	11.81	0.0002	0.999
Ni(II)	10.19	0.0001	0.999

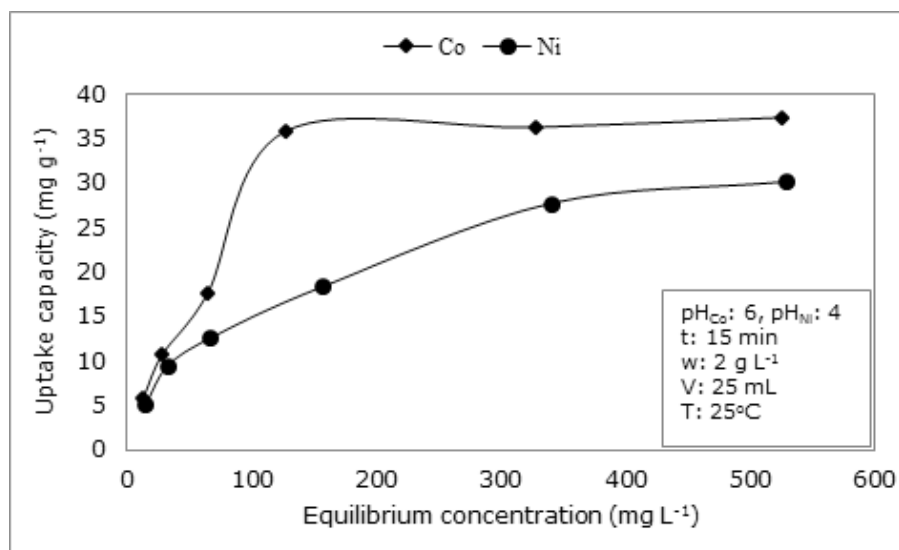


**Figure 4:** Variation of Co(II) and Ni(II) uptake capacity with initial concentration.

Isotherms interpret the sorption equilibrium and provide data on the amount of metal ion on sorbent phase and in the solution. According to Langmuir's theory, sorption occurs in certain homogeneous regions on the sorbent surface. Langmuir equation (21) is written as follows:

$$\frac{C_e}{q_e} = \frac{1}{q_m} + \frac{C_0}{q_m} \quad (\text{Eq. 7})$$

where  $q_m$  is the maximum quantity of the metal per unit mass of sorbent ( $\text{mg g}^{-1}$ ),  $C_e$  is the equilibrium

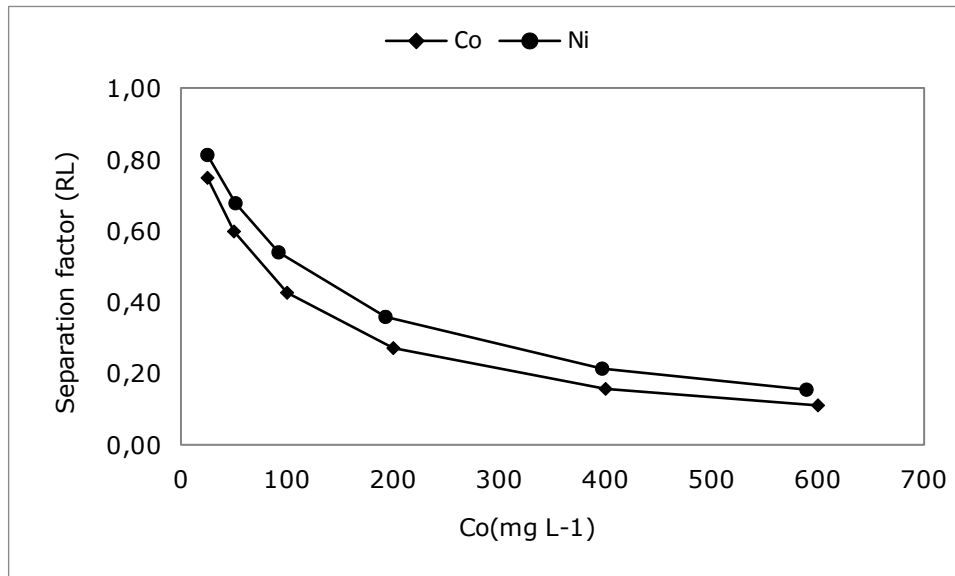
concentration ( $\text{mg L}^{-1}$ ), and  $b$  is a constant associated with sorption energy ( $\text{L mg}^{-1}$ ).

Table 3 presents the obtained  $q_m$ ,  $b$ , and  $R^2$  values. High  $R^2$  values indicate that the sorption of both metals could be explained well by the Langmuir model.

Separation factor ( $R_L$ ) is a dimensionless constant expressed by Webber and Chakravorti (22). It is derived from the Langmuir model and is calculated as in Eq. (8):

$$R_L = \frac{1}{1 + bC_0} \quad (\text{Eq. 8})$$

where  $b$  is the constant from Langmuir equation ( $\text{L mg}^{-1}$ ), and  $C_0$  is initial metal ion concentration ( $\text{mg L}^{-1}$ ). The sorption is considered favorable if the calculated value of  $R_L$  is between zero and one ( $0 < R_L < 1$ ). The variation of  $R_L$  values with initial  $\text{Co(II)}$  and  $\text{Ni(II)}$  concentration was plotted as illustrated in Figure 5. The biosorption was favorable in the whole concentration range under investigation.



**Figure 5:** Variation of separation factor depending on the initial metal concentration.

Freundlich adsorption isotherm are represented as in Eqs. (9) and (10):

$$q_e = K_f C_e^{\frac{1}{n}} \quad (\text{Eq. 9})$$

$$\ln q_e = \ln K_f + \frac{1}{n} \ln C_e \quad (\text{Eq. 10})$$

where  $q_e$  is the metal uptake per unit mass of the sorbent at equilibrium ( $\text{mg g}^{-1}$ ),  $C_e$  is the equilibrium concentration,  $K_f$  is the constant related to adsorption capacity and  $n$  is the constant of adsorption intensity. Freundlich isotherm parameters are shown in Table 3. If we examine the  $R^2$  values, we can deduce that the biosorption data do not fit the Freundlich isotherm well.

Dubinin-Radushkevich (D-R) equation is described as in Eq. (11):

$$\ln q_e = \ln q_m - \beta \epsilon^2 \quad (\text{Eq. 11})$$

$\epsilon$ , the Polanyi potential is given by Eq. (12):

$$\epsilon = RT \ln \left( 1 + \frac{1}{C_e} \right) \quad (\text{Eq. 12})$$

where  $\beta$  is the mean free energy constant ( $\text{mol}^2 \text{J}^2$ )<sup>-1</sup>,  $q_e$  is the quantity of metal sorbed at equilibrium ( $\text{mg g}^{-1}$ ),  $q_m$  is the theoretical saturation capacity ( $\text{mg g}^{-1}$ ),  $T$  is the temperature (K) and  $R$  is the gas constant. The adsorption mean free energy  $E$  ( $\text{kJ mol}^{-1}$ ) is obtained as follows:

$$E = \frac{1}{\sqrt{2\beta}} \quad (\text{Eq. 13})$$

When the  $E$  value is below  $8 \text{ kJ mol}^{-1}$ , the sorption process can be considered as physical sorption. If the  $E$  value is within  $8 - 16 \text{ kJ mol}^{-1}$ , the mechanism is chemical sorption. D-R isotherm data are summarized in Table 3.  $E$  value for both metal ions was obtained as  $0.10 \text{ kJ mol}^{-1}$ . These values indicate that physical sorption plays a dominant role in both biosorption processes.

The maximum  $\text{Co(II)}$  and  $\text{Ni(II)}$  uptake ( $q_m$ ) values of various biosorbents are illustrated in Table 4. It was determined that the maximum uptake

capacities obtained for Co(II) and Ni(II) in the present study were higher than most of the values found in similar studies.

### The Effect of Temperature

Metal uptake slightly decreased with temperature variation from 303 to 323 K (Figure 6). The

obtained results revealed that the alteration of temperature determined no remarkable impact on metal uptake. When the temperature shifted from 303 to 323 K, Co(II) and Ni(II) uptake decreased from 10.42 mg g<sup>-1</sup> to 9.63 mg g<sup>-1</sup> and from 10.80 mg g<sup>-1</sup> to 10.11 mg g<sup>-1</sup>, respectively.

**Table 3:** Langmuir, Freundlich and D-R isotherm parameters for Co(II) and Ni(II) biosorption on *Narcissus tazetta* L. leaf powder.

	Langmuir			Freundlich			D-R		
	q <sub>m</sub> (mg g <sup>-1</sup> )	b(L mg <sup>-1</sup> )	R <sup>2</sup>	K <sub>f</sub>	n	R <sup>2</sup>	q <sub>m</sub> (mg g <sup>-1</sup> )	E(kJ mol <sup>-1</sup> )	R <sup>2</sup>
Co(II)	43.48	0.014	0.985	1.917	1.941	0.899	27.89	0.10	0.753
Ni(II)	35.97	0.009	0.987	1.617	2.082	0.984	19.85	0.10	0.721

**Table 4:** Cobalt and nickel ion uptake (q<sub>m</sub>) data of various biosorbents.

Biosorbent	Maximum Cobalt Uptake (mg g <sup>-1</sup> )	Maximum Nickel Uptake (mg g <sup>-1</sup> )	Reference
<i>Ficus Religiosa</i> leaf powder	3.60	-	(1)
Protonated rice bran	-	46.51	(4)
<i>Sargassum glaucescens</i>	10.11	28.73	(6)
Modified <i>Aspergillus flavus</i>	31.06	32.26	(7)
Crab Shell Particles	322.6	-	(8)
<i>Cone biomass of Thuja orientalis</i>	-	12.42	(23)
Black carrot residues	5.350	5.745	(24)
Coir pith	12.82	15.95	(25)
<i>Narcissus tazetta</i> L. Leaf Powder	43.48	35.97	Present Study

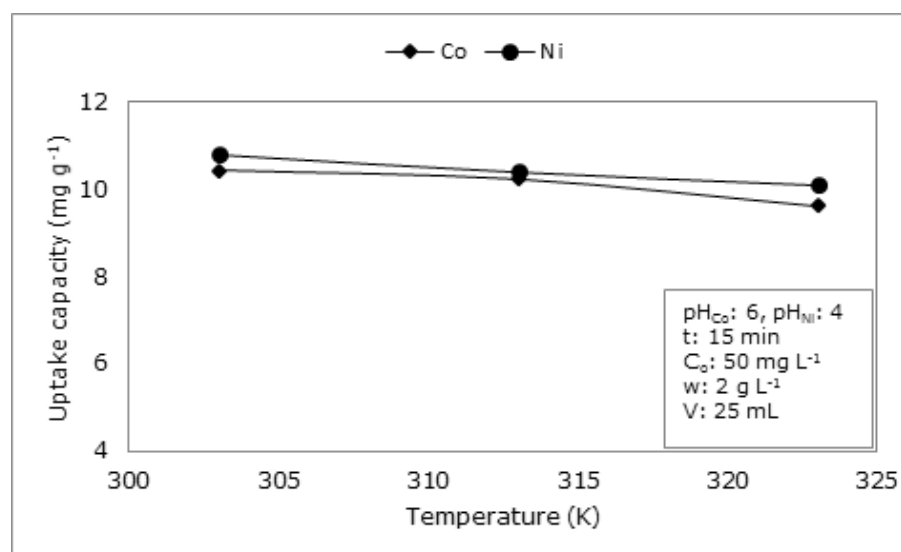


**Figure 6:** Influence of temperature on uptake capacity.

Thermodynamic data provides information about the spontaneity of the biosorption process. The enthalpy ( $\Delta H^\circ$ ), entropy ( $\Delta S^\circ$ ) and Gibbs free energy ( $\Delta G^\circ$ )

changes were estimated using Eqs. (14), (15) and (16) (26).

$$K_D = \frac{C_0 - C_e}{C_e} \times \frac{V}{m} \quad (\text{Eq. 14})$$

$$\ln K_D = \frac{\Delta S^0}{R} - \frac{\Delta H^0}{RT} \quad (\text{Eq. 15})$$

$$\Delta G^0 = \Delta H^0 - T \Delta S^0 \quad (\text{Eq. 16})$$

where  $K_D$  is the thermodynamic equilibrium constant ( $\text{mL g}^{-1}$ ),  $T$  is the temperature (K),  $R$  is the universal gas constant ( $8.314 \text{ J mol}^{-1} \text{ K}^{-1}$ ),  $V$  is the solution volume (mL), and  $m$  is the mass (g) of the biosorbent. From the slope and intercept of Van't Hoff plot ( $\ln K_D$  versus  $1/T$ )  $\Delta H^0$  and  $\Delta S^0$  values were obtained.

Thermodynamic data concerning Co(II) and Ni(II) biosorption are presented in Table 5.  $\Delta G^0$  values

were found negative at 303, 313, and 323 K, indicating that the biosorption process was spontaneous for both metal ions.

The negative  $\Delta H^0$  value denotes that biosorption is an exothermic process. The positive  $\Delta S^0$  value points out the increase in disorder with the flow of Co(II) and Ni(II) ions towards the sorbent surface. Generally,  $\Delta G^0$  values for physical sorption are from  $-20$  to  $0 \text{ kJ mol}^{-1}$ , while chemisorption occurs in the range of  $-80$  to  $-400 \text{ kJ mol}^{-1}$  (27).  $\Delta G^0$  values obtained in the present study support that the mechanism involved in biosorption is physical sorption.

### The Effect of Biosorbent Dosage

As shown in Figure 7, Co(II)'s biosorption efficiency (%) increased from 21.06 to 45.30% with the variation of biosorbent dosage from 0.4 to 4.0  $\text{g L}^{-1}$ .

Similar behavior was observed for Ni(II) ions. An increase in the biosorption efficiency (%) from 25.35 to 43.52% could be seen with the variation of biosorbent dosage in the same range.

**Table 5:** Thermodynamic data for Co(II) and Ni(II) biosorption.

Ions	$\Delta H^0$ ( $\text{kJ mol}^{-1}$ )	$\Delta S^0$ ( $\text{kJ mol}^{-1} \text{ K}^{-1}$ )	$\Delta G^0$ ( $\text{kJ mol}^{-1}$ )		
			303 K	313 K	323 K
Co(II)	-5.62	0.031	-15.013	-15.023	-15.633
Ni(II)	-4.35	0.035	-14.955	-15.305	-15.655

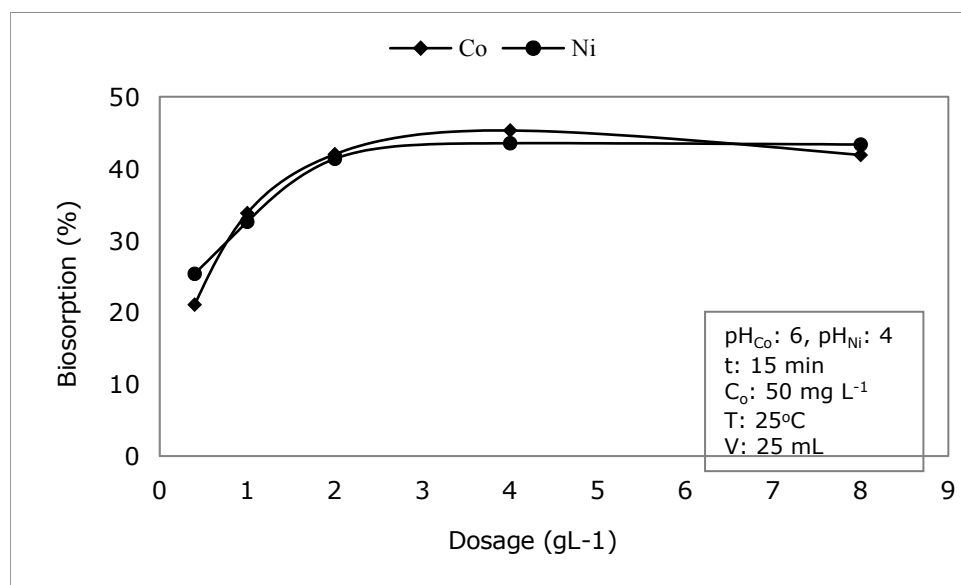


**Figure 7:** Effect of biosorbent dosage on biosorption efficiency (%).

### CONCLUSION

In this study, novel biomaterial biosorption behaviors, *Narcissus tazetta L.* leaf powder towards Co(II) and Ni(II) ions, were investigated. The maximum Co(II) and Ni(II) uptake were obtained at pH 6 and pH 4, respectively. The biosorption process was rapid, and the equilibrium was achieved

in 15 min for both metal ions. Biosorption kinetics fit the pseudo-second-order model well. The sorption isotherm data were best explained by Langmuir isotherm. The monolayer Co(II) and Ni(II) sorption capacities were 43.48 and 35.97  $\text{mg g}^{-1}$ , respectively. It has been determined that temperature does not have a significant impact on biosorption. The thermodynamic parameters

evaluation revealed that the Co(II) and Ni(II) biosorption processes were exothermic and spontaneous. When the biosorbent dosage increased in the range of 0.2 – 4.0 g L<sup>-1</sup>, biosorption efficiency (%) of Co(II) and Ni(II) increased from 21.06 to 45.30% and 25.35 to 43.52%, respectively. Overall results indicate that the removal of Co(II) and Ni(II) from dilute solutions by *Narcissus tazetta* L. leaf powder, which is costless and readily available in vast amount, is promising.

### ACKNOWLEDGEMENTS

The authors would like to thank Ms. Dilara Yörür, Ms. Ezgi Çelik, and Mr. Ümit Emre Kartal for their contribution in the laboratory.

### REFERENCES

- Krishna B, Venkateswarlu P. Influence of *Ficus religiosa* leaf powder on biosorption of cobalt. *Ind J Chem Technol.* 2011 Sep;18:381–90.
- Pahlavanzadeh H, Keshtkar AR, Safdari J, Abadi Z. Biosorption of nickel(II) from aqueous solution by brown algae: Equilibrium, dynamic and thermodynamic studies. *Journal of Hazardous Materials.* 2010 Mar;175(1–3):304–10. DOI: <https://doi.org/10.1016/j.jhazmat.2009.10.004>.
- Koivula R, Harjula R, Lehto J. 63 Ni and 57 Co Uptake and Selectivity of Tin Antimonates of Different Structure. *Separation Science and Technology.* 2003 Jan 10;38(15):3795–808. DOI: <https://doi.org/10.1081/SS-120024231>.
- Zafar MN, Nadeem R, Hanif MA. Biosorption of nickel from protonated rice bran. *Journal of Hazardous Materials.* 2007 May;143(1–2):478–85. DOI: <https://doi.org/10.1016/j.jhazmat.2006.09.055>.
- Vijayaraghavan K, Jegan J, Palanivelu K, Velan M. Biosorption of cobalt(II) and nickel(II) by seaweeds: batch and column studies. *Separation and Purification Technology.* 2005 Jul;44(1):53–9. DOI: <https://doi.org/10.1016/j.seppur.2004.12.003>.
- Esmaeili A, Aghababai Beni A. Biosorption of nickel and cobalt from plant effluent by *Sargassum glaucescens* nanoparticles at new membrane reactor. *Int J Environ Sci Technol.* 2015 Jun;12(6):2055–64. DOI: <https://doi.org/10.1007/s13762-014-0744-3>.
- Foroutan R, Esmaeili H, Rishchri SD, Sadeghzadeh F, Mirahmadi S, Kosarifard M, et al. Zinc, nickel, and cobalt ions removal from aqueous solution and plating plant wastewater by modified *Aspergillus flavus* biomass: A dataset. *Data in Brief.* 2017 Jun;12:485–92. DOI: <https://doi.org/10.1016/j.dib.2017.04.031>.
- Vijayaraghavan K, Palanivelu K, Velan M. Biosorption of copper(II) and cobalt(II) from aqueous solutions by crab shell particles. *Bioresource Technology.* 2006 Aug;97(12):1411–9. DOI: <https://doi.org/10.1016/j.biortech.2005.07.001>.
- Tounsadi H, Khalidi A, Abdennouri M, Barka N. Biosorption potential of *Diplotaxis harra* and *Glebionis coronaria* L. biomasses for the removal of Cd(II) and Co(II) from aqueous solutions. *Journal of Environmental Chemical Engineering.* 2015 Jun;3(2):822–30. DOI: <https://doi.org/10.1016/j.jece.2015.03.022>.
- Prasad MNV, Freitas H. Removal of toxic metals from solution by leaf, stem and root phytomass of *Quercus ilex* L. (holly oak). *Environmental Pollution.* 2000 Nov;110(2):277–83. DOI: [https://doi.org/10.1016/S0269-7491\(99\)00306-1](https://doi.org/10.1016/S0269-7491(99)00306-1).
- Hanks GR. Commercial production of *Narcissus* bulbs. In: *Narcissus and Daffodil.* London: Taylor and Francis; 2002. p. 53–130.
- İnan S, Özkan B. Eu (III) 'un *Narcissus Tazetta* L. Yaprak Tozu Üzerine Biyosorpsiyonu. *Deu Muhendislik Fakultesi Fen ve Muhendislik.* 2019 Sep 20;21(63):955–66. DOI: <https://doi.org/10.21205/deufmd.2019216324>.
- Brigante M, Zanini G, Avena M. Effect of humic acids on the adsorption of paraquat by goethite. *Journal of Hazardous Materials.* 2010 Dec;184(1–3):241–7. DOI: <https://doi.org/10.1016/j.jhazmat.2010.08.028>.
- Fu H, Quan X. Complexes of fulvic acid on the surface of hematite, goethite, and akaganeite: FTIR observation. *Chemosphere.* 2006 Apr;63(3):403–10. DOI: <https://doi.org/10.1016/j.chemosphere.2005.08.054>.
- Wei W, Yang L, Zhong W, Cui J, Wei Z. Mechanism of enhanced humic acid removal from aqueous solution using poorly crystalline hydroxyapatite nanoparticles. *Digest Journal of Nanomaterials and Biostructures.* 2015;10(2):663–80.
- Akar T, Kaynak Z, Ulusoy S, Yuvaci D, Ozsari G, Akar ST. Enhanced biosorption of nickel(II) ions by silica-gel-immobilized waste biomass: Biosorption characteristics in batch and dynamic flow mode. *Journal of Hazardous Materials.* 2009 Apr;163(2–3):1134–41. DOI: <https://doi.org/10.1016/j.jhazmat.2008.07.084>.

17. Lagergren S. About the theory of so-called adsorption of solution substances. 1898;24(4):147–56.
18. Ho YS, McKay G. Sorption of dye from aqueous solution by peat. *Chemical Engineering Journal*. 1998 Jun;70(2):115–24. DOI: [https://doi.org/10.1016/S0923-0467\(98\)00076-1](https://doi.org/10.1016/S0923-0467(98)00076-1).
19. Ho YS, McKay G. The sorption of dye from aqueous solution by peat. *Water Res*. 1999; 33(2): 578-84. DOI: [https://doi.org/10.1016/S0923-0467\(98\)00076-1](https://doi.org/10.1016/S0923-0467(98)00076-1).
20. Mahajan G, Sud D. Kinetics and equilibrium studies of Cr(VI) metal ion remediation by *Arachis hypogea* shells: A green approach. *BioResources*. 2011;6(3):3324–38. URL: [https://ojs.cnr.ncsu.edu/index.php/BioRes/article/download/BioRes\\_06\\_3\\_3324\\_Mahajan\\_S\\_Kinetic\\_Sorption\\_Cr6\\_Arachis/1121](https://ojs.cnr.ncsu.edu/index.php/BioRes/article/download/BioRes_06_3_3324_Mahajan_S_Kinetic_Sorption_Cr6_Arachis/1121).
21. Langmuir I. The adsorption of gases on plane surfaces of glass, mica and platinum. *J Am Chem Soc*. 1918 Sep;40(9):1361–403. DOI: <https://doi.org/10.1021/ja02242a004>.
22. Weber TW, Chakravorti RK. Pore and solid diffusion models for fixed-bed adsorbers. *AIChE J*. 1974 Mar;20(2):228–38. DOI: <https://doi.org/10.1002/aic.690200204>.
23. Malkoc E. Ni(II) removal from aqueous solutions using cone biomass of *Thuja orientalis*. *Journal of Hazardous Materials*. 2006 Sep 21;137(2):899–908. DOI: <https://doi.org/10.1016/j.jhazmat.2006.03.004>.
24. Guzel F, Yakut H, Topal G. Determination of kinetic and equilibrium parameters of the batch adsorption of Mn(II), Co(II), Ni(II) and Cu(II) from aqueous solution by black carrot (*Daucus carota* L.) residues. *Journal of Hazardous Materials*. 2008 May 30;153(3):1275–87. DOI: <https://doi.org/10.1016/j.jhazmat.2007.09.087>.
25. Parab H, Joshi S, Shenoy N, Lali A, Sarma US, Sudersanan M. Determination of kinetic and equilibrium parameters of the batch adsorption of Co(II), Cr(III) and Ni(II) onto coir pith. *Process Biochemistry*. 2006 Mar;41(3):609–15. DOI: <https://doi.org/10.1016/j.procbio.2005.08.006>.
26. Nayak AK, Pal A. Green and efficient biosorptive removal of methylene blue by *Abelmoschus esculentus* seed: Process optimization and multivariate modeling. *Journal of Environmental Management*. 2017 Sep;200:145–59. DOI: <https://doi.org/10.1016/j.jenvman.2017.05.045>.
27. Gerçel Ö, Özcan A, Özcan AS, Gerçel HF. Preparation of activated carbon from a renewable bio-plant of *Euphorbia rigida* by H<sub>2</sub>SO<sub>4</sub> activation and its adsorption behavior in aqueous solutions. *Applied Surface Science*. 2007 Mar;253(11):4843–52. DOI: <https://doi.org/10.1016/j.apsusc.2006.10.053>.



## Drug Discovery and Treatment of an Emerging Pandemic Infection Covid-19

Mishra Arunesh K.<sup>1</sup>  , Pratibha<sup>1</sup>  , and Das Ratnesh<sup>1\*</sup>  

<sup>1</sup>Department of Chemistry, Dr. Harisingh Gour Central University, Sagar- 470003 (M.P.), INDIA  
IGNTU, Amarkantak, M.P., INDIA

**Abstract:** In the last decades, two serious coronaviruses have appeared in humans and animals, SARS-CoV (severe acute respiratory syndrome) and MERS-CoV (middle east respiratory syndrome) are also contagious viruses that causes ARDS stands for acute respiratory distress syndrome. SARS-CoV in 2003 and MERS-CoV in 2012 are characterized as a high mortality rate. This novel human respiratory coronaviruses, also known as SARS n-CoV or SARS-CoV-2, are needed to rapidly provide therapeutic options to reduce and prevent the spread of this outbreak. For such infections, there are currently no scientifically approved precautions or anti - viral products authorized.; therefore, effective remedial and preventive strategies have to be developed that can be easily applied to this newly emerging epidemic. In addition to all these, some therapeutic options are also being evaluated that are used for Covid-19, which includes inhibitory virus molecules or molecules that target specific replication and transcription enzymes. Since the drugs remdesivir, lopinavir-ritonavir, favipiravir, camostat mesylate, chloroquine, and hydroxychloroquine were originate closely stand high successful in controlling infection, Covid-19 looks promising. The research on Covid-19, discuss the efficacy of the several drug and vaccines against Covid-19 and previous outbreaks of SARS and MERS, and provide recommendations for new modes of treatment, assessment, and clinical research on such terrible epidemic. This paper will summarize and discuss the main biological characteristics of SARS-CoV-2 and the current scenario of emerging Covid-19 infections, as well as explain the current therapeutic medications treating Covid-19, based on the clinical trial data.

**Keywords:** 2019-new coronavirus, epidemic, vaccines & antiviral drugs, acute respiratory distress syndrome (ARDS), remdesivir, chloroquine.

**Submitted:** March 27, 2021. **Accepted:** June 13, 2021.

**Cite this:** Mishra AK, Pratibha, Das R. Drug Discovery and Treatment of an Emerging Pandemic Infection Covid-19. JOTCSA. 2021;8(3):715-22.

**DOI:** <https://doi.org/10.18596/jotcsa.897044>.

**\*Corresponding author. E-mail:** [ratneshdas1@gmail.com](mailto:ratneshdas1@gmail.com).

### INTRODUCTION

The World Health Organization (WHO) expressed concern after taking cognizance of this after coming to light on several fast-spreading viral pneumonia cases due to unknown reasons in the Hubei province of Wuhan city of China on December 31, 2019. Later, on January 7, 2020, it was self-confirmed by China's scientific research institutes that the real reason behind viral pneumonia serious acute respiratory symptoms would be a new form of coronavirus. SARS-CoV-2

is a virus that causes SARS (1). After which, by the international committee on taxonomy of viruses on February 11, 2020, the novel coronavirus was named SARS-CoV-2 is a coronavirus that causes extreme acute respiratory syndrome (2). The WHO then dubbed the SARS-CoV-2-caused disorder Coronavirus 2019 (Covid-19) (3). Severe acute respiratory syndrome coronavirus 2 (SARS-CoV-2) viruses are single-stranded RNA viruses with ~30,000 nucleotides and a group of highly diverse, non-fragmented positive-sense, that In animal species, it causes infectious, enteric, hepatic, and

neural ailments, including human belong to the order Nidovirales, family Coronaviridae, genus *Betacoronavirus*, and the species belong to the severe acute respiratory syndrome-related coronavirus (SARS-CoV) (4–8).

In the late 1960s, Tyrrell, one of the virologists with his colleagues, was investigating the effects of the virus on humans. While observed within an electron microscope, infectious bronchitis virus, mouse hepatitis virus, and swine's transmissible gastroenteritis virus were all shown to still be morphologically similar (9). This new virus group was called coronavirus due to a corona-like surface and was future authoritatively recognized as the virus's novel gene (10). As research on the pathogenetics and epidemiology of humanoid coronaviruses progressed, the character of animal coronaviruses was increasing quickly. In which it was observed that coronaviruses cause disorder trendy many animal classes, plus rats, chickens, dogs, cats, mice, and pig are all examples of animals. The research involved in animal studies focuses only on respiratory disorders. The key research included gastrointestinal, hepatitis, and encephalitis in mice; the pathogenesis of these disorder conditions remained diverse also multipart, suggesting that the gene as an entire could cause an extensive range of diseases (11). Much has been known about the epidemiology of human respiratory coronaviruses using serological techniques. According to recent studies,

respiratory coronavirus infections are more common in temperate climates in wintertime and spring than in the summer and decrease (12). In 2002–2003, SARS, a severe acute respiratory syndrome known as coronavirus, emerged from southerly China, spreading worldwide as an epidemic (13).

Many species, including cats, cows, bats, horses, and humans, are susceptible to coronavirus pathogens. There are currently seven forms of coronaviruses identified, four of which (229E, NL63, OC43, and KHU1) cause slight to modest breathing contaminations similar to the general cold, which do not have many side effects and these actions are fatal. One and two types, the SARS-CoV and the MERS-CoV, can origin severe breathing infections that are more fatal, causing humans and animals vulnerable to severe illnesses. Whereas the seventh type recently discovered in China is the novel coronavirus or Covid-19 that occurs in humans, Covid-19 is primarily respiratory or gastrointestinal tap affects humans through infection whose symptoms are that they can be up spironia as more severe lower respiratory infections from the common cold (14). Many diseases in humans are spread by coronaviruses, most of which are associated with mild clinical symptoms, including SARS-CoV, a novel betacavavirus that originates from Guangdong, southern China is spread all over the world (15).

#### Severe acute respiratory syndrome coronavirus 2 (SARS-CoV-2)

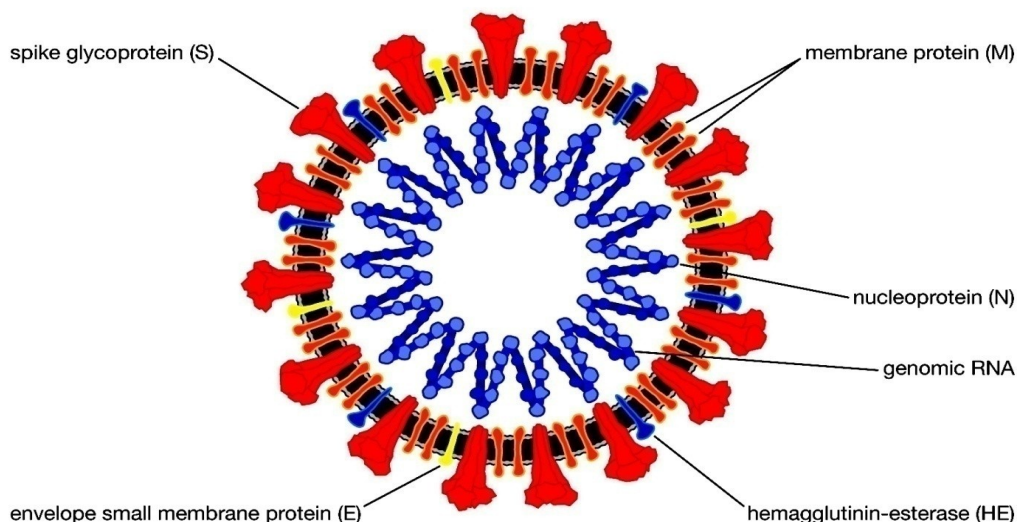


**Figure 1.** Cartoon illustration of the severe acute respiratory syndrome SARS CoV-2 structure.

The nucleic acid of the SARS CoV-2 virus is around 30 kb long, polyadenylated in a positive manner and single-stranded. RNA is the major identified viral RNA code meant for a large poly-protein

(Figure 1). The mutation is a natural phenomenon of nature in which climate change also plays an important role. Furthermore, if two viruses infect the same cell simultaneously, coronavirus (SARS-

CoV-2) is capable of genetic recombination. The cytoplasm of infected cells is where all coronaviruses originate, from the endoplasmic reticulum to the cytoplasmic vesicles. Within that time period, the vesicles are then extruded or expelled from of the cell, as well as the cell is killed (16). Viruses include structural S-spike proteins (external spikey glycoproteins), N-nucleocapsid proteins (which are found within the phospholipid bilayer), and non-structural proteins are all encoded by separate genetic loci on the virus's RNA. The nucleocapsid, which is made up of genomic RNA and nucleocapsid proteins, is at the heart of the virion (17).

### Pandemic Outbreak in Current Scenario

At present, the cases of coronavirus in the whole world have reached over 9,060,870, indicating that North America, India, Brazil, Turkey, and Russia are the main pillars of Covid-19, Europe (France, Britain, Italy, Germany, Spain, etc.) the major in the Americas. The United States and East Asia

China are mainly vulnerable to the coronavirus, which has resulted in a huge quantity of expiries and growing rates. The speedy growth of the worldwide coronavirus is also happening in the countries of the Indian subcontinent, which is a large population center; the WHO has also continuously issued guidelines for health care and control strategies to countries like India, thorough exchange of research, technology and public health information for active illness regulator and protective administration must be Radan. The best way to avoid disease transmission is to use the most widely adopted practice, social distinction, and work from a home model, which includes limitations on foreign and local visits, as well as complete lockdown over a broad geographic region. These countries' revealed activities include sanitation adaptation through technology, mass diagnosis and quarantine, and complete lockdown. It is critical to comprehend and implement their preventive public health model as a strategy.

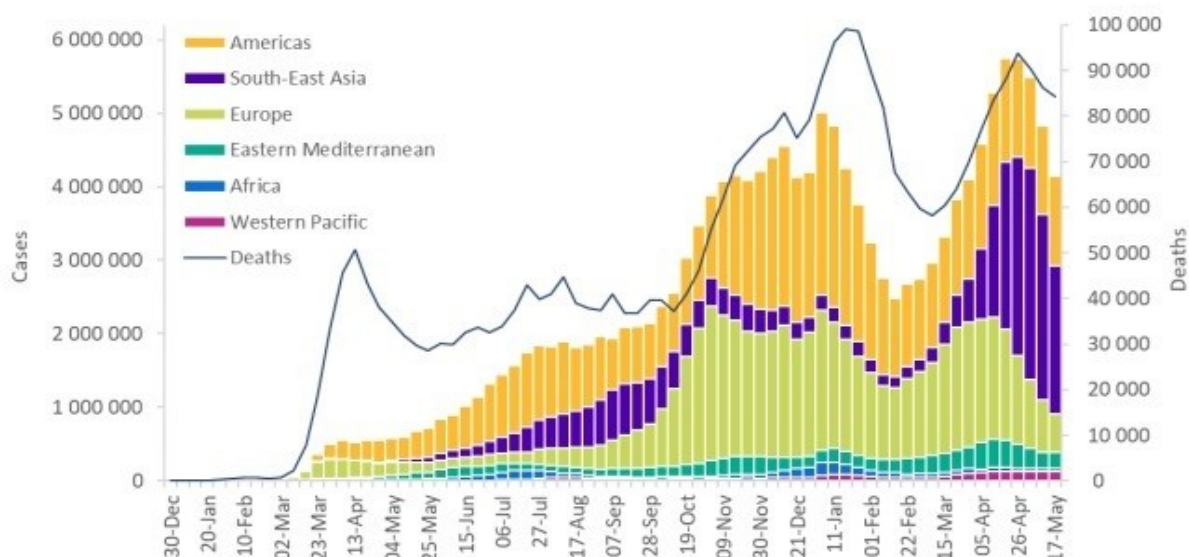


**Figure 2:** Covid-19 cases reported weekly by WHO Region, and global deaths, as of 23 May 2021\*\*

From December 31, 2019, to May 22, 2021, conferring to the WHO, there are 162,773,940 cases of Covid-19 universal (giving to the case definitions and trial strategies applied in the affected countries), and 3,375,573 worldwide deaths occurred as of May 22, 2020, supreme figures of cases have remained testified in USA (32,605,236), India (24,965,463), Brazil (15,856,534), France (5,783,787), Turkey (5,117,374), Russia (4,949,573), United Kingdom (4,450,781), Italy (4,159,122), Germany (3,598,846) Spain (3,598,452), Argentina

(3,514,683), Colombia (3,103,333), Poland (2,855,190) and Iran (2,751,166). The global epidemic caused by covid-19 has caused the highest number of deaths (605,805) in the United States so far and India's death toll (274,390). The deaths reported by other countries like Brazil (434,715), France (106,859) Turkey (44,760), Russia (116,211), United Kingdom (127,679), Italy (124,126), Germany (86,160) Spain (79,281), Argentina (70,253), Colombia (80,780), Poland (71,675) and Iran (76,936).

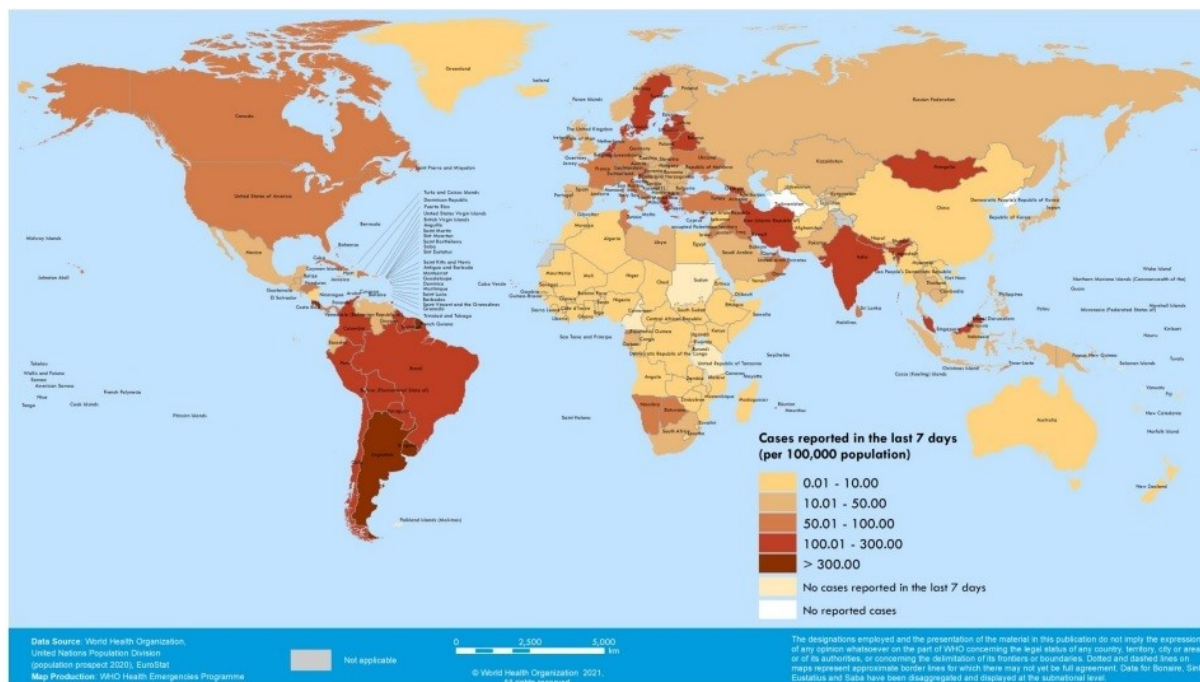


**Figure 3:** Covid-19 cases per 100,000 population reported by countries, territories, and areas, 17 May – 23 May 2021\*\*

### Antiviral Drugs with Therapeutic Potential Against the SARS-CoV-2

In direction of avoid the rapid growing of Covid-19, intensive monitoring of disease warrants and rapid dissemination of isolation protocols is vital. It is well known that no drug or vaccine has been developed yet. That is why the aim of current treatment strategies is only symptomatic care and oxygen therapy. However, prophylactic vaccination is crucial for the early prevention of an epidemic or pandemic related to Covid-19. Here is no finding of drug for the handling of Covid-19 contamination or prophylactic drugs. The patient's condition and the habit of handwashing, face covers, and other hygiene steps are all essential in treating respiratory aerosol/droplet infections caused by patients. Covid-19 will reduce the risk of transmission and be helpful in patient care due to this. Diagnostic testing of the effectiveness of the new antiviral drug Remdesivir. The first use of this drug has been used on various animals in diseases

related to the Ebola virus, SARS, and MERS virus (18). Scientists around the world are increasingly trying to find vaccines and drugs to treat infections transmitted by Covid-19. More than 30 agents, including Due to this type of research, natural products from Western medicine and conventional Chinese medicines have been identified as having emphatic effectiveness against Covid-19. Any of these compounds have been tested in clinical trials and have shown promise in combating Covid-19 (19). For Covid-19 treatment, the National Health Commission of the People's Republic of China recommends IFN- and lopinavir/ritonavir. This recommendation is focused on past studies have shown that this drugs lower death rates in patients undergoing SARS. In the most recent version of the Guidelines, antivirals such as interferon (IFN-), lopinavir/ritonavir, chloroquine phosphate, ribavirin, and arbidol are recommended for the prevention, diagnosis, and treatment of novel coronaviruses (20).

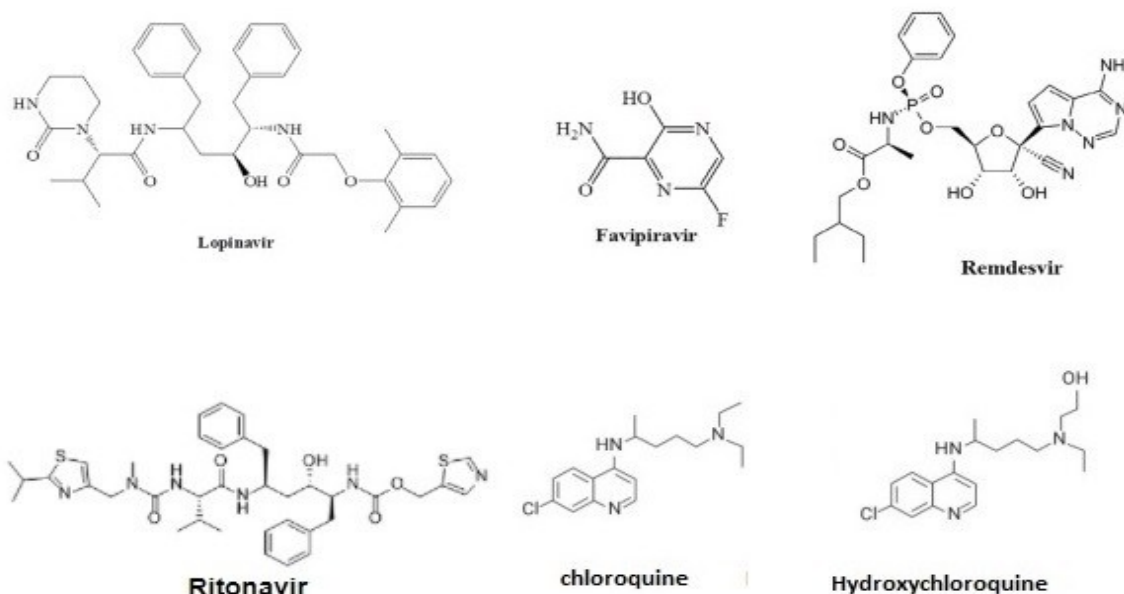


**Figure 4:** Chemical structural formula of some therapeutic agents (drugs) against SARS CoV-2.

Previous research has shown that the RNA polymerase is responsible for virus-related duplication in host cells and that the remdesivir drug acts as an inhibitor, preventing infection from being transmitted and in rhesus macaques as a pre-proliferation prophylaxis as a prevention, rehabilitation therapy, and it reduced disorder, virus replication, and lung injury. Several countries around the world, including the United States, are increasingly using hydroxychloroquine drugs for patients with uncontrolled Covid-19 infection, which showed strong in-vitro movement in contradiction of SARS-COV-2 preclinical proliferation (21). Recent research has found that the IFN- compound, a wide-ranging antiviral agent widely cast-off to take care of hepatitis, weakens the life cycle and reduces the effects of infection by disrupting SARS-CoV reproduction in vitro and decreases the effects of infection (22). Chu et al. discovered that ribavirin has a wide-ranging of antiviral effects then that lopinavir/ritonavir has SARS-CoV motion in vitro against SARS CoV-2 in medical studies (23). Chloroquine is an antimalarial medicine that stayed discovered to have wide-ranging antiviral effects in 2006 (24). Arbidol, an antiviral drug used to treat the influenza virus, was found to effectively prevent SARS-CoV-2 contamination in vitro at concentrations of 10 to 30  $\mu\text{M}$  in one sample (25). China approved Favipiravir, an anti-influenza medication, to treat novel influenza on February 15, 2020. This drug is currently being tested for Covid-19 therapy. Favipiravir is a new type of RNA-dependent RNA polymerase (RDRP) inhibitor with anti-influenza virus properties and the ability to stop the reproduction of flavi-, alpha-, phylo-,

market-region, noro- and other RNA viruses (26). Patients with extreme Covid-19 pneumonia with hyper inflammatory syndrome and acute respiratory failure reacted to tocilizumab effectively and consistently, with substantial therapeutic changes, according to a recent prospective study in a single centre with 100 patients from Italy (27). Dexamethasone was found to reduce 28-day mortality in patients hospitalised with Covid-19 who were getting either intrusive respiratory support or oxygen alone at the time of trial, but not in those who were not getting mechanical ventilation (28). Caly et al., reported that Ivermectin, an FDA-approved anti-parasitic drug that has previously demonstrated to have broad-spectrum anti-viral activity in vitro, is an inhibitor of the SARS-CoV-2 virus (29).

#### Vaccines Against SARS CoV-2

Policy makers from various countries have traditionally demanded a growing number of clinical trials with a majority of patients and a high number of resources for human vaccine production. These safeguards conclude that the best vaccine product is secure and appropriate for various demographic groups prior to commercialization. Unlike SARS and MERS, which appeared to reconcile spontaneously after territorial pandemics, the global scale of the Covid-19 outbreaks has rendered vaccine production a top priority. This pressing need has prompted a variety of approaches to vaccine production. Regulatory bodies from around the world have demanded that the number of clinical trials on corona virus-infected people be increased, as well as the testing of different vaccines. Before being

approved for commercial use, these studies ensure that the final vaccine product is safe and effective for different population subgroups (30). The WHO has also used this dataset to better understand global vaccination access discrepancies, utilising

this evidence to support recommendations for increased financial support for COVAX, a WHO-backed worldwide project aiming at ensuring equitable access to Covid-19 vaccinations (31).

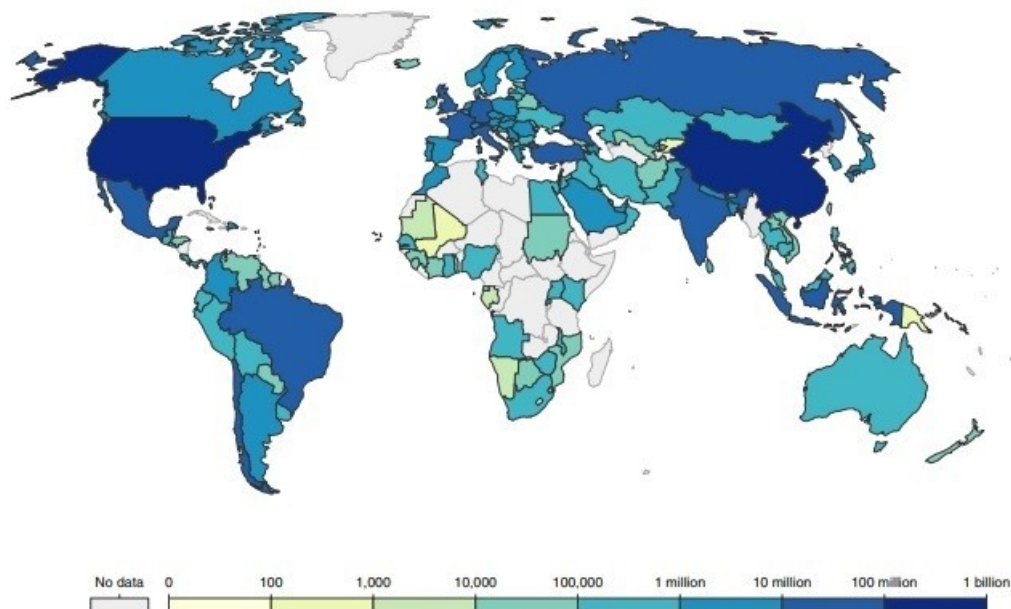


**Figure 5:** Cumulative number of Covid-19 doses administered by country. Total number of Covid-19 vaccine doses administered as of 7 April 2021 (Ref. 29).

More than 100 vaccines against SARS-CoV-2 are being developed, according to WHO reports. Vaccination can help contain SARS-COV-2 epidemics by preventing infection or lowering the severity of sickness, virus shedding, and spread. SARS-COV-2 vaccines have been developed using DNA and RNA-based vaccines, subunit (recombinant protein) vaccines, viral vector vaccines, live-attenuated virus vaccines, recombinant protein vaccines and inactivated virus vaccines (32).

## CONCLUSION

Covid-19, an infection that has become a global epidemic and is spreading at a very alarming rate worldwide. Side effects of Covid-19 can be predicted to cause more infection than SARS or MERS and also lead to faster deaths. Assuming WHO, it can be said that SARS-CoV-2 is more infectious than SARS or MERS. As the Covid-19 outbreak banquets crosswise the biosphere, scientists are scrambling to find medications that may be successful in fighting the virus. There are currently no antivirals that have been shown to be effective against Covid-19. Covid-19 is being treated with medicines that have previously been used to treat other diseases. Efforts are also being made to create medical tests to determine the effectiveness of the medications. However, given the current severe global epidemic situation and

the urgent need for medical treatment, further studies should be undertaken as soon as possible to identify a new vaccine or treatment and to effectively manage this health crisis. Covid-19 is a virus that can be spread from person to person. Covid-19 can be effectively minimized by interventions such as comprehensive contact tracing followed by quarantine and isolation, by the influence of travel bans, wearing covers, wash hands, and sanitizing outsides.

## REFERENCES

1. Wang M, Zhou M, Ji G, Ye L, Cheng Y, Feng Z, et al. Mask crisis during the Covid-19 outbreak. *European Review for Medical and Pharmacological Sciences*. 2020;3397-9. URL: <https://www.europeanreview.org/wp/wp-content/uploads/3397-3399.pdf>.
2. International Committee on Taxonomy of Viruses. The ICTV Report on Virus Classification and Taxon Nomenclature. June 14, 2021 (<https://talk.ictvonline.org/ictv-reports/>)
3. Ghebreyesus TA, Swaminathan S. Scientists are sprinting to outpace the novel coronavirus. *The Lancet*. 2020 Mar;395(10226):762-4. DOI: [https://doi.org/10.1016/S0140-6736\(20\)30420-7](https://doi.org/10.1016/S0140-6736(20)30420-7).
4. Huang C, Wang Y, Li X, Ren L, Zhao J, Hu Y, et

- al. Clinical features of patients infected with 2019 novel coronavirus in Wuhan, China. *The Lancet*. 2020 Feb;395(10223):497–506. DOI: [https://doi.org/10.1016/S0140-6736\(20\)30183-5](https://doi.org/10.1016/S0140-6736(20)30183-5).
5. Rota PA. Characterization of a Novel Coronavirus Associated with Severe Acute Respiratory Syndrome. *Science*. 2003 May 30;300(5624):1394–9. DOI: <https://doi.org/10.1126/science.1085952>.
6. Woo PCY, Lau SKP, Huang Y, Yuen K-Y. Coronavirus Diversity, Phylogeny and Interspecies Jumping. *Exp Biol Med (Maywood)*. 2009 Oct;234(10):1117–27. DOI: <https://doi.org/10.3181/0903-MR-94>.
7. Chan JFW, Li KSM, To KKW, Cheng VCC, Chen H, Yuen K-Y. Is the discovery of the novel human betacoronavirus 2c EMC/2012 (HCoV-EMC) the beginning of another SARS-like pandemic? *Journal of Infection*. 2012 Dec;65(6):477–89. DOI: <https://doi.org/10.1016/j.jinf.2012.10.002>.
8. Chan JF-W, Lau SK-P, Woo PC-Y. The emerging novel Middle East respiratory syndrome coronavirus: The “knowns” and “unknowns.” *Journal of the Formosan Medical Association*. 2013 Jul;112(7):372–81. DOI: <https://doi.org/10.1016/j.jfma.2013.05.010>.
9. McIntosh K, Becker WB, Chanock RM. Growth in suckling-mouse brain of “IBV-like” viruses from patients with upper respiratory tract disease. *Proceedings of the National Academy of Sciences*. 1967 Dec 1;58(6):2268–73. DOI: <https://doi.org/10.1073/pnas.58.6.2268>.
10. Pal M, Berhanu G, Desalegn C, Kandi V. Severe Acute Respiratory Syndrome Coronavirus-2 (SARS-CoV-2): An Update. *Cureus [Internet]*. 2020 Mar 26 [cited 2021 Jun 14]; URL: <https://www.cureus.com/articles/29589-severe-acute-respiratory-syndrome-coronavirus-2-sars-cov-2-an-update>
11. Haring J, Perlman S. Mouse hepatitis virus. *Current Opinion in Microbiology*. 2001 Aug 1;4(4):462–6. DOI: [https://doi.org/10.1016/S1369-5274\(00\)00236-8](https://doi.org/10.1016/S1369-5274(00)00236-8).
12. McIntosh K, Kapikian AZ, Turner HC, Hartley JW, Parrott RH, Chanock RM. Seroepidemiologic Studies of Coronavirus Infection in Adults and Children. *American Journal of Epidemiology*. 1970 Jun;91(6):585–92. DOI: <https://doi.org/10.1093/oxfordjournals.aje.a121171>.
13. Peiris J, Lai S, Poon L, Guan Y, Yam L, Lim W, et al. Coronavirus as a possible cause of severe acute respiratory syndrome. *The Lancet*. 2003 Apr;361(9366):1319–25. DOI: [https://doi.org/10.1016/S0140-6736\(03\)13077-2](https://doi.org/10.1016/S0140-6736(03)13077-2).
14. Zhu N, Zhang D, Wang W, Li X, Yang B, Song J, et al. A Novel Coronavirus from Patients with Pneumonia in China, 2019. *N Engl J Med*. 2020 Feb 20;382(8):727–33. DOI: <https://doi.org/10.1056/NEJMoa2001017>.
15. Peiris JSM, Guan Y, Yuen KY. Severe acute respiratory syndrome. *Nat Med*. 2004 Dec;10(S12):S88–97. DOI: <https://doi.org/10.1038/nm1143>.
16. Holmes KV. SARS coronavirus: a new challenge for prevention and therapy. *J Clin Invest*. 2003 Jun 1;111(11):1605–9. DOI: <https://doi.org/10.1172/JCI18819>.
17. Fehr AR, Perlman S. Coronaviruses: An Overview of Their Replication and Pathogenesis. In: Maier HJ, Bickerton E, Britton P, editors. *Coronaviruses [Internet]*. New York, NY: Springer New York; 2015 [cited 2021 Jun 14]. p. 1–23. (Methods in Molecular Biology; vol. 1282). URL: [http://link.springer.com/10.1007/978-1-4939-2438-7\\_1](http://link.springer.com/10.1007/978-1-4939-2438-7_1).
18. de Wit E, Feldmann F, Cronin J, Jordan R, Okumura A, Thomas T, et al. Prophylactic and therapeutic remdesivir (GS-5734) treatment in the rhesus macaque model of MERS-CoV infection. *Proc Natl Acad Sci USA*. 2020 Mar 24;117(12):6771–6. DOI: <https://doi.org/10.1073/pnas.1922083117>.
19. Qiu T, Liang S, Dabbous M, Wang Y, Han R, Toumi M. Chinese guidelines related to novel coronavirus pneumonia. *Journal of Market Access & Health Policy*. 2020 Jan 1;8(1):1818446. DOI: <https://doi.org/10.1080/20016689.2020.1818446>.
20. Ko W-C, Rolain J-M, Lee N-Y, Chen P-L, Huang C-T, Lee P-I, et al. Arguments in favour of remdesivir for treating SARS-CoV-2 infections. *International Journal of Antimicrobial Agents*. 2020 Apr;55(4):105933. DOI: <https://doi.org/10.1016/j.ijantimicag.2020.105933>.
21. Gautret P, Lagier J-C, Parola P, Hoang VT, Meddeb L, Mailhe M, et al. Hydroxychloroquine and azithromycin as a treatment of Covid-19: results of an open-label non-randomized clinical trial. *International Journal of Antimicrobial Agents*. 2020 Jul;56(1):105949. DOI: <https://doi.org/10.1016/j.ijantimicag.2020.105949>.
22. Stockman LJ, Bellamy R, Garner P. SARS:

- Systematic Review of Treatment Effects. Low D, editor. PLoS Med. 2006 Sep 12;3(9):e343. DOI: <https://doi.org/10.1371/journal.pmed.0030343>.
23. Chu CM. Role of lopinavir/ritonavir in the treatment of SARS: initial virological and clinical findings. Thorax. 2004 Mar 1;59(3):252-6. DOI: <https://doi.org/10.1136/thorax.2003.012658>.
24. Savarino A, Di Trani L, Donatelli I, Cauda R, Cassone A. New insights into the antiviral effects of chloroquine. The Lancet Infectious Diseases. 2006 Feb;6(2):67-9. DOI: [https://doi.org/10.1016/S1473-3099\(06\)70361-9](https://doi.org/10.1016/S1473-3099(06)70361-9).
25. Zhang Y, Xu Q, Sun Z, Zhou L. Current targeted therapeutics against Covid-19: Based on first-line experience in China. Pharmacological Research. 2020 Jul;157:104854. DOI: <https://doi.org/10.1016/j.phrs.2020.104854>.
26. Delang L, Abdelnabi R, Neyts J. Favipiravir as a potential countermeasure against neglected and emerging RNA viruses. Antiviral Research. 2018 May;153:85-94. DOI: <https://doi.org/10.1016/j.antiviral.2018.03.003>.
27. Toniati P, Piva S, Cattalini M, Garrafa E, Regola F, Castelli F, et al. Tocilizumab for the treatment of severe Covid-19 pneumonia with hyperinflammatory syndrome and acute respiratory failure: A single center study of 100 patients in Brescia, Italy. Autoimmunity Reviews. 2020 Jul;19(7):102568. DOI: <https://doi.org/10.1016/j.autrev.2020.102568>.
28. Article O. Dexamethasone in Hospitalized Patients with Covid-19 — Preliminary Report. 2020;1-11.
29. Caly L, Druce JD, Catton MG, Jans DA, Wagstaff KM. The FDA-approved drug ivermectin inhibits the replication of SARS-CoV-2 in vitro. Antiviral Research. 2020 Jun;178:104787. DOI: <https://doi.org/10.1016/j.antiviral.2020.104787>.
30. Black S, Bloom DE, Kaslow DC, Pecetta S, Rappuoli R. Transforming vaccine development. Seminars in Immunology. 2020 Aug;50:101413. DOI: <https://doi.org/10.1016/j.smim.2020.101413>.
31. Mathieu E, Ritchie H, Ortiz-Ospina E, Roser M, Hasell J, Appel C, et al. A global database of Covid-19 vaccinations. Nat Hum Behav [Internet]. 2021 May 10 [cited 2021 Jun 14]; URL: <http://www.nature.com/articles/s41562-021-01122-8>.
32. Liu X, Liu C, Liu G, Luo W, Xia N. Covid-19: Progress in diagnostics, therapy and vaccination. Theranostics. 2020;10(17):7821-35. DOI: <https://doi.org/10.7150/thno.47987>.



## Improved Photocatalytic Degradation of Methyl Orange Dye in UV Light Irradiation by $K_2Ti_6O_{13}$ Nanorods

Kiran K S<sup>1</sup>  and Lokesh S V<sup>1</sup> 

<sup>1</sup>Department of Nanotechnology, Visvesvaraya Technological University, Center for PG Studies-Bangalore Region, Muddenahalli, Chikkaballapura (D)-562101, Karnataka, India.

**Abstract:** The  $K_2Ti_6O_{13}$  nanorods (KTNRs) were synthesized by Molten Salt Solution method (MSS) using  $TiO_2$  nanoparticles and potassium chloride as precursors. As synthesized KTNRs was characterized by powder X-ray diffraction to know the crystallinity, scanning electron microscopy confirms the rod type morphology with diameter 10 to 12 nm with length up to 80 nm, functional groups were studied with FT-IR spectroscopy, optical property of KTNRs showed the bandgap energy  $E_g = 3.41$  eV by UV-Vis spectrophotometry. The synthesized KTNRs was used as photocatalyst for degradation of the methyl orange dye under UV light illumination. The degradation of methyl orange dye followed the pseudo first order rate law. The kinetics and mechanism of MO dye degradation dye was studied for different photocatalyst dosage 5, 10 and 15 mg of KTNRs, maximum for rate constant is found for 10 mg of photocatalyst.

**Keywords:** Photocatalyst, Potassium Titanate nanorods, methyl orange degradation.

**Submitted:** July 09, 2020. **Accepted:** June 14, 2021.

**Cite this:** Kiran K, Lokesh S. Improved Photocatalytic Degradation of Methyl Orange Dye in UV Light Irradiation by  $K_2Ti_6O_{13}$  Nanorods. JOTCSA. 2021;8(3):723-30.

**DOI:** <https://doi.org/10.18596/jotcsa.766952>.

**\*Corresponding author. E-mail:** [lokeshsampangi@gmail.com](mailto:lokeshsampangi@gmail.com).

### INTRODUCTION

The purification of water contaminated by cyanide is refined by titanium dioxide ( $TiO_2$ ) by photocatalytic method (1) for the first time. After that the research community has investigated many nanocomposite materials with different nanostructured materials were used to find the solutions for environmental pollution problem. These nanocomposites were more attractive for environmental issues because of their properties like non-toxic, photo-stable, low cost, and insoluble in water.

Similarly, the nanocomposites consisting of one-dimensional (1 D) nanostructures like nanowire, nanotubes, nanobelts, and nanorods have also engrossed the extraordinary interests due to their size dependent optical, magnetic, chemical, electronic, mechanical, and thermal properties and

their promising applications in nanodevices (2-8). Even though there are large number of nanomaterials, titanium dioxide-related materials and their one-dimensional nano structured materials because of large specific surfaces and there by improving promising applications in decontamination, purification and decomposition of environmental pollutants photocatalytically (9-12).

Beside the high photocatalytic activity, potassium titanate has the distinctive crystal structure made up of layered titanium oxide layers and inter layer cations, which exhibits the brilliant ion exchange and intercalation ability. The general formula of potassium titanates consists of  $K_2Ti_nO_{2n+1}$ . Numerous methods have been developed to synthesize one-dimensional potassium titanates' nanostructures (13) with flux method (14-17). Alkali metal titanates such as  $K_2Ti_4O_9$  and  $K_2Ti_6O_{13}$  have great mechanical property by incorporating

metals and plastics (18,19). Many researchers follow the hydrothermal method (20–22) for synthesizing the 1-D  $K_2Ti_6O_{13}$  nanostructures. In this work, we have reported the synthesis of  $K_2Ti_6O_{13}$  nanorods by molten salt solution method and their potential application as photocatalyst in degrading the methyl orange dye in UV light irradiation are investigated.

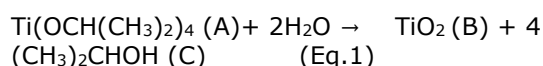
## MATERIALS AND METHODS

### Materials

Potassium chloride (99%) was purchased from SD Fine Chemicals, titanium (IV) isopropoxide (97%) and methyl orange were procured from Sigma Aldrich. The chemicals procured are of analytical grade and used without any further purification. Milli Q, deionized (DI) water is used throughout the experiment for preparing the solutions.

### Synthesis of $TiO_2$ nanoparticles

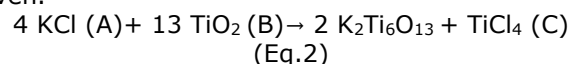
Initially, titanium(IV) isopropoxide of 2 mL volume was added to 25 mL of DI water and continuously stirred using magnetic stirrer at 400 rpm for 30 minutes at room temperature; the resultant solution was further transferred to a silica crucible and heated at 150 °C using electric bunsen burner leading to the formation of  $TiO_2$  nanoparticles as titanium(IV) isopropoxide reacts with water, leaving other components to evaporate. The resultant powder was dried at 120 °C for 2 h and then fine ground for 5 minutes in an agate mortar (23).



- (A) titanium (IV) isopropoxide  
(B) titanium dioxide  
(C) Iso propyl alcohol

### Synthesis of $K_2Ti_6O_{13}$ nanorods

The potassium titanate nanorods are synthesized by using molten salt solution method. 0.05 g of titanium dioxide nanoparticles and 7.5 g of potassium chloride were thoroughly mixed and ground consistently in an agate mortar for 0.5 h. Then an alumina crucible is obtained and the mixture is transferred to it and annealed at 850 °C for 3 h in the furnace. At this higher temperature, the reaction mixture would be in molten state. The alumina crucible is allowed to cool naturally to reach room temperature and in this cooling step crystallinity of the  $K_2Ti_6O_{13}$  would take place in the presence of molten potassium chloride. The synthesized product was collected, washed many times to remove the unreacted potassium chloride with DI, and dried at 80 °C overnight in hot air oven.



- (A) Potassium chloride  
(B) Titanium dioxide  
(C) Titanium(IV) chloride

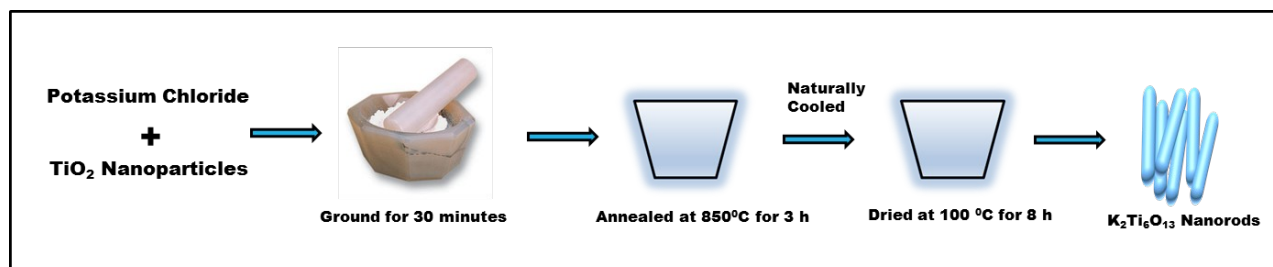


**Figure 1:** Schematic representation of Synthesis of  $K_2Ti_6O_{13}$  nanorods.

### Characterization Techniques

The synthesized  $K_2Ti_6O_{13}$  nanorods were characterized by various advanced analytical spectroscopic methods such as the powder X-ray diffraction (PXRD) study were performed using Rigaku Ultima IV diffractometer using Cu K $\alpha$  radiation with  $\lambda=0.15406$  nm in the range 10° - 70° for phase confirmation. In transmittance mode UV-Visible absorption spectrophotometry was performed by a Perkin Elmer Lambda 750 in the range of 200-800 nm. The Optical Bandgap  $E_g$  was measured by plotting  $(\alpha h\nu)^2$  versus photon energy  $E_v$ . Morphology of the synthesized  $K_2Ti_6O_{13}$  nanorods were confirmed by Scanning Electron Microscopy Vega 3 Tescan. Functional group study

was performed by Fourier Transform Infrared spectroscopy with a Perkin Elmer Spectrum Two.

## RESULTS AND DISCUSSION

### Powder XRD analysis

The powder X-ray diffraction patterns of as synthesized  $K_2Ti_6O_{13}$  nanorods was as shown in Figure 2. The XRD patterns were completely matched with the standard literature JCPDS card number 74-0275 with no additional impurities. The diffraction patterns indexed as pure monoclinic system with C2/m phase (24) of  $K_2Ti_6O_{13}$  with  $a=15.58$  Å,  $b=3.820$  Å,  $c=9.112$  Å, and  $\beta=99.764^\circ$ . The intense diffraction peak corresponding to hkl values (200) was for  $2\theta$ ,

11.34 degrees. The crystallite size of the as synthesized product was calculated using Scherrer's equation: The size of the nanoparticles was calculated by using Scherrer's formula  $D=0.9\lambda/\beta\cos\theta$  where D is the crystalline size,  $\lambda$  is

wavelength of X-rays,  $\beta$  is full width half maximum of the diffraction peak and  $\theta$  is the Bragg's diffraction angle of the diffraction peaks. The average particle size was found to be and average crystallite found to be 52nm.

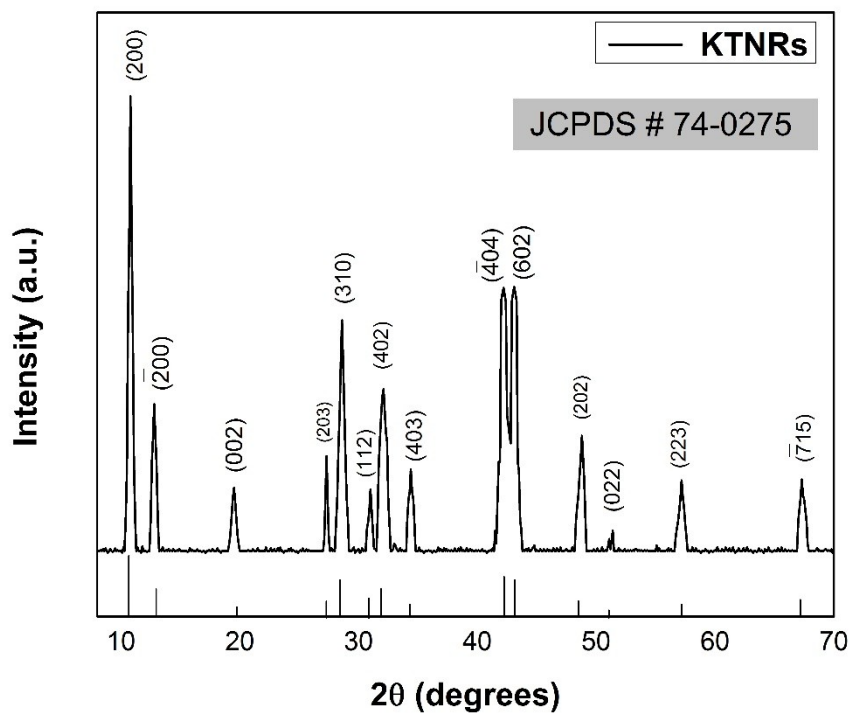


**Figure 2:** XRD patterns of potassium titanate nanorods.

#### Scanning Electron Microscopic analysis

The Scanning electron microscopic (SEM) images were used to analyze the morphology of the as-synthesized potassium titanate nanorods. Figure 4

a) and b) show the synthesized potassium titanate nanorods at 1.0  $\mu\text{m}$  and 10  $\mu\text{m}$ , respectively. Morphology of the samples were found to be rod-shaped.

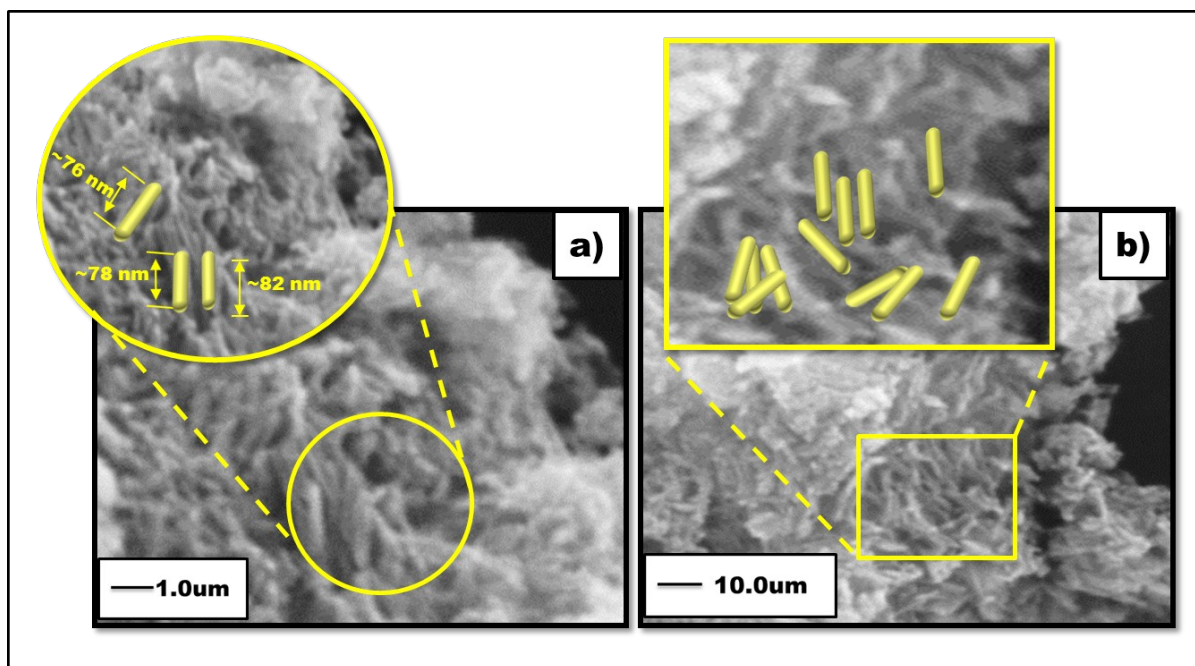


**Figure 3:** SEM images of K<sub>2</sub>Ti<sub>6</sub>O<sub>13</sub> nanorods at magnifications **a)** 1.0 μm **b)** 10 μm.

#### EDAX analysis

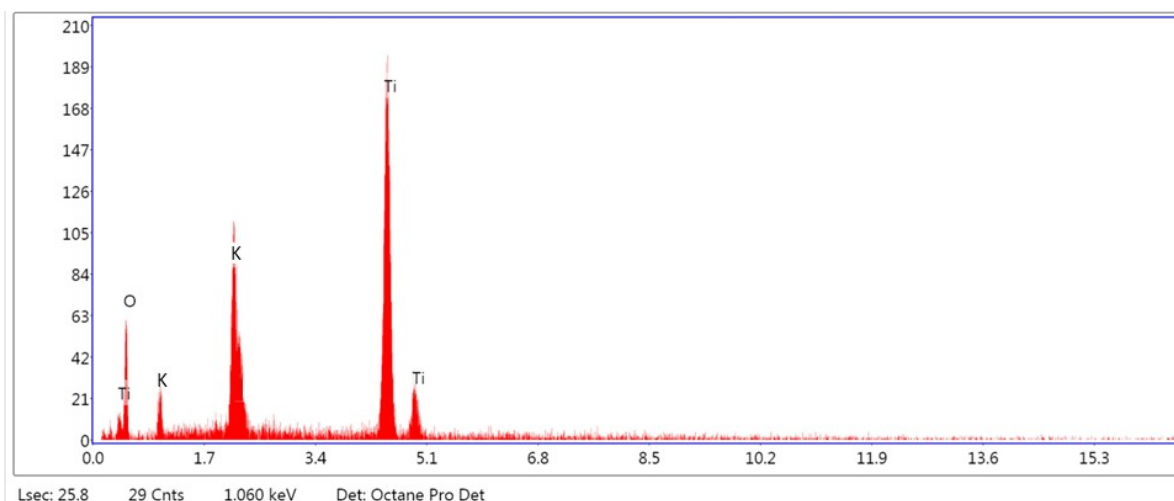


**Figure 4:** EDX elemental analysis spectra of K<sub>2</sub>Ti<sub>6</sub>O<sub>13</sub> nanorods.

In order to determine the composition of the as synthesized products examined by Energy Dispersive X-ray spectroscopy (EDAX). Figure 4 shows the elemental analysis data.

**Table 1:** Elemental data of K<sub>2</sub>Ti<sub>6</sub>O<sub>13</sub> nanorods.

Element	Weight %	Atomic %
O	24.28	42.73
K	9.53	13.81
Ti	66.19	43.46

The as-synthesized product from molten salt synthesis method are pure and free from

impurities and the ratio was found to be 1:3 for potassium to titanium atomic ratio.

#### UV-Visible spectrophotometry

The UV-Vis absorption spectra and Bandgap energy plot was shown in Figure 5 (a) & (b) Bandgap energy  $E_g$  plot. Absorption spectra for potassium titanate nanorods was  $\lambda_{max} = 325$  nm (25). Because there is a transformation in the structure from spherical particle type to rod type. This creates a unique electronic property. Bandgap energy  $E_g$  is 3.41 eV for as-synthesized potassium titanate nanorods were calculated from the plot,  $(ah\nu)^2$  v/s photon energy eV, which is very close to literature value (26).

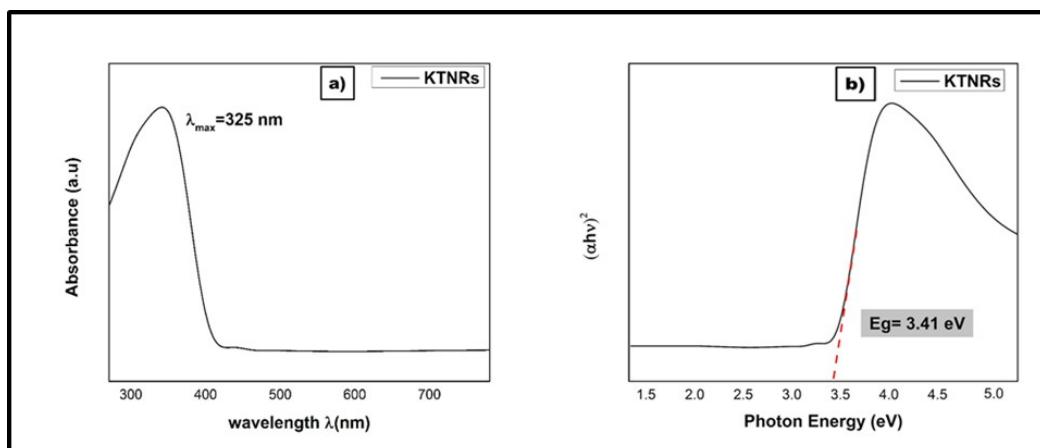


**Figure 5 a)** UV-Visible absorption plot absorbance (a.u.) v/s wavelength  $\lambda$  (nm) of KTNRs **b).** Bandgap energy  $E_g$  of KTNRs plot,  $(\alpha h\nu)^2$  v/s photon energy eV.

### FT IR analysis

FTIR for potassium titanate nanorods was as shown in Figure 6. The two prominent absorptions were observed at  $3358.3\text{ cm}^{-1}$  and  $1640.8\text{ cm}^{-1}$  which are designated to O-H bending vibrations

and H-O-H bending vibrations of the adsorbed water molecules. Ti-O bending vibrations were observed at  $550\text{ cm}^{-1}$ . At  $723.7\text{ cm}^{-1}$  is assigned to the vibration of Ti-O-Ti bond in the lattice (27).

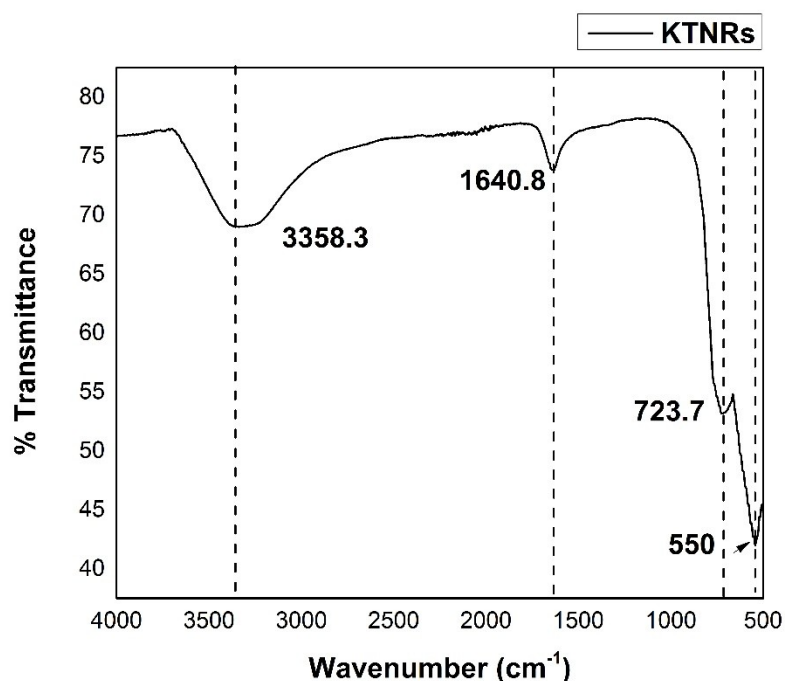


**Figure 6:** FTIR spectra of KTNRs.

### Photocatalytic degradation of methyl orange dye

Under UV light illumination, the degradation of MO (4-[[[4-dimethylamino)phenyl]-azo]benzenesulfonic acid sodium salt) by the photocatalyst was analyzed by using an absorption-based on UV-Vis spectroscopic technique. Photocatalytic tests were carried out in a beaker made up of quartz (150 mL) under stirring at room temperature, being filled with an

aqueous suspension (100 mL) containing 10 ppm of MO dye and catalyst (0.10 g/L). A 300 W high pressure mercury lamp was positioned at 10 cm away from the quartz beaker, suspension was bubbled continuously with air.

Prior to irradiation, the solution mixture was ultrasonicated for 15 min, then stirred for 0.5 h in dark condition to achieve the adsorption/desorption equilibrium. The

concentration of MO after equilibrium was analyzed by recording the absorption band maximum ( $\lambda_{\max}$  464 nm) in the absorption spectra and taken as the initial concentration ( $C_0$ ). During the photocatalysis, the suspension was extracted at an interval of 30 min, concentration (C), ( $C/C_0$ ) of MO during the photo degradation were proportional to the normalized maximum absorbance and derived from the changes in the dye's absorption profile at a given time interval. For comparison,  $K_2Ti_6O_{13}$  nanorods were characterized under the same conditions.

The degradation efficiency ( $n$ ) was measured by using following formula  $n=(1-C)/C_0$  where,  $C_0$  is

the initial concentration before irradiation with light and C is the concentration of dye after irradiation. The degradation efficiency of MO was analyzed using UV-Vis spectrometer. Peaks were observed to be at 464 nm and were assigned as the absorption of the  $\pi$ -system (28), which was indicative of the degradation of methyl orange dye shown in Figure 7 a) and Percentage of degradation in 7 b). In Figure 7 c) Degradation of MO can be seen with time. Initially the absorbance was 0.9412 and gradually decreased with time and irradiation of UV-Vis light to 0.0252 at 240 min. The rate constant was found to be  $0.000314 \text{ min}^{-1}$  for 10 mg of photocatalytic dosage.

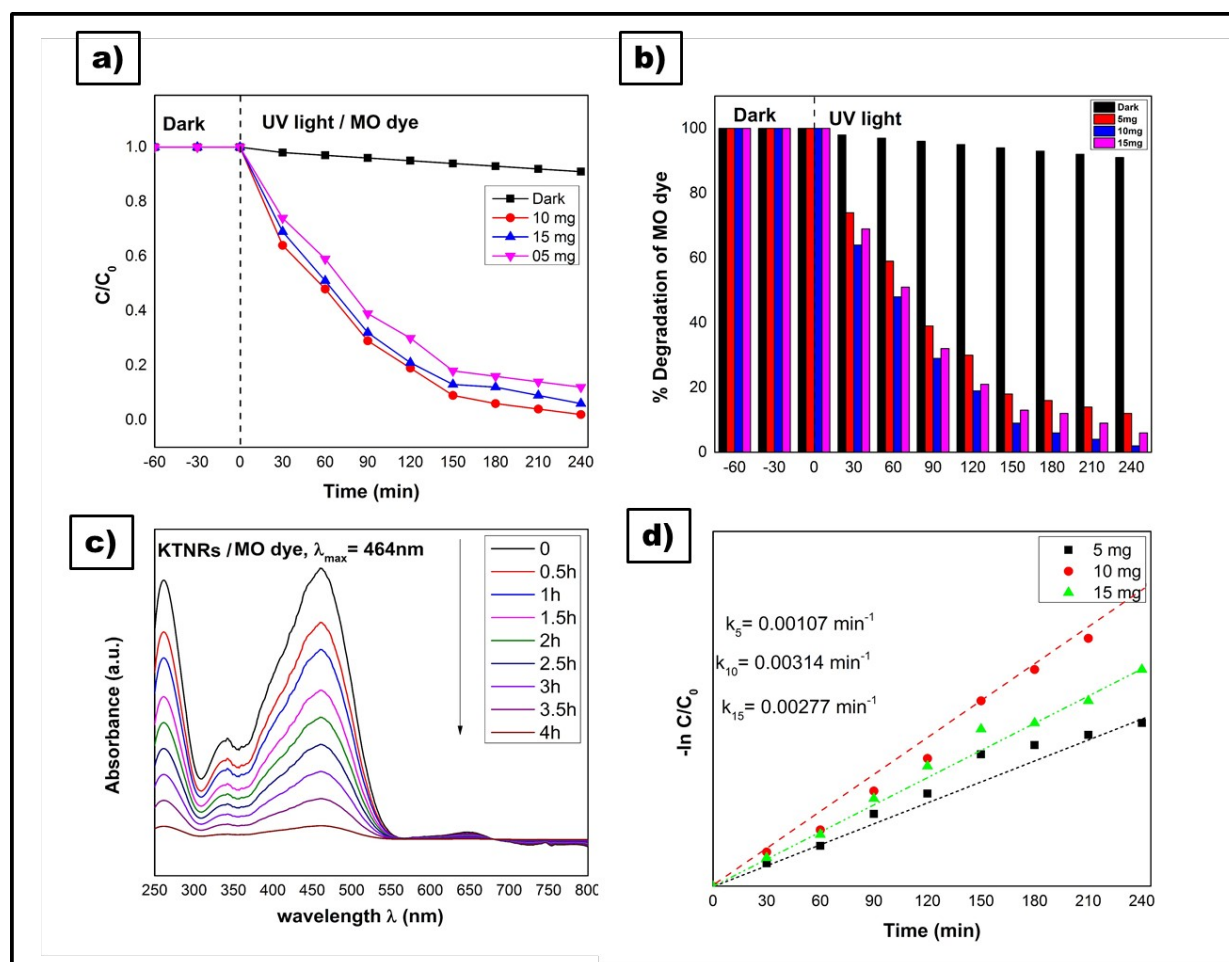


**Figure 7:** Photocatalytic degradation of  $K_2Ti_6O_{13}$  nanorods of different photocatalyst loading **a)** Concentration  $C/C_0$  v/s Irradiation Time (min) **b)** Percentage degradation v/s Irradiation Time (min) **c)** Absorbance (a. u.) v/s wavelength  $\lambda$ (nm) of 10 mg KTNRs **d)** rate constant plot:  $-\ln C/C_0$  v/s Time (min)

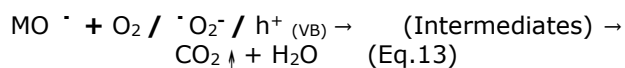
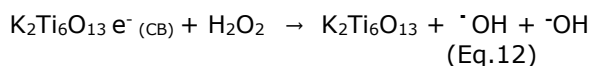
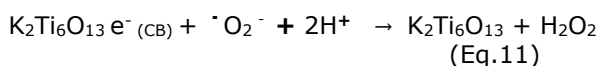
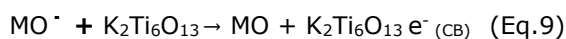
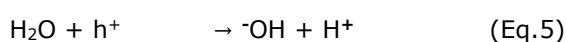
The same photocatalytic degradation reaction is repeated keeping all the conditions same but changing the weight of photocatalyst. The effect of photocatalytic dosage was varied from 5 mg and 15 mg. The rate constant was found more for 10 mg photocatalyst than 5 mg and 15 mg due to the availability of number of active sites on the surface

of the sample increases with increasing the amount of photocatalyst. In this way, the number of superoxide and hydroxyl radicals also increases. However, the rate of reaction decreases due to the covering the active sites of the suspension for photocatalyst. There by the light radiation will not fall on the active sites to proceed the reaction.

**Table 2:** Photocatalytic dosage and rate constant of the reaction for KTNRs.

For photocatalytic degradation of MO dye by KTNRs with 10 ppm concentration	Photocatalytic dosage	Rate constant, min <sup>-1</sup>
	5 mg	0.000107
	10 mg	0.000314
	15 mg	0.000277

The K<sub>2</sub>Ti<sub>6</sub>O<sub>13</sub> nanorods has a structure as that of semiconductors, on irradiating to UV light generates the electron hole pairs after attaining the equilibrium/desorption in dark condition. The photo generated electron hole pairs follows the reaction and gradually degrade the MO dye to CO<sub>2</sub> and H<sub>2</sub>O. The plausible reaction mechanism (29,30) as follows:



The degraded products are environmentally friendly. Hence the K<sub>2</sub>Ti<sub>6</sub>O<sub>13</sub> nanorods can be used as promising photocatalysts for the degradation of methyl orange dye.

## CONCLUSIONS

The potassium titanate nanorods were efficiently synthesized by molten salt solution method. The as synthesized K<sub>2</sub>Ti<sub>6</sub>O<sub>13</sub> nanorods were in pure monoclinic phase with rod-like structure with average 10<sup>-12</sup> nm diameter and length up to 80 nm. The K<sub>2</sub>Ti<sub>6</sub>O<sub>13</sub> nanorods showed higher photocatalytic activity of azo dye methyl orange under UV light irradiation. Hence it exhibited as a prominent photocatalyst. Three different dosage such as 5, 10 and 15 mg was examined for photocatalytic activity, rate constant was maximum for 10 mg, even though as the size decreases the active site increases, but the rate of

reaction decreases due to the blocking of the active sites of the suspension for photocatalyst.

## ACKNOWLEDGEMENTS

Authors acknowledge the financial support from DST-Science and Engineering Research Board, Government of India, File no. SB/EMEQ-171/2014.

## REFERENCES

- Frank SN, Bard AJ. Heterogeneous photocatalytic oxidation of cyanide and sulfite in aqueous solutions at semiconductor powders. *J Phys Chem.* 1977;81(15):1484-8. DOI: <https://doi.org/10.1021/j100530a011>.
- Ge M, Cao C, Huang J, Li S, Chen Z, Zhang K-Q, et al. A review of one-dimensional TiO<sub>2</sub> nanostructured materials for environmental and energy applications. *J Mater Chem A.* 2016;4(18):6772-801. DOI: <https://doi.org/10.1039/C5TA09323F>.
- Lieber CM. One-dimensional nanostructures: Chemistry, physics & applications. *Solid State Communications.* 1998;107(11):607-16. DOI: [https://doi.org/10.1016/S0038-1098\(98\)00209-9](https://doi.org/10.1016/S0038-1098(98)00209-9).
- Xie JL, Guo CX, Li CM. Construction of one-dimensional nanostructures on graphene for efficient energy conversion and storage. *Energy Environ Sci.* 2014 30;7(8):2559. DOI: <https://doi.org/10.1039/C4EE00531G>.
- Cho C-P, Perng T-P. One-Dimensional Organic and Organometallic Nanostructured Materials. *j nanosci nanotechnol.* 2008;8(1):69-87. DOI: <https://doi.org/10.1166/jnn.2008.N14>.
- Nowak DJ, Hirabayashi S, Bodine A, Greenfield E. Tree and forest effects on air quality and human health in the United States. *Environmental Pollution.* 2014;193:119-29. DOI: <https://doi.org/10.1016/j.envpol.2014.05.028>.
- Xu Y, Zhang B. Recent advances in porous Pt-based nanostructures: synthesis and electrochemical applications. *Chem Soc Rev.* 2014;43(8):2439. DOI: <https://doi.org/10.1039/c3cs60351b>.
- Kilinc N, Cakmak O, Kosemen A, Ermek E, Ozturk S, Yerli Y, et al. Fabrication of 1D ZnO nanostructures on MEMS cantilever for VOC sensor application. *Sensors and Actuators B: Chemical.* 2014;202:357-64. DOI: <https://doi.org/10.1016/j.snb.2014.05.078>.
- Kasuga T, Hiramatsu M, Hoson A, Sekino T, Niihara K. Formation of Titanium Oxide Nanotube. *Langmuir.* 1998 1;14(12):3160-3. DOI: <https://doi.org/10.1021/ja9713816>.

10. Kasuga T, Hiramatsu M, Hoson A, Sekino T, Niihara K. Titania Nanotubes Prepared by Chemical Processing. *Adv Mater*. 1999;11(15):1307-11.
11. Anderson C, Bard AJ. An Improved Photocatalyst of TiO<sub>2</sub>/SiO<sub>2</sub> Prepared by a Sol-Gel Synthesis. *J Phys Chem*. 1995;99(24):9882-5. DOI: <https://doi.org/10.1021/j100024a033>.
12. Ma S, Li R, Lv C, Xu W, Gou X. Facile synthesis of ZnO nanorod arrays and hierarchical nanostructures for photocatalysis and gas sensor applications. *Journal of Hazardous Materials*. 2011;192(2):730-40. DOI: <https://doi.org/10.1016/j.jhazmat.2011.05.082>.
13. Cao J, Wang A, Yin H, Shen L, Ren M, Han S, et al. Selective Synthesis of Potassium Titanate Whiskers Starting from Metatitanic Acid and Potassium Carbonate. *Ind Eng Chem Res*. 2010 6;49(19):9128-34. DOI: <https://doi.org/10.1021/ie101154q>.
14. Choy J-H, Han Y-S. A combinative flux evaporation-slow cooling route to potassium titanate fibres. *Materials Letters*. 1998;34(3-6):111-8. DOI: [https://doi.org/10.1016/S0167-577X\(97\)00157-2](https://doi.org/10.1016/S0167-577X(97)00157-2).
15. Makarova NM, Kulapina EG, Tret'yachenko EV, Gorokhovskii AV, Zakharevich AM. Effect of the sorption of polyoxyethylated nonylphenols on the surface structure of potassium polytitanate. *Russ J Phys Chem*. 2014;88(12):2209-13. DOI: <https://doi.org/10.1134/S0036024414120206>.
16. Wang X, Li Y. Solution-Based Synthetic Strategies for 1-D Nanostructures. *Inorg Chem*. 2006 1;45(19):7522-34. DOI: <https://doi.org/10.1021/ic051885o>.
17. Yuan Z-Y, Zhang X-B, Su B-L. Moderate hydrothermal synthesis of potassium titanate nanowires. *Appl Phys A*. 2004 Apr;78(7):1063-6. DOI: <https://doi.org/10.1007/s00339-003-2165-x>.
18. Yu D, Wu J, Zhou L, Xie D, Wu S. The dielectric and mechanical properties of a potassium-titanate-whisker-reinforced PP/PA blend. *Composites Science and Technology*. 2000 Mar;60(4):499-508. DOI: [https://doi.org/10.1016/S0266-3538\(99\)00149-9](https://doi.org/10.1016/S0266-3538(99)00149-9).
19. Murakami R, Matsui K. Evaluation of mechanical and wear properties of potassium acid titanate whisker-reinforced copper matrix composites formed by hot isostatic pressing. *Wear*. 1996 Dec;201(1-2):193-8. DOI: [https://doi.org/10.1016/S0043-1648\(96\)07239-0](https://doi.org/10.1016/S0043-1648(96)07239-0).
20. Wang BL, Chen Q, Wang RH, Peng L-M. Synthesis and characterization of K<sub>2</sub>Ti<sub>6</sub>O<sub>13</sub> nanowires. *Chemical Physics Letters*. 2003 Jul;376(5-6):726-31. DOI: [https://doi.org/10.1016/S0009-2614\(03\)01068-6](https://doi.org/10.1016/S0009-2614(03)01068-6).
21. Du GH, Chen Q, Han PD, Yu Y, Peng L-M. Potassium titanate nanowires: Structure, growth, and optical properties. *Phys Rev B*. 2003 Jan 30;67(3):035323. DOI: <https://doi.org/10.1103/PhysRevB.67.035323>.
22. Wang RH, Chen Q, Wang BL, Zhang S, Peng L-M. Strain-induced formation of K<sub>2</sub>Ti<sub>6</sub>O<sub>13</sub> nanowires via ion exchange. *Appl Phys Lett*. 2005 Mar 28;86(13):133101. DOI: <https://doi.org/10.1063/1.1890470>.
23. Hanaor DAH, Chironi I, Karatchevtseva I, Triani G, Sorrell CC. Single and mixed phase TiO<sub>2</sub> powders prepared by excess hydrolysis of titanium alkoxide. *Advances in Applied Ceramics*. 2012 Apr;111(3):149-58. DOI: <https://doi.org/10.1179/1743676111Y.0000000059>.
24. Cid-Dresdner H, Buerger MJ. The crystal structure of potassium hexatitanate K<sub>2</sub>Ti<sub>6</sub>O<sub>13</sub>. *Zeitschrift für Kristallographie - Crystalline Materials* [Internet]. 1962 Jan [cited 2021 Jun 14];117(1-6). DOI: <https://doi.org/10.1524/zkri.1962.117.16.411>.
25. Saleh TA, Gupta VK. Photo-catalyzed degradation of hazardous dye methyl orange by use of a composite catalyst consisting of multi-walled carbon nanotubes and titanium dioxide. *Journal of Colloid and Interface Science*. 2012 Apr;371(1):101-6. DOI: <https://doi.org/10.1016/j.jcis.2011.12.038>.
26. Siddiqui MA, Chandel VS, Azam A. Comparative study of potassium hexatitanate (K<sub>2</sub>Ti<sub>6</sub>O<sub>13</sub>) whiskers prepared by sol-gel and solid state reaction routes. *Applied Surface Science*. 2012 Jul;258(19):7354-8. DOI: <https://doi.org/10.1016/j.apsusc.2012.04.018>.
27. Pan H, Wang X, Xiao S, Yu L, Zhang Z. Preparation and characterization of TiO<sub>2</sub> nanoparticles surface-modified by octadecyltrimethoxysilane. *Ind J Eng&Mat Sci*. 2013 Dec;20:561-7. URL: <http://nopr.niscair.res.in/bitstream/123456789/25584/1/IJEMS%2020%286%29%20561-567.pdf>.
28. Liu G, Wu T, Zhao J, Hidaka H, Serpone N. Photoassisted Degradation of Dye Pollutants. 8. Irreversible Degradation of Alizarin Red under Visible Light Radiation in Air-Equilibrated Aqueous TiO<sub>2</sub> Dispersions. *Environ Sci Technol*. 1999 Jun;33(12):2081-7. DOI: <https://doi.org/10.1021/es9807643>.
29. Veldurthi NK, Velchuri R, Pola S, Prasad G, Muniratnam NR, Vithal M. Synthesis, characterization and silver/copper-nitrogen substitutional effect on visible light driven photocatalytic performance of sodium hexatitanate nanostructures: Silver/copper-nitrogen substituted sodium hexatitanate. *J Chem Technol Biotechnol*. 2015 Aug;90(8):1507-14. DOI: <https://doi.org/10.1002/jctb.4466>.
30. Choi J, Cui M, Lee Y, Kim J, Yoon Y, Jang M, et al. Synthesis, characterization and sonocatalytic applications of nano-structured carbon based TiO<sub>2</sub> catalysts. *Ultrasonics Sonochemistry*. 2018 May;43:193-200. DOI: <https://doi.org/10.1016/j.ultsonch.2018.01.010>.



## Equilibrium, Kinetic Data, and Adsorption Mechanism for Lead Adsorption onto Polyacrylamide Hydrogel

Imane LEBKIRI<sup>1,\*</sup> , Brahim ABBOU<sup>1</sup> , Lamyia KADIRI<sup>1</sup> ,  
 Abdelkarim OUASS<sup>1</sup> , Abdelhay ELAMRI<sup>1</sup> , Hanae OUADDARI<sup>2</sup> ,  
 Omar ELKHATTABI<sup>1</sup> , Ahmed LEBKIRI<sup>1</sup> , El Housseine RIFI<sup>1</sup> 

<sup>1</sup>Laboratory of Advanced Materials and Process Engineering, Faculty of Sciences, Ibn Tofail University – Kenitra – Morocco.

<sup>2</sup>Laboratory of Materials Membranes and Environment, Department of Chemistry, Faculty of Sciences and Technologies of Mohammedia, University of Hassan II, Casablanca, Morocco.

**Abstract:** The present study focuses on the effect of experimental parameters (pH, temperature, gel mass, metal concentration, contact time) on the performance of lead adsorption by polyacrylamide hydrogels. The results obtained showed that the retention of Pb<sup>2+</sup> ions is closely linked to these parameters. The adsorbent gels equilibrate with the metal solution after 180 minutes, and the maximum adsorption capacity is 442.31 mg/g. In addition, the adsorption obeys the pseudo-second-order kinetics and Langmuir isotherm. Desorption of the micropollutant retained by the hydrogel was also studied using 0.1 M of HCl solution. The desorption was rapid, and the efficiency exceeded 90% after a contact time of 90 minutes.

**Keywords:** Adsorption, lead, water treatment, hydrogel, polyacrylamide.

**Submitted:** April 09, 2021. **Accepted:** June 15, 2021.

**Cite this:** Lebkiri I, Abbou B, Kadiri L, Ouass A, Elamri A, Ouaddari H, et al. Equilibrium, Kinetic Data, and Adsorption Mechanism for Lead Adsorption onto Polyacrylamide Hydrogel. JOTCSA. 2021;8(3):731-48.

**DOI:** <https://doi.org/10.18596/jotcsa.912479>.

**\*Corresponding author.** E-mail: [imane.lebkiri@gmail.com](mailto:imane.lebkiri@gmail.com)

### INTRODUCTION

It is well known that heavy metals such as cadmium, lead, copper, and mercury are toxic to humans and other living organisms when their concentration exceeds the tolerance limit. Unlike organic contaminants, heavy metals are not biodegradable and accumulate in living organisms. Heavy metals are increasingly being released, either directly or indirectly, into the environment, particularly in developing countries (1).

Our attention has been focused on lead, which is considered one of the toxic metals that accumulate

slowly in living organisms from the food chain and has several harmful effects on human health (2).

Eliminating these types of pollutants is always a big challenge. Numerous studies have developed several treatment processes to reduce the amount of these contaminants in aquatic environments (3,4). The adsorption process is one of the methods that has shown outstanding cost-effectiveness in contaminants removal of a different nature, including organic pollutants and heavy metals (5,6). Besides, the research and development of new adsorbents, with a high capacity for adsorption, abundant, economically profitable, and effective for treating wastewater is

a great challenge. Thus, in recent years, a great importance has been attached to functionalized polymers because of their low cost and high capacity to adsorption different pollutants, especially the possibility of their regeneration (7-9).

Through the literature, polyacrylamide (PAAM) is one of the most widely used polymers (10,11). This material can absorb large amounts of water compared to other polymers (12). Polyacrylamide is a functionalized polymer containing a large number of amide groups that grant an excellent selectivity for the elimination of several organic pollutants and minerals (13). Due to its low cost, recoverable, eco-friendly, high adsorption capacity, and its use without any modification, PAAM can be a great adsorbent for heavy metal removal from wastewater (14,15). Moreover, one of the essential advantages of using this polymer is its structure containing abundant active sites that can fix metal species. Also, the shape and the mechanical rigidity of the adsorbent promote the separation procedure at the end of the adsorption experience. Various studies have investigated the PAAM hydrogel as a heavy metals adsorbent, such as the removal of mercury ions from aqueous solutions by Ramadan et al. (2010) (16); the removal of chromium ions from industrial lean methyl diethanolamine solvents (MDEA) by Pal and Banat (2015) (17) and the copper adsorption by S. Moulay et al. (2013) (18).

This work aims to study the effect of the physical-chemical parameters linked on the one hand to metallic solution and on the other hand to the polymeric matrix. The optimization of these parameters allows defining the amount of gel needed to treat a given metal solution volume. The equilibrium data were analyzed using various adsorption isotherms and kinetics.

## EXPERIMENTAL SECTION

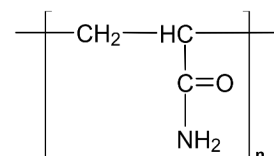
### Adsorbate

The stock solution of lead is prepared from the corresponding salt:  $Pb(NO_3)_2$  supplied by the company SOLVACHIM (Casablanca, Morocco). The solution studied is prepared by successive dilutions of the stock solution until the desired concentration is obtained.

### Adsorbent

The material used in this work is polyacrylamide (PAAM), whose chemical formula is  $[-C_2H_3CONH_2-]_n$  (Figure 1). It's a polymer made by radicalic polymerization of acrylamide and bisacrylamide. PAAM is a superabsorbent hydrogel with transparent beads of non-porous surface aspect supplied by Sigma-Aldrich (Saint Louis,

USA) (CAS number: 9003-05-8, purity: 99.99%, MW: 150000).



### Adsorption Experiments

The adsorption experiments were carried out in a static regime in a stirred reactor at a fixed temperature ( $25 \text{ }^\circ\text{C} \pm 2 \text{ }^\circ\text{C}$ ). The system was adjusted to the desired pH by adding small volumes of 0.01 or 0.1 mol/L HCl, or NaOH supplied by the company SOLVACHIM (Casablanca, Morocco). The quantities of metal adsorbed and the metal removal efficiency was calculated from the concentrations in the solutions, before and after adsorption according to the following equations (19,20):

$$Q = \frac{C_i - C_f}{m} * V \quad (\text{Eq. 1})$$

$$R\% = \frac{(C_i - C_f)}{C_i} * 100 \quad (\text{Eq. 2})$$

Where: Q is the adsorbed amount of lead at equilibrium (mg/g), R% is the lead removal efficiency (%),  $C_i$  and  $C_f$ , respectively, the initial and equilibrium lead concentration (mg/L), m is the mass of adsorbent (g) and V the volume of the lead solution (L).

The FT-IR spectra were obtained by 70 Vertex instrument of Bruker brand. The analysis was done by scanning from  $4000 \text{ cm}^{-1}$  to  $400 \text{ cm}^{-1}$  with a resolution of  $4 \text{ cm}^{-1}$ . X-ray diffraction analyses were recorded using a PANalytical X'Pert HighScore Plus diffractometer using Cu-K $\alpha$  radiation ( $1.5418 \text{ \AA}$ ) at a goniometer rate of  $2\theta = 4^\circ/\text{min}$ . SEM analysis was carried out using QUATTRO S, FEI. The heavy metal content analysis was carried out by optical emission spectrometry coupled to inductive plasma ICP-OES (Ultima2, Horiba Jobin Yvon).

### Desorption Experiments

To assess the regenerative property of our adsorbent PAAM, HCl was tested as an eluent (supplied by the company SOLVACHIM (Casablanca, Morocco)). The gels loaded with lead are each immersed in 40 mL of a 0.1 M HCl solution. The experiment was stirred and performed at  $25 \text{ }^\circ\text{C}$ . Then the PAAM beads were collected from the solution, washed with distilled

water to remove acid excess acid, neutralized with 0.1 M NaOH, and washed again to remove NaOH excess. Then the beads were reused in the next cycle of the adsorption experiment. The adsorption-desorption experiments were carried out for five cycles.

### Model to Experimental Data

- Adsorption kinetics analysis was calculated using (21):  
The pseudo-second-order rate equation as (22):

The pseudo-first-order rate equation as (23):

$$\frac{dQ_t}{dt} = K_2(Q_e - Q_t)^2 \Rightarrow \frac{t}{Q_t} = \frac{1}{K_2 Q_e^2} + \frac{1}{Q_e} t \quad (\text{Eq. 3})$$

$$\frac{dQ_t}{dt} = K_1(Q_e - Q_t) \Rightarrow \ln(Q_e - Q_t) = \ln Q_e - K_1 t \quad (\text{Eq. 4})$$

Where  $K_1$  is the pseudo-first-order rate constant (g/mg min),  $K_2$  is the pseudo-second-order rate constant (g/mg min),  $Q_e$  and  $Q_t$  are the metal uptake (mg/g) at equilibrium and at time  $t$ , respectively.

- The Freundlich sorption isotherm equation is given below (24):

$$Q = K_f \frac{C_e^1}{n} \Rightarrow \log(Q) = \log(k_f) + \frac{1}{n} \log(C_e) \quad (\text{Eq. 5})$$

Where  $K_f$  (mg/g) represents the adsorption capacity, and  $n$  represents the degree of dependence of adsorption with equilibrium concentration.

The Langmuir sorption isotherm equation is given below (25):

$$Q_t = Q_m \frac{K_L C_e}{1 + K_L C_e} \Rightarrow \frac{C_e}{Q_t} = \frac{1}{K_L Q_m} + \frac{C_e}{Q_m} \quad (\text{Eq. 6})$$

Furthermore, the separation factor ( $R_L$ ) was used to determine whether the adsorption was favorable or not. The  $R_L$  was calculated from the following equation:

$$R_L = \frac{1}{1 + K_L C_0} \quad (\text{Eq. 7})$$

Where  $C_0$  and  $C_e$  represent the initial and equilibrium concentration of heavy metals (mg/L);  $Q_m$  is the adsorption capacity (mg/g), and  $K_L$  is related to the energy of adsorption (L/mg).

For the thermodynamic studies, the Eyring equation was used (26):

$$\ln K_d = \left( \frac{\Delta S}{R} \right) - \left( \frac{\Delta H}{R} \right) \frac{1}{T} \quad \text{and} \quad (\text{Eq. 8})$$

$$\Delta G = -RT \ln K_d \ln K_d = \left( \frac{\Delta S}{R} \right) - \left( \frac{\Delta H}{R} \right) \frac{1}{T}$$

Where  $K_d = Q_e / C_e$  is the sorption distribution constant and  $Q_e$  the adsorption capacity at equilibrium (mg/g), and  $C_e$  is the amount of  $Pb^{2+}$  in solution at equilibrium (mg/L),  $R$  ideal gas constant (8,314 J.mol<sup>-1</sup>.K<sup>-1</sup>) and  $T$  the temperature (K),  $\Delta G^\circ$  is the Gibbs free energy (J/mol),  $\Delta S$  the entropy (J/kmol) and  $\Delta H$  the enthalpy (J/mol).

## RESULTS AND DISCUSSION

### Characterization of PAAM

#### X-ray diffraction

X-ray diffraction makes it possible to determine the structure of the polymer studied. Figure 2 shows the X-ray diffraction pattern of the polymer in powder form. The absence of peaks in this figure's spectrum shows that the polymer studied is an amorphous product (27,28).

#### FTIR spectroscopy of PAAM

An infrared spectroscopic (IR) study of PAAM gels before and after lead adsorption was performed (Figure 3). The purpose of this study is to understand the mechanism of fixation of  $Pb^{2+}$  ions by polyacrylamide. The study is based on the comparison of the spectra of free and doped lead polymers.

The spectrum of blank PAAM shows two peaks at 3465.44 cm<sup>-1</sup> due to the valence vibration of the amino group N-H stretching (primary amine) (29–31). The absorption peak at 2923 cm<sup>-1</sup> could be attributed to the C-H elongation vibration of the CH<sub>2</sub> group. The adsorption peak at 1639 cm<sup>-1</sup> confirms the presence of C=O and that at 1382 cm<sup>-1</sup> corresponds to the valence vibration of C-N, whereas that at 998 cm<sup>-1</sup> and 622 cm<sup>-1</sup> corresponds to the valence vibration of NH<sub>2</sub> (32–34).

The first change observed after lead adsorption appears at the peaks corresponding to the N-H vibration; they become wider and intense with the appearance of a new band of N-H at 1561.44 cm<sup>-1</sup>. A bending vibration is observed at 1615 cm<sup>-1</sup> corresponding to the double band C=O; after the adsorption of the lead, this band becomes more intense. The vibration bands C-H, CH<sub>2</sub>, and C-N, do not change the spectra of the formed complex. They are therefore not involved in the coordination of  $Pb^{2+}$  to the PAAM polymer.

The observations presented above show that PAAM probably acts as a bidentate ligand, coordinating with the metal  $Pb^{2+}$  center by two bonds to the CO and  $NH_2$  groups (Figure 4). This coordination leads

to a chemical crosslinking of the polymer and thus the repulsion of the water molecules present in the polymer network. This explains the deflation of the gel after lead adsorption (35).

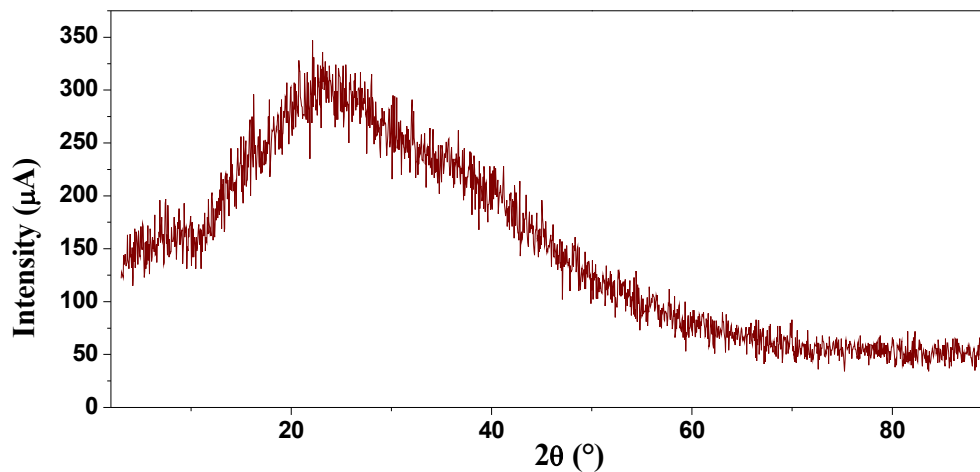


**Figure. 2:** X-ray diffraction of PAAM.

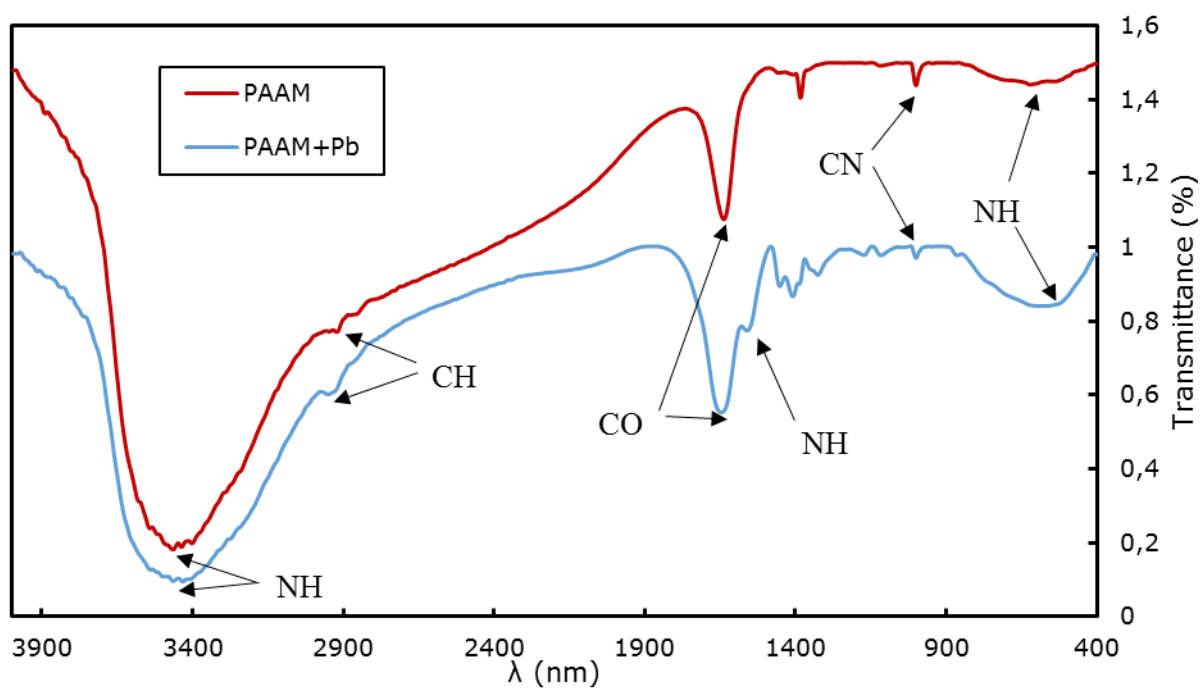


**Figure 3:** IR spectrometry of PAAM hydrogel and lead charged PAAM.

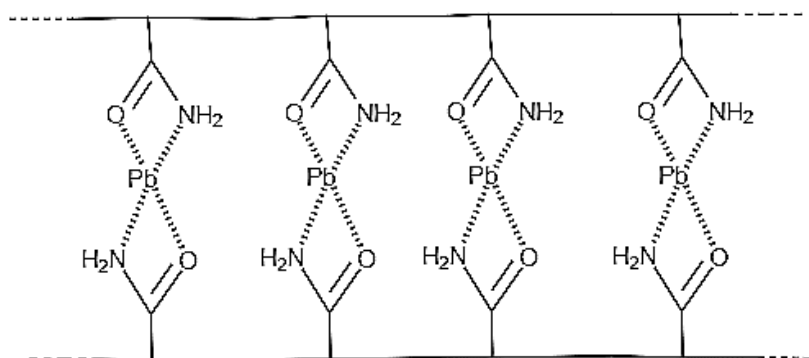


**Figure 4:** PAAM-Pb complex.

#### *SEM analysis*

Figure 5 (a) shows the SEM micrograph of the lead-containing gel, and Figure 5 (b) shows the EDX mapping of the region shown in (a), the lead, shown in turquoise blue, is present in the gel in a random distribution. Figure 5 (c) shows the EDX spectrum of the same region and peaks are corresponding to Pb, N, and O; these last two elements should be present in a PAAM polymer; carbon is detected, but this corresponds to the carbon in the gel and the carbon ribbon. Pb peak is present; it confirms the presence of lead on the gel (36).

#### **Effects of Different Experimental Parameters on Adsorption of Lead by PAAM**

##### *Effect of contact time*

Experiments were performed to determine the time required for the metal removal process to reach equilibrium. The study consists of placing, in a temperature-controlled cell, a volume of 100 mL of 20 ppm of lead solution and 0.026 g of PAAM gel. The whole is stirred at 25 °C until equilibrium. The following curve represents the simultaneous variations of the concentration and the pH of the metallic solution versus time.

According to Figure 6, we notice two phases: the first one is fast from 0 to 30 minutes, and the second phase is slow from 60 until 180 minutes when equilibrium is reached. This is relating to the wide availability of the free active sites of PAAM at the beginning of the experience, which becomes weak over time (37).

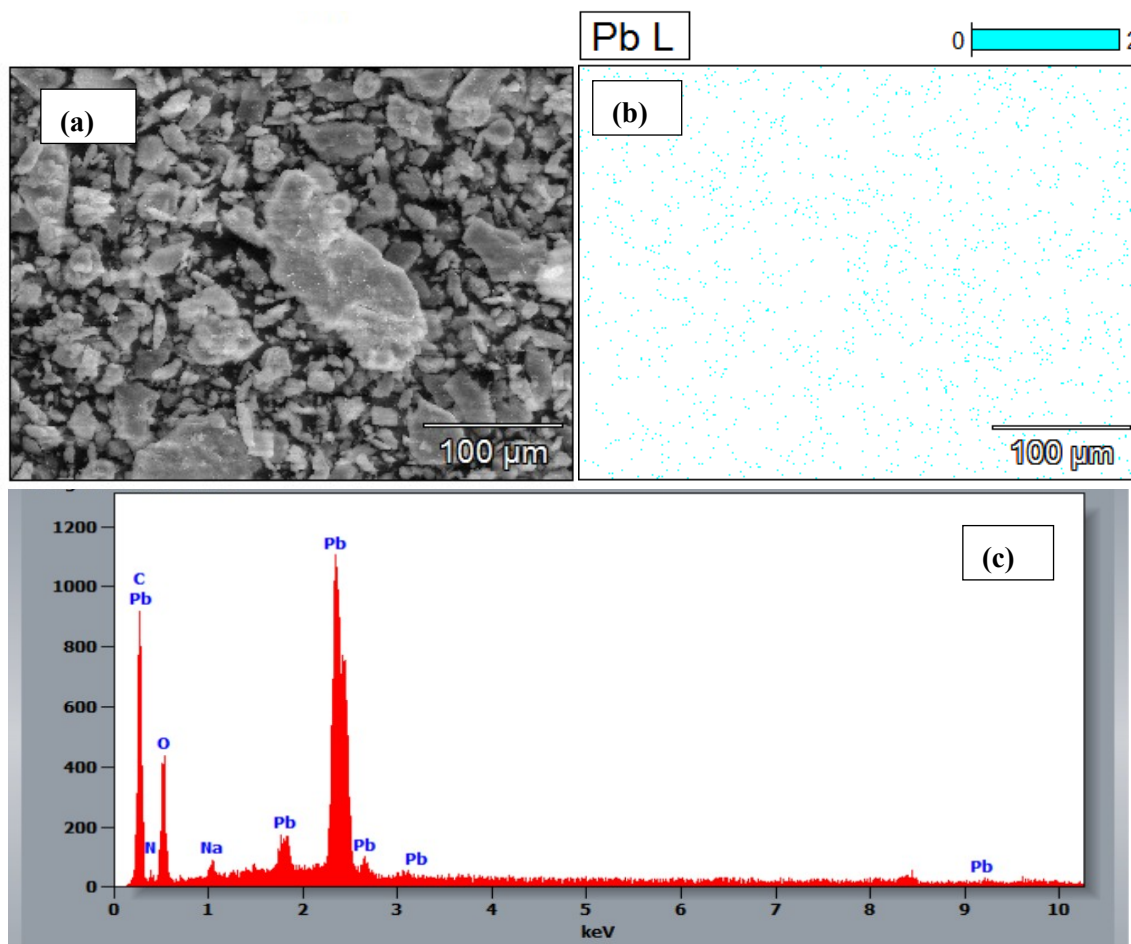


Figure 5: EDX analysis coupled with the SEM of the lead-laden PAAM

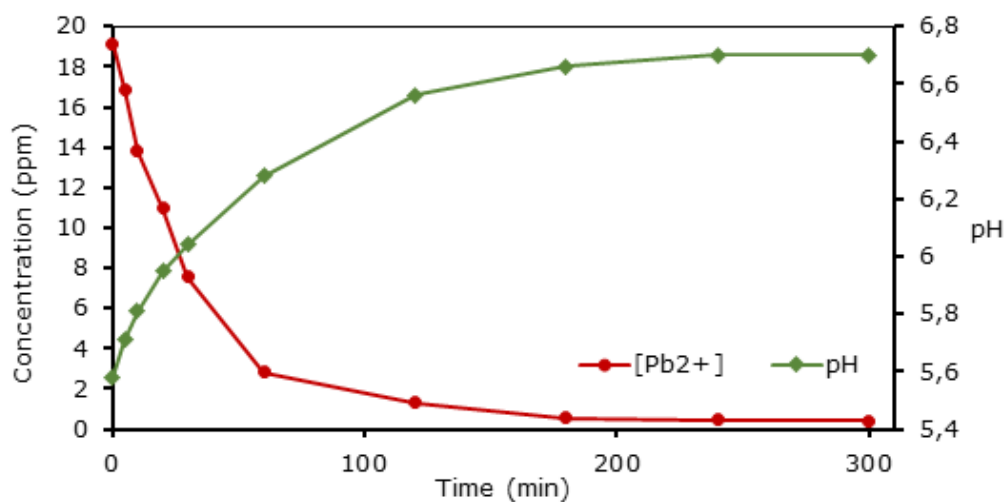


Figure 6: Evolution of lead concentration and pH over time (V=100 mL, T=25 °C, pH=5, m=0.026 g, [Pb<sup>2+</sup>]=20 ppm).

At the same time, we observe an increase in the pH, ranging from 5.5 to 6.7. The increase in pH shows that the gel equilibrates with the solution

loaded with metal by consuming H<sup>+</sup> (19). In our operating conditions, we record an adsorption efficiency close to 97%.

*Effect of adsorbent dose*

Studying the effect of PAAM's mass on lead adsorption allows us to determine the optimal mass that will be used throughout our study. For this purpose, we put PAAM masses varying from 0.007 to 0.08 g each in contact with 100 mL of metal solution. The results obtained are shown in Figure 7. According to the results, the percentage of lead elimination by PAAM increases rapidly with the increase in the mass of the adsorbent to the value of 0.026 g. Beyond this value, the increase in adsorbent content slightly affects the adsorption of the lead until reaching an equilibrium of 100%. This is explained by the fact that by adding the adsorbent, more active centers will be available to adsorb  $Pb^{2+}$  ions. Therefore the system reaches an equilibrium state for an initial lead concentration of 20 ppm (38). Finally, 0.026 g will be considered and used as optimal mass.

*Effect of pH*

pH has a remarkable influence on the process of removing metal cations in aqueous solutions by adsorption, as it directly affects the surface load and the nature of the ion species of adsorbates. In this context, the effect of pH on the adsorption of lead by PAAM gel was studied at different values: 2, 3, 4, 5, and 6. Masses of PAAM are put in contact with lead solutions. According to Figure 8, it can be observed that the adsorption efficiency of lead increases with increasing pH. Indeed, at acidic pH, the adsorption yield is almost equal to 16%, and it increases with increasing pH until reaching a

maximum corresponding to equilibrium at pH = 4, where the yield is equal to 97% (39). This can be explained by the fact that at low pH values, the surface of the adsorbent would be surrounded by  $H^+$ , which would decrease the interaction of  $Pb^{2+}$  with the sites of the adsorbent due to repulsive forces. The decrease in adsorption at low pH values may be due to the high concentration and high mobility of the  $H^+$ , which are preferentially adsorbed than metal ions (40). On the other hand, the gels' deflation at a more acidic pH prevents the diffusion of metal ions in the gel. With the increase in pH, the quantity of protons in solution decreases, the competition between  $H^+$  and  $Pb^{2+}$  for the occupation of surface sites becomes less strong, hence increasing adsorption yield.

*Effect of the temperature*

Temperature is a significant parameter in the adsorption process. To study the influence of this parameter, experiments were carried out at different temperatures (25, 35, 45, and 55 °C) using a thermostat. The resulting mixture was stirred until equilibrium. Figure 9 represents the effect of temperature in the performance of lead adsorption by the PAAM. Based on the results obtained, we find that the increase in temperature causes an increase in the adsorption efficiency (41). In fact, the increase in temperature leads to the expansion of the polymer's macromolecular chain, promoting the metal's adsorption. These results show that the adsorption process is probably endothermic.

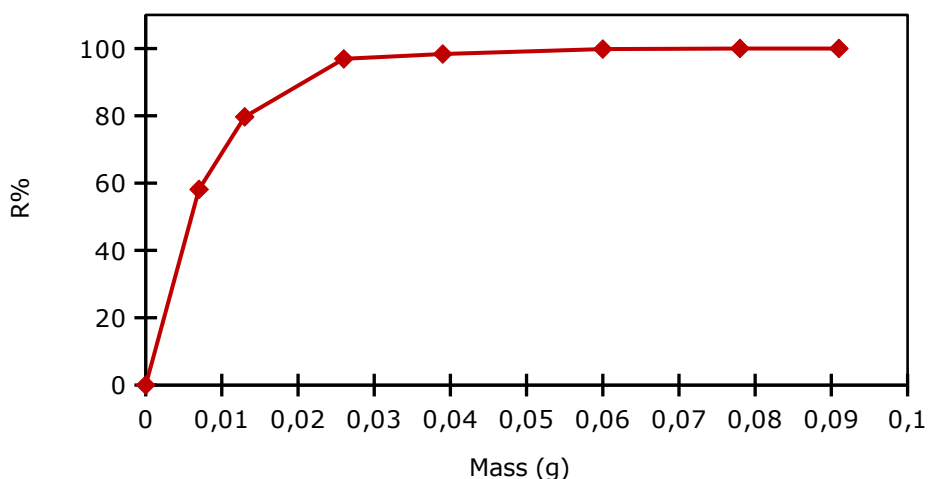


**Figure 7:** Effect of the mass of the PAAM polymer on the adsorption of lead ( $T=25\text{ }^{\circ}\text{C}$ ,  $[Pb^{2+}]=20\text{ ppm}$ ,  $pH=5$ ,  $t=3\text{ h}$ ,  $V=100\text{ mL}$ ).

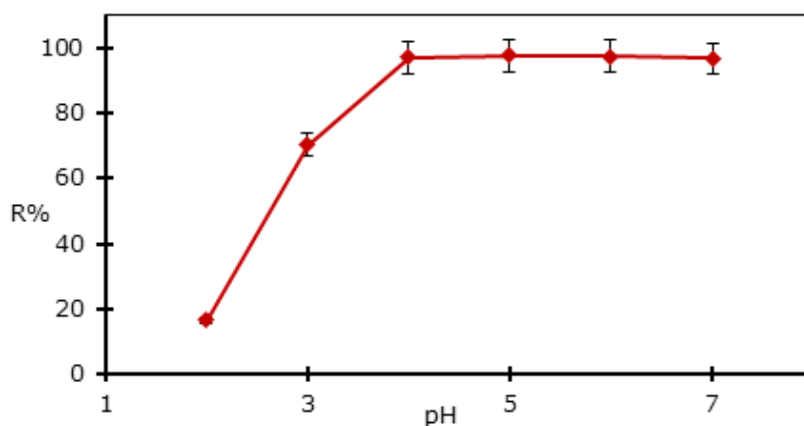


**Figure 8:** Effect of the pH on adsorption lead by PAAM (T=25 °C, m=0.026 g, V=100 mL, [Pb<sup>2+</sup>] =20 ppm).

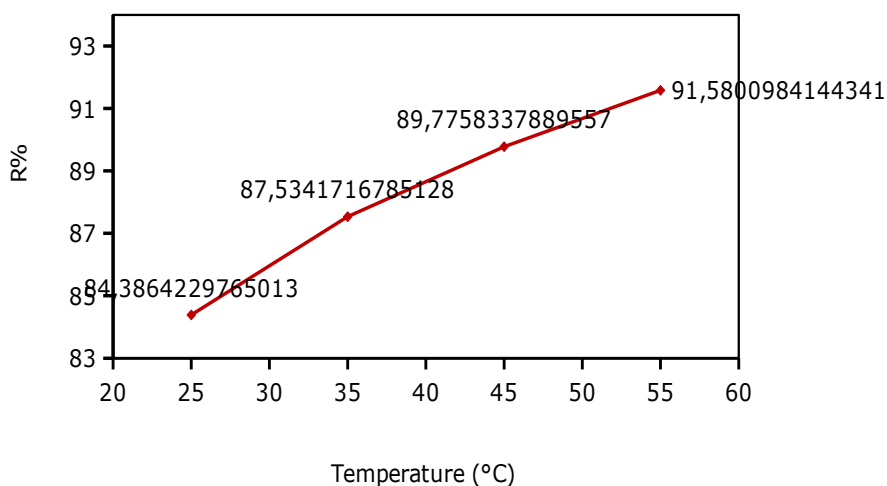


**Figure 9:** Effect of the temperature on lead adsorption by PAAM (m=0.026 g, V=100 mL, pH=5, [Pb<sup>2+</sup>]=20 ppm, t =3 h)

*Effects of ionic strength*

The effect of ionic strength on the sorption of lead ions onto PAAM was studied by conducting experiments at different concentrations of NaCl (25, 50, 100, 200, and 300 mg/L) (Figure 10). We observe from the figure that the amount of Pb ions

decreased with an increase in the ionic strength of the electrolyte solution. This can be explained, probably, by the competition of lead ions with other ions to adhere with the adsorbent. This result is confirmed by previous work concerned with water treatment (42,43).

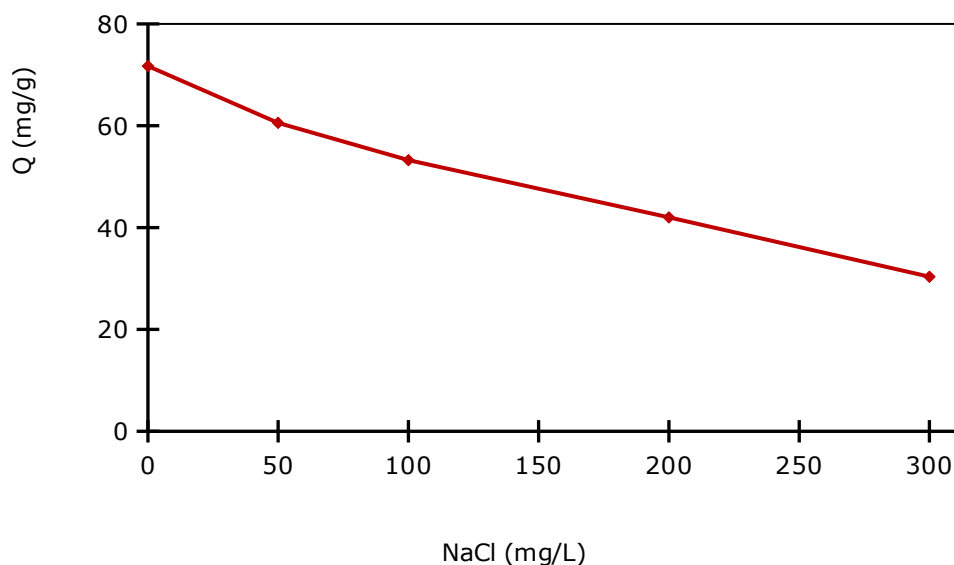


**Figure 10:** Effect of various ionic strength on lead adsorption by PAAM ( $m=0.026$  g,  $V=100$  mL,  $T= 25$  °C,  $pH=5$ ,  $[Pb] = 20$  ppm,  $t=3$  h).

#### *Effect of the initial lead concentration*

The initial concentration of the pollutant has an important influence on the retention capacity of the support. To study its effect, solutions of lead at different concentrations: 20, 50, 100, 150, 200, 300, and 500 ppm were considered. It appears from Figure 11 that the initial concentration of the metal actually influences the retention process. Indeed, the ability to fix the ions increases as the lead solution's content increases. A maximum is

obtained for a concentration close to 200 ppm, where the retention capacity of lead reaches 442.31 mg/g. This can be explained by the depletion of all existing active sites at the surface of the support (44). Besides, the increase in concentration induces the increase in the driving force of the concentration gradient, thus increasing the diffusion of dye molecules in solution through the surface of the adsorbent (45).

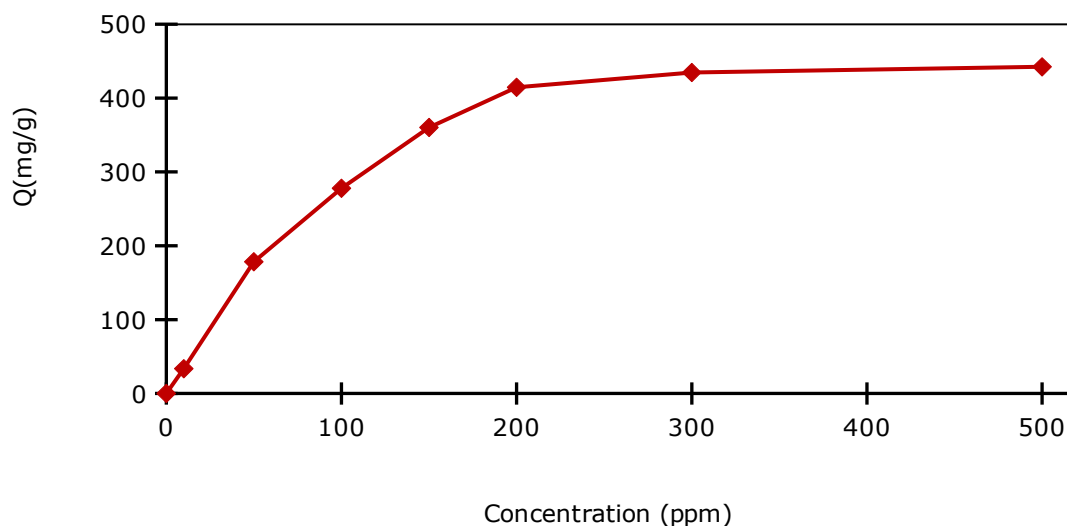


**Figure 11:** Adsorption capacity versus the initial lead concentration.

#### **Isotherms and Kinetics of Lead Adsorption by PAAM**

##### *Adsorption isotherm*

The adsorption capacity of lead by PAAM gels was studied as a function of the initial lead

concentration. The experimental conditions are identical to those used previously. The initial concentration of lead varies from 20 to 500 ppm. The results obtained were modeled by two empirical models: Langmuir and Freundlich. These

two models provide a widely used tool for elucidating the adsorption mechanism and quantifying adsorbent/adsorbate affinity.

Figure 12 (a, b) represents the isotherms of lead adsorption by PAAM. It is observed that the adsorption is satisfactorily described by the Langmuir model ( $R^2 = 0.9994$ ), reflecting the homogeneous nature of the surface of this solid (PAAM).

Table 1 represents the various parameters calculated from the Langmuir and Freundlich

models. According to these results, it can be seen that the maximum adsorbed quantity obtained by the Langmuir model 454.54 mg/g is very close to that obtained experimentally 442.31 mg/g, the correlation coefficient  $R^2 = 0.9994$  is close to unity, and the separation factor  $R_L < 1$  implying that the adsorption of lead on PAAM is favorable (46). This reinforces the validity of the Langmuir model, which is based on monolayer coverage and the absence of interactions between the entities adsorbed on sites of the same nature. These results agree with previous work on other supports loaded with Pb, cited in the literature (47,48).

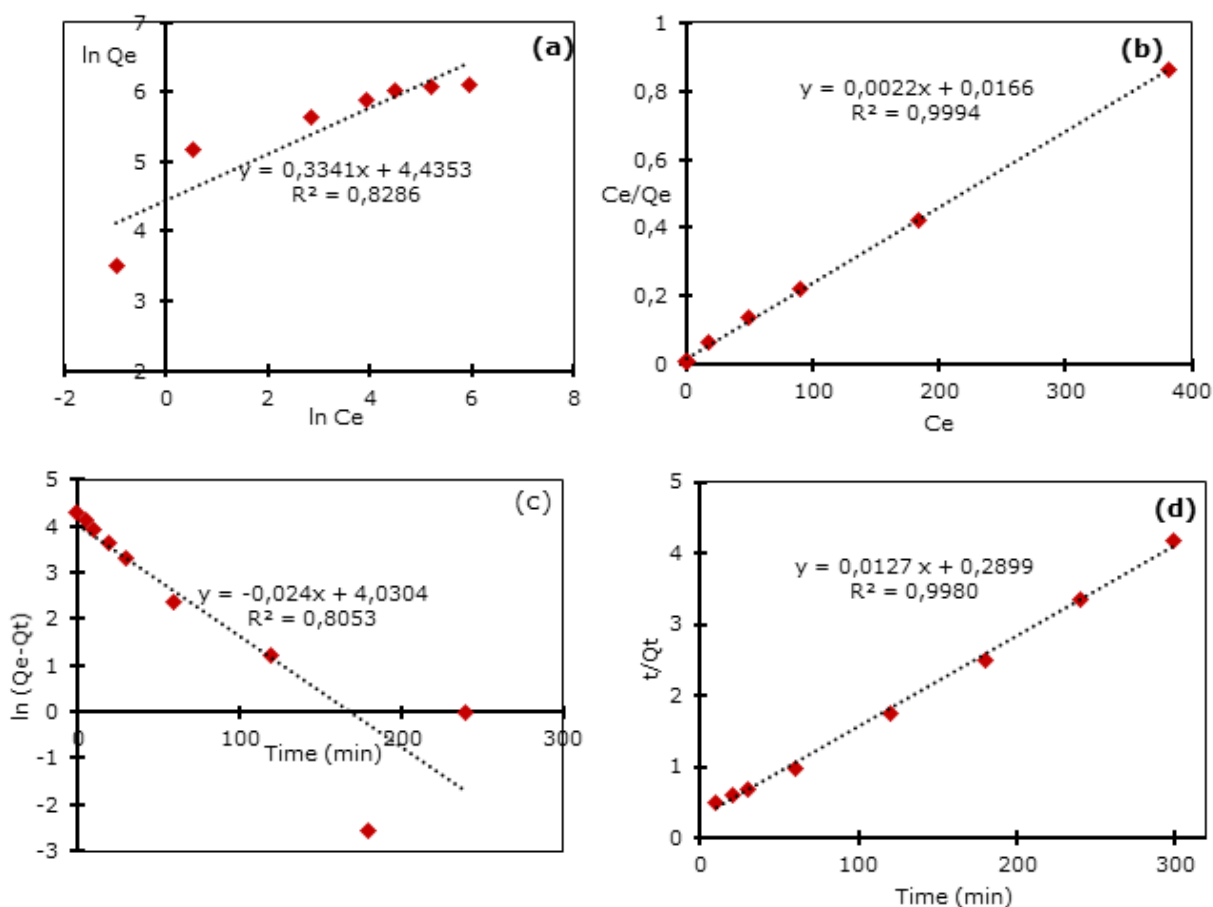


**Figure 12:** Freundlich (a), Langmuir (b) isotherms and Pseudo-first-order (c), Pseudo second-order (d) kinetics applied to lead<sup>2+</sup> ion adsorption by PAAM.

*Adsorption kinetics*

Two kinetic models were applied to describe the mechanism of lead adsorption by PAAM gels: Pseudo first-order kinetic model and pseudo second-order kinetic model (Figure 12 c, d). The purpose of applying these models is to provide general expressions capable of describing the adsorption kinetics of solutes on a surface.

Table 2 represents the various kinetic parameters calculated from the graphic representation of these models. The calculated kinetic parameters are K1, K2, and Qe (adsorption quantity) for both models. The value of the amount of lead adsorption calculated from the pseudo-second-order model is the closest to that determined experimentally, which indicates the suitability of using this model to describe the adsorption of lead by PAAM. The

correlation coefficient of the pseudo-second-order model is of the order of 0.998. For the pseudo-first-order model, the correlation coefficient is 0.8053. These data confirm that the pseudo-second-order kinetic model is the most reliable to describe the adsorption of lead by PAAM. This model suggests that the lead adsorption depends on the adsorbate and the adsorbent and that a chemisorption process is involved in this sorption and physisorption. This is in good agreement with previous work on other supports loaded with Pb, cited in the literature (49,50).

*Thermodynamic study*

Determining thermodynamic parameters is very important to understand the effect of temperature

on adsorption better. In principle, it can also predict the strength of the bonds between the adsorbent and the adsorbate.

Figure 13 shows the  $\ln K_d=f(1/T)$  curve for the adsorption of lead by PAAM. The thermodynamic parameters of this process are shown in Table 3. The standard enthalpy value is positive, which confirms that the adsorption process is endothermic. It is accepted that the binding energies of physical adsorption are generally between -20 and 0 kJ/mol, while the energies of a chemical bond are in the range of -80 to -400 kJ/mol (51). In our case, the enthalpy is equal to 18 kJ/mol, which means that the adsorption of lead by PAAM is physical in nature.

**Table 1:** Parameters of the Langmuir and Freundlich equations for lead adsorption by PAAM.

Langmuir isotherm				Freundlich isotherm			
$Q_{m, exp}$ (mg/g)	$Q_m$ (mg/g)	$K_L$ (L/mg)	$R^2$	$R_L$	$K_f$ (mg/g)	$1/n$	$R^2$
<b>442.32</b>	454.54	0.13	0.9994	0.453-0.0149	84.37	0.3341	0.8286

**Table 2:** Kinetics parameter of lead adsorption by PAAM.

Pseudo-first-order				Pseudo-second-order		
$Q_{max}$ (mg/g)	$K_1$ (g/mg.min)	$Q_e$ (mg/g)	$R^2$	$K_2$ (g/mg.min)	$Q_e$ (mg/g)	$R^2$
<b>71.99</b>	0.024	56.28	0.8053	0.00055461	78.86	0.9980

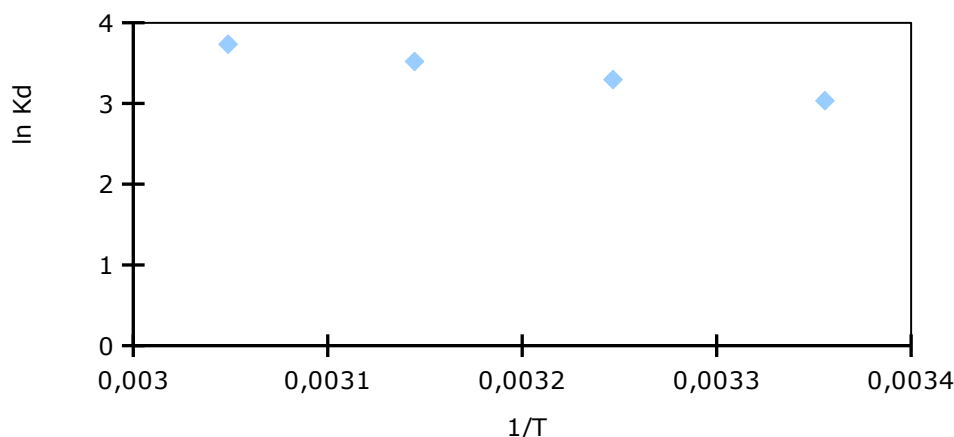


**Figure 13:** Van't Hoff plot of lead adsorption by PAAM.

**Table 3:** Thermodynamic parameters of lead adsorption by PAAM.

T (K)	$\Delta G$ (J/mol)	$\Delta H$ (J/mol)	$\Delta S$ (J/k,mol)	$R^2$
<b>298</b>	-7355.03			
<b>308</b>	-8257.65	18879.43	88.62	0.9996
<b>318</b>	-9103.93			
<b>328</b>	-9961.30			

### Desorption of Lead Ions from PAAM

Among the characteristics and requirements that an adsorbent must have is its regeneration and reuse in adsorption. In fact, the adsorbents must be able to be regenerated by elution to recover the adsorbed metal. The results showed HCl is effective in removing the adsorbed metal. Figure 14 shows the adsorption and desorption yields of

metals during the five cycles of adsorption-desorption. It can be seen that the rate of desorption was generally above 97%, and the adsorption efficiency was hardly affected. These results indicate that the polyacrylamide beads would have great potential in practical applications for the removal of metal ions as well as for their recovery.

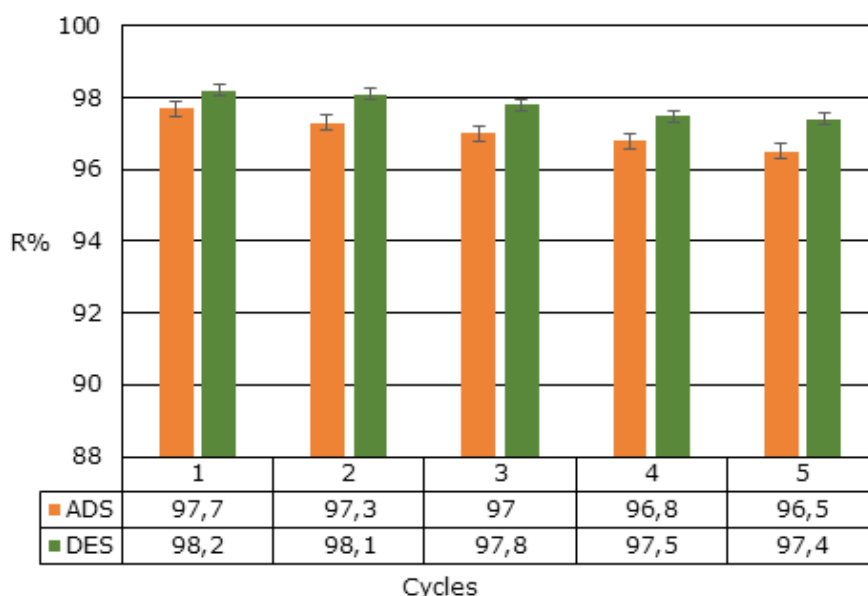


**Figure 14:** Adsorption and desorption of lead by PAAM.

To better visualize the desorption process, samples were taken from the HCl solution during desorption, diluted, and then dosed. Changes in the concentration of lead over time are shown in Figure 15. The equilibrium is reached at approximately 90 minutes, which shows that the desorption kinetics is 2 times faster than the adsorption kinetics. This can be explained by the low swelling of the metal-laden PAAM, which decreases the path traveled inside the gel and accelerates the diffusion of species during desorption.

### Adsorption of Bivalent Cations by PAAM

To study the adsorption of other metals by PAAM, we introduced a magnitude of 0.026 g of PAAM gel in  $Pb^{2+}$ ,  $Cd^{2+}$ , and  $Cu^{2+}$  solutions with the same concentration ( $10^{-4}$  M) (Figure 16). The curves obtained show quick adsorption for the three ions for the first 30 minutes. However, the equilibrium

is reached after 3 hours of contact regardless of the adsorbed metal. The maximum adsorption amounts reached are 71.6 mg/g, 46.8 mg/g and 28 mg/g of  $Pb^{2+}$ ,  $Cu^{2+}$  and  $Cd^{2+}$ , respectively. It is clear that the PAAM adsorb Pb ions more than other metallic ions. These results can be attributed to the affinity of the polymeric hydrogel vis-a-vis certain metals; in fact, it can be influenced by the valency and the ionic size of the heavy metals once hydrated (52,53). At equal valence, a low-hydrated cation has more affinity than a high-hydrated cation. The smaller the non-hydrated radius of a cation, the stronger its hydrated radius, because it attracts water molecules more strongly. At equal valence, therefore, it is the voluminous cations that will be fixed preferentially and lead ions are voluminous, more than copper and cadmium, that's why they are more adsorbed by the adsorbent.

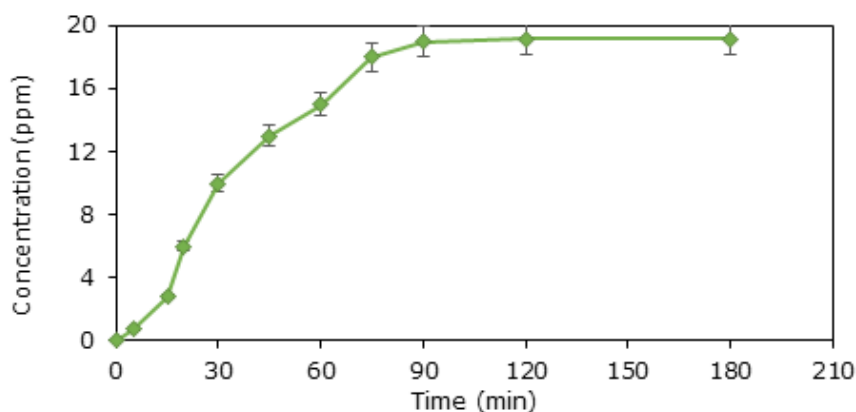


Figure 15: Kinetics desorption of lead by PAAM using HCl as eluent.

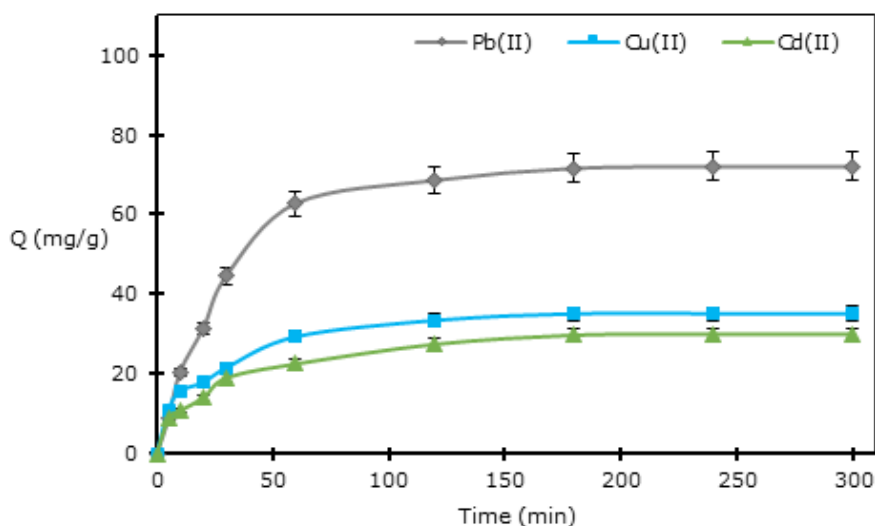


Figure 16: Absorption capacity of divalent cations by PAAM versus time.

**Comparison with Other Adsorbents**

It is found that the adsorption amount of PAAM among the highest capacities of hydrogels, and herein lies the novelty and the importance of using

PAAM hydrogel in heavy metal adsorption. Table 4 has shown various hydrogels that have been studied previously for the removal of Pb ions.

**Table 4:** Comparative study of the adsorption of PAAM by different hydrogels.

Adsorbent	Adsorption capacity (mg/g)	Reference
Chitosan hydrogel beads	124.2	(54)
Poly(N-isopropylacrylamide-co-benzo18-crown-6-acrylamide)	142	(55)
bentonite/ sodium lignosulfonate graft-polymerized with acrylamide and maleic anhydride (BLPAMA)	218.04	(56)
Acid hydrolysis lignin-g-poly-(acrylic acid)	235	(57)
poly (acrylamide-co-itaconic acid)/multi-walled carbon nanotubes (P(AAm-co-IA)/MWCNTs)	107.36	(58)
Polyacrylamide	442.31	Present work
poly (AA)-bentonitesuperabsorbent composites (SAC)	1666.67	(59)

**CONCLUSION**

Given the intense interest in superabsorbent polymers in recent years, we tested the potential of polyacrylamide to adsorb lead. The study of the influence of the experimental parameters showed that the equilibrium was reached after 180 minutes, and the decrease in the concentration of lead was accompanied by an increase in the pH of the solution, which implies that the gel equilibrates with the metal solution by fixing H<sup>+</sup> protons. The increase in pH promoted the adsorption of the metal; a maximum was reached from pH = 4. At high lead concentrations, the gel reached its maximum metal load, about 442.31 mg/g.

Adsorption isotherm was studied on the considered concentration interval where the Langmuir model well represents experimental data. Linear representations of kinetic curves have shown that the pseudo-second-order model gives the best match compared to the pseudo-first-order.

**ACKNOWLEDGMENT**

The authors gratefully acknowledge the Technical Support Units for Scientific Research (UATRS) under the National Center for Scientific and Technical Research (CNRST), especially to Hanae OUADDARI for the analytical services and instrumentations.

**REFERENCES**

1. Burakov AE, Galunin EV, Burakova IV, Kucherova AE, Agarwal S, Tkachev AG, et al. Adsorption of heavy metals on conventional and nanostructured materials for wastewater treatment purposes: A review. *Ecotoxicology and Environmental Safety*. 2018 Feb;148:702–12. DOI: <https://doi.org/10.1016/j.ecoenv.2017.11.034>.
2. Boudrahem F, Aissani-Benissad F, Soualah A. Adsorption of Lead(II) from Aqueous Solution by Using Leaves of Date Trees As an Adsorbent. *J Chem Eng Data*. 2011 May 12;56(5):1804–12. DOI: <https://doi.org/10.1021/jc100770j>.
3. Akpor O, Muchie M. Remediation of heavy metals in drinking water and wastewater treatment systems: Processes and applications. *Int J Phys Sci*. 2010;5(12):1807–17. DOI: <https://doi.org/10.5897/IJPS.9000482>.
4. Es-sahbany H, Berradi M, Nkhili S, Hsissou R, Allaoui M, Loutfi M, et al. Removal of heavy metals (nickel) contained in wastewater-models by the adsorption technique on natural clay. *Materials Today: Proceedings*. 2019;13:866–75. DOI: <https://doi.org/10.1016/j.matpr.2019.04.050>.

5. Dhir B, Kumar R. Adsorption of Heavy Metals by Salvinia Biomass and Agricultural Residues. *International journal of environmental research (IJER)*. 2010;4(3):427–32. URL: <https://www.sid.ir/en/Journal/ViewPaper.aspx?ID=182202>.

6. Es-sahbany H, Hsissou R, El Hachimi ML, Allaoui M, Nkhili S, Elyoubi MS. Investigation of the adsorption of heavy metals (Cu, Co, Ni and Pb) in treatment synthetic wastewater using natural clay as a potential adsorbent (Sale-Morocco). *Materials Today: Proceedings*. 2021;45:7290–8. DOI: <https://doi.org/10.1016/j.matpr.2020.12.1100>.

7. Siqueira DF, Reiter J, Breiner U, Stadler R, Stamm M. Competitive Adsorption of Functionalized Polymers. *Langmuir*. 1996 Jan;12(4):972–9. DOI: <https://doi.org/10.1021/la950519m>.

8. Huang Y, Zhao W, Zhang X, Peng H, Gong Y. Thiol-ene synthesis of thioether/carboxyl-functionalized polymers for selective adsorption of silver (I) ions. *Chemical Engineering Journal*. 2019 Nov;375:121935. DOI: <https://doi.org/10.1016/j.cej.2019.121935>.

9. Es-sahbany H, El Hachimi ML, Hsissou R, Belfaquir M, Es-sahbany K, Nkhili S, et al. Adsorption of heavy metal (Cadmium) in synthetic wastewater by the natural clay as a potential adsorbent (Tangier-Tetouan-Al Hoceima – Morocco region). *Materials Today: Proceedings*. 2021;45:7299–305. DOI: <https://doi.org/10.1016/j.matpr.2020.12.1102>.

10. Kim S, Iyer G, Nadarajah A, Frantz J, Spongberg A. Polyacrylamide Hydrogel Properties for Horticultural Applications. *Int J Polym Anal Character*. 2010 Apr;15(5):307–18. DOI: <https://doi.org/10.1080/1023666X.2010.493271>.

11. Kaşgöz H, Özgümüş S, Orbay M. Modified polyacrylamide hydrogels and their application in removal of heavy metal ions. *Polymer*. 2003 Mar;44(6):1785–93. DOI: [https://doi.org/10.1016/S0032-3861\(03\)00033-8](https://doi.org/10.1016/S0032-3861(03)00033-8).

12. Lira LM, Martins KA, Torresi SIC de. Structural parameters of polyacrylamide hydrogels obtained by the Equilibrium Swelling Theory. *European Polymer Journal*. 2009 Apr;45(4):1232–8. DOI: <https://doi.org/10.1016/j.eurpolymj.2008.12.022>.

13. Bertrand T, Peixinho J, Mukhopadhyay S, MacMinn CW. Dynamics of Swelling and Drying in a

- Spherical Gel. *Phys Rev Applied*. 2016 Dec;6(6):064010. DOI: <https://doi.org/10.1103/PhysRevApplied.6.064010>.
14. Moreno-Sader K, García-Padilla A, Realpe A, Acevedo-Morantes M, Soares JBP. Removal of Heavy Metal Water Pollutants (Co 2+ and Ni 2+ ) Using Polyacrylamide/Sodium Montmorillonite (PAM/Na-MMT) Nanocomposites. *ACS Omega*. 2019 Jun 30;4(6):10834–44. DOI: <https://doi.org/10.1021/acsomega.9b00981>.
15. Wiśniewska M, Fijałkowska G, Szewczuk-Karpisz K. The mechanism of anionic polyacrylamide adsorption on the montmorillonite surface in the presence of Cr(VI) ions. *Chemosphere*. 2018 Nov;211:524–34. DOI: <https://doi.org/10.1016/j.chemosphere.2018.07.198>.
16. Ramadan H, Ghanem A, El-Rassy H. Mercury removal from aqueous solutions using silica, polyacrylamide and hybrid silica-polyacrylamide aerogels. *Chemical Engineering Journal*. 2010 May 1;159(1-3):107–15. DOI: <https://doi.org/10.1016/j.cej.2010.02.051>.
17. Pal P, Banat F. Removal of Contaminants from Industrial Lean Amine Solvent Using Polyacrylamide Hydrogels Optimized by Response Surface Methodology. *Adsorption Science & Technology*. 2015 Jan;33(1):9–24. DOI: <https://doi.org/10.1260/0263-6174.33.1.9>.
18. Moulay S, Bensacia N, Garin F, Fechete I, Boos A. Polyacrylamide-Based Sorbents for the Removal of Hazardous Metals. *Adsorption Science & Technology*. 2013 Aug;31(8):691–709. DOI: <https://doi.org/10.1260/0263-6174.31.8.691>.
19. Ouass A, Essaadaoui Y, Kadiri L, Lebkiri I, Lafreme C, Cherkaoui M, et al. Adsorption of Cr (III) from aqueous solution by two forms of a superabsorbant polymer: parametric study and effect of activation mode. Boukdir A, El Mabrouki M, editors. *E3S Web Conf*. 2018;37:02001. DOI: <https://doi.org/10.1051/e3sconf/20183702001>.
20. Kadiri L, Lebkiri A, Rifi EH, Ouass A, Essaadaoui Y, Lebkiri I, et al. Kinetic studies of adsorption of Cu (II) from aqueous solution by coriander seeds (*Coriandrum Sativum*). Boukdir A, El Mabrouki M, editors. *E3S Web Conf*. 2018;37:02005. DOI: <https://doi.org/10.1051/e3sconf/20183702005>.
21. Lagergren S. Zur theorie der sogenannten adsorption gelöster stoffe. *Kungliga Svenska Vetenskapsakademiens Handlingar*. 1898;24(4):1–39.
22. Essaadaoui Y, Lebkiri A, Rifi EH, Kadiri L, Ouass A. Adsorption of cobalt from aqueous solutions onto Bark of Eucalyptus. *Mediterr J Chem*. 2018 Sep 15;7(2):145–55. DOI: <https://doi.org/10.13171/mjc72/01808150945-essaadaoui>.
23. Essaadaoui Y, Lebkiri A, Rifi E, Kadiri L, Ouass A. Adsorption of lead by modified Eucalyptus camaldulensis barks: equilibrium, kinetic and thermodynamic studies. *DWT*. 2018;111:267–77. DOI: <https://doi.org/10.5004/dwt.2018.22191>.
24. Freundlich H. Über die adsorption in lösungen. *Z Phys Chem*. 1907;57(1):385–470.
25. Huang J, Liu Y, Jin Q, Wang X, Yang J. Adsorption studies of a water soluble dye, Reactive Red MF-3B, using sonication-surfactant-modified attapulgite clay. *Journal of Hazardous Materials*. 2007 May;143(1-2):541–8. DOI: <https://doi.org/10.1016/j.jhazmat.2006.09.088>.
26. Chakir A, Bessiere J, Kacemi KEL, Marouf B. A comparative study of the removal of trivalent chromium from aqueous solutions by bentonite and expanded perlite. *Journal of Hazardous Materials*. 2002 Nov;95(1-2):29–46. DOI: [https://doi.org/10.1016/S0304-3894\(01\)00382-X](https://doi.org/10.1016/S0304-3894(01)00382-X).
27. Baron RI, Bercea M, Avadanei M, Lisa G, Biliuta G, Coseri S. Green route for the fabrication of self-healable hydrogels based on tricarboxy cellulose and poly(vinyl alcohol). *International Journal of Biological Macromolecules*. 2019 Feb;123:744–51. DOI: <https://doi.org/10.1016/j.ijbiomac.2018.11.107>.
28. Kadiri L, Lebkiri A, Rifi E, Essaadaoui Y, Ouass A, Lebkiri I, et al. Characterization of coriander seeds "coriandrum sativum." *International Journal of Scientific and Engineering Research*. 2017;8(7):2303–8.
29. Yuan N, Xu L, Zhang L, Ye H, Zhao J, Liu Z, et al. Superior hybrid hydrogels of polyacrylamide enhanced by bacterial cellulose nanofiber clusters. *Materials Science and Engineering: C*. 2016 Oct;67:221–30. DOI: <https://doi.org/10.1016/j.msec.2016.04.074>.
30. Liu R, Liang S, Tang X-Z, Yan D, Li X, Yu Z-Z. Tough and highly stretchable graphene oxide/polyacrylamide nanocomposite hydrogels. *J Mater Chem*. 2012;22(28):14160. DOI: <https://doi.org/10.1039/c2jm32541a>.

31. Zhou C, Wu Q, Lei T, Negulescu II. Adsorption kinetic and equilibrium studies for methylene blue dye by partially hydrolyzed polyacrylamide/cellulose nanocrystal nanocomposite hydrogels. *Chemical Engineering Journal*. 2014 Sep;251:17–24. DOI: <https://doi.org/10.1016/j.cej.2014.04.034>.
32. Yang Z, Yang H, Jiang Z, Cai T, Li H, Li H, et al. Flocculation of both anionic and cationic dyes in aqueous solutions by the amphoteric grafting flocculant carboxymethyl chitosan-graft-polyacrylamide. *Journal of Hazardous Materials*. 2013 Jun;254–255:36–45. DOI: <https://doi.org/10.1016/j.jhazmat.2013.03.053>.
33. Wei X, Tao J, Li M, Zhu B, Li X, Ma Z, et al. Polyacrylamide-based inorganic hybrid flocculants with self-degradable property. *Materials Chemistry and Physics*. 2017 May;192:72–7. DOI: <https://doi.org/10.1016/j.matchemphys.2017.01.064>.
34. Yang F, Li G, He Y-G, Ren F-X, Wang G. Synthesis, characterization, and applied properties of carboxymethyl cellulose and polyacrylamide graft copolymer. *Carbohydrate Polymers*. 2009 Aug;78(1):95–9. DOI: <https://doi.org/10.1016/j.carbpol.2009.04.004>.
35. Ismi I, Rifi E, Lebkiri A, Oudda H. Spectral characterization of PA–Cu under two polymeric forms and their complex PA–Cu. *J Mater Environ Sci*. 2015;6(2):343–8.
36. Vijayalakshmi K, Devi BM, Latha S, Gomathi T, Sudha PN, Venkatesan J, et al. Batch adsorption and desorption studies on the removal of lead (II) from aqueous solution using nanochitosan/sodium alginate/microcrystalline cellulose beads. *International Journal of Biological Macromolecules*. 2017 Nov;104:1483–94. DOI: <https://doi.org/10.1016/j.ijbiomac.2017.04.120>.
37. Anirudhan TS, Unnithan MR, Divya L, Senan P. Synthesis and characterization of polyacrylamide-grafted coconut coir pith having carboxylate functional group and adsorption ability for heavy metal ions. *J Appl Polym Sci*. 2007 Jun 15;104(6):3670–81. DOI: <https://doi.org/10.1002/app.25002>.
38. Zendejdel M, Barati A, Alikhani H. Removal of heavy metals from aqueous solution by poly(acrylamide-co-acrylic acid) modified with porous materials. *Polym Bull*. 2011 Jul;67(2):343–60. DOI: <https://doi.org/10.1007/s00289-011-0464-5>.
39. Li N, Bai R, Liu C. Enhanced and Selective Adsorption of Mercury Ions on Chitosan Beads Grafted with Polyacrylamide via Surface-Initiated Atom Transfer Radical Polymerization. *Langmuir*. 2005 Dec;21(25):11780–7. DOI: <https://doi.org/10.1021/la051551b>.
40. Cao J, Tan Y, Che Y, Xin H. Novel complex gel beads composed of hydrolyzed polyacrylamide and chitosan: An effective adsorbent for the removal of heavy metal from aqueous solution. *Bioresource Technology*. 2010 Apr;101(7):2558–61. DOI: <https://doi.org/10.1016/j.biortech.2009.10.069>.
41. Payne KB, Abdel-Fattah TM. Adsorption of Divalent Lead Ions by Zeolites and Activated Carbon: Effects of pH, Temperature, and Ionic Strength. *Journal of Environmental Science and Health, Part A*. 2004 Dec 27;39(9):2275–91. DOI: <https://doi.org/10.1081/ESE-200026265>.
42. Xiao Y, Xue Y, Gao F, Mosa A. Sorption of heavy metal ions onto crayfish shell biochar: Effect of pyrolysis temperature, pH and ionic strength. *Journal of the Taiwan Institute of Chemical Engineers*. 2017 Nov;80:114–21. DOI: <https://doi.org/10.1016/j.jtice.2017.08.035>.
43. El-Bayaa AA, Badawy NA, AlKhalik EA. Effect of ionic strength on the adsorption of copper and chromium ions by vermiculite pure clay mineral. *Journal of Hazardous Materials*. 2009 Oct 30;170(2–3):1204–9. DOI: <https://doi.org/10.1016/j.jhazmat.2009.05.100>.
44. Yu B, Zhang Y, Shukla A, Shukla SS, Dorris KL. The removal of heavy metals from aqueous solutions by sawdust adsorption – removal of lead and comparison of its adsorption with copper. *Journal of Hazardous Materials*. 2001 Jun;84(1):83–94. DOI: [https://doi.org/10.1016/S0304-3894\(01\)00198-4](https://doi.org/10.1016/S0304-3894(01)00198-4).
45. Deniz F, Saygideger SD. Investigation of adsorption characteristics of Basic Red 46 onto gypsum: Equilibrium, kinetic and thermodynamic studies. *Desalination*. 2010 Nov;262(1–3):161–5. DOI: <https://doi.org/10.1016/j.desal.2010.05.062>.
46. Ouass A, Ismi I, Elaidi H, Lebkiri A, Cherkaoui M, Rifi E. Mathematical Modeling Of The Adsorption Of Trivalent Chromium By The Sodium Polyacrylate Beads. *J Mater Environ Sci*. 2017;8:3448–56.
47. Largitte L, Pasquier R. A review of the kinetics adsorption models and their application to the adsorption of lead by an activated carbon. *Chemical Engineering Research and Design*. 2016 May;109:495–504. DOI: <https://doi.org/10.1016/j.cherd.2016.02.006>.

48. Sekar M, Sakthi V, Rengaraj S. Kinetics and equilibrium adsorption study of lead(II) onto activated carbon prepared from coconut shell. *Journal of Colloid and Interface Science*. 2004 Nov;279(2):307-13. DOI: <https://doi.org/10.1016/j.jcis.2004.06.042>.
49. Robati D. Pseudo-second-order kinetic equations for modeling adsorption systems for removal of lead ions using multi-walled carbon nanotube. *J Nanostruct Chem*. 2013 Dec;3(1):55. DOI: <https://doi.org/10.1186/2193-8865-3-55>.
50. Özacar M, Şengil İA, Türkmenler H. Equilibrium and kinetic data, and adsorption mechanism for adsorption of lead onto valonia tannin resin. *Chemical Engineering Journal*. 2008 Sep;143(1-3):32-42. DOI: <https://doi.org/10.1016/j.cej.2007.12.005>.
51. Rathinam A, Maharshi B, Janardhanan SK, Jonnalagadda RR, Nair BU. Biosorption of cadmium metal ion from simulated wastewaters using *Hypnea valentiae* biomass: A kinetic and thermodynamic study. *Bioresource Technology*. 2010 Mar;101(5):1466-70. DOI: <https://doi.org/10.1016/j.biortech.2009.08.008>.
52. Fifi U, Winiarski T, Emmanuel E. Assessing the Mobility of Lead, Copper and Cadmium in a Calcareous Soil of Port-au-Prince, Haiti. *IJERPH*. 2013 Nov 4;10(11):5830-43. DOI: <https://doi.org/10.3390/ijerph10115830>.
53. Gomes PC, Fontes MPF, da Silva AG, de S. Mendonça E, Netto AR. Selectivity Sequence and Competitive Adsorption of Heavy Metals by Brazilian Soils. *Soil Sci Soc Am J*. 2001 Jul;65(4):1115-21. DOI: <https://doi.org/10.2136/sssaj2001.6541115x>.
54. Yan WL, Bai R. Adsorption of lead and humic acid on chitosan hydrogel beads. *Water Research*. 2005 Feb;39(4):688-98. DOI: <https://doi.org/10.1016/j.watres.2004.11.007>.
55. Ju X-J, Zhang S-B, Zhou M-Y, Xie R, Yang L, Chu L-Y. Novel heavy-metal adsorption material: ion-recognition P(NIPAM-co-BCAm) hydrogels for removal of lead(II) ions. *Journal of Hazardous Materials*. 2009 Aug 15;167(1-3):114-8. DOI: <https://doi.org/10.1016/j.jhazmat.2008.12.089>.
56. Yao Q, Xie J, Liu J, Kang H, Liu Y. Adsorption of lead ions using a modified lignin hydrogel. *J Polym Res*. 2014 Jun;21(6):465. DOI: <https://doi.org/10.1007/s10965-014-0465-9>.
57. Sun Y, Ma Y, Fang G, Li S, Fu Y. Synthesis of Acid Hydrolysis Lignin-g-Poly-(Acrylic Acid) Hydrogel Superabsorbent Composites and Adsorption of Lead Ions. *BioResources*. 2016 May;11(3):5731-42. URL: <https://ojs.cnr.ncsu.edu/index.php/BioRes/article/view/7960>.
58. Mohammadinezhad A, Marandi GB, Farsadrooh M, Javadian H. Synthesis of poly(acrylamide-co-itaconic acid)/MWCNTs superabsorbent hydrogel nanocomposite by ultrasound-assisted technique: Swelling behavior and Pb (II) adsorption capacity. *Ultrasonics Sonochemistry*. 2018 Dec;49:1-12. DOI: <https://doi.org/10.1016/j.ultsonch.2017.12.028>.
59. Bulut Y, Akçay G, Elma D, Serhatlı IE. Synthesis of clay-based superabsorbent composite and its sorption capability. *Journal of Hazardous Materials*. 2009 Nov;171(1-3):717-23. DOI: <https://doi.org/10.1016/j.jhazmat.2009.06.067>.





## Pharmacophore Modeling in Drug Discovery: Methodology and Current Status

Muhammed Tilahun Muhammed<sup>1\*</sup>  , Esin Aki-Yalcin<sup>2</sup>  

<sup>1</sup>Suleyman Demirel University, Faculty of Pharmacy, Department of Pharmaceutical Chemistry, 32000, Isparta, Turkey.

<sup>2</sup>Ankara University, Faculty of Pharmacy, Department of Pharmaceutical Chemistry, 06100, Ankara, Turkey.

**Abstract:** A pharmacophore describes the framework of molecular features that are vital for the biological activity of a compound. Pharmacophore models are built by using the structural information about the active ligands or targets. The pharmacophore models developed are used to identify novel compounds that satisfy the pharmacophore requirements and thus expected to be biologically active. Drug discovery process is a challenging task that requires the contribution of multidisciplinary approaches. Pharmacophore modeling has been used in various stages of the drug discovery process. The major application areas are virtual screening, docking, drug target fishing, ligand profiling, and ADMET prediction. There are several pharmacophore modeling programs in use. The user must select the right program for the right purpose carefully. There are new developments in pharmacophore modeling with the involvement of the other computational methods. It has been integrated with molecular dynamics simulations. The latest computational approaches like machine learning have also played an important role in the advances achieved. Moreover, with the rapid advance in computing capacity, data storage, software and algorithms, more advances are anticipated. Pharmacophore modeling has contributed to a faster, cheaper, and more effective drug discovery process. With the integration of pharmacophore modeling with the other computational methods and advances in the latest algorithms, programs that have better performance are emerging. Thus, improvements in the quality of the pharmacophore models generated have been achieved with this new developments.

**Keywords:** Computational approaches, computer-aided drug design, drug discovery, molecular modeling, pharmacophore.

**Submitted:** April 25, 2021. **Accepted:** June 25, 2021.

**Cite this:** Muhammed M, Aki-Yalçın E. Pharmacophore Modeling in Drug Discovery: Methodology and Current Status. JOTCSA. 2021;8(3):749-62.

**DOI:** <https://doi.org/10.18596/jotcsa.927426>.

**\*Corresponding author.** E-mail: [muh.tila@gmail.com](mailto:muh.tila@gmail.com)

### INTRODUCTION

Drug discovery and development is an expensive and complex process that takes more than 10 years (1). Drug design and discovery is a challenging task that needs the involvement of multidisciplinary approaches. Computer-aided drug design (CADD) methods are mainly employed in the early to mid-stage of the drug discovery process. CADD methods have contributed much to the drug discovery process with the rapid advance in computing capacity, data storage, software and algorithms (2-4). CADD has applications in target fishing, target

validation, hit identification and selection of the lead and its optimization (5). Herein, pharmacophore modeling, which is among the CADD methods, is reviewed.

A pharmacophore is a molecular frame that describes the vital features responsible for the biological activity of a molecule (6). Pharmacophore models are generated to increase the understanding about the ligand-protein interactions. They can be employed in identifying new molecules that satisfy the pharmacophore requirements and thus expected to be active (7). Pharmacophore models can be built

by using the structural information about the active ligands that bind to the target if the target structure is not available. This is known as ligand-based pharmacophore modeling approach (8). In conditions where the structure of the target is available, pharmacophore models can be built by using the structural properties of the target. This is known as structure-based pharmacophore modeling approach (Figure 1) (7).

There are several pharmacophore modeling tools in use. HipHop, HypoGen, Pharmer, PHASE, GASP,

PharmaGist, PharmMapper, MOE, LigandScout, and GALAHAD are examples of softwares used for pharmacophore model generation (5). With the use of such softwares, pharmacophore modeling has been employed at the various stages of the drug discovery process (9). Virtual screening, drug target fishing, ligand profiling, docking and ADMET (absorption, distribution, metabolism, excretion, toxicity) prediction are among its popular application areas (Figure 1) (10–12).

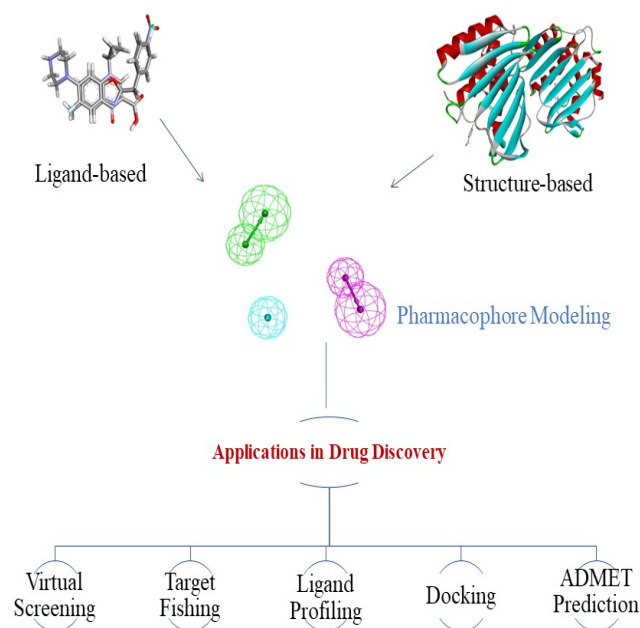


**Figure 1:** Overview of pharmacophore modeling and its applications.

The scope of the application of pharmacophore modeling in the drug discovery process has been increased by solving the challenges being faced. There are challenges in pharmacophore scoring functions used in virtual screening, modeling ligand flexibility, molecular alignment, and selection of training sets (13). In order to overcome these challenges the contribution of the other computational methods is crucial. Thus, the integration of pharmacophore modeling with the other computational methods is performed in a way that solves some of these limitations (14). For example, pharmacophore modeling has been integrated with molecular dynamics simulations. With this integration better pharmacophore models have been built (15). Furthermore, with the contribution of the latest computational approaches such as machine learning the advances in pharmacophore modeling has got momentum (16).

In this study, the general principles of pharmacophore modeling and its major application areas in the drug discovery process are explained. Moreover, the challenges faced and their probable

solutions through the advances in the computational methods are covered. This work aims to fill the information gap observed in pharmacophore modeling and to provide an updated information for the academia and the pharmaceutical industry.

## PRINCIPLES OF PHARMACOPHORE MODELING

The pharmacophore concept was introduced by Paul Ehrlich in the early 1900s. Then, the term pharmacophore was coined and defined as molecular features that bears (phoros) the necessary properties for the biological activity of a drug (pharmakon) (17). In those year's pharmacophore was understood as chemical or functional groups on a molecule that are responsible for the biological activity. IUPAC (International Union of Pure and Applied Chemistry) defined pharmacophore as the sum of steric and electronic properties that are required for the interaction of a molecule with a target and thus provide the biological activity (13).

Pharmacophore is a pattern of features responsible for the biological activity of a compound. This shows that the concept of pharmacophore is more of about features than chemical groups. Each atom or group of a compound that shows features associated with molecular recognition can be converted into a pharmacophore pattern (18,19). Molecular pharmacophore patterns can be hydrogen bond donors (HBD), hydrogen bond acceptors (HBA), positive features, negative features, aromatic rings, hydrophobic features and their combinations (20,21).

A pharmacophore model includes several patterns arranged in a particular 3D (three dimensional) pattern. Each pattern is depicted by a typical sphere containing radius that determines the deviation tolerance from the exact position. There are also various other displaying ways. These patterns can be displayed as a single pattern or their combinations (22).

There are two principal approaches of pharmacophore modeling that are used in the drug discovery process: Ligand-based pharmacophore modeling and structure-based pharmacophore modeling. In the ligand-based pharmacophore modeling approach, novel ligands are designed by using a set of active ligands available (23). This approach is employed if the target structure is not available. In a similar manner, the structure-based pharmacophore approach is employed when the structure of the target protein is available (24).

In the ligand-based pharmacophore modeling, first active ligands are identified by using the literature available or database search. The data set is split into a training set and test set. Then, feature analysis of the training set ligands is done. The common features are detected through the alignment of the active ligands. The next step is pharmacophore model generation and ranking of the generated models. Finally, pharmacophore model validation is performed and the best pharmacophore model is selected depending on the results obtained (23,25).

In the structure-based pharmacophore modeling, selection and preparation of target protein structure is the first step. The second step is binding site prediction. Then, complementary chemical features of the binding site amino acids and their layouts are identified by analyzing it carefully. After this, the pharmacophore features, which should be optimized by the adjusted tools in the programs employed, are generated. Finally, crucial pharmacophore features responsible for the activity are selected (7). LigandScout (26), MOE (27), Pocket v2 (28) and Snooker (29) are among the commonly used softwares for structure-based pharmacophore modeling. Similarly, there are various softwares and servers used in pharmacophore modeling. The commonly employed programs and servers are summarized in the alphabetical order (Table 1).

**Table 1:** Programs and servers used in pharmacophore modeling.

<b>Program/Server</b>	<b>Brief Description</b>
CATALYST-HipHop (30)	CATALYST is now part of the BIOVIA Discovery Studio. It consists of algorithms used in pharmacophore generation: HipHop and HypoGen. HipHop gives the alignment of active ligands against a specific target and finds the three dimensional arrangements of common features by overlapping various structures.
CATALYST-HypoGen (8)	It generates hypotheses that are able to estimate the activity of molecules quantitatively by using biological analysis data. Thus, it allows the correlation of the structural and activity data for pharmacophore modeling.
GALAHAD (31)	The program uses modified genetic algorithm and fixes certain shortcomings of the GASP program and thus increases its performance. It increases the computational speed by using prebuilt structures as a starting point.
GASP (32)	GASP is available in the SYBYL package. It uses genetic algorithm for the detection of pharmacophores. Unlike the other pharmacophore determinations, conformational search is carried out instantly in the GASP process and is an integral part of the program. A single low energy structure and random spinings are applied to examine conformational changes before superimposing on each input compound.
LigandScout (26)	Though it is possible to perform both structure-based and ligand-based pharmacophore modeling with LigandScout, it is among the first programs specialized in structure-based pharmacophore modeling. Especially, if the structure of the target protein is present in its ligand bound state, LigandScout is widely used.
MOE (27)	MOE is able to perform ligand-based and structure-based

	pharmacophore modeling. Model building is performed by the pairwise alignment of the active ligands. It is recommended to decrease the magnitude of the training set by grouping similar molecules.
PharmaGist (33)	It is a freely accessible server used in ligand-based pharmacophore generation. This web server detects pharmacophores via multiple flexible alignments of the input molecules.
Pharmer (34)	It is a pharmacophore method that makes searching based on the width and complexity of the query instead of the molecular library screened. It is a very fast method and its source code is available under an open-source license.
PharmMapper (35)	It is a freely accessible web server used for the identification of potential targets for the input ligands. It calculates pharmacophores by using semi-rigid pharmacophore mapping.
PHASE (36)	It is provided by Schrödinger package. It is a convenient approach used in drug discovery with or without its receptor structure. It creates a hypothesis from one or more ligands, protein-ligand complexes and apo proteins. It has a special algorithm designed for use in optimization of lead compounds and virtual screening.

### APPLICATIONS OF PHARMACOPHORE MODELING IN DRUG DISCOVERY

Pharmacophore modeling is employed in virtual screening, fishing drug targets, ligand profiling, docking, and ADMET prediction. New perspectives are also expected for various applications of pharmacophore modeling in the future due to the simplicity and versatility of the concept. In this way, besides the applications explained here, it may have applications in polypharmacology, drug repurposing and side effect prediction (24). In order to explain

the scope of the application of pharmacophore modeling in drug discovery, publications in the last two decades are depicted here (Figure 2). These figures are the average of the number of documents published in Scopus, PubMed, and ScienceDirect. They are obtained by searching in these search engines using 'pharmacophore modeling' and 'drug discovery' as keywords. As illustrated by the publications generated, the use of pharmacophore modeling in drug discovery has been increasing (Figure 2).

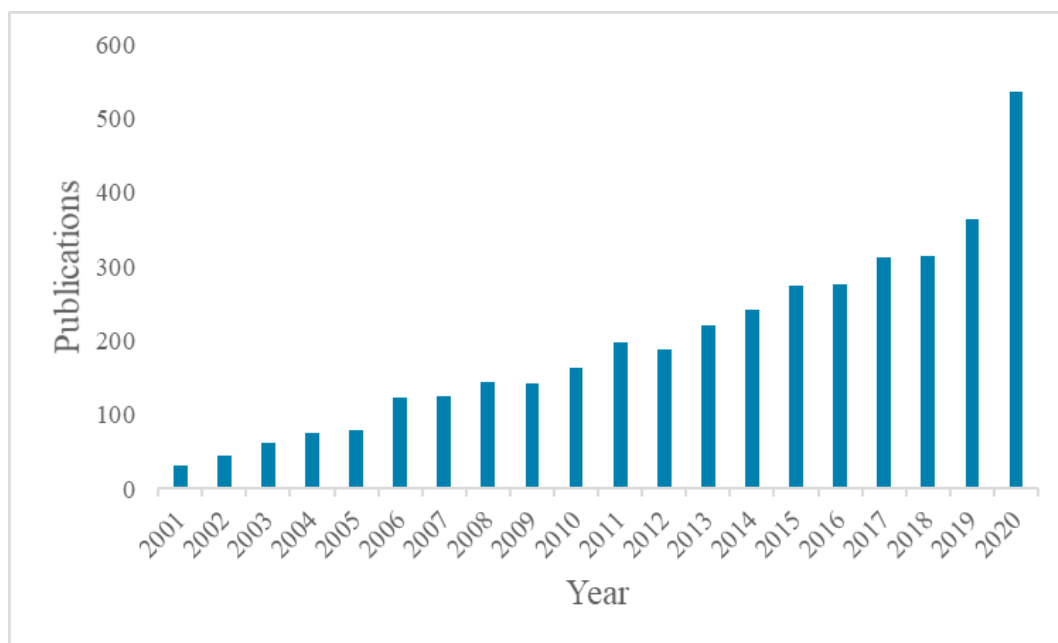


**Figure 2:** Publications in the application of pharmacophore modeling in drug discovery.

#### Applications in virtual screening

Pharmacophore modeling is frequently used in virtual screenings to identify compounds that trigger the intended biological activity. Therefore, researchers generate a pharmacophore model that

codes the 3D structure of the desired interaction pattern correctly. There are various options to create a pharmacophore model according to the information about the query protein target. When several active ligands and their inactive derivatives

are available, separating the ligand data into training set and test set, for the validation of the pharmacophore models generated, is a common practice (37).

For example, pharmacophore modeling and virtual screening together with docking were used to identify novel *Mycobacterium tuberculosis* InhA (MtInhA) inhibitors. In this work, pharmacophore models were built using 36 known crystal structures of MtInhA. By the combination of ligand-based and structure-based data, four pharmacophore features were used to filter compounds that can meet the essential binding features of MtInhA. The compounds obtained from the pharmacophore-based virtual screening of the ZINC database was docked to compare the binding mode and score of the screened compounds. After thorough analysis of the *in silico* results, experimental testing was performed on six selected ligands. Three of these compounds were found to be potential InhA inhibitors (38).

In a recent work, pharmacophore modeling was used to repurpose drugs available in DrugBank for the fight against COVID-19. In this work, some potential candidates that can be used in the fight against the Coronavirus pandemic were screened (39).

#### **Applications in drug target fishing**

When mechanism of action of drug molecules isn't well known, CADD can be used to elucidate the mechanism. Chemoinformatics-based similarity search tools are used for the identification of similar ligands with known mechanisms of action (40). However, pharmacophore modeling can also be used for other purposes that are different from searching for molecules with a pharmacophore query. The compound under investigation can be the query and the purpose here is to determine the pharmacophore model that may be suitable for the compound. Such pharmacophore models can be developed manually or retrieved from the databases (41). Furthermore, this method can be used to find a target for a particular molecule whose activity is still unknown. For example, many plant metabolites have been investigated and several possible drug targets have been found for them (42).

#### **Applications in ligand profiling**

Pharmacophore modeling is utilized in ligand profiling to estimate the possible targets, their adverse effects and suggest new targets for drugs. Not only structure-based pharmacophore modeling but also ligand-based pharmacophore modeling is utilized in ligand profiling however structure-based pharmacophore modeling is preferable (43). Pharmacophore modeling can be an alternative to molecular docking for profiling of ligands (44).

In a study conducted by using pharmacophore modeling-based ligand profiling, targets are assigned correctly. In this study, through both structure-based and ligand-based pharmacophores, 16 metabolites from *Ruta graveolens* were screened against a dataset of 2208 pharmacophore models. The computational results were validated by experimental setups with a special focus on AChE (acetylcholinesterase), HRV (human rhinovirus) coat protein and CB2 (cannabinoid receptor type 2). The experimental results confirmed the binding profile obtained from the pharmacophore modeling (42).

#### **Applications in docking**

There are various means to combine pharmacophore-based and docking-based molecular modeling approaches. This may overcome some of the drawbacks of both approaches and may lead to generate better results. Pharmacophore models can be used as initial filters to reduce the number of molecules to be docked, during the docking process as pharmacophore guides and after docking as filters to select ligands and rank the poses (45). Pharmacophore models are used as filters to determine molecules that meet the basic structural and chemical functionality requirements of the query before molecular docking (46). Before the evaluation using docking, pharmacophore is utilized as a search query to filter the ligand database. Pharmacophore-constrained docking is also applicable in docking softwares available and permits certain types of ligand-protein interactions to exist in the docking pose (47). Similarly, pharmacophore models can be used in post-docking filtering to identify the correct binding mode of a compound (47,48). Therefore, pharmacophore models can be used in enriching the top ranking docking results (49).

For instance, pharmacophore and docking were used to filter Chk-1 (checkpoint kinase-1) inhibitors from a compound database. The pharmacophore model was used as initial filter in searching for small compounds that can interact with the adenine region of Chk-1 through a HBA and a HBD features. Then, docking was undertaken by incorporating these interactions in the pose identification. For each ligand, multiple poses were saved and rescoring was carried out. At the end of the study, compounds with potential binding affinity were identified (50). In another recent study, pharmacophore modeling and docking were used to discover new dual adenosine A1/A2A receptor antagonists (51).

#### **Applications in ADMET**

Low ADMET property is among the principal reasons for the failure of drug development efforts (52). Therefore, the necessity of determining ADMET properties in the early stages of the drug development process is generally accepted. Pharmacophore modeling methods are used in

estimating ADMET properties early to reduce the failures in the endeavor to develop novel drugs (53).

It is possible to use pharmacophore models in identifying the likely interactions between the drug and its metabolizer enzymes by comparing the similar chemical features of tested compounds and drugs whose ADMET profile is well known (54). For instance, a pharmacophore model that is able to estimate the binding of a drug-like molecule to some CYP (cytochrome P450) enzymes was generated by using the interactions of known drugs with CYP enzymes and the probable degradation by these enzymes was assessed (55). Similarly, ADMET pharmacophore model was generated for the 5'-diphospho-glucuronosyl transferase, which are enzymes related to drug excretion (56).

### CHALLENGES IN PHARMACOPHORE MODELING

There are limitations in pharmacophore modeling that should be overcome. Therefore, there are new efforts to solve such problems and thus increase the quality of the applied modeling (57).

One of the application areas of pharmacophore modeling is virtual screening by pharmacophore. However, there are no good scoring functions used in virtual screening by pharmacophore (58). Here, the extent of matching of the ligand to the pharmacophore query is usually expressed by the RMSD between the patterns of the query and atoms of the compound. However, this measurement does not consider the similarity with known inhibitors and thus cannot estimate the overall similarity with the receptor. Therefore, compounds that match the pharmacophore query may differ from the other known inhibitors and contain functional groups that cannot bind with the receptor binding site. This makes the molecules inactive though they are perfect matches (59).

Another challenging problem in pharmacophore-based virtual screening is higher 'false positive' rates, that is, the virtual hit ligands may not be biologically active (13). This limitation may result from lack of the required hypothesis, quality of the pharmacophore model and discrepancies from the real biological conditions. Using expertises, exhaustive validation, including important information about the target and integrating with the other computational methods need to be considered to overcome this drawback (60).

Modeling ligand flexibility is also an important challenge. To solve this, structure analysis based on predetermined structure databases or during the pharmacophore process can be used. The method based on predetermined structure databases has been found to have a better performance (61). However, there are deficiencies in virtual screening

by pharmacophore that is performed using the method depending on predetermined structural databases. These databases consist of a few low energy structures per molecule. If the structure of an active ligand is missing, there is a possibility of not detecting it (62). This is especially true for various structures with rotatable bonds of small molecular functional groups like hydroxyl. It would be hard to differentiate the various rotations by RMSD value difference during structure generation. Generally, pharmacophore search tools can rotate such bonds during the matching process to find the right directional conformations of small flexible polar functional groups. The other limitation is the absence of a clear way to create a pharmacophore query (63).

Similarly, in structure-based pharmacophore modeling protein flexibility and ligand conformational flexibility are the major challenges. These limitations can be overcome by generating the pharmacophore model using docked complex built through flexible docking or by the generation and alignment of the models from protein-ligand molecular dynamics simulations simultaneously. In other words, combination of the structure-based approach with flexible docking and molecular dynamics simulations may alleviate these drawbacks (64). Furthermore, in structure-based approach generation of pharmacophore models is not straightforward. Especially, when various combination of features are likely, each pharmacophore model may lead to different set of compounds (65).

Molecular alignment is a difficult matter in pharmacophore modeling. Molecular alignments can be classified as point-based and feature-based approaches according to their basic nature. In the point-based algorithms, double atoms, fragments or chemical pattern points are overlapped using low square matching. The need for predetermined connection points is a major drawback of this approach. The feature-based algorithms use molecular domain determinants, often represented by Gaussian function sets, to create alignments. Development of new alignment methods continues (66).

The other challenging issue in the practical job is the right selection of the training set molecules. Although this issue is non-technical and straightforward, it may confuse users. The type of ligand molecule, size of the dataset and chemical variety have been shown to significantly affect the final pharmacophore model generated (13).

### ADVANCES IN PHARMACOPHORE MODELING

The scope and depth of the utilization of pharmacophore modeling in the drug discovery process are increasing (Figure 2). As a result, in

order to keep up with the new developments in the area, contribution of the other computational methods is in need (45). Herein, the latest methods in the integration of the pharmacophore modeling with molecular dynamics (MD) simulations and the contribution of machine learning to its advance are presented. The necessity of the integration of it with the other computational methods is apparent as it is demonstrated by its applications in the last three years (Table 2). Thus, more integrational approaches with the other complementary computational methods are anticipated (18). Moreover, the new approaches will help to overcome the difficulties encountered in pharmacophore modeling.

**Integration with molecular dynamics simulations**

Since ligands and receptors are dynamic bodies, it is clear that ligand-receptor complexes and thus the underlying interactions are also dynamic. Based on this concept, researchers began to integrate MD

simulations in the generation of better pharmacophore models (67). In recent years most of the pharmacophore modeling implementations in the drug discovery process are in combination with MD simulations (Table 2). Thus, the integration of pharmacophore generation with MD simulations will have a profound effect on the improvement of this approach.

HSRP (hydration site restricted pharmacophore), SILCS (site identification by ligand competitive saturation) and dynophores are examples for methods that use conformations obtained from MD simulations for pharmacophore building (16). In the HSRP approach, the aim is to reduce the number of pharmacophore features by determining hydration points on the surface of the protein (68). The SILCS method uses the binding hot spots of probe compounds in MD simulations for the generation of pharmacophore models (69). On the other hand, the dynophore represents the fully automated integration of MD simulations with the pharmacophore generation (70).

**Table 2:** Recent applications of pharmacophore modeling in combination with other computational methods.

<b>Aim of the Study</b>	<b>Major Findings</b>	<b>Other Computational Methods Used</b>
Identification of 20S proteasome inhibitors (71)	Five promising compounds that might inhibit the $\beta$ 5 subunit of 20S proteasome were identified.	Virtual screening, molecular docking, and MD simulations
Identification of new <i>Mycobacterium tuberculosis</i> MurG inhibitors (72)	Ten potential inhibitors of MurG were identified.	Homology modeling, virtual screening, molecular docking, and MD simulations
Development of inhibitors against HER family proteins (73)	A lead compound with better properties than the reference ligand, afatinib, was found.	Molecular docking, ADMET property analysis, virtual screening and MD simulations
Identification of novel caspase-1 inhibitors (74)	Four compounds that can be leads for the development of new anti-inflammatory agents were identified.	Virtual screening, molecular docking, MD simulations and ADMET property analysis
Identification of novel compounds that inhibit TNF $\alpha$ and/or TNFR1 (75)	Fifteen promising leading compounds that can serve as novel TNF $\alpha$ and/or TNFR1 inhibitors were identified.	Molecular docking, virtual screening and ADMET property analysis
Identification of new therapeutic agents against resistant tuberculosis by targeting DNA Gyrase B (76)	Seven potential selective inhibitors of Gyrase B were detected.	MD simulations, virtual screening and molecular mechanics
Designing of new DprE1 inhibitors for tuberculosis (77)	A potential lead compound that can be used as DprE1 inhibitor was identified.	Molecular docking, free binding energy estimations, MD simulations, and ADMET property analysis
Elucidation of key interactions between SARS-CoV-2 main protease (Mpro) and its possible inhibitors (78)	Residual key for the interactions between SARS-CoV-2 Mpro and three drug candidates were revealed.	MD simulations
Exploration of novel drugs	Eight molecules that might	Homology modeling,

against COVID-19 by inhibiting its receptor binding domain (79)	hinder the attachment of the Spike protein of novel Coronavirus to the host receptor were predicted.	molecular docking, virtual screening and ADMET property analysis
Identification of new potential Coronavirus inhibitors (80)	Ten potential Coronavirus inhibitors were identified.	Virtual screening, molecular docking and MD simulations
Identification of new molecules for the regulation of glutamate signaling pathway (81)	Two potential dual negative allosteric modulator compounds against mGluRs in neurodegenerative diseases were identified.	Virtual screening, MD simulations and ADMET property analysis
Discovery of novel TNF- $\alpha$ inhibitors (82)	Sixteen molecules with better binding affinity than the previously known TNF- $\alpha$ inhibitors were identified.	Molecular docking, virtual screening, MD simulations, and free binding energy estimations
Identification of new GSTP1-1 inhibitors (83)	Four promising hGSTP1-1 enzyme inhibitors were screened.	Virtual screening and ADMET analysis

### Involvement of machine learning

The improvements in computing capacity and the available data have contributed much to the drug discovery process. Machine learning, which is a subfield of artificial intelligence (AI), has been used in pharmacophore modeling over the last years. In the era of big data, machine learning methods have developed into more efficient approaches such as deep learning. Thus, several machine learning methods that use the concept of pharmacophores have been developed (16). In addition to this, machine learning has been used in improving the scoring functions (84).

HSPHarm (hot spots guided receptor based pharmacophores), PharmIF (pharmacophore based interaction fingerprint) and DeepSite are examples for machine learning approaches trained with pharmacophores. The HSPHarm trains random forest decision trees with pharmacophoric descriptors to decrease the number of pharmacophore features (85). The PharmIF trains support vector machine (SVM) with pharmacophoric fingerprints to rank docking poses of small molecules (86). The DeepSite trains convolutional neural network (CNN) with pharmacophoric descriptors to find out cavities and calculate binding affinities (87).

### CONCLUSION

Pharmacophore is a pattern of features responsible for the biological activity of a molecule. There are various programs used in the generation of pharmacophore models. The pharmacophore models developed are used to identify new molecules that satisfy the pharmacophore requirements and thus expected to be biologically active.

Pharmacophore modeling has several applications at the various stages of the drug discovery process. Pharmacophore modeling is widely employed in virtual screenings to identify the molecules that

trigger the desired biological activity. Pharmacophore models are also used as filters to identify molecules that meet the pharmacophore requirements prior, during and after docking. Furthermore, pharmacophore models are used in drug target fishing, ligand fishing, and ADMET property predictions.

It is possible to overcome the challenges encountered in pharmacophore modeling by using the other advanced computational methods. For instance, pharmacophore modeling has been integrated with molecular dynamics simulations. This has the potential to alleviate problems faced in the modeling of the ligand flexibility. Lack of good scoring functions used in virtual screening by pharmacophore is another challenge observed. Machine learning can be used in improving such scoring functions as it has been employed in various computational approaches. Therefore, with the new advances in pharmacophore modeling, it is possible to develop pharmacophore models with better properties.

In short, pharmacophore modeling has played its own role in the drug discovery process. Improvements in computing capacity, increase in the available data, integration with the other computational methods and involvement of the latest algorithms have enhanced the quality of the pharmacophore models generated. As the quality of the pharmacophore model developed increases, its potential role in the drug discovery also increases. With this in mind, further improvements that will increase the quality of the pharmacophore models are still required.

### REFERENCES

1. Deore A, Dhumane J, Wagh R, Sonawane R. The Stages of Drug Discovery and Development Process.

- Asian J Pharma Res Dev. 2019;7(6):62–7. DOI: <https://doi.org/10.22270/ajprd.v7i6.616>.
2. Sliwoski G, Kothiwale S, Meiler J, Lowe EW. Computational methods in drug discovery. *Pharmacol Rev.* 2014;66(1):334–95. DOI: <https://doi.org/10.1124/pr.112.007336>.
3. Anh Vu L, Thi Cam Quyen P, Thuy Huong N. In silico Drug Design: Prospective for Drug Lead Discovery. *Int J Eng Sci Invent [Internet].* 2015;4(10):60–70. URL: [www.ijesi.org/7C%7CVolumewww.ijesi.org](http://www.ijesi.org/7C%7CVolumewww.ijesi.org).
4. Macalino SJY, Gosu V, Hong S, Choi S. Role of computer-aided drug design in modern drug discovery. *Arch Pharm Res.* 2015;38(9):1686–701. DOI: <https://doi.org/10.1007/s12272-015-0640-5>.
5. Prachayasittikul V, Worachartcheewan A, Shoombuatong W, Songtawe N, Simeon S, Prachayasittikul V, et al. Computer-Aided Drug Design of Bioactive Natural Products. *Curr Top Med Chem.* 2015;15(18):1780–800. URL: <https://www.ingentaconnect.com/content/ben/ctmc/2015/00000015/00000018/art00004>.
6. Guner O. History and Evolution of the Pharmacophore Concept in Computer-Aided Drug Design. *Curr Top Med Chem.* 2005;2(12):1321–32. DOI: <https://doi.org/10.2174/1568026023392940>.
7. Sanders MPA, McGuire R, Roumen L, De Esch IJP, De Vlieg J, Klomp JPG, et al. From the protein's perspective: The benefits and challenges of protein structure-based pharmacophore modeling. *Medchemcomm.* 2012;3(1):28–38. DOI: <https://doi.org/10.1039/C1MD00210D>.
8. Lin, Shu-Kun Sutter, J.M. Hoffman R. HypoGen: An automated system for generating predictive 3D pharmacophore models. In: Güner O, editor. *Pharmacophore Perception, Development and Use in Drug Design.* International University Line; 2000. p. 171–89.
9. Gao Q, Yang L, Zhu Y. Pharmacophore Based Drug Design Approach as a Practical Process in Drug Discovery. *Curr Comput Aided-Drug Des.* 2010;6(1):37–49. DOI: <https://doi.org/10.2174/157340910790980151>.
10. Langer T, Hoffmann RD. Pharmacophore Modelling: Applications in Drug Discovery. *Expert Opin Drug Discov.* 2006;1(3):261–7. DOI: <https://doi.org/10.1517/17460441.1.3.261>.
11. Vel EP, Guti PA. Generation of pharmacophores and classification of drugs using protein-ligand complexes Generación de farmacóforos y clasificación de drogas utilizando complejos proteína-ligando Geração de farmacóforos e classificação de fármacos usando-se complexo prote. *Rev Colomb Química.* 2012;41(3):337–48. URL: [http://www.scielo.org.co/scielo.php?pid=S0120-28042012000300001&script=sci\\_arttext&lng=en](http://www.scielo.org.co/scielo.php?pid=S0120-28042012000300001&script=sci_arttext&lng=en).
12. Schuster D. 3D pharmacophores as tools for activity profiling. *Drug Discov Today Technol.* 2010;7(4):e205–11. DOI: <https://doi.org/10.1016/j.ddtec.2010.11.006>.
13. Yang SY. Pharmacophore modeling and applications in drug discovery: Challenges and recent advances. *Drug Discov Today.* 2010;15(11–12):444–50. DOI: <https://doi.org/10.1016/j.drudis.2010.03.013>.
14. Vazquez J, Lopez M, Gibert E, Herrero E, Luque FJ. Merging ligand-based and structure-based methods in drug discovery: An overview of combined virtual screening approaches. *Molecules.* 2020;25:4723–50. DOI: <https://doi.org/10.3390/molecules25204723>.
15. Zeng L, Guan M, Jin H, Liu Z, Zhang L. Integrating pharmacophore into membrane molecular dynamics simulations to improve homology modeling of G protein-coupled receptors with ligand selectivity: A2A adenosine receptor as an example. *Chem Biol Drug Des.* 2015;86(6):1438–50. DOI: <https://doi.org/10.1111/cbdd.12607>.
16. Schaller D, Šribar D, Noonan T, Deng L, Nguyen TN, Pach S, et al. Next generation 3D pharmacophore modeling. *Wiley Interdiscip Rev Comput Mol Sci.* 2020;10(4):1–20. DOI: <https://doi.org/10.1002/wcms.1468>.
17. Güner OF, Bowen JP. Setting the record straight: The origin of the pharmacophore concept. *J Chem Inf Model.* 2014;54(5):1269–83. DOI: <https://doi.org/10.1021/ci5000533>.
18. Kaserer T, Beck KR, Akram M, Odermatt A, Schuster D, Willett P. Pharmacophore models and pharmacophore-based virtual screening: Concepts and applications exemplified on hydroxysteroid dehydrogenases. *Molecules.* 2015;20(12):22799–832. DOI: <https://doi.org/10.3390/molecules201219880>.
19. Bajorath J. Pharmacophore. In: Schwab M, editor. *Encyclopedia of Cancer.* Berlin Heidelberg: Springer; 2015. p. 2–5. ISBN: 978-3-540-47648-1.
20. McGregor MJ, Muskal SM. Pharmacophore fingerprinting. 1. Application to QSAR and focused library design. *J Chem Inf Comput Sci.* 1999;39(3):569–74. DOI: <https://doi.org/10.1021/ci980159j>.

21. Horvath D, Mao B, Gozalbes R, Barbosa F, Rogalski SL. Strengths and Limitations of Pharmacophore-Based Virtual Screening. *Chemoinformatics Drug Discov.* 2005;23:117–40. DOI: <https://doi.org/10.1002/3527603743.ch5>.
22. Sheridan RP, Rusinko A, Nilakantan R, Venkataraghavan R. Searching for pharmacophores in large coordinate data bases and its use in drug design. *Proc Natl Acad Sci U S A.* 1989;86(20):8165–9. DOI: <https://doi.org/10.1073/pnas.86.20.8165>.
23. Noha SM, Schuster D. Pharmacophore modeling. In: Lill MA, editor. *In Silico Drug Discovery and Design.* 2013. p. 80–93. ISBN: 9781909453029.
24. Horvath D. Pharmacophore-Based Virtual Screening. In: Bajorah J, editor. *Chemoinformatics and Computational Chemical Biology.* Springer; 2011. p. 261–97. ISBN: 9781493957934.
25. Leelananda SP, Lindert S. Computational methods in drug discovery. *Beilstein J Org Chem.* 2016;12:2694–718. DOI: <https://doi.org/10.3762/bjoc.12.267>.
26. Wolber G, Langer T. LigandScout: 3-D pharmacophores derived from protein-bound ligands and their use as virtual screening filters. *J Chem Inf Model.* 2005;45(1):160–9. DOI: <https://doi.org/10.1021/ci049885e>.
27. Vilar S, Cozza G, Moro S. Medicinal chemistry and the Molecular Operating Environment (MOE): Application of QSAR and molecular docking to drug discovery. *Curr Top Med Chem.* 2008;8(18):1555–72. DOI: <https://doi.org/10.2174/156802608786786624>.
28. Chen J, Lai L. Pocket v.2: Further developments on receptor-based pharmacophore modeling. *J Chem Inf Model.* 2006;46(6):2684–91. DOI: <https://doi.org/10.1021/ci600246s>.
29. Sanders MPA, Verhoeven S, De Graaf C, Roumen L, Vroiling B, Nabuurs SB, et al. Snooker: A structure-based pharmacophore generation tool applied to class A GPCRs. *J Chem Inf Model.* 2011;51(9):2277–92. DOI: <https://doi.org/10.1021/ci200088d>.
30. Barnum D, Greene J, Smellie A, Sprague P. Identification of common functional configurations among molecules. *J Chem Inf Comput Sci.* 1996;36:563–71. DOI: <https://doi.org/10.1021/ci950273r>.
31. Richmond NJ, Abrams CA, Wolohan PRN, Abrahamian E, Willett P, Clark RD. GALAHAD: 1. Pharmacophore identification by hypermolecular alignment of ligands in 3D. *J Comput Aided Mol Des.* 2006;20(9):567–87. DOI: <https://doi.org/10.1007/s10822-006-9082-y>.
32. Patel Y, Gillet VJ, Bravi G, Leach AR. A comparison of the pharmacophore identification programs: Catalyst, DISCO and GASP. *J Comput Aided Mol Des.* 2002;16(8–9):653–81. DOI: <https://doi.org/10.1023/A:1021954728347>.
33. Schneidman-Duhovny D, Dror O, Inbar Y, Nussinov R, Wolfson HJ. PharmaGist: a webserver for ligand-based pharmacophore detection. *Nucleic Acids Res.* 2008;36 (Web Server issue):223–8. DOI: <https://doi.org/10.1093/nar/gkn187>.
34. Koes, DR, Camacho CJ. Pharmer: Efficient and exact pharmacophore search. *J Chem Inf Model.* 2011;51(6):1307–14. DOI: <https://doi.org/10.1021/ci200097m>.
35. Liu X, Ouyang S, Yu B, Liu Y, Huang K, Gong J, et al. PharmMapper server: A web server for potential drug target identification using pharmacophore mapping approach. *Nucleic Acids Res.* 2010;38(SUPPL. 2):5–7. DOI: <https://doi.org/10.1093/nar/gkq300>.
36. Dixon SL, Smondyrev AM, Rao SN. PHASE: A novel approach to pharmacophore modeling and 3D database searching. *Chem Biol Drug Des.* 2006;67(5):370–2. DOI: <https://doi.org/10.1111/j.1747-0285.2006.00384.x>.
37. Qing X, Lee XY, De Raeymaeker J, Tame JR, Zhang KY, De Maeyer M, et al. Pharmacophore modeling: Advances, limitations, and current utility in drug discovery. *J Receptor Ligand Channel Res.* 2014;7:81–92. DOI: <https://doi.org/10.2147/JRLCR.S46843>.
38. Pauli I, Dos Santos RN, Rostirolla DC, Martinelli LK, Ducati RG, Timmers LFSM, et al. Discovery of new inhibitors of mycobacterium tuberculosis InhA enzyme using virtual screening and a 3D-pharmacophore-based approach. *J Chem Inf Model.* 2013;53(9):2390–401. DOI: <https://doi.org/10.1021/ci400202t>.
39. Rampogu S, Lee KW. Pharmacophore Modelling-Based Drug Repurposing Approaches for SARS-CoV-2 Therapeutics. *Front Chem.* 2021;9(May):1–10. DOI: <https://dx.doi.org/10.3389/fchem.2021.636362>.
40. Medina-Franco JL. Advances in computational approaches for drug discovery based on natural products. *Rev Latinoam Quim.* 2013;41(2):95–110. URL: [http://www.scielo.org.mx/scielo.php?pid=S0370-59432013000200003&script=sci\\_arttext&tlng=en](http://www.scielo.org.mx/scielo.php?pid=S0370-59432013000200003&script=sci_arttext&tlng=en).

41. Koutsoukas A, Simms B, Kirchmair J, Bond PJ, Whitmore A V., Zimmer S, et al. From in silico target prediction to multi-target drug design: Current databases, methods and applications. *J Proteomics*. 2011;74(12):2554–74. DOI: <https://doi.org/10.1016/j.jprot.2011.05.011>.
42. Rollinger JM, Schuster D, Danzl B, Schwaiger S, Markt P, Schmidtke M, et al. In silico target fishing for rationalized ligand discovery exemplified on constituents of *Ruta graveolens*. *Planta Med*. 2009;75(3):195–204. DOI: <https://doi.org/10.1055%2Fs-0028-1088397>.
43. Rognan D. Structure-based approaches to target fishing and ligand profiling. *Mol Inform*. 2010;29(3):176–87. DOI: <https://doi.org/10.1002/minf.200900081>.
44. Rella M, Rushworth CA, Guy JL, Turner AJ, Langer T, Jackson RM. Structure-based pharmacophore design and virtual screening for novel Angiotensin Converting Enzyme 2 inhibitors. *J Chem Inf Model*. 2006;46(2):708–16. DOI: <https://doi.org/10.1021/ci0503614>.
45. Caporuscio F, Tafi A. Pharmacophore Modelling: A Forty Year Old Approach and its Modern Synergies. *Curr Med Chem*. 2011;18(17):2543–53. DOI: <https://doi.org/10.2174/092986711795933669>.
46. Paliwal S, Mittal A, Sharma M, Pandey A, Singh A, Paliwal S. Pharmacophore and molecular docking based identification of novel structurally diverse PDE-5 inhibitors. *Med Chem Res*. 2015;24(2):576–87. DOI: <https://doi.org/10.1007/s00044-014-1144-4>.
47. Peach ML, Nicklaus MC. Combining docking with pharmacophore filtering for improved virtual screening. *J Cheminform*. 2009;1(1):1–15. DOI: <https://doi.org/10.1186/1758-2946-1-6>.
48. Hindle SA, Rarey M, Buning C, Lengauer T. Flexible docking under pharmacophore type constraints. *J Comput Aided Mol Des*. 2002;16(2):129–49. DOI: <https://doi.org/10.1023/A:1016399411208>.
49. Mobley DL, Lim NM, Wymer KL. Blind prediction of HIV integrase binding from the SAMPL4 challenge. *J Comput Aided Mol Des*. 2014;28(4):327–45. DOI: <https://doi.org/10.1007/s10822-014-9723-5>.
50. Lyne PD, Kenny PW, Cosgrove DA, Deng C, Zabudoff S, Wendoloski JJ, et al. Identification of Compounds with Nanomolar Binding Affinity for Checkpoint Kinase-1 Using Knowledge-Based Virtual Screening. *J Med Chem*. 2004;47(8):1962–8. DOI: <https://doi.org/10.1021/jm030504i>.
51. Wang M, Hou S, Wei Y, Li D, Lin J. Discovery of novel dual adenosine A1/A2A receptor antagonists using deep learning, pharmacophore modeling and molecular docking. *PLoS Comput Biol*. 2021;17(3):1–23. DOI: <https://doi.org/10.1371/journal.pcbi.1008821>.
52. Alavijeh MS, Palmer AM. The pivotal role of drug metabolism and pharmacokinetics in the discovery and development of new medicines. *Curr Opin Investig drugs J*. 2004;7(8):755–63.
53. Guner O, Bowen J. Pharmacophore modeling for ADME. *Curr Top Med Chem*. 2013;13(11):1327–42. URL: <https://www.ingentaconnect.com/content/ben/ctmc/2013/00000013/00000011/art00007>.
54. Mohan CG. Structural Bioinformatics: Applications in Preclinical Drug Discovery Process. Challenges and Advances in Computational Chemistry and Physics. Springer Nature; 2019. 25–55 p. ISBN: 978-3-030-05281-2.
55. De Groot MJ, Ekins S. Pharmacophore modeling of cytochromes P450. *Adv Drug Deliv Rev*. 2002;54(3):367–83. DOI: [https://doi.org/10.1016/S0169-409X\(02\)00009-1](https://doi.org/10.1016/S0169-409X(02)00009-1).
56. Sorich MJ, Miners JO, McKinnon RA, Smith PA. Multiple pharmacophores for the investigation of human UDP-glucuronosyltransferase isoform substrate selectivity. *Mol Pharmacol*. 2004;65(2):301–8. DOI: <https://doi.org/10.1124/mol.65.2.301>.
57. Hassan Baig M, Ahmad K, Roy S, Mohammad Ashraf J, Adil M, Haris Siddiqui M, et al. Computer Aided Drug Design: Success and Limitations. *Curr Pharm Des*. 2016;22(5):572–81. URL: <https://www.ingentaconnect.com/content/ben/cpd/2016/00000022/00000005/art00008>.
58. Hamza A, Wei N-N, Zhan C-G. Ligand-Based Virtual Screening Approach Using a New Scoring Function. *J Chem Inf Model*. 2012;52(4):963–74. DOI: <https://doi.org/10.1021/ci200617d>.
59. Scior T, Bender A, Tresadern G, Medina-Franco JL, Martínez-Mayorga K, Langer T, et al. Recognizing pitfalls in virtual screening: A critical review. *J Chem Inf Model*. 2012;52(4):867–81. DOI: <https://doi.org/10.1021/ci200528d>.
60. Chandrasekaran B, Agrawal N, Kaushik S. Pharmacore development. In: Encyclopedia of bioinformatics and computational biology: ABC of bioinformatics. Elsevier; 2019. p. 677–87.
61. Wolber G, Seidel T, Bendix F, Langer T. Molecule-pharmacophore superpositioning and pattern

- matching in computational drug design. *Drug Discov Today*. 2008;13(1-2):23-9. DOI: <https://doi.org/10.1016/j.drudis.2007.09.007>.
62. Gimeno A, Ojeda-Montes MJ, Tomás-Hernández S, Cereto-Massagué A, Beltrán-Debón R, Mulero M, et al. The light and dark sides of virtual screening: What is there to know? *Int J Mol Sci*. 2019;20(6):1375-99. DOI: <https://doi.org/10.3390/ijms20061375>.
63. Kirchmair J, Wolber G, Laggner C, Langer T. Comparative performance assessment of the conformational model generators omega and catalyst: A large-scale survey on the retrieval of protein-bound ligand conformations. *J Chem Inf Model*. 2006;46(4):1848-61. DOI: <https://doi.org/10.1021/ci060084g>.
64. Drwal MN, Griffith R. Combination of ligand- and structure-based methods in virtual screening. *Drug Discov Today Technol*. 2013;10(3):e395-401. DOI: <https://doi.org/10.1016/j.ddtec.2013.02.002>.
65. Vancaerenbroeck R, De Raeymaecker J, Lobbstaël E, Gao F, De Maeyer M, Voet A, et al. In silico, in vitro and cellular analysis with a kinome-wide inhibitor panel correlates cellular LRRK2 dephosphorylation to inhibitor activity on LRRK2. *Front Mol Neurosci*. 2014;7:1-19. DOI: <https://doi.org/10.3389/fnmol.2014.00051>.
66. Dror O, Shulman-Peleg A, Nussinov R, Wolfson HJ. Predicting molecular interactions in silico: I. A guide to pharmacophore identification and its applications to drug design. *Curr Med Chem*. 2004;11:71-90. DOI: <https://doi.org/10.2174/0929867043456287>.
67. Damm KL, Carlson HA. Exploring experimental sources of multiple protein conformations in structure-based drug design. *J Am Chem Soc*. 2007;129(26):8225-35. DOI: <https://doi.org/10.1021/ja0709728>.
68. Hu B, Lill MA. Protein pharmacophore selection using hydration-site analysis. *J Chem Inf Model*. 2012;52(4):1046-60. DOI: <https://doi.org/10.1021/ci200620h>.
69. Yu W, Lakkaraju SK, Raman EP, MacKerell AD. Site-Identification by Ligand Competitive Saturation (SILCS) assisted pharmacophore modeling. *J Comput Aided Mol Des*. 2014;28(5):491-507. DOI: <https://doi.org/10.1007/s10822-014-9728-0>.
70. Sydow D. *Dynophores: Novel Dynamic Pharmacophores*. [Berlin]: Humboldt-Universität zu Berlin; 2015.
71. Arba M, Nur-Hidayat A, Surantaadmaja SI, Tjahjono DH. Pharmacophore-based virtual screening for identifying  $\beta 5$  subunit inhibitor of 20S proteasome. *Comput Biol Chem*. 2018;77(August):64-71. DOI: <https://doi.org/10.1016/j.compbiolchem.2018.08.009>.
72. Saxena S, Abdullah M, Sriram D, Guruprasad L. Discovery of novel inhibitors of mycobacterium tuberculosis murg: Homology modelling, structure based pharmacophore, molecular docking, and molecular dynamics simulations. *J Biomol Struct Dyn*. 2018;36(12):3184-98. DOI: <https://doi.org/10.1080/07391102.2017.1384398>.
73. James N, Ramanathan K. Ligand-Based Pharmacophore Screening Strategy: a Pragmatic Approach for Targeting HER Proteins. *Appl Biochem Biotechnol*. 2018;186(1):85-108. DOI: <https://doi.org/10.1007/s12010-018-2724-4>.
74. Patel S, Modi P, Chhabria M. Rational approach to identify newer caspase-1 inhibitors using pharmacophore based virtual screening, docking and molecular dynamic simulation studies. *J Mol Graph Model*. 2018;81:106-15. DOI: <https://doi.org/10.1016/j.jmgm.2018.02.017>.
75. Saddala MS, Huang H. Identification of novel inhibitors for TNF $\alpha$ , TNFR1 and TNF $\alpha$ -TNFR1 complex using pharmacophore-based approaches. *J Transl Med [Internet]*. 2019;17(1):1-16. DOI: <https://doi.org/10.1186/s12967-019-1965-5>.
76. Kashyap A, Singh PK, Satpati S, Verma H, Silakari O. Pharmacophore modeling and molecular dynamics approach to identify putative DNA Gyrase B inhibitors for resistant tuberculosis. *J Cell Biochem*. 2019;120(3):3149-59. DOI: <https://doi.org/10.1002/jcb.27579>.
77. KB S, Kumari A, Shetty D, Fernandes E, DV C, Jays J, et al. Structure based pharmacophore modelling approach for the design of azaindole derivatives as DprE1 inhibitors for tuberculosis. *J Mol Graph Model*. 2020;101:107718. DOI: <https://doi.org/10.1016/j.jmgm.2020.107718>.
78. Yoshino R, Yasuo N, Sekijima M. Identification of key interactions between SARS-CoV-2 main protease and inhibitor drug candidates. *Sci Rep*. 2020;10(1):1-8. DOI: <https://doi.org/10.1038/s41598-020-69337-9>.
79. Shehroz M, Zaheer T, Hussain T. Computer-aided drug design against spike glycoprotein of SARS-CoV-2 to aid COVID-19 treatment. *Heliyon*. 2020;6(10):e05278. DOI: <https://doi.org/10.1016/j.heliyon.2020.e05278>.
80. Battisti V, Wieder O, Garon A, Seidel T, Urban E, Langer T. A Computational Approach to Identify Potential Novel Inhibitors against the Coronavirus

SARS-CoV-2. Mol Inform. 2020;39(10):1–8. DOI: <https://doi.org/10.1002/minf.202000090>.

81. Prabhu SV, Singh SK. Energetically optimized pharmacophore modeling to identify dual negative allosteric modulators against group I mGluRs in neurodegenerative diseases. J Biomol Struct Dyn. 2020;38(8):2326–37. DOI: <https://doi.org/10.1080/07391102.2019.1640794>.

82. Jade DD, Pandey R, Kumar R, Gupta D. Ligand-based pharmacophore modeling of TNF- $\alpha$  to design novel inhibitors using virtual screening and molecular dynamics. J Biomol Struct Dyn. 2020;0(0):1–17. DOI: <https://doi.org/10.1080/07391102.2020.1831962>.

83. Bolelli K, Ertan-Bolelli T. Pharmacophore-based virtual screening of novel GSTP1-1 inhibitors. J Turkish Chem Soc Sect A Chem. 2018;5(3):1279–86. DOI: <https://doi.org/10.18596/jotcsa.466458>.

84. Ain QU, Aleksandrova A, Roessler FD, Ballester PJ. Machine-learning scoring functions to improve structure-based binding affinity prediction and virtual screening. Wiley Interdiscip Rev Comput Mol Sci. 2015;5(6):405–24. DOI: <https://doi.org/10.1002/wcms.1225>.

85. Barillari C, Marcou G, Rognan D. Hot-spots-guided receptor-based pharmacophores (HS-pharm): A knowledge-based approach to identify ligand-anchoring atoms in protein cavities and prioritize structure-based pharmacophores. J Chem Inf Model. 2008;48(7):1396–410. DOI: <https://doi.org/10.1021/ci800064z>.

86. Sato T, Honma T, Yokoyama S. Combining machine learning and pharmacophore-based interaction fingerprint for in silico screening. J Chem Inf Model. 2010;50(1):170–85. DOI: <https://doi.org/10.1021/ci900382e>.

87. Jiménez J, Doerr S, Martínez-Rosell G, Rose AS, De Fabritiis G. DeepSite: Protein-binding site predictor using 3D-convolutional neural networks. Bioinformatics. 2017;33(19):3036–42. DOI: <https://doi.org/10.1093/bioinformatics/btx350>.





## Synthesis and Characterization of Some Transition Metals Complex Salts of Pyridinium Iodide Ionic Liquids: Application On Extractive Desulfurization

Assim A. SABAH\*  

**Abstract:** The ionic liquid of pyridine base [emPy]I was prepared. Then, a series of complex salts were designed from it with some transition metal chlorides Fe(III), Co(II), Ni(II) and Cu(II) as Lewis acids. The compounds were characterized by spectroscopic and physical methods such as nuclear magnetic resonance  $^1\text{H-NMR}$ , infrared spectroscopy "FT-IR", electronic spectrum "UV", mass spectroscopy "MS", elemental analysis "CHN", magnetic susceptibility, molar conductivity, and other methods. The thermal stability of these compounds was also verified within the temperature range of (25-1000 °C). [emPy]I and its complex salts were tested in the extractive desulfurization process EDS. The procedure treats them with the model fuel of sulfur content of 2000 ppm, prepared from dissolving dibenzothiophene DBT in n-hexane. The ratio of sulfur removal was estimated using the GC-FID technique. The optimal conditions for EDS process were studied, and the possibility of reusing the extractant more than once without regeneration.

**Keywords:** Pyridine-based-ionic liquids, extractive desulfurization, complex salts, Lewis acids.

**Submitted:** May 24, 2021. **Accepted:** June 27, 2021.

**Cite this:** Sabah A. Synthesis and Characterization of Some Transition Metals Complex Salts of Pyridinium Iodide Ionic Liquids: Application On Extractive Desulfurization. JOTCSA. 2021;8(3):763-74.

**DOI:** <https://doi.org/10.18596/jotcsa.942318>.

**\*Corresponding author. E-mail:** [assimsabah@uomosul.edu.iq](mailto:assimsabah@uomosul.edu.iq).

### INTRODUCTION

The combustion process in vehicle engines generates emissions of sulfur gases, affecting pollution control equipment in vehicles and increasing pollution. To increase the efficiency of pollution control equipment, it is preferable to significantly reduce the sulfur content in the fuel (1-3).

The processes of hydrodesulfurization (HDS) has a good efficiency. Still, they have limited use, especially for aromatic sulfur compounds. Further, in aromatic sulfur compounds, the HDS process can cause a high cost. It requires particular temperature and pressure conditions, affecting the rest of the fuel components such as olefinic compounds and reducing the octane number. Also, the harsh conditions may affect catalysts used in the process (4, 5). Therefore, the choice of an

appropriate approach for desulfurization depends mainly on the percentage and types of sulfur compounds in the fuel. It is possible to use alternative methods like oxidation desulfurization (ODS), adsorption desulfurization (ADS), and others (6-8). One of the essential alternative methods used is extraction desulfurization EDS, especially for aromatic sulfur compounds such as thiophene, benzothiophene, and their derivatives. The EDS process is carried out under appropriate laboratory conditions of temperature and pressure and does not require special equipment; thus, it does not change the fuel's chemical structure and physical properties, and the octane number value is not reduced (3, 9-12).

The most important solvents used in the EDS process are acetonitrile and pyrrolidine, DMF, and DMSO. It is noticed that the selectivity to extract the sulfur compounds is not accessible due to the

proximity of polarity with some other aromatic compounds. The efficiency of the extraction process does not exceed 50% at most, which means that large quantities of solvent are used. Therefore, it is better to use other materials that help in increasing the selectivity of sulfur compounds, and among these materials are ionic liquids (ILs) (11, 13, 14). Ionic liquids are among the promising materials and solvents for having distinct properties such as viscosity, thermal stability, and solubility. It is possible to control and change the properties of ionic fluids by changing the anion or the cation. The solubility of (ILs) in the fuel is an essential factor in its use in the EDS process. On the other hand, the solubility of ionic liquids with a nitrogen base in fuel increases nitrogen gas emissions ( $\text{NO}_x$ ), leading to increasing pollution and increasing the cost of reuse of ionic liquids. For these reasons, ionic liquids that do not dissolve in the fuel must be chosen for EDS of sulfur compounds (6, 15-17).

Some pyridine-based ionic liquids have been tested in the EDS process after tested for their non-solubility in the fuel (diesel) by analyzing the treated fuel using (HPLC). The results showed that there was no package belonging to the ionic liquids. It was found that the efficiency of extraction increases with the increase of the aromatic character of the sulfur compounds (thiophene (T) < benzothiophene (BT) < dibenzothiophene DBT) under the same conditions (18, 19). In general, ionic liquids that do not contain a transition metal have low efficiency in the EDS process. The results confirmed that ionic liquids containing metals are more efficient than the ionic liquid alone and more efficient than the metal halide under the same conditions EDS. Many ionic liquids containing transition metal chlorides are used, such as non-hydrous  $\text{FeCl}_3$  and  $\text{CuCl}$  with 3-butyl-1-methylimidazolium chloride [BMIM]Cl have been used in EDS. The amount of sulfur removed increases with metallic elements due to the increased acidity (20-22).

In this work, some pyridine-based ionic liquids were tested with some transition metal halides in

the EDS process using a model of diesel oil containing DBT as an aromatic sulfur compound. The optimal conditions for extractive desulfurization were also determined.

## EXPERIMENTAL PART

All chemical compounds used are of high purity and from trustworthy international companies without treatment. The chemical compounds were prepared and characterized according to the approved methods (6, 23-26).

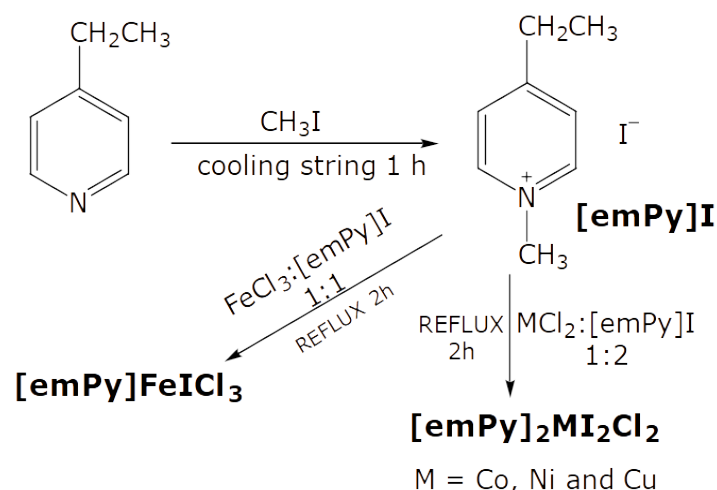
### Preparation of the Compounds

*Preparation of 4-ethyl-1-methylpyridinium iodide [emPy]I:*

The ionic liquid [emPy]I was prepared by reacting 4-ethyl pyridine with methyl iodide in a molar ratio (1:1) by adding methyl iodide slowly and gradually with continuous stirring for one hour with cooling; the reaction is exothermic. An additional excess amount of methyl iodide is added to obtain a higher yield of the product. After completion, the brown-yellow precipitate was formed, unreacted methyl iodide was removed by washing the product formed with n-hexane for more than one time.

*Preparation of complex salts of 4-ethylpyridinium iodide [emPy]FeCl<sub>3</sub>, [emPy]<sub>2</sub>MI<sub>2</sub>Cl<sub>2</sub> (M= Co, Ni and Cu):*

Some transition metal complex salts of the [emPy]I were prepared by reacting molar ratios (2:1) of the [emPy]I: metal chloride ( $\text{CoCl}_2$ ,  $\text{NiCl}_2$ , and  $\text{CuCl}_2$ ) and with a ratio (1:1) of the [emPy]I: iron(III) chloride ( $\text{FeCl}_3$ ). The reaction is done by dissolving the ionic liquid with an appropriate amount of ethanol (10 mL) and adding the metal chloride dissolved in water (10 mL), and adding it gradually, refluxing the mixture for two hours with continuous stirring. After the end of the reaction, the solution is concentrated in half by evaporation, left for 24 hours, the complex salt precipitates, and then the solution is filtered and the precipitate washed with diethyl ether. Scheme 1 shows the preparation of compounds.

**Scheme 1:** Preparation of the compounds.*Characterization of the prepared compounds*

All the prepared compounds were well characterized using various physical and spectroscopic methods. <sup>1</sup>H-NMR was carried out by using DMSO-d<sub>6</sub> as a solvent (Bruker Avance DPX 400 MHz). Elemental analysis was measured by Flash EA 1112 Series Thermo electron corporation. The GC-Mass is obtained using a Trio-1000 mass spectrometer; an infrared spectrum is carried out by JASCO Canvas FT/IR 4200 (KBr and CsI disks). At the same time, atomic absorption spectrophotometry was measured by SensAA GCB scientific equipment system (Avanta 2.02 software). A Shimadzu 1800 spectrometer UV-Vis was used for collecting electronic spectra, and magnetic susceptibility was tested by using Sherwood MK1, an electrothermal melting point 9100 was used to determine the melting points. The thermal study was tested using Mettler Toledo TGA\DSC with STARe evaluation software virgin (15.01) at 25-1000 °C with a ramping heat rate of 10 °C/min under air. Conductivity was recorded via the HANNA EC214 conductivity meter. Gas chromatography was carried out by using (STRUMENTAZIONE 4200 CARLO ERBA) FID-

detector, the programmed temperature: Intake injector temperature: 280 °C, detector temperature: 275 °C, oven temperature: 125 °C for 3 min then ramping till 185 °C for 10 min. Gases' flow rate details: hydrogen gas: 1 kg / cm<sup>2</sup>, make up gas (air): 1 kg/cm<sup>2</sup>, air: 1.5 kg / cm<sup>2</sup>, helium gas: 2 kg/cm<sup>2</sup>. Column properties: Name: SE-30, length: 28 m, diameter: 0.50 mm, film thickness: 1.2 μm. Table 1 shows the quantitative analysis and physical data of the prepared compounds.

*Extraction desulfurization analysis*

The model fuel oil contained 2000 ppm dibenzothiophene DBT, and it was prepared by dissolving DBT in n-hexane in weight percentage. All prepared compounds were used for EDS using 100 mL quick-fit conical flask 10 mL of model fuel mixing with salts at 25 °C with a specific time, SK-L180. Pro linear array laboratory shaker used for shaking (350 rpm) to optimize the best conditions and make systematic testing with a different time and concentration. The concentration of DBT before and after the treatment was measured by GC-FID equipment; hexadecane C<sub>16</sub> was used as the reference.

**Table 1:** Quantitative analysis and physical data of the prepared compounds.

No.	Compounds	CHN calcd./ (found)			M%	Cl%	Color	m.p °C
		C%	H%	N%				
1	[emPy]I C <sub>8</sub> H <sub>12</sub> IN	38.57 (38.23)	4.86 (4.62)	5.62 (5.44)	---	---	Brown yellow	45
2	[emPy]FeICl <sub>3</sub> C <sub>8</sub> H <sub>12</sub> Cl <sub>3</sub> INFe	23.36 (22.43)	2.94 (2.61)	3.41 (3.24)	13.58 (14.32)	25.86 (26.43)	Black red	80
3	[emPy] <sub>2</sub> CoICl <sub>3</sub> C <sub>16</sub> H <sub>24</sub> Cl <sub>3</sub> IN <sub>2</sub> Co	35.82 (35.03)	4.51 (4.22)	5.22 (4.85)	10.98 (11.32)	19.82 (20.42)	Dark olive	140
4	[emPy] <sub>2</sub> NiICl <sub>3</sub> C <sub>16</sub> H <sub>24</sub> Cl <sub>3</sub> IN <sub>2</sub> Ni	35.83 (34.67)	4.51 (4.42)	5.22 (5.02)	10.94 (11.14)	19.83 (20.78)	Olive	90
5	[emPy] <sub>2</sub> CuICl <sub>3</sub> C <sub>16</sub> H <sub>24</sub> Cl <sub>3</sub> IN <sub>2</sub> Cu	35.51 (35.03)	4.47 (4.32)	5.18 (4.84)	11.74 (12.22)	19.65 (20.76)	Brown	160

## RESULTS AND DISCUSSION

## Characterization of ionic liquid and its complex salts

The structure of IL as [emPy]I was confirmed with spectroscopy ( $^1\text{H-NMR}$ , FTIR, and UV-Vis), elemental analysis, and high resolution mass spectrometry.  $^1\text{H-NMR}$  ( $\text{DMSO-d}_6$ , 400 MHz):  $\delta$ 1.255 (3H- $\text{CH}_3$ , t,  $J = 7.56$  Hz),  $\delta$ 2.904 (2H- $\text{CH}_2$ ,

q,  $J = 7.56$  Hz),  $\delta$ 4.288 (3H- $\text{CH}_3$ , s),  $\delta$ 8.006 (2H-Ar, d,  $J = 6.40$  Hz),  $\delta$ 8.860 (2H-Ar, d,  $J = 6.52$  Hz). MS  $m/z$  (relative intensity): 122 (0.02%), 119 (1.30%), 118 (14.50%), 117 (3.37%), 92 (2.03%), 91 (51.80%), 90 (2.12%), 75 (3.62%), 74 (100.00%), 73 (5.75%), 72 (0.39%). Figures 1 and 2 show the  $^1\text{H-NMR}$  of [emPy]I and the cation mass spectra, respectively.

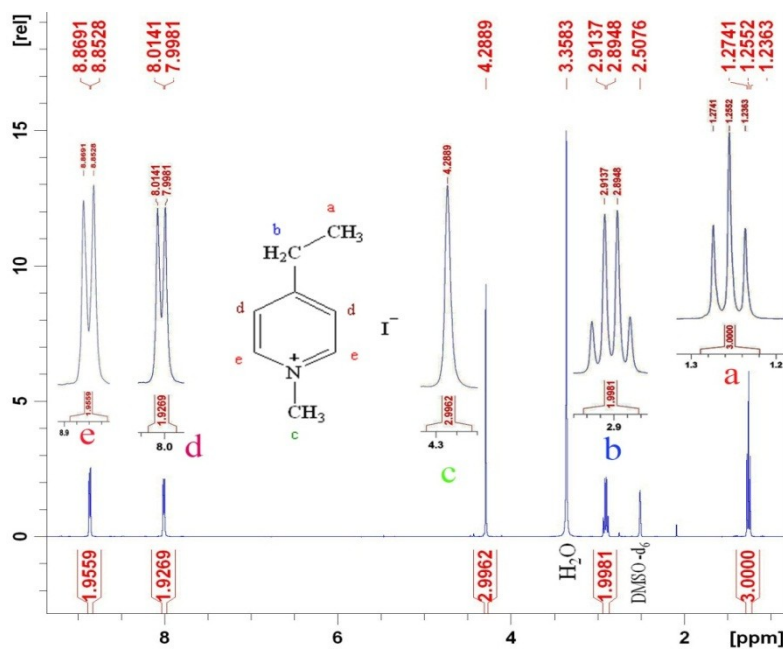


Figure 1:  $^1\text{H-NMR}$  analysis of [emPy]I.

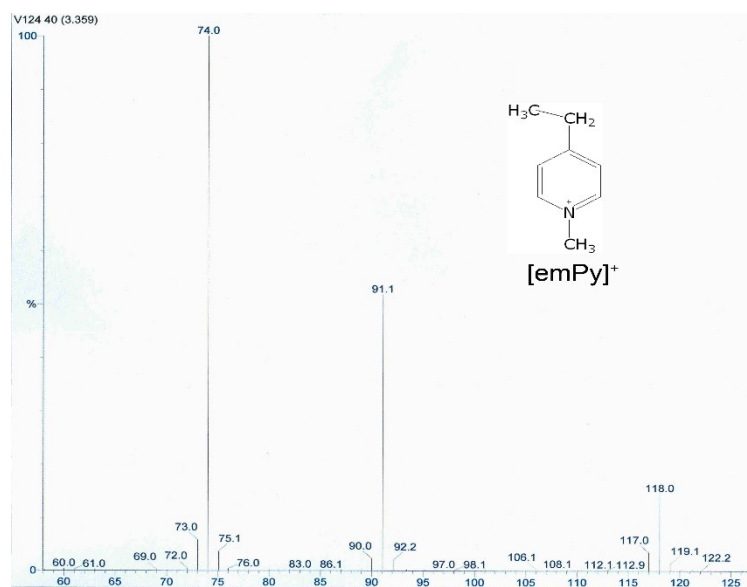


Figure 2: Positive ion mass spectrum of [emPy] $^+$ .

The infrared measurements were made using the KBr disk of the region ( $600\text{--}4000$   $\text{cm}^{-1}$ ), while the CsI disk within the ( $200\text{--}500$   $\text{cm}^{-1}$ ) region was used. The stretching frequencies of the pyridine aromatic ring of [emPy]I and its complex salts were investigated, and  $\nu(\text{C}=\text{C})$  group appeared in

the region of ( $1608\text{--}1646$   $\text{cm}^{-1}$ ). While  $\nu(\text{C}=\text{N})$  and  $\nu(\text{C}-\text{N})$  bands appeared in the region ( $1430\text{--}1473$   $\text{cm}^{-1}$ ) and ( $1110\text{--}1245$   $\text{cm}^{-1}$ ) respectively, while the  $\nu(\text{C}-\text{H})$  bands appeared in the ( $3019\text{--}3370$   $\text{cm}^{-1}$ ) region (27, 28). The new active group  $\nu(\text{N}^+-\text{CH}_3)$  was noticed at ( $2356\text{--}2854$   $\text{cm}^{-1}$ ), while the metal-

halide bond  $\nu(\text{M-X})$  ( $\text{X} = \text{Cl}, \text{I}$ ) appeared at (239-331  $\text{cm}^{-1}$ ) all these values matching with literature (27-29). Table 2 shows the stretching frequencies

of the main active groups in the prepared compounds.

**Table 2:** Stretching frequencies ( $\text{cm}^{-1}$ ) of FT/IR spectral data of prepared compounds.

No.	Compounds	$\nu(\text{C}=\text{C})$	$\nu(\text{C}=\text{N})$	$\nu(\text{C}-\text{N})$	$\nu(\text{C}-\text{H})$	$\nu(\text{N}+\text{CH}_3)$	$\nu(\text{M}-\text{X})$
1	[emPy]I	1643s	1473m	1187m	3019s	---	---
2	[emPy]FeICl <sub>3</sub>	1608m	1454m	1214s	3370s	2356w	239s,331s
3	[emPy] <sub>2</sub> CoICl <sub>3</sub>	1643s	1446w	1118m	3320s	2854w	254m,316s
4	[emPy] <sub>2</sub> NiICl <sub>3</sub>	1646s	1454w	1110m	3336s	2368w	242s,327s
5	[emPy] <sub>2</sub> CuICl <sub>3</sub>	1612m	1430m	1245w	3359s	2846w	246s,331s

DMF was used in the electronic spectra as a solvent. Also, the magnetic susceptibility was measured at a temperature of 25 °C to investigate the geometrical shape of complex salts. The results proved the tetrahedral shape of complex salts and using conductivity to verify the ionic state of the prepared salts at the same temperature by using DMF as a solvent with concentration  $10^{-3}$  M. The

percentage of metal in the complex salt was measured by the atomic absorption technique, which showed a good match with theoretical values, as well as similar the other works (30-35). Table 3 clarifies the spectral, magnetic susceptibility, and conductivity data of prepared compounds.

**Table 3: Spectral, magnetic susceptibility, and conductivity data**

No.	Compounds	Bands $\text{cm}^{-1}$	Suggested transitions	$\mu_{\text{eff}}(\text{BM})$	Conductivity ( $\text{ohm}^{-1}.\text{cm}^2.\text{mol}^{-1}$ )
1	[emPy]I	28248	$n \rightarrow \pi^*$	---	74
		34602	$\pi \rightarrow \pi^*$		
2	[emPy]FeICl <sub>3</sub>	11961	$^5\text{E} \rightarrow ^5\text{T}_2$	5.72	79
		12562			
3	[emPy] <sub>2</sub> CoICl <sub>3</sub>	14836	$^4\text{A}_2(\text{F}) \rightarrow ^4\text{T}_2(\text{F})$ $^4\text{A}_2(\text{F}) \rightarrow ^4\text{T}_1(\text{F})$ $^4\text{A}_2(\text{F}) \rightarrow ^4\text{T}_1(\text{P})$	4.20	145
		16477			
		17761			
4	[emPy] <sub>2</sub> NiICl <sub>3</sub>	12610	$^3\text{T}_1(\text{F}) \rightarrow ^3\text{T}_2(\text{F})$ $^3\text{T}_1(\text{F}) \rightarrow ^3\text{A}_2(\text{F})$ $^3\text{T}_1(\text{F}) \rightarrow ^3\text{T}_1(\text{P})$	3.61	140
		14164			
		14310			
5	[emPy] <sub>2</sub> CuICl <sub>3</sub>	14310	$^2\text{T}_2 \rightarrow ^2\text{E}$	2.42	144

The thermal stability of the prepared compounds was tested. As shown in Figure 3, the ionic liquid shows good stability up to 250 °C, as it decomposes in two primary stages (the first loses 70% by weight, and the second loses 20% by weight). The isothermal stability was studied for [emPy]I at 100 °C up to 120 min; it is proved that the compounds stable at this temperature as well as same in previous studies literature (36-38). The

thermal stability of the complex salts was also measured under the same thermal conditions. All the prepared compounds showed good stability below 100 °C, within the operational conditions for the desulfurization extractive process EDS. The Ni(II) complex salt loses the moisture water (10% mass loss) below 100 °C. Figure 4 shows the thermogravimetric analysis curve of all prepared compounds.

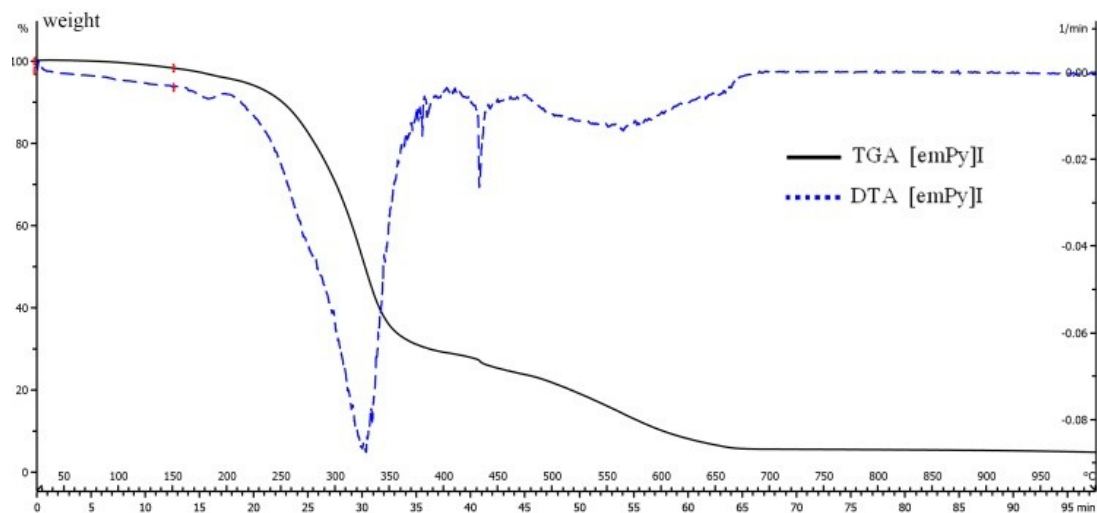


Figure 3: TGA and DTA analyses of [emPy]I.

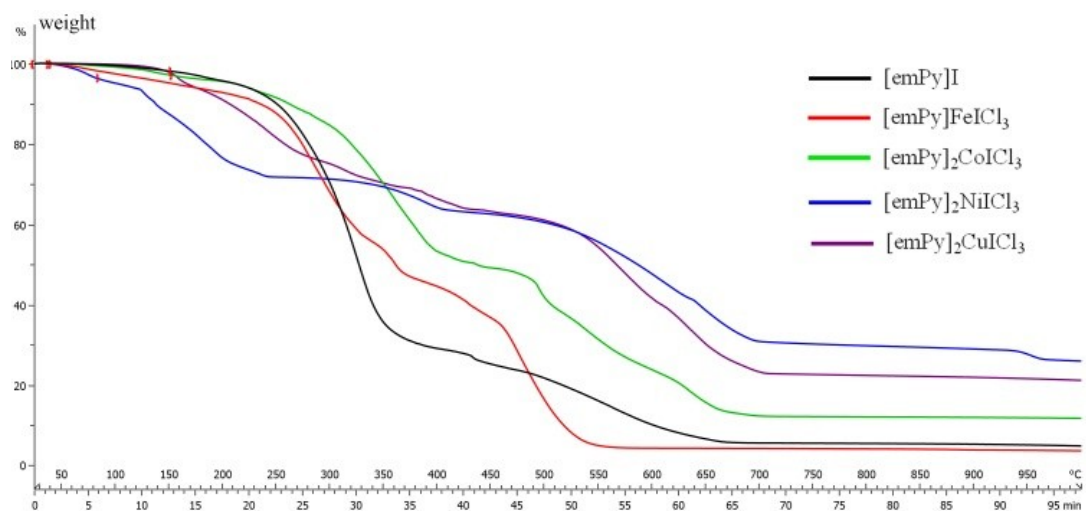


Figure 4: TGA analyses of prepared compounds.

#### EDS optimization conditions analysis

For optimizing the best conditions in EDS process, the model oil was treated with several reaction conditions (concentration, time, and temperature) through systematic experiments. All tests carried at 25 °C, to choose the best compound, 10 mL of 2000 ppm DBT was tested with 0.05 g of extractant dissolved in 5 mL of DMSO with 30 min of shaking. Figure 5 clarifies the result of EDS with mentioned conditions.

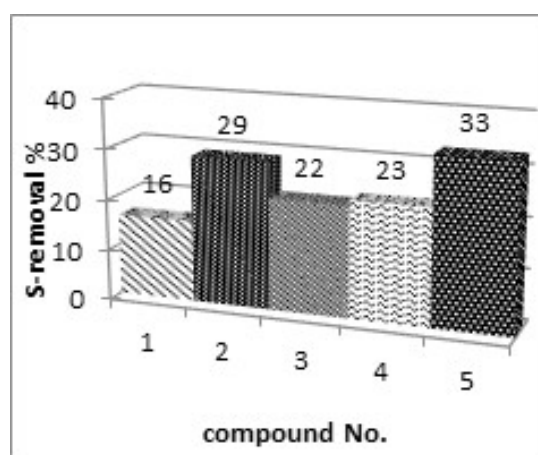
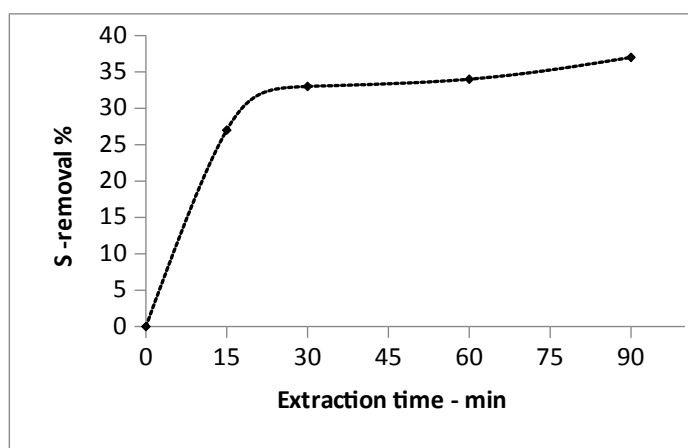


Figure 5: S-removal in condition: 2000 ppm of DBT, 30 min and 0.05 g of extractant at 25 °C.

Ionic liquids of pyridine have one of the essential extracting factors used in desulfurization processes (39, 40), and from the results in Figure 5, the [emPy]I (IL) gave 16% of sulfur removal, as the

proposed removal mechanism depends on the interference of aromatic electrons in the sulfur compounds with their counterparts in a pyridine ring ( $\pi$ - $\pi$  interactions), which depends on electron density (6, 41). The extractant factor efficiency depends on the type of the cation and type of the anion, as all the compounds under study have the same cation. Therefore, the difference in the efficiency of desulfurization is attributed to the anion. From a comparison of the results, it becomes clear that the complex salts have a higher efficiency than the ionic liquid alone. Lewis acids (metal chlorides) act as extraction agents in

addition to the ionic liquid. The proposed mechanism is the interference of sulfur and aromatic electrons in sulfur compounds with the metal ( $M = \text{Fe(II)}, \text{Ni(II)}, \text{Co(II)}$  and  $\text{Cu(II)}$ ) and the halide bound with the metal (6, 26, 42). In general, Lewis acids show less ability in desulfurization processes than complex salts, which confirms the important role of ionic liquids, while the previous work have better efficiency as they use a large amounts of extractants (3, 15, 43). The copper complex salt  $[\text{emPy}]_2\text{CuICl}_3$  has been chosen for study the best condition as shown in the Figures 6-8.



**Figure 6:** Effect the time of extraction, treatment conditions: 2000 ppm DBT and 0.05 g of  $[\text{emPy}]_2\text{CuICl}_3$  at 25 °C.

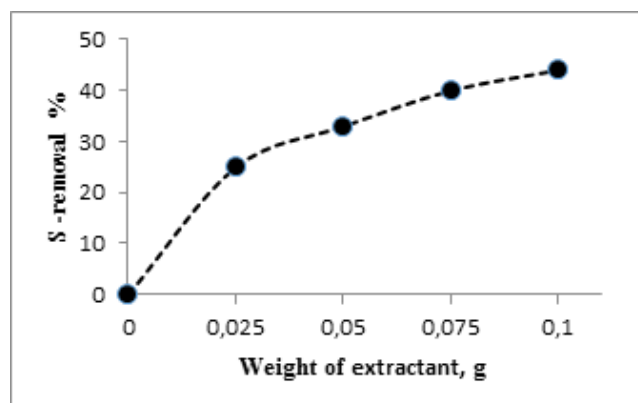


**Figure 7:** Effect the concentration of extractant  $[\text{emPy}]_2\text{CuICl}_3$ , treatment conditions: 2000 ppm DBT and 30 min at 25 °C.

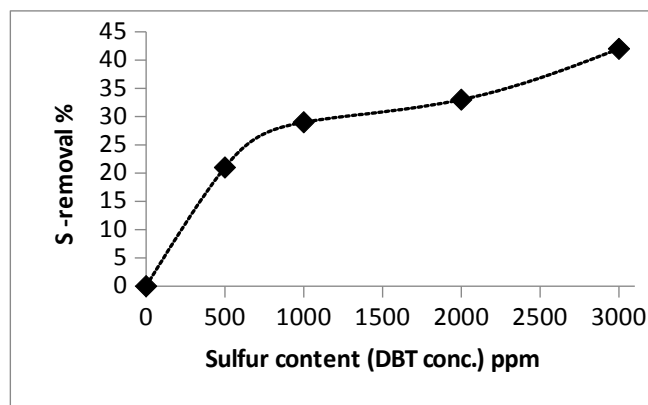


**Figure 8:** Effect the concentration of DBT, treatment conditions: 30 min, 0.05 g of [emPy]<sub>2</sub>CuICl<sub>3</sub> at 25 °C.

Through the above diagrams (Figures 6-8), we notice that increasing the time has a positive effect on the efficiency of the extraction process, but it is limited. The increase in the concentration of complex salt reflects positively on the efficiency of the sulfur removal process, which matches the literature (6, 41), but with very few differences, and is not economically feasible. Furthermore, increasing the sulfur content leads to an increase in the efficiency of the extraction process in a limited way. The use of high concentrations of sulfur content may negatively affect the reusability of complex salt or ionic liquid more than once

without regeneration. It is possible to suggest that the optimal conditions for the extraction process are (time = 30 minutes, complex salt concentration, 0.05 g, and the sulfur content DBT is 1000 ppm).

#### Extractants reusability tests

The ionic liquid [emPy]I and its complex salts were tested for the reusability experiment without regeneration, where the prepared compounds were used three times, and the reuse results showed less efficiency than the use of extractant for the first time as fresh extractant, as shown in Table 4.

**Table 4:** EDS efficiency after three times of usage of extractant (reaction conditions: time = 30 min, extractant weight = 0.05 g and DBT concentration = 2000 ppm) at 25 °C.

No.	Compounds	Sulfur removal %		
		1 <sup>st</sup>	2 <sup>nd</sup>	3 <sup>rd</sup>
1	[emPy]I	16%	13%	10%
2	[emPy]FeICl <sub>3</sub>	29%	20%	16%
3	[emPy] <sub>2</sub> CoICl <sub>3</sub>	22%	10%	10%
4	[emPy] <sub>2</sub> NiICl <sub>3</sub>	23%	13%	10%
5	[emPy] <sub>2</sub> CuICl <sub>3</sub>	33%	22%	13%

## CONCLUSION

The new ionic liquids prepared from pyridine-base compensators showed promising efficacy in the EDS process, especially those containing Lewis acids (transition metal chlorides). The results showed that the efficiency of the extraction process increased when the concentration of the extracted material increased, as well as when the extraction time increased, furthermore, the increase in the sulfur concentration in the oil model. The study also showed the possibility of reusing the ionic liquid and its complex salts without regeneration but with less EDS efficiency. The prepared compounds also showed good thermal stability under the experimental conditions used in the extraction sulfur removal processes.

## ACKNOWLEDGMENT

The author is grateful to the University of Mosul for funding this work and the Department of Chemistry, the University of Liverpool, for use the laboratory features and analysis measurements.

## REFERENCES

- Zhang S, Zhang Q, Zhang ZC. Extractive desulfurization and denitrogenation of fuels using ionic liquids. *Industrial & Engineering Chemistry Research*. 2004;43(2):614-22. DOI: <https://doi.org/10.1021/ie030561>.
- Min W. A unique way to make ultra low sulfur diesel. *Korean Journal of Chemical Engineering*. 2002;19(4):601-6. DOI: <https://doi.org/10.1007/BF02699303>.

3. Chen X, Yuan S, Abdeltawab AA, Al-Deyab SS, Zhang J, Yu L, et al. Extractive desulfurization and denitrogenation of fuels using functional acidic ionic liquids. *Separation and Purification Technology*. 2014;133:187-93. DOI: <https://doi.org/10.1016/j.seppur.2014.06.031>.
4. Babich I, Moulijn J. Science and technology of novel processes for deep desulfurization of oil refinery streams: a review. *Fuel*. 2003;82(6):607-31. DOI: [https://doi.org/10.1016/S0016-2361\(02\)00324-1](https://doi.org/10.1016/S0016-2361(02)00324-1).
5. Wang Y, Li H, Zhu W, Jiang X, He L, Lu J, et al. The extractive desulfurization of fuels using ionic liquids based on FeCl<sub>3</sub>. *Petroleum Science and Technology*. 2010;28(12):1203-10. DOI: <https://doi.org/10.1080/10916460903066148>.
6. Zhang L, Wang J, Sun Y, Jiang B, Yang H. Deep oxidative desulfurization of fuels by superbase-derived Lewis acidic ionic liquids. *Chemical Engineering Journal*. 2017;328:445-53. DOI: <https://doi.org/10.1016/j.cej.2017.07.060>.
7. Kianpour E, Azizian S. Polyethylene glycol as a green solvent for effective extractive desulfurization of liquid fuel at ambient conditions. *Fuel*. 2014;137:36-40. DOI: <https://doi.org/10.1016/j.fuel.2014.07.096>.
8. Li C, Li D, Zou S, Li Z, Yin J, Wang A, et al. Extraction desulfurization process of fuels with ammonium-based deep eutectic solvents. *Green Chemistry*. 2013;15(10):2793-9. DOI: <https://doi.org/10.1039/C3GC41067F>.
9. Meier P, Reed L, Greenwood G. Removing gasoline sulfur. *Hydrocarbon Engineering*. 2001;6(1): 26-8. URL: <https://www.osti.gov/etdeweb/biblio/20218722>.
10. Song Z, Zhou T, Qi Z, Sundmacher K. Systematic method for screening ionic liquids as extraction solvents exemplified by an extractive desulfurization process. *ACS Sustainable Chemistry & Engineering*. 2017;5(4):3382-9. DOI: <https://doi.org/10.1021/acssuschemeng.7b00024>.
11. Paucar NE, Kiggins P, Blad B, De Jesus K, Afrin F, Pashikanti S, et al. Ionic liquids for the removal of sulfur and nitrogen compounds in fuels: a review. *Environmental Chemistry Letters*. 2021:1-24. DOI: <https://doi.org/10.1007/s10311-020-01135-1>.
12. Sun L, Su T, Li P, Xu J, Chen N, Liao W, et al. Extraction coupled with aerobic oxidative desulfurization of model diesel using a B-type Anderson polyoxometalate catalyst in ionic liquids. *Catalysis Letters*. 2019;149(7):1888-93. DOI: <https://doi.org/10.1007/s10562-019-02791-x>.
13. Yu G, Wu X, Wei L, Zhou Z, Liu W, Zhang F, et al. Desulfurization of diesel fuel by one-pot method with morpholinium-based Brønsted acidic ionic liquid. *Fuel*. 2021;296:120551. DOI: <https://doi.org/10.1016/j.fuel.2021.120551>.
14. Ren Z, Wei L, Zhou Z, Zhang F, Liu W. Extractive desulfurization of model oil with protic ionic liquids. *Energy & Fuels*. 2018;32(9):9172-81. DOI: <https://doi.org/10.1021/acs.energyfuels.8b01936>.
15. Yang H, Jiang B, Sun Y, Hao L, Huang Z, Zhang L. Synthesis and oxidative desulfurization of novel lactam-based Brønsted-Lewis acidic ionic liquids. *Chemical Engineering Journal*. 2016;306:131-8. DOI: <https://doi.org/10.1016/j.cej.2016.07.044>.
16. Bhutto AW, Abro R, Gao S, Abbas T, Chen X, Yu G. Oxidative desulfurization of fuel oils using ionic liquids: A review. *Journal of the Taiwan Institute of Chemical Engineers*. 2016;62:84-97. DOI: <https://doi.org/10.1016/j.jtice.2016.01.014>.
17. Jiang B, Yang H, Zhang L, Zhang R, Sun Y, Huang Y. Efficient oxidative desulfurization of diesel fuel using amide-based ionic liquids. *Chemical Engineering Journal*. 2016;283:89-96. DOI: <https://doi.org/10.1016/j.cej.2015.07.070>.
18. Kulkarni PS, Afonso CA. Deep desulfurization of diesel fuel using ionic liquids: current status and future challenges. *Green Chemistry*. 2010;12(7):1139-49. DOI: <https://doi.org/10.1039/C002113J>.
19. Gao H, Zeng S, Liu X, Nie Y, Zhang X, Zhang S. Extractive desulfurization of fuel using N-butylpyridinium-based ionic liquids. *RSC Advances*. 2015;5(38):30234-8. DOI: <https://doi.org/10.1039/C5RA03762J>.
20. Dharaskar SA, Wasewar KL, Varma MN, Shende DZ. Extractive deep desulfurization of liquid fuels using Lewis-based ionic liquids. *Journal of Energy*. 2013;2013. DOI: <https://doi.org/10.1155/2013/581723>.
21. Ko NH, Lee JS, Huh ES, Lee H, Jung KD, Kim HS, et al. Extractive desulfurization using Fe-containing ionic liquids. *Energy & Fuels*. 2008;22(3):1687-90. DOI: <https://doi.org/10.1021/ef7007369>.
22. Hao Y, Hao Y-J, Ren J, Wu B, Wang X-J, Zhao D, et al. Extractive/catalytic oxidative mechanisms over [Hnmp] Cl· x FeCl<sub>3</sub> ionic liquids

towards the desulfurization of model oils. *New Journal of Chemistry*. 2019;43(20):7725-32. DOI: <https://doi.org/10.1039/C9NJ00691E>.

23. Brown LC, Hogg JM, Swadźba-Kwaśny M. Lewis acidic ionic liquids. *Ionic Liquids II*. 2017;185-224. DOI: [https://doi.org/10.1007/978-3-319-89794-3\\_7](https://doi.org/10.1007/978-3-319-89794-3_7).

24. Singh SK, Savoy AW. Ionic liquids synthesis and applications: An overview. *Journal of Molecular Liquids*. 2020;297:112038. DOI: <https://doi.org/10.1016/j.molliq.2019.112038>.

25. Ren T-J, Zhang J, Hu Y-H, Li J-P, Liu M-S, Zhao D-S. Extractive desulfurization of fuel oil with metal-based ionic liquids. *Chinese Chemical Letters*. 2015;26(9):1169-73. DOI: <https://doi.org/10.1016/j.ccllet.2015.05.023>.

26. Wang J, Zhang L, Sun Y, Jiang B, Chen Y, Gao X, et al. Deep catalytic oxidative desulfurization of fuels by novel Lewis acidic ionic liquids. *Fuel processing technology*. 2018;177:81-8. DOI: <https://doi.org/10.1016/j.fuproc.2018.04.013>.

27. Earle MJ, McCormac PB, Seddon KR. Regioselective alkylation in ionic liquids. *Chemical Communications*. 1998(20):2245-6. DOI: <https://doi.org/10.1039/A806328A>.

28. Ding Y-S, Zha M, Zhang J, Wang S-S. Synthesis, characterization and properties of geminal imidazolium ionic liquids. *Colloids and Surfaces A: Physicochemical and Engineering Aspects*. 2007;298(3):201-5. DOI: <https://doi.org/10.1016/j.colsurfa.2006.10.063>.

29. Moshikur RM, Chowdhury MR, Wakabayashi R, Tahara Y, Kamiya N, Moniruzzaman M, et al. Ionic liquids with N-methyl-2-pyrrolidonium cation as an enhancer for topical drug delivery: Synthesis, characterization, and skin-penetration evaluation. *Journal of Molecular Liquids*. 2020;299:112166. DOI: <https://doi.org/10.1016/j.molliq.2019.112166>.

30. Liu Q-S, Yan P-F, Yang M, Tan Z-C, Li C-P, Welz-Biermann U. Dynamic viscosity and conductivity of ionic liquids [Cnpy][NTf2](n= 2, 4, 5). *Acta Physico-Chimica Sinica*. 2011;27(12):2762-6. URL: <https://www.ingentaconnect.com/content/apcs/apcs/2011/00000027/00000012/art00007#expand/collapse>.

31. Pereiro AB, Araújo JM, Oliveira FS, Bernardes CE, Esperança JM, Lopes JNC, et al. Inorganic salts in purely ionic liquid media: the development of high ionicity ionic liquids (HIILs).

*Chemical communications*. 2012;48(30):3656-8. DOI: <https://doi.org/10.1039/C2CC30374D>.

32. Peppel T, Köckerling M. Investigations on a series of ionic liquids containing the [CoIIBr3quin] – anion (quin= quinoline). *Crystal Growth & Design*. 2011;11(12):5461-8. DOI: <https://doi.org/10.1021/cg2010419>.

33. Boudalis AK, Rogez G, Heinrich B, Raptis RG, Turek P. Towards ionic liquids with tailored magnetic properties: bmim+ salts of ferro- and antiferromagnetic Cu II3 triangles. *Dalton Transactions*. 2017;46(36):12263-73. DOI: <https://doi.org/10.1039/C7DT02472J>.

34. Okuhata M, Funasako Y, Takahashi K, Mochida T. A spin-crossover ionic liquid from the cationic iron (III) Schiff base complex. *Chemical Communications*. 2013;49(69):7662-4. DOI: <https://doi.org/10.1039/C3CC44199G>.

35. Nacham O, Clark KD, Yu H, Anderson JL. Synthetic strategies for tailoring the physicochemical and magnetic properties of hydrophobic magnetic ionic liquids. *Chemistry of Materials*. 2015;27(3):923-31. DOI: <https://doi.org/10.1021/cm504202v>.

36. Tamura T, Yoshida K, Hachida T, Tsuchiya M, Nakamura M, Kazue Y, et al. Physicochemical properties of glyme-Li salt complexes as a new family of room-temperature ionic liquids. *Chemistry Letters*. 2010;39(7):753-5. DOI: <https://doi.org/10.1246/cl.2010.753>.

37. D'Anna F, Gunaratne HN, Lazzara G, Noto R, Rizzo C, Seddon KR. Solution and thermal behaviour of novel dicationic imidazolium ionic liquids. *Organic & Biomolecular Chemistry*. 2013;11(35):5836-46. DOI: <https://doi.org/10.1039/C3OB40807H>.

38. Quitevis EL, Bardak F, Xiao D, Hines L, Son P, Bartsch R, et al. OKE Spectroscopy and Molecular Dynamics Simulations of Nonpolar and Polar Molecules in Ionic Liquids. *Ionic liquids: Science and Applications*, Visser AE, Bridges NJ, Rogers RD, Eds; 2012. DOI: <https://doi.org/10.1021/bk-2012-1117.ch013>.

39. Francisco M, Arce A, Soto A. Ionic liquids on desulfurization of fuel oils. *Fluid Phase Equilibria*. 2010;294(1-2):39-48. DOI: <https://doi.org/10.1016/j.fluid.2009.12.020>.

40. Rodríguez-Cabo B, Rodríguez H, Rodil E, Arce A, Soto A. Extractive and oxidative-extractive desulfurization of fuels with ionic liquids. *Fuel*. 2014;117:882-9. DOI: <https://doi.org/10.1016/j.fuel.2013.10.012>.

41. Zhang M, Zhu W, Xun S, Li H, Gu Q, Zhao Z, et al. Deep oxidative desulfurization of dibenzothiophene with POM-based hybrid materials in ionic liquids. *Chemical Engineering Journal*. 2013;220:328-36. DOI: <https://doi.org/10.1016/j.cej.2012.11.138>.

42. Chen X, Guo H, Abdeltawab AA, Guan Y, Al-Deyab SS, Yu G, et al. Brønsted–Lewis acidic ionic liquids and application in oxidative desulfurization of diesel fuel. *Energy & Fuels*. 2015;29(5):2998-3003. DOI: <https://doi.org/10.1021/acs.energyfuels.5b00172>.

43. Gao H, Zeng S, He H, Dong H, Nie Y, Zhang X, et al. Deep desulfurization of gasoline fuel using FeCl<sub>3</sub>-containing lewis-acidic ionic liquids. *Separation Science and Technology*. 2014;49(8):1208-14. DOI: <https://doi.org/10.1080/01496395.2013.868487>.





## Non-destructive Detection of Sesame Oil Adulteration by Portable FT-NIR, FT-MIR, and Raman Spectrometers Combined with Chemometrics

Ahmed Menevseoglu<sup>1\*</sup>  

<sup>1</sup>Gumushane University, Faculty of Engineering and Natural Sciences, Department of Food Engineering, Gumushane, 29100, Turkey

**Abstract:** Edible oils are often adulterated with fixed oils because of their high quality and price. Sesame oil is prone to adulteration due to its high commodity value and popularity. Therefore, a rapid, simple, and non-invasive method to detect adulteration in sesame oil is necessary for quality control purposes. Handheld and portable FT-NIR, FT-MIR, and Raman spectrometers are easy to operate, non-destructive, rapid, and easy to transport for in-situ assessments as well as being cheaper alternatives to traditional instruments. This study aimed to evaluate three different vibrational spectroscopic techniques in detecting sesame oil adulteration with sunflower and canola oil. Sesame oils were adulterated with fixed oils at different concentrations (0 – 25%) (w/w). Spectra were collected with portable devices and analyzed using Soft Independent Modelling of Class Analogy (SIMCA) to generate a classification model to authenticate pure sesame oil and Partial Least Squares Regression (PLSR) to predict the levels of the adulterant. For confirmation, the fatty acid profile of the oils was determined by gas chromatography (GC). In all three instruments, SIMCA provided distinct clusters for pure sesame oils and adulterated samples with interclass distance (ICD) over 3. Furthermore, FT-NIR and FT-MIR showed excellent performance in predicting adulterant levels with  $r_{val} > 0.96$ . Specifically, the FT-MIR unit provided more precise classification and PLSR prediction models over FT-NIR and Raman units. Still, all the units can be used as an alternative method to traditional methods such as GC, GC-MS, etc. These units showed great potential for in-situ surveillance to detect sesame oil adulterations.

**Keywords:** Sesame oil, adulteration, portable devices, NIR, MIR, Raman.

**Submitted:** May 21, 2021. **Accepted:** July 08, 2021.

**Cite this:** Menevseoglu A. Non-destructive Detection of Sesame Oil Adulteration by Portable FT-NIR, FT-MIR, and Raman Spectrometers Combined with Chemometrics. JOTCSA. 2021;8(3):775–86.

**DOI:** <https://doi.org/10.18596/jotcsa.940424>.

**\*Corresponding author. E-mail:** [amenevseoglu@gumushane.edu.tr](mailto:amenevseoglu@gumushane.edu.tr), Tel.: +90-456-233-10-00/1849.

### INTRODUCTION

Sesame oil is a seed oil extracted from *Sesamum indicum* L. Because it provides many health benefits and contains antioxidants, polyunsaturated fatty acids, tocopherols, sesamin and sesamol, which are cardioprotective functional components, it is becoming more popular and demanded worldwide (1,2). Sesame oil consists of up to 48% linoleic acid, 43% oleic acid, 12% palmitic acid, and 7% stearic acid (3). Sesame oil is used in foods as a flavor enhancer, in shortening, cosmetics, and pharmaceuticals (4,5).

China, Myanmar, India, and Nigeria are the leading countries for sesame oil production, followed by Japan (6). The largest sesame oil producer, China, had an annual production of 302,354 tons (29%), followed by Myanmar with 168,100 tons (16%), India with 87,200 tons (8%), Nigeria with 54,000 tons (5%), and Japan with 52,700 tons (5%) in 2018 (6). Sesame oil is a premium oil, therefore an expensive oil, which increases the concern of authentication. Sunflower, canola, maize, and soybean oils are the most common oils used for adulterations in sesame oil (7).

Conventional analytic techniques such as GC, HPLC, NMR, and IMS have focused on specific marker compounds in the pure oils (4). These traditional methods focus on targeted approaches that pre-define the chemical marker for their identification and quantification; however, those can be failed to detect unexpected adulterants that cannot be determined through the selected method (8). Although these methods susceptible and accurate, they require transportation of samples to the facilities where analysis is carried, are invasive, expensive, time-consuming, and require high-cost instrumentation and maintenance and complex sample preparation (9). Vibrational spectroscopy techniques (VST) combined with multivariate data analysis can be used as an alternative to the conventional techniques because VST can provide rapid, precise, and sensitive chemical information of the samples. Besides, a non-targeted approach using VST focuses on all chemical compounds without knowing the sample's chemical structure, which could then be compared with the pure sample's fingerprint profile (10). The performance of VST on the detection of adulteration in the edible oils has been evaluated in the literature, including olive oil (8), avocado oil (11), and sesame oil (12). With the advancement of microelectromechanical systems, fibers, sensors, optical parts, and detectors have been assisted the miniaturization of vibrational spectroscopy units. These units can provide *in-situ* analysis, real-time assessments, rapid and cost-efficient results because there is no need to transport the samples and convenience to the food industry and food control agencies (13).

This study aimed to evaluate the performance of three different vibrational spectroscopy techniques and portable devices on the authentication of sesame oil.

## MATERIALS and METHODS

### Materials

Sesame oils (32 different commercial products), sunflower oils (6 different commercial products), canola oils (6 different commercial products) were purchased from various local markets in Istanbul, Turkey, and Columbus, OH, USA. Sunflower and canola oil were selected because both oils were cheaper than sesame oil and could be used as adulterants in sesame oil. Samples were stored at 4 °C until further analysis to prevent any oxidative changes in the oil. One of the pure sesame oils was chosen randomly, and it was adulterated with 5, 10, 15, 20, and 25% (w/w) sunflower oil and canola oil, separately. Adulteration with adulterant levels lower than 10% may not be feasible economically; therefore, it may limit the use in food fraud practices, and high adulterant levels may be easily detected by sensory without any

instrument used. Therefore, a 5-25% range was selected to imitate realistic and practical applications in the adulteration of oils (14).

### Methods

#### NIR

The NIR of the oil samples were collected using micro-NeoSpectra (Si-Ware Systems, Cairo, Egypt) (Figure 1), a compact Fourier Transform Near-Infrared (FT-NIR) sensor equipped with a single-chip Michelson interferometer with monolithic Opto-electro-mechanical structure with a single uncooled indium-gallium-arsenide (InGaAs) photodetector. A total of 50  $\mu\text{L}$  of oil sample were deposited on the unit's sensor, and the spectra were collected at the range of 7400–3920  $\text{cm}^{-1}$  in absorbance mode and with a 16  $\text{cm}^{-1}$  resolution. Samples were scanned for 15 seconds to increase the signal-to-noise ratio. Spectral data collection was carried out in duplicate.

#### MIR

A total of 50  $\mu\text{L}$  of the oil sample was placed on the IR crystal. The FT-IR 5500 (Agilent Technologies Inc., Santa Clara, CA) (Fig. 1) spectrometer equipped with a temperature-controlled 5-bounce ZnSe crystal set to 40 °C. The spectra were collected at 4  $\text{cm}^{-1}$  resolution over a range from 4000 to 650  $\text{cm}^{-1}$ , and an interferogram of 64 scans co-added to increase the signal-to-noise ratio. Spectral data collection was carried out in duplicate.

#### Raman

Three milliliters of oil sample were placed in a 10-mm light path quartz cuvette (Hellma Analytics, Mulheim, Germany), and the Raman spectra were collected using a WP 1064 compact portable Raman spectrometer (Wasatch Photonics, Durham, NC, USA) (Figure 1). The Raman unit was equipped with an Indium Gallium Arsenide (InGaAs) detector and a laser source operating at 1064 nm. The spectra were collected from 1855 to 200  $\text{cm}^{-1}$  with a resolution of 4  $\text{cm}^{-1}$ , and 3 scans were co-added to improve the signal-to-noise ratio of the spectrum with an integration time of 3000 ms. A background spectrum was acquired in between every sample to eliminate the environmental variations. Spectral data were displayed in terms of scattered light by the sample and viewed using Enlighten™ software (Wasatch Photonics, Durham, NC, USA). Spectral data collection was carried out in duplicate.

#### GC (Reference method)

The fatty acid profile was determined using a fatty acid methyl ester (FAME) procedure (15) with slight modifications. A total of 100  $\mu\text{L}$  oil sample was dissolved in 1 mL of n-hexane in a microcentrifuge tube; after adding 20  $\mu\text{L}$  of 2 N potassium hydroxide in methanol, the mixture was

vortexed for a minute. The microcentrifuge tube set aside for the phase separation, and a 750  $\mu\text{L}$  of an aliquot from the upper part was removed into another microcentrifuge tube with a pinch of anhydrous sodium sulfate. The tube was centrifuged at 13.2 rpm for 5 min, and the upper part ( $\sim 500 \mu\text{L}$ ) was transferred into a borosilicate glass vial. Samples were analyzed using an Agilent 6890 (Santa Clara, CA, USA) GC, with a flame ionization detector (FID) and an HP G1513A autosampler and a tray. Fatty acids were eluted through an HP-88 100 m  $\times$  0.25 mm  $\times$  0.2  $\mu\text{m}$  column (Agilent, Santa Clara, CA, USA), and helium was used as a carrier gas. A total of 1  $\mu\text{L}$  of the sample was injected with a split ratio of 20:1. The oven temperature was set at 110  $^{\circ}\text{C}$  for 1 min, then increased to 220  $^{\circ}\text{C}$  (5  $^{\circ}\text{C}/\text{min}$ ) and held for 15 min. The injector temperature was 220  $^{\circ}\text{C}$ , and the detector temperature was 250  $^{\circ}\text{C}$ . The identification of the fatty acids was achieved by comparing each peak's retention time against the reference standards (Supelco®37 Component FAME Mix, Sigma Aldrich, St. Louis, MO, USA). GC analyses for each sample were carried out in duplicate.

### Data Analysis

A multivariate data analysis software (Pirouette version 4.5, Infometrix Inc., Bothell, WA, USA) was used to analyze the spectral data.

### SIMCA

A supervised pattern recognition technique relies on a confidence region for each class after PCA is applied. Observations are projected in each PC that decides if the observation belongs to that class or not. Because the spectra are complex, SIMCA is required for obtaining meaningful information of the data matrix (16). More information can be found in the literature (17-19). SIMCA was used to determine the pure samples and adulterated sesame oils. Known classes (sesame, sunflower, and canola oils) were used to create a classification algorithm to identify the correct classes (80% of the total samples). Then, the validation data set (20% of the samples that were not used in the classification model) was informed to evaluate the model. SIMCA was evaluated based on three-dimension class projection, misclassification (if the sample was predicted in the correct class), and interclass distance (ICD).

### PLSR

Partial Least Square Regression (PLSR) was used to evaluate the fitness of the model using the standard error of cross-validation (SECV), standard error of prediction (SEP), coefficient of correlation ( $r$ ), and outlier diagnostics. PLSR is one of the

most used multivariate data analyses used for correlated, noisy, and multi-X variables. For example, data obtained from FT-NIR, FT-MIR, and Raman can have thousands of data points (X variable, i.e., FT-MIR – from 3500  $\text{cm}^{-1}$  to 800  $\text{cm}^{-1}$ ). PLSR includes the PCA features where thousands of variables can be compressed into few latent variables called factors, predictors, or components. Detailed information for PLSR can be found in the literature (20-23). Samples with large residuals indicating the samples with structure do not fit in the model, and high leverage indicates the sample or variable have very much impact on the calibration model were considered as outliers (not shown in the data).

## RESULTS AND DISCUSSION

### SIMCA Results – FT-NIR Spectra

Due to NIR spectra's complexity, and to make the interpretation more straightforward, the spectra were mean-centered, second derivative, and smoothly transformed before the SIMCA analysis to obtain better spectral characteristics (with a second-order poly-nominal filter with a 19-point window). Even though many pre-processing options were tried, the best results were obtained using a 19-point window (i.e., 21, 25, 35-point). SIMCA was used to generate a classification algorithm for the oils. Figure 2A shows the SIMCA 3D projection to classify sesame oil, sunflower oil, and canola oil. Based on the SIMCA, all oil samples were clustered very distinctly ( $\text{ICD} > 19$ ). Figure 2B shows the classification's discriminating power, which expresses the variables (wavenumber ( $\text{cm}^{-1}$ )) responsible for the classification. Peak identifications were made based on the literature (24,25). Around 4386  $\text{cm}^{-1}$ , the combination of C-H stretching vibration can be observed. The peak at 4876  $\text{cm}^{-1}$  is associated with the C-H vibration of cis-unsaturation. Lastly, the peak at 5660  $\text{cm}^{-1}$  is related to the first overtone of the C-H stretching vibration of chemical groups (i.e., methylene). Figure 2C shows the FT-NIR prediction. The prediction model indicated that adulterated samples were clustered from pure samples. Moreover, two out of eight validation samples (not used in calibration set) did not fit in the model, and GC data confirmed that those samples' fatty acid profile was different from pure samples. Only one sample was misclassified when comparing FT-MIR and Raman results. Figure 2D shows the score plot of the model, indicating that using two factors was enough to represent the model with  $\sim 97\%$ . Overall, a miniaturized FT-NIR spectrometer combined with SIMCA showed that FT-NIR could be an alternative method for detecting sesame oil adulteration with cheap vegetable oils.

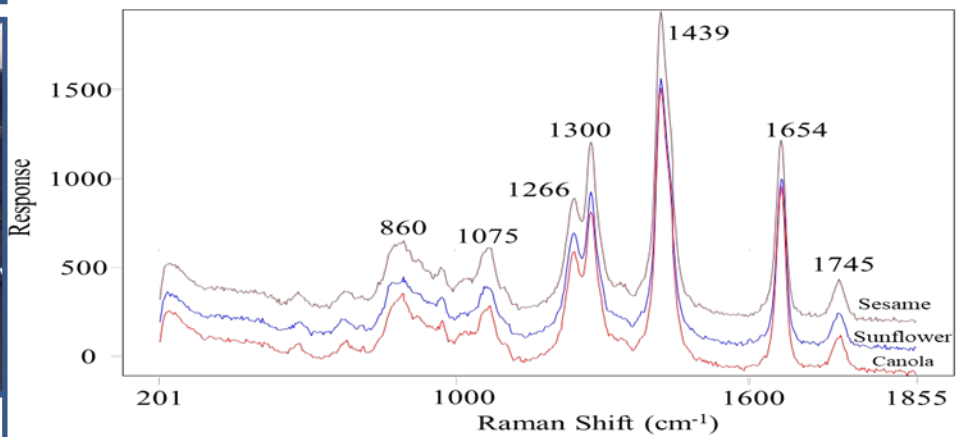
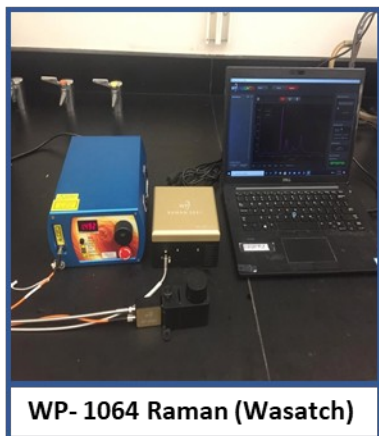
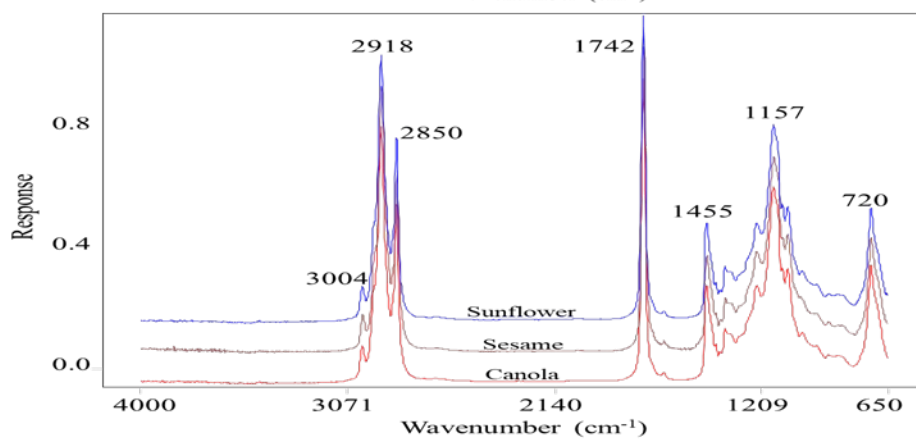
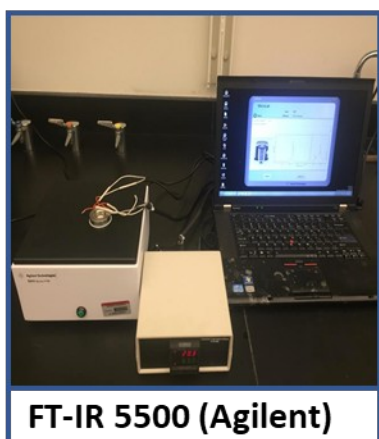
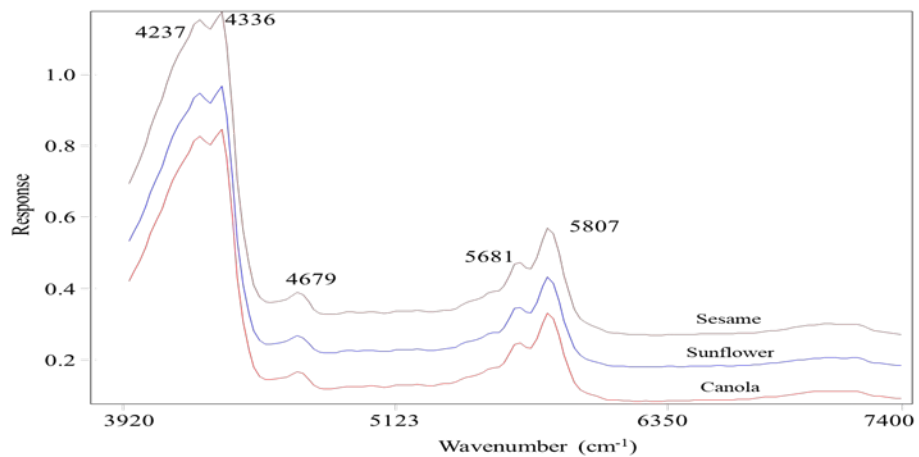


**Figure 1:** Commercial portable and handheld FT-NIR, FT-MIR and Raman spectrometers, and the spectra of oils obtained from them.

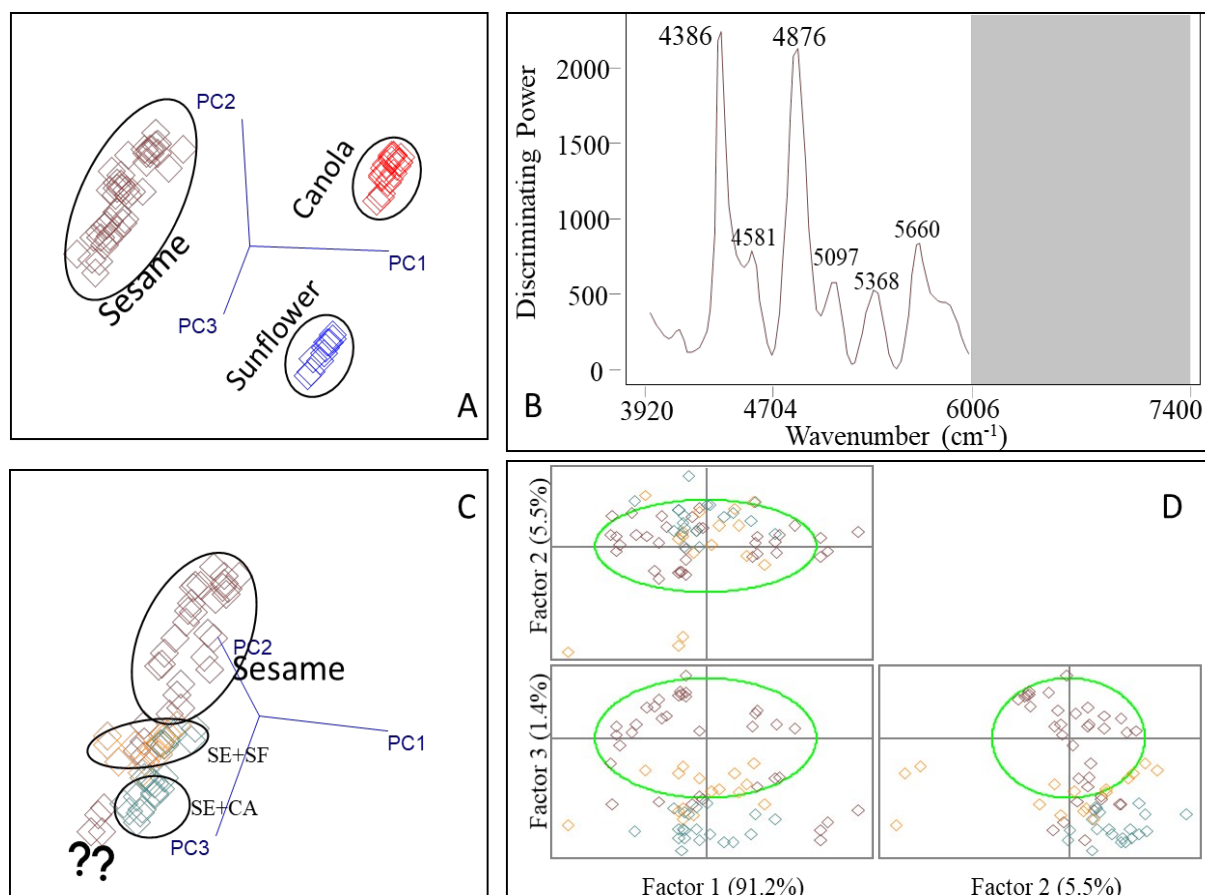


**Figure 2:** SIMCA 3D projection obtained from FT-NIR spectral data (2A), discriminating power obtained from SIMCA (2B), Validation model of SIMCA (2C), score plot for validation model (2D). SE: sesame oil; SF: sunflower oil; CA: canola oil; ? mark: suspected sample.

### SIMCA Results – FT-MIR Spectra

Before the SIMCA analysis, the spectra were mean-centered, local-scoped, first-derivative, normalized, and smooth-transformed (19-point window) for improving spectral characteristics. Figure 3A shows SIMCA 3D projection obtained from FT-MIR spectral data. The samples were clustered distinctly with  $ICD > 10$ . Based on the ICD value, FT-NIR was slightly better than FT-MIR. Figure 3B shows the discriminating power, and the peaks assignment was made based on previous studies (26,27). The peaks around in the range of  $3024 - 2864 \text{ cm}^{-1}$  associated with C-H stretching of methyl and methylene groups ( $\text{CH}_2$  symmetric and  $\text{CH}_3$  asymmetric stretching),  $1836 - 1709 \text{ cm}^{-1}$  related to  $-\text{C}=\text{O}$  ester stretching vibration (C-O stretching esters of fatty acids),  $1450 - 1377 \text{ cm}^{-1}$  associated with C-H bending (symmetrical and scissoring) vibrations of  $\text{CH}_2$  and  $\text{CH}_3$  groups.

Although the oil spectral profile seems similar, triglyceride composition would impact the band intensities and slight shifts in the wavenumbers for functional groups. Figure 3C shows the prediction model. Similar to the FT-NIR results, adulterated samples were clustered very distinctly. Besides, three out of eight external validation samples did not fit in the model, and GC results were confirmed the fatty acid profile of those samples were different than pure sesame oils. SIMCA results indicated that even with low adulterant levels (5%) could be detected by FT-MIR spectrometer. Figure 3D shows the score plot of the SIMCA validation model obtained from FT-MIR spectral data indicating that using three factors was enough to represent the prediction model with  $\sim 88\%$  of all variables. Overall, portable FT-MIR unit showed great performance in detecting sunflower and canola oil adulterations in sesame oil.

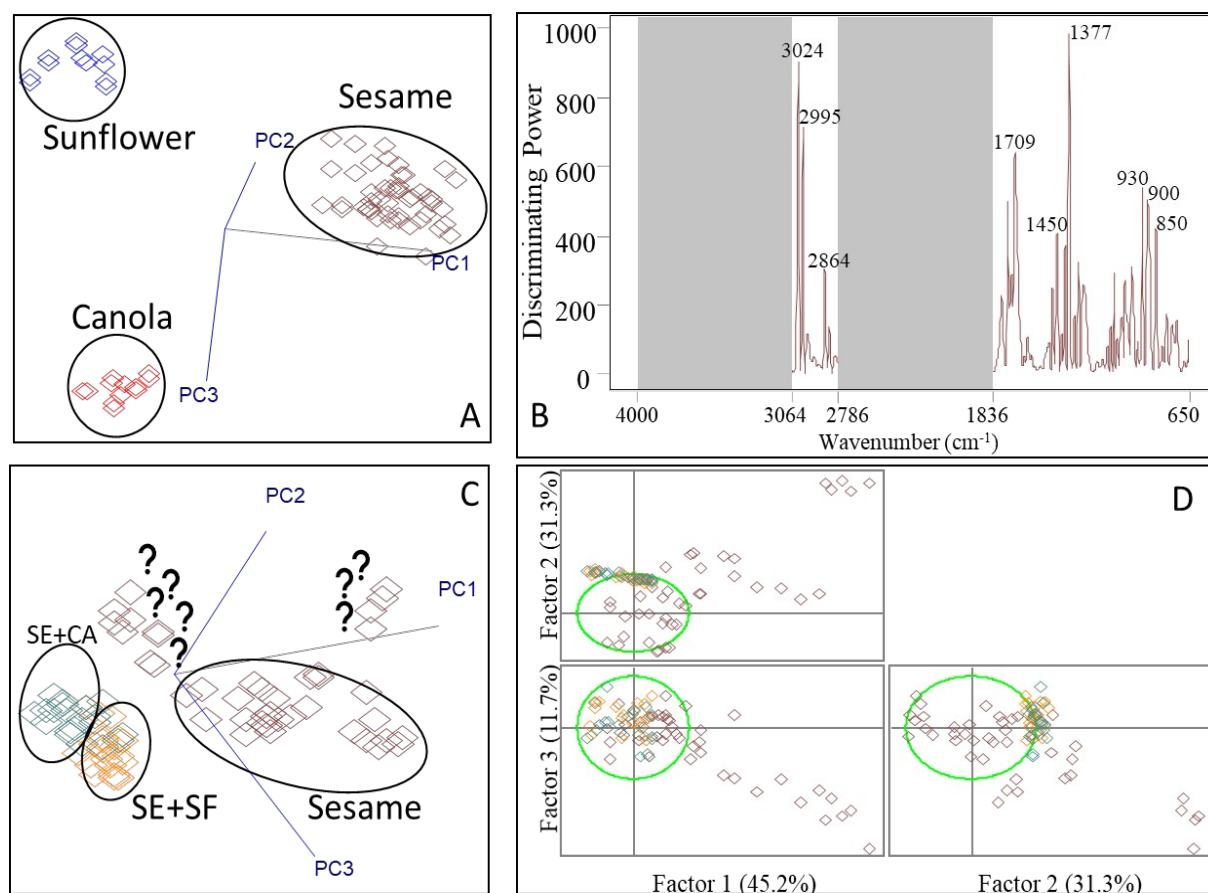


**Figure 3** SIMCA 3D projection obtained from FT-MIR spectral data (3A), discriminating power obtained from SIMCA (3B), Validation model of SIMCA (3C), score plot for validation model (3D). SE: sesame oil; SF: sunflower oil; CA: canola oil; ? mark: suspected sample.

### SIMCA Results – Raman Spectra

Similar to previously mentioned techniques, spectral data were mean-centered, locally scoped, second-derivative, and smooth-transformed (19-point window). Figure 4A shows the classification of three oils. Based on the spectral data, all three oils were clustered distinctly with  $ICD > 5$ . The classification obtained from Raman spectral data was slightly worse than both FT-MIR and FT-NIR data based on the ICD value. A possible explanation for this result would be the due less scanning region (wavenumber) in our Raman spectrometer. For instance, FT-MIR covers 3064 – 2786  $cm^{-1}$ , which region associated with  $CH_2$  and  $CH_3$ ; however, Raman covers up to 1855  $cm^{-1}$  in our unit. Figure 4B shows the discriminating power for classification. 1445  $cm^{-1}$ , associated with  $-CH_2$  bending vibrational mode, is the most powerful

band for classification. 1291  $cm^{-1}$  (twisting  $-CH_2$ ), 1640  $cm^{-1}$  and 1657  $cm^{-1}$  (stretching  $cis-R-HC=CH-R$ ) were also powerful bands for classification. The peaks assignments were made based on the literature (28). Figure 4C shows the validation model. Similar to FT-MIR unit, Raman spectrometer detected the adulterated samples, and three suspected samples which then confirmed by GC-FID, and those were clustered distinctly. SIMCA results indicated that a Raman spectrometer could detect as low as 5% adulteration in sesame oil. Figure 4D shows the score plot for validation model indicated three factors were enough to represent the prediction model with  $\sim 93\%$  of all variables. Overall, the portable Raman spectrometer showed good performance in detecting sesame oil adulteration with sunflower and canola oil.

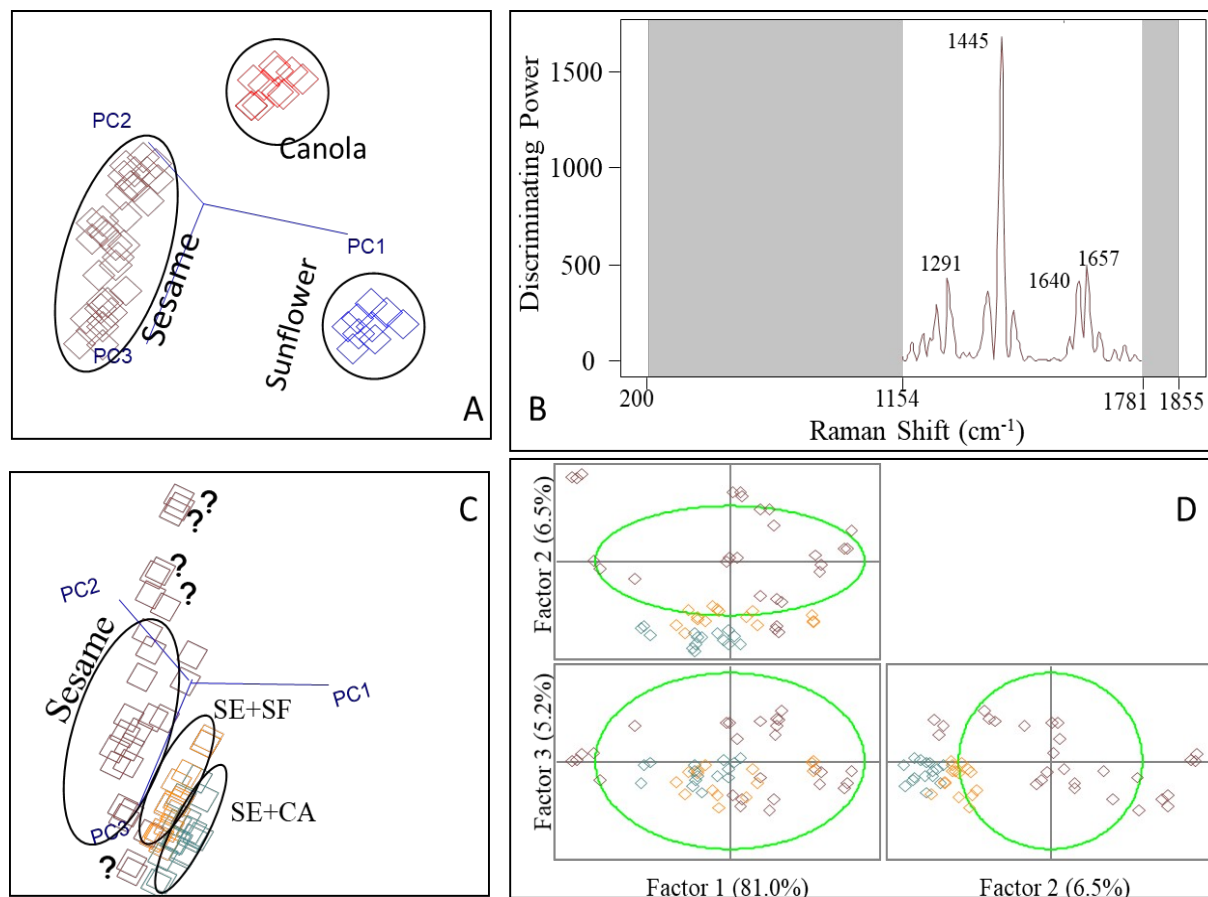


**Figure 4** SIMCA 3D projection obtained from Raman spectral data (4A), discriminating power obtained from SIMCA (4B), Validation model of SIMCA (4C), score plot for validation model (4D). SE: sesame oil; SF: sunflower oil; CA: canola oil; ? mark: suspected sample.

#### PLSR Results – FT-NIR, FT-MIR, and Raman Spectra

Table 1 shows the prediction performance of three vibrational spectroscopy units for predicting adulterant levels in sesame oil. The optimum factors for predicting models were between four to six. Although the performance would be slightly better if more factors were used, using more factors would include noise or irrelevant components that would cause overfitting the model. Likewise, using fewer factors than optimum number would cause underfitting associated with

less variance than needed (29). PLSR models of the oils yielded high SECV, high SEP,  $r_{cal}$ , and  $r_{val}$  values, indicating the accuracy of the prediction models. Correlation coefficient value ( $r$ ) is accepted as an excellent prediction over 0.90, and suitable prediction over 0.80 (30). FT-NIR, FT-MIR, and Raman units showed excellent performance in predicting adulterant levels ( $r_{val} > 0.90$ ). Portable FT-MIR unit showed superior performance over handheld FT-NIR and portable Raman units since it provided lower SEP, and higher  $r_{val}$ .

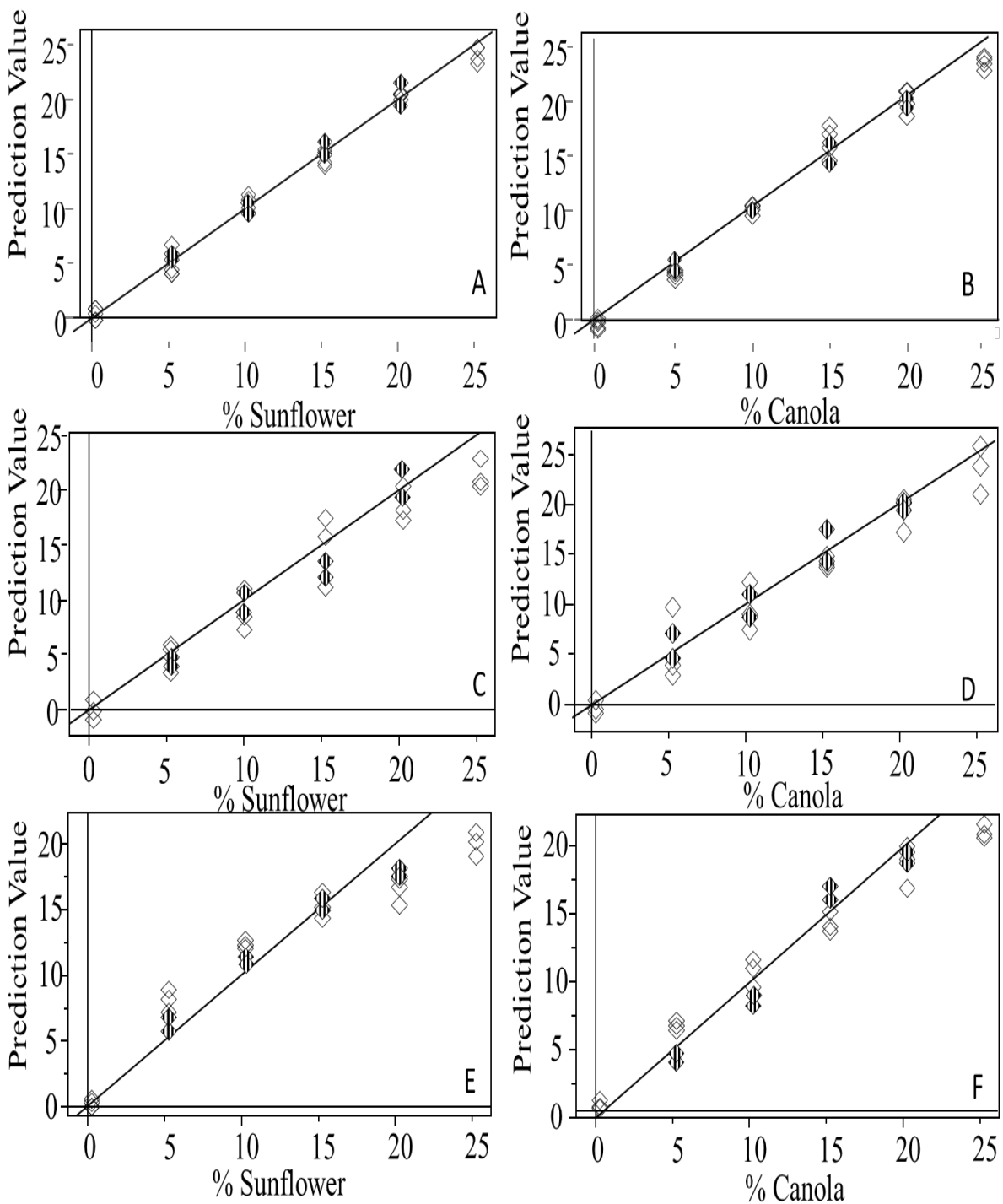


**Figure 5** Partial Least Square Regression (PLSR) calibration and validation plots for sunflower oil levels (5A), canola oil (5B) obtained from FT-NIR unit, 5C and 5D obtained from FT-MIR unit, 5E and 5F obtained from Raman unit. Empty squares: calibration model; filled squares: validation model.

**Table 1:** Statistical performance of the prediction models developed using FT-NIR, FT-MIR, and Raman spectrometers for adulteration levels in sesame oil.

Unit	Parameter	Calibration model					Validation model			
		Range <sup>a</sup>	N <sup>b</sup>	F <sup>c</sup>	SECV <sup>d</sup>	r <sub>cal</sub> <sup>e</sup>	Range	N	SEP <sup>f</sup>	r <sub>val</sub> <sup>g</sup>
FT-NIR	SFO	0-25	18	5	1.17	0.994	5.0-20.0	12	2.03	0.976
	CAO	0-25	18	6	1.76	0.985	5.0-20.0	12	2.28	0.969
FT-MIR	SFO	0-25	18	6	1.41	0.990	5.0-20.0	12	1.82	0.978
	CAO	0-25	18	4	0.95	0.996	5.0-20.0	12	1.36	0.988
Raman	SFO	0-25	18	5	2.83	0.937	5.0-20.0	12	3.23	0.898
	CAO	0-25	18	4	2.87	0.924	5.0-20.0	12	3.26	0.909

<sup>a</sup>The unit of the range is %. <sup>b</sup>Number of samples used in calibration models. <sup>c</sup>The number of factors. <sup>d</sup>Standard error of cross-validation. <sup>e</sup>Correlation coefficient of cross-validation. <sup>f</sup>Standard error of prediction. <sup>g</sup>Correlation coefficient of prediction for external validation. SFO: Sunflower oil. CAO: Canola oil.

## CONCLUSIONS

In this study, sesame oil adulteration with sunflower and canola oil was aimed to be determined by portable FT-NIR, FT-MIR, and Raman spectrometers. Developed SIMCA and PLSR models showed that sesame oil adulteration could be detected rapidly, non-destructively, and reliably by using portable vibrational spectroscopy units. Based on portable units' and GC results, three out of 32 samples were suspected as being adulterated. FT-MIR spectrometer showed slightly better performance than FT-NIR, superior performance than Raman spectrometers. These techniques may detect sunflower and canola oil adulterations in sesame oil as low as 5%. These portable units can provide government agencies and the oil industry an alternative method to the traditional methods.

## FUNDING

This research received no external funding.

## CONFLICT OF INTEREST

The author declares no conflict of interest.

## ACKNOWLEDGMENTS

The author would like to thank Prof. Luis E. Rodriguez-Saona and Didem Peren Aykas, PhD (The Ohio State University, Department of Food Science and Technology) for their technical support rendered during this study.

## REFERENCES

1. Ozulku G, Yildirim RM, Toker OS, Karasu S, Durak MZ. Rapid detection of adulteration of cold pressed sesame oil adulterated with hazelnut, canola, and sunflower oils using ATR-FTIR

spectroscopy combined with chemometric. Food Control. 2017 Dec;82:212–6. DOI:

<https://doi.org/10.1016/j.foodcont.2017.06.034>.

2. Wang R, Liu K, Wang X, Tan M. Detection of Sesame Oil Adulteration Using Low-Field Nuclear Magnetic Resonance and Chemometrics. International Journal of Food Engineering. 2019 Jul 26;15(7):20180349. DOI:

<https://doi.org/10.1515/ijfe-2018-0349>.

3. Gharby S, Harhar H, Bouzoubaa Z, Asdadi A, El Yadini A, Charrouf Z. Chemical characterization and oxidative stability of seeds and oil of sesame grown in Morocco. Journal of the Saudi Society of Agricultural Sciences. 2017 Apr;16(2):105–11. DOI: <https://doi.org/10.1016/j.jssas.2015.03.004>.

4. Zhang L, Shuai Q, Li P, Zhang Q, Ma F, Zhang W, et al. Ion mobility spectrometry fingerprints: A rapid detection technology for adulteration of sesame oil. Food Chemistry. 2016 Feb;192:60–6. DOI:

<https://doi.org/10.1016/j.foodchem.2015.06.096>.

5. Warra A. Sesame (*Sesamum indicum* L.) Seed Oil Methods of Extraction and its Prospects in Cosmetic Industry: A Review. Bayero J Pure App Sci. 2012 Apr 6;4(2):164–8. DOI: <https://doi.org/10.4314/bajopas.v4i2.33>.

6. FAO. FAOSTAT online statistical service [Internet]. FAO; 2018. Available from: <http://faostat.fao.org/>.

7. Seo H-Y, Ha J, Shin D-B, Shim S-L, No K-M, Kim K-S, et al. Detection of Corn Oil in Adulterated Sesame Oil by Chromatography and Carbon Isotope Analysis. J Am Oil Chem Soc. 2010 Jun;87(6):621–6. DOI: <https://doi.org/10.1007/s11746-010-1545-6>.

8. Aykas DP, Karaman AD, Keser B, Rodriguez-Saona L. Non-Targeted Authentication Approach for Extra Virgin Olive Oil. *Foods*. 2020 Feb 20;9(2):221. DOI: <https://doi.org/10.3390/foods9020221>.
9. Subramanian A, Alvarez VB, Harper WJ, Rodriguez-Saona LE. Monitoring amino acids, organic acids, and ripening changes in Cheddar cheese using Fourier-transform infrared spectroscopy. *International Dairy Journal*. 2011 Jun;21(6):434-40. DOI: <https://doi.org/10.1016/j.idairyj.2010.12.012>.
10. Tengstrand E, Rosén J, Hellenäs K-E, Åberg KM. A concept study on non-targeted screening for chemical contaminants in food using liquid chromatography-mass spectrometry in combination with a metabolomics approach. *Anal Bioanal Chem*. 2013 Feb;405(4):1237-43. DOI: <https://doi.org/10.1007/s00216-012-6506-5>.
11. Quiñones-Islas N, Meza-Márquez OG, Osorio-Revilla G, Gallardo-Velazquez T. Detection of adulterants in avocado oil by Mid-FTIR spectroscopy and multivariate analysis. *Food Research International*. 2013 Apr;51(1):148-54. DOI: <https://doi.org/10.1016/j.foodres.2012.11.037>.
12. Chen H, Lin Z, Tan C. Fast quantitative detection of sesame oil adulteration by near-infrared spectroscopy and chemometric models. *Vibrational Spectroscopy*. 2018 Nov;99:178-83. DOI: <https://doi.org/10.1016/j.vibspec.2018.10.003>.
13. Rodriguez-Saona L, Aykas DP, Borba KR, Urtubia A. Miniaturization of optical sensors and their potential for high-throughput screening of foods. *Current Opinion in Food Science*. 2020 Feb;31:136-50. DOI: <https://doi.org/10.1016/j.cofs.2020.04.008>.
14. Miaw CSW, Sena MM, Souza SVC de, Ruisanchez I, Callao MP. Variable selection for multivariate classification aiming to detect individual adulterants and their blends in grape nectars. *Talanta*. 2018 Dec;190:55-61. DOI: <https://doi.org/10.1016/j.talanta.2018.07.078>.
15. Ichihara K, Shibahara A, Yamamoto K, Nakayama T. An improved method for rapid analysis of the fatty acids of glycerolipids. *Lipids*. 1996 May;31(5):535-9. DOI: <https://doi.org/10.1007/BF02522648>.
16. De Maesschalck R, Candolfi A, Massart DL, Heuerding S. Decision criteria for soft independent modelling of class analogy applied to near infrared data. *Chemometrics and Intelligent Laboratory Systems*. 1999 Apr;47(1):65-77. DOI: [https://doi.org/10.1016/S0169-7439\(98\)00159-2](https://doi.org/10.1016/S0169-7439(98)00159-2).
17. Wold S. Pattern recognition by means of disjoint principal components models. *Pattern Recognition*. 1976 Jul;8(3):127-39. DOI: [https://doi.org/10.1016/0031-3203\(76\)90014-5](https://doi.org/10.1016/0031-3203(76)90014-5).
18. Lavine BK. Clustering and Classification of Analytical Data. In: Meyers RA, editor. *Encyclopedia of Analytical Chemistry* [Internet]. Chichester, UK: John Wiley & Sons, Ltd; 2000 [cited 2021 Jul 17]. p. a5204. Available from: <https://onlinelibrary.wiley.com/doi/10.1002/9780470027318.a5204>.
19. Ballabio D, Todeschini R. Infrared Spectroscopy for Food Quality Analysis and Control Multivariate Classification for Qualitative Analysis. In: Sun D-W, editor. *Infrared Spectroscopy for Food Quality Analysis and Control*. 1st edition. Burlington, MA: Elsevier; 2009. p. 83-104. ISBN: 978-0-12-374136-3.
20. Haaland DM, Thomas EV. Partial least-squares methods for spectral analyses. 1. Relation to other quantitative calibration methods and the extraction of qualitative information. *Anal Chem*. 1988 Jun 1;60(11):1193-202. DOI: <https://doi.org/10.1021/ac00162a020>.
21. Jong SD. PLS fits closer than PCR. *J Chemometrics*. 1993 Nov;7(6):551-7. DOI: <https://doi.org/10.1515/jpme.1998.26.4.325>.
22. Brereton RG. Introduction to multivariate calibration in analytical chemistry. *Analyst*. 2000;125(11):2125-54. DOI: <https://doi.org/10.1039/b003805i>.
23. Wold S, Sjöström M, Eriksson L. PLS-regression: a basic tool of chemometrics. *Chemometrics and Intelligent Laboratory Systems*. 2001 Oct;58(2):109-30. DOI: [https://doi.org/10.1016/S0169-7439\(01\)00155-1](https://doi.org/10.1016/S0169-7439(01)00155-1).
24. Hourant P, Baeten V, Morales MT, Meurens M, Aparicio R. Oil and Fat Classification by Selected Bands of Near-Infrared Spectroscopy. *Appl Spectrosc*. 2000 Aug;54(8):1168-74. URL: <http://as.osa.org/abstract.cfm?URI=as-54-8-1168>.
25. Yang H, Irudayaraj J, Paradkar M. Discriminant analysis of edible oils and fats by FTIR, FT-NIR and FT-Raman spectroscopy. *Food Chemistry*. 2005 Nov;93(1):25-32. DOI: <https://doi.org/10.1016/j.foodchem.2004.08.039>.
26. Aykas DP, Rodriguez-Saona LE. Assessing potato chip oil quality using a portable infrared spectrometer combined with pattern recognition

analysis. Anal Methods. 2016;8(4):731–41. DOI: <https://doi.org/10.1039/C5AY02387D>.

27. Rodriguez-Saona LE, Giusti MM, Shotts M. Advances in Infrared Spectroscopy for Food Authenticity Testing. In: Advances in Food Authenticity Testing [Internet]. Elsevier; 2016 [cited 2021 Jul 17]. p. 71–116. Available from: <https://linkinghub.elsevier.com/retrieve/pii/B9780081002209000047>

28. Covaciu F-D, Berghian-Grosan C, Feher I, Magdas DA. Edible Oils Differentiation Based on the Determination of Fatty Acids Profile and Raman Spectroscopy—A Case Study. Applied Sciences. 2020 Nov 24;10(23):8347. DOI: <https://doi.org/10.3390/app10238347>.

29. Abdi H. Partial least squares regression and projection on latent structure regression (PLS Regression). WIREs Comp Stat. 2010 Jan;2(1):97–106. DOI: <https://doi.org/10.1002/wics.51>.

30. Urbanocuadrado M, Luquedecastro M, Perezjuan P, Gomezniето M. Comparison and joint use of near infrared spectroscopy and Fourier transform mid infrared spectroscopy for the determination of wine parameters. Talanta. 2005 Mar 31;66(1):218–24. DOI: <https://doi.org/10.1016/j.talanta.2004.11.011>.





## A Self-Healing Material Based on Microcapsules of Poly(Urea-Formaldehyde)/Bis-Propargyl-Succinate Containing in Polyurethane Matrix

Thi Sinh VO<sup>1\*</sup>  , Tran Thi Bich Chau VO<sup>2</sup>  , Nhan Duy Pham<sup>3</sup>  , and Thi Ngoc Huyen Lai<sup>4</sup> 

<sup>1</sup>School of Mechanical Engineering, Sungkyunkwan University, Suwon 16419, Korea.

<sup>2</sup>Department of Industrial Management, Can Tho University, Can Tho, Vietnam.

<sup>3</sup>Department of Chemistry, Memorial University of Newfoundland, St. John's, NF A1B 3X7, Canada.

<sup>4</sup>School of Advance Materials Science & Engineering, Sungkyunkwan University, Suwon 16419, Korea.

**Abstract:** With the development of current technology, several concepts of self-healing materials (SHMs) have recently been proposed, and capsule-based SHMs are explored. In our study, a terminal alkyne compound (bis-propargyl-succinate, BPS) is concerned as a healing agent to be used as a core material, and poly(urea-formaldehyde) (PUF) is employed as a wall shell. Besides, the chemical, morphological and thermal properties of the microcapsules (MCs) are also determined by Fourier-transform infrared spectroscopy (FTIR), gas chromatography (GC), thermogravimetric analysis (TGA), and optical microscopy (OM). Additionally, the MCs have better thermal stability up to 257 °C with the rough outer surface. The MCs have successfully encapsulated 75.0% of BPS with a size range of 63 – 125 μm and PUF shell thickness range of 5.72 – 11.35 μm; moreover, the stability of MCs is well maintained within 50 days at room temperature basing on the solvent extraction method. Concomitantly, self-healing ability is activated by the breakup of the MCs as cracks, then the healing agent (BPS) is released into the cracked regions to react with azide groups of the polymeric matrix. The BPS in the MCs is moved to cracked regions, which involves MCs diameter and weight fraction of PUF capsules. Moreover, the self-healing ability can reach high when BPS amounts (i.e., SHMs containing 5% and 10% of MCs) are available sufficiently to be outrightly filled into the cracked regions. Thereby, MCs' size and weight fraction can be reasonably selected to result in an optimal healing capacity for a pre-established size of cracks.

**Keywords:** Microcapsules, healing agent, urea-formaldehyde, self-healing materials.

**Submitted:** May 08, 2021. **Accepted:** July 09, 2021.

**Cite this:** Vo TS, Vo TTBC, Pham ND, Lai TNH. A Self-Healing Material Based on Microcapsules of Poly(Urea-Formaldehyde)/Bis-Propargyl-Succinate Containing in Polyurethane Matrix. JOTCSA. 2021;8(3):787-802.

**DOI:** <https://doi.org/10.18596/jotcsa.934775>.

**\*Corresponding author. E-mail:** [vtsinh92@skku.edu](mailto:vtsinh92@skku.edu).

### INTRODUCTION

Currently, several concepts of self-healing materials (SHMs) have recently been considered. At the same time, SHM is an artificial or synthetically-created material to be automatically

repaired damages to themselves without any external diagnosis or human intervention. The SHMs can be classified primarily into different approaches basing on self-healing mechanisms (i.e., vascular, capsule-based, and intrinsic). The approaches also diversify by various damaged

volumes to can heal, as well as the healing ability can be repeated in the same location and the rate of healing, leading to each approach having advantages and challenges to investigate. Moreover, microcapsule (MC)-based SHMs contain a healing agent that is capsuled and protected from different globular shells when the damages break them, at the same time that the self-healing mechanism is based on releasing the healing agent in the MCs to react with the polymeric matrix at the damaged region. The polymer shell walls are created from a number of techniques to protect the core materials (healing agents) containing inside them; in particular, the most common methods relate to the shell formation at the interface of droplets in an oil-in-water emulsion (1). Additionally, the damages and cracks regularly appear on/in the polymeric materials during a used long-term, which loses their necessary functions and impacts to their mechanical properties (2-5). The fabrication methods of SHMs are concerned as a significant role in maintaining the necessary properties of materials; thus, the source materials have a self-healing ability in the damaged polymeric matrix is considered as a healing agent that is truly attracted to can investigate its abilities (3-6).

Simultaneously, polyurethane (PU) is one of synthetic polymers, that is formed from a polycondensation reaction of a terminal hydroxyl group-contained pre-polymer and a di-isocyanate (or a polyisocyanate) (7-9). A typical classification utilized for powerful and selective reactions is mentioned to a "azide-alkyne" click reaction that is conducted by compounds containing azide and alkyne groups (10-13). Here, a terminal alkyne ( $-C\equiv C-$ ) compound can be well prepared through one-step method with a suitable molar ratio of reactants as shown in our previous works (13, 14), while glycidyl azide polyol (GAP, a pre-polymer) is known an azide ( $-N_3$ ) compound containing terminal hydroxyl ( $-OH$ ) group that can well react with isocyanate ( $-N=C=O$ ) compound to form an azide group-contained PU matrix (13, 14). Remarkably, the preliminary healing ability on the SHMs has been investigated in the first study of ours (13), which was based on the direct injection method by the various assuming cuts on the GAP-based PUs, the as-prepared bis-propargyl-succinate (BPS) was then injected to repair the damaged regions (assuming cuts) of the GAP-based PUs. Thus, this is a precondition to continue conducting an investigation of PU/MCs-based SHMs in this study, as well as which can be a novel SHMs on the basic of "azide-alkyne" click reaction between an azide group-contained polymeric matrix (the as-prepared GAP-based PU) and a terminal alkyne compound-contained healing agent (the as-prepared BPS). Specifically, it uses only

one type of healing agent (alkyne compound)-contained capsule instead of two different healing agents (azide and alkyne compounds)-contained capsules on a polymeric matrix (polyisobutylene) by Gragert et al. (15), or one healing agent (the azide compound)-contained capsule on a polymeric matrix (alkyne-graphene oxide) with the use of copper-catalyzed azide-alkyne (CuAAC) click reaction by Akhan et al. (16). As limitation of the use of CuAAC regarding to diffusion of the participating reactants, Dohler et al. (17) performed more extensively in variety of multivalent azide/alkyne compounds and polymers grafted with various molecular weights, viscosities, and functional group densities. Further, Saikia et al. (18) also designed an azide-alkyne cycloaddition-based SHMs through azide-multiwall carbon nanotubes with poly(*t*-butyl acrylate) and alkyne compound-contained capsule embedded in an epoxy matrix. On the basic of any damaging event occurs in the epoxy matrix, the healing liquid could dissolve the implanted catalyst from the matrix to occur the crosslinking reaction between azide and alkyne leading to healing the cracks, as well as investigated the influences of temperature and healing time (18).

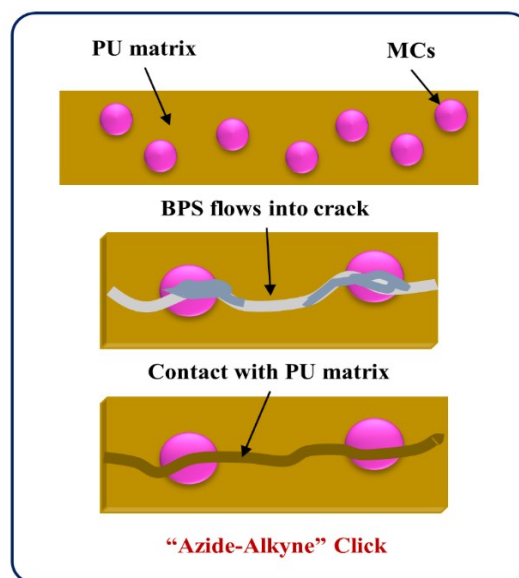


**Figure 1:** Self-healing mechanism of PU/MCs-based SHMs using "azide-alkyne" click.

Thereby, a terminal alkyne compound BPS is concerned as a healing agent to be used as a core material, and poly(urea-formaldehyde) (PUF) is employed as a wall shell. BPS was prepared through an esterification reaction in our previous works (13, 14), while PUF/BPS MCs are fabricated in an oil-in-water emulsion to conduct surveys of chemical, morphological, and thermal properties of the as-prepared MCs based on Fourier-transform infrared spectroscopy (FTIR), gas chromatography

(GC), thermogravimetric analysis (TGA), and optical microscopy (OM). Concomitantly, the stability of the as-prepared MCs is also investigated at room temperature following a storage time cycle by the solvent extraction method. Moreover, the self-healing ability of SHMs is activated by the breakup of the above MCs as cracks, an amount of healing agent liquid (BPS) in the MCs is released to move into the cracked regions, conducting a reaction of "azide-alkyne" click [i.e., azide groups of the polymeric matrix (GAP-based PU) and alkyne groups of healing agent (BPS)] (12, 19, 20) (Figure 1). Besides, the influences of MCs content, diameter, and crack types on PU/MCs-based SHMs are also investigated. These can open a new approach for the fabrication of capsule-based SHMs from GAP-based PU matrices.

## MATERIALS AND METHODS

### Materials

GAP polyols were offered from the Korean Company. Poly(ethylene-alt-maleic anhydride) (EMA,  $M_w = 100,000 - 500,000$ ) was provided from Sigma company. Ammonium chloride 98+% was obtained from the Alfa Aesar company. Resorcinol 98.0% and Urea 99.0% were purchased from Samchun Company. Formaldehyde solution 37.0% were offered from Junsei Chemical Co., Ltd (Japan). BPS was synthesized via an esterification reaction in our previous work to be continued using as a core material in this study (13).

### Fabrication of PUF/BPS MCs

MCs are fabricated in an oil-in-water emulsion by the in-situ polymerization method. 2.50 g of urea, 0.25 g of ammonium chloride, and 0.25 g of resorcinol are added and stirred into EMA aqueous solution (0.5 wt%) at 55 °C. The pH solution is adjusted (i.e., pH = 2.60 – 3.50) by hydrochloric acid (HCl) and sodium hydroxide (NaOH). Especially, 1-octanol is supplemented into the above solution to avoid surface bubbles. The BPS is added slowly to obtain an emulsion and stabilized for 10 min. Thereafter, the formaldehyde solution is added to achieve a 1/1.9 molar ratio of formaldehyde/urea. After 4 h, the suspension of MCs is separated, as based on filter papers under vacuum. Finally, the MCs are washed with a solvent mixture (distilled water: n-hexane), which then are air-dried for 24 – 48 h. Herein, sieves (Chung Gye Sang Gong SA) are employed to separate the sizes of the MCs.

### Preparation of PU/MCs-based SHMs

GAP polyol (8.00 g) is dried at 60 °C under vacuum and cooled down to 25 °C – 30 °C. Then, IPDI (0.45 g) is quickly added and stirred in the GAP polyol (25 – 30 °C). Next, 0.15 g of TPB solution (20 wt% in BZ), 0.24 g of DNS solution (12.5 wt% in BZ), and 0.44 g of MCs (5 wt% of PU) are added and stirred under vacuum. Finally, the above mixture is filled into a mold (3 cm x 8 cm) to continue removing the bubbles under vacuum (30 °C, 3 h); the curing process of PU/MCs-based SHMs is conducted in the oven (60 °C, 7 days) (13, 14). The reaction scheme of PU/MCs-based SHMs is described in Figure 2.

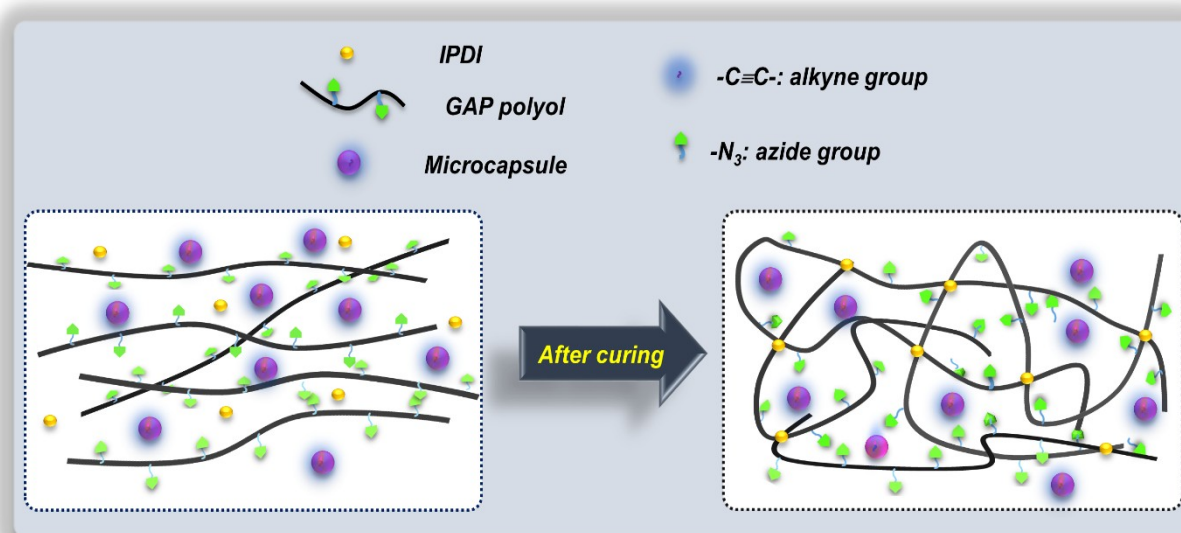


**Figure 2:** Formation scheme of PU/MCs-based SHMs.

### Instruments of analysis

Fourier-transform infrared spectroscopy (FT-IR) of the samples is scanned in the 4000 – 400  $\text{cm}^{-1}$

region (Nicolet 380, Ietled Co.). Thermogravimetric (TGA) curves of the samples are conducted from 50 to 850 °C with a ramp rate of 20 °C min<sup>-1</sup> under the dry nitrogen atmosphere (20 mL/min) by a Seiko Exstar6000 (TGA4000, PerkinElmer). Surface morphology of the as-prepared MCs is performed with an optical microscope (OM) (Olympus SZX12) and i-Solution™ IMTcamCCD Digital Camera. The diameter of the as-prepared MCs is determined from Standard Testing Sieves (Chung Gye Sang Gong SA). A gas chromatograph (GC) (Shimadzu, Inc.) with a 320 μm internal diameter capillary column and flame ionization detector is employed to determine the core materials in MCs. The GC samples are prepared by adding MCs into a vial containing acetone, which is then filtered and collected the liquid to measure.

## RESULTS AND DISCUSSION

### Morphological characterization of PUF/BPS MCs

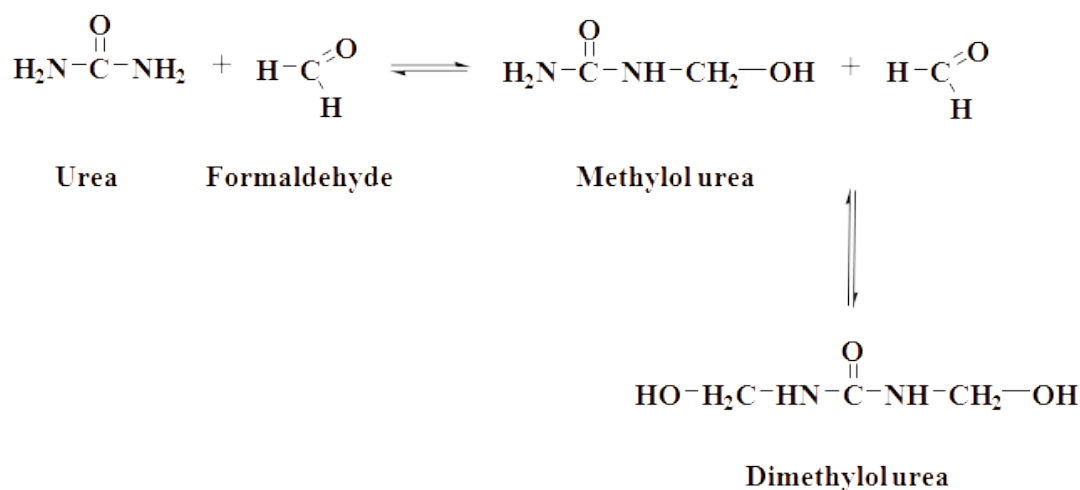


**Figure 3:** Formation scheme of methylol urea and dimethylol urea.

Furthermore, the encapsulation of BPS in the PUF capsules takes place simultaneously during the formation of crosslinked PUF. Urea and formaldehyde are all soluble in an aqueous medium, which can react to each other to form PUF as mentioned above in an acidic environment and 55 °C. During the initial stage of the in-situ polymerization, the urea-formaldehyde molecule is rich with polar groups (i.e., methylol urea, dimethylol urea, or low molecular weight compound) is compatible with water. Besides, the number of polar groups will gradually decrease with an increase in polymer molecular weight, which reduced the hydrophilicity of PUF molecules

A chemical method with in-situ polymerization has been applied for the fabrication of MCs (1). In this process, the polymerization is conducted in/on the continuous phase of the interface through the dispersed core material. Initially, a polymer with low molecular weight (i.e., prepolymer) will be formed; as time goes on, it grows in size. It means that this polymer will deposit on the surface of the dispersed core material, thereby generating a solid capsule shell. In the fabrication process of the MCs, the PUF/BPS MCs have been rinsed with distilled water: n-hexane, which then are air-dried at room temperature—resulting from that the yield of spherical MCs was obtained to 82.0% after air-dried 2 days. Besides, the formation of poly(urea-formaldehyde) (PUF) capsules has been included a possible reaction of urea and formaldehyde to attain methylol urea and dimethylol urea (Figure 3) during in-situ polymerization, which continues a condensation under acidic conditions to collect the PUF wall shell in Figure 4. Herein, BPS is concerned as a healing agent to be encapsulated in PUF capsules.

to separate from the aqueous phase and deposited on the already emulsified oil droplets (i.e., hydrophobic organic phase) after this molecular weight attained a certain value. The PUF shell thickness has been optimized in order that this PUF shell contains the maximum amount of core material. Here, the diameter of the prepared PUF/BPS MCs is separated from standard testing sieves. Four standard testing sieves with different mesh sizes (180, 150, 125, and 63 μm) were used to separate the particles. The PUF/BPS MCs size range of 63 – 125 μm (Figure 5) is chosen to apply for the preparation process of SHMs.

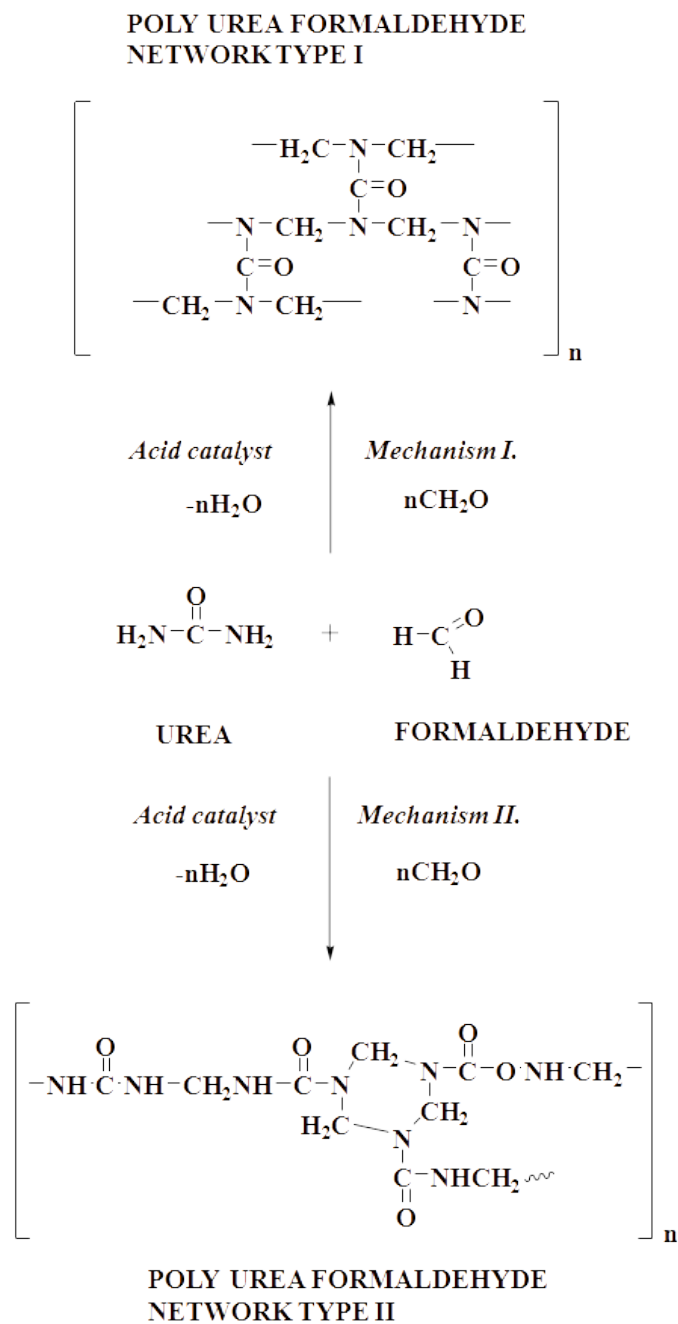


**Figure 4:** Possible formation of PUF during in-situ polymerization.

In Figure 5, it shows the OM micrographs of MCs morphology. Overall, the microencapsulation efficiency of the prepared PUF/BPS MCs has occurred condensation reaction for the PUF wall shell; its strength cannot endure the treatment such as washing and separation (Standard testing sieves) because PUF particles have been moved out the capsules. At the same time, most of the prepared PUF/BPS MCs are round globules; the PUF particles will deposit much around the capsules leading to the outer surface of the MCs

becoming rougher, as well as the MCs are tightly clustered together. Furthermore, the PUF particles deposit around the capsules and separate out the capsules, indicating that the inner surface of the capsule is smoother than the outer surface of the capsule. In other words, the polymeric membrane is formed to be protected the MCs well. Additionally, the less thickness MCs did not rupture after they were separated via standard testing sieves.

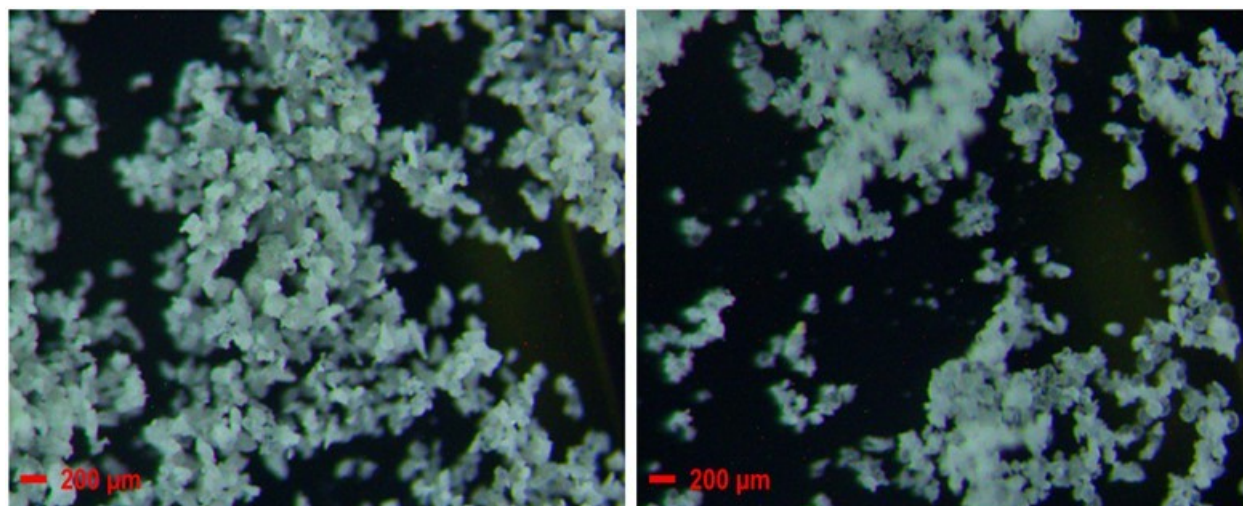


**Figure 5:** OM micrographs of PUF/BPS MCs.

### Encapsulation ability of BPS into the PUF capsules

MCs are prepared from the PUF shell and the filled BPS to be characterized through different instrumental techniques. In particular, chemical characterization of the as-prepared MCs is investigated by FTIR spectroscopy, as shown in Figure 6. For PUF spectra (Figure 6A), peaks of O-H and N-H stretching vibrations are assigned at  $3390\text{ cm}^{-1}$ , and a peak at  $2969\text{ cm}^{-1}$  is the stretching vibration of saturated H-C-H symmetry and inverse symmetry. Besides, the peaks at  $1652\text{ cm}^{-1}$ ,  $1560\text{ cm}^{-1}$ , and  $1251\text{ cm}^{-1}$  belong to NH-CO-NH, N-H, and C-O-C stretching vibrations, respectively. A peak of C-H bending vibration is observed at  $1382\text{ cm}^{-1}$ ; C-N stretching vibrations are assigned at  $1194\text{ cm}^{-1}$  and  $1116\text{ cm}^{-1}$ . These results confirm that the shell material is successfully created from PUF wall shell basing on

in-situ polymerization. Furthermore, in BPS spectra (Fig. 6B), C-H stretching and bending vibrations are observed at  $2946$  and  $1417\text{ cm}^{-1}$ , respectively. Peaks of C-O stretching vibration are assigned at  $1309\text{ cm}^{-1}$  and  $1147\text{ cm}^{-1}$ . Besides, special H-C≡C and C≡C stretching vibrations in BPS are absorbed in  $3257\text{ cm}^{-1}$  and  $2133\text{ cm}^{-1}$ , respectively. Peaks at  $1724\text{ cm}^{-1}$ ,  $960\text{ cm}^{-1}$ , and  $798\text{ cm}^{-1}$  belong to C=O stretching vibration, ≡C-H bending vibration, and  $-(\text{CH}_2)_2-$  unit stretching vibration. Overall, there is a matching of core material (BPS) and shell material (PUF) in PUF/BPS MCs spectra (Figure 6B), as well as the spectra of BPS and the core material inside the MCs, have also been confirmed a matching at above-mentioned characteristic peaks. Hence, it manifests that BPS-core material has been successfully encapsulated in the PUF capsules.

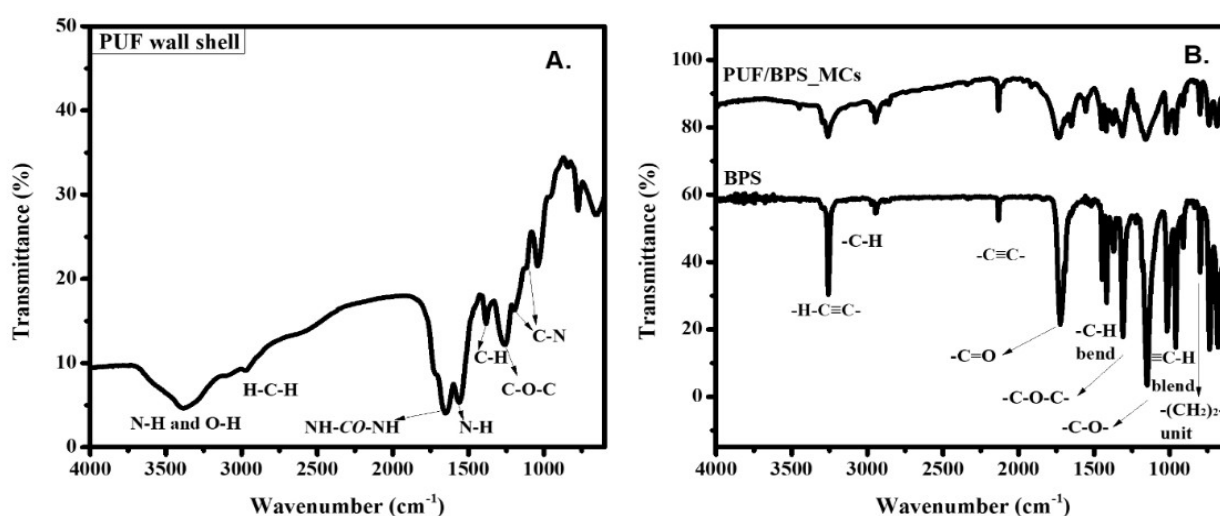


**Figure 6:** FT-IR spectra of PUF wall shell (A), PUF/BPS MCs, and BPS (B).

To further evaluate MCs' characterization and the storage ability of BPS in the MCs, a gas chromatograph is applied to estimate the appearance of core material successfully encapsulated in the shell material. Here, the mixture of acetone and MCs are sealed to recognize the presence of BPS into the MCs for one week, as well as the core material has enough time to diffuse from the PUF capsules into the solvent. GC instrument is employed for the filtered solution

to can assess the presence of core material. From the GC results of this filtered solution, there is the only peak of acetone solvent, indicating that the core material is still kept in shell material during 5 days (Figure 7A); however, two peaks of core material (BPS) have appeared in this filtered solution after one week (Figure 7B). This result is also similar to the above FTIR report for successfully encapsulated BPS in UF shell material and the storage ability of BPS in the MCs.

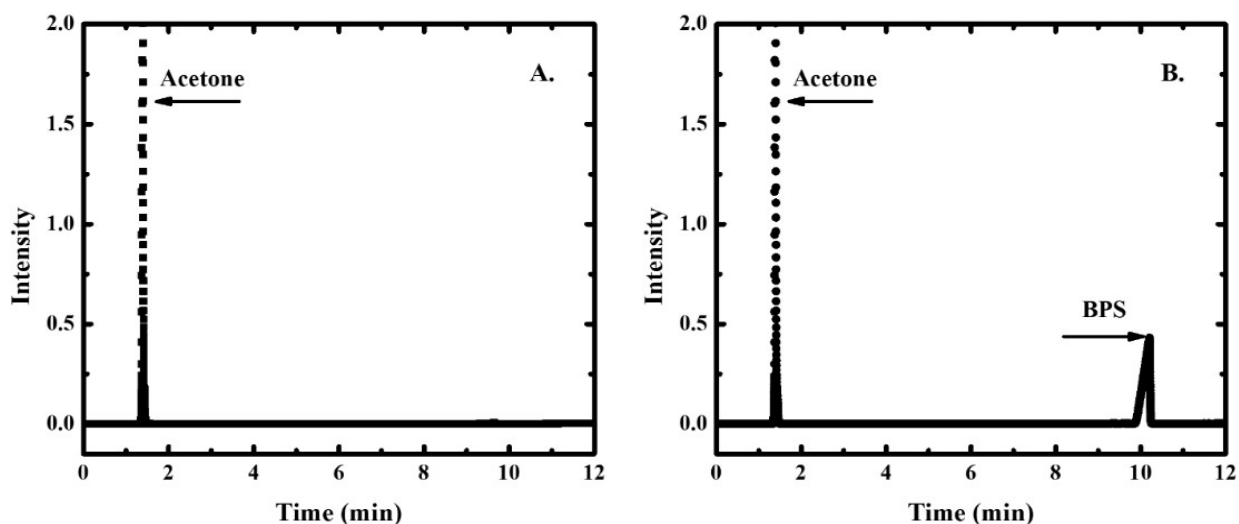


**Figure 7:** GC curves of a (Acetone: MCs) mixture after 5 days (A) and 7 days (B).

#### Content of BPS and PUF shell thickness in PUF/BPS MCs

The identification of BPS content in MCs is concerned as a major factor. In order to determine the content of BPS in the prepared MCs, five mixtures of PUF/BPS have been prepared as follows: 100/0, 30/70, 20/80, 10/90, and 0/100 (% wt/wt), which are then measured by TGA instrument as shown in Figure 8 (A, B). The calibration curve for BPS content versus weight loss of BPS will be constructed (Figure 8C) from the above-prepared mixtures, so the relationships of the content of BPS and the weight loss of BPS is calculated as shown in Equation 1, where  $y$  is the

content of BPS, and  $x$  is the weight loss of BPS from the TGA curve. Based on Equation 1, the content of BPS in the prepared MCs can be identified, resulting in that the content of BPS in the prepared MCs achieved 75.0% [As shown in Figure 10, the obtained weight loss of BPS ( $WL = \sim 77.0\%$ , at  $210\text{ }^{\circ}\text{C}$ ) on the TGA curve of PUF/BPS MCs is considered as  $x$ -value that can be added in Eq. (1) to calculate the content of BPS ( $y$ -value)]. At the same time, this method can be seen as a new one to identify the core material content in the MCs.

$$y = 0.1781x^2 + 0.8300x + 0.0001 \quad (\text{Eq. 1})$$

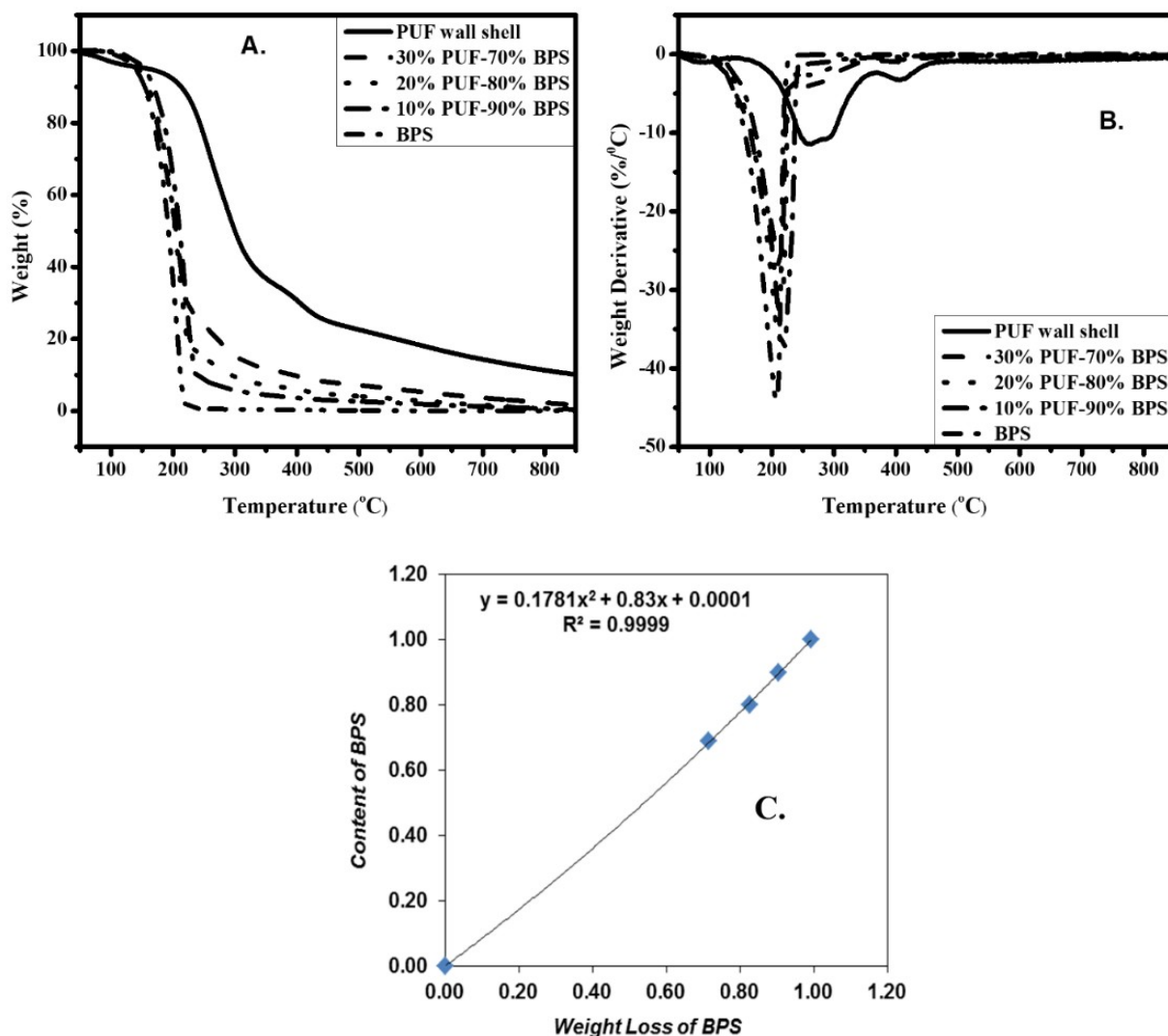


**Figure 8:** TGA (A) and DTG (B) curves of five mixtures. Calibration curve for content of BPS versus weight loss of BPS (C).

In addition to the above-mentioned identification method of the content of the core material, the content of BPS in the prepared MCs can also be determined by the solvent extraction method. The PUF/BPS MCs are crushed in a mortar with pestle. A solvent mixture (ethanol and acetone) is employed to dissolve and extract the core material from these MCs. Next, the insoluble PUF shell is filtered, washed, and dried for 12 – 24 h. The content of encapsulated core material ( $E_c$ ) in the prepared MCs is calculated by Equation 2;  $W_s$  and

$W_i$  are the weight of the sample and the insoluble shell's weight, respectively. As a result, the content of BPS in the PUF/BPS MCs has been attained to 73.0%. As such, the calculated contents of core material are similar in the two methods as mentioned above.

$$E_c = \frac{(W_s - W_i)}{W_s} \cdot 100\% \quad (\text{Eq. 2})$$

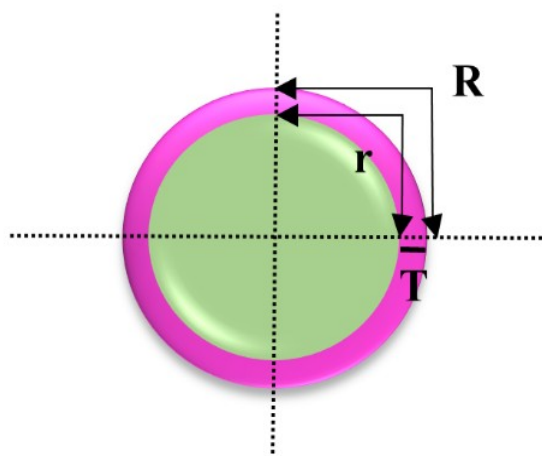


**Figure 9:** Schematic diagram of PUF/BPS MCs.

Additionally, the determination of the PUF shell thickness in PUF/BPS MCs is truly significant. The MC is supposed as a round globule (Figure 9) to calculate this PUF shell thickness in this study. The mass of PUF shell is shown in Equation 3,  $M_s$  is considered as the mass of PUF shell;  $R$  and  $r$  are seen with an order to as the MCs radius and the core of the MCs radius, and  $\rho_s$  is defined as the PUF density (1.180 g/cm<sup>3</sup> (21, 22)). Besides, the mass of BPS is shown in Equation 4,  $M_c$  is the mass of BPS, and  $\rho_c$  is the density of BPS (1.17 g/cm<sup>3</sup>). The content of BPS ( $P$ ) and the thickness of PUF shell ( $T$ ) are presented with an order in Equations 5 and 6. Hence, from Equations 3 to 6, it is truly easy to obtain the thickness of the PUF shell (Equation 7).

$$\frac{4}{3} \cdot \pi \cdot R^3 \cdot \rho_s - \frac{4}{3} \cdot \pi \cdot r^3 \cdot \rho_s = M_s \quad (\text{Eq. 3})$$

$$\frac{4}{3} \cdot \pi \cdot r^3 \cdot \rho_c = M_c \quad (\text{Eq. 4})$$

$$P = \frac{M_c}{M_c + M_s} \cdot 100\% \quad (\text{Eq. 5})$$

$$T = R - r \quad (\text{Eq. 6})$$

$$T = R \cdot \left( 1 - \frac{\sqrt[3]{\rho_s \cdot P}}{\rho_c - \rho_c \cdot P + \rho_s \cdot P} \right) \quad (\text{Eq. 7})$$

Based on the above Equation 7, the thicknesses of PUF shell are identified to be 5.72 – 11.35  $\mu\text{m}$  according to 63 – 125  $\mu\text{m}$  of diameters of MCs and 75.0% of MCs BPS content; concomitantly, the MCs fill percentage is estimated to be 76.0% by volume.

### Thermal properties of PUF/BPS MCs

In addition to identifying the BPS content in the PUF/BPS MCs based on a TGA instrument, this instrument is also employed in an investigation of the thermal property of the PUF/BPS MCs, as well as the thermal stability of the MCs is considered as a significant factor in the practical application (23-25), the thermal analysis of the prepared MCs involve to both the PUF shell and BPS (core agent) to be conducted for the further characterization. Specifically, Figure 10 (A, B) displays TGA and DTG curves of PUF wall shell, PUF/BPS MCs, and BPS. In TGA and DTG curves of PUF wall shell, it shows that a little weight loss at  $\sim 100$   $^{\circ}\text{C}$  is primarily attributed to the elimination of free formaldehyde and an entrapped residual water (3, 26-30); in particular, the weight loss at 249  $^{\circ}\text{C}$  and 355  $^{\circ}\text{C}$  are primarily ascribed to the PUF's decomposition. The residual undergoes extensive fragmentation above 500  $^{\circ}\text{C}$  (26-30). Additionally, the thermal degradation of MCs containing BPS is further much complexed than that of PUF shell material. The as-prepared MCs are better thermal stability through the weight loss at 257  $^{\circ}\text{C}$  and 418  $^{\circ}\text{C}$ , while the core material (BPS) degradation is initiated at 210  $^{\circ}\text{C}$  as shown in TGA and DTG curves. Hence, it is further confirmed that the as-prepared MCs truly contain both PUF (shell material) and BPS (core material), which is suitable with the above FTIR and GC reports.

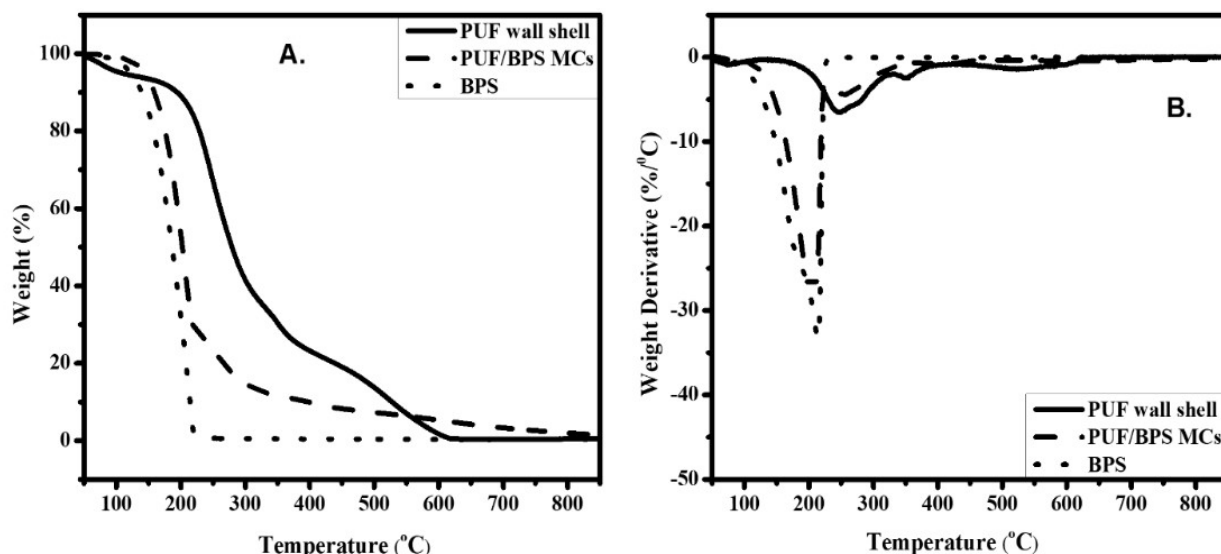


Figure 10: TGA (A) and DTG (B) curves of PUF wall shell, PUF/BPS MCs and BPS.

**Stability of PUF/BPS MCs**

In the practical application of the MCs, the storage ability (or stability) is seen as a significant factor; therefore, the stability of PUF/BPS MCs in this study is truly necessary to be investigated. Herein, the PUF/BPS MCs are crushed in a mortar and pestle mentioned in the solvent extraction method. A solvent mixture (ethanol and acetone) is employed to dissolve and extract the core material from these MCs. Next, the insoluble PUF shell is filtered, washed meticulously, and dried for 12 – 24 h. The core content in the MCs at the initial time and at storage time is calculated by Equation 2, then the weight loss of MCs in the storage time is calculated by Equation 8,  $E_{c1}$  and  $E_{c2}$  are initial content of core material and content of core material during the storage time, respectively.

$$WL = \frac{E_{c1} - E_{c2}}{E_{c1}} \cdot 100\% \quad (\text{Eq. 8})$$

As shown in Figure 11, it indicates that the stability of MCs is well maintained within 50 days at room temperature, the weight loss of the MCs is about 0.20 wt% within 50 days, as well as the significant role of PUF shell in BPS protection. The weight loss of the PUF/BPS MCs becomes higher with the increasing tested storage time. At the same time, the weight loss of MCs in the storage time involves the diffusion of the core material over the PUF shell and the elimination of free-formaldehyde (22, 23) primarily. As such, this study can open an approach for preparing the PUF/BPS MCs are employed as healing agents.

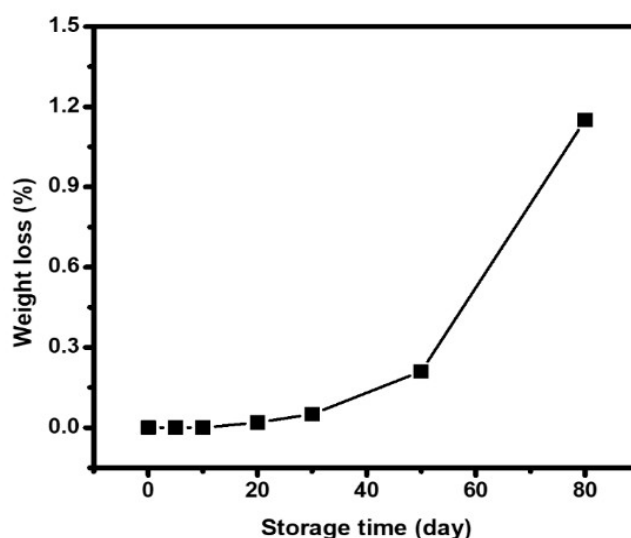
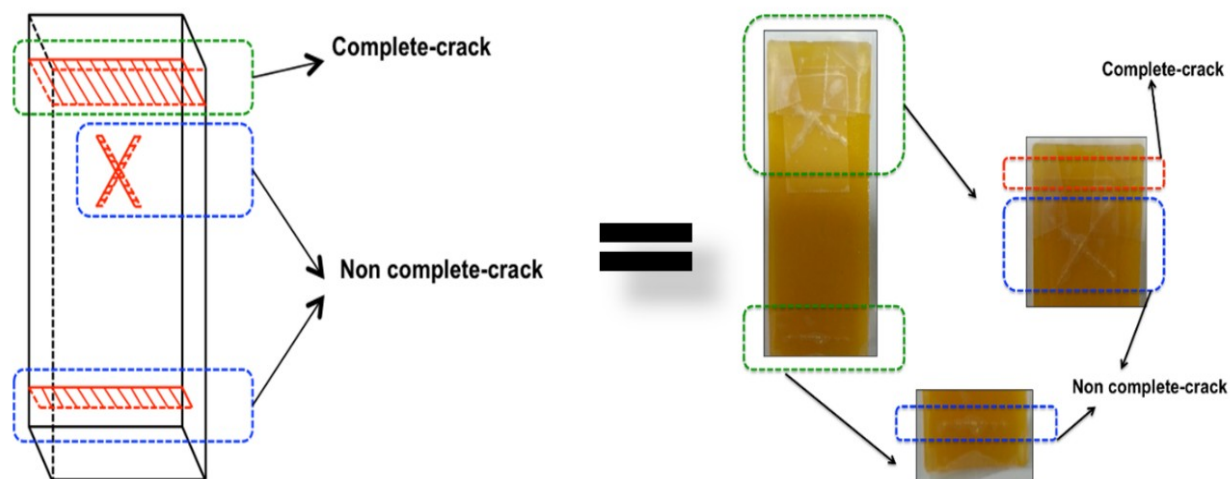


Figure 11: Weight loss of PUF/BPS MCs at room temperature.

**Self-healing ability of PU/MCs-based SHMs**

As known, a healing agent is encapsulated and protected in globular capsules when damages break them. The self-healing mechanism is performed by releasing the healing agent to react with the polymeric matrix at the damage region. In particular, MC is seen as one of many applications of polymer to protect specific functional materials

from or to release them into an outer phase for a long time. Herein, the self-healing ability of the PU/MCs-based SHMs is activated by rupture of the MCs in response to cracks, then an amount of BPS liquid in the MCs is released to move into the cracked regions, conducting reaction with the azide groups of the polymeric matrix (GAP-based PU) via "azide-alkyne" click.



**Figure 12:** Schematic of complete-crack and non-complete-crack on PU/MCs-based SHMs.

Gragert et al. (15) conducted an investigation of two different healing agents (azide and alkyne compounds)-contained capsules on a high-molecular-weight poly(isobutylene) matrix, resulting that the specimens could be recovered after 5 days at 25 °C (91%) or 3 days at 60 °C (107%) through the shear-induced click cross-linking. Akhan et al. (16) preformed a survey of one healing agent (azide compound)-contained capsule on an alkyne-graphene oxide matrix with the use of CuAAC click reaction, leading to improving the self-healing efficiency through an incorporation of the low molecular weight self-healing agent within the microcapsule. Besides, Saikia et al. (18) designed an azide-alkyne cycloaddition-based SHMs through azide-multiwall carbon nanotubes with poly(*t*-butyl acrylate) and alkyne compound-contained capsule embedded in an epoxy matrix, manifesting that this SHM recovered as much as 65% of its original fracture toughness. Herein, the self-healing ability of the as-prepared PU/MCs-based SHMs on the basis of only one type of healing agent (alkyne compound)-contained capsule is surveyed through various weight ratios of MCs and cracks. PU/MCs-based SHMs have been prepared by adding the PUF/BPS MCs into PU matrix with four different weight ratios of the MCs (i.e.: 5, 10, 25, and 40%). After the curing process of PU/MCs-based SHMs, these samples are cut following the complete-crack and non-complete-crack, which are then put into oven at 60 °C as described in Figures 12 and 13. The

resulting that the prepared SHMs have not self-healed at various cracked regions after 7 days, it means that the BPS amount in the MCs is not enough to conduct reacting with the azide groups of PU matrix at the cracked regions. However, these cannot explain that the calculated BPS amount in the MCs is quantitatively correct. Thus, to further investigate that, BPS is injected into crack regions of above PU/MCs-based SHMs to be manually delivered to the cracked regions using a syringe, which are then put into an oven (60 °C) for 7 days (Figure 13). For the SHMs containing 5% and 10% of MCs, "azide-alkyne" click has occurred completely at various cracked regions, except for the complete-cracked region of the SHMs containing 10% of MCs. The "azide-alkyne" click has not effectively occurred at each cracked region of the SHMs containing 25% and 40% of MCs, although an amount of BPS has been injected manually into the cracked regions from a syringe. It means that the amount of the MCs actually occupies more than that of the azide groups of PU matrix at the cracked regions. Although the BPS liquid on the surface of each sample disappeared after 7 days as shown in Figures 13 (3 and 4), they are injected manually into the cracked regions, indicating that injected BPS has diffused into samples to react with the azide groups of PU matrix. However, the diffusion regions in the phenomena have not yet been clearly explained here.

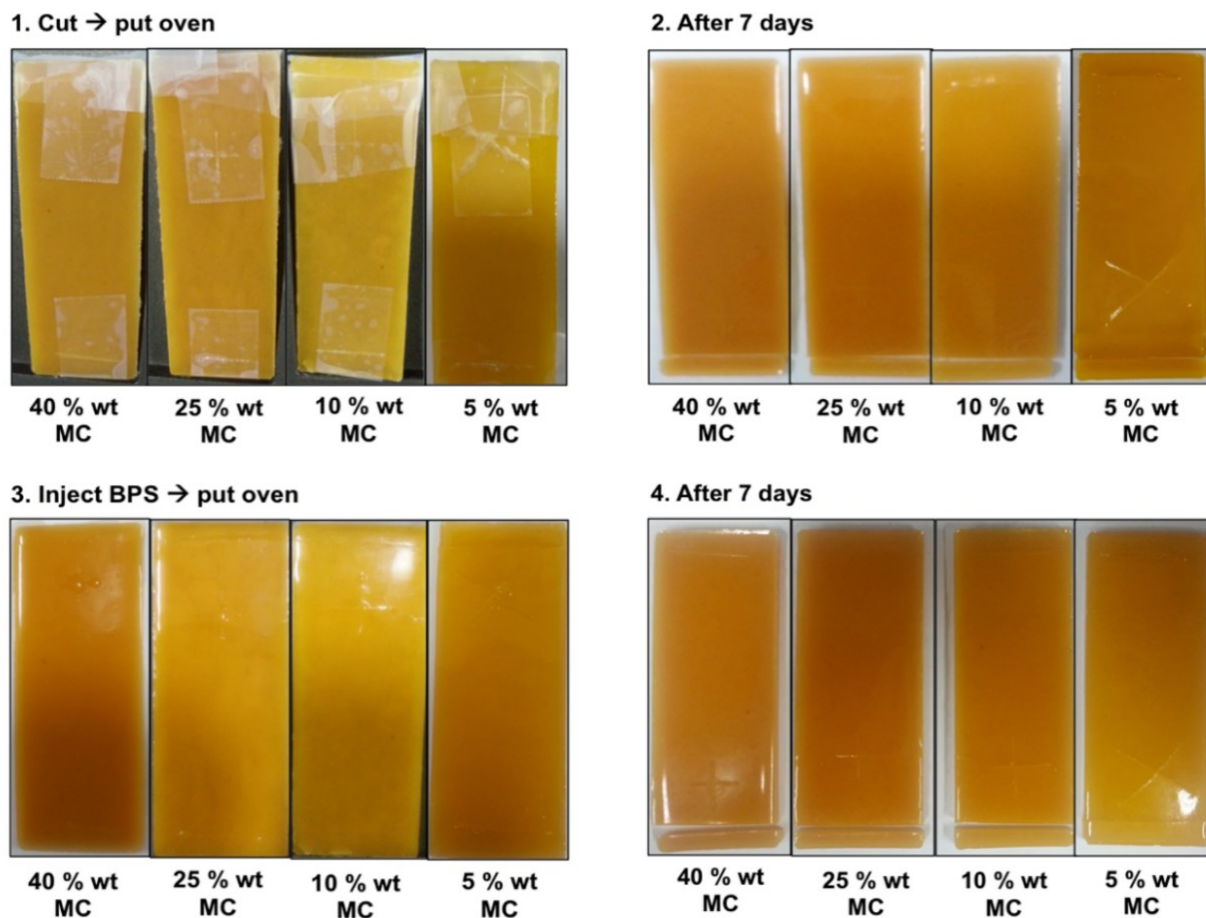


**Figure 13:** Influence of weight ratios of the MCs and injected BPS into PU/BPS-based SHMs.

In order to further explain the results mentioned above, an SHM containing MCs has been randomly distributed, as shown in Figure 14. It is assumed that a planar crack has occurred in this material system. All MCs then are intersected by the plane, and which will be broken to release core material. Besides, the number of broken MCs ( $n$ ) is calculated by Equation 9,  $N$  is seen as the total number of MCs in the sample, and  $P$  is the probability of a broken MC. It means that the MCs are evenly distributed in the sample; the probability should be based on Equation 10;  $\rho_s$ ,  $A$ ,  $d_c$ , and  $M_s$  are the density of the sample, the crack area, the diameter of the MCs, and the total mass of the sample, respectively. Besides, the total number of MCs in the PU/MCs-based SHMs can be calculated on the MCs weight fraction from Equation 11;  $\phi$  and  $m_c$  are the mass fraction and the mass of MCs, respectively. The amount of delivered BPS ( $m$ ) from the cracked area is calculated by Equation 12,  $m_h$  is the total mass of BPS delivered, assuming all MCs intersected by the cracked region are broken. From Equations 9 – 12, the available, total mass of BPS for delivery per unit crack area is calculated by Equation 13. The above-mentioned total mass of BPS is proportional

to both the weight fraction and the diameter of MCs (Table 1), as well as the self-healing ability can be controlled by both available BPS amount at the cracked region and achieved self-healing status.

$$n = P \cdot N \quad (\text{Eq. 9})$$

$$P = \frac{\rho_s \cdot A \cdot d_c}{M_s} \quad (\text{Eq. 10})$$

$$N = \frac{\phi \cdot M_s}{m_c} \quad (\text{Eq. 11})$$

$$m = \frac{m_h}{A} = \frac{n \cdot m_c}{A} \quad (\text{Eq. 12})$$

$$m = \rho_s \cdot \phi \cdot d_c \quad (\text{Eq. 13})$$

Furthermore, based on the visually observed results of the above samples (Figure 13), the samples have been designed with different cracks and MCs weight fractions to investigate the self-healing ability. These results manifest that the observed healing performance is a combination of MCs' weight fraction and diameter in this material

system. Overall, it is supposed that the self-healing ability can depend on the amount of available BPS – healing agent, which can be supported from Equation 13. As a result, the BPS amount delivered autonomically from MCs is not enough to reach effectively the self-healing ability (Table 1). Here, the best healing capacity has been achieved for the SHMs containing 5% and 10% of MCs. Moreover, the MC's weight fraction and diameter relationship also affect the amount of core agent in the MCs distributed at the cracked region. According to some references, the PUF capsules with rougher surfaces and larger diameters are beneficial to appreciate the self-healing efficiency of polymeric composites (1, 31). At the same time, the appreciated self-healing ability can be achieved by delivering much the healing agent into the cracked regions; according to theory, which suitable weight fractions of MCs can accomplish. However, for an actual self-

healing efficiency, it can much depend on the necessary properties of the final product (i.e., its bonding strength with polymeric matrix, density, thickness, etc.).

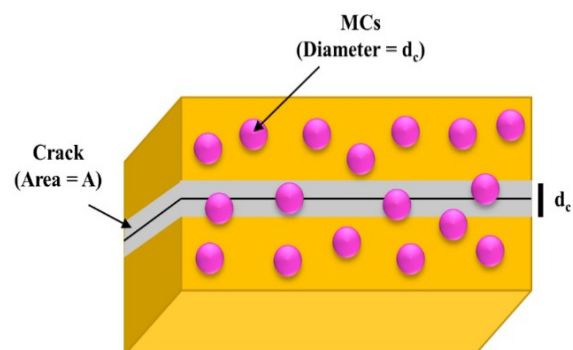


**Figure 14:** Schematic of PUF/BPS MCs in PU matrix.

**Table 1:** The amount of delivered BPS normalized by crack area.

Samples	$d_c$ ( $\mu\text{m}$ )	$\rho_s$ ( $\text{g}/\text{cm}^3$ )	$\Phi$ (%)	$m$ ( $\text{g}/\text{cm}^2$ )* $10^4$
<b>5 wt% MCs</b>	63 – 125	1.306	5	4.11 – 8.16
<b>10 wt% MCs</b>	63 – 125	1.306	10	8.23 – 16.33
<b>25 wt% MCs</b>	63 – 125	1.306	25	20.57 – 40.81
<b>40 wt% MCs</b>	63 – 125	1.306	40	32.91 – 65.30

## CONCLUSIONS

In summary, the PUF shell has been prepared successfully by the in-situ polymerization. The PUF particles are precipitated through the fine powder formation and bonded to the surface of MCs. Concomitantly, the as-prepared MCs consist of both PUF – shell material and BPS – core agent, which are prepared successfully with up to 82.0% yield achieved based on the in-situ polymerization process of PUF shell. Additionally, the MCs have better thermal stability up to 257 °C with the rough outer surface. The MCs have successfully encapsulated 75.0% of BPS with a size range of 63 – 125  $\mu\text{m}$  and the PUF shell thickness range of 5.72 – 11.35  $\mu\text{m}$ ; moreover, the stability of MCs is well maintained within 50 days at room temperature based on the solvent extraction method. In addition, the as-prepared PUF/BPS MCs have been employed to fabricate PU/MCs-based SHMs containing various weight ratios of the MCs, suggesting that the BPS amount is delivered autonomically through using MCs is too low to

reach the self-healing ability effectively. Besides, the best healing performance has been achieved for the SHMs containing 5% and 10% of MCs when an amount of BPS has been injected manually into the cracked regions, indicating that the healing ability could be investigated. However, its bonding strength with polymeric matrix, thickness, density, etc., also involves self-healing efficiency. These can open an approach for the fabrication of capsule-based SHMs, and the characterization and reaction rate of the capsule-based SHMs can also be investigated in the next work.

## REFERENCES

1. Brown EN, Kessler MR, Sottos NR, White SR. In situ poly(urea-formaldehyde) microencapsulation of dicyclopentadiene. *Journal of Microencapsulation*. 2003;20(6):719–30. DOI: <https://doi.org/10.3109/02652040309178083>.
2. Yuan L, Liang G, Xie J, Li L, Guo J. Preparation and characterization of poly(urea-formaldehyde)

- microcapsules filled with epoxy resins. *Polymer*. 2006;47(15):5338–49. DOI: <https://doi.org/10.1016/j.polymer.2006.05.051>.
3. Suryanarayana C, Rao KC, Kumar D. Preparation and characterization of microcapsules containing linseed oil and its use in self-healing coatings. *Progress in Organic Coatings*. 2008;63(1):72–8. DOI: <https://doi.org/10.1016/j.porgcoat.2008.04.008>.
4. Cosco S, Ambrogi V, Musto P, Carfagna C. Properties of poly(urea-formaldehyde) microcapsules containing an epoxy resin. *Journal of Applied Polymer Science*. 2007;105(3):1400–11. DOI: <https://doi.org/10.1002/app.26263>.
5. Keller MW, Sottos NR. Mechanical Properties of Microcapsules Used in a Self-Healing Polymer. *Experimental Mechanics*. 2006;46(6):725–33. DOI: <https://doi.org/10.1007/s11340-006-9659-3>.
6. Ghorbanzadeh Ahangari M, Fereidoon A, Jahanshahi M, Sharifi N. Effect of nanoparticles on the micromechanical and surface properties of poly(urea-formaldehyde) composite microcapsules. *Composites Part B: Engineering*. 2014;56:450–5. DOI: <https://doi.org/10.1016/j.compositesb.2013.08.071>.
7. Acik G, Karabulut HRF, Altinkok C, Karatavuk AO. Synthesis and characterization of biodegradable polyurethanes made from cholic acid and L-lysine diisocyanate ethyl ester. *Polymer Degradation and Stability*. 2019;165:43–8. DOI: <https://doi.org/10.1016/j.polymdegradstab.2019.04.015>.
8. Caraculacu AA, Coseri S. Isocyanates in polyaddition processes. Structure and reaction mechanisms. *Progress in Polymer Science*. 2001;26(5):799–851. DOI: [https://doi.org/10.1016/S0079-6700\(00\)00033-2](https://doi.org/10.1016/S0079-6700(00)00033-2).
9. Acik B, Acik G, Erdemi H. Synthesis and characterization of bile acid, poly ( $\epsilon$ -caprolactone) and L-lysine diisocyanate ethyl ester based polyurethanes and investigation of their biodegradability properties. *European Polymer Journal*. 2021;146:110247. DOI: <https://doi.org/10.1016/j.eurpolymj.2020.110247>.
10. Binder WH, Sachsenhofer R. 'Click' Chemistry in Polymer and Material Science: An Update: 'Click' Chemistry in Polymer and Material Science: An Update. *Macromolecular Rapid Communications*. 2008;29(12–13):952–81. DOI: <https://doi.org/10.1002/marc.200800089>.
11. Díaz DD, Punna S, Holzer P, McPherson AK, Sharpless KB, Fokin VV, et al. Click chemistry in materials synthesis. 1. Adhesive polymers from copper-catalyzed azide-alkyne cycloaddition. *Journal of Polymer Science Part A: Polymer Chemistry*. 2004;42(17):4392–403. DOI: <https://doi.org/10.1002/pola.20330>.
12. Rostovtsev VV, Green LG, Fokin VV, Sharpless KB. A stepwise Huisgen cycloaddition process: copper(I)-catalyzed regioselective "ligation" of azides and terminal alkynes. *Angewandte Chemie International Edition*. 2002;41(14):2596–9. DOI: [https://doi.org/10.1002/1522-3773\(20020715\)41:14<2596::AID-ANIE2596>3.0.CO;2-4](https://doi.org/10.1002/1522-3773(20020715)41:14<2596::AID-ANIE2596>3.0.CO;2-4).
13. Vo TS, Vo TTBC. Preparation and Characterization of Bis-Propargyl-Succinate, and its Application in Preliminary Healing Ability of Crosslinked Polyurethane using "Azide-Alkyne" Click. *Journal of Engineering Science and Technology Review*. 2020;13(4):110–6. DOI: <https://doi.org/10.25103/jestr.134.10>.
14. Vo TS, Vo TTBC, Tien TT, Sinh NT. Enhancement of mechanical property of modified polyurethane with bis-butyl succinate. *Journal of the Turkish Chemical Society Section A: Chemistry*. 2021;8(2):519–26. DOI: <https://doi.org/10.18596/jotcsa.878515>.
15. Gragert M, Schunack M, Binder WH. Azide/Alkyne-"Click"-Reactions of Encapsulated Reagents: Toward Self-Healing Materials. *Macromolecular Rapid Communications*. 2011;32(5):419–25. DOI: <https://doi.org/10.1002/marc.201000687>.
16. Akhan S, Oktay B, Özdemir OK, Madakbaş S, Kayaman Apohan N. Polyurethane graphene nanocomposites with self-healing properties by azide-alkyne click reaction. *Materials Chemistry and Physics*. 2020;254:123315. DOI: <https://doi.org/10.1016/j.matchemphys.2020.123315>.
17. Döhler D, Michael P, Binder WH. Autocatalysis in the Room Temperature Copper(I)-Catalyzed Alkyne-Azide "Click" Cycloaddition of Multivalent Poly(acrylate)s and Poly(isobutylene)s. *Macromolecules*. 2012;45(8):3335–45. DOI: <https://doi.org/10.1021/ma300405v>.
18. Saikia BJ, Dolui SK. Preparation and characterization of an azide-alkyne cycloaddition based self-healing system via a semiencapsulation method. *RSC Advances*. 2015;5(112):92480–9. DOI: <https://doi.org/10.1039/C5RA17666B>.

19. Tornøe CW, Christensen C, Meldal M. Peptidotriazoles on solid phase: [1,2,3]-triazoles by regioselective copper(i)-catalyzed 1,3-dipolar cycloadditions of terminal alkynes to azides. *The Journal of Organic Chemistry*. 2002;67(9):3057–64. DOI: <https://doi.org/10.1021/jo011148j>.
20. Gorman IE, Willer RL, Kemp LK, Storey RF. Development of a triazole-cure resin system for composites: Evaluation of alkyne curatives. *Polymer*. 2012;53(13):2548–58. DOI: <https://doi.org/10.1016/j.polymer.2012.04.002>.
21. Osemeahon SA, Barminas JT. Development of amino resin for emulsion paint formulation: reactive blending of methylol urea with soybean oil. *African Journal of Biotechnology*. 2007;6(6):803-9. DOI: <https://doi.org/10.4314/ajb.v6i6.56907>.
22. Osemeahon SA, Barminas JT. Study of some physical properties of urea formaldehyde and urea proparaldehyde copolymer composite for emulsion paint formulation. *International Journal of Physical Sciences*. 2007; 2: 169-177. DOI: <https://doi.org/10.5897/IJPS.9000533>.
23. Liu Q, Zhang J, Liu W, Guo F, Pei J, Zhu C, et al. Preparation and characterization of self-healing microcapsules embedding waterborne epoxy resin and curing agent for asphalt materials. *Construction and Building Materials*. 2018;183:384–94. DOI: <https://doi.org/10.1016/j.conbuildmat.2018.06.185>.
24. Liao LP, Zhang W, Zhao Y, Li WJ. Preparation and Characterization of Microcapsules for Self-healing Materials. *Chemical Research in Chinese Universities*. 2010; 26: 496-500.
25. Cai X, Fu D, Qu A. Effects of processing conditions on the properties of epoxy resin microcapsule. *J Wuhan Univ Technol-Mat Sci Edit*. 2015;30(4):689–94. DOI: <https://doi.org/10.1007/s11595-015-1213-7>.
26. Arshad MA, Maaroufi A, Benavente R, Pinto G. Kinetics of the thermal degradation mechanisms in urea-formaldehyde cellulose composites filled with zinc particles. *Journal of Materials Science: Materials in Electronics*. 2017;28(16):11832–45. DOI: <https://doi.org/10.1007/s10854-017-6991-6>.
27. Arshad MA, Maaroufi A, Benavente R, Pinto G. Thermal degradation of urea-formaldehyde cellulose composites filled with aluminum particles: Kinetic approach to mechanisms. *Journal of Applied Polymer Science*. 2017;134(19). DOI: <https://doi.org/10.1002/app.44826>.
28. Arshad MA, Maaroufi A, Pinto G, El-Barkany S, Elidrissi A. Morphology, thermal stability and thermal degradation kinetics of cellulose-modified urea-formaldehyde resin. *Bulletin of Materials Science*. 2016;39(6):1609–18. DOI: <https://doi.org/10.1007/s12034-016-1304-x>.
29. Jadhao MM, Paliwal LJ, Bhawe NS. Resin II: Thermal degradation studies of terpolymer resins derived from 2,2'-dihydroxybiphenyl, urea, and formaldehyde. *Journal of Applied Polymer Science*. 2006;101(1):227–32. DOI: <https://doi.org/10.1002/app.23224>.
30. Camino G, Operti L, Trossarelli L. Mechanism of thermal degradation of urea-formaldehyde polycondensates. *Polymer Degradation and Stability*. 1983;5(3):161–72. DOI: [https://doi.org/10.1016/0141-3910\(83\)90007-1](https://doi.org/10.1016/0141-3910(83)90007-1).
31. Brown EN, White SR, Sottos NR. Retardation and repair of fatigue cracks in a microcapsule toughened epoxy composite—Part II: In situ self-healing. *Composites Science and Technology*. 2005;65(15):2474–80. DOI: <https://doi.org/10.1016/j.compscitech.2005.04.053>.





## Application of Oxidative Coupling Reaction using Brucine and Sodium Periodate as Chromogenic Reagent for the Assay of Perindopril Erbumine in Formulations

Thuttgartunta Manikya Sastry<sup>1\*</sup> and Karipeddi Ramakrishna<sup>2</sup>

<sup>1</sup>Department of Chemistry, Gayatri Vidya Parishad College of Engineering (Autonomous), Madhrawada, Visakhapatnam – 530047, India

<sup>2</sup>Department of Chemistry, Institute of Science, GITAM (Deemed to be University), Rushikonda, Visakhapatnam- 530045, India

**Abstract:** The drug Perindopril Erbumine (PE), an ACE inhibitor, and can be used to treat the patients with hypertension and cardiac failure problems. A sensitive, inexpensive, and precise analytical technique has been developed for the estimation of Perindopril in bulk and formulations. The procedure involves the development of color by forming an oxidative coupling reaction between drug (PE) and Brucine/ $\text{IO}_4^-$ ). The formed colored species were measured at  $\lambda_{\text{max}}=520$  nm. The developed method showed linearity within the concentration limits of 8-24  $\mu\text{g mL}^{-1}$ . The linear correlation coefficient (r) and molar absorptivity were found to be 0.9999 and  $9.16 \times 10^3 \text{ mol}^{-1}\text{cm}^{-1}$ . % Recovery  $\pm$  SD values were in the range of 99.16 - 100.7 ( $\pm 0.41$  -  $\pm 0.8$ ) (n=3) which indicates the accuracy of the developed method. The interference of other excipients that are commonly present in formulations is found to be negligible. Precision and accuracy of the proposed method were confirmed by Student's t-test and F-tests at 95% confidence limits with (n-1) degrees of freedom. The validity parameters of the proposed method were calculated by ICH guidelines.

**Keywords:** Spectrophotometry, perindopril erbumine, brucine, coversyl and perigard-DF.

**Submitted:** June 24, 2020. **Accepted:** July 11, 2021.

**Cite this:** Sastry T, Ramakrishna K. Application of Oxidative Coupling Reaction using Brucine and Sodium Periodate as Chromogenic Reagent for the Assay of Perindopril Erbumine in Formulations. JOTCSA. 2021;8(3):803–10.

**DOI:** <https://doi.org/10.18596/jotcsa.757440>.

**\*Corresponding author.** E-mail: [tmsastry@yahoo.com](mailto:tmsastry@yahoo.com).

### INTRODUCTION

Pharmacodynamic agents refer to group of drugs which activate or reduce various functions of the body so as to bring some relief to the body without healing the disease. These are generally used as depressants or stimulants, blocking agents, antianginal, anticoagulants, antihypertensive agents, anti-acne and ACE inhibiting agents, etc. In the present investigation, the drug used namely perindopril erbumine (PDE) is referred to as one of the categories of the aforesaid agents called as angiotensin converting enzyme inhibitor (ACE

inhibitor). It is used as a medicine for patients having the problems like hypertension and cardiac failure. ACE inhibitor (1) inhibits the transfer of angiotensin (AT-I) into angiotensin (AT-II).

The molecular formula of Perindopril Erbumine (PPE) is  $\text{C}_{23}\text{H}_{43}\text{N}_3\text{O}_5$ . Its IUPAC name is "(2S, 3aS, 7aS)-1-[(S)-N-[(S)-1-carboxy-butyl]-alanyl]hexahydro-2-indolincarboxylic acid, 1-ethylester (2), compound with tertiary-butylamine (1:1)" (Figure 1). The drug (PDE) is listed in the British Pharmacopoeia (3), Remington (4), and Physician's desk reference (5). A survey of the literature

revealed that UV (6,7), HPLC (8-11), RP-HPLC (12-18), spectrofluorimetric (19,20), UV-Visible spectrophotometric (21-24), kinetic spectrophotometric (25,26), LC-MS (27,28), and GC-MS (29) methods were reported for the estimation of PPE. It was found that there are very few spectrophotometric methods are reported for the assay of PPE. The authors made an attempt to develop and validate spectrophotometric method for PPE in bulk form and formulations using Brucine -  $\text{IO}_4^-$  as chromogenic reagent.

## MATERIALS AND METHODS

### Instrumentation

Precise and accurate wavelength measurements were made using UV wavelength scanning double beam spectrophotometer (UNICAM UV-500, Thermo Electron Corporation, UK) and visible scanning spectrophotometer (SL-177 of Elico, Elico India). Digital pH meter (Elico LI 120) was used for measuring PH of the samples. All materials were weighed using Dhona 200D analytical balance with an accuracy of  $\pm 0.1$  mg.

### Preparation of Brucine (BCN) Solution, $\text{NaIO}_4$ Solution

Reagents belonging to investigative grade, bulk, and formulation samples were made using deionized water. Brucine (BCN) (Loba; 0.2%,  $5.06 \times 10^{-3}$  M) was prepared by dissolving 200 mg of brucine initially in a minimum amount of 0.16 M  $\text{H}_2\text{SO}_4$  and then made up to 100 mL with distilled water. Sodium metaperiodate (AR grade, BDH; 0.2%,  $9.35 \times 10^{-3}$  M) solution was prepared by dissolving sodium metaperiodate (200 mg) in 100 mL deionized water and standardized by iodometric method. Sulfuric acid (AR grade, Qualigens; 2.3N) was prepared by mixing 6.4 mL of 18 M conc.  $\text{H}_2\text{SO}_4$  to 50 mL of deionized water initially, followed by diminishing to 100 mL with the same solvent (deionized water).

### Preparation of Standard Perindopril Erbumine Solution (ppe)

We dissolved 100 mg of perindopril erbumine in a minimum quantity of 0.1 M sodium hydroxide solution followed by dilution to 100 mL with distilled water to prepare the standard stock solution ( $\text{mg mL}^{-1}$ ). The released free erbumine was extracted with 10.0 mL of chloroform. The aqueous solution free from erbumine was used as the stock solution. It is further diluted stepwise with distilled water to obtain working standard solutions of concentration of  $200 \mu\text{g mL}^{-1}$

### Procedure for Formulations

Coversyl (Serdia Pharmaceuticals (India) Pvt Ltd., India), Coversyl plus (Serdia Pharmaceutical Ind. Ltd., India), Perigard-DF (Glenmark Pharmaceuticals Ltd., India), and Aceon (Solvay Pharmaceuticals, Inc.) containing perindopril erbumine were procured from local market. Tablets equivalent to 2 mg, 4 mg and 8 mg per tablet respectively were selected for this study. Tablet powder equivalent to 100 mg was taken for extraction with chloroform (4 x 25.0 mL portions) and filtered. The filtrate was taken and extracted three times with 0.1 M NaOH using a separating funnel. Stock solution ( $\text{mg mL}^{-1}$ ) was prepared diluting the aqueous alkaline extract to 100 mL with deionized water. The working standard of  $200 \mu\text{g mL}^{-1}$  solutions was made by diluting a portion of the above stock solution and analyzed as per the developed analytical method.

### Calibration Curve of Perindopril Erbumine by UV Method

100 mg of bulk drug sample was dissolved in 100 mL of distilled water to prepare the stock solution ( $\text{mg mL}^{-1}$ ). The working standard solution concentration of  $100 \mu\text{g mL}^{-1}$  was prepared from an aliquot portion of 10.0 mL of the above stock solution. The absorption spectrum was recorded on a spectrophotometer within the UV region against a reagent blank (Figure 3). A portion of the working standard drug solution (1.0 – 3.0 mL, conc.  $100 \mu\text{g mL}^{-1}$ ) was taken in a series of 10.0 mL calibrated tubes, and diluted to 10.0 mL with doubly distilled water. The absorbance was measured at 204 nm against deionized water as blank. The concentration of the drug sample was calculated using its calibration curve (Fig.4). The UV absorption method was chosen as a reference method.

### Protocol of Proposed Method

Aliquots of standard drug solution [1.0 – 3.0 mL,  $200 \mu\text{g mL}^{-1}$ ], 3.0 mL of  $5.067 \times 10^{-3}$  M brucine, 1.5 mL of  $9.35 \times 10^{-3}$  M  $\text{NaIO}_4$  solution and 2.0 mL of 2.3 N sulfuric acid were added successively into a series of calibrated tubes. The volume was brought up to 10.0 mL with distilled water and kept in boiling water bath for 20 min. The solutions were cooled to room temperature and the volume was made up to 25 mL with distilled water. The absorbances were measured at 520 nm against a similar reagent blank within 30 min. The stability of colored species was found as 40 minutes, afterwards the absorbance was found to decrease which may be due to the decomposition of the oxidative coupling product. The amount of PPE was computed from its calibration graph (Figure 5).

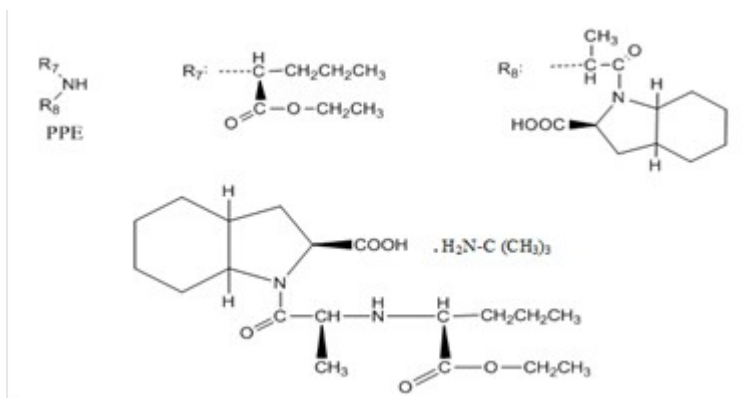


**Figure 1:** Structure of Perindopril Erbumine (PPE).

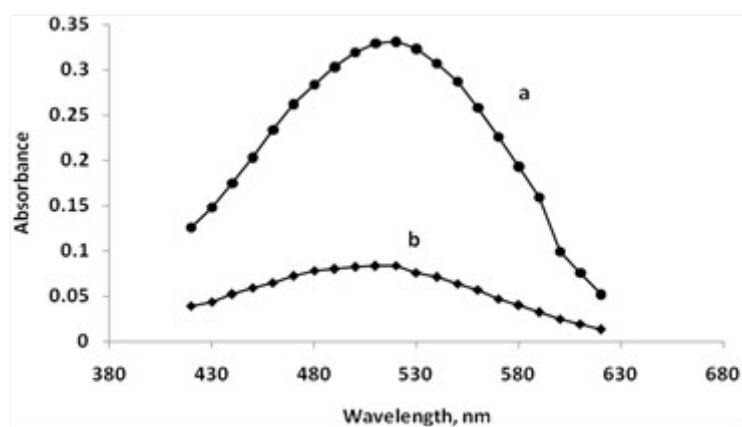


**Figure 2:** Absorption spectrum of PPE - Brucine - NaIO<sub>4</sub> method. a) PPE-Brucine -NaIO<sub>4</sub> method ([PPE]= $3.62 \times 10^{-5}$  M [BCN]= $6.08 \times 10^{-4}$  M; [NaIO<sub>4</sub>]=  $5.61 \times 10^{-4}$  M; [H<sub>2</sub>SO<sub>4</sub>]=  $1.84 \times 10^{-4}$  M ) b) Blank Vs deionized water.

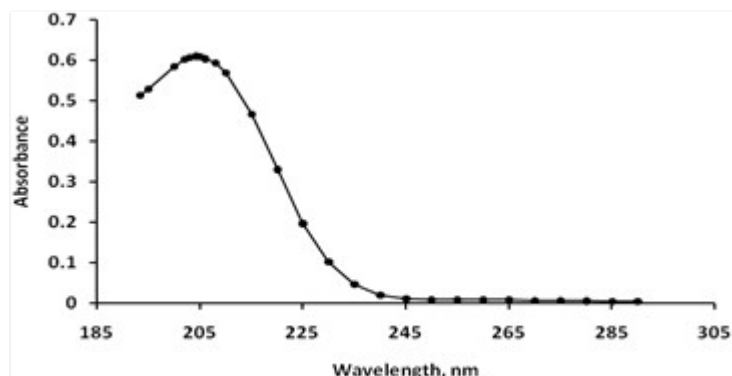


**Figure 3:** Absorption Spectrum of Perindopril ([PPE] =  $4.53 \times 10^{-6}$  M).

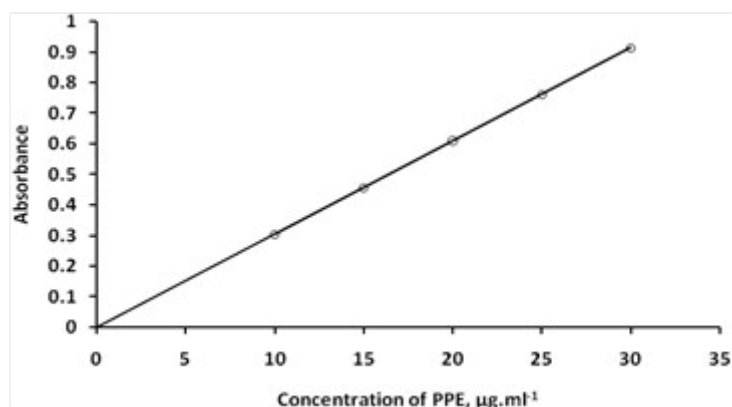


**Figure 4:** Calibrated Curve of Perindopril ( $[PPE] = [4.53 \times 10^{-6} M]$ ).

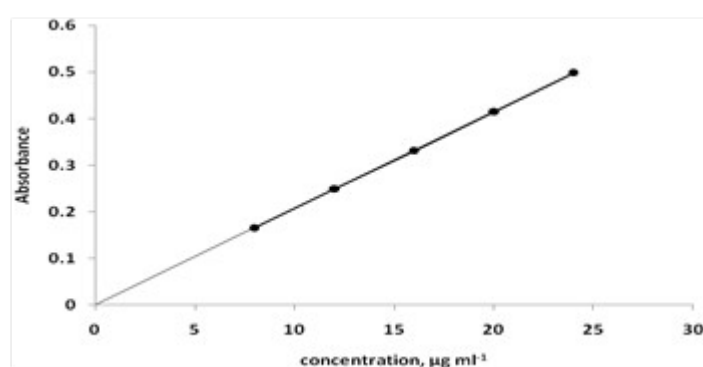
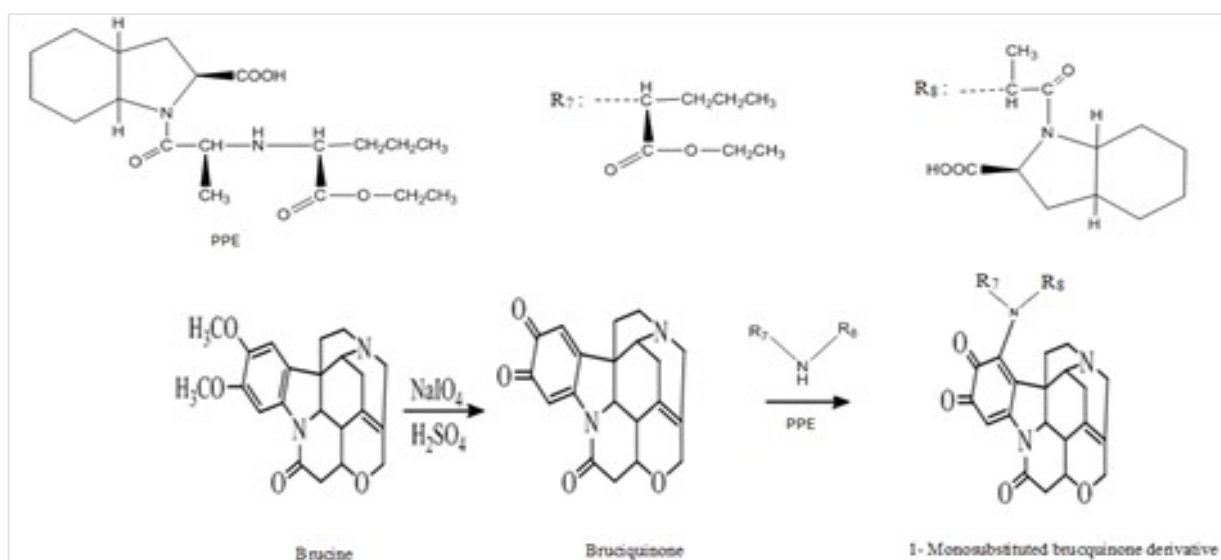


**Figure 5:** Beer's law plot of PPE-Brucine ( $BCN$ )- $NaIO_4$  method ( $[BCN] = 6.08 \times 10^{-4} M$ ;  $[NaIO_4] = 5.61 \times 10^{-4} M$ ;  $[H_2SO_4] = 1.84 \times 10^{-4} M$ ).



**Scheme 1:** Oxidative coupling reaction of perindopril erbumine with brucine-periodate.

**Table 1:** Validation of PPE-BCN the method.

Wavelength	520 nm
Molar absorptivity	$9.16 \times 10^3 \text{ L mol}^{-1}\text{cm}^{-1}$
Beer's Law limits	8 – 24 $\mu\text{g mL}^{-1}$
Limit of detection	$1.0 \times 10^{-2} \mu\text{g mL}^{-1}$
Correlation coefficient	0.9999
Limit of quantification	$1.1 \times 10^{-1} \mu\text{g mL}^{-1}$
Relative Standard Deviation*	0.56
% of error	
0.01 Confidence Limits	0.59
0.05 Confidence Limits	0.93

\*Estimation of six observations.

## RESULTS AND DISCUSSION

### Absorption Spectrum of Perindopril-Brucine System

For the selection of analytical wavelength, the sample solution containing fixed quantity of drug (PPE), brucine solution, and other furnished variables as outlined in the analytical procedure was scanned in the visible wavelength region 350 – 800 nm against the reagent blank. The spectrum of the oxidative coupling product observed to have maximum wavelength at 520 nm which was selected for the analysis. The spectrum of reagent blank against isopropanol solvent was also measured (Figure 2).

### Mechanism for Oxidative Coupling Product Formation Reaction

In the present investigation, the chemistry of colored species was studied. Sastry et al reported brucine-periodate reagent for the spectrophotometric determinations of sulfur-containing compounds and tryptophan (30). In the present investigation, the bruciquinone formed from brucine and periodate undergoes nucleophilic attack on the most electron-rich portion of the coupler (-NH-) in PPE (free from erbumine) to give 1-monosubstituted bruciquinone derivative which is presented in Scheme 1.

### Validation of Analytical Data

Following (ICH) guidelines (31), the developed method was validated for various optical and regressive characteristics such as slope, intercept, correlation coefficient, LOD, LOQ sensitivity, RSD, and percentage of error.

### Linear Relationship

The developed analytical procedure showed the linear relationship within the Beer's law range (8 – 24  $\mu\text{g mL}^{-1}$ ). Beer's law plot ( $n = 6$ ) was measured under optimum conditions and found consisting of linearity with a high correlation coefficient ( $r$ ) value 0.9999. The standard calibration curve drawn at five concentration levels. Results are given in Table 1.

### Limits of LOD and LOQ

Limit of detection (LOD) and Limit of quantification (LOQ) were calculated using the below given expressions.

$$(\text{LOD}) = 3.3 \times S_a / b \quad (1)$$

$$(\text{LOQ}) = 10 \times S_a / b \quad (2)$$

Where  $b$  is the slope of the calibrated curve and  $S_a$  is the standard deviation of the intercept.

### Sensitivity

The sensitivity of the developed method was measured in terms of molar absorptivity ( $\epsilon_{\text{max}}$ ), limit of detection, and limit of quantification. Results of molar absorptivity, LOD, and LOQ are  $9.16 \times 10^3$ ,  $1.0 \times 10^{-2} \mu\text{g.mL}^{-1}$ , and  $1.1 \times 10^{-1} \mu\text{g.mL}^{-1}$ , respectively (Table 1).

### Sandell's Sensitivity

It is measured as "smallest weight of substance that can be detected in column of unit cross section". The Sandell's sensitivity is the concentration of the analyte (in  $\mu\text{g mL}^{-1}$ ) which will give an absorbance of 0.001 in a cell of path length 1 cm. Units of Sandell's sensitivity ( $S$ ) is given as  $\mu\text{g cm}^{-2}$ , and its value was found as  $4.82 \times 10^{-2} \mu\text{g.cm}^{-2}$ .

### Selectivity of Method

Selectivity for the assay analytical procedure was calculated by analyzing standard drug sample solution in the presence of excipients that are commonly present in formulations. The excipients namely microcrystalline cellulose, magnesium stearate, lactose, and titanium dioxide. The results of developed method indicated that no interference from the excipients present in formulations.

### Precision

Precision of the analytical procedure expresses "the closeness of agreement between a series of measurement obtained from six determinations of sample solution under prescribed conditions". The intra-day precision was calculated by measuring "absorbance of sample solution of particular concentration within the linearity range at regular intervals on the same day". The inter-day precision

was calculated by measuring "absorbance of sample solution of same concentration at a fixed time in three consecutive days". The precision of developed method expressed in terms of relative standard deviation (RSD) for the smallest concentration indicating good precision. Results are presented in Table 1.

### Accuracy

Accuracy of analytical procedure was calculated as "percentage of error between the measured mean concentrations and taken concentrations". The accuracy and precision was checked by comparing the result of developed and UV reference method statistically through Student's t- and F- tests at theoretical values of 95% confidence limits with

(n-1) degrees of freedom. It was observed that the values obtained for t- and F- tests for the proposed method are found to be lower than the tabulated values 29 of 2.57 and 5.05 respectively. % Recovery  $\pm$  SD values were in the range of 99.16-100.7 (+ 0.41 -  $\pm$  0.8) (n=3) which indicates the accuracy of developed method. Results of accuracy are given in Table-2. The interference of other excipients that are commonly present in dosage forms is found to be negligible. The proposed method is found to be sensitive and more accurate within the Beer's law range with reference to correlation coefficient value compared to literature methods (Table 3).

**Table 2:** Estimation of Perindopril-Erbumine (PPE) in formulations.

Formulation Batches	Quantity (mg)	Quantity found by PPE-BCN method (mg)*	95% confidence limit values F - Test	95% confidence limit values t- Test	UV reference Value
I	2	2.01 $\pm$ 0.021	1.86	0.87	2.00 $\pm$ 0.005
II	4	3.99 $\pm$ 0.028	2.69	0.18	4.00 $\pm$ 0.003
III	4	3.96 $\pm$ 0.16	1.15	1.70	4.00 $\pm$ 0.017
IV	8	8.05 $\pm$ 0.06	3.86	0.61	7.99 $\pm$ 0.021

\*Average value of six observations.

### CONCLUSION

Sensitivity of the technique lies only on the nature of the reaction with an appropriate chromogenic reagent selected but not on the sophistication of the instrument. The method developed is specific to be recommended for routine analysis in bulk and formulations as a substitute to GLC, HPLC, GC-MS, and LC-MS, etc. in quality control laboratories where the sophisticated and expensive instruments are not available.

### ACKNOWLEDGEMENTS

The authors are grateful to the management of Gayatri Vidya Parishad College of Engineering (Autonomous), Visakhapatnam for providing research laboratory facilities

### REFERENCES

1. Sweetman S C. In Martindale: The complete Drug Reference. Brayfield A, Buckingham R (eds). 36th Edition, Vol II, Pharmaceutical Press, London. 2009; p.928. ISBN: 9780857113672.
2. Budavari S (editor). The Merck Index: An Encyclopedia of Chemicals, Drugs and Biologicals. Merck & Co. Inc., 12th edition, White House Station, New Jersey. 1996; ISBN: 9780412756504.

3. British Pharmacopoeia : British pharmacopoeial Commission Office, vol I & vol II, London, UK. 2009; p. 4612.

4. Joseph PR and Alfonso R. Remington's The Science and Practice of Pharmacy, Publisher, Lippincott Williams & Wilkins, 20th Edition, Baltimore, Maryland, USA. 2000; p. 1281. ISBN: 0-7817-4673-6.

5. Montvale, NJ. P.D.R.: 'Physicians' desk reference', 54th Edn., Medical Economics Company Publisher, U.S. 2000; p. 3057. ISBN: 9781563633300.

6. Nayak SP, Pillai S. Simultaneous estimation of amlodipine besylate and perindopril erbumine by UV spectrophotometric method. Res J of Pharmacy and Technol. 2011; 4: 735-8.

7. Kale SS, Bakal RL, Chandewar AV, Sakhare RS. Two wavelength method for estimation of indapamide and perindopril erbumine in combined tablet dosage form. Res J Pharmacy Technol. 2011; 4: 545-8.

8. El-Gizawy SM, Abdelmageed OH, Derayea SM, Omar MA, Abdel-Megied AM. Chiral separation of perindopril erbumine enantiomers using high performance liquid chromatography and capillary

- electrophoresis. *Anal Methods*. 2014;6(3):825–30. DOI: <https://doi.org/10.1039/C3AY42056F>.
9. Gizawy SM, Bebawy LI, Abdelmageed OH, Omar MA, Deryea SM, Abdel-Megied AM. High Performance Liquid Chromatography, TLC-Densitometry, and First-Derivative Spectrophotometry for Simultaneous Determination of Amlodipine and Perindopril in Bulk Powder and its Tablets. *Journal of Liquid Chromatography & Related Technologies*. 2013 Apr;36(10):1323–39. DOI: <https://doi.org/10.1080/10826076.2012.686141>.
10. Pattan SR, Patni AC, Mali RA, Patni CJ, Godge RK, Bhawar HS and Marathe RP. Analytical method development and validation of perindopril erbumine and amlodipine besylate in bulk and tablet dosage form by HPLC. *Indian Drugs*. 2013;50:32–5.
11. Singh M, Kaskhedikar SG, Singhvi G, Soni L. HPLC estimation of perindopril erbumine in tablet dosage form. *Asian J Chem*. 2011; 23: 3909-11.
12. Chaudhary AB, Patel R, Chaudhary S. Determination of losartan potassium and perindopril erbumine in tablet formulations by reversed-phase HPLC. *International Journal of ChemTech Research*. 2010;2:1141–6.
13. Mastanamma S, Saidulu P, Sravanthi A, Rajitha E. Stability Indicating Validated RP-HPLC Method for Simultaneous Determination of Hydralazine Hydrochloride and Isosorbide Dinitrate in Bulk and Pharmaceutical Dosage Form. *Int J Pharm Sci Rev Res*. 2016;28:141–8.
14. Dugga HHT, Peraman R, Nayakanti D. Stability-Indicating RP-HPLC Method for the Quantitative Analysis of Perindopril Erbumine in Tablet Dosage Form. *Journal of Chromatographic Science*. 2014 Apr 1;52(4):315–20. DOI: <https://doi.org/10.1093/chromsci/bmt031>.
15. Joseph J, Philip B, Sundarapandian M. Method development and validation for simultaneous estimation of perindopril erbumine and indapamide by RP-HPLC in pharmaceutical dosage forms. *International Journal of Pharmacy and Pharmaceutical Sciences*. 2011;3(4):288–93.
16. Oza C, Prajapati J, Mehta P. RP-HPLC method for the determination of losartan potassium and perindopril erbumine in combined tablet dosage form. *International Journal of Pharma and Bio Sciences*. 2011;2(1):709–7015.
17. Prajapati J, Patel A, Patel M, Prajapati N, Prajapati R. Analytical method development and validation of Amlodipine besylate and Perindopril erbumine in combine dosage form by RP-HPLC. *International Journal of PharmTech Research*. 2011;3(2):801–8.
18. Prameela Rani A, Bala Sekaran C. A validated RP-HPLC method for the determination of Perindopril Erbumine in pharmaceutical formulations. *Int J PharmTech Res*. 2009; 1(3): 575-8.
19. Fael H, Sakur AA-H. Novel Spectrofluorimetric Method for the Determination of Perindopril Erbumine Based on Fluorescence Quenching of Rhodamine B. *J Fluoresc*. 2015 Nov;25(6):1577–84. DOI: <https://doi.org/10.1007/s10895-015-1666-2>.
20. Fael H, Sakur AA-H. Novel Spectrofluorimetric Method for the Determination of Perindopril Erbumine Based on Charge Transfer Reaction with 7-Hydroxycoumarin. *J Fluoresc*. 2015 Jul;25(4):811–8. DOI: <https://doi.org/10.1007/s10895-015-1596-z>.
21. Sridevi N, Jahnavi G, Sekaran CB. Spectrophotometric analysis of perindopril erbumine in bulk and tablets using bromophenol blue. *Der Pharmacia Lettre*. 2012;4(1):159–69.
22. Rahman N, Rahman H, Khatoon A. Development of Spectrophotometric Method for the Determination of Perindopril Erbumine in Pharmaceutical Formulations Using 2, 4 dinitrofluorobenzene. *J Chil Chem Soc*. 2012;57(2):1069–73. DOI: <https://doi.org/10.4067/S0717-97072012000200002>.
23. Rahman N, Rahman H. Quantitative analysis of perindopril erbumine in pharmaceutical preparations by spectrophotometry via ternary complex formation with Zn(II) and eosin and charge transfer complexation with iodine. *Spectroscopy*. 2011;25(2):123–36. DOI: <https://doi.org/10.1155/2011/106936>.
24. Rahman N, Rahman H, Haque SM. Kinetic spectrophotometric method for the determination of perindopril erbumine in pure and commercial dosage forms. *Arabian Journal of Chemistry*. 2017 Feb;10:S831–8. DOI: <https://doi.org/10.1016/j.arabjc.2012.12.017>.
25. Rahman N, Anwar N, Kashif M. Optimized and Validated Initial-Rate Method for the Determination of Perindopril Erbumine in Tablets. *Chem Pharm Bull*. 2006;54(1):33–6. DOI: <https://doi.org/10.1248/cpb.54.33>.
26. Jain DS, Subbaiah G, Sanyal M, Pande UC, Shrivastav P. First LC-MS/MS electro spray

ionization validated method for the quantification of perindopril and its metabolite perindoprilat in human plasma and its application to bioequivalence study. *Journal of Chromatography B*. 2006 Jun;837(1-2):92-100. DOI: <https://doi.org/10.1016/j.jchromb.2006.04.008>.

27. Nirogi RVS, Kandikere VN, Shukla M, Mudigonda K, Maurya S, Komarneni P. High-throughput quantification of perindopril in human plasma by liquid chromatography/tandem mass spectrometry: application to a bioequivalence study. *Rapid Commun Mass Spectrom*. 2006 Jun 30;20(12):1864-70. DOI: <https://doi.org/10.1002/rcm.2529>.

28. Maurer HH, Kraemer T, Arlt JW. Screening for the Detection of Angiotensin-Converting Enzyme Inhibitors, Their Metabolites, and AT II Receptor Antagonists. *Therapeutic Drug Monitoring* [Internet]. 1998;20(6). URL: <https://journals.lww.com/drug-monitoring/Fulltext>

[/1998/12000/Screening\\_for\\_the\\_Detection\\_of.22.a.spx](#).

29. Massart DL, editor. *Chemometrics: a textbook*. Amsterdam; New York: New York, NY, U.S.A: Elsevier; Distributors for the U.S. and Canada, Elsevier Science Pub. Co; 1988. 488 p. (Data handling in science and technology). ISBN: 978-0-444-42660-4.

30. Rao GR, Murthy SSN, Rao EV. Spectrophotometric determination of some sulphur compounds and tryptophan with brucine and sodium metaperiodate, *Indian Drugs*. 1985; 22: 484-8.

30. International Conference on Harmonisation Expert Working Group. International conference on harmonisation of technical requirements for registration of pharmaceuticals for human use. ICH harmonised tripartite guideline. Guideline for good clinical practice. 1997 CFR & ICH Guidelines. 1997;



## Synthesis of Tricyclic Quinoline Derivatives from 5- and 6-Aminoindazoles and 5-Aminoindole under Conventional Way and Microwave System

Adnane HALIMA SALEM <sup>1\*</sup>  , Abdellah MILOUDI <sup>1, 2</sup>  

<sup>1</sup> Fine Chemistry Laboratory, Chemistry Department, Faculty of Exact and Applied Sciences, University Oran 1, BP1524, El Mnaouer, 31100, Oran, Algeria

<sup>2</sup> Department of Preparatory Classes in Science and Technology, National Polytechnic School of Oran Maurice-Audin, BP1523, El Mnaouer, 31100, Oran, Algeria

**Abstract:** Targeted tricyclic quinolines were prepared from the corresponding aminoindazolic and indolic derivatives as starting materials using two comparative methods; conventional heating and microwave irradiation. We noticed that the syntheses of 5-amino-1-methylindazole and 5-aminoindole were abandoned due to their conversion to fluorescent products one week after free contact with air and acetone. As a result of this finding, we decided to condense the relevant amine with acetone or mesityl oxide to confirm our hypothesis. We show that the amine is converted to the derived quinoline through these condensation processes. Subsequently, this reaction was extended to the aminoindazole derivatives of positions 5 and 6, yielding the appropriate quinoline derivatives. Similarly, 5-aminoindole exhibited the same reactivity. By applying the corresponding NMR and centesimal techniques, the resulting structures were identified.

**Keywords:** 5- and 6- aminoindazole, 5-aminoindole, quinoline, acetone, mesityl oxide.

**Submitted:** March 29, 2021. **Accepted:** June 02, 2021.

**Cite this:** Halima Salem A, Miloudi A. Synthesis of Tricyclic Quinoline Derivatives from 5- and 6-Aminoindazoles and 5-Aminoindole under Conventional Way and Microwave System. JOTCSA. 2021;8(3):811-20.

**DOI:** <https://doi.org/10.18596/jotcsa.904598>.

\*Corresponding author. E-mail: [221halimasalem.adnane@gmail.com](mailto:221halimasalem.adnane@gmail.com).

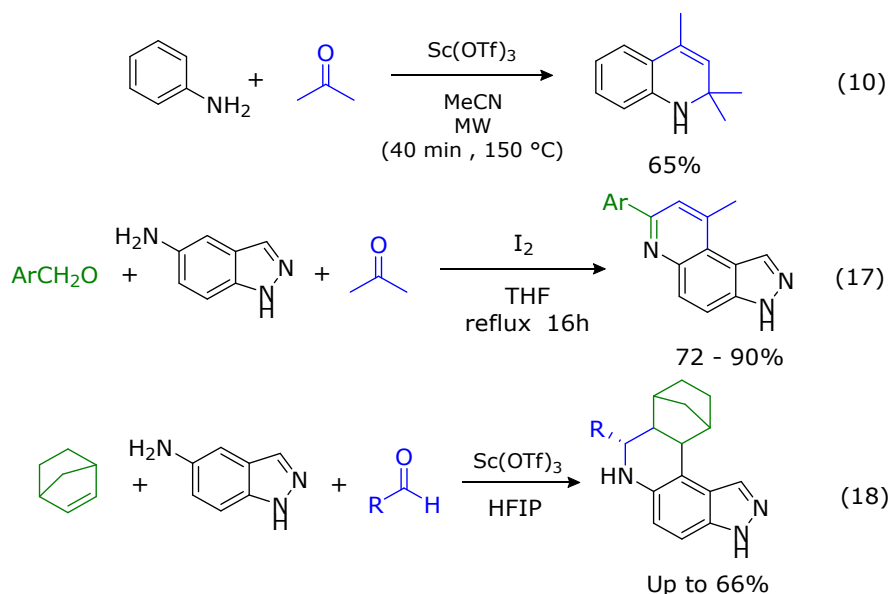
### INTRODUCTION

Throughout this century, significant research has been conducted on the synthesis and development of new heterocyclic compounds containing various heteroatoms, namely nitrogen, oxygen, and sulfur; the goal of this work is to produce products with active biological properties that are comparable to those found in nature (1–3). Indazole and quinoline derivatives are pharmacologically important, forming the basic structure of several drugs treating arthritis (4), gynecological disorders, anti-inflammatory (5), the derivatives of isoxazole, thiazoles, and quinoline cyanopyridine, have very good anticancer and antimicrobial

activity (6–8). A brief overview of their general preparation methods is necessary; more detailed studies were conducted to synthesize derivatives of quinoline starting from a series of carbonyl (9–19), while scandium ion was used as a catalyst in place of iodine to modify the Skraup reaction in order to increase yield in less time when microwave irradiation was used (13). W.Xiang-Shan and co-worker used a method to obtain quinoline derivatives via three-component reactions of aldehydes, aminoindazole, and thiopyranone (20); recently, a tetrahydro-3H-pyrazolo[4,3-f]quinoline core was synthesized using Povarov multicomponent reaction, the product's proof is its efficiency against cell cancer

(21) (Figure 1), we were then interested on the simple, and eco-friendly methods, synthesis of these types of heterocycles with fast,

#### Literature



#### This work

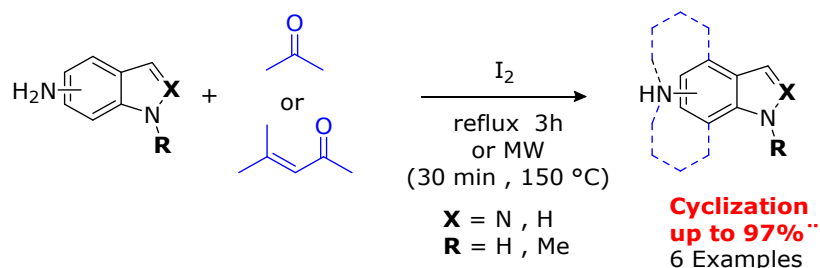


**Figure 1:** Similar reactions described in the literature.

## EXPERIMENTAL SECTION

**General Remarks:** Melting points were measured on a *Büchi Melting Point* apparatus and are not corrected. Microwave reactor for microwave-assisted extractions: *Monowave 450* from *Anton Paar*, The  $^1\text{H}$  and  $^{13}\text{C}$  NMR spectra were measured on a *Bruker Avance 300 Spectrometer* operating at 300 MHz (300 MHz for  $^1\text{H}$  and 100 MHz for  $^{13}\text{C}$ ). The chemical shift was recorded as units relative to  $\text{DMSO-d}_6$  or  $\text{CDCl}_3$  as the solvent unless otherwise stated, and  $J$  values in Hertz. Combustion analyses were performed in the *Microanalysis Laboratory of the National Center for Scientific Research in Vernaison in France*. Separations by chromatography were performed with Merck on "silica gel 60" (60 – 230 mesh).

### Condensation of aminoindazoles into quinoline

#### Method a

A dry 250 mL bi-necked flask was charged with 2.50 g (17.01 mmol) of 1-methyl-5-aminoindazole,

with 5 mol% (0.215 g, 0.850 mmol) of iodine, into a solution of acetone of 200 mL (variable quantity according to the number of mole of amine used). The solution is carried under reflux for 3 hours, the solution was washed with water, the solvent was removed under reduced pressure, and the residue is purified by chromatography on a column with eluent: EtOAc / petroleum Ether (1/1 v/v).

#### Method b

In sealed tube charged with stirring bar, a solution of 5-aminoindazole (0.133 g, 1 mmol) in 5 mL of acetone was added 5 mol% of iodine; the reaction mixture was heated at 150 °C with 400 W during 30 min, the solution was washed with water the solvent was removed under reduced pressure, the residue is purified by chromatography on column with eluent: EtOAc / petroleum ether (1/1 v/v).

#### Method c

A dry 250 mL bi-necked flask was charged with an equimolar mixture of 1-methyl-5-aminoindazole (2.50 g, 17.01 mmol) and of mesityl oxide (1.67 g,

17.01 mmol) with 5 mol% of iodine (0.215 g, 0.850 mmol), in solution in 200 mL of acetone. The solution is carried under reflux for 3 hours. After filtration and evaporation, the residue is purified by chromatography on the column, eluent: EtOAc / petroleum ether (1/1 v/v).

**3,7,7,9-Tetramethyl-6,7-dihydro-3H-pyrazolo[4,3-f] quinoline I** method **c** :

3.75 g , 97%, method **a** : 1.33 g, 34%, m.p. 148 °C, <sup>1</sup>H-NMR (300 MHz, DMSO-d<sub>6</sub>, δ, ppm) : 7.88 (1H, s), 7.23 (1H, d, J = 8.7 Hz), 6.76 (1H, d, J = 8.7 Hz), 5.72 (1H, s), 5.21 (1H, s), 3.92 (3H, s), 2.19 (3H, s), 1.19 (6H, s). <sup>13</sup>C-NMR (100 MHz, DMSO-d<sub>6</sub>) δ: 138.7, 135.1, 130.3, 128.9, 127.6 (Ar-C), 120.7, 116.5, 109.4, 109.2 (Ar-CH), 50.7 (-NH-C(CH<sub>3</sub>)<sub>2</sub>), 35.3 (>N-CH<sub>3</sub>), 29.7 (2x-CH<sub>3</sub>), 21.7 (-CH<sub>3</sub>). Anal. calcd for C<sub>14</sub>H<sub>17</sub>N<sub>3</sub>: C, 73.98; H, 7.54; N, 18.49. Found: C, 73.39; H, 7.34; N, 18.52.

**7,7,9-Trimethyl-6,7-dihydro-3H-pyrazolo[4,3-f] quinoline III**, method **b**: 0,96 g, 45%, method **c** : (1.33 g, 10 mmol) of 5-aminoindazole, mesityl oxide (0.98 g, 10 mmol), iodine 5 mol% and 100 mL of acetone: 0.6 g, 28%, <sup>1</sup>H-NMR (300 MHz, DMSO-d<sub>6</sub>, δ, ppm): 12.42 (1H, s), 7.69 (1H, s), 6.92 (1H, d, J = 8.7 Hz), 6.47 (1H, d, J = 8.7 Hz), 5.38 (1H, s), 4.94 (1H, s), 1.96 (3H, s), 0.94 (6H, s). <sup>13</sup>C-NMR (100 MHz, DMSO-d<sub>6</sub>) δ: 139.5, 138.6, 129.1, 127.3, 125.1 (Ar-C), 120.1, 116.7, 110.2, 109.2 (Ar-CH), 50.8 (-NH-C(CH<sub>3</sub>)<sub>2</sub>), 29.8 (2x-CH<sub>3</sub>), 21.7 (-CH<sub>3</sub>).

**(1,3-Dimethyl-buta-1,3-dienyl)-(1H-indazol-5-yl)-amine IV** , method **c** : (1.33 g, 10 mmol) of 5-aminoindazole, mesityl oxide (0.98 g, 10 mmol), iodine 5 mol % and 100 mL of acetone : 0.51 g, 24%, <sup>1</sup>H-NMR (300 MHz, DMSO-d<sub>6</sub>, δ, ppm): 12.66 (1H, s), 7.95 (1H, s), 7.09 (1H, d, J = 8.7 Hz), 6.57 (1H, d, J = 8.8 Hz), 5.50 (2H, d, J = 8.3 Hz), 5.21 (1H, s), 4.89 (1H, d, J = 5.1), 3.72 (1H, s), 3.33 (3H, s), 1.00 (3H, s). <sup>13</sup>C-NMR (100 MHz, DMSO-d<sub>6</sub>) δ: 143.6, 138.4, 135.2 (Ar-C), 120.4, 118.3, 118.4, 106.9 (Ar-CH), 125.4 (-N-C(CH<sub>3</sub>)=C-), 125.2 (H<sub>2</sub>C=C(CH<sub>3</sub>)-), 105.8 (H<sub>2</sub>C=C(CH<sub>3</sub>)-), 74.3 (-N-C(CH<sub>3</sub>)=C-), 27.1, 21.5 (-CH<sub>3</sub>).

**7,7,9-Trimethyl-6,7-dihydro-1H-pyrazolo[3,4-f] quinoline V**, method **c**: a mixture of (1 g, 7.220 mmol) of 6-aminoindazole, mesityl oxide (0.737 g, 7.220 mmol), iodine 5 mol % (0.361 mmol , 0,091 g) and 100 mL of acetone, 1.130 g, 74%, m.p. 190°C, <sup>1</sup>H-NMR (300 MHz, DMSO-d<sub>6</sub>, δ, ppm): 12.06 (1H, s), 7.69 (1H, s), 7.28 (1H, d, J = 8.4 Hz) 6.48 (1H, d, J = 8.5 Hz), 6.16 (1H, s), 5.10 (1H, s); 2.25 (3H, s), 1.21 (6H, s). <sup>13</sup>C-NMR (100 MHz, DMSO-d<sub>6</sub>) δ: 143.5, 142.2, 138.6, 127.3, 125.4 (Ar-C), 120.4, 117.84, 116.9, 110.1 (Ar-CH), 50.7 (-NH-C(CH<sub>3</sub>)<sub>2</sub>), 29.8 (2x-CH<sub>3</sub>), 21.3

(-CH<sub>3</sub>).

**1,7,7,9-Tetramethyl-6,7-dihydro-1H-pyrazolo[3,4-f] quinoline VI**, method **a**: (0.147 g ,1 mmol) of 1-methyl-6-aminoindazole in 10 mL of acetone, with 5 mol % of iodine give 49%, 0.136 g. A mixture of 1-methyl 6-aminoindazole (0.195 g, 1.326 mmol), mesityl oxide (0.131 g, 1.326 mmol), in 30 mL of methanol, acetone and glacial acetic acid (1/1/1 v/v/v), activated by 10 mol% Pd/C, 0.135 g, 48%, m.p. 92°C, <sup>1</sup>H-NMR (300 MHz, DMSO-d<sub>6</sub>, δ, ppm): 8.16 (1H, s), 7.68 (1H, d, J = 7.5 Hz), 6.79 (1H, d, J = 8.5 Hz), 5.40 (1H, d, J = 4.7 Hz), 4.23 (3H, s), 2.74 (3H, s), 1.58 (6H, s). <sup>13</sup>C-NMR (100 MHz, DMSO-d<sub>6</sub>) δ: 144.9, 144.3, 139.0, 136.9, 133.9 (Ar-C), 120.9, 117.2, 112.1, 99.9 (Ar-CH), 50.9 (-NH-C(CH<sub>3</sub>)<sub>2</sub>), 39.3 (>N-CH<sub>3</sub>), 29.4 (2x-CH<sub>3</sub>), 27.5 (-CH<sub>3</sub>).

**Condensation of aminoindole into quinoline In the presence of acetone**

A dry 250 mL bi-necked flask was charged with 1.45 g (10.98 mmol) of 5-aminoindole, with 5 mol % (0.14 g, 0.549 mmol) of iodine, into a solution of 100 mL of acetone (variable quantity according to the number of moles of amine used). The solution is carried under reflux for 3 hours. After evaporation, the residue is purified by chromatography on the column, eluent: CH<sub>2</sub>Cl<sub>2</sub> / n-pentane (1/1 v/v). Compound **II** is isolated with a 42% yield, 0.98 g.

**In the presence of mesityl oxide**

A dry 250 mL bi-necked flask was charged with an equimolar mixture of 5-aminoindole (0.265 g, 2.023 mmol) and of mesityl oxide (0.198 g, 2.023 mmol) with 5 mol% of iodine (0.026 g, 0.101 mmol), in solution in 50 mL of acetone. The solution is carried under reflux for 3 hours. After filtration and evaporation, the residue is purified by chromatography on the column, eluent: CH<sub>2</sub>Cl<sub>2</sub>/ n-pentane (1/1 v/v). Compound **II** is isolated with a 50% yield, 0.215 g.

**7,7,9-Trimethyl-6,7-dihydro-3H-pyrrolo[3,2-f] quinoline II**, m.p. 118°C, <sup>1</sup>H-NMR (300 MHz, DMSO-d<sub>6</sub>, delta, ppm): 10.71 (1H, s), 7.14 (1H, d, J = 2.3 Hz), 7.04 (1H, d, J = 8.3 Hz), 6.48 (1H, d, J = 8.5 Hz), 6.44 (1H, sbr), 5.17 (1H, s), 2.20 (3H, s), 1.17 (6H, s). <sup>13</sup>C-NMR (100 MHz, DMSO-d<sub>6</sub>) δ: 137.5, 130.9, 130.1, 127.3, 124.7 (Ar-C), 124.5, 113.2, 111.7, 110.9, 100.9 (Ar-CH), 50.6 (-NH-C(CH<sub>3</sub>)<sub>2</sub>), 29.4 (2x-CH<sub>3</sub>), 22.3 (-CH<sub>3</sub>).

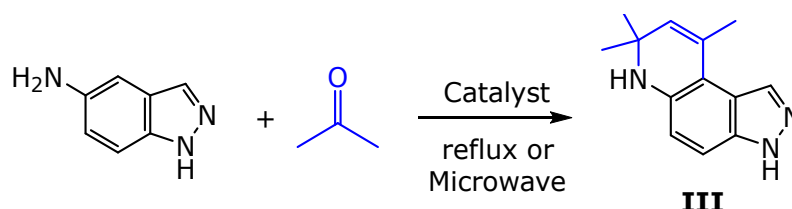
**RESULTS AND DISCUSSION**

**Test of Catalysts**

The treatment of 5-aminoindazole with different catalysts in acetone under reflux and microwave afforded to the corresponding quinoline **III** in good yield (Scheme 1).

Our first study focused on the absence of a catalyst; any progress was found neither under reflux nor a microwave system (Table 1, Entry **1**). The same reaction was carried out with iodine in different amounts 5 mol%, 10 mol%, and 20 mol %, the given result in yield is the same 45% (Table 1, Entry **2**), showing that a higher amount of catalyst has no influence on the reaction. Some transition metals were also used to catalyze our reaction under the same conditions, copper (CuI,

CuCl, CuSO<sub>4</sub>), iron (FeCl<sub>3</sub>), manganese (MnO), and bismuth (BiCl<sub>3</sub>) in their salt form give fewer interesting results (0-25%) as shown in (Table 1, Entry **3-8**). ZnCl<sub>2</sub> performs the reaction as iodine does and led us to the desired product **III** with a 45% yield (Table 1, Entry **10**). I<sub>2</sub> was chosen instead of ZnCl<sub>2</sub> to catalyze the reaction because of its non-toxic, inexpensive, and eco-friendly nature (22-27).



**Scheme 1:** Cyclization of 5-aminoindazole with acetone under different conditions.

**Table 1:** Optimization of yield for **III** using different catalysts under reflux.

Entry	Catalyst	Time (h)	yield% <sup>b</sup>
<b>1</b> <sup>a</sup>	-	3	ND <sup>a</sup>
<b>2</b> <sup>a</sup>	<b>I<sub>2</sub></b>	<b>3</b>	<b>45</b> <sup>a</sup>
<b>3</b>	CuI	3	Trace
<b>4</b>	CuCl	3	20
<b>5</b>	CuSO <sub>4</sub>	3	ND
<b>6</b>	BiCl <sub>3</sub>	3	25
<b>7</b>	FeCl <sub>3</sub>	3	25
<b>8</b>	MnO	3	ND
<b>9</b>	PdCl <sub>2</sub>	3	23
<b>10</b> <sup>a</sup>	<b>ZnCl<sub>2</sub></b>	<b>3</b>	<b>45</b> <sup>a</sup>

<sup>a</sup> Reaction tested under microwave system (30 min, 150 °C, 400 W), <sup>b</sup> isolated yield, ND: not detected

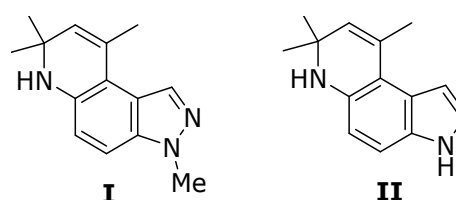
#### Optimization of the conditions for microwave irradiation

The choice of the optimal condition reaction under microwave irradiation was studied, the same substrate has been condensed in the presence of acetone catalyzed by iodine, starting with temperature from 100 °C during 30 min of reaction, we observed a formation of compound **III** with 20% of yield, after increasing the heating we reached 150 °C corresponding to 45% of yield, some impurities were spotted above this temperature, we then fixed it and changed the time of reaction, after 5 min under irradiation no evolution was observed, the structure **III** begins to be formed from the 15th min, the isolated yield indicates 12% and start increasing until 45% and stabilizes after 30 min of reaction. The reaction under reflux was privileged compared to microwave irradiation because it requires less drastic conditions insight of the power and temperature needed to get our desired structures.

#### Formation of quinolines

Having noted, we observed a transformation of 5-amino-1-methylindazole and the 5-aminoindole bunched with the free air into quinoline **I** and **II** (Figure 2).

Test reaction of condensation on the products transformed lead to the same structure of quinoline **I** and **II** in both cases, even with acetone or mesityl oxide.

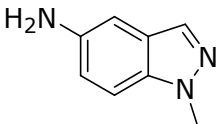
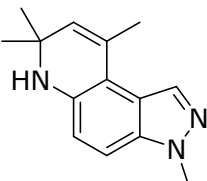
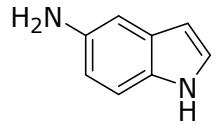
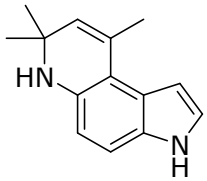
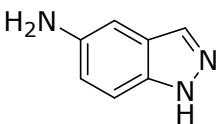
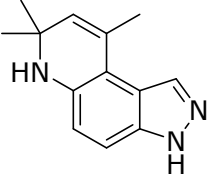
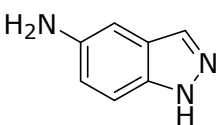


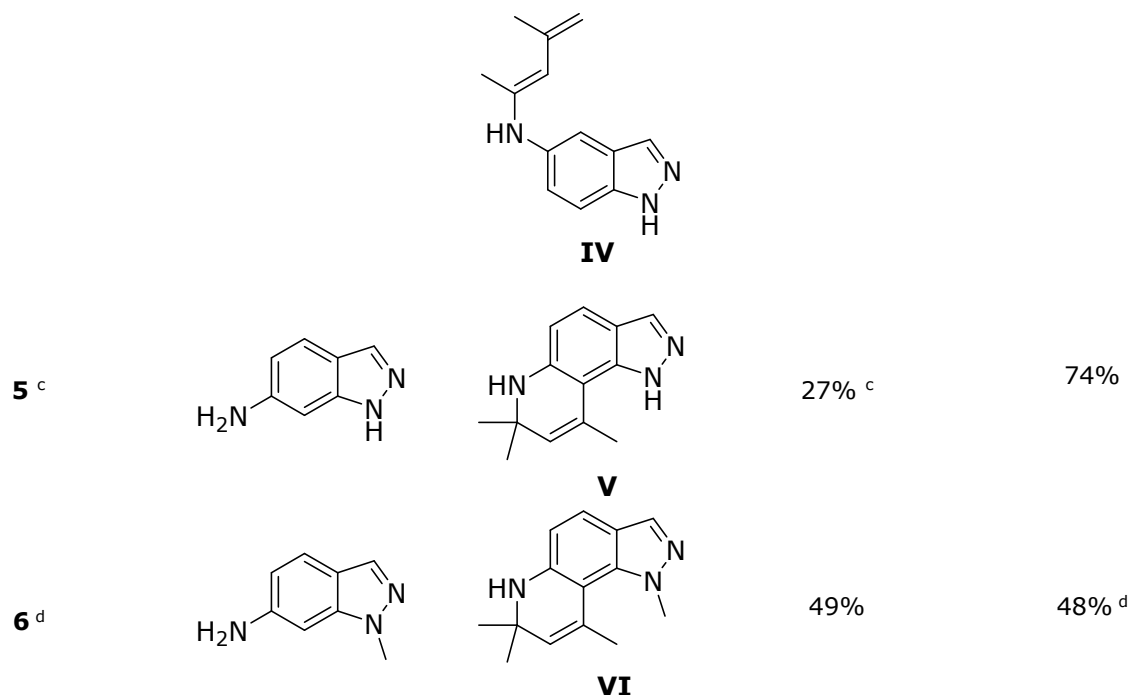
**Figure 2.** Quinolines **I** and **II** formed from 5-amino-1-methylindazole and the 5-aminoindole respectively.

After 3 hours in refluxing the 5-amino-1-methylindazole with acetone in the catalytic medium of iodine, we observed the formation of the product **I** with a yield of 34%. However, the 5-amino-1-methylindazole treated with mesityl oxide in the presence of iodine led to a similar product of structure **I** with a yield of 97% (Table 2, Entry **1**). After carrying out the proton and carbon 13 NMR spectra, a study of spectral fragmentation of mass shows the presence of a molecular mass of 227 amu and a chemical ionization of the peak  $[M + 1]^+$  is equal to 228 amu ( $M + H^+$ ) and two other significant peaks of fragmentation  $M/Z = 29$  for ion  $NCH_3^+$  and  $M/Z = 41$  for ion  $HCN^+$ . The addition of the 5-aminoindole with acetone in the presence of a catalytic quantity of iodine under reflux led to the same structure **II**, which is obtained with a reaction yield of 42%. However, the action of mesityl oxide on the 5-aminoindole, under the same conditions, gives us the structure **II** with a yield of 50%, as shown in (Table 2 (Entry **2**). We realized that the reaction of 5-aminoindazole in the presence of acetone produces the compound **III** with 45% of yield (Table 2,

Entry **3**), then we observed the formation of another product **IV** in addition to our predicted one **III** by using mesityl oxide under identical conditions, the two current structures were formed in competition with less difference in yield 24% and 28% respectively (Table 2, Entries **3-4**). For this phenomenon, two mechanisms were suggested, a different attack of the mesityl oxide on 5-aminoindazole (Scheme 3, 4). However, the condensation of the 6-aminoindazole with mesityl oxide led to the compound **V** with an output of 74%, illustrating a more interesting result against the condensation with acetone which gives a 27% yield (Table 2, Entry **5**). The structure **VI** was formed with 49% in yield under the same conditions as the previously formed quinolines; in order to increase this last and to observe the best condensation, the 6-amino-1-methylindazole condenses with mesityl oxide in the presence of a mixture of the solvent of  $CH_3OH/CH_3COCH_3/CH_3CO_2H$  catalyzed by Pd / C (12), the competitor's condition shows any evolution in yield and give 48% of quinoline **VI** (Table 2, Entry **6**).

**Table 2.** Formation of quinoline derivatives using acetone and mesityl oxide.

Entry <sup>a</sup>	Amine	Product	Yield using acetone <sup>b</sup>	Yield using mesityl oxide <sup>b</sup>
<b>1</b>			34%	97%
<b>2</b> <sup>c</sup>			42% <sup>c</sup>	50%
<b>3</b> <sup>c</sup>			45% <sup>c</sup>	28%
<b>4</b>			ND	24%



<sup>a</sup> Reaction condition: solvent: acetone, reflux (3h), 5 mol% I<sub>2</sub> as the catalyst.

<sup>b</sup> Isolated yield, ND: not detected.

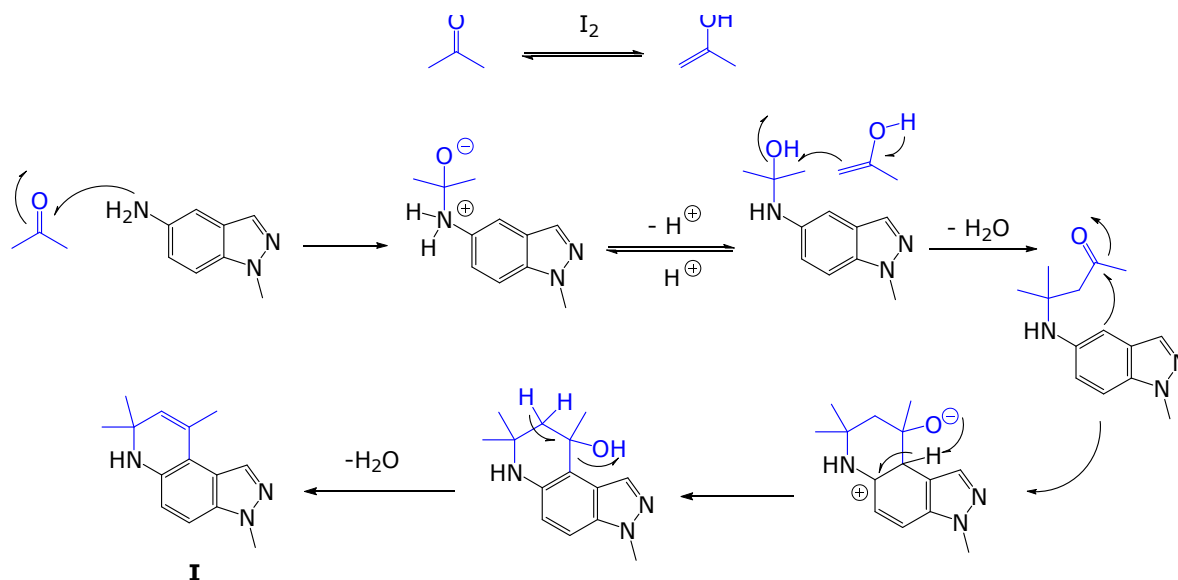
<sup>c</sup> Reaction was also tested under microwave irradiation (150 °C, 400 W, 30 min).

<sup>d</sup> Reaction condition : solvent : CH<sub>3</sub>OH/CH<sub>3</sub>COCH<sub>3</sub>/CH<sub>3</sub>CO<sub>2</sub>H ,reflux (3h), 10 mol% Pd / C (12) as catalyst.

### Proposed mechanisms

The mechanism proposed is shown in (Scheme 2), iodine participates in equilibrium form of acetone into enol, the amine attacks the carbonyl functional

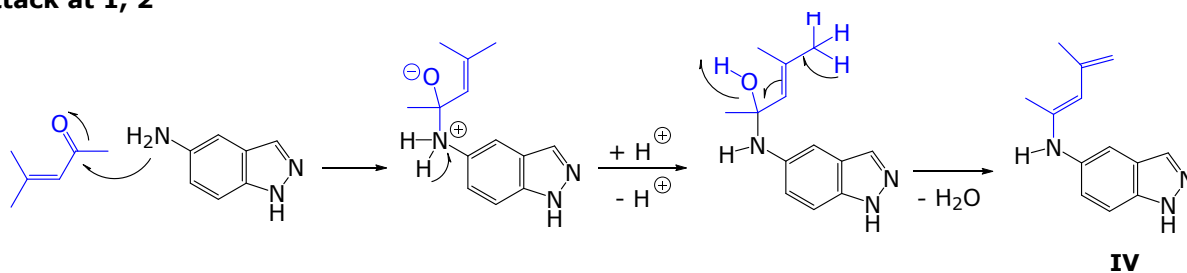
group then a Diels-Alder reaction naturally takes place spawning dehydration. Finally, structure **I** is produced following a cyclization step.



**Scheme 2.** The suggested mechanism for obtaining structure **I** using acetone.

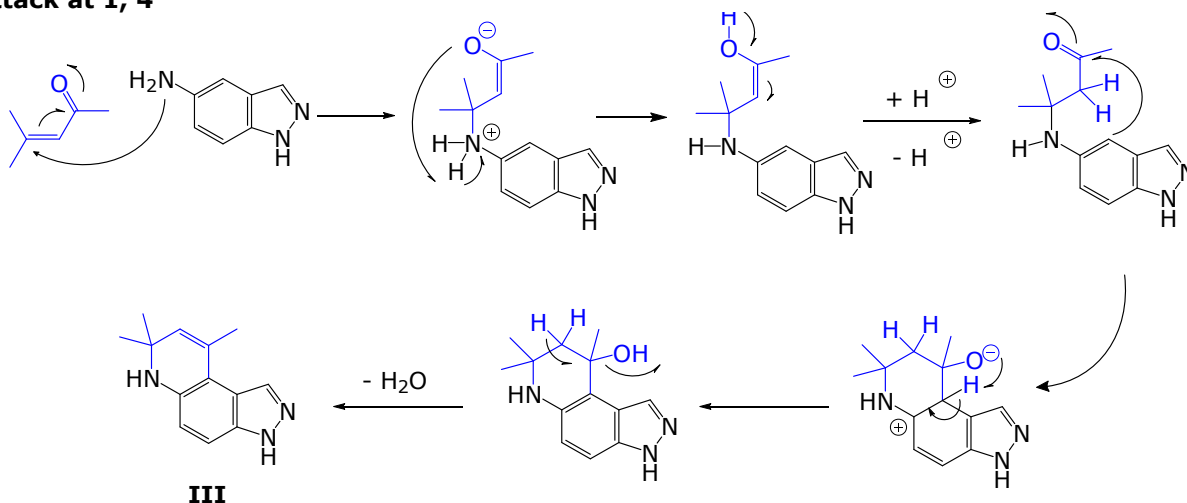
The two structures **IV** and **V** were formed because of the considerable difference of amine's attack on mesityl oxide. Structure **IV** was undoubtedly formed when the amine reacts favorably with the

carbonyl function disadvantaging the cyclization (Scheme 3).

**Attack at 1, 2****Scheme 3.** The mechanism suggested obtaining structure **IV** using mesityl oxide.

On the other hand, the amine reacts correctly with the aliphatic alkene vacating place to the

cyclization naturally done by the carbonyl function (Scheme 4).

**Attack at 1, 4****Scheme 4.** The mechanism suggested obtaining structure **III** using mesityl oxide.**CONCLUSION**

In conclusion, a simple and eco-friendly approach has been demonstrated to synthesize different quinolines with a different yield up to 97% starting from indazolic and indolic structures by condensation using acetone and mesityl oxide in a catalytic medium of iodine, the conventional way and the microwave system of the condensation reaction generate the same results, on this cause that the reflux reaction was chosen as the leading precursor to obtain our final structures in order to avoid the energy consumption at elevated temperature which can assist polymerization.

**ACKNOWLEDGEMENTS**

The authors are grateful to Prof Dr.El Abed, university Oran 1, Algeria. Furthermore, we thank the Algerian "Ministry of Higher Education and scientific research and DGRSDT" for financial support.

**REFERENCES**

1. Kang YK, Shin KJ, Yoo KH, Seo KJ, Hong CY, Lee C-S, et al. Synthesis and antibacterial activity of new carbapenems containing isoxazole moiety. *Bioorganic & Medicinal Chemistry Letters*. 2000 Jan;10(2):95–9. DOI: [https://doi.org/10.1016/S0960-894X\(99\)00646-0](https://doi.org/10.1016/S0960-894X(99)00646-0).
2. Kochetkov NK, Sokolov SD. Recent developments in isoxazole chemistry. In: *Advances in Heterocyclic Chemistry* [internet]. Elsevier; 1963 [cited 2021 jun 4]. p. 365–422. ISBN: 978-0-12-020602-5.
3. Gezegen H, Gürdere MB, Dincer A, Özbek O, Koçyiğit ÜM, Taslimi P, et al. Synthesis, molecular docking, and biological activities of new cyanopyridine derivatives containing phenylurea. *Arch Pharm*. 2021 Apr;354(4):2000334. DOI: <https://doi.org/10.1002/ardp.202000334>.
4. Sironi M, Massimiliano I, Transidico P, Pinza M, Sozzani S, Mantovani A, et al. Differential effect of

- benzylamine on pro- versus anti-inflammatory cytokine production: Lack of inhibition of interleukin-10 and interleukin-1 receptor antagonist. *Int J Clin Lab Res.* 2000 Mar;30(1):17–9. DOI: <https://doi.org/10.1007/s005990070028>.
5. Párkányi C, Schmidt DS. Synthesis of 5-chloro-2-methyl-3-(5-methylthiazol-2-yl)-4(3H)-quinazolinone and related compounds with potential biological activity. *Journal of Heterocyclic Chemistry.* 2000 Jul;37(4):725–9. DOI: <https://doi.org/10.1002/jhet.5570370409>.
6. Xiao K, Zhang H-J, Xuan L-J, Zhang J, Xu Y-M, Bai D-L. Stilbenoids: Chemistry and bioactivities. In: *Studies in natural products chemistry* [internet]. Elsevier; 2008 [cited 2021 jun 4]. p. 453–646. ISBN: 978-0-444-53180-3.
7. Özbek O, Gürdere MB. Synthesis and anticancer properties of 2-aminothiazole derivatives. *Phosphorus, Sulfur, and Silicon and the Related Elements.* 2021 May 4;196(5):444–54. DOI: <https://doi.org/10.1080/10426507.2020.1871347>.
8. Özbek O, Usta NC, Gürdere MB, Aslan ON, Budak Y, Ceylan M. Synthesis and antibacterial screening of novel 2-(4-(aryl)thiazol-2-yl)-3a,4,7,7a-tetrahydro-1H-indolo[4,7-ethano]indole-1,3(2H)-dione derivatives. *Phosphorus, Sulfur, and Silicon and the Related Elements.* 2017 Oct 3;192(10):1153–7. DOI: <https://doi.org/10.1080/10426507.2017.1354209>.
9. Poursattar Marjani A, Khalafy J, Salami F, Mohammadlou M. Tin(II) chloride catalyzed synthesis of new pyrazolo[5,4-b]quinolines under solvent-free conditions. *Synthesis.* 2015 Jun;47(11):1656–60. DOI: <https://doi.org/10.1055/s-0034-1380189>.
10. Edwards JP, Ringgenberg JD, Jones TK. Lewis-acid catalyzed reaction of 2-isopropenylaniline with ketones: Improved synthesis of 2,2,4-trisubstituted 1,2-dihydroquinolines. *Tetrahedron Letters.* 1998 Jul;39(29):5139–42. DOI: [https://doi.org/10.1016/S0040-4039\(98\)01010-7](https://doi.org/10.1016/S0040-4039(98)01010-7).
11. Leis J. Conformational dynamics and equilibria in amides [PhD thesis]. [Tartu, Estonia]: University of Tartu; 1998.
12. Manske RHF, Kulka M. The Skraup synthesis of quinolines. In: *Organic Reactions* [internet]. Hoboken, NJ, USA. p. 59–98. ISBN: 978-0-471-26418-7.
13. Theoclitou M-E, Robinson LA. Novel facile synthesis of 2,2,4 substituted 1,2-dihydroquinolines via a modified Skraup reaction. *Tetrahedron Letters.* 2002 May;43(21):3907–10. DOI: [https://doi.org/10.1016/S0040-4039\(02\)00614-7](https://doi.org/10.1016/S0040-4039(02)00614-7).
14. Walter H, Sauter H, Winkler T. Eine neue einfache synthese spirocyclischer 1H-chinolin-derivate. *Helv Chim Acta.* 1992 Jun 24;75(4):1274–80. DOI: <https://doi.org/10.1002/hlca.19920750428>.
15. Li X, Mao Z, Wang Y, Chen W, Lin X. Molecular iodine-catalyzed and air-mediated tandem synthesis of quinolines via three-component reaction of amines, aldehydes, and alkynes. *Tetrahedron.* 2011 May;67(21):3858–62. DOI: <https://doi.org/10.1016/j.tet.2011.03.087>.
16. Hamann LG, Winn DT, Pooley CLF, Tegley CM, West SJ, Farmer LUCJ, ET AL. Nonsteroidal progesterone receptor antagonists based on a conformationally-restricted subseries of 6-aryl-1,2-dihydro-2,2,4-trimethylquinolines. *Bioorganic & Medicinal Chemistry Letters.* 1998 Oct;8(19):2731–6. DOI: [https://doi.org/10.1016/S0960-894X\(98\)00482-X](https://doi.org/10.1016/S0960-894X(98)00482-X).
17. Wu Y-C, Liu L, Li H-J, Wang D, Chen Y-J. Skraup–Doebner–Von Miller quinoline synthesis revisited: Reversal of the regiochemistry for  $\gamma$ -aryl- $\beta,\gamma$ -unsaturated  $\alpha$ -ketoesters. *J Org Chem.* 2006 Aug;71(17):6592–5. DOI: <https://doi.org/10.1021/jo060290n>.
18. Eisch JJ, Dluzniewski T. Mechanism of the Skraup and Doebner–Von Miller quinoline syntheses. Cyclization of  $\alpha,\beta$ -unsaturated n-aryliminium salts via 1,3-diazetidinium ion intermediates. *J Org Chem.* 1989 Mar;54(6):1269–74. DOI: <https://doi.org/10.1021/jo00267a010>.
19. Johnson JV, Rauckman BS, Baccanari DP, Roth B. 2,4-Diamino-5-benzylpyrimidines and analogs as antibacterial agents. 12. 1,2-Dihydroquinolylmethyl analogs with high activity and specificity for bacterial dihydrofolate reductase. *J Med Chem.* 1989 Aug;32(8):1942–9. DOI: <https://doi.org/10.1021/jm00128a042>.
20. Wang W, Yin M-Y, Zhang M-M, Wang X-S. Iodine-catalyzed synthesis of thiopyrano[3,4-c]quinoline derivatives via imino-Diels–Alder reaction. *Journal of Chemical Research.* 2012 Jun;36(6):318–21. DOI: <https://doi.org/10.3184/174751912X13352797144052>.
21. Dayal N, Wang M, Sintim HO. HSD1787, a tetrahydro-3H-pyrazolo[4,3-f]quinoline compound synthesized via Povarov reaction, potently inhibits proliferation of cancer cell lines at nanomolar concentrations. *ACS Omega.* 2020 Sep 22;5(37):23799–807. DOI: <https://doi.org/10.1021/acscomega.1c01010>.

<https://doi.org/10.1021/acsomega.0c03001>.

22. Wang G-W, Gao J. Selective formation of spiro dihydrofurans and cyclopropanes through unexpected reaction of aldehydes with 1,3-dicarbonyl compounds. *Org Lett*. 2009 Jun 4;11(11):2385–8. DOI:

<https://doi.org/10.1021/ol900451d>.

23. Mal D, De SR. Total synthesis of euplectin, A natural product with a chromone fused indenone.

*Org Lett*. 2009 Oct 1;11(19):4398–401. DOI:

<https://doi.org/10.1021/ol901817r>.

24. Parvatkar PT, Parameswaran PS, Tilve SG. An expeditious  $i$  2 -catalyzed entry into 6 H -indolo[2,3- b ]quinoline system of cryptotackieine.

*J Org Chem*. 2009 Nov 6;74(21):8369–72. DOI:

<https://doi.org/10.1021/jo901361x>.

25. Zeng L-Y, Cai C. Iodine catalyzed one-pot multicomponent synthesis of a library of compounds containing tetrazolo[1,5- a ]pyrimidine core. *J Comb Chem*. 2010 Jan 11;12(1):35–40. DOI:

<https://doi.org/10.1021/cc9000983>.

26. Das B, Balasubramanyam P, Krishnaiah M, Veeranjanyulu B, Reddy GC. Iodine-catalyzed efficient hydrophosphonylation of N -tosyl aldimines. *J Org Chem*. 2009 Jun 5;74(11):4393–5. DOI:

<https://doi.org/10.1021/jo9003162>.

27. Cho C-H, Neuenswander B, Lushington GH, Larock RC. Solution-phase parallel synthesis of a multi-substituted benzo[ b ]thiophene library. *J COMB CHEM*. 2009 Sep 14;11(5):900–6. DOI:

<https://doi.org/10.1021/cc9000604>.





## Synthesis, Characterization, and Adsorption Properties of Highly Microporous Structured Activated Carbon

İlhan KÜÇÜK<sup>1,2</sup>  , Yunus ÖNAL<sup>3</sup>  

<sup>1</sup> Department of Chemistry, Faculty of Art and Science, Inonu University, 44280 Malatya, Turkey

<sup>2</sup> Muş Alparslan University, 49250, Muş, Turkey

<sup>3</sup> Department of Chemical Engineering, Faculty of Engineering, Inonu University, 44280 Malatya, Turkey

**Abstract:** The aim of this study is to synthesize activated carbon with high surface area from peach kernel shells which is an agricultural waste. In this study, activated carbon synthesis was carried out by using CO<sub>2</sub> at 2 different temperatures (800 and 900 °C) with physical activation from products carbonized at 4 different temperatures (300, 400, 500, and 600 °C) and 2 different N<sub>2</sub> gas flow rates (100 and 500 mL/min). After carbonization, solid, liquid, and gas yields of the materials were calculated. The surface area of activated carbons synthesized was calculated by BET analysis and the differences in the surface area were shown by changing the synthesis conditions. Surface areas vary between 340.15 and 686.74 m<sup>2</sup>/g. In samples pores formed were examined by DFT plus. It was found that most of these pores consist of micropores. Also, the structures of the samples were examined with SEM and XRD analyses. Methylene blue removal of the synthesized samples was studied and the results were compared.

**Keywords:** Biomass, carbonization, physical activation, activated carbon.

**Submitted:** June 16, 2020. **Accepted:** July 12, 2021.

**Cite this:** Küçük İ, Önal Y. Synthesis, Characterization, and Adsorption Properties of Highly Microporous Structured Activated Carbon. JOTCSA. 2021;8(3):821-34.

**DOI:** <https://doi.org/10.18596/jotcsa.753579>.

**\*Corresponding author. E-mail:** [yunus.onal@inonu.edu.tr](mailto:yunus.onal@inonu.edu.tr).

### INTRODUCTION

Activated carbon, known as activated charcoal, is a high surface area, amorphous and graphite-free carbonaceous compound. Activated carbons, which do not have a chemical formula, differ from each other with their surface areas, advanced and adjustable pores, mechanical strength, high reactive surface chemistry, adsorption capacities, the raw materials they are synthesized, the activation method used and chemicals used (1-5).

One of the most important properties of activated carbons is that they have a porous structure that causes the surface area to grow. Besides its porous structure, pore volume and diameter are important. The formation of pores in activated carbons starts at the carbonization stage. Through physical and chemical activation, these pores gain volume and

open if there are closed pores. The formation of the pores is as follows (6):

✓ Volatile components in the raw material leave the structure by heating the raw material in an inert environment.

✓ These components, which move away from the raw material, pore on the raw material according to the size of the structure.

✓ If the displaced structure is in the middle of the solid, the internal pressure will increase in the solid and will open micro channels as this structure moves away.

The pore distribution and pore diameter in an activated carbon vary depending on the type of raw material used and the carbonization temperature (7).

In recent years, research has been increased towards the use of agricultural waste products for the synthesis of activated carbon. These biomass products are sustainable, cheap, and rich sources of carbon. This feature makes them the suitable raw material for the synthesis of activated carbon. In respect of environmental concern, these agricultural wastes will get decayed finally with time, but most of them reduce slowly and create pollution. The best way to address these issues is to use them as precious material. Along with having a good source of carbon, these biomaterial wastes include other elements and compounds, which can be exploited cleverly according to the application (8). Some agricultural wastes synthesized from activated carbon coffee husks (9), durian shells (10), olive stones (11), rice straw (12), oil palm fibers (13), walnut shells (14), rice husks (15), waste apricot (16), cherry stones (17), banana peels (18), sawdust (19), rice bran (20), almond shells (21), tea waste (22), herb residues (23), corn cobs (24), rice hulls (25), sugarcane bagasse (26), cotton stalks (27), orange peels (28), date stones (29), coconut husks (30), etc.

Activated carbon is an adsorbent acquired from carbonaceous substances with a disorganized crystallographic shape, constituted through randomly dispensed microcrystals. This microcrystalline shape is constructed from standard systems which include graphene sheets and fullerene or quasi-graphitic fragments. However, this microcrystalline association does not enlarge on a macroscopic scale ensuing in a disordered and surprisingly nanoporous shape. Consequently, those substances gift excessive surface area, extensive type of practical groups and a pore length distribution. All those traits supply them an outstanding potential to adsorb a remarkable range of molecules (31). In addition to this potential, it is used in many different fields. Some of those purification (32), nuclear power stations (33), gas separation (34), energy storage (35), catalysis (36), water treatment (37), pharmaceutical (38), capacitors (39), petroleum industries (40), etc.

Adsorption, which is one of the most used areas of activated carbons, takes place through the pores on the surface of the activated carbon. The substance to be adsorbed enters through these pores and interacts with the outer surface of the activated carbon and adheres to that region. Adsorption takes place in this manner. However, for the adsorption to take place, the material to be adsorbed must pass through the pores of the activated carbon. If these pores are small or if the material to be adsorbed is larger than the pores, adsorption cannot take place (41).

In this study, activated carbon synthesis was made from peach kernel shells which are agricultural

waste. In this study, carbonization temperature, carbonization gas flow and activation temperature were changed. The synthesized active carbons were compared with each other.

## EXPERIMENTAL

### Synthesis of the Activated Carbon

Supplied with peach kernel shells (Bursa, Turkey) was used without applying any pretreatment except for washing with water. These shells were firstly subjected to pyrolysis process and the synthesis of activated carbon was made on solid char. A three-zone furnace was used for the pyrolysis process of peach kernel shell. The furnace was placed in the steel reactor with the help of a steel cuvette by taking approximately  $500 \pm 25$  g and subjected to pyrolysis in nitrogen atmosphere. Pyrolysis was carried out at 300, 400, 500, and 600 °C. The furnace started at room temperature and increased to 10 °C per minute to the final temperature. When it reached the final temperature, the furnace remained stable for 1 hour and was then allowed to cool to room temperature. Nitrogen gas atmosphere was used in all of these processes and nitrogen gas flow was made with the help of a manometer. Nitrogen gas for the samples was tested by means of manometer pyrolysis at 100 and 500 mL/min gas flow rates. The pyrolysis liquid was collected by means of the back cooler connected to the outlet end of the steel reactor.

Char obtained was placed in a three-zone furnace by means of a glass reactor and the physical activation was carried out. Two different activation temperatures (800 and 900 °C) were studied. At these temperatures, CO<sub>2</sub> gas was used for activation and the gas flow was fixed to a flow of 100 mL/min by means of a manometer. In this activation process, the furnace increased from 10 °C per minute starting from room temperature and remained at the final temperature for 1 hour.

### Preparation of Methylene Blue

The methylene blue used in the study was placed in a beaker and kept in an oven at 105° for 6 hours. Then 1 gram of methylene blue was taken and 1000 ppm, 1 liter stock solution was prepared.

### Adsorption

The prepared stock solution was diluted to 100 ppm and 0,1 grams of activated carbon sample was added to 100 mL and mixed for approximately 24 hours by magnetic stirrer (pH 6.2 at room temperature). The received solutions were filtered through a syringe filter and measured at 660 nm in a UV-Vis device.

### Equipment

Carbonization process with Protherm PZF 12/50/700 furnace, activation process with Protherm PZF 12/60/600 furnace were carried out.

### Analysis

UV-Vis analyses were performed with a Shimadzu UV-2100S, SEM analyses were carried out with a Leo EV040 brand scanning electron microscope, XRD were realized with a Rigaku RadB-DMAX II computer-controlled X-ray diffractometer, and BET (Brunauer-Emmett-Teller) measurements were performed with a Micromeritics Tristar 3000, and elemental analyses were realized with a CHNS-932 (LECO) Elemental Analyzer.

### RESULTS AND DISCUSSION

Biomass is converted to solid (char), liquid, and gas by pyrolysis process. These transformations vary depending on the biomass species and pyrolysis conditions. Table 1 shows the solid, liquid, and gas transformations of the peach kernel shell used as raw material as a result of the process.

**Table 1:** Solid, liquid and gas yields as a result of pyrolysis process.

Temperature / N <sub>2</sub> Gas Flow	Solid Yield %	Liquid Yield %	Gas Yield %
300 °C/ 100 mL/min	41.5	39.91	18.59
300 °C/ 500 mL/min	43.02	37.55	19.43
400 °C/ 100 mL/min	34.24	37.04	28.72
400 °C/ 500 mL/min	33.62	34.22	32.16
500 °C/ 100 mL/min	29.55	33.1	37.35
500 °C/ 500 mL/min	29.01	36.17	34.82
600 °C/ 100 mL/min	27.03	37.25	35.72
600 °C/ 500 mL/min	27.03	31.29	41.68

Peach kernel shell was subjected to pyrolysis at four different temperatures (300, 400, 500, and 600 °C) and solid, liquid and gas yields were calculated. Solid yield decreased with increasing temperature. It is seen that gas yield increases while liquid yield decreases with increasing temperature. Although the change in pyrolysis gas flow rate changed the solid, liquid and gas yields excessively at some temperatures, the change in some temperatures was very low.

The BET analysis results of the synthesized activated carbons are shown in Table 2. According to these results, the surface area varies between 686.74 and 340.15 m<sup>2</sup>/g. The highest surface area was achieved at an activation temperature of 800 °C in N<sub>2</sub> gas flow of 100 mL/min at 500 °C carbonization temperature. Table 2 shows that the change in temperature of pyrolysis caused changes in surface areas. Increasing the pyrolysis temperature up to 500 °C caused a positive change in the surface areas, while the rise to 600 °C showed a negative change in the surface areas. The change in the gas flow rate of pyrolysis caused changes in the samples. There was no order in these changes. The increased gas flow rate, except for 2 samples, caused a decrease in surface areas. The change in the activation temperature caused the surface area to change. In particular, the increase in activation temperature increased the surface area of samples. Since one of the objectives in activated carbons is the increased surface, it is necessary to work at high activation temperature when using CO<sub>2</sub> for high surface area activated carbons. Also, when we look at the synthesized activated carbons, we can usually mention two types of pores. Table 2 shows that activated carbons are composed of micropore and mesopore. Some samples were found to consist entirely of

micropores. In particular, the activated carbon synthesized at low carbonization temperature and low activation temperature is entirely composed of micropores. Increased carbonization temperature increased mesopore formation. Also, the increased gas flow rate increased the amount of mesopore in the samples. Another parameter, namely activation temperature, positively affected mesopore formation. Table 2 shows the total volume, micro and meso volumes of the activated carbons. Almost all of the samples consisted of micro volumes. In some samples, meso volumes were not observed at all, whereas in some samples a small amount was observed. Increased activation temperature caused micro volume to increase.

In the literature (42), activated carbon synthesis have been made from peach kernel shell. However, chemical activation method was generally used in these studies. In very few physical activation the results of activation temperature and carbonization temperature on activated carbon using CO<sub>2</sub> were not investigated. In some studies, physical activation was performed with water vapor. However, even with this activation, the activated carbons synthesized differ from each other. Compared with the studies in the literature, this study showed differences in many ways. The surface areas of the synthesized activated carbons were smaller than those synthesized by chemical activation in the literature (43). This is due to the fact that the chemical agent can directly contact the surface while the CO<sub>2</sub> hits the surface. However, during this contact, the chemical agent affected the surface and the active carbons have increased the ratio of mesopore. In this study, the amount of mesopore is less. In the literature (31), water vapor is used in activated carbons synthesized by physical activation. It is seen that the use of water vapor

causes more development of pores. When the water molecule contacted the biomass, it caused the pores to grow by contacting the pore walls in the cavities formed by carbonization. However, since the CO<sub>2</sub> molecule was larger than the water molecule, it could not provide expansion in the walls and expanded into the pore center. Therefore, the amount of mesopore is very high in water vapor studies in the literature. As the surface area will increase with increasing mesopore amount, the surface area in these studies is higher than the surface areas of the synthesized active carbons.

Figure 1 shows that the pore distribution ranges in the samples. Samples generally have pore distributions ranging from 1 nm to 2 nm. These pore distributions show the micropores formed in the structure. As in Table 2, the micropore ratio was found to be high in the samples. These results

showed parallelism with the pore distribution graph and confirmed the structure.

One of the ways of characterizing activated carbons is N<sub>2</sub> adsorption graphs. N<sub>2</sub> adsorption graphs provide information about the pores of activated carbons. Six types of adsorption plots were defined by IUPAC (International Union of Pure and Applied Chemistry). Each graph tells us about the pores of activated carbons by following different N<sub>2</sub> adsorption. N<sub>2</sub> adsorption graphs of the synthesized activated carbons are given in Figure 2. According to the graph in Figure 2, the N<sub>2</sub> adsorption graph is similar to type 1. Type 1 graphs are generally N<sub>2</sub> adsorption graphs seen in microporous and low surface area activated carbons. In the graph, adsorption at low pressure increases rapidly. This increase is due to microporous. The adsorption stops with the filling of micropores in the structure and the graph proceeds in a straight way.

**Table 2:** BET analysis results of activated carbons.

Carbonization		Physical Activation								
Temp. (°C)	N <sub>2</sub> Gas Flow (min/mL)	Temp. (°C/100 mL CO <sub>2</sub> )	S <sub>BET</sub> m <sup>2</sup> /g	S <sub>micro</sub> m <sup>2</sup> /g	S <sub>meso</sub> m <sup>2</sup> /g	V <sub>T</sub> cm <sup>3</sup> /g	V <sub>micro</sub> cm <sup>3</sup> /g	V <sub>meso</sub> cm <sup>3</sup> /g	dp nm	
300	100	800	340.15	340.15	-	0.19	0.17	0.02	-	
300	500	800	353.48	353.48	-	-	0.18	-	-	
300	100	900	445.42	412.06	33.35	0.22	0.21	0.01	2	
300	500	900	417.42	408.03	9.38	0.20	0.21	-	1.94	
400	100	800	596.73	69.81	526.9	0.55	0.03	0.52	3.74	
400	500	800	378.05	373.27	4.78	0.18	0.19	-	1.92	
400	100	900	458.24	426.67	31.56	0.228	0.224	0.004	1.99	
400	500	900	451.8	427.63	24.17	-	0.22	-	-	
500	100	800	686.74	-	686.7	0.68	0.02	0.66	4.01	
500	500	800	356.99	356.99	-	-	0.19	-	-	
500	100	900	422.53	402.39	20.13	0.20	0.21	-	1.97	
500	500	900	447.65	412.41	35.23	0.22	0.21	0.01	1.99	
600	100	800	349.23	343.24	5.98	0.18	0.05	0.13	-	
600	500	800	345.42	345.42	-	-	0.18	-	-	
600	100	900	427.13	399.99	27.14	0.21	0.21	-	2	
600	500	900	412.89	409	3.88	-	0.21	-	-	

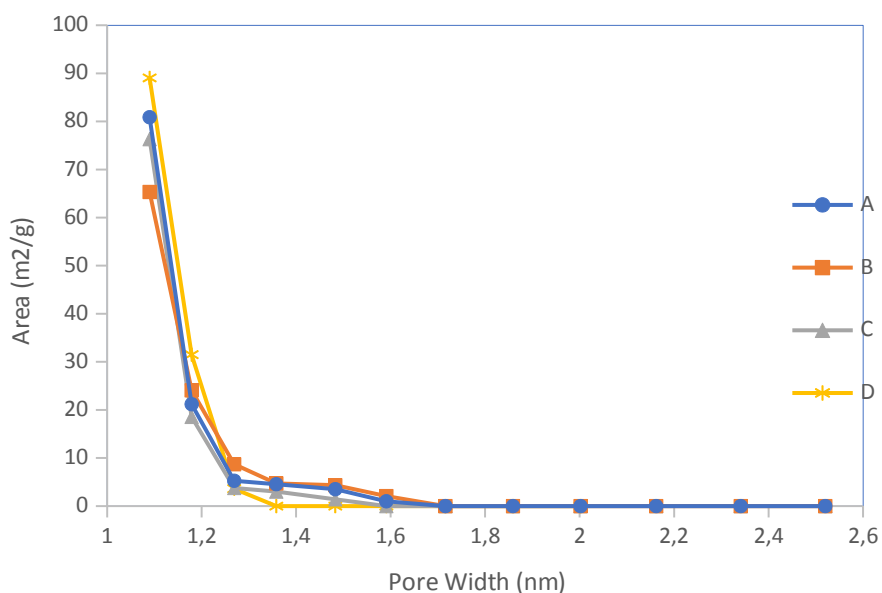


**Figure 1:** Pore size distribution of activated carbon sample A. Activated carbon sample at 500 °C 100 mL/min N<sub>2</sub> carbonization and at 900 °C with 100 mL/min CO<sub>2</sub> activation B. Activated carbon sample at 400 °C 100 mL/min N<sub>2</sub> carbonization and at 900 °C with 100 mL/min CO<sub>2</sub> activation C. Activated carbon sample at 600 °C 100 mL/min N<sub>2</sub> carbonization and at 800 °C with 100 mL/min CO<sub>2</sub> activation D. Activated carbon sample at 300 °C 100 mL/min N<sub>2</sub> carbonization and at 800 °C with 100 mL/min CO<sub>2</sub> activation.

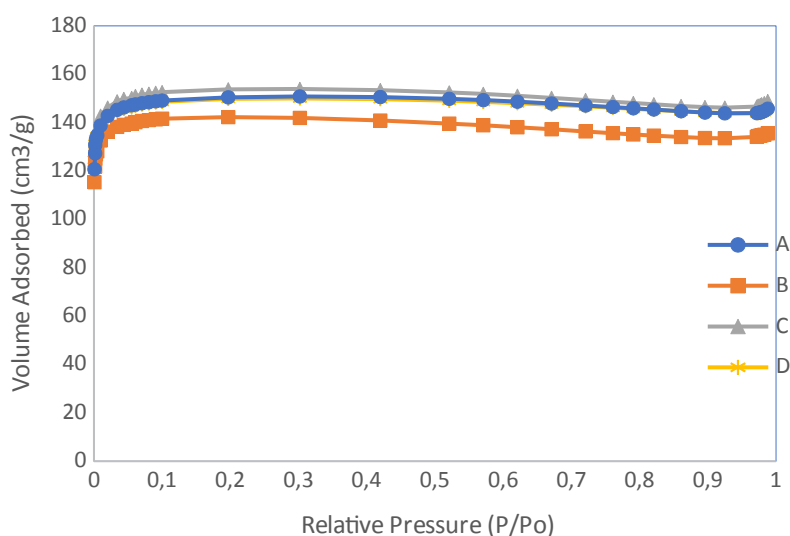


**Figure 2:** Adsorption isotherms of N<sub>2</sub> A. Activated carbon sample at 500 °C 500 mL/min N<sub>2</sub> carbonization and at 900 °C with 100 mL/min CO<sub>2</sub> activation B. Activated carbon sample at 500 °C 100 mL/min N<sub>2</sub> carbonization and at 900 °C with 100 mL/min CO<sub>2</sub> activation C. Activated carbon sample at 400 °C 100 mL/min N<sub>2</sub> carbonization and at 900 °C with 100 mL/min CO<sub>2</sub> activation D. Activated carbon sample at 300 °C 100 mL/min N<sub>2</sub> carbonization and at 900 °C with 100 mL/min CO<sub>2</sub> activation.

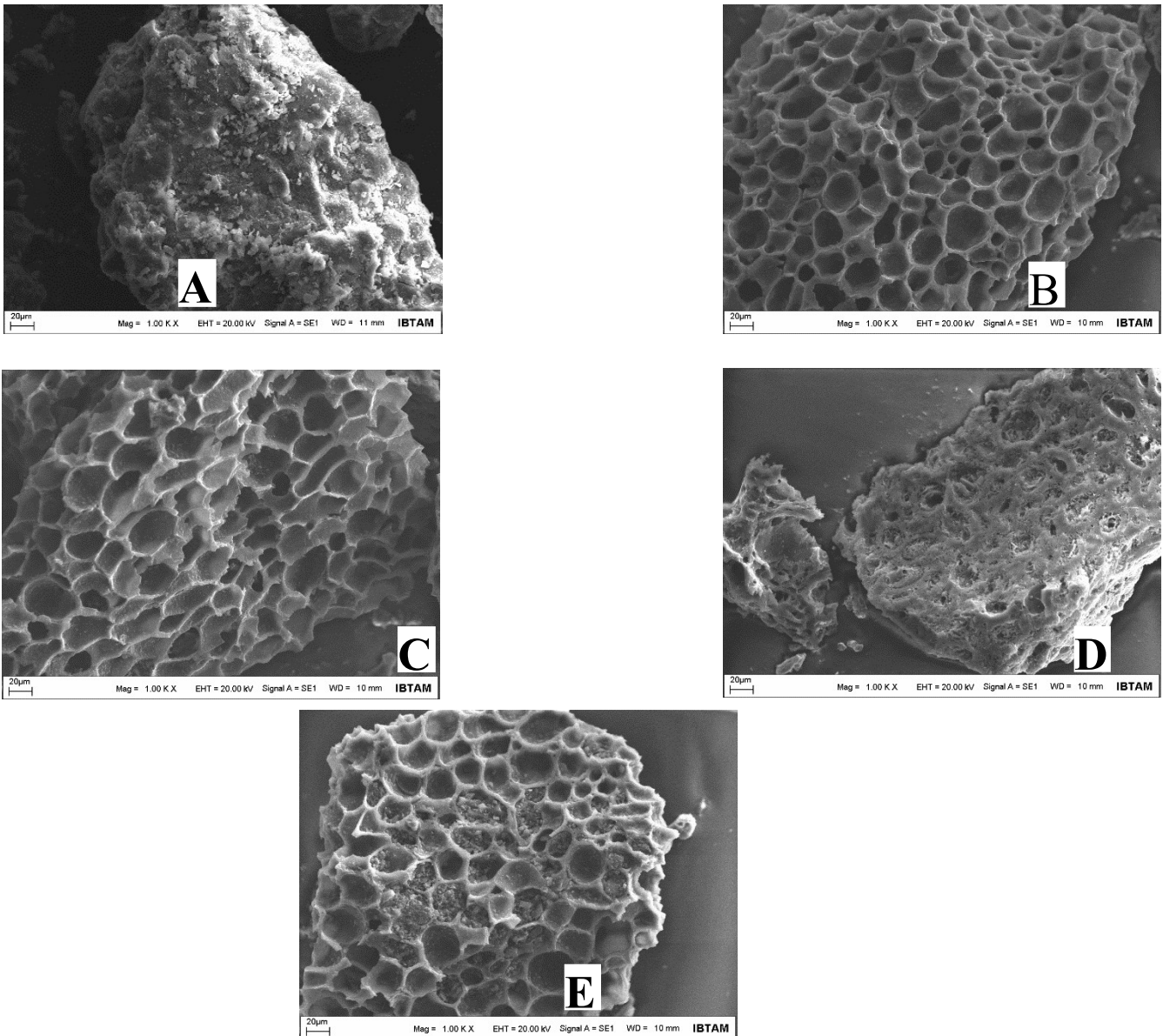


**Figure 3:** A. SEM image of raw peach shell B. Activated carbon sample at 500 °C 100 mL/min N<sub>2</sub> carbonization and at 800 °C with 100 mL/min CO<sub>2</sub> activation C. Activated carbon sample at 500 °C 500 mL/min N<sub>2</sub> carbonization and at 900 °C with 100 mL/min CO<sub>2</sub> activation. D. Activated carbon sample at 400 °C 100 mL/min N<sub>2</sub> carbonization and at 800 °C with 100 mL/min CO<sub>2</sub> activation. E. Activated carbon sample at 400 °C 100 mL/min N<sub>2</sub> carbonization and at 900 °C with 100 mL/min CO<sub>2</sub> activation.

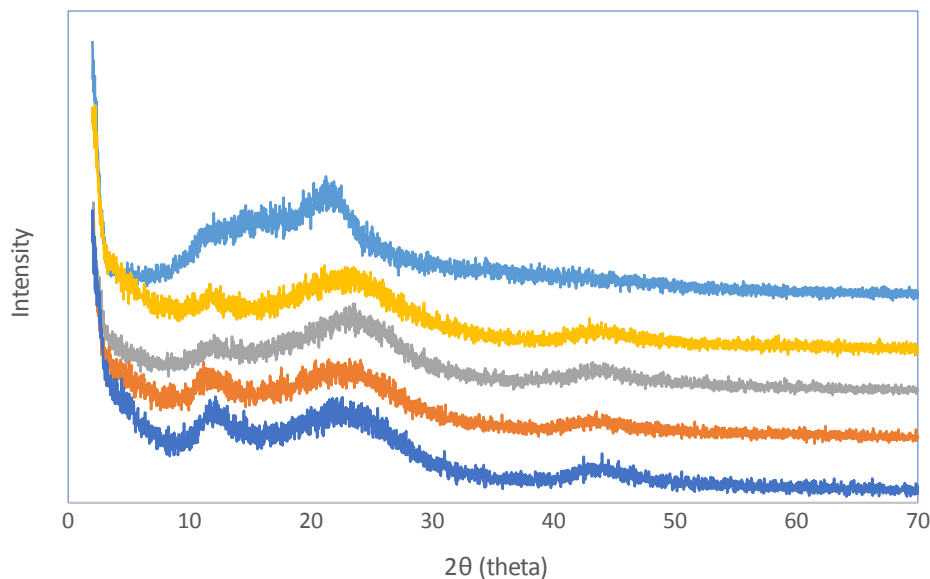


**Figure 4:** XRD chart of samples. A. XRD chart of raw peach shell. B. Activated carbon sample at 400 °C 100 mL/min N<sub>2</sub> carbonization and at 800 °C with 100 mL/min CO<sub>2</sub> activation. C. Activated carbon sample at 400 °C 100 mL/min N<sub>2</sub> carbonization and at 900 °C with 100 mL/min CO<sub>2</sub> activation. D. Activated carbon sample at 500 °C 100 mL/min N<sub>2</sub> carbonization and at 800 °C with 100 mL/min CO<sub>2</sub> activation. E. Activated carbon sample at 500 °C 500 mL/min N<sub>2</sub> carbonization and at 900 °C with 100 mL/min CO<sub>2</sub> activation

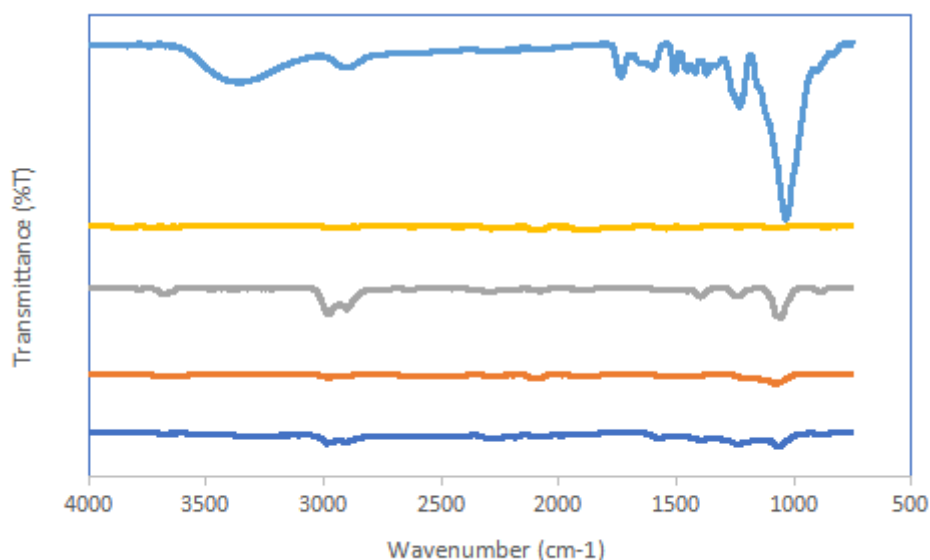


**Figure 5:** FTIR spectra of raw material and activated carbon samples. A. Raw material. B. Activated carbon sample at 400 °C 100 mL/min N<sub>2</sub> carbonization and at 800 °C with 100 mL/min CO<sub>2</sub> activation. C. Activated carbon sample at 400 °C 100 mL/min N<sub>2</sub> carbonization and at 900 °C with 100 mL/min CO<sub>2</sub> activation. D. Activated carbon sample at 500 °C 100 mL/min N<sub>2</sub> carbonization and at 800 °C with 100 mL/min CO<sub>2</sub> activation. E. Activated carbon sample at 500 °C 500 mL/min N<sub>2</sub> carbonization and at 900 °C with 100 mL/min CO<sub>2</sub> activation.

One of the methods used to characterize activated carbons is SEM analysis. Thanks to SEM analysis, we see the pores of the activated carbons. SEM images of the synthesized activated carbons and peach kernel shell used as raw materials are shown in Figure 3. According to SEM images, peach kernel shell does not show pores on its surface without any

pretreatment. The formation of pores on the surface is seen as a result of activated carbon synthesis.

XRD analysis of synthesized activated carbons and peach kernel shell is shown in Figure 4. When the raw materials and activated carbons were examined, no crystalline structure was found in the

structure. Amorphous is observed in the structures. In the peach kernel shell used in the synthesis of activated carbon, a small amount of regular structure is encountered. In particular, the peak of about  $22^\circ$  is defined as the cellulose peak and is seen in cellulose-structured materials. During the synthesis of activated carbon, this regular structure was disrupted by heat and partially lost this peak intensity in activated carbon samples.

The FTIR spectroscopy technique was used to identify the functional groups on the surface on activated carbons and the raw material. According to the FTIR spectra in Figure 5, the band belongs to OH stress vibrations at approximately  $3450\text{ cm}^{-1}$ , band around  $2850\text{ cm}^{-1}$  indicates the C-H stretching vibrations, the band seen at about  $1700\text{ cm}^{-1}$  originates from C=O, band at about  $1600\text{ cm}^{-1}$  belongs to the C=C bond vibration of alkenes. Band at about  $1000\text{ cm}^{-1}$  is the peak of vibrations caused by C-OH and C-O-C bonds.

Elemental analysis results of synthesized activated carbons and raw material are given in Table 3. According to Table 3, It is seen that the carbon amounts of the synthesized activated carbons are approximately 7-71% higher than the raw materials. In addition, the carbon content of the synthesized activated carbons that are exposed to a high activation temperature is generally less than the others. Activated carbons synthesized at the same carbonization temperature and activation temperature of  $800\text{ }^\circ\text{C}$  appear to reduce the amount of carbon at an increased gas flow rate. However, at the activation temperature of  $900\text{ }^\circ\text{C}$  this was the opposite. The hydrogen content of the synthesized active carbons decreased approximately 5 times compared to the raw material.

Adsorption, which is one of the most commonly used application fields of activated carbons, was studied. In this work, methylene blue adsorption capacities of activated carbons were examined. The

adsorption capacity of the synthesized activated carbons was found to be very low. The reason for this is methylene blue, which is the molecule to be adsorbed, and the reason is the diameter of the pores formed on the activated carbon. If the molecule to be adsorbed passes through the pores on the activated carbon, it will bind to the atoms on the outer surface of the pores through secondary interactions. Because the methylene blue molecule did not pass through the pores on the activated carbon this phenomenon could not occur. The synthesized activated carbons have very small pore diameters. DFT results show how small and narrow the pore diameters change. Therefore, these results are quite natural.

## CONCLUSIONS

In this study, it is aimed to synthesize activated carbon with narrow pore distribution from peach seed peel, which is an agricultural waste. In the study, carbonization was made at 4 different temperatures and 2 different gas flows, and  $\text{CO}_2$  was used for activation. As a result of the characterization of the samples, it was observed that micropores were abundant and showed a narrow pore distribution according to the DFT plus data. The micropore ratio in the prepared activated carbons varied depending on the temperature and gas flow rate. No micropores were observed in one sample, although some samples consisted entirely of micropores. In the elemental analysis of activated carbons, the amount of carbon showed a maximum increase of 71% compared to the raw material. In the study, the adsorption capacity of methylene blue studied in the samples with narrow pore distribution was quite low, while adsorption was not observed in some samples. Although the activated carbons prepared in this study are not suitable for methylene blue adsorption, it can be checked whether they are suitable by using different applications.

**Table 3:** Elementary analysis results of raw materials and activated carbons.

Carbonization		Physical Activation				
Temperature °C	N <sub>2</sub> Gas Flow dk/mL	Temperature (°C/100 mL CO <sub>2</sub> )	C	H	N	S
	Raw Materials		50.45	5.68	0.072	-
300	100	800	79.27	1.03	0.28	-
300	500	800	78.25	1.132	0.32	-
300	100	900	54.07	1.317	0.184	-
300	500	900	57.74	1.063	0.242	-
400	100	800	86.27	0.98	-	-
400	500	800	74.85	1.628	0.276	-
400	100	900	62.06	0.59	-	-
400	500	900	69.40	1.219	0.132	-
500	100	800	86.53	0.97	-	-
500	500	800	79.76	1.607	0.268	-
500	100	900	65.90	1.509	0.138	0.053
500	500	900	74.34	0.64	-	-
600	100	800	84.00	1.39	0.215	-
600	500	800	77.46	1.412	0.259	-
600	100	900	76.81	0.59	-	-
600	500	900	82.77	1.009	0.173	0.054

**Table 4:** Methylene blue adsorption capacity of activated carbons.

Carbonization		Physical Activation		
Temperature °C	N <sub>2</sub> Gas Flow dk/mL	Temperature (°C/100 mL CO <sub>2</sub> )	S <sub>BET</sub> m <sup>2</sup> /g	Adsorption Capacity q <sub>e</sub> (mg/g)
300	100	800	340.15	2.98
300	500	800	353.48	0.89
300	100	900	445.42	12
300	500	900	417.42	9.69
400	100	800	596.73	1.44
400	500	800	378.05	-
400	100	900	458.24	24.1
400	500	900	451.8	16.29
500	100	800	686.74	-
500	500	800	356.99	-
500	100	900	422.53	9.69
500	500	900	447.65	7.74
600	100	800	349.23	-
600	500	800	345.42	-
600	100	900	427.13	8.15
600	500	900	412.89	7.93

**ACKNOWLEDGEMENT**

This study was supported by the unit of Scientific Researches of Inonu University in Malatya, Turkey; Project no: FDI-2017-680

**REFERENCES**

1. Ayinla RT, Dennis J, Zaid H, Sanusi Y, Usman F, Adebayo L. A review of technical advances of recent palm bio-waste conversion to activated carbon for energy storage. *Journal of cleaner production*. 2019;229:1427-42. [<DOI>](#)
2. Mayyas M, Sahajwalla V. Carbon nano-sponge with enhanced electrochemical properties: A new understanding of carbon activation. *Chemical Engineering Journal*. 2019;358:980-91. [<DOI>](#)
3. Khan JH, Marpaung F, Young C, Lin J, İslam MT, Alsheri SM, Ahamad T, Alhokbany N, Ariga K, Shrestha LK, Yamauchi Y, Wu KC, Hossain MSA, Kim J. Jute-derived microporous/mesoporous carbon with ultra-high surface area using a chemical activation process. *Microporous Mesoporous Materials*. 2019;274:251-6. [<DOI>](#)
4. Zhang Y, Song X, Xu Y, Shen H, Kong X, Xu H. Utilization of wheat bran for producing activated carbon with high specific surface area via NaOH activation using industrial furnace. *Journal of cleaner production*. 2019;210:366-75. [<DOI>](#)
5. Sharma M, Joshi M, Nigam S, Shree S, Avasthi DK, Adelung R, Srivastava SK, Mishra YK. ZnO tetrapods and activated carbon based hybrid composite: Adsorbents for enhanced decontamination of hexavalent chromium from aqueous solution. *Chemical Engineering Journal*. 2019;358:540-51. [<DOI>](#)
6. Abdullah MO, Tan IW, Lim LS. Automobile adsorption air-conditioning system using oil palm biomass-based activated carbon: a review. *Renewable Sustainable Energy Reviews*. 2011; 15:2061-72. [<DOI>](#)
7. Hu Z, Srinivasan M. Mesoporous high-surface-area activated carbon. *Microporous Mesoporous Materials*. 2001;43:267-75. [<DOI>](#)
8. Sinha P, Banerjee S, Kar K.K. Characteristics of activated carbon. *Springer Series in Materials Science*. 2020. ISBN: 978-3-030-43009-2
9. Oliveira L, Pereira E, Guimaraes R, Vallone A, Pereira M, Mesquita JP, Sapag K. Preparation of activated carbons from coffee husks utilizing FeCl<sub>3</sub> and ZnCl<sub>2</sub> as activating agents. *Journal of Hazardous Materials*. 2009;165:87-94. [<DOI>](#)
10. Chandra TC, Mirna M, Sudaryanto Y, Ismadji S. Adsorption of basic dye onto activated carbon prepared from durian shell: Studies of adsorption equilibrium and kinetics. *Chemical Engineering Journal*. 2007;127:121-9. [<DOI>](#)
11. Martinez ML, Torres MM, Guzman CA, Maestri DM. Preparation and characteristics of activated carbon from olive stones and walnut shells. *Industrial crops products*. 2006;23:23-8. [<DOI>](#)
12. Gao P, Liu Z-H, Xue G, Han B, Zhou M-H. Preparation and characterization of activated carbon produced from rice straw by (NH<sub>4</sub>)<sub>2</sub>HPO<sub>4</sub> activation. *Bioresource technology*. 2011;102:3645-8. [<DOI>](#)
13. Foo K, Hameed B, Microwave-assisted preparation of oil palm fiber activated carbon for methylene blue adsorption. *Chemical Engineering Journal*. 2011;166:792-5. [<DOI>](#)
14. Gonzalez JF, Roman S, González-García CM, Nabais JV, Ortiz AL. Porosity development in activated carbons prepared from walnut shells by carbon dioxide or steam activation. *Industrial engineering chemistry research*. 2009;48:7474-81. [<DOI>](#)
15. Chen Y, Zhu Y, Wang Z, Li Y, Wang L, Ding L, Gao X, Ma Y, Guo Y. Application studies of activated

carbon derived from rice husks produced by chemical-thermal process—A review, *Advances in colloid interface science*, 2011;163:39-52. [<DOI>](#)

16. Demirbas E, Kobya M, Sulak M. Adsorption kinetics of a basic dye from aqueous solutions onto apricot stone activated carbon. *Bioresource technology*. 2008;99:5368-73. [<DOI>](#)

17. Angin D. Production and characterization of activated carbon from sour cherry stones by zinc chloride. *Fuel*. 2014;115:804-11. [<DOI>](#)

18. Van Thuan T, Quynh BTP, Nguyen TD, Bach LG. Response surface methodology approach for optimization of Cu<sup>2+</sup>, Ni<sup>2+</sup> and Pb<sup>2+</sup> adsorption using KOH-activated carbon from banana peel. *Surfaces Interfaces*. 2017;6:209-17. [<DOI>](#)

19. Srinivasakannan C, Bakar MZA. Production of activated carbon from rubber wood sawdust. *Biomass and Bioenergy*.2004;27;89-96. [<DOI>](#)

20. Suzuki R, Andrade A, Sousa J, Rollemberg M. Preparation and characterization of activated carbon from rice bran. *Bioresource technology*. 2007;98:1985-91. [<DOI>](#)

21. Mohan D, Sarswat A, Singh VK, Alexandre-Franco M, Pittman Jr. C. Development of magnetic activated carbon from almond shells for trinitrophenol removal from water. *Chemical Engineering Journal*. 2011;172:1111-25. [<DOI>](#)

22. Yagmur E, Ozmak M, Aktas Z. A novel method for production of activated carbon from waste tea by chemical activation with microwave energy. *Fuel*. 2008;87:3278-85. [<DOI>](#)

23. Yang J, Qiu K. Development of high surface area mesoporous activated carbons from herb residues. *Chemical engineering journal*. 2011;167:148-54. [<DOI>](#)

24. Bagheri N, Abedi J, Adsorption of methane on corn cobs based activated carbon. *Chemical Engineering Research Design*. 2011;89:2038-43. [<DOI>](#)

25. Teker M, Saltabaş Ö, İmamoğlu M. Adsorption of cobalt by activated carbon from the rice hulls. *Journal of Environmental Science Health Part A*. 1997;32:2077-86. [<DOI>](#)

26. Krishnan KA, Anirudhan T. Uptake of heavy metals in batch systems by sulfurized steam activated carbon prepared from sugarcane bagasse pith. *Industrial Engineering Chemistry Research*. 2002;41:5085-93. [<DOI>](#)

27. Deng H, Zhang G, Xu X, Tao G, Dai J. Optimization of preparation of activated carbon from cotton stalk by microwave assisted phosphoric acid-chemical activation. *Journal of Hazardous Materials*. 2010;182:217-24. [<DOI>](#)

28. Fernandez ME, Nunell GV, Bonelli PR, Cukierman AL. Activated carbon developed from orange peels: Batch and dynamic competitive adsorption of basic dyes. *Industrial Crops Products*. 2014;62:437-45. [<DOI>](#)

29. Alhamed YA. Adsorption kinetics and performance of packed bed adsorber for phenol removal using activated carbon from dates' stones. *Journal of Hazardous Materials*. 2009;170:763-70. [<DOI>](#)

30. Gupta VK, Jain R, Shrivastava M, Nayak A. Equilibrium and thermodynamic studies on the adsorption of the dye tartrazine onto waste "coconut husks" carbon and activated carbon. *Journal of Chemical Engineering Data*. 2010;55:5083-90. [<DOI>](#)

31. Pallares J, Cencerrado GA, Arauzo I. Production and characterization of activated carbon from barley straw by physical activation with carbon dioxide and steam. *Biomass and Bioenergy*. 2018;115:64-73. [<DOI>](#)

32. Jurado-Sanchez B, Sattayasamitsathit S, Gao W, Santos L, Fedorak Y, Sing Vv, Orozco J, Galarnyk M, Wang J. Self-Propelled Activated Carbon Janus Micromotors for Efficient Water Purification. *Small*. 2015;11:499-506. [<DOI>](#)
33. Matsuo T, Nishi T. Activated carbon filter treatment of laundry waste water in nuclear power plants and filter recovery by heating in vacuum. *Carbon*. 2000;38(5):709-14. [<DOI>](#)
34. Sircar S, Golden T, Rao M. Activated carbon for gas separation and storage. *Carbon*. 1996;34(1):1-12. [<DOI>](#)
35. Fang B, Binder L. A modified activated carbon aerogel for high-energy storage in electric double layer capacitors. *Journal of power sources*. 2006;163; 616-22. [<DOI>](#)
36. Faria P, Órfão J, Pereira M. Activated carbon catalytic ozonation of oxamic and oxalic acids. *Applied Catalysis B: Environmental*. 2008;79:237-43. [<DOI>](#)
37. Rivera-Utrilla J, Sánchez-Polo M, Gómez-Serrano V, Alvarez P, Alvim-Ferraz M, Dias J. Activated carbon modifications to enhance its water treatment applications. An overview. *Journal of hazardous materials*. 2011;187:1-23. [<DOI>](#)
38. Snyder AS, Adham S, Redding AM, Cannon FS, Decarolis J, Oppenheimer J, Wert EC, Yoon Y. Role of membranes and activated carbon in the removal of endocrine disruptors and pharmaceuticals, *Desalination*, 2007;202:156-81. [<DOI>](#)
39. Park JH, Park OO. Hybrid electrochemical capacitors based on polyaniline and activated carbon electrodes. *Journal of Power Sources*. 2002;111:185-0. [<DOI>](#)
40. Anirudhan T, Sreekumari S, Bringle C. Removal of phenols from water and petroleum industry refinery effluents by activated carbon obtained from coconut coir pith. *Adsorption*. 2009;15;439. [<DOI>](#)
41. Vargas AM, Cazetta AL, Kunita MH, Silva TL, Almeida VC. Adsorption of methylene blue on activated carbon produced from flamboyant pods (*Delonix regia*): Study of adsorption isotherms and kinetic models. *Chemical Engineering Journal*. 2011;168:722-30. [<DOI>](#)
42. Anyika C, Asri NAM, Majid ZA, Yahya A, Jaafar J. Synthesis and characterization of magnetic activated carbon developed from palm kernel shells. *Nanotechnology for Environmental Engineering*. 2017; 2: 16. [<DOI>](#)
43. Prauchner JM, Sapag K, Reinoso RF. Tailoring biomass-based activated carbon for CH<sub>4</sub> storage by combining chemical activation with H<sub>3</sub>PO<sub>4</sub> or ZnCl<sub>2</sub> and physical activation with CO<sub>2</sub>. 2016;110:138-47. [<DOI>](#)





## Synthesis, Characterization, and Use of Lanthanide Chelate of $\beta$ -Diketonate Based Ligand as a Luminescent Biolabel

Semanur Sen Yuvayapan<sup>1</sup>  , Alper Tolga Colak<sup>1\*</sup>  , Onur Sahin<sup>2</sup>  ,  
and Cumali Celik<sup>3</sup>  

<sup>1</sup> Department of Chemistry, Faculty of Arts and Sciences, Dumlupinar University, Kutahya, Turkey

<sup>2</sup> Department of Occupational Health & Safety, Faculty of Health Sciences, Sinop University, Sinop, Turkey

<sup>3</sup> Department of Property Protection and Security, Yalova Vocational School, Yalova University, Yalova, Turkey

**Abstract:** In this study, we aimed to synthesize a  $\beta$ -diketonate-based ligand and its Eu(III) complex which are used for luminescent biolabel. For this purpose, we chose acetophenone as the starting material which contains methyl group at the alpha position of the ketone group. Firstly, we obtained 4,4,5,5,6,6,7,7-octafluoro-3,8-dihydroxy-1,10-diphenyldeca-2,8-diene-1,10-dione (H<sub>2</sub>ODIT) ligand in a reaction between acetophenone and diethyloctafluoroadipate with Claisen condensation. This ligand was characterized by <sup>1</sup>H-NMR, <sup>13</sup>C-NMR, and mass spectral analyses. We obtained a single crystal H<sub>2</sub>ODIT as characterized by X-ray analysis. At the second step, in order to bind H<sub>2</sub>ODIT to the antibody, it is reacted with chlorosulfonic acid. As a result of this reaction, the functional group of -ClSO<sub>2</sub> was bound to the structure. The structure of H<sub>2</sub>CODIT was characterized by NMR and mass spectral analysis. In the third step, to understand the usability of the ligand as a biolabel, the complex compound was synthesized with EuCl<sub>3</sub>. The complex compound was excited with UV light at 306 nm wavelength, specific hypersensitive <sup>5</sup>D<sub>0</sub> → <sup>7</sup>F<sub>2</sub> phosphorescence electronic transition of the Eu(III) was observed which proved that the luminescent H<sub>2</sub>CODIT molecule can work as a biolabel.

**Keywords:** Beta-diketonate, Claisen condensation, europium(III) complex, keto-enol tautomerism, luminescence, biolabel.

**Submitted:** June 09, 2021. **Accepted:** July 18, 2021.

**Cite this:** Sen Yuvayapan S, Colak AT, Sahin O, Celik C. Synthesis, Characterization, and Use of Lanthanide Chelate of  $\beta$ -Diketonate Based Ligand as a Luminescent Biolabel. JOTCSA. 2021;8(3):835-50.

**DOI:** <https://doi.org/10.18596/jotcsa.949970>.

**\*Corresponding author. E-mail:** [tolga.colak@dpu.edu.tr](mailto:tolga.colak@dpu.edu.tr).

### INTRODUCTION

The investigation of luminescence properties of complexes of rare earth elements was introduced upon the excitation of europium  $\beta$ -diketone complexes by ultraviolet light in 1942 (1). Biomedical and biolabeling of europium  $\beta$ -diketone complexes have been a subject of interest since then.

Lanthanides are known for their atomic emission properties. Europium is a versatile lanthanide; a myriad of luminescence applications of europium such as biomedical sensor, diagnosis, drug delivery, and optical screening exist (2-7). One of the most striking properties of the complexes that contain lanthanides is absorption of light with a specific wavelength followed by a reflection with a distinct wavelength. Either a ligand or a metal center are responsible for such absorption behavior. Energy is emitted through various ways,

which are fluorescence or phosphorescence, heat, and a photochemical product (8). In the Ln(III)-ligand bonding, 4f electrons are screened by the electrons of 5s<sup>2</sup> and 5p<sup>6</sup> so that they can rarely take place in covalent interactions with ligands. The covalency of a Ln(III)-ligand bond is around 5-7%. As a result of this screening, transitions are considered weak in respect to both absorption and emission. It is a difficult task to excite 4f electrons directly unless subjected to a laser, even for highly luminescent materials. Ln(III) ions cannot fluoresce through absorbing UV light (6,9). The lanthanide ion depends on fluorescence ligands in order to transfer to <sup>5</sup>D<sub>j</sub> energy level through a viable mechanism, and the absorption of light is similar to an antenna. The long lifetime of the excited states of complex lanthanide ions (0.2-1.5 ms), large Stokes slip (over 200 nm), and emission at visible region makes them attractive ions in terms of possessing narrow and sharp emission bands (2). Visible emission spectrum of Eu<sup>3+</sup> results from <sup>5</sup>D<sub>0</sub>→<sup>7</sup>F<sub>j</sub> transition, and transitions at specific wavelength are: 594 nm (<sup>5</sup>D<sub>0</sub>→<sup>7</sup>F<sub>1</sub>); 617 nm (<sup>5</sup>D<sub>0</sub>→<sup>7</sup>F<sub>2</sub>); 659 nm (<sup>5</sup>D<sub>0</sub>→<sup>7</sup>F<sub>3</sub>), (10).

Eu<sup>3+</sup> complexes usually provide higher sensitivity, which accounts for their very strong preference among lanthanides. Eu<sup>3+</sup> complexes exhibit some distinct properties such as i) performing absorption pinnacle at UV region (about 330 nm) and fluorescence emission at 615 nm, ii) possessing a narrow emission band, iii) considerable lifetime of the triplet state of their complexes under excitation (longer than 100 μs), iv) indicating low background signal, v) demonstrating sharp emission peaks, and vi) not causing any radioactive contamination.

β-diketones or 1,3-diketones consist of two carbonyl groups separated by a carbon atom, which is an α-carbon. On the other hand, carbonyl substituents can be either alkyl, fluorinated alkyl, or aromatic/heteroaromatic groups. The selection of functional groups affect the properties of Eu(III) complexes. For instance, solubility and volatility are increased in organic solvents when branched alkyl chains such as tert-butyl group are introduced. Perfluorinated alkyl groups increase the Lewis acidity. Aromatic β-diketones better absorb light when compared to aliphatic ones. Furthermore, functional groups affect the energy state of the ligand (singlet and triplet), (11). Fluorescent intensity increases when an electron donor (R<sub>1</sub>) and acceptor (R<sub>2</sub>) are introduced in the same ligand for β-diketonato (R<sub>1</sub>COHCOR<sub>2</sub>)-Eu complexes (12).

The selection of the ligands that will be constituted with europium(III) depends on the application. The ligands used as biolabeling in medical diagnostic kits can be divided into 4 main categories: i)

ligands exhibiting no luminescent property, ii) polyamino carboxylate based luminescent ligands (PAC based), iii) β-Diketone based luminescent ligands, and iv) other luminescent ligands (13).

Luminescent lanthanide β-diketones have a wide range of applications, including electroluminescent device and sensors, lasers, and bioanalysis (14). Eu(III) complexes are established to be stable in aqueous solutions of β-diketonates, covalently bonded to the protein easily due to their tendency to chlorosulfonation, and possessing highly luminescent character. Their lesser side products in reactions, ease of their synthesis, and cost-effective synthesis can be counted as other advantages (15).

Ultrasensitive bioanalytical kits of analysis are based on the detection of the existence of analyte that bonds to the material of interest or measurement of the concentration (5). The applications regarding the use of luminescent lanthanide complexes in bioanalysis date back to 1983 (16). Most of them are designed for biochemical evaluation or qualitative measurement of specific antibodies or any antigen. Within the possibility of involving radioactive atoms (<sup>125</sup>I, <sup>3</sup>H, and <sup>14</sup>C) that generate signals for some regions, many labels are available. In addition, enzymes, fluorescent probes, chemiluminescent compounds, metals, and metal chelates and liposomes, as non-radioactive labels, can be used due to their numerous advantages (17). This study aims to synthesize the non-radioactive label Eu(III) complex.

Employing ketone and fluorine compounds as precursors, a very limited number of compounds synthesized via Claisen condensation can be found in the literature. Most of them contain aromatic rings. Despite the vast number of synthesis of lanthanide-β-diketone complexes, very few of them have been utilized in biomolecular labeling (11) by reason of them being only bidentate that makes them have a limited stability. In order to go beyond this limit, tetradentate ligands comprise of two β-diketones in a molecule were synthesized. These ligands were then used in immunoanalysis for designation of various biomolecules (18,19). This study focuses on the synthesis of tetradentate β-diketonate based luminescent ligand with eight fluorine atoms and two aromatic rings and its availability on biomolecular labeling.

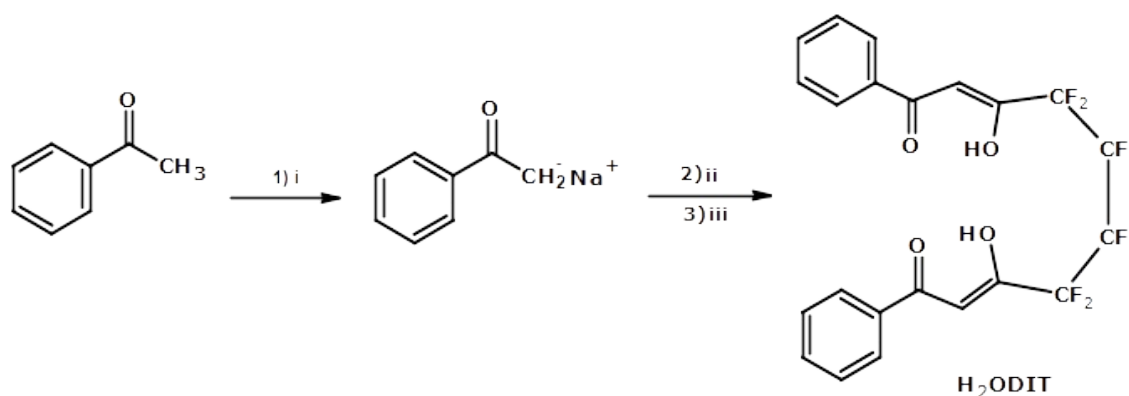
## MATERIALS AND METHODS

EuCl<sub>3</sub>, acetophenone, dimethyloctafluoroadipate (DEOFA), sodium methoxide (NaOCH<sub>3</sub>), chlorosulfonic acid (HSO<sub>3</sub>Cl), diethyl ether, ethanol, and 1,4-dioxane were all provided by Sigma-Aldrich and used without any purification. NMR

analysis were carried out by using a Bruker Biospin NMR Spectrometer with data acquisition by taking advantage of an Avance III 400 MHz instrument. FTIR studies were run by a Bruker Vertex 70 FT-IR. UV-visible electronic spectra were obtained by a Shimadzu UV-2450 spectrophotometer. Mass spectrometry of the complexes were performed by an Agilent 6530 Accurate Mass Q-TOF LC/MS. X-ray single crystallography of H<sub>2</sub>ODIT ligand was studied by using D8-QUEST diffractometer with a graphite-monochromatic Mo-K $\alpha$  light source at 296 K. The structure was examined by SHELX-2013 (20,21) through direct methods and least squares method was applied to refine the matrix at F<sup>2</sup> by taking advantage of WINGX software. Crystalline X-Ray Diffraction data was acquired from Bruker APEX-II (22) diffractometer. Molecular diagrams were generated by MERCURY software (23). Supramolecular analysis was run by WinGX software (24). Luminescence spectrum of the complex was obtained by Perkin Elmer LS55 fluorescence spectrophotometer.

### Synthesis of (2Z,8Z)-4,4,5,5,6,6,7,7-octafluoro-3,8-dihydroxy-1,10-diphenyldeca-2,8-diene-1,10-dione (H<sub>2</sub>ODIT)

In order to form the acetophenone sodium salt, NaOCH<sub>3</sub> and 50 mL of diethyl ether in catalytic amount were placed in a two-necked round-bottom flask connected to a refrigeration apparatus. Acetophenone (2.50 g, 20 mmol) was slowly added into the flask, and the solution was stirred for 1 h. The observed color was pale light yellow. DEOFA (3.60 g, 10 mmol) was added in this solution dropwise. A yellow color was observed. Thin layer chromatography was employed in order to determine the reaction time, amount of matter, and purity in a specific timespan. *n*-Hexane-chloroform (1:3, v:v) mixture was used for chromatographic analysis. The solution was stirred for 5 days at room temperature followed by the evaporation of the solvent. The residue was dissolved with water. pH adjustment (pH=6) was later carried out with 15% H<sub>2</sub>SO<sub>4</sub>. Precipitated substance at acidic medium was dried and crystallized from ethanol-1,4-dioxane (3:2, v:v) mixture (Scheme 1). Yield: 2.50 g (48.5 %).

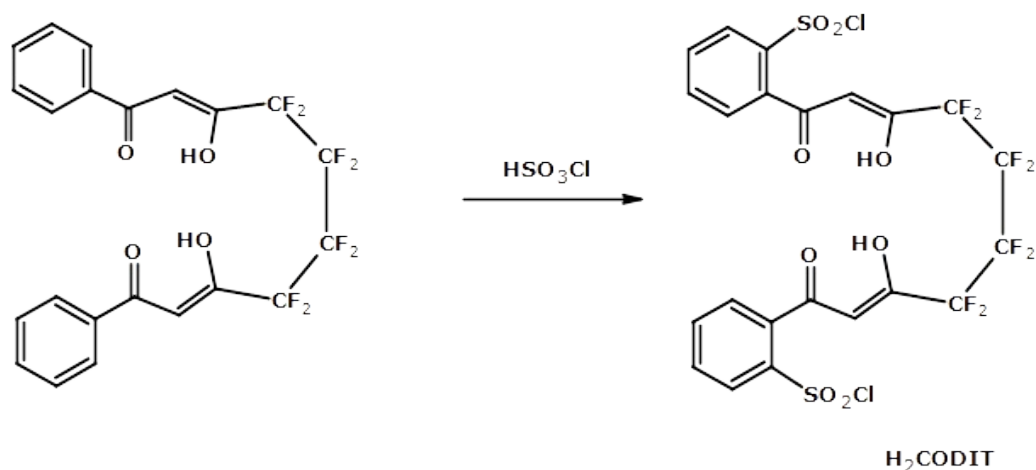


**Scheme 1:** Reagents and conditions. (i) NaOCH<sub>3</sub>, diethyl ether, rt, 1 h; (ii) DEOFA, rt, 5 days; (iii) H<sub>2</sub>SO<sub>4</sub>, H<sub>2</sub>O.

### Synthesis of (2Z,8Z)-1,10-bis(benzene-1-sulfonyl chloride)-4,4,5,5,6,6,7,7-octafluoro-3,8-dihydroxydeca-2,8-diene-1,10-dione (H<sub>2</sub>CODIT)

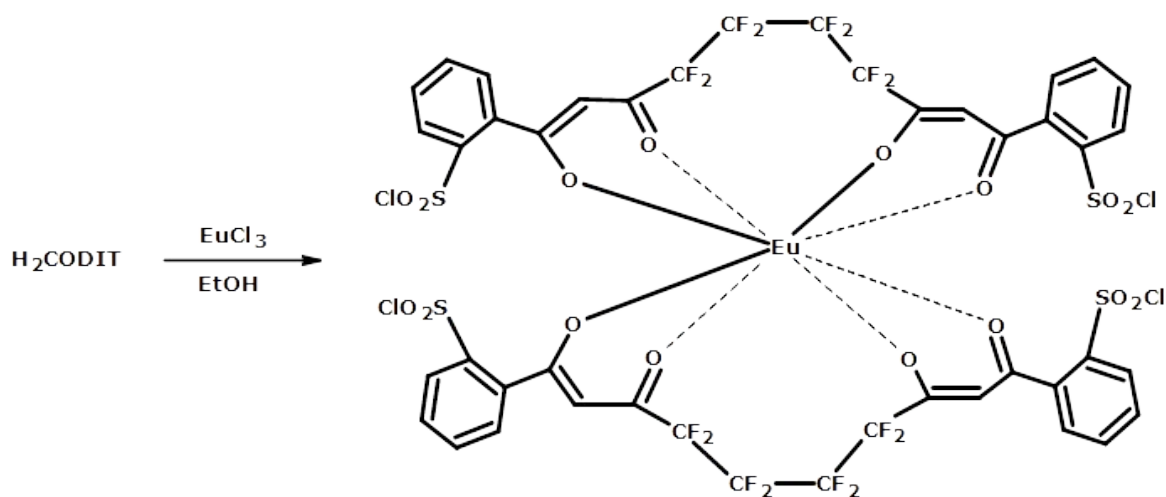
H<sub>2</sub>ODIT (0.98 g, 2 mmol) compound was added slowly in HSO<sub>3</sub>Cl (5 mL) that was placed in a balloon under refrigeration apparatus. The color of the solution turned to light green from yellow

followed by a dark green color when the whole material was introduced into the solution. The solution was stirred for 5 days at room temperature. To abandon the excess chlorosulfonic acid, solution was dripped onto ice-water. A yellow solid was formed in ice-water. The solution was then filtered, rinsed with cold water, and dried (Scheme 2). Yield: 0,99 g (72%).

**Scheme 2:** Synthesis of H<sub>2</sub>CODIT compound.**Synthesis of the Eu(III) complex**

Chlorosulfonated ligand (H<sub>2</sub>CODIT) (0.97 g, 1.4 mmol) was dissolved in ethanol. EuCl<sub>3</sub> (0.18 g, 0.70 mmol) was introduced in the stirring solution resulting that complexation occurs very rapidly.

Subsequent to abandoning of ethanol, the obtained solid material was rinsed with water and diethyl ether followed by drying (Scheme 3). Yield: 0.87 g (81%).

**Scheme 3.** Synthesis of Eu(III) complex.**RESULTS AND DISCUSSION****Spectroscopic studies**

While the structure of the synthesized H<sub>2</sub>ODIT compound was illuminated via <sup>1</sup>H-NMR and <sup>13</sup>C-NMR spectroscopy, mass spectrometry, X-ray single crystal diffraction and FT-IR techniques, <sup>1</sup>H-NMR and <sup>13</sup>C-NMR spectroscopy, mass spectrometry, and FT-IR were employed for the characterization of the H<sub>2</sub>CODIT ligand. Structural properties of the complex was determined by FT-IR, mass, luminescence spectroscopy, and UV-Visible techniques.

**FTIR spectra**

ATR technique was employed in obtaining the FTIR spectra of the ligands and complexes in the range

of 4000-550 cm<sup>-1</sup> and characteristic vibrations were determined.

FTIR spectrum of DEOFA is given in Figure 1a. The absorption band at 1778 cm<sup>-1</sup> results from C=O stretching (-CO-OR). Two other absorption bands at 1181 and 1142 cm<sup>-1</sup> were observed and these bands were assigned to -CF<sub>2</sub> group vibrations. The stretching vibration absorption band at 2994 cm<sup>-1</sup> could be assigned to the aliphatic C-H group.

In the FTIR spectrum of H<sub>2</sub>ODIT compound (Figure 1b), the peaks observed at 1595 and 1565 cm<sup>-1</sup> belong to tautomeric state keto and enol form carbonyls ν(C=O), respectively. ν(C=C) and ν(C-O) vibration bands of enol form correspond to 1466 and 1228 cm<sup>-1</sup>, respectively. Two sharp peaks at

1185 and 1156  $\text{cm}^{-1}$  belong to  $\nu(\text{CF}_2)$  vibrations. The intense peak observed at 751  $\text{cm}^{-1}$  results from the vibration that belongs to the monosubstituted benzene ring (25).

$\nu(\text{SO}_2\text{Cl})$  vibration peak is observed in FTIR spectrum of the  $\text{H}_2\text{CODIT}$  compound (Figure 1c) apart from  $\text{H}_2\text{ODIT}$  compound. Asymmetric vibration of sulfonyl chloride group gives a peak at 1343  $\text{cm}^{-1}$ . On the other hand, two peaks at 842 and 806  $\text{cm}^{-1}$  exhibit the disubstituted bonding to benzene ring (25).

FTIR spectrum of Eu(III) complex is given in Figure 1d. The peak observed at 1604  $\text{cm}^{-1}$  relates to the  $\nu(\text{C}=\text{O})$  vibration of keto form carbonyl that does not bond to the metal in  $\text{H}_2\text{CODIT}$  compound. On the other hand, peaks observed at 1564  $\text{cm}^{-1}$  and 1404  $\text{cm}^{-1}$  belong to  $\nu(\text{C}=\text{O})$  and  $\nu(\text{C}=\text{C})$  vibrations of enolic structure, respectively. Characteristic vibration bands shift to lower frequencies in  $\beta$ -diketone complex for the free ligand. This shift arises from the acidic proton loss of enolic structure from hydroxyl group and bonding of enolic hydroxyl oxygen and enolic carbonyl oxygen to the metal ion in the chelate mode (26). The peak that is coherent to the  $\nu(\text{CF}_2)$  vibrations in the ligand is at 1240  $\text{cm}^{-1}$  and  $\nu(\text{SO}_2\text{Cl})$  vibrations result in the peak at 1171  $\text{cm}^{-1}$  (25). The emergent absorption band observed at 510  $\text{cm}^{-1}$  in the complex suggests the existence of Eu-O coordination bond (27,28).

### Mass Spectra

Mass spectrometric results obtained from  $\text{H}_2\text{ODIT}$  molecule in chloroform solution are presented in Figure 2. Investigating the mass spectrometry of  $\text{H}_2\text{ODIT}$  ligand, addition of one hydrogen to this ligand results in a strong molecular ion peak at  $m/z$  495.08 that corresponds to the  $[\text{H}_2\text{ODIT} + \text{H}]^+$  ion. The peak observed at  $m/z$  517.07 corresponds to the  $[\text{H}_2\text{ODIT} + \text{Na}]^+$  ion whereas the peak at  $m/z$  518.07 belongs to the  $[\text{H}_2\text{ODIT} + \text{Na} + \text{H}]^+$  ion.

$\text{H}_2\text{ODIT}$  structure is supported by the mass spectrometric data.

The mass spectra of ligand  $\text{H}_2\text{CODIT}$  was recorded in chloroform solution is presented in Figure 3a. The mass spectra of  $\text{H}_2\text{CODIT}$  showed accurate molecular ion peak at  $m/z$  691.03, matched with the theoretical value. Two molecular ion peaks at 690.34 and 693.99 in the spectrum correspond to one hydrogen atom subtraction and two hydrogen atoms addition in the molecular ion peak, respectively.

Mass spectrum that belongs to Eu(III) complex in ethanol as solvent is given in Figure 3b. The product ion at  $m/z$  1532.78 in the spectrum was observed through the introduction of protonated ion were resulted from the molecular ion peak of the ligand. The structure shown in the spectrum, which has the most bonding abundance, has a peak at  $m/z$  1018.23.

### NMR Spectroscopy

$^1\text{H}$ -NMR and  $^{13}\text{C}$ -NMR spectra of the ligands were recorded in benzene- $d_6$  as solvent.  $^1\text{H}$  NMR and  $^{13}\text{C}$ -NMR of  $\text{H}_2\text{ODIT}$  are presented in Figures 4 and 5, respectively. Due to the symmetry of the compounds in the solution, half of the molecules were taken into consideration when the spectra were being acquired.

For  $^1\text{H}$  NMR spectrum of the  $\text{H}_2\text{ODIT}$  ligand, the triplet that belongs to the  $\text{H}_a$  proton bonded to aromatic ring was observed in the range of 6.92-6.89 ppm whereas the triplet that belongs to  $\text{H}_b$  protons in the range of 7.07-7.03 ppm. The doublet belonging to  $\text{H}_c$  protons were observed in the range of 7.45-7.43 ppm. The singlet at 6.42 ppm that belong to the active alpha proton ( $-\text{CH}$ ) neighboring the carbonyl group suggests the formation of the ( $-\text{HC}=\text{C}$ ) functional group, as a result of keto-enol tautomeric equilibrium in the structure, and a possible intramolecular hydrogen bond ( $\text{O}-\text{H}\cdots\text{O}$ ), (Figure 4a).



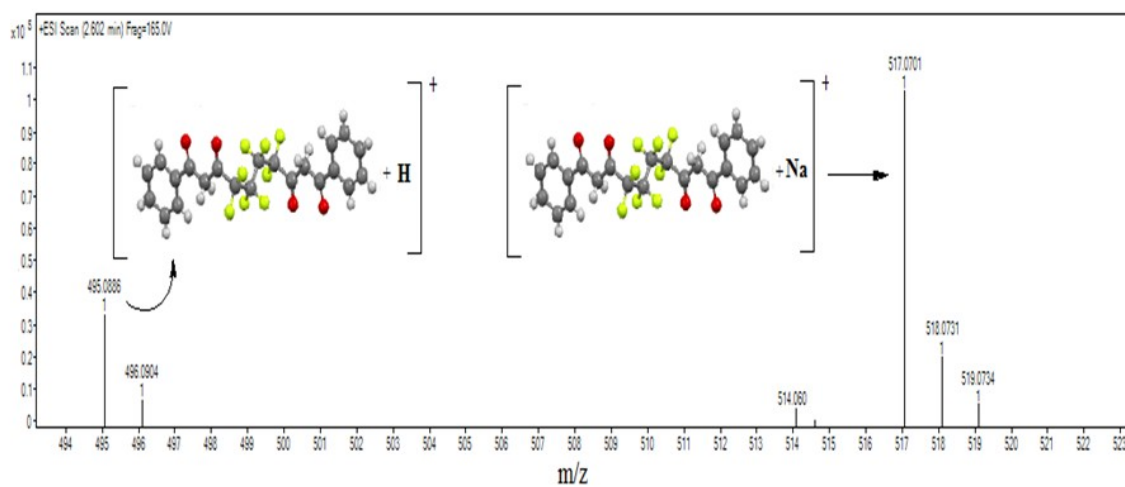
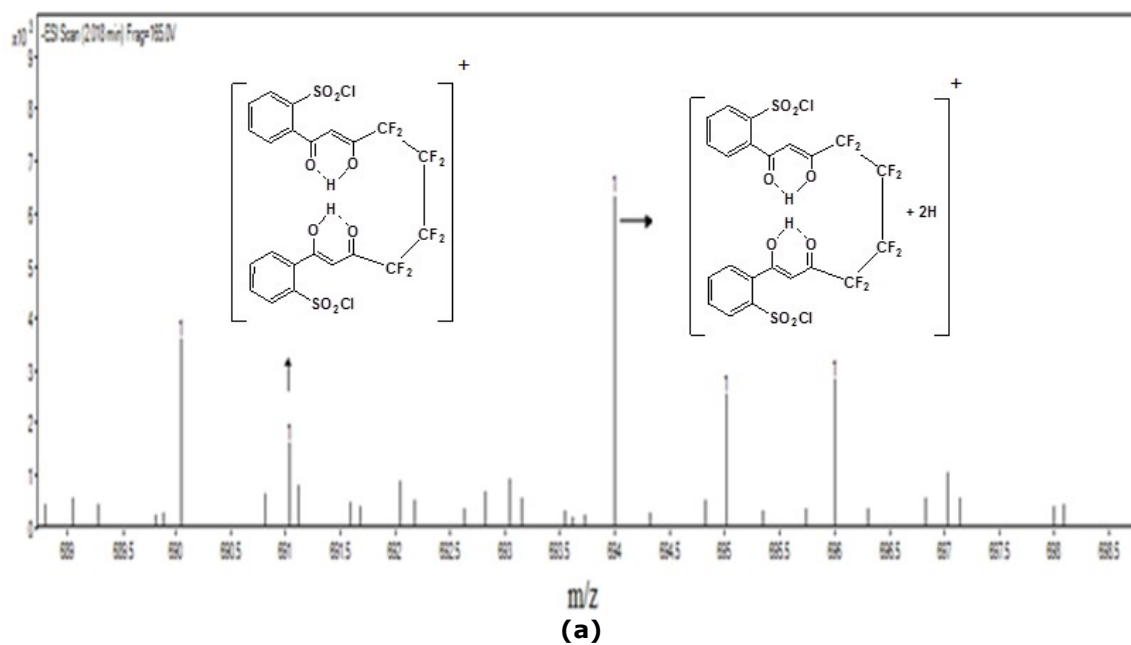
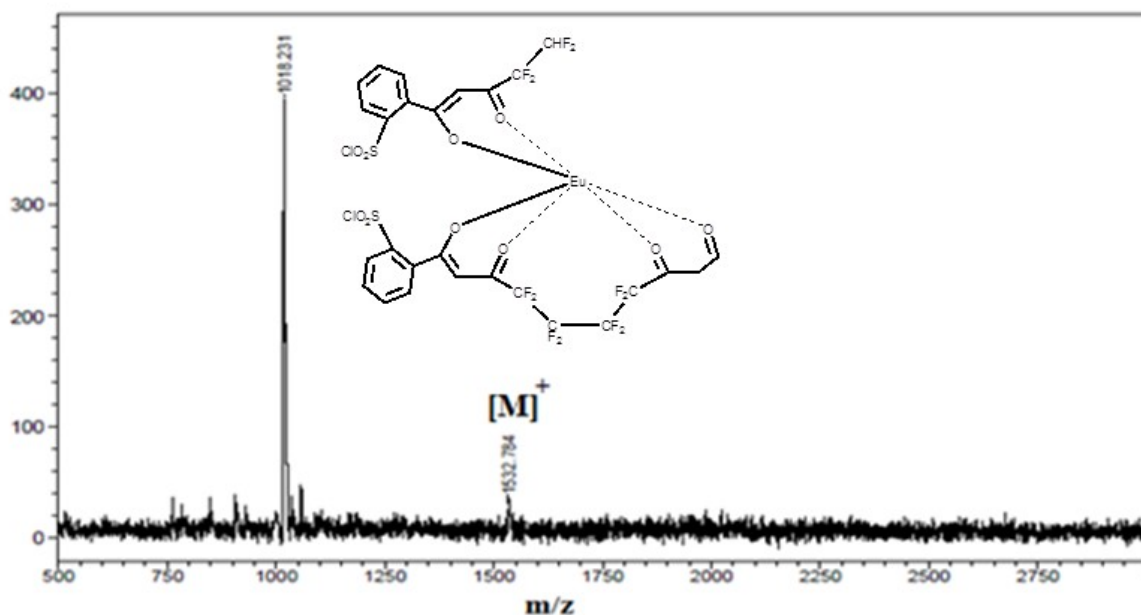


Figure 2: Mass spectrum of H<sub>2</sub>ODIT ligand.



(b)



(b)

**Figure 3:** Mass spectra of the compounds: (a) H<sub>2</sub>CODIT, (b) Eu(III) chelate.

When the <sup>1</sup>H NMR spectrum of H<sub>2</sub>CODIT ligand was investigated, H<sub>a</sub> and H<sub>b</sub> protons bonded to aromatic ring were observed in the range of 7.45-7.44 and 7.42-7.41 ppm as two doublets, respectively. On the other hand, H<sub>c</sub> proton was detected in the range of 7.02-7.06 ppm as triplet, and H<sub>d</sub> protons were detected in the range of 6.92-6.90 ppm also as triplet. Active alpha proton belonging to the H<sub>2</sub>CODIT ligand was established at 6.41 ppm as singlet (Figure 4b).

When the <sup>13</sup>C-NMR spectrum of the H<sub>2</sub>ODIT ligand was observed, the peaks that belong to aromatic ring carbons are surveyed in the range of 127.21-132.94 ppm. The carbon, which

belongs to (-HC=) group, exhibiting keto-enol tautomer balance in the structure resonated at 93.27 ppm. Keto and enol carbons are characterized at 184.94 and 179.09 ppm, respectively. The peaks at 109.95 and 126.97 ppm belong to the carbon of (-CF<sub>2</sub>) group (Figure 5a).

The carbons bonded to the aromatic ring in the <sup>13</sup>C-NMR spectrum of H<sub>2</sub>CODIT ligand resonated in the range of 126.97-132.95 ppm. Keto-enol tautomeric equilibrium exhibits a peak at 93.28 ppm, belonging to the (-HC=) group. Keto tautomer carbonyl carbon and enol carbon resonated at 184.94 ppm and 178.83 ppm, respectively (Figure 5b).

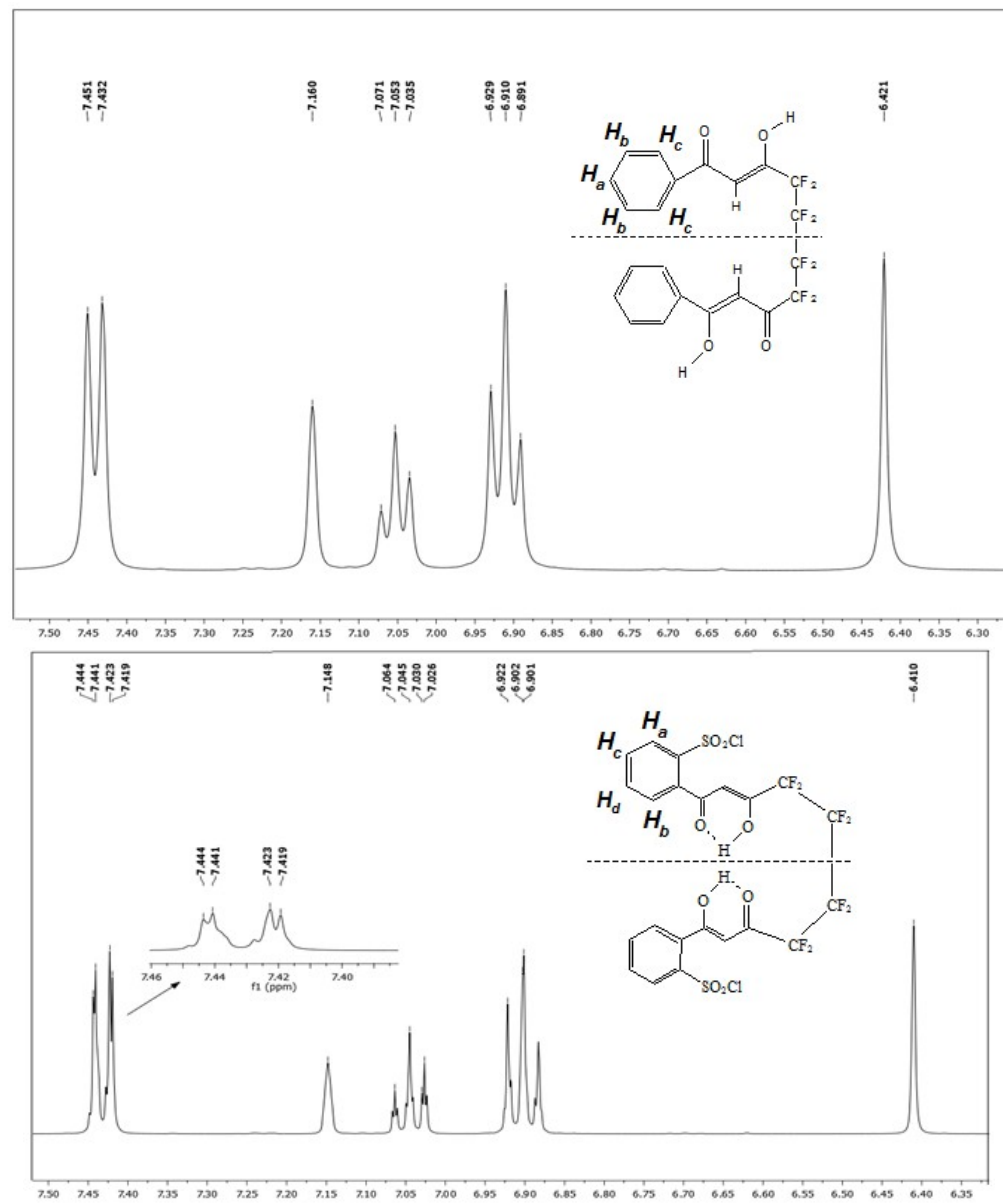


**Figure 4:** <sup>1</sup>H NMR spectra of the ligands: (top) H<sub>2</sub>ODIT, (bottom) H<sub>2</sub>CODIT.



### UV-Visible Spectra

UV-visible absorption spectrum of H<sub>2</sub>ODIT compound was observed in a 10<sup>-4</sup> M ethanolic solution (Figure 6a). The band at 265 nm visible light short wavelength belongs to aromatic ring  $\pi \rightarrow \pi^*$  transition. The second band observed at

318 nm wavelength belongs to  $n \rightarrow \pi^*$  electronic transition of keto and enol carbonyl group of the tautomer. Lastly, the band observed at 329 nm ( $\epsilon = 38660 \text{ L mol}^{-1} \text{ cm}^{-1}$ ) corresponds to  $\pi \rightarrow \pi^*$  transition of conjugation and delocalization of the ligand in the electronic system (29,30).

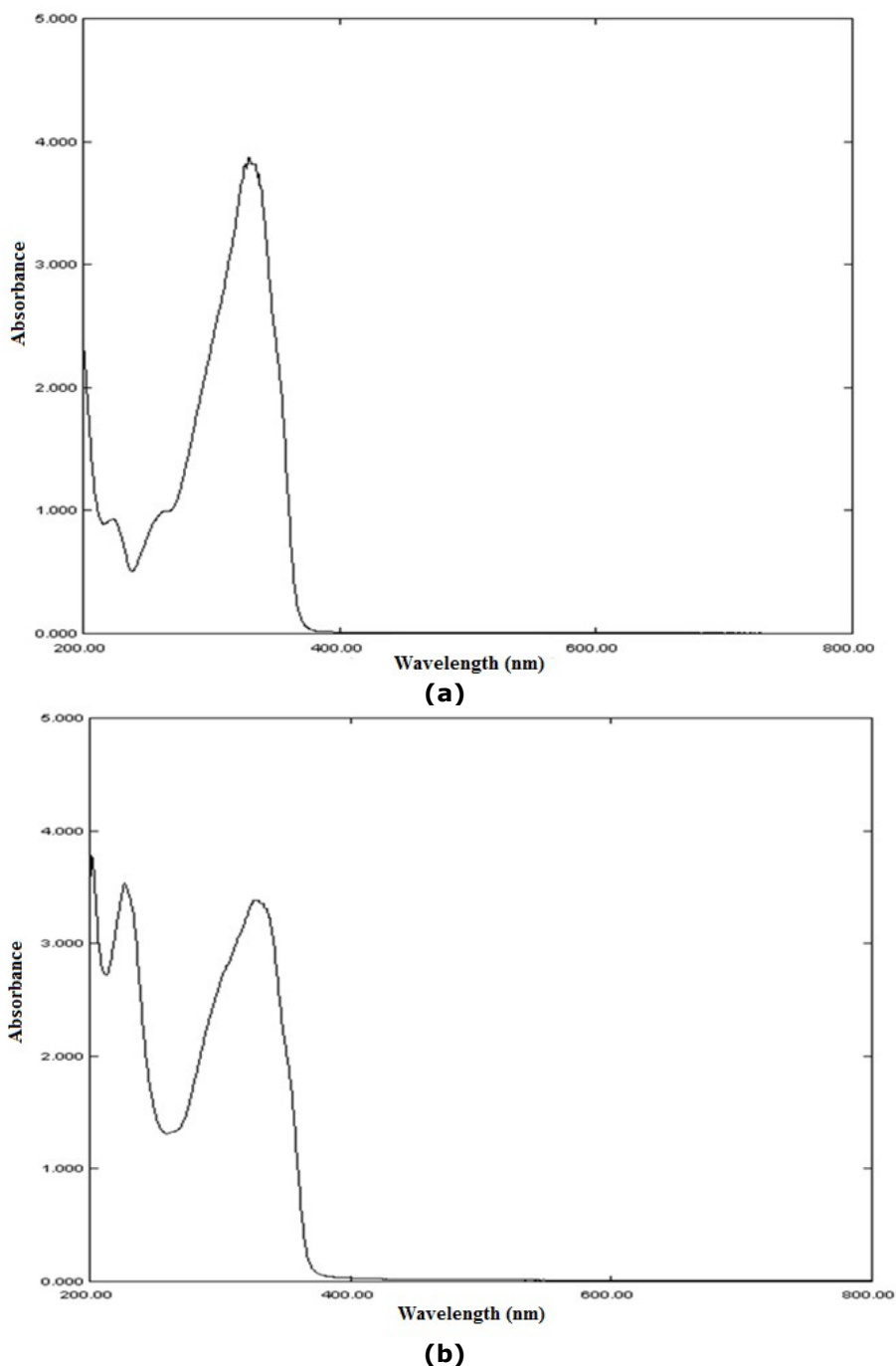


**Figure 6:** UV-visible spectra of (EtOH, 1.0×10<sup>-4</sup> M), (a) H<sub>2</sub>ODIT, (b) H<sub>2</sub>CODIT ligands.

H<sub>2</sub>CODIT compound was characterized in 10<sup>-4</sup> M ethanolic solution (Figure 6b). Three absorption bands at 268, 318 and 325 nm ( $\epsilon = 33850$

$\text{L mol}^{-1} \text{ cm}^{-1}$ ) resulting from  $\pi \rightarrow \pi^*$  and  $n \rightarrow \pi^*$  electronic transition were observed at UV-visible absorption spectrum.

UV-Visible spectrum of the complex in  $10^{-4}$  M aqueous solution has an  $\epsilon$  value of  $91600 \text{ L mol}^{-1} \text{ cm}^{-1}$  at 268 nm, which belongs to  $n \rightarrow \pi^*$  and  $n \rightarrow \pi^*$  transitions whereas the band at 321.5 nm

possessing a considerably high value of  $\epsilon = 28980 \text{ L mol}^{-1} \text{ cm}^{-1}$  belongs to the charge transfer to the metal from the ligand (Figure 7).

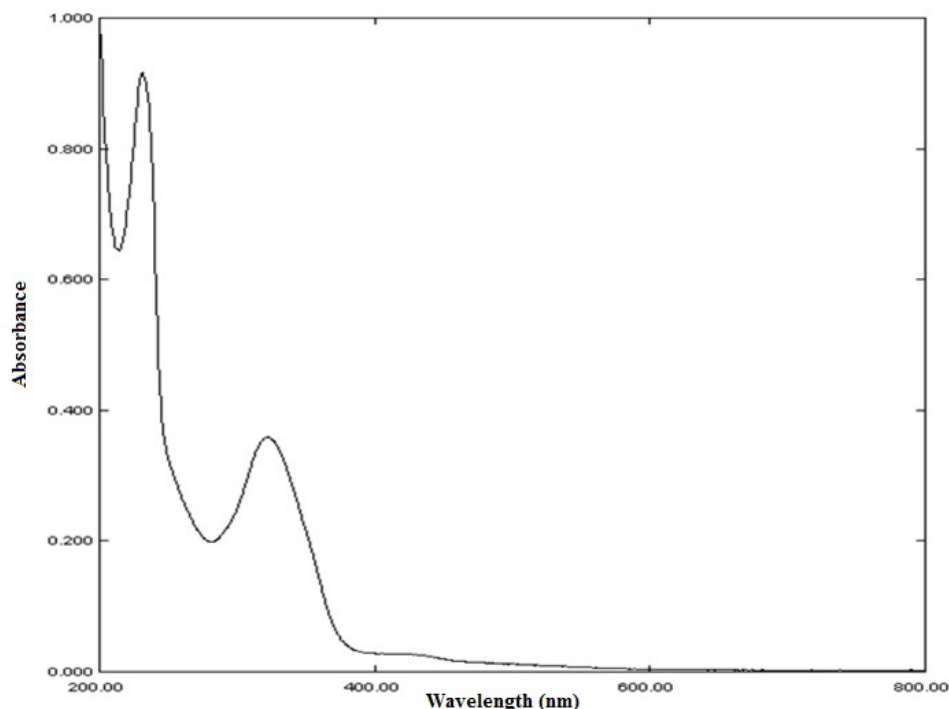


**Figure 7:** UV-Visible spectrum of the complex ( $\text{H}_2\text{O}$ ,  $1.0 \times 10^{-5} \text{ M}$ ).

### X-Ray Diffraction Analysis

Crystallographic data and refinement details of  $\text{H}_2\text{ODIT}$  are presented in Table 1; selected bond distances, angles and hydrogen bond geometries are listed in Table 2.  $\text{H}_2\text{ODIT}$  ligand belongs to the  $P2_1/c$  space group. As seen in Figure 8, a center of symmetry located on the mid position  $(1/2, 1/2, 0)$  of C-C [C11-C11<sup>i</sup>] bond exists. The C9-O2 bond is typical double

bond [ $1.245(2) \text{ \AA}$ ], while the C7-O1 bond is single bond [ $1.314(2) \text{ \AA}$ ]. The molecules of  $\text{H}_2\text{ODIT}$  are connected by  $n \cdots n$  interactions. The  $n \cdots n$  contact between the phenyl rings may stabilize the structure, with centroid-centroid distance of  $3.992(3) \text{ \AA}$ . As seen in Figure 9,  $n \cdots n$  interactions maintain the packing along [111] direction.

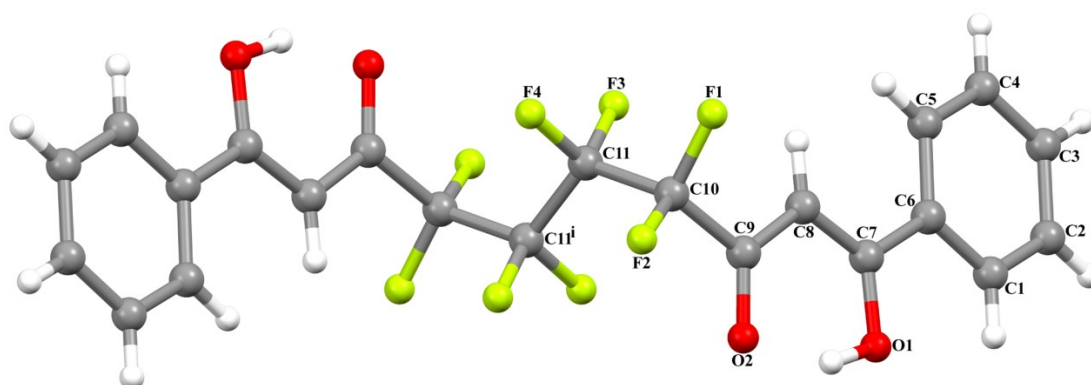


**Figure 8:** The molecular structure of H<sub>2</sub>ODIT showing the atom numbering scheme. [(i) -x+1, -y+1, -z].

**Table 1.** Crystal data and structure refinement parameters for H<sub>2</sub>ODIT.

Empirical formula	C <sub>22</sub> H <sub>14</sub> F <sub>8</sub> O <sub>4</sub>
Formula weight	494.33
Crystal system	Monoclinic
Space group	P2 <sub>1</sub> /c
<i>a</i> (Å)	8.168 (5)
<i>b</i> (Å)	11.385 (5)
<i>c</i> (Å)	11.425 (5)
$\beta$ (°)	104.042 (5)
<i>V</i> (Å <sup>3</sup> )	1030.7 (9)
<i>Z</i>	2
<i>D<sub>c</sub></i> (g cm <sup>-3</sup> )	1.593
$\mu$ (mm <sup>-1</sup> )	0.16
$\theta$ range (°)	3.1-28.3
Measured refls.	20454
Independent refls.	2552
<i>R</i> <sub>int</sub>	0.027
<i>S</i>	1.06
<i>R</i> <sub>1</sub> / <i>wR</i> <sub>2</sub>	0.043/0.114
$\Delta\rho_{\max}/\Delta\rho_{\min}$ (eÅ <sup>-3</sup> )	0.28/-0.18

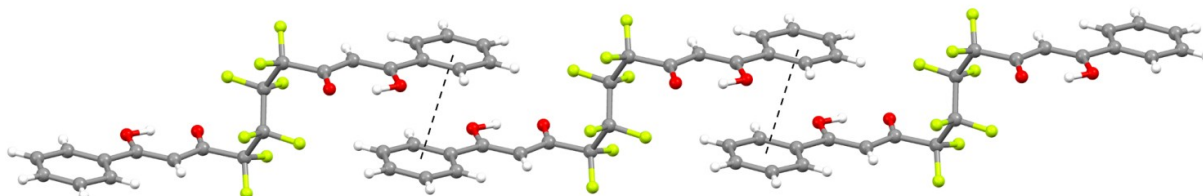


**Figure 9.** The n...n interactions in H<sub>2</sub>ODIT.

**Table 2:** Selected bond distances and angles, hydrogen bond parameters for H<sub>2</sub>ODIT (Å, °).

Bond distances (Å)				
C10-F1	1,3596 (19)	C10-F2	1.3478 (18)	
C11-F3	1,3475 (18)	C11-F4	1,3519 (18)	
C9-O2	1,245 (2)	C7-O1	1,314 (2)	
Bond angles (°)				
C7—O1—H1A	105.0 (19)	O2—C9—C8	125.77 (15)	
O1—C7—C8	120.67 (15)	O1—C7—C6	115.02 (14)	
F2—C10—F1	107.33 (13)	F3—C11—F4	107.70 (13)	
Hydrogen bond parameters (Å, °)				
D—H...A	D—H	H...A	D...A	D—H...A
O1—H1A...O2	0.95 (3)	1.67 (3)	2.552 (2)	153

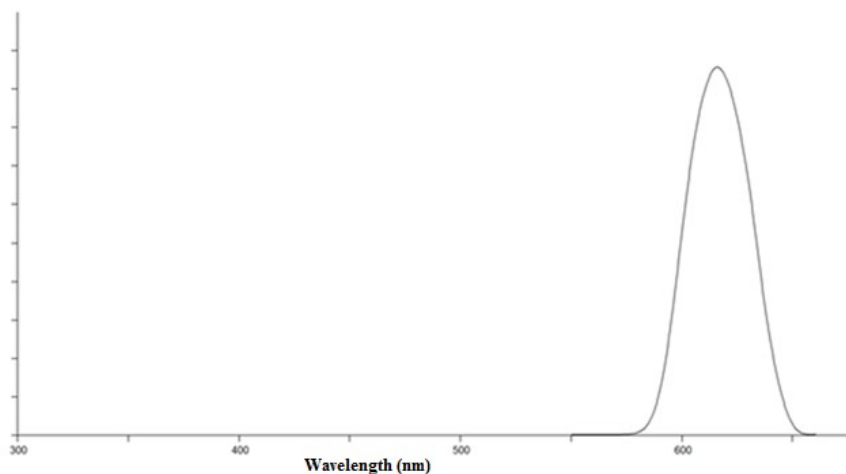
### Photoluminescent Properties of the Complex

Data acquisition in regards to excitation and radiation spectra for various modes such as luminescence, phosphorescence, and bioluminescence is available in modern photoluminescent spectroscopy. Acquiring the excitation spectrum, excitation chromator scans keeping a specific radiation wavelength constant while excitation wavelength is kept constant when radiation monochromator scans in obtaining a radiation spectrum.

Eu(III) radiation usually consists of stripes at red spectral region. This ion corresponds to

transitions from excited <sup>5</sup>D<sub>0</sub> of 4f configuration to <sup>7</sup>F<sub>j</sub> (j = 0 to 6) level. The most intense red emission line results from <sup>5</sup>D<sub>0</sub> → <sup>7</sup>F<sub>1</sub> magnetic dipole transitions, ranging between 610 and 630 nm wavelength.

Excitation and radiation spectra of the complex, in its solid state, was recorded at room temperature with a scan interval of λ<sub>ex</sub>:15 nm/λ<sub>em</sub>:15.0 nm. Eu(III) complex was excited by UV light at 306 nm. The emission band observed at 615 nm corresponds to <sup>5</sup>D<sub>0</sub> → <sup>7</sup>F<sub>2</sub> electrical dipole transition (Figure 10).

**Figure 10:** Emission spectrum of the complex (H<sub>2</sub>O, 1.0x10<sup>-5</sup> M).

### CONCLUSION

A novel β-diketone based ligand and its Eu(III) complex has been synthesized in pursuit of advancing a biolabel in techniques for labeling biomolecules in this study. H<sub>2</sub>ODIT and H<sub>2</sub>CODIT ligands were elucidated by using <sup>13</sup>C-NMR, <sup>1</sup>H-NMR, mass spectrometry and FTIR spectroscopic techniques. Furthermore, X-ray analysis of single crystal synthesis of H<sub>2</sub>ODIT

ligand was carried out. As a result, this ligand prefers enolic structure in the equilibrium of keto-enol tautomer. H<sub>2</sub>CODIT ligand was synthesized with EuCl<sub>3</sub> complex, and luminescent analysis was carried out in order to investigate the viability of its biolabeling.

**SUPPLEMENTARY DATA**

Crystallographic data for the structural analysis has been deposited with the Cambridge Crystallographic Data Centre, CCDC No. 1817092. Copies of this information may be obtained free of charge from the Director, CCDC, 12 Union Road, Cambridge CB2 1EZ, UK (fax: +44-1223-336033; e-mail: [deposit@ccdc.cam.ac.uk](mailto:deposit@ccdc.cam.ac.uk) or [www: http://www.ccdc.cam.ac.uk](http://www.ccdc.cam.ac.uk)).

**ACKNOWLEDGMENTS**

This study has been supported by TÜBİTAK BİDEB 2210-C Master's Scholarship Program for Priority Fields.

**REFERENCES**

- Weissman SI. Intramolecular Energy Transfer The Fluorescence of Complexes of Europium. *The Journal of Chemical Physics*. 1942;10(4):214-7. [<DOI>](#)
- Richardson FS. Terbium (III) and europium (III) ions as luminescent probes and stains for biomolecular systems. *Chemical Reviews*. 1982;82(5):541-52.
- Hemmilä I. Fluoroimmunoassays and immunofluorometric assays. *Clinical Chemistry*. 1985;31(3):359-70. [<DOI>](#)
- Gudgin Dickson EF, Pollak A, Diamandis EP. Ultrasensitive bioanalytical assays using time-resolved fluorescence detection. *Pharmacology & Therapeutics*. 1995;66(2):207-35. [<DOI>](#)
- Gudgin Dickson EF, Pollak A, Diamandis EP. Time-resolved detection of lanthanide luminescence for ultrasensitive bioanalytical assays. *Journal of Photochemistry and Photobiology B: Biology*. 1995;27(1):3-19. [<DOI>](#)
- Hemmilä I, Laitala V. Progress in Lanthanides as Luminescent Probes. *J Fluoresc*. 2005;15(4):529-42. [<DOI>](#)
- Armelaio L, Quici S, Barigelletti F, Accorsi G, Bottaro G, Cavazzini M, et al. Design of luminescent lanthanide complexes: From molecules to highly efficient photo-emitting materials. *Coordination Chemistry Reviews*. 2010;254(5-6):487-505. [<DOI>](#)
- Melby L, Rose N, Abramson E, Caris J. Synthesis and fluorescence of some trivalent lanthanide complexes. *Journal of the American Chemical Society*. 1964;86(23):5117-25.
- Choppin GR, Peterman DR. Applications of lanthanide luminescence spectroscopy to solution studies of coordination chemistry. *Coordination Chemistry Reviews*. 1998;174(1):283-99. [<DOI>](#)
- Andres J, Chauvin A. Luminescence. In: Atwood D, editor. *The Rare Earth Elements: Fundamentals and Applications Lanthanides: Luminescence Applications*. John Wiley and Sons; 2012. p. 135-52. ISBN: 978-1-118-63263-5.
- Binnemans K. Rare-Earth Beta-Diketonates. In: Gschneidner KA, editor. *Handbook on the physics and chemistry of rare earths*. 1. ed. Amsterdam: Elsevier North Holland; 2005. p. 107-272. ISBN: 978-0-444-52028-9.
- Yuan J, Matsumoto K. Synthesis of a New Tetradentate .BETA.-Diketonate-Europium Chelate That Can Be Covalently Bound to Proteins in Time-Resolved Fluorometry. *Anal Sci*. 1996;12(5):695-9. [<DOI>](#)
- Hagan AK, Zuchner T. Lanthanide-based time-resolved luminescence immunoassays. *Anal Bioanal Chem*. 2011;400(9):2847-64. [<DOI>](#)
- Räsänen M, Takalo H, Rosenberg J, Mäkelä J, Haapakka K, Kankare J. Study on photophysical properties of Eu(III) complexes with aromatic  $\beta$ -diketones - Role of charge transfer states in the energy migration. *Journal of Luminescence*. 2014;146:211-7. [<DOI>](#)
- Zhang L, Wang Y, Ye Z, Jin D, Yuan J. New Class of Tetradentate  $\beta$ -Diketonate-Europium Complexes That Can Be Covalently Bound to Proteins for Time-Gated Fluorometric Application. *Bioconjugate Chem*. 2012;23(6):1244-51. [<DOI>](#)
- Siitari H, Hemmilä I, Soini E, Lövgren T, Koistinen V. Detection of hepatitis B surface antigen using time-resolved fluoroimmunoassay. *Nature*. 1983;301(5897):258-60. [<DOI>](#)
- Darwish IA. Immunoassay Methods and their Applications in Pharmaceutical Analysis: Basic Methodology and Recent Advances. *Int J Biomed Sci*. 2006;2(3):217-35. [<URL>](#)

18. Yuan J, Matsumoto K. Synthesis of a new tetradentate  $\beta$ -diketonate-europium chelate and its application for time-resolved fluorimetry of albumin. *Journal of Pharmaceutical and Biomedical Analysis*. 1997;15(9-10):1397-403. [<DOI>](#)
19. Wang G, Yuan J, Matsumoto K, Hu Z. Homogeneous Time-Resolved Fluorescence DNA Hybridization Assay by DNA-Mediated Formation of an EDTA-Eu(III)- $\beta$ -Diketonate Ternary Complex. *Analytical Biochemistry*. 2001;299(2):169-72. [<DOI>](#)
20. Sheldrick GM. A short history of SHELX. *Acta Crystallogr A Found Crystallogr*. 2008;64(1):112-22. [<DOI>](#)
21. Sheldrick GM. Crystal structure refinement with SHELXL. *Acta Crystallogr C Struct Chem*. 2015;71(1):3-8. [<DOI>](#)
22. Anonymous. APEX2. Bruker AXS, Inc., Madison, Wisconsin, USA; 2013.
23. Macrae CF, Bruno IJ, Chisholm JA, Edgington PR, McCabe P, Pidcock E, et al. Mercury CSD 2.0 - new features for the visualization and investigation of crystal structures. *J Appl Crystallogr*. 2008;41(2):466-70. [<DOI>](#)
24. Farrugia LJ. WinGX and ORTEP for Windows: an update. *J Appl Crystallogr*. 2012;45(4):849-54. [<DOI>](#)
25. Erdik E. *Organik kimyada spektroskopik yöntemler*. Ankara: Gazi Büro Kitabevi; 2008. ISBN: 978-975-7373-04-9.
26. Bhise N, Al-Horaibi S, Gaikwad S, Rajbhoj A. Synthesis, Spectral Characterization, Antimicrobial, Anti-Inflammatory, Antioxidant, And Cyclic Voltammetric Studies Of  $\beta$ -Diketone And Its Metal Complexes. *Rasayan J Chem*. 2019;12(1):101-13. [<DOI>](#)
27. Yang C, Xu J, Ma J, Zhu D, Zhang Y, Liang L, et al. An efficient long fluorescence lifetime polymer-based sensor based on europium complex as chromophore for the specific detection of F<sup>-</sup>, CH<sub>3</sub>COO<sup>-</sup>, and H<sub>2</sub>PO<sub>4</sub><sup>-</sup>. *Polym Chem*. 2012;3(9):2640. [<DOI>](#)
28. Nakamoto K. *Infrared and Raman spectra of inorganic and coordination compounds*. 6th ed. Hoboken, N.J: Wiley; 2009. 23 p. ISBN: 978-0-471-74493-1.
29. Charette J, Neiryck G, Teyssié Ph. Structural dependence of absorption spectra of  $\beta$ -diketonate chelates. II. Ultraviolet 1. *J Phys Chem*. 1961;65(5):735-9. [<DOI>](#)
30. Sultan R, Gadamsetti K, Swavey S. Synthesis, electrochemistry and spectroscopy of lanthanide(III) homodinuclear complexes bridged by polyazine ligands. *Inorganica Chimica Acta*. 2006;359(4):1233-8. [<DOI>](#)



## Synthesis of Nitrogen- and Oxygen-Containing Heterocyclic Compounds Using Nanocatalyst: A Review

Atish Roy , Anil Kumar Bahe , Aayushi Chanderiya , Hemlata Dangi ,  
Pratibha Mishra , Arunesh K. Mishra , and Ratnesh Das\* 

Department of Chemistry, Dr. Hari Singh Gour University, Sagar, M.P. India.

**Abstract:** In organic synthesis, nanocatalysts play a significant role. Nitrogen- and oxygen-containing based heterocyclic atoms are the substantial and essential primary units available in different organically dynamic characteristic items, industrial and pharmaceutical, and agrochemicals. Nanoparticles (NPs) or nanoclusters (NCs) have high synergist action; the maintainable and financial advantages of the convention are the exceptional returns of items, short response time, primary stir-up method, and utilization of a non-poisonous and reusable impetus the response. The current review looks at the various forms of nanocatalysts used to form heterocyclic compound synthesis and some other important ring functionalization.

**Keywords:** Heterocyclic atoms, nanoclusters, pharmaceutical, agrochemicals, nanoparticle (NPs), green chemistry.

**Submitted:** March 27, 2021. **Accepted:** July 06, 2021.

**Cite this:** Roy A, Bahe A, Chanderiya A, Dangi H, Mishra P, Mishra A, et al. Synthesis of Nitrogen- and Oxygen-Containing Heterocyclic Compounds Using Nanocatalyst: A Review. JOTCSA. 2021;8(3):821-32.

**DOI:** <https://doi.org/10.18596/jotcsa.904246>.

**\*Corresponding author. E-mail:** [ratneshdas1@gmail.com](mailto:ratneshdas1@gmail.com).

### INTRODUCTION

The carbon-nitrogen bond arrangement is a significant manufactured advance in natural combination for creating N-heterocyclic particles, which assume a real job in the union of modern polymers, agrochemical, besides organically dynamic drug products (1). The 2,3-benzopyrrole core is one of the most seriously considered primary examples by manufactured just as organic scientific experts (2) because of the natural organic exercises. Nanoparticles (NPs) are great impetuses for the natural union, and however, during the movement of a synthetic response, they show the extraordinary inclination to total and misshape. Thus, they need help to achieve their synthetic and actual security as catalysts. Nitrogen-containing heterocyclic compounds are vital applications because of their abundance in nature. Several nitrogen-containing heterocyclic

compounds exhibit many biological activities like antibacterial, antiarthritis, antiasthmatic, and many other types of biological activities (3-5).

Nitrogen-containing heterocycles also show their essential role as ligands, explosives, stabilizers in photography (6-8). The synthesis of such compounds by eco-friendly methods is of great interest to the research community. Oxygen-containing heterocycles have displayed a very wide range of biological and therapeutic properties (9). This chromene moiety, which belongs to a naturally occurring oxygen-heterocyclic class, shows a wide range of biological activity. These compounds can be used as antioxidant agents, antifungal agents, anticancer agents etc. (10).

Heterocyclic compounds are structural units present in various biologically active natural products and pharmaceuticals (11). However, due

to a lack of substrate, the extent and generality of a particular 2,3-benzopyrrole's synthesis have sometimes been reduced. As a result, developing reliable and cost-effective methods for synthesizing 2,3-benzopyrroles from readily available starting materials is still challenging (12). One of the most pressing issues and problems in recent decades has been the use of nanoscience in the advancement of ecology, drug, and most notably, catalysts. Nanoscience and green chemistry have unique compatibility and accuracy due to the efficient implementation of

nanotechnology in manufacturing greener goods, making nanoscience a savior in environmental and energy challenges (13). Due to their high reactivity, sustainability, ease of recapture, and opportunity to recycle, metallic nanoparticles have recently been widely used as alternative catalysts in organic synthesis. Metal nanoparticle catalyzed reactions have many advantages over traditional metal-catalyzed reactions, including low catalyst loading, low cost, strong atom efficiency, higher yields, shorter reaction time, and the opportunity to recycle catalysts (14).

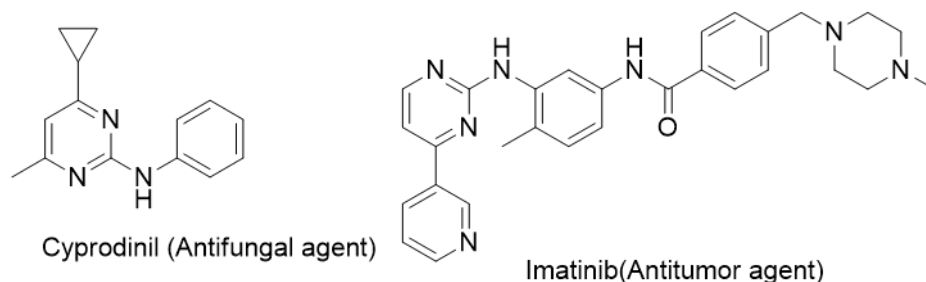
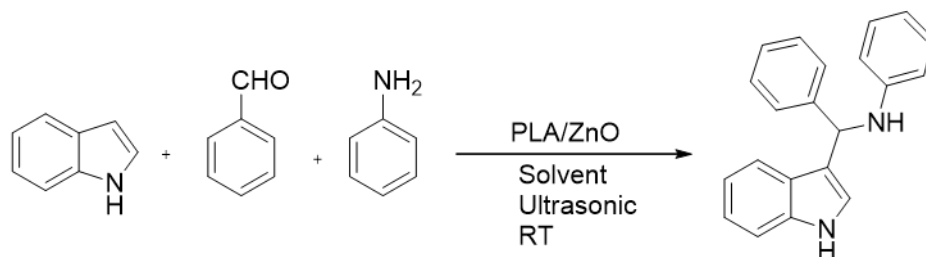


**Figure 1:** The structures of cyprodinil and imatinib.

### Formation of 3-Substituted 2,3-Benzopyrrole in Water Using Polymer-Attached ZnO NPs as a Eco-Friendly Catalyst

3-Amino alkylated 2,3-benzopyrroles were synthesized by Tauhid Shaikh et al. in the presence of ZnO nanoparticles. 2,3-Benzopyrroles react with benzaldehyde and aniline to form 3-amino alkylated 2,3-benzopyrroles. Polylactic acid (PLA) includes a hydrophobic region around ZnO, which is naturally hydrophilic. PLA can absorb organic molecules, as shown by its use in the drug

delivery framework; thus, this nanocomposite can serve as an amphiphilic catalyst. By absorbing substrate molecules, PLA may improve the accessibility of the catalyst (ZnO) (15). To investigate the effect of solvent on reaction results, a model reaction was carried out in various solvents, such as N,N-dimethylformamide (DMF), p-dioxane, dimethyl sulfoxide ((CH<sub>3</sub>)<sub>2</sub>SO), acetonitrile, oxolane, acetone, and H<sub>2</sub>O. The best result is found in the presence of water.

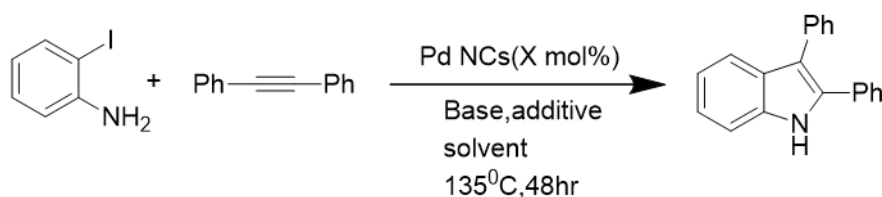


**Scheme 1:** Synthesis of 3-amino-alkylated 2,3-benzopyrrole. Adapted from (15).

### Larock's 2,3-Benzopyrrole Synthesis Using N, N-Dimethylformamide-Stabilized Pd Nanocluster

In the presence of a Pd nanocluster, Kaito Onishi et al. synthesized 2-iodoanilines with alkynes to produce 2,3-disubstituted 2,3-benzopyrroles. This reaction took place in the absence of ligands and with low catalyst loadings. The most effective solvent was DMF, which created an isolated yield of 88%. Then there were mixed solvents like DMF/H<sub>2</sub>O (1:1) and N-methyl pyrrolidone

(NMP)/H<sub>2</sub>O (1:1). A trace amount of product was obtained when DMF/H<sub>2</sub>O (1:1) was used. When NMP/H<sub>2</sub>O (1:1) was used, the product was obtained in 28% yield, and various additives are used, but NaCl was the best additive; product yield was 69 percent without the addition of NaCl. As reported in the palladium complex-catalyzed Larock 2,3-benzopyrrole synthesis, salts such as NaCl increased the catalytic activity by synthesizing a chloride-ligated zerovalent palladium species (16).

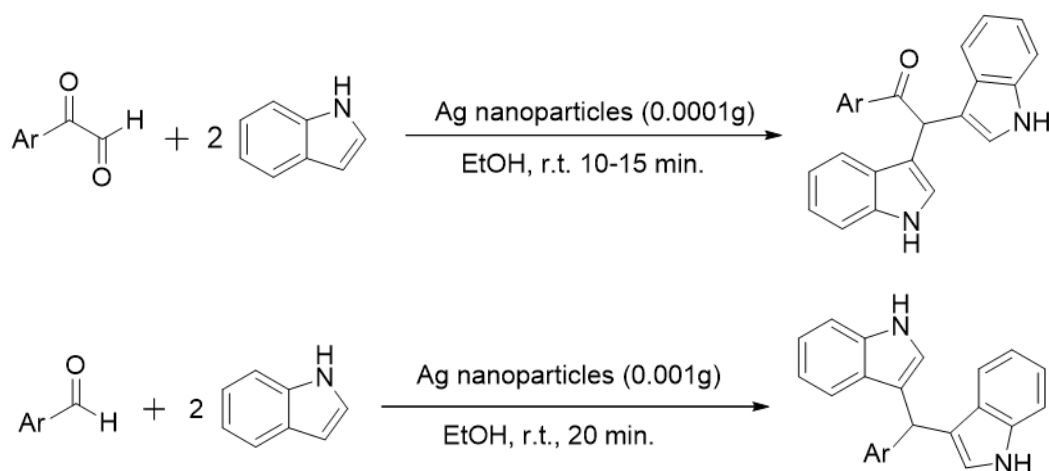


**Scheme 2:** Synthesis of 2,3-disubstituted 2,3-benzopyrrole. Adapted from (16).

### Synthesis of Bis(indolyl)methanes Using an Efficient and Versatile Reagent, Ag NPs

Aromatic aldehyde and 2,3-benzopyrrole react to form bis(indolyl)methanes in the presence of Ag nanoparticles. This is an outline of a modest, mild, and effective method to the fusion of bis(indolyl) methane and its derivatives because the most active cruciferous compounds for promoting healthy estrogen metabolism and inducing apoptosis in human cancer cells are

bis(indolyl)methanes, at 25 °C, an optimized number of nano-Ag arranged the reaction of benzaldehyde and 2,3-benzopyrrole. When Ag nanoparticles take less than 0.001 mol, the yield of the product also decreases. Several Lewis acids catalyzed a mixture of products in EtOH at 25 °C, but the best synthesis formed is in the presence of Ag NPs. Some solvents yielded like CHCl<sub>3</sub> (55%), CH<sub>3</sub>CN (42%), H<sub>2</sub>O (20%), but EtOH gave 94% yield (17).

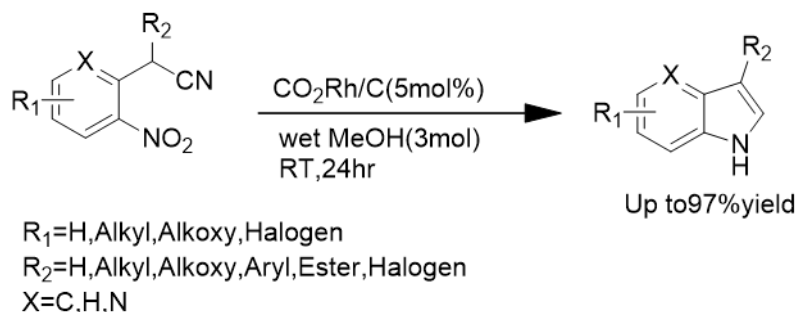


**Scheme 3:** Synthesis of bis(indolyl)methanes. Adapted from (17).

### Synthesis of 2,3-Benzopyrrole of 2-Nitrobenzyl Cyanide in the Presence of Co-Rh Heterobimetallic NPs

Reductive cyclization of two 2-Nitrobenzyl Cyanide in the presence of heterobimetallic Cobalt-Rhodium

NPs yields 2,3-Benzopyrrole (14). They have higher catalytic efficiency compared to monometallic NPs. Heterobimetallic NPs have recently been concerned with much consideration as catalysts (18).



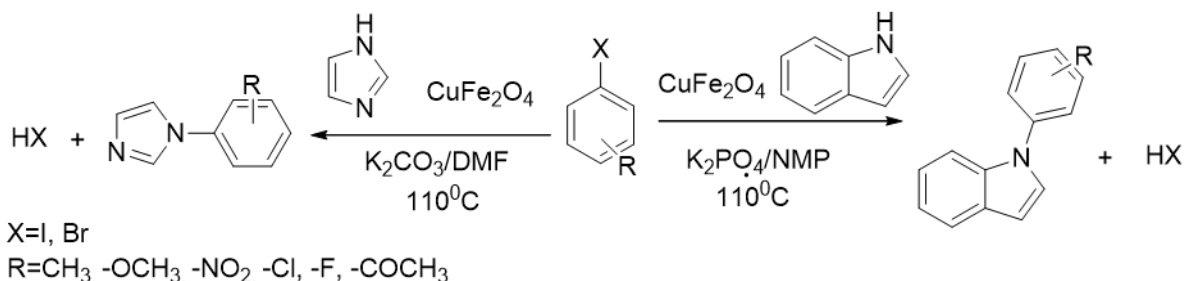
**Scheme 4:** Synthesis of 2,3-benzopyrrole. Adapted from (18).

### Synthesis of N-arylation of 2,3-Benzopyrrole and Imidazole with Aryl Halide in the Presence of CuFe<sub>2</sub>O<sub>4</sub> Magnetic NPs

2,3-Benzopyrrole and imidazole N-arylation reactions with various aryl halides in the presence of CuFe<sub>2</sub>O<sub>4</sub> nanoparticles. In the below ligand-free

circumstances, the reaction yields well to excellent with  $\text{CuFe}_2\text{O}_4$  nanoparticles as the catalyst. Furthermore,  $\text{CuFe}_2\text{O}_4$  NPs could be recycled six times, lacking down their operation (19). Optimization of reaction taken in different solvents

and bases such as 1. NMP 97%, 2. DMF 82%, 3.  $\text{CH}_3\text{CN}$  22%, 4.  $\text{CH}_2\text{Cl}_2$  26%, 5. Toluene 15%, and 6.  $\text{K}_3\text{PO}_4$  97% 7.  $\text{Et}_3\text{N}$  35%, 8.  $\text{K}_2\text{CO}_3$  71%, 9.  $\text{KOH}$  64%, 10.  $\text{Na}_3\text{PO}_4 \cdot 12\text{H}_2\text{O}$  58% 11.  $\text{Cs}_2\text{CO}_3$  78%.

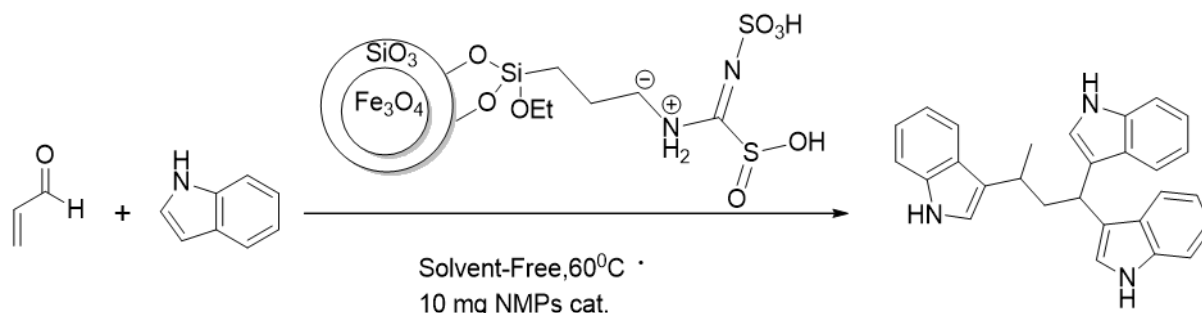


**Scheme 5:** Synthesis of N-Arylindole and N-Arylimidazole. Adapted from (19).

### Synthesis of 1,1,3-tris(1H-indol-3-yl) Alkanes in Attendance of Silica-Coated Magnetic Nanoparticle

Proposed a straightforward and worthy system for the amalgamation of 1,1,3-tris(1H-indol-3-yl) alkanes catalyzed with MNPs-TUD-SO<sub>3</sub>H. As per the response pathway to start with, the carbonyl gathering of a  $\beta$ -unsaturated compound will be initiated within sight of MNPs-TUD-SO<sub>3</sub>H impetus and shaped the dynamic halfway. 2,3-Benzopyrrole effectively assaulted to this insecure halfway, and the item relating gives due to the 1,4- and 1,2-increments. Subsequent stage followed by

initiation of existing moderate through attractive nanoparticles MNPs-TUD-SO<sub>3</sub>H and a nucleophilic response of the third atom of 2,3-benzopyrrole with this halfway that in the end this synergistic cycle finished by eliminating a water atom and the ideal item 1,1,3-tris(1H-indol-3-yl) alkane was created at present of the novel nanostructured impetus. The authors related that the reaction between crotonaldehyde and 2,3-benzopyrrole was considered under the same reaction condition in the presence of 10 mol% thiourea dioxide as a catalyst. The corresponding 1,1,3-tri(1H-indol-3-yl) alkane was synthesized in 40% yield (20).

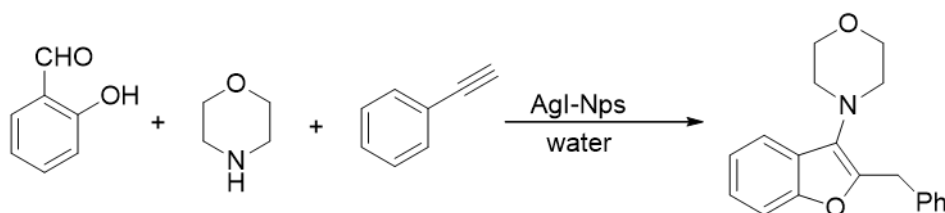


**Scheme 6:** Synthesis of 1,1,3-tris(1H-indol-3-yl)alkanes. Adapted from (20).

### One-Pot Synthesis of Benzofurans under Aqueous Conditions Using Silver Iodide NPs

In the existence of a silver iodide nanocatalyst, the reaction of salicylaldehyde, morpholine, and phenylacetylene produce 2,3-disubstituted benzofuran in aqueous media. First, in this condensation reaction, reagents, such as copper iodide, copper chloride, silver bromide, and silver

iodide, were used to test the efficiency of the catalytic activity. We discovered that silver iodide is the best catalyst for this reaction, so we ran the model reaction with silver iodide nanoparticles. Furthermore, compared to bulk AgI, silver iodide NPs produced outstanding yields in quicker response times (21).

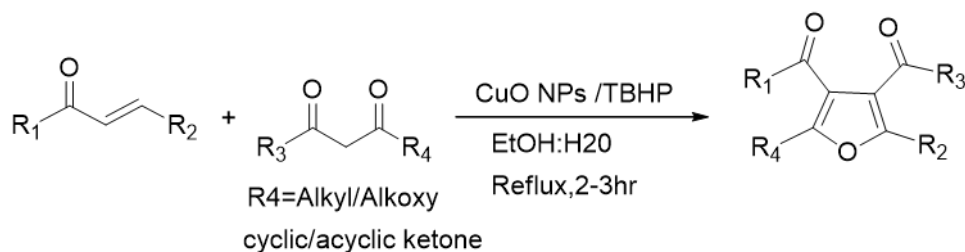


**Scheme 7:** Synthesis of 2,3-disubstituted benzofuran. Adapted from (21).

### Synthesis of Poly-Substituted Furans Catalyzed CuO NPs in an Aqueous Medium

MnO<sub>2</sub> interceded ZnCl<sub>2</sub> and helped blend of 3,4-dicarbonylfuran subsidiaries in corrosive acidic medium, according to Zhuo et al. The Zhuo technique had a few limitations, such as the use of an abundance measure of ZnCl<sub>2</sub>/MnO<sub>2</sub> as an impetus that was not reusable, unforgiving reaction conditions (refluxing in a corrosive acidic medium at 130 °C), and a longer response time (24 h). It lowered segregated yields of items (15-

80%). The addition of 2-methylpropane-2-peroxol as an oxidizing agent (1 eq.) increases the yield and decreases the reaction time significantly (3 h). After 12 hours of refluxing a mixture of A (1 millimole), B (5 mmol), and CuONPs (10 milligrams) in the presence of CuO nanoparticles (10 milligrams), 40% of the required furan derivative was obtained. The addition of 2-methylpropane-2-peroxol as an oxidizing agent (1 eq.) increases product amount and decreases response time significantly (3 h) (22).

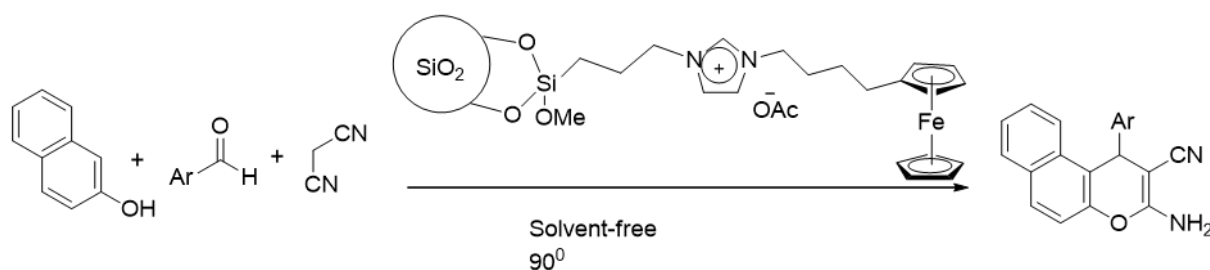


**Scheme 8:** Synthesis of 3,4-dicarbonylfuran. Adapted from (22).

### Synthesis of Naphthopyran Derivatives, Using Novel Ferrocene-Based Ionic Liquid Supported on Silica Nanoparticles

The model reactions were 2-naphthol, benzaldehyde, and malononitrile. For this reason, the efficiency of (SiO<sub>2</sub>@Im-Fc [OAc]) was investigated employing a change of solvents, temperatures, and quantities of synthesized nanocatalyst to find a more efficient, convenient, and rapid method for the synthesis of naphthopyran derivatives. The findings are summarized in this report. For the model reaction

at room temperature in the presence of 30 mg nanocatalyst, a variety of traditional organic solvents such as EtOH, CH<sub>2</sub>Cl<sub>2</sub>, CHCl<sub>3</sub>, CH<sub>3</sub>CN, and H<sub>2</sub>O, as well as solvent-free conditions, were screened. At ordinary temperatures, various traditional solvents provided low to moderate yields. Surprisingly, the best results were obtained without the use of any solvents. The model reaction was then performed in varying amounts of nanocatalyst (5 to 50 mg) and at different temperatures (23).

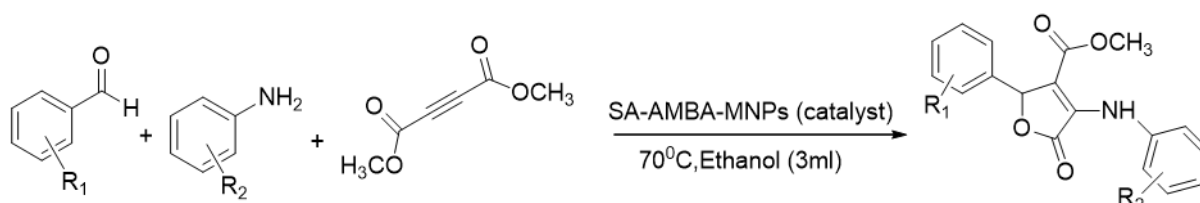


**Scheme 9:** Synthesis of naphthopyran derivatives. Adapted from (23).

### Synthesis of 3,4,5-Trisubstituted Furan-2(5H)-one Derivative Using 4-carboxybenzylsulfamic Acid Supported on Magnetic NPs

In the presence of magnetic NPs aided by 4-carboxybenzylsulfamic acid, the combination of trisubstituted furan derivatives from aryl aldehydes, various anilines, and dimethyl acetylene dicarboxylate. Designing heterogeneous

hybrid catalysts to synthesize furans, such as 4-carboxybenzylsulfamic acid-functionalized  $\text{Fe}_3\text{O}_4$  nanoparticles (SA-AMBA-MNPs) as a new green and magnetically simple distinguishable catalyst (24). The reaction was carried out using various solvents and amounts of catalyst, with the best results obtained using ethanol catalyst at 20 mg at 70 °C for two hours and a yield of 92%.

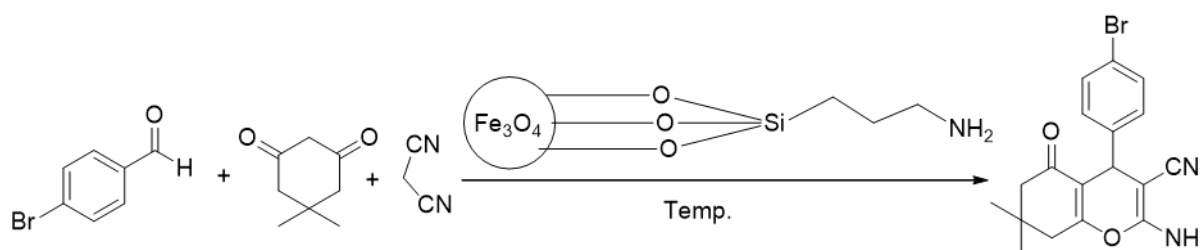


**Scheme 10:** Synthesis of 3,4,5-trisubstituted furan-2(5H)-one. Adapted from (24).

### Amine-Functionalized $\text{SiO}_2@ \text{Fe}_3\text{O}_4$ NPs are Used in a One-Pot Multi-Component Synthesis of Bioactive 2-Amino-4H-Benzo[b]Pyrans

Formation of 2-amino-4-(4-bromophenyl)-7,7-dimethyl-5-oxo-5,6,7,8-tetrahydro-4H-chromene-3-carbonitrile required the use of amine-

functionalized  $\text{SiO}_2@ \text{Fe}_3\text{O}_4$  NPs from p-bromobenzaldehyde, propanedinitrile, and dimedone. The lack of a catalytic product led to an absence of 2-amino-4H-benzo[b]pyrans. Raising the quantity of catalyst by 2 to 10 mg resulted in a higher percentage yield of the formula (25).

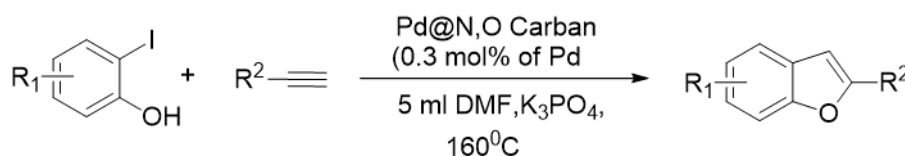


**Scheme 11:** Synthesis of 2-amino-4-(4-bromophenyl)-7,7-dimethyl-5-oxo-5,6,7,8-tetrahydro-4H-chromene-3-carbonitrile. Adapted from (25).

### Synthesis of Benzofurans from Terminal Alkynes and Indophenols using Recyclable Palladium NPs under the Ligand-Free Condition

The authors developed highly efficient and robust heterogeneous reaction supported by Pd nanoparticles on N, O-dual-doped hierarchical porous carbon using a one-pot tandem reaction of o-iodophenols with terminal alkynes. The catalyst allowed for sequential intermolecular Sonogashira cross-coupling followed by cyclization of o-iodophenols with terminal alkynes to synthesize a variety of 2-benzofurans under copper- and ligand-free conditions (26). The reagent allowed

successive intermolecular Sonogashira reactions after recirculating o-iodophenols with terminal alkynes to produce a variety of 2-benzofuran derivatives under copper- and ligand-free conditions with a selectivity of 60%. Various bases were used in the reaction, including  $\text{Na}_2\text{CO}_3$ ,  $\text{K}_2\text{CO}_3$ ,  $\text{Cs}_2\text{CO}_3$ ,  $\text{K}_3\text{PO}_4$ ,  $\text{NaO}^t\text{Bu}$ ,  $\text{KOH}$ ,  $\text{DBU}$  (1,8-diazabicyclo[5.4.0]undec-7-ene), and  $\text{TEA}$  (triethylamine). Under similar conditions, it was discovered that  $\text{K}_3\text{PO}_4$  with two equivalents to the reactant was the best option for superior catalytic efficiency in terms of equal operation and selectivity (a full conversion with up to 96% selectivity).



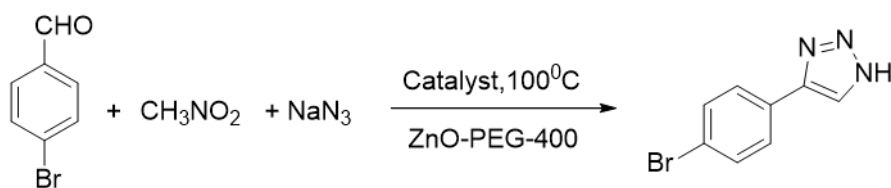
**Scheme 12:** Synthesis of benzofurans. Adapted from (26).

### A One-Pot Three-Component Reaction Catalyzed by Zinc Oxide NPs: A Simple Synthesis of 4-ArylNH1,2,3 Triazoles

Synthesis of NH-triazoles in the presence of ZnO nanoparticles using 4-bromobenzaldehyde, nitromethane, and sodium azide as model substrates. A wide variety of solvents, both organic and aqueous, were studied. Surprisingly, the yield of the desired items varies significantly in each case. It can be shown that when PEG-400 was used as a solvent at 100 °C, the best results were obtained. The reaction can also proceed when

aqueous was also carried out in the water, but the product yield was meager.

Following that, several solvents were investigated, including dichloromethane (DCM), DMF, dimethylsulfoxide (DMSO), ethylene glycol, and toluene, but the yields of NH-triazoles were inferior. The cycloaddition reaction of 4-bromobenzaldehyde, nitromethane, and sodium azide was also performed in PEG-400 solvent at 80 °C to optimize the temperature. Notably, at this temperature, the product's yield decreased (27).

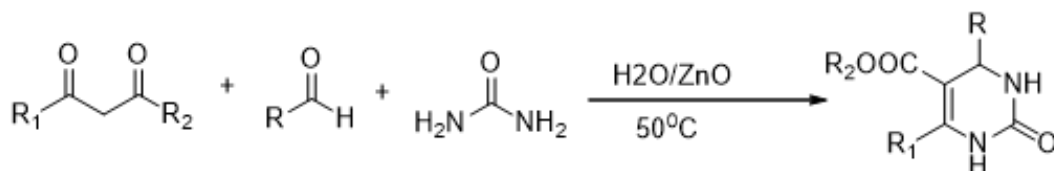


**Scheme 13:** Synthesis of 4-arylNH-1,2,3-triazoles. Adapted from (27).

### ZnO NPs are Used to Synthesize 3,4-Dihydropyrimidin-2(1H)-(thio)one Derivatives

It's a Biginelli reaction in which aldehyde, diketones, and urea were used as starting materials. As a solvent, H<sub>2</sub>O was used. The response took place at 50 °C. ZnO nanoparticles catalyze this reaction. These types of responses are not able to proceed without the use of

catalysts. It is observed that this reaction produces a small yield of desired products without catalyst after straining the reaction mixture for 28 hours. However, when catalysts were used, the result of the desired outcome was good to excellent. Moreover, the time for the completion of the reaction was about half an hour at mild temperature (28).

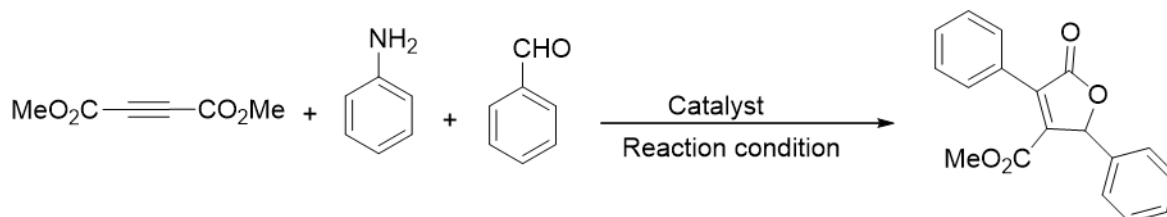


**Scheme 14:** Synthesis of 3,4-dihydropyrimidin-2(1H)-(thio)one derivatives. Adapted from (28).

### Synthesis of Furan Derivatives using Highly Efficient Silica-Coated Magnetic NPs by Multi-Component Reaction

The derivatives of furan are formed when aniline, aromatic aldehyde, and dialkylacetylenedicarboxylate react. This reaction proceeds at room temperature, and the catalyst used for this process was silica-coated magnetic NPs. Only 0.004 g of catalyst was used for the response. Observations have shown that as the catalyst volume increases from 0.004 to 0.006, the

product yields do not change. So it can be concluded that the best quantity of catalyst was 0.004 g. A trace amount of product was obtained in the catalyst shortage (29). At room temperature, 4 mg of catalyst was measured in different solvents such as aqueous medium, ethyl alcohol, methyl alcohol, and acetonitrile. As can be shown, ethyl alcohol is the perfect solvent designed for this conversion, yielding 93% of the time.

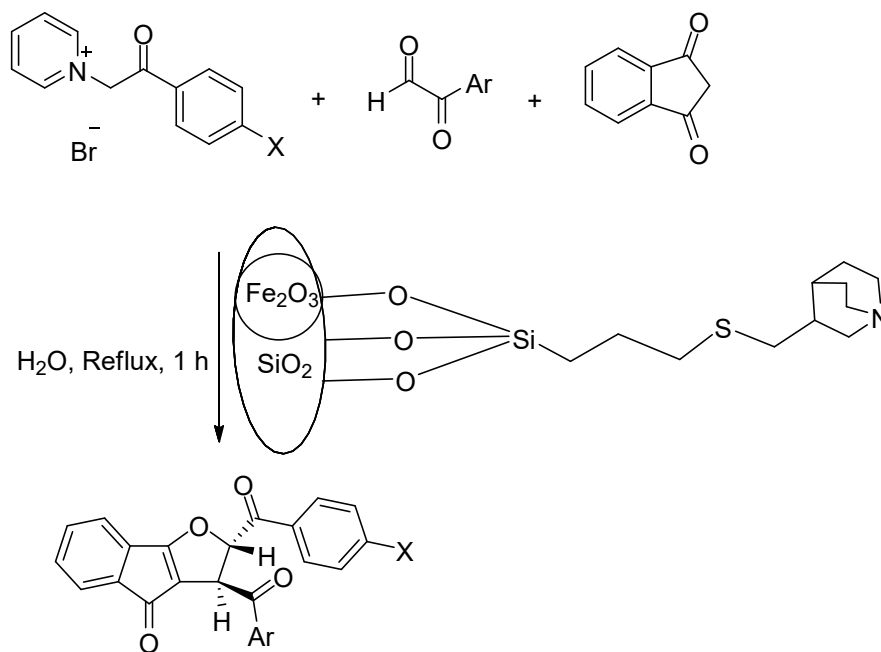


**Scheme 15:** Synthesis of methyl-oxo-2,4-diphenyl-2,5-dihydrofuran-3-carboxylate. Adapted from (29).

**Synthesis of Trans-dihydroindeno[1,2-b]furans in the Presence of a Nano-Fe<sub>2</sub>O<sub>3</sub>-Quinuclidine-based Catalyst**

When N-arylpyridinium bromide, 1,3-diketohydrindene, and arylglyoxal were reacted in

the equimolar condition in the presence of nano-Fe<sub>2</sub>O<sub>3</sub>-quinuclidine in aqueous media for 1.5 hours, the best product will come from the Ar group 4-NO<sub>2</sub>C<sub>6</sub>H<sub>4</sub> and the X group Cl, with a 94% overall yield (30).

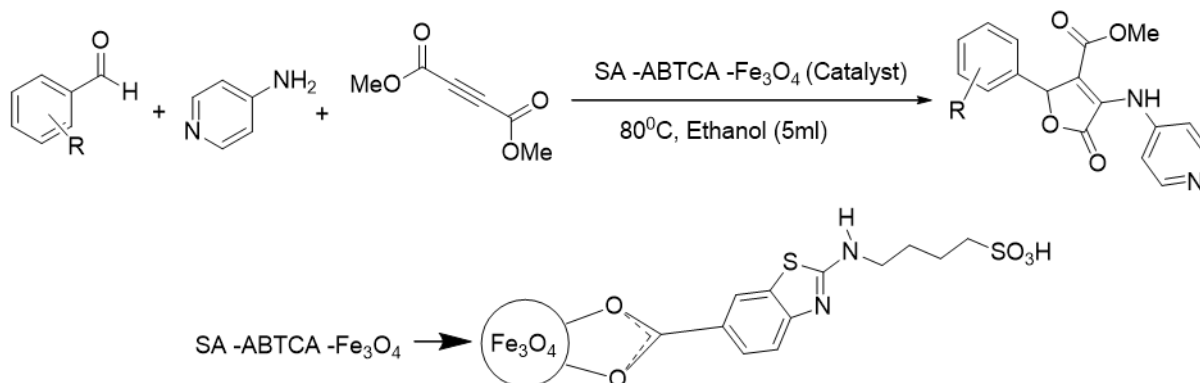


**Scheme 16:** Synthesis of trans-dihydroindeno[1,2-b]furans. Adapted from (30).

**Synthesis of Novel Furan-2(5H)-One's Derivatives Utilize Magnetic Nanoparticle and their Antibacterial Activities**

Fe<sub>3</sub>O<sub>4</sub> nanoparticles functionalized with 2-amino-1,3-benzothiazole-6-carboxylic acid (SA-ABTCA-Fe<sub>3</sub>O<sub>4</sub>) were synthesized as a new heterogeneous catalyst containing inorganic and organic parts.

The product shows antimicrobial action. This synthesis was carried out at different temperatures (25, 80 °C), varying the quantity of SA-ABTCA-Fe<sub>3</sub>O<sub>4</sub> as catalyst (5, 10, 15 mg). The results showed that 15 mg of SA-ABTCA-Fe<sub>3</sub>O<sub>4</sub> at 80°C was the best condition (31).

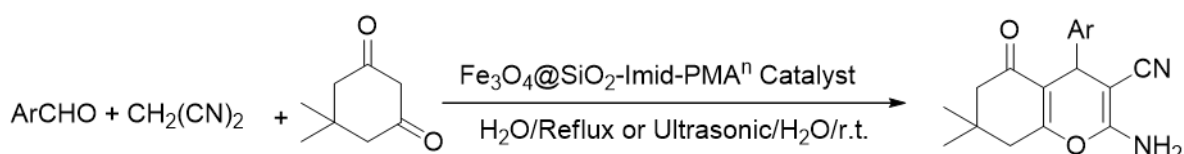


**Scheme 17:** Synthesis of novel furan-2(5H)-one derivatives. Adapted from (31).

### One-pot Multi-Constituent Synthesis of Tetrahydrobenzo[b]pyran Using Heterogeneous Nanoparticle

The one-pot multi-component reaction of aldehydes, active methylene groups such as malononitrile, and dimedone in the presence of  $\text{Fe}_3\text{O}_4 @\text{SiO}_2\text{-imid-PM}$  have been developed to synthesize various derivatives of tetrahydrobenzo[b]pyran and 3,4-dihydropyrano[c]chromene under different conditions such as reflux in water, ultrasonic irradiations nanoparticles behave as a magnetic catalyst. Because of their magnetic property, these catalysts can quickly be recovered from the

reaction mixture.  $\text{H}_2\text{O}$ , EtOH, MeOH, EtOAc,  $\text{CHCl}_3$ , and  $\text{CH}_3\text{CN}$  were used as solvents to complete the reaction using 20 mg  $\text{Fe}_3\text{O}_4 @\text{SiO}_2\text{-imid-PM}$ . The data showed that the response went smoothly in refluxing  $\text{H}_2\text{O}$ , producing the desired product's high yields. Under reflux, this multi-component condensation can also be achieved in solvents such as ethanol and methanol as they are protic solvents. These solvents yield 87% and 79% of desired product, respectively. However, this reaction can take more time and produce less yield of desired outcomes in the presence of aprotic solvents like  $\text{CHCl}_3$ , EtOAc, and  $\text{CH}_3\text{CN}$  (32).

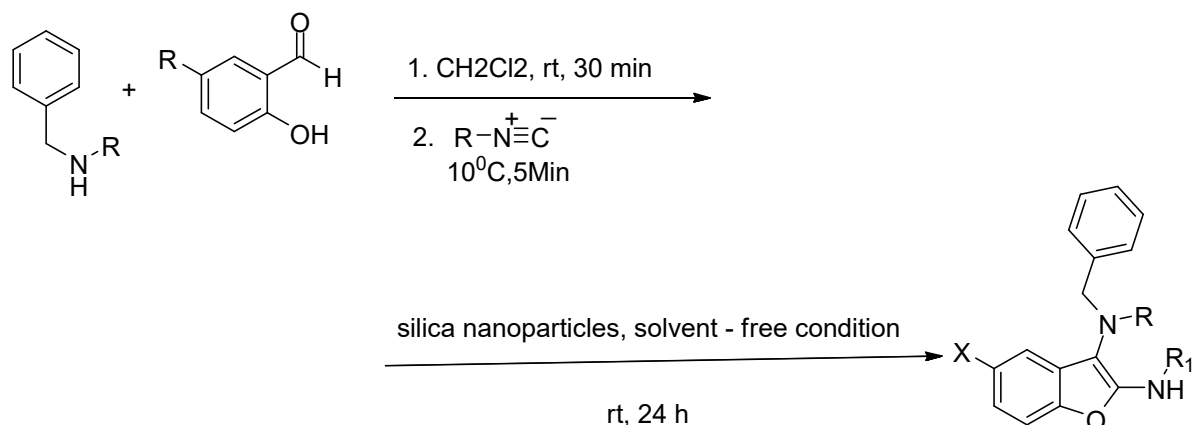


**Scheme 18:** Synthesis of tetrahydrobenzo[b]pyran derivatives. Adapted from (32).

### Synthesis of Benzo[b]furan and its Derivatives Using Green Nanocatalyst

Isocyanides, 2° amines, and 2-hydroxybenzaldehyde derivative

benzo[b]furan derivatives by utilizing silica NPs in a one-pot multi-component reaction (33). The best results and yield (95%) were obtained, when  $\text{R}_1=(1,3,3\text{-tetramethylbutyl})$ ,  $\text{R}(\text{Benzyl})$ ,  $\text{X}, (\text{NO}_2)$

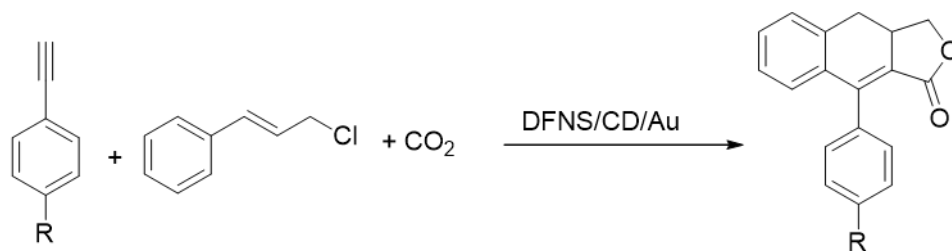


**Scheme 19:** Synthesis of benzo[b]furan derivatives. Adapted from (33).

### Interpolation of $\text{CO}_2$ into Aryl Alkynes Followed by Allylic Chlorides using Nanocatalyst

Heterocyclic compounds were synthesized by utilizing catalyzed carbonylation cinnamyl chloride

and the derivative of phenylacetylene in the presence of  $\text{CO}_2$  gas. The reactions were done in the presence of DFNS/-CD/Au NPs. Approximately 98% of the product is obtained (34).

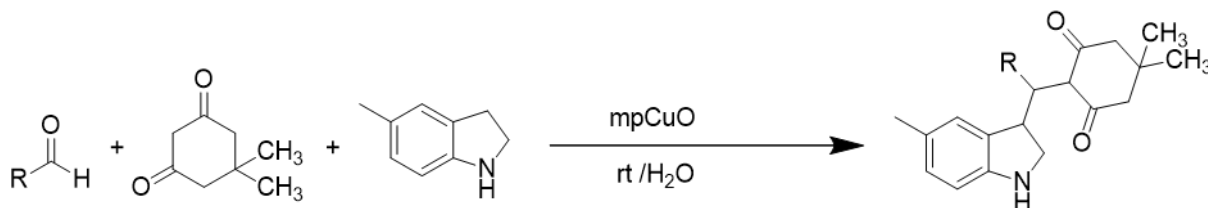


**Scheme 20:** Synthesis of furan derivatives. Adapted from (34).

### Porous CuO Catalyzed Green Synthesis of Some Novel 3-Alkylated Indoles

The green synthesis of some novel 3-alkylated indoles as active antitubercular agents was catalyzed by porous CuO. In 10 mL of water, a solution of indole (1 millimole), dimedone (1 millimole), and substituted aldehyde (1 millimole) were stirred at room temperature until the reaction was completed in the presence of 0.04 mmol

mpCuO as a heterogeneous catalyst. The solid compound that resulted was filtered out and then treated with DMF. To recover mpCuO particles, the mixture was centrifuged for a long time at 2500 rpm. After that, the organic solution was poured into water, purified, and recrystallized from ethanol before being dried under a vacuum to obtain the pure product (35).



**Scheme 21:** Synthesis of novel 3-alkylated indoles. Adapted from (35).

### CONCLUSION

The most commonly used strategies and mechanistic descriptions of various nanoparticles and some nitrogen oxygen-containing heterocyclic compounds were discussed. The effect of solvent role in the reaction was investigated. From a mechanical standpoint, the catalyst's most notable characteristic is its ability to be reused up to three times or more without losing its efficacy. As a result, this catalyst outperforms other non-magnetic catalysts in several respects. Easy process, smoother reaction, adequate recovery, and reversibility of the nanocatalysts are appealing and exciting features of this procedure.

### REFERENCES

- Weinstein DS, Gong H, Doweiko AM, Cunningham M, Habte S, Wang JH, et al. Azaxanthene Based Selective Glucocorticoid Receptor Modulators: Design, Synthesis, and Pharmacological Evaluation of (S)-4-(5-(1-((1,3,4-Thiadiazol-2-yl)amino)-2-methyl-1-oxopropan-2-yl)-5H-chromeno[2,3-b]pyridin-2-yl)-2-fluoro-N,N-dimethylbenzamide (BMS-776532) and Its Methylene Homologue (BMS-791826). *Journal of Medicinal Chemistry*. 2011;54(20):7318-33. DOI: <https://doi.org/10.1021/jm200879j>.
- Evdokimov NM, Kireev AS, Yakovenko AA, Antipin MYu, Magedov IV, Kornienko A. One-Step Synthesis of Heterocyclic Privileged Medicinal Scaffolds by a Multicomponent Reaction of Malononitrile with Aldehydes and Thiols. *The Journal of Organic Chemistry*. 2007;72(9):3443-53. DOI: <https://doi.org/10.1021/jo070114u>.
- Gupta S, Khurana JM. An efficient approach for the synthesis of 5-hydroxy-chromeno[2,3-b]pyridines under catalyst and solvent free conditions. *Green Chemistry*. 2017;19(17):4153-6. DOI: <https://doi.org/10.1039/C7GC01463E>.

2017;19(17):4153-6. DOI: <https://doi.org/10.1039/C7GC01463E>.

- El-Saghier AMM, Naili MB, Rammash BKh, Saleh NA, Kredan KM. Synthesis and antibacterial activity of some new fused chromenes. *Arkivoc*. 2007 Nov 12;2007(16):83-91. DOI: <https://doi.org/10.3998/ark.5550190.0008.g09>.
- Ghorab M, Al-Said M, Nissan Y. Dapson in Heterocyclic Chemistry Part VI: Synthesis and Molecular Docking of Some Novel Sulfonebiscompounds of Expected Anticancer Activity. *Arzneimittelforschung*. 2012;62(11):497-507. DOI: <https://doi.org/10.1055/s-0032-1323660>.
- Mukhopadhyay S, Lasri J, Guedes da Silva MFC, Januário Charmier MA, Pombeiro AJL. Activation of C-CN bond of propionitrile: An alternative route to the syntheses of 5-substituted-1H-tetrazoles and dicyanoplatinum(II) species. *Polyhedron*. 2008;27(13):2883-8. DOI: <https://doi.org/10.1016/j.poly.2008.06.031>.
- Singh RP, Verma RD, Meshri DT, Shreeve JM. Energetic Nitrogen-Rich Salts and Ionic Liquids. *Angewandte Chemie International Edition*. 2006;45(22):3584-601. DOI: <https://doi.org/10.1002/anie.200504236>.
- Li J, Ren T, Liu H, Wang D, Liu W. The tribological study of a tetrazole derivative as additive in liquid paraffin. *Wear*. 2000;246(1-2):130-3. DOI: [https://doi.org/10.1016/S0043-1648\(00\)00500-7](https://doi.org/10.1016/S0043-1648(00)00500-7).
- Pakdel S, Akhlaghinia B, Mohammadinezhad A. Fe<sub>3</sub>O<sub>4</sub>@Boehmite-NH<sub>2</sub>-CoII NPs: An Environment Friendly Nanocatalyst for Solvent Free Synthesis of Coumarin Derivatives Through Pechmann Condensation Reaction. *Chemistry Africa*. 2019;2(3):367-76. DOI: <https://doi.org/10.1007/s42250-019-00042-5>.
- Ochieng PJ, Kusuma WA, Rafi M, Sumaryada T. Deciphering the Action Mechanism of Indonesia Herbal Decoction in the Treatment of Type II Diabetes Using a

Network Pharmacology Approach. *International Journal of Pharmacy and Pharmaceutical Sciences*. 2017;9(3):243. DOI: <https://doi.org/10.22159/ijpps.2017v9i3.16413>.

11. Yamaguchi J, Yamaguchi AD, Itami K. C-H Bond Functionalization: Emerging Synthetic Tools for Natural Products and Pharmaceuticals. *Angewandte Chemie International Edition*. 2012;51(36):8960-9009. DOI: <https://doi.org/10.1002/anie.201201666>.

12. Riadi Y. UV Light Mediated Palladium-Catalyzed Synthesis of 2-Substitutedpyrido[2,3- d ]pyrimidines. *Polycyclic Aromatic Compounds*. 2019;1-6. DOI: <https://doi.org/10.1080/10406638.2019.1665554>.

13. Ojha NK, Zyryanov GV, Majee A, Charushin VN, Chupakhin ON, Santra S. Copper nanoparticles as inexpensive and efficient catalyst: A valuable contribution in organic synthesis. *Coordination Chemistry Reviews*. 2017;353:1-57. DOI: <https://doi.org/10.1016/j.ccr.2017.10.004>.

14. Nagarapu L, Aneesa, Peddiraju R, Apuri S. HClO<sub>4</sub>-SiO<sub>2</sub> as a novel and recyclable catalyst for the synthesis of 2,4,6-triarylpyridines under solvent-free conditions. *Catalysis Communications*. 2007;8(12):1973-6. DOI: <https://doi.org/10.1016/j.catcom.2007.08.003>.

15. Shaikh T, Sharma A, Kaur H. Ultrasonication-Assisted Synthesis of 3-Substituted Indoles in Water Using Polymer Grafted ZnO Nanoparticles as Eco-Friendly Catalyst. *ChemistrySelect*. 2019;4(1):245-9. DOI: <https://doi.org/10.1002/slct.201802702>.

16. Onishi K, Oikawa K, Yano H, Suzuki T, Obora Y. N,N -Dimethylformamide-stabilized palladium nanoclusters as a catalyst for Larock indole synthesis. *RSC Advances*. 2018;8(21):11324-9. DOI: <https://doi.org/10.1039/C8RA01410H>.

17. Sadeghi B, Tavasoli FA, Hassanabadi A. Ag Nanoparticles: An Efficient and Versatile Reagent for Synthesis of Bis(indolyl)methanes. *Synthesis and Reactivity in Inorganic, Metal-Organic, and Nano-Metal Chemistry*. 2015;45(9):1396-400. DOI: <https://doi.org/10.1080/15533174.2015.1016315>.

18. Choi I, Chung H, Park JW, Chung YK. Active and Recyclable Catalytic Synthesis of Indoles by Reductive Cyclization of 2-(2-Nitroaryl)acetonitriles in the Presence of Co-Rh Heterobimetallic Nanoparticles with Atmospheric Hydrogen under Mild Conditions. *Organic Letters*. 2016;18(21):5508-11. DOI: <https://doi.org/10.1021/acs.orglett.6b02659>.

19. Nakhate AV, Yadav GD. Hydrothermal Synthesis of CuFe<sub>2</sub>O<sub>4</sub> Magnetic Nanoparticles as Active and Robust Catalyst for N- arylation of Indole and Imidazole with Aryl Halide. *ChemistrySelect*. 2017;2(8):2395-405. DOI: <https://doi.org/10.1002/slct.201601846>.

20. Zolfigol MA, Ayazi-Nasrabadi R. Synthesis of the first magnetic nanoparticles with a thiourea dioxide-based sulfonic acid tag: application in the one-pot synthesis of 1,1,3-tri(1H-indol-3-yl) alkanes under mild and green conditions. *RSC Advances*. 2016;6(73):69595-604. DOI: <https://doi.org/10.1039/C6RA11620E>.

21. Safaei-Ghomi J, Ghasemzadeh MA. Silver iodide nanoparticle as an efficient and reusable catalyst for the one-pot synthesis of benzofurans under aqueous conditions. *Journal of Chemical Sciences*. 2013;125(5):1003-8. DOI: <https://doi.org/10.1007/s12039-013-0451-5>.

22. Payra S, Saha A, Guchhait S, Banerjee S. Direct CuO nanoparticle-catalyzed synthesis of poly-substituted furans via oxidative C-H/C-H functionalization in aqueous medium. *RSC Advances*. 2016;6(40):33462-7. DOI: <https://doi.org/10.1039/C6RA04181G>.

23. Teimuri-Mofrad R, Gholamhosseini-Nazari M, Payami E, Esmati S. Novel ferrocene-based ionic liquid supported on silica nanoparticles as efficient catalyst for synthesis of naphthopyran derivatives. *Research on Chemical Intermediates*. 2017;43(12):7105-18. DOI: <https://doi.org/10.1007/s11164-017-3061-x>.

24. Khodaei MM, Alizadeh A, Haghipour M. Supported 4-carboxybenzyl sulfamic acid on magnetic nanoparticles as a recoverable and recyclable catalyst for synthesis of 3,4,5-trisubstituted furan-2(5H)-one derivatives. *Journal of Organometallic Chemistry*. 2018;870:58-67. DOI: <https://doi.org/10.1016/j.jorgchem.2018.06.012>.

25. Singh P, Yadav P, Mishra A, Awasthi SK. Green and Mechanochemical One-Pot Multicomponent Synthesis of Bioactive 2-amino-4 H -benzo[ b ]pyrans via Highly Efficient Amine-Functionalized SiO<sub>2</sub>@Fe<sub>3</sub>O<sub>4</sub> Nanoparticles. *ACS Omega*. 2020;5(8):4223-32. DOI: <https://doi.org/10.1021/acsomega.9b04117>.

26. Ji G, Duan Y, Zhang S, Yang Y. Synthesis of benzofurans from terminal alkynes and iodophenols catalyzed by recyclable palladium nanoparticles supported on N,O-dual doped hierarchical porous carbon under copper- and ligand-free conditions. *Catalysis Today*. 2019;330:101-8. DOI: <https://doi.org/10.1016/j.cattod.2018.04.036>.

27. Phukan P, Agarwal S, Deori K, Sarma D. Zinc Oxide Nanoparticles Catalysed One-Pot Three-Component Reaction: A Facile Synthesis of 4-Aryl-NH-1,2,3-Triazoles. *Catalysis Letters*. 2020;150(8):2208-19. DOI: <https://doi.org/10.1007/s10562-020-03143-w>.

28. Hassanpour A, Khanmiri RH, Abolhasani J. ZnO Nanoparticles as an Efficient, Heterogeneous, Reusable, and Ecofriendly Catalyst for One-Pot, Three-Component Synthesis of 3,4-Dihydropyrimidin-2(1 H )-(thio)one Derivatives in Water. *Synthetic Communications*. 2015;45(6):727-33. DOI: <https://doi.org/10.1080/00397911.2014.987350>.

29. Shirzaei M, Mollashahi E, Taher Maghsoodlou M, Lashkari M. Novel synthesis of silica-coated magnetic nano-particles based on acidic ionic liquid, as a highly efficient catalyst for three component system leads to furans derivatives. *Journal of Saudi Chemical Society*. 2020;24(2):216-22. DOI: <https://doi.org/10.1016/j.jscs.2020.01.001>.

30. Vatanchian R, Mosslemin MH, Tabatabaee M, Sheibani A. Synthesis of Trans-Dihydroindeno[1,2-

- b]Furans via Nano  $\gamma$ -Fe<sub>2</sub>O<sub>3</sub>-Quinuclidine-Based Catalyst in an Aqueous Medium. *Journal of Chemical Research*. 2018;42(12):598–600. DOI: <https://doi.org/10.3184/174751918X15411641337056>.
31. Hao F, Wang X, Mohammadnia M. Preparation and Characterization of a Novel Magnetic Nano Catalyst for Synthesis and Antibacterial Activities of Novel Furan-2(5H)-Ones Derivatives. *Polycyclic Aromatic Compounds*. 2021;1–15. DOI: <https://doi.org/10.1080/10406638.2021.1887298>.
32. Esmailpour M, Javidi J, Dehghani F, Nowroozi Dodeji F. A green one-pot three-component synthesis of tetrahydrobenzo[b]pyran and 3,4-dihydropyrano[c]chromene derivatives using a Fe<sub>3</sub>O<sub>4</sub>@SiO<sub>2</sub>-imid-PMA n magnetic nanocatalyst under ultrasonic irradiation or reflux conditions. *RSC Advances*. 2015;5(34):26625–33. DOI: <https://doi.org/10.1039/C5RA01021G>.
33. Ramazani A, Rouhani M, Joo SW. Silica Nanoparticles from Rice Husk Ash: A Green Catalyst for the One-Pot Three-Component Synthesis of Benzo[B]Furan Derivatives. *Advanced Materials Research*. 2014;875–877:202–7. DOI: <https://doi.org/10.4028/www.scientific.net/AMR.875-877.202>.
34. Wang Z, Li X, Feng L, Liu B, Shamsa F. DFNS/ $\alpha$ -CD/Au as a Nanocatalyst for Interpolation of CO<sub>2</sub> into Aryl Alkynes Followed by SN<sub>2</sub> Coupling with Allylic Chlorides. *Catalysis Letters*. 2021;151(7):1911–22. DOI: <https://doi.org/10.1007/s10562-020-03451-1>.
35. Khan GA, War JA, Naikoo GA, Pandit UJ, Das R. Porous CuO catalysed green synthesis of some novel 3-alkylated indoles as potent antitubercular agents. *Journal of Saudi Chemical Society*. 2018;22(1):6–15. DOI: <https://doi.org/10.1016/j.jscs.2016.03.009>.



## An Overview of the Polymeric Materials that can be Used to Prevent Metal Corrosion: A Review

Abhishek Dwivedi<sup>1\*</sup> , Prem Kumar Bharti<sup>1</sup> , Sudhish Kumar Shukla<sup>2</sup> 

<sup>1</sup>Integral University, Lucknow, India

<sup>2</sup>Manav Rachna University, Faridabad, India

**Abstract:** Traditional study has discovered that natural materials such as wood are scarce and that synthetic materials can serve as suitable substitutes. Polymer chemicals, plant materials, chemical compounds, inorganic compounds, and other corrosion inhibitors all use metals. When technology fails, corrosion is one of the most severe consequences, causing harm to the financial system, natural resources, and people's lives. Natural materials such as wood are scarce, according to traditional research, and synthetic materials may serve as suitable replacements. Polymers as corrosion inhibitors have piqued researchers' attention from both a theoretical and practical standpoint. It has been seen from the research that natural polymer inhibitors exhibits more than 90% efficiency and good surface cover on carbon steel surface. A summary of forms of corrosion, corrosion processes, and recent work on the application of polymer inhibitors on the basis of parameters such as cost, convenience of use, environmental impact, and reliability has been reviewed.

**Keywords:** Corrosion, polymer inhibitor, metal, acids.

**Submitted:** May 17, 2021. **Accepted:** July 20, 2021.

**Cite this:** Dwivedi A, Bharti P, Shukla S. An Overview of the Polymeric Materials that can be Used to Prevent Metal Corrosion: A Review. JOTCSA. 2021;8(3):863-72.

**DOI:** <https://doi.org/10.18596/jotcsa.894374>.

**\*Corresponding author. E-mail:** [abhishekdwivedi2003@hotmail.com](mailto:abhishekdwivedi2003@hotmail.com).

### INTRODUCTION

When surfaces deteriorate due to chemical reactions with their surroundings, then corrosion happens. Rusting can also occur in plastics, concrete, and wood, although it is more prevalent in metals. Corrosion is the formation of more solid products as a result of surface reactions in a chemical or electrochemical reaction as metals or alloys are attacked in their environments such as air, water, or

dust. The most commonly used metal is iron (usually steel), and the corrosion of this metal is the subject of the following question. Corrosion is shown by the rusting of iron ( $\text{Fe}_2\text{O}_3 \cdot \text{H}_2\text{O}$ ) and the forming of a green carbonate film  $[(\text{Cu CO}_2 + \text{Cu}(\text{OH})_2)]$  on copper (1-5).

Metals are generated by their ores (oxide, chloride, sulfides etc.) found in Earth's crust by different metallurgical processes.

**Table 1:** A table showing that most of the materials decay overtime.

Material	Type of decay	Mitigation actions
Wood	Fungi, Insects, and Sun+rain	Chemicals, Paint/varnish
Steel	Rust	Galvanizing, Painting
Concrete	Cracking / Spalling	Corrosion-resistant rebar
Stone	Wear, Damage by Pollution	Usually none taken
Glass	Breaks	Tempered glass
Polymer	Become brittle under UV light	Improved polymer grades
Aluminum	Pitting over time, possible galvanic	Galvanic corrosion can be prevented

	corrosion	
Copper	Forms a green patina over time	None
Stainless steel	No decay	None required

**Corrosion Research Explanations**

As per IUPAC, "Corrosion is an irreversible interfacial reaction of a material (metal, ceramic, polymer) with its environment which results in its consumption or dissolution into the material of a component of the environment. Often, but not necessarily, corrosion results in effects detrimental to the usage of the material considered. Exclusively physical or mechanical processes such as melting and evaporation, abrasion or mechanical fracture are not included in the term corrosion"

Corrosion can affect our lives in a variety of ways, from the inconvenience of a seized nut on our vehicles to a disaster caused by a combustion chamber break in a jet plane engine. Understanding corrosion processes aids in product design and selection to ensure high levels of safety. The most important factor in corrosion prevention is safety, but economy is also important (6). Corrosion costs money not only because the object must be removed, but also because time and processing materials are wasted (7,8). Studies also shown that metallic building depreciation has an important impact on the economies of all countries, including roads, transport, accommodation, construction and development, and government. The need for expensive retrofits is eliminated by proper construction. Corrosion management should be considered during the facility's commissioning and service (9,10). Corrosion in buildings and installations can be avoided by applying appropriate inhibitors to water cooling and increasing the distribution of impressed current cathodic safety. In the United States, the cost of corrosion, both direct and indirect, is expected to be about \$279 billion a year, or 3.2 percent of GDP (GDP). In India, the direct cost of corrosion is projected to be \$26.1 billion (2.4 percent of GDP) (11-17). Corrosion engineering is the science of preventing and controlling corrosion. Corrosion is estimated to save \$9.3 billion in costs. The most serious effects of infrastructural defects are the loss of financial wealth, natural resources, and human lives. Metals are commonly used as automotive parts in modern times, which makes them mostly corrupt. Alloys are the only viable option, but not the most strong. Corrosive production is an ordinary phenomenon which transforms a polished metal, such as oxide, hydroxide and sulfide, into a chemically stable state. It decreases the strength, appearance, and fluid and gas permeability of the material and structural properties. It was found to form the studies that the rate of corrosion on mild steel in different conditions like dry, marine, humid (additional to different agents) has been stated as 0.001, 0.02, 0.2 mmpy, respectively.

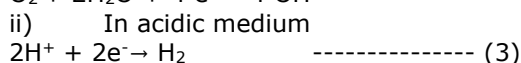
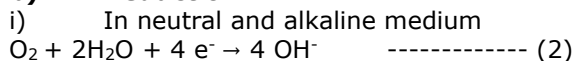
**Mechanism of Corrosion**

Corrosion chemistry is complex, but can be divided into an electrochemical phase. An anode during corrosion occurs at a certain point on the surface of an iron material. The electrons formed at this anodic position, when H<sup>+</sup> is present, flow through the metal in a separate position and reduce oxygen (which is assumed to be accessible from H<sub>2</sub>CO<sub>3</sub> produced by carbon dioxide dissolution into water in a moist atmosphere). The ion of hydrogen in water is present in order to dissolve other acid oxides in the atmosphere. This place is a cathode used as basic two reactons.

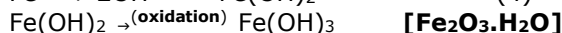
**a) Oxidation**



**b) Reduction**



**a) Formation of rust**



**Rust -- (5)**

The concept of corrosion must be expanded to include microbially mediated causes based on a better understanding of how different microorganisms in soil and water function. Chemical and electrochemical corrosion, high temperature and low temperature corrosion, wet corrosion and dry corrosion, etc. are all examples of corrosion. (18-20).

**Two Forms of Corrosion**

When there is no humidity or dampness to aid corrosion, dry corrosion occurs, and the metal oxidizes on its own, whereas metals undergo wet corrosion as a result of electron movement, which includes two measures: oxidation and decrease.

Metal iotas lose electrons during oxidation. The electrons in decrease are then picked up by the surrounding condition. The anode is the metal that lacks electrons. The cathode is the second metal, fluid, or gas that absorbs electrons, while the medium is the electrolyte (21-23).

Micro-corrosion cells are created due to the heterogeneity in metal or in corrosive environment. These cells are classified as Galvanic Cell and Concentration Cell, which represents two dissimilar metals, are immersed in electrolyte / corrosive environment as well as the concentration of the electrolyte is not uniform around the metal respectively.

The several forms of corrosion have been discussed as **Uniform Corrosion**, which represents dissolution of iron or zinc piece in acid solution, **Galvanic Corrosion** in steel pipe connected to copper plumbing, **Pitting Corrosion** where failure occurs suddenly, **Intergranular Corrosion** due to localized attack occurs adjacent to grain boundaries, **Fretting Corrosion** due to mechanical action of solid body on the metal under load and moving condition, **Selective Leaching** due to removal of one of the element from alloy by corrosion process, **Stress Corrosion** due to the fact that it occurs in specific corrosive environment and **Crevice Corrosion** (8,21,23,24).

### Inhibitors

Inhibitors are compounds that are applied to the corrosion medium when corrosion occurs in a damp atmosphere to slow the rate of corrosion by delaying the anodic and/or cathodic processes. A significant part of the cost can be minimized by using inhibitors.

**NACE** defined inhibitors as "A substance which retards corrosion when added to an environment in appropriate concentration" whereas **ISO** defined as "A chemical substance which decreases the corrosion rate when present in the corrosion system at a suitable concentration without significantly change in the concentration of any other corrosive agent".

Many of the researchers discussed that a good corrosion inhibitor must act as cost-effective, chemically inert, a good inhibitor of dissolution of metal and environmental friendly as well as, it should not decompose during service condition, and inhibit the diffusion of hydrogen into metal (6,20,25,26).

### LITERATURE REVIEW

One significant pattern in present day human advancement is to impact slow substitution of common materials particularly made of wood through whichever altogether engineered materials otherwise adjusted characteristic resources. The quick industrial development of numerous nations demonstrates the shrinkage in metal assets. Clearly, metals are critical in current building yet many can be severely influenced by corrosion since they are related with high vitality. In the cutting edge age, it is basic to alter the properties of a metal and additionally combinations as per customized particulars intended for target applications. Be that as it may, after the alterations the serious issues related with the metallic materials is its destructive nature. The degree of consumption relies upon the material synthesis and the idea of the earth to which it is uncovered. Loss of economy, regular assets, and human lives includes serious issues of corrosion, due to if there should be an occurrence of

infrastructural breakdown. So it is exceptionally imperative to step into new improvements in consumption alleviation. Counteraction of corrosion of materials in destructive condition is a difficult one. Various techniques have traditionally been used to minimize intake, including cathodic safety, progression monitoring, decreasing quality of the metal pollutant, and using surface therapy approaches as well as consolidating suitable composites (27). In any case, corrosion inhibitors have proved to be the most simple and cost-effective method of ensuring and preventing acidic media use. Those same inhibitors restrict use and prevent metal corrosion damage to mechanical ships, equipment, and surfaces. Since inorganic and natural inhibitors are poisonous and costly, recent attempts have been made to find ways to guard against corrosion (28,29). Numerous analysts have as of late centred around corrosion avoidance strategies utilizing green inhibitors for mild steel in acidic solution for imitate modern procedures.

Some papers suggested triazines, anilinopropionates, polymers, dyes, drugs, ionic liquids, natural products (plant extract) N-(6-methoxyquinolin-4-yl)-pentane-1,4-diamine (MPD), N'-(7-chloroquinolin-4-yl)-N,N-diethyl-pentane-1,4-diamine (CDPD), thiosemicarbazide, phenyl isothiocyanate, N-phenylhydrazine-1,2-dicarbothioamide (PDA) and azorubine dye (AZB), streptomycin, cephalixin, ceftadizime (CZD), and eco-friendly polyaspartic acid (PASP) (25,30-40) as different effective class of corrosion inhibitors on mild steel in HCl and H<sub>2</sub>SO<sub>4</sub> solution interface and found the inhibitor efficiency to be about 90% and more respectively. To increase the counter consumption and scale restriction properties of metal surfaces, an uncovered multi-use bearer of mesoporous titanium dioxide whiskers (TiO<sub>2</sub>(w)) (41) was contrived in epoxy covering and altered by ethylenediamine tetra (methylene phosphonic corrosive) (EDTMPA) and imidazoline, whereas (42) ginger concentrate as consumption inhibitor from normal assets was concentrated to forestall corrosion of mild steel in corrosive media. (43) PASAC3, PASAC 11 and PASAC13 organic corrosion inhibitors were examined for carbon steel in cooling water.

Several researches reviewed the use of polymers (25,44), organic compounds (34,45-47), natural products (48,49) and so on as corrosion inhibitors (50). The combination of carbon (C) and iron (Fe) forms carbon steel which in broad forms are utilized in marine applications, atomic, petroleum product power plants, transport, concoction preparing, development, mining, and metal handling hardware because of its expense and accessibility. Notwithstanding, corrosions are probably going to assault carbon steel in forceful condition, yet in addition in ordinary condition. The majority of the successful inhibitors have an issue concerning

biocompatibility, biodegradability, bioaccumulation and harmfulness arrangement that is destructive to the ocean-living space. Inhibitors can be divided into four categories to be specific; anodic inhibitors, cathodic inhibitors, blended inhibitors, and unpredictable consumption inhibitors. The assessment of inhibitors type can be portrayed by electrochemical or submersion test by adding recognized measure of inhibitor into arrangements which are ordinarily seawater.

The section put forth will discuss selective polymers having versatile corrosion inhibition properties i.e., same polymer as corrosion inhibitor for different metals and media (51). The major water-soluble polymeric systems discussed are polyacrylic acid, polyacrylamide, polyvinyl alcohol, polyethylene glycol, polyvinyl pyrrolidone, polyethylene imine, polyelectrolytes, polyphosphates, and natural polymers. Rheology alteration, surface sealing, personal hygiene, and oilfield formulation, corrosion inhibitors, polymer flooding, precious metal-ion recovery, and colloid stabilization are only a few of the uses for these water soluble polymers. Some of the synthetic polymers like polyacrylic acid, polyvinyl alcohol, sulfonated polystyrene, etc. (52,53), have extensively been used in medicinal field for drug delivery, implants, medical devices and injectable polymer conjugates. The inhibitor efficiency of N1,N1-diallyl-N6,N6,N6,N5-tripropylhexane-1,6-diaminium (NDTHDC), for carbon steel in 15 percent HCl solution and found that poly-NDTHDC is better than NDTHDC in 1000 mg/L inhibitor and was used in weight loss, electrochemical, and surface testing techniques. The efficacy of the inhibition increased but afterwards fell at 60 °C of the combination (54). There are a few consumption control techniques to alter the materials viable, which incorporates cathodic insurance, (22,55,56); anodic insurance, (57,58) and alloying. The utilization of substance inhibitors, (59,60) was the principle corrosion counteraction method in which change of the earth was considered. This technique is regularly considered as the best and common sense strategy for corrosion avoidance because of its simplicity of use. A few works have been accounted for the consumption restraint of various metals in different destructive conditions. At first consideration was fixated on natural mixes. It was audited (61) that the quantity of announced natural mixes while other papers (62–65) has talked about the different heterocyclic mixes utilized as corrosion inhibitors. Worldwide awareness on the natural effect of the natural mixes established the framework for the improvement of earth sympathetic mixes as green inhibitors. Green inhibitors incorporate normal plant materials and non-harmful, eco-benevolent polymers (66–68) in their audit articles secured the distinctive revealed plant materials for consumption hindrance of metals.

Polymers, copolymers, joined polymers, and polymer composites have also become more common as natural antioxidants in recent years (69). (70,71) in their articles investigated the polymers for consumption counteraction applications. The elite of the polymeric consumption inhibitors is because of its bigger size and various utilitarian tying down gatherings. The polymers essentially get adsorbed on the metal surface through the binding down gatherings and ensure slightly additional substrate than that of the corresponding monomers. Polymeric mixtures were tried for their capability to control the corrosion procedure utilizing traditional and electrochemical systems. The adequacy of the inhibitors was assessed using electrochemical techniques such as potentiodynamic polarization, potentiostatic polarization, direct polarization, and electrochemical impedance spectroscopy. Some other extraordinary systems utilized for the assessment of polymeric corrosion inhibitors were talked about in detail. (72) According to some papers, polymer is a good covering medium for plain carbon (soft) steel to prevent corrosion in an acidic medium like hydrochloric acid. At high current thickness, polymerization of the shielding operator frames enormous and circular miniaturized scale particles with a rough surface. Polymerization of the polymer covering at low current thickness, on the other hand, produces a smooth and homogeneous polymer film. To have surface insurance, electro-polymerization of a polymer on the exterior of a metal may be used. In 1 M HCl, poly(vinyl liquor cysteine) [PVAC] worked well as a mild steel ingestion inhibitor. In an oxalic corrosive form, ammonium persulfate was used to create a water-dissolvable leading polymer composite poly(vinyl liquor cysteine) (20). Examined polymers which act both as antiscalant and inhibitors and resulted that corrosion happens because of synthetic and electrochemical responses. Creator expressed that the natural mixes adsorb superficially and interface with the surface. Leading polymers and biodegradable polymeric materials may likewise assume imperative job in future to shield materials from decay. (61) Using UV, FTIR, and SEM-EDX to characterize a composite, (73,74) discovered that with an increasing focus on the hindrance proficiency (IE) of chitosan biopolymer, it is able to minimize its intake of copper by 3% using electrochemical (polarization and impedance) and weight reduction calculations combined with morphology tests. (75) Via a weight reduction technique and a potentiodynamic polarization test, the influence of thiocarbanilide (TCB) corrosion inhibitor behavior of high carbon steel in 1 M, H<sub>2</sub>SO<sub>4</sub>, and HCl corrosive arrangements was investigated. The natural compound worked effectively in corrosive solutions at all focuses with standard TCB restriction mastery, according to the data collected. It was discovered that TCB adheres

to the Langmuir and Frumkin isotherm models of adsorption.

Polyacrylamide (PACM), prepared by radical polymerization technique using ammonium persulfate (APS) as initiator under nitrogen atmosphere (76) tested polymers act as mixed anodic and cathodic inhibitor in the 1.0 M HCl 96% efficiency at room temperature. Many researchers found that oil and gas industries are most suffering from the problem of corrosion (77). Some of the works investigated that because of oxygen, corrosive environments, CO<sub>2</sub> and H<sub>2</sub>S defilement, polymeric corrosion inhibitors for the use at metal surface, to hold consumption rates under control, researchers must use weight measurement, EIS, potentiodynamic, and polarization tests to find effective inhibitors for versatile materials. Polymers, unlike small atom consumption inhibitors, have a wider range of applications and greater film-forming capabilities, which may significantly enhance protective obstruction capabilities. This audit counted the most well-known polymeric structures utilized as consumption inhibitors for various phases of the oil and gas investigation, generation and transportation enterprises. Among corrosion alleviation procedures, the utilization of consumption inhibitors despite everything stays to be one of the most financially reasonable techniques in controlling the corrosion rate since these materials can without much of a stretch be applied through bunch as well as ceaseless medications with least measures of material with the point of limiting incomplete or complete shutdowns in the plants. Be that as it may, when contrasted with little atom inhibitors, polymeric materials are not yet as broadly utilized. Polymers, on the other hand, have a considerable capacity for outperforming the showcase of small particle inhibitors while holding the fixation to a minimum due to the intrinsic advantages of these macromolecules, such as stronger film shaping operators, a few possible attachment focuses, and extremely adaptable depolymerization. Polyamine corrosion inhibitors that have been modified with carboxylic corrosive, heterocyclic moieties, thiols, disulfides, and phosphorus-containing useful gatherings are appropriate for joining on the metal surfaces of different hardware and transmission pipelines that are widely utilized. Polymerization techniques are becoming more and more regulated, different designs, stretched, hyper expanded, dendrimeric, and so on, might be increasingly suitable in tending to the exceptionally destructive media experienced when it comes to the oil and gas industries (78). In this analysis, it is mentioned that the inhibition efficiency increases significantly with the increase of theobromacocoa peel polar extract TCPE content using for the examination of corrosion inhibition efficiency of 0.3% C mild steel bar, however, (79,80) in a number of violent media, both natural

and synthetic polymers have proven useful to resist metal corrosion.

Many researchers found that oil and gas industries are most suffering from the problem of corrosion. It was investigated that the due cause of it may be oxygen, acid stimulation, CO<sub>2</sub> and H<sub>2</sub>S defilement in the environment. It was proposed by the researchers that the versatile nature inhibitors with multi-functionality and better film-forming capabilities like polymeric corrosion inhibitors may be the better solution there. Polymeric corrosion inhibitors have been found one of the market-place solutions for minimizing the rate of corrosion since these chemicals can be easily spread by lot and/or ongoing treatments with limited material volumes in order to prevent partial or complete plant interference. Polymeric materials have been shown to be stronger film-forming agents (81,82), several potential binding sites, are highly stable for derivatives and are likely to exceed the performance of small molecular inhibitors while retaining a low concentration.

#### Industrial Applications of Corrosion Inhibitors

- Refinery industries: Film forming long chain amines are used as corrosion inhibitors.
- Power Plants: Nitrites, Chromate, Phosphate, Benzotriazoles are used in cooling water.
- Steel Industry: During pickling of steel organic mixed inhibitors are used.
- Acidification of Oil Well: Thermally stable inhibitors are used. e.g. acetylenic compounds, cinnamaldehydes, quaternary salts, and Mannich bases are used as inhibitors.
- Automobiles: For control of internal corrosion of coolants nitrites, phosphonates, Silicates, benzoates, and mercaptans are used.
- For controlling external corrosion, rust proofing pigments are used.
- Reinforce concrete – Calcium Nitrite, calcium stearate, and tannic acid are used.

#### DISCUSSION

The preceding literature provides an outline of various forms of corrosion, the ingestion process, and previous research on the use of natural polymers as mild steel corrosion inhibitors (83,84). According to the preceding discussion, conventional plant eliminates are viable sustainable consumption inhibitors, but polymers seem to be more suitable for use by the steel specimen. In sulfuric or hydrochloric corrosive medium, reduction of weight, with impedance electrochemistry, were mainly used and confirmed by potentiodynamic polarization and surface morphology techniques about corrosion restraint. There is still a lot of untapped potential, especially in the computational visualization of large concentrate divisions on steel specimen. It will really aid in the establishment of specific

components for corrosion resistance. Work on the investigations of genuine modern emanating to genuine circumstances is constrained. Some corrosion prevention techniques have been suggested, including raising awareness of high corrosion threats and potential savings, dispelling the misconception that there is little that can be done about corrosion, increasing corrosion savings by sound corrosion protection by updating rules, regulations, standards, and management procedures, and staff training and instruction in corrosion prevention.

Additional research into these plant-based materials in other destructive conditions, such as carbon dioxide, sulfur dioxide, and hydrogen sulfide, is required, while polymers such as linear insulated polymer (polyacrylic acid, polyvinyl alcohol, polystyrene).

(52,53,85), cross-linked insulated polymer (aniline-formaldehyde derivatives copolymer), and conducting polymers (polyanthranilic acid, sulfonated polyaniline) seem to have a wide range of applications and potential. Frequency experiments for potential approaches should also be carried out in order to revolutionize these traditional mixes and effectively replace the regular synthetic concoctions that are currently used to monitor corrosion using best inhibitor for corrosion with methods such as chemical process, weight loss method, electrochemical, and atomic analysis of surface using microscopy, among others.

#### ACKNOWLEDGEMENT

The manuscript communication number provided by the Research and Development Cell, Integral University, Lucknow is: IU/R&D/2021-MCN0001131

#### REFERENCES

1. Asworth V, Booker C, Charlton H, Fairhurst J. a Short Introduction To Corrosion and Its Control Corrosion of Metals and Its Prevention. Corrosion&Protection/Bm. 2012;1-9.
2. Evans UR. Corrosion, Causes and prevention: An engineering problem. J Soc Chem Ind [Internet]. 1926 Aug 13;45(33):582-3. URL: <http://doi.wiley.com/10.1002/jctb.5000453306>
3. Raja PB, Ismail M, Ghoreishiamiri S, Mirza J, Ismail MC, Kakooei S, Rahim AA. Reviews on Corrosion Inhibitors: A Short View. Chemical Engineering Communications. 2016;203(9): 1145-56. DOI: <https://doi.org/10.1080/00986445.2016.1172485>
4. Wranglen G. An introduction to corrosion and protection of metals. Anti-Corrosion Methods Mater. 1972;19(11):5.
5. Zarras P, Stenger-Smith JD. Corrosion processes and strategies for prevention: An introduction. In: Makhlof ASH, editor. Handbook of Smart Coatings for Materials Protection. Woodhead Publishing Limited; 2014. p. 3-28. ISBN: 978-0-85709-680-7.
6. Hari kumar, S., Karthikeyan, S., A.Jeeva, P., Sundaramali G. A Review on Corrosion Inhibition of Aluminium with Special Reference to Green Inhibitors. Int J Recent Sci Res Vol. 2012;3(2):61-7.
7. Hammonds P. An Introduction to Corrosion and its Prevention. Compr Chem Kinet. 1989;28(C):233-79.
8. Natarajan KA. Corrosion: Introduction - Definitions and Types [Internet]. NPTEL Web Course. 2014. p. 1-9. URL: <https://nptel.ac.in/content/storage2/courses/113108051/module1/lecture1.pdf>
9. Aramide FO. Corrosion Inhibition of AISI / SAE Steel in a Marine Environment. 2009;(15):47-52.
10. Deshpande PP, Jadhav NG, Gelling VJ, Sazou D. Conducting polymers for corrosion protection: A review. J Coatings Technol Res. 2014;11(4):473-94.
11. Tsoeunyane MG, Makhatha ME, Arotiba OA. Corrosion Inhibition of Mild Steel by Poly(butylene succinate)-L-histidine Extended with 1,6-diisocynatohexane Polymer Composite in 1 M HCl. Int J Corros [Internet]. 2019 Mar 3;2019:1-12. URL: <https://www.hindawi.com/journals/ijc/2019/7406409/>
12. Kruger J. Cost of Metallic Corrosion. In: Uhlig's Corrosion Handbook: Third Edition. Revie RW (Ed) 2011. p. 15-20. ISBN: 978-0-470-08032-0.
13. The Annual Cost of Corrosion to Ohio [Internet]. 2007. URL: <http://www.brown.senate.gov/imo/media/doc/OhioCorrosion.pdf>
14. Bhaskaran R, Bhalla L, Sarin V. Cost of corrosion protection in Indian oil & petroleum products transmission pipelines - A case study. Int J Appl Bus Econ Res. 2016;14(7):5169-80.
15. Bhaskaran, R, Palaniswamy, N, Rengaswamy, NS. Cost of Corrosion and Corrosion Auditing in Indian Industries. Corros Res. 2011;27(Supplement):1-35.
16. NACE International. NACE-international Cost of corrosion study unveiled. Mater Perform 2. 2002; (July):20.

17. Biezma M V, Cristóbal JRS. Methodology to study cost of corrosion. *Corros Eng Sci Technol* [Internet]. 2005;40(4):344–52. DOI: <https://doi.org/10.1179/174327805X75821>
18. Shukla SK, Ebenso EE. Corrosion inhibition, adsorption behavior and thermodynamic properties of streptomycin on mild steel in hydrochloric acid medium. *Int J Electrochem Sci*. 2011;6(8):3277–91.
19. Yi Y, Liu G, Jin Z, Feng D. The use of conducting polyaniline as corrosion inhibitor for mild steel in hydrochloric acid. *Int J Electrochem Sci*. 2013;8(3):3540–50.
20. Subramania A, Sundaram NTK, Priya RS, Muralidharan VS. Polymeric corrosion INHIBITORS - An Overview. *Bull Electrochem*. 2004;20(February):49–58.
21. Elayaperumal K, Raja VS. Forms of Corrosion. In: Revie RW, editor. *Corrosion Failures: Theory, Case Studies, and Solutions*. 2015. p. 1–26. ISBN: 978-0-470-45564-7.
22. Roberge PR. *Handbook of Corrosion Engineering*. 2nd ed. United States: The McGraw-Hill Companies; 2012. 1057 p. ISBN: 9780071750370.
23. Fortana M., Mita M. The Eight forms of corrosion and the corrective measures. 1953; URL: [eprints.nmlindia.org/3414/1/137-148.PDF](http://eprints.nmlindia.org/3414/1/137-148.PDF)
24. McCafferty E. Introduction to corrosion science [Internet]. *Introduction to Corrosion Science*. New York: Springer Berlin Heidelberg; 2010. 1–575 p. ISBN: 978-1-4419-0454-6.
25. Umoren SA, Solomon MM. Recent Developments on the Use of Polymers as Corrosion Inhibitors - A Review. *Open Mater Sci J*. 2014;8:39–54.
26. Revie RW, Uhlig HH. *Corrosion and Corrosion Control Handbook* [Internet]. 4th ed. Hoboken, NJ, USA: John Wiley & Sons, Inc.; 2008. 495 p. URL: <http://doi.wiley.com/10.1002/9780470277270>
27. Chigondo M, Chigondo F. Recent Natural Corrosion Inhibitors for Mild Steel: An Overview. *J Chem* [Internet]. 2016;2016:1–7. URL: <http://www.hindawi.com/journals/jchem/2016/6208937/>
28. Abdel-Gaber AM, Abd-El-Nabey BA, Sidahmed IM, El-Zayady AM, Saadawy M. Inhibitive action of some plant extracts on the corrosion of steel in acidic media. *Corros Sci*. 2006;48(9):2765–79.
29. Sastri VS. Types of corrosion inhibitor for managing corrosion in underground pipelines. In: *Underground Pipeline Corrosion* [Internet]. Sawston, United Kingdom: Woodhead Publishing Limited; 2014. p. 166–211. DOI: <http://dx.doi.org/10.1533/9780857099266.1.166>.
30. Shukla SK. Corrosion inhibitive effect of N- ( 6-methoxyquinolin-8-yl ) -pentane-1 , 4- diamine on mild steel / sulphuric acid solution interface. *J Mater Environ Sci*. 2015;6(6):1779–86.
31. Zeino A, Abdulazeez I, Khaled M, Jawich MW, Obot IB. Mechanistic study of polyaspartic acid (PASP) as eco-friendly corrosion inhibitor on mild steel in 3% NaCl aerated solution. *J Mol Liq* [Internet]. 2018;250:50–62. DOI: <http://dx.doi.org/10.1016/j.molliq.2017.11.160>.
32. Habibiyani A, Ramezanzadeh B, Mahdavian M, Kasaeian M. Facile size and chemistry-controlled synthesis of mussel-inspired bio-polymers based on Polydopamine Nanospheres: Application as eco-friendly corrosion inhibitors for mild steel against aqueous acidic solution. *J Mol Liq* [Internet]. 2020;298:111974. DOI: <https://doi.org/10.1016/j.molliq.2019.111974>.
33. Singh K. AK, Shukla K. SK, Quraishi MA. Ultrasound mediated Green synthesis of Hexa-hydro Triazines. *J Mater Environ Sci*. 2011;2(4):403–6.
34. Shukla SK, Quraishi MA. 4-Substituted anilinomethylpropionate: New and efficient corrosion inhibitors for mild steel in hydrochloric acid solution. *Corros Sci*. 2009;51(9):1990–7.
35. Kabanda MM, Shukla SK, Singh AK, Murulana LC, Ebenso EE. Electrochemical and quantum chemical studies on calmagite and fast sulphone black f dyes as corrosion inhibitors for mild steel in hydrochloric medium. *Int J Electrochem Sci*. 2012;7(9):8813–31.
36. Salem H, Samir E. Determination of cefotaxime, cefoperazone, ceftazidime and cefadroxil using surface plasmon resonance band of silver nanoparticles. *Brazilian J Pharm Sci*. 2018;54(3):1–9.
37. Shukla SK, Murulana LC, Ebenso EE. Inhibitive effect of imidazolium based aprotic ionic liquids on mild steel corrosion in hydrochloric acid medium. *Int J Electrochem Sci*. 2011;6(9):4286–95.
38. Shukla SK, Ebenso EE. Effect of condensation product of thiosemicarbazide and phenyl isothiocyanate on corrosion of mild steel in sulphuric acid medium. *Int J Electrochem Sci*. 2012;7(12):12134–45.
39. Singh AK, Shukla SK, Singh M, Quraishi MA. Inhibitive effect of ceftazidime on corrosion of mild steel in hydrochloric acid solution. *Mater Chem Phys*. 2011;129(1–2):68–76.

40. Chai C, Xu Y, Shi S, Zhao X, Wu Y, Xu Y, et al. Functional polyaspartic acid derivatives as eco-friendly corrosion inhibitors for mild steel in 0.5 M H<sub>2</sub>SO<sub>4</sub> solution. *RSC Adv.* 2018;8(44):24970–81.
41. Wang C, Wang H, Hu Y, Liu Z, Lv C, Zhu Y, et al. Anti-Corrosive and Scale Inhibiting Polymer-Based Functional Coating with Internal and External Regulation of TiO<sub>2</sub> Whiskers. *Coatings* [Internet]. 2018;8(2):29. URL: <http://www.mdpi.com/2079-6412/8/1/29>.
42. Fidrulsi A, Suryanto, Mahmood M. Ginger extract as green corrosion inhibitor of mild steel in hydrochloric acid solution. In: *IOP Conference Series: Materials Science and Engineering*. IOP Conf. Series: Materials Science and Engineering; 2017. p. 1–6.
43. Harabor I, Nechifor G, Branzoi V, Branzoi F, Carbon I. Investigation of Some Organic Polymers As Corrosion Inhibitors on Carbon Steel in Cooling Water System. *UPBSci Bull, Series B.* 2016;78(3):145–60.
44. Fathima Sabirneeza AA, Geethanjali R, Subhashini S. Polymeric Corrosion Inhibitors for Iron and Its Alloys: A Review. *Chem Eng Commun.* 2015;202(2):232–44.
45. Aljeaban NA, Goni LKMO, Alharbi BG, Jafar Mazumder MA, Ali SA, Chen T, et al. Polymers Decorated with Functional Motifs for Mitigation of Steel Corrosion: An Overview. Huang J-C, editor. *Int J Polym Sci* [Internet]. 2020;2020:9512680. DOI: <https://doi.org/10.1155/2020/9512680>.
46. Sakhri A, Perrin FX, Benaboura A, Aragon E, Lamouri S. Corrosion protection of steel by sulfodoped polyaniline-pigmented coating. *Prog Org Coatings* [Internet]. 2011;72(3):473–9. DOI: <http://dx.doi.org/10.1016/j.porgcoat.2011.06.005>.
47. Loto RT, Ayozie BU, Loto CA. Electrochemical study of the corrosion inhibition effect of 3-cyanophenyl compound on 420 martensitic stainless steel in strong acid media. *IOP Conf Ser Mater Sci Eng.* 2019;613(1).
48. Quraishi MA, Ahamad I, Singh AK, Shukla SK, Lal B, Singh V. N-(Piperidinomethyl)-3-[(pyridylidene)amino]isatin: A new and effective acid corrosion inhibitor for mild steel. *Mater Chem Phys.* 2008;112(3):1035–9.
49. Amin MA, Ei-rehim SSA, El-sherbini EEF, Hazzazi OA, Abbas MN. Polyacrylic acid as a corrosion inhibitor for aluminium in weakly alkaline solutions . Part I: Weight loss , polarization , impedance EFM and EDX studies. *Corros Sci* [Internet]. 2009;51(3):658–67. DOI: <http://dx.doi.org/10.1016/j.corsci.2008.12.008>.
50. Ismail A. A review of Green Corrosion Inhibitor for mild steel in seawater. *ARNP J Eng Appl Sci* [Internet]. 2016 Jul;11(14):8710–4. URL: [http://www.arnpjournals.org/jeas/research\\_papers/rp\\_2016/jeas\\_0716\\_4665.pdf](http://www.arnpjournals.org/jeas/research_papers/rp_2016/jeas_0716_4665.pdf).
51. Kausar A. Corrosion prevention prospects of polymeric nanocomposites: A review. *J Plast Film Sheeting* [Internet]. 2019 Apr 11;35(2):181–202. URL: <http://journals.sagepub.com/doi/10.1177/8756087918806027>.
52. DWIVEDI A, BHARTI P, SHUKLA S. Surface assimilation and corrosion inhibition characteristic of water soluble Polyvinyl Alcohol on mild steel surface in 0.5M HCl solution. *J Turkish Chem Soc Sect A Chem* [Internet]. 2021 Jan 11;8(1):219–30. URL: <https://dergipark.org.tr/en/doi/10.18596/jotcsa.794721>.
53. Dwivedi A, Bharti PK, Shukla SK. Interaction of water soluble polyacrylic acid with mild steel / hydrochloric acid interface. In: *International Conference on Contemporary Research in Mechanical Engineering with focus on Materials and Manufacturing* [Internet]. Lucknow--India: IOP Conference Series: Materials Science and Engineering; 2018. p. 1–11. URL: <https://iopscience.iop.org/article/10.1088/1757-899X/404/1/012044>.
54. Odewunmi NA, Solomon MM, Umoren SA, Ali SA. Comparative studies of the corrosion inhibition efficacy of a dicationic monomer and its polymer against API X60 steel corrosion in simulated acidizing fluid under static and hydrodynamic conditions. *ACS Omega.* 2020;5(42):27057–71. DOI: <https://doi.org/10.1021/acsomega.0c02345>.
55. Shittu MD, Olawale JO, Adeoye MO, Oluwasegun KM, Adebayo KM, Ige OO. Investigation of corrosion resistance of polystyrene as an inhibitor in hydrochloric and tetra-oxo sulphate VI acids. *Int J Mater Chem.* 2014;4(1):9–13.
56. Desai PS, Kapopara SM. Inhibiting effect of anisidines on corrosion of aluminium in hydrochloric acid. *Indian J Chem Technol.* 2009;16(6):486–91.
57. Cecchetto L, Delabouglise D, Petit J. On the mechanism of the anodic protection of aluminium alloy AA5182 by emeraldine base coatings Evidences of a galvanic coupling. 2007;52:3485–92.
58. Praveen BM, Venkatesha T V, Naik YA, Prashantha K. Corrosion studies of carbon nanotubes – Zn composite coating. *Surface and*

- Coatings Technology. 2007;201:5836-42. DOI: <https://doi.org/10.1016/j.surfcoat.2006.10.034>.
59. Yang F, Li X, Qiu S, Zheng W, Zhao H, Wang L. Water soluble trianiline containing polyurethane (TAPU) as an efficient corrosion inhibitor for mild steel. *Int J Electrochem Sci*. 2017;12(6):5349-62.
60. Oyama T. Encyclopedia of Polymeric Nanomaterials [Internet]. Kobayashi S, Müllen K, editors. Encyclopedia of Polymeric Nanomaterials. Berlin, Heidelberg: Springer Berlin Heidelberg; 2020. 1-11 p. URL: <http://link.springer.com/10.1007/978-3-642-36199-9>.
61. Abdul Rahiman AFS, Sethumanickam S. Corrosion inhibition, adsorption and thermodynamic properties of poly(vinyl alcohol-cysteine) in molar HCl. *Arab J Chem* [Internet]. 2017;10:S3358-66. DOI: <http://dx.doi.org/10.1016/j.arabjc.2014.01.016>.
62. Li Z, Zhu A, Yang J. One-Pot Three-Component Mild Synthesis of 2-Aryl-3-(9-alkylcarbazol-3-yl)thiazolin-4-ones. *J Heterocycl Chem*. 2012;49(Scheme 1):1458-61.
63. Metcalf RL. Indigo and Indigo Colorants. *Ullmann's Encycl Ind Chem*. 2000;13837329:264-322. ISBN: 9783527304103.
64. Dos Pereira JDS, Neri JM, Emerenciano DP, De Freitas GRS, Felipe MBMC, De Souza MÂF, et al. Experimental and theoretical analysis of an oxazinoquinoxaline derivative for corrosion inhibition of AISI 1018 steel. *Quim Nova*. 2018;41(3):243-50.
65. Stanly Jacob K, Parameswaran G. Corrosion inhibition of mild steel in hydrochloric acid solution by Schiff base furoin thiosemicarbazone. *Corros Sci* [Internet]. 2010;52(1):224-8. URL: <http://dx.doi.org/10.1016/j.corsci.2009.09.007>.
66. Antonijevic MM, Petrovic MB. Copper Corrosion Inhibitors . A review. *Rev Lit Arts Am* [Internet]. 2008;3(1):1-28. URL: <http://www.electrochemsci.org/papers/vol3/3010001.pdf>.
67. Quraishi MA, Shukla SK. Poly(aniline-formaldehyde): A new and effective corrosion inhibitor for mild steel in hydrochloric acid. *Mater Chem Phys*. 2009;113(2-3):685-9. DOI: <https://doi.org/10.1016/j.matchemphys.2008.08.028>.
68. Srimathi M, Rajalakshmi R, Subhashini S. Polyvinyl alcohol-sulphanilic acid water soluble composite as corrosion inhibitor for mild steel in hydrochloric acid medium. *Arab J Chem* [Internet]. 2014;7(5):647-56. DOI: <http://dx.doi.org/10.1016/j.arabjc.2010.11.013>.
69. Guo J, Yuan S, Jiang W, Lv L, Liang B, Pehkonen SO. Polymers for combating biocorrosion. *Front Mater*. 2018;5(March).
70. Umoren SA. Polymers as Corrosion Inhibitors for Metals in Different Media - A Review. *Open Corros J* [Internet]. 2009;2(1):175-88. URL: <http://benthamopen.com/ABSTRACT/TOCORRJ-2-175>.
71. Arthur DE, Jonathan A, Ameh PO, Anya C. A review on the assessment of polymeric materials used as corrosion inhibitor of metals and alloys. *Int J Ind Chem* [Internet]. 2013;4(1):2. URL: <http://www.industchem.com/content/4/1/2>.
72. Alsingery RMD. Polypyrrole as a Perfect Corrosion Inhibitor for Mild Steel in Hydrochloric Acid Solution Cyclic Voltammetry. *Int J ChemTech Res*. 2017;10(9):1058-65.
73. Oukhrib R, El Ibrahim B, Bourzi H, El Mouaden K, Jmiai A, El Issami S, et al. Quantum chemical calculations and corrosion inhibition efficiency of biopolymer "chitosan" on copper surface in 3%NaCl. *J Mater Environ Sci*. 2017;8(1):195-208.
74. Zhang QH, Hou BS, Li YY, Zhu GY, Liu HF, Zhang GA. Two novel chitosan derivatives as high efficient eco-friendly inhibitors for the corrosion of mild steel in acidic solution. *Corros Sci*. 2020;164.
75. Loto RT, Loto CA, Joseph O, Olanrewaju G. Adsorption and corrosion inhibition properties of thiocarbanilide on the electrochemical behavior of high carbon steel in dilute acid solutions. *Results Phys* [Internet]. 2016;6:305-14. DOI: <http://dx.doi.org/10.1016/j.rinp.2016.05.013>.
76. Azzam EMS, El-Salam HMA, Mohamed RA, Shaban SM, Shokry A. Control the corrosion of mild steel using synthesized polymers based on polyacrylamide. *Egypt J Pet* [Internet]. 2018;27(4):897-910. DOI: <https://doi.org/10.1016/j.ejpe.2018.01.006>.
77. Tiu BDB, Advincula RC. Polymeric corrosion inhibitors for the oil and gas industry: Design principles and mechanism. *React Funct Polym* [Internet]. 2015;95:25-45. DOI: <http://dx.doi.org/10.1016/j.reactfunctpolym.2015.08.006>.
78. Yetri Y, Emriadi, Jamarun N, Gunawarman. Corrosion Inhibition Efficiency of Mild Steel in Hydrochloric Acid by Adding Theobroma Cacao Peel Extract. *International Conference on Biological, Chemical and Environmental Sciences*. 2014;15-9. DOI: <http://dx.doi.org/10.15242/IICBE.C614002>.

79. Hussain AK, Sudin I, Basheer UM, Yusop MZM. A review on graphene-based polymer composite coatings for the corrosion protection of metals. *Corros Rev.* 2019;37(4):343–63.
80. Keramatinia M, Ramezanzadeh B, Mahdavian M. Green production of bioactive components from herbal origins through one-pot oxidation/polymerization reactions and application as a corrosion inhibitor for mild steel in HCl solution. *J Taiwan Inst Chem Eng.* 2019;105:134–49. DOI: <https://doi.org/10.1016/j.jtice.2019.10.005>.
81. Rokaya D, Srimaneepong V, Sapkota J, Qin J, Siraleartmukul K, Siriwongrungson V. Polymeric materials and films in dentistry: An overview. *J Adv Res [Internet].* 2018;14:25–34. DOI: <https://doi.org/10.1016/j.jare.2018.05.001>.
82. Umoren SA, Solomon MM. Protective polymeric films for industrial substrates: A critical review on past and recent applications with conducting polymers and polymer composites/nanocomposites. *Prog Mater Sci [Internet].* 2019;104:380–450. DOI: <https://doi.org/10.1016/j.pmatsci.2019.04.002>.
83. Ismail AS, Farag AA. Experimental, theoretical and simulation studies of extracted crab waste protein as a green polymer inhibitor for carbon steel corrosion in 2 M H<sub>3</sub>PO<sub>4</sub>. *Surfaces and Interfaces [Internet].* 2020;19:100483. DOI: <https://doi.org/10.1016/j.surfin.2020.100483>.
84. Jafar Mazumder MA. Synthesis, characterization and electrochemical analysis of cysteine modified polymers for corrosion inhibition of mild steel in aqueous 1 M HCl. *RSC Adv.* 2019;9(8):4277–94. DOI: <https://doi.org/10.1039/C8RA09833F>.
85. Dharmalingam V, Sahayaraj P, Amalraj A, Prema A. Poly ( acrylic acid ) and Sodium gluconate as effective corrosion inhibitors for mild steel in chloride environment. *International Journal of ChemTech Research.* 2017;10(5):630–41.



## *cis*-2 and *trans*-2-eicosenoic Fatty Acids Inhibit *Mycobacterium tuberculosis* Virulence Factor Protein Tyrosine Phosphatase B

Lalu Rudyat Telly Savalas<sup>1\*</sup>  , Asih Chomsa Lestari<sup>2</sup>  , Munirah Munirah<sup>3</sup>  ,  
Suryawati Farida<sup>3</sup>  , Dedy Suhendra<sup>3</sup>  , Dina Asnawati<sup>3</sup>  , Jannatin 'Ardhuha<sup>1</sup>  ,  
Baiq Nila Sari Ningsih<sup>1,4</sup>  , and Jufrizal Syahr<sup>5</sup>  

<sup>1</sup>Department of Mathematics and Natural Sciences, Faculty of Teacher Training and Education, University of Mataram, Jl. Majapahit No. 62 Mataram, Nusa Tenggara Barat, Indonesia 83125.

<sup>2</sup>National Agency of Drugs and Food Control, Jl. Catur Warga Mataram, Nusa Tenggara Barat, Indonesia 83121.

<sup>3</sup>Department of Chemistry, Faculty of Mathematics and Natural Sciences, University of Mataram, Jl. Majapahit No. 62 Mataram, Nusa Tenggara Barat, Indonesia 83125.

<sup>4</sup>Division of Physical Science, Faculty of Science, Prince Songkla University, Hat Yai, Songkla 90110, Thailand.

<sup>5</sup>Department of Chemistry, Universitas Muhammadiyah Riau, Jl. KH. Ahmad Dahlan No.88, Pekanbaru, Riau 28156, Indonesia.

**Abstract:** The present study aims to investigate the potential inhibitory effect of eicosenoic fatty acids on protein tyrosine phosphatase B of *Mycobacterium tuberculosis* (PtpB). PtpB is recognized to play a vital role in *Mycobacterium tuberculosis* (Mtb) successful latent infection. It prevents the fusion even between phagocytosed mycobacteria with lysosomes so that the bacteria escape from degradation. We have over-expressed recombinant Mtb PtpB within *Escherichia coli* BL21(DE3), and further, we have used the protein for inhibition assay with *cis*-2 and *trans*-eicosenoic fatty acids. It is revealed that at a concentration of 16  $\mu$ M, *cis*-2- and *trans*-2-eicosenoic fatty acids can inhibit PtpB by 63.72% and 74.67%, respectively. Docking analysis has confirmed strong interactions of PtpB with *cis*-2 and *trans*-2-eicosenoic fatty acids, with the binding energy of -60.40 and -61.60 kcal/mol, respectively. These findings underline both fatty acids' high potential to be further investigated to discover drugs against latent tuberculosis infection.

**Keywords:** Eicosenoic fatty acid, latent tuberculosis infection, protein tyrosine phosphatase B, molecular docking.

**Submitted:** March 26, 2021. **Accepted:** July 26, 2021.

**Cite this:** Savalas L, Lestari A, Munirah M, Farida S, Suhendra D, Asnawati D, et al. *cis*-2 and *trans*-2-eicosenoic Fatty Acids Inhibit *Mycobacterium tuberculosis* Virulence Factor Protein Tyrosine Phosphatase B. JOTCSA. 2021;8(3):873-82.

**DOI:** <https://doi.org/10.18596/jotcsa.896489>.

**\*Corresponding author.** E-mail: [telly@unram.ac.id](mailto:telly@unram.ac.id). Phone +62 (0370) 623873, Fax +62 (0370) 634918

### INTRODUCTION

The World Health Organization estimates that Mtb infects one-fourth of the world population in a latent fashion (1,2). Although not all infections develop into active tuberculosis cases, the number of people with tuberculosis (TB) is still very high. There are 10 million new TB cases with a death rate of 1.2 million registered annually (1).

At the onset of *M. tuberculosis* infection, macrophages -the host cells that act as the first line of the defense system- engulf the bacteria in a process called phagocytosis. Phagocytosis results in membrane-enclosed structures called phagosomes. Phagosomes undergo a series of maturation processes by fusion with early endosomes, late endosomes, and lysosomes. This maturation process includes several stages to form early,

intermediate, and, finally, mature phagolysosomes (3). The presence of specific marker proteins characterizes each stage. The mature form of phagolysosome is a membrane-enclosed structure with an acidic lumen (pH 4.5) containing an array of lysosome-derived proteases/hydrolases and reactive oxygen species (ROS). They collectively serve as host weapons to degrade invading bacterial cells (4).

Together with monocytes and dendritic cells, macrophages constitute the mononuclear phagocyte system (MPS). The hallmark of this system is the recognition and elimination of pathogens (5). *Mtb* and related species, however, are equipped with the ability to evade the hostile environment of macrophage cells. *Mtb* does this by secreting different types of molecules that can interfere and prevent phagosome fusion with lysosomes, which are otherwise lethal for the *Mtb* bacteria. They include mycobacterial lipid and glycolipid such as trehalose-6,6'-dimycolate (TDM) and lipoarabinomannan (LAM), respectively. TDM has been shown to facilitate *Mtb* survival by decreasing phagosomal acidification and phagolysosomal fusion in murine macrophage (6). LAM was reported to inhibit early phagosomal markers (7). The mycobacterial may also secrete proteins or enzymes, such as protein tyrosine phosphatase A (PtpA), protein tyrosine phosphatase B (PtpB), secretory acid phosphatase M, zinc-dependent metalloprotease 1, lipoamide dehydrogenase C, serine/threonine protein kinase G (PknG), and PEGRS62 protein (5,8). These proteins have been demonstrated to play important roles in the *Mtb* survival from macrophage elimination. Once the bacteria escaped from the degradation process, they enter a latent infection phase (9). This so-called latent tuberculosis infection (LTBI) can last for years and even decades before resurrecting into active TB (10). Therefore, understanding the interactions between the *Mtb* pathogen and host macrophages is essential to overcome tuberculosis.

PtpA and PtpB are among the proteins secreted by *Mtb*, and both of them play a role in facilitating the persistence of mycobacterial infection (11). Deletion of PtpA and PtpB reduces *Mtb* survival within macrophages and dramatically reduces the *Mtb* bacillary load in the lung of chronic guinea pigs (12,13). Researchers proposed PtpA to interfere with the formation of the acidic lysosome by blocking the V-type proton pump responsible for the lysosome's acidification (14,15). The void of acidification eventually switches the lysosomal hydrolases into an inactive form, a condition that favors *Mtb*'s survival (16). Likewise, PtpB protein phosphatase is also known to promote mycobacterial survival from host degradation. A

recent report suggested that PtpB reduces the expression of proinflammatory cytokines as well as the apoptosis of macrophages (17). It also limits macrophages' bactericidal responses by inhibiting NF- $\kappa$ B and MAPK signaling pathways (18). Therefore, these phosphatases constitute a high potential to be research targets due to their essential role in *Mtb* infection.

It has recently been shown that *cis*-2 and *trans*-2-eicosenoic fatty acids can inhibit PtpA (19). A few reports suggest that PtpA and PtpB have common inhibitors, although the inhibitory effect may vary (20). In this context, the present study aims to reveal whether *cis*-2 and *trans*-2-eicosenoic fatty acids can also inhibit PtpB.

## MATERIALS AND METHODS

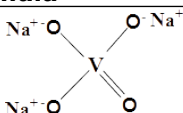
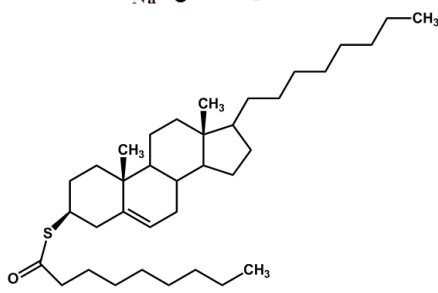
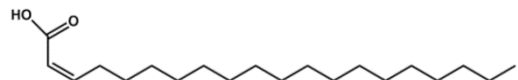
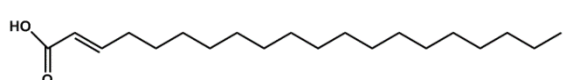
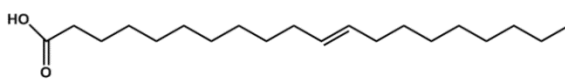
### Materials

Recombinant plasmid pET-30a bearing *M. Tuberculosis PtpB* is maintained in *Escherichia coli* strain XL1-Blue. The strain BL21(DE3) of *E. Coli* was used for expression. Bacterial growth media was standard lysogeny broth (LB), which consisted of 0.5% yeast extract (BD), 1% Tryptone (Bio Basic), 1% NaCl (Merck), 2% bacto agar (Difco) for plated culture, and 25  $\mu$ g/mL kanamycin (Bioworld). The inducer of gene expression was Isopropyl 1-thio- $\beta$ -D-galactopyranoside (IPTG), supplied by Thermo Scientific, whereas the substrate for PtpB was *para*-nitrophenyl phosphate (pNPP, Sigma). Materials for SDS PAGE were acrylamide and bis-acrylamide (Bio Basic), sodium dodecyl sulfate (Bio Basic), tetramethylethylenediamine (Bio Basic), ammonium persulfate (Bio Basic), glycine (Bio Basic), beta-mercaptoethanol (Sigma), bromophenol blue, and Coomassie Brilliant Blue (Sigma), dithiothreitol (Sigma) and protein ladder (Thermo Scientific). Sample degradation by protease was prevented by the addition of Phenylmethylsulfonyl fluoride (PMSF, Sigma). Guanidine hydrochloride (GuHCl) was purchased from MP BioScience.

Inhibitor *cis*-2- and *trans*-2-eicosenoic fatty acids were purchased from Larodan AB. *Trans*-11-eicosenoic acid and sodium orthovanadate were purchased from Sigma. S-((3S,10R,13R)-10,13-dimethyl-17-octyl-2,3,4,7,8,9,10,11,12,13,14,15,16,17-tetradecahydro-1H-cyclopenta[a]phenanthren-3-yl) nonanethioate or DTP was purchased from Interbioscreen. The inhibitors structures are shown in Table 1.

DMSO (MP BioScience) was used as the solvent for the substrate in the presence of imidazole (Thermo Scientific). Graphics were plotted in Graphpad Prism 7. Docking analysis was performed by Discovery Studio (Accelrys, San Diego, CA, USA).

**Table 1:** Compounds tested their inhibitory effect on PtpB.

No	Compound	Structure/formula	Note
1	Sodium orthovanadate		general inhibitor for phosphatases as a control (21)
2	DTP*		proposed to inhibit PtpB (22)
3	<i>cis</i> -2-eicosenoic acid		PtpA inhibitor (19)
4	<i>trans</i> -2-eicosenoic acid		PtpA inhibitor (19)
5	<i>trans</i> -11-eicosenoic acid		a related fatty acid with double bond position lies apart from carboxyl group

\*) DTP: S-((3S,10R,13R)-10,13-dimethyl-17-octyl-2,3,4,7,8,9,10,11,12,13,14,15,16,17-tetradecahydro-1H-cyclopenta[a]phenanthren-3-yl) nonanethioate

## Methods

### Expression and Production of PtpB

The recombinant pET30a plasmid bearing the Mtb *PtpB* gene was used to transform *Escherichia coli* BL21(DE3). Expression of PtpB under the control of T7 promoter within the pET30a vector was induced by adding 0.5 mM IPTG to the culture of transformant *E. coli* (23) in its early log phase, i.e., when the culture reached to OD<sub>600</sub> of ~0.3. Incubation of *E. coli* culture was prolonged at 37 °C with a shaking speed of 250 rpm and harvested after 4 hours of induction. The high PtpB expression leads to the formation of an inclusion body (IB), which is further subjected to the recovery process described below.

### Recovery of PtpB and activity assay

Recovery of PtpB from inactive IB was made resolubilization and dialysis against refolding buffer, as described elsewhere (24). Briefly, IB was washed three times with wash buffer (50 mM Tris pH 8; 0.1 mM NaCl; 0.1 mM EDTA, 5% glycerol; 0.1 mM DTT, and 5% Triton X-100). In each washing step, IB suspension was sonicated and recovered by centrifugation at 14,000 rpm at 4 °C for 10 minutes. No Triton X-100 was added in the second and third washing steps. The washed IB was further dissolved in the same buffer containing 6 M GuHCl and shaken vigorously (250 rpm) until a clear lysate was observed. The denatured protein was transferred into a dialysis tube (Carolina Biological Supply Company) with a cutoff between 12,000 to 14,000 Daltons. The dialysis was undertaken against

refolding buffer (20 mM Tris pH 8; 5 mM EDTA; 5 mM DTT; 50 mM NaCl, 20% glycerol, and 0.32 M GuHCl) overnight. On the next day, the refolding buffer was exchanged, and dialysis further proceeded for two hours. The buffer exchange and dialysis cycle were subsequently repeated for two times.

A time-course curve that shows the activity of recombinant PtpB was created by plotting the absorbance of *para*-nitrophenol over time. pNP is the product of *para*-nitrophenyl phosphate hydrolysis by PtpB. The reaction was carried out in a 96 well-plate containing 40 µL of 100 mM imidazole, 20 µL of 50 mM pNPP substrate, 135 µL milli-Q water, and 5 µL of recovered PtpB in a total volume of 200 µL. The reaction was allowed to proceed within the spectrophotometer chamber (Multiskan Go, Thermo Scientific). The spectrophotometer was set to automatically record the absorbance at 410 nm in five minutes intervals for two hours.

### Inhibition of PtpB with *cis*-2 and *trans*-2-eicosenoic fatty acids

We have performed an inhibition assay of PtpB with a procedure adapted from Mascarello et al. (20). The reaction mixture contained 100 ng PtpB (in phosphate buffer, pH 8.0), 20 mM imidazole, 20 mM pNPP substrate, 16 µM inhibitor (Table 1), and Milli-Q water to complete the reaction volume to 200 µL in a 96-well plate. The reaction was carried out at 37 °C. After 15 minutes, the reaction was stopped

by the addition of 80  $\mu$ L of 0.25 M NaOH, and the absorbance was recorded at 410 nm immediately. PtpB activity was calculated by the following equation:

$$A = \frac{Vol \times \Delta A_{410}}{\epsilon \times time}$$

Where

A : activity (Unit)

Vol : reaction mixture volume ( $\mu$ L)

$\Delta A_{410}$  : sample absorption - blank absorption, measured at 410 nm

$\epsilon$  : molar extinction of pNP ( $1.78 \times 10^4 \text{ M}^{-1} \cdot \text{cm}^{-1}$ )

t : measurement time (minutes)

### Molecular Docking

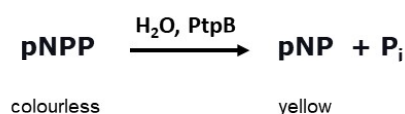
In order to describe the interaction between PtpB with the inhibitor molecules, we have performed docking analysis by using the software Discovery Studio (Biovia, Accelrys, San Diego USA). The protein structure of PtpB was retrieved from RCSB Protein Data Bank with accession number 1YWF.

## RESULTS AND DISCUSSION

The required material for the inhibition assay was prepared by over-expressing the *Mtb PtpB* gene in *E. coli* BL21(DE3). We found that the protein exists as an IB (Figure 1A). Despite initially being inactive

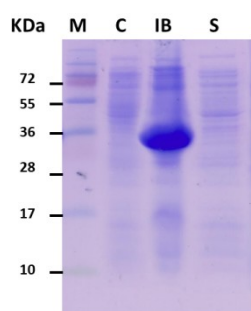
protein, expression as IB offered a high protein level that can be recovered by an established procedure to gain protein with sufficient purity for inhibition assays. As shown in Figure 1B, re-solubilization with 6 M GuHCl followed by dialysis effectively removes the excessive salt. The application of GuHCl gave a better result compared to previous work with 8 M urea (24). The observation might come from the relatively efficient solubilization of the IB by GuHCl compared to urea (25).

The re-solubilized protein was active, as shown by its ability to cleave pNPP substrate into para-nitrophenol and phosphate.

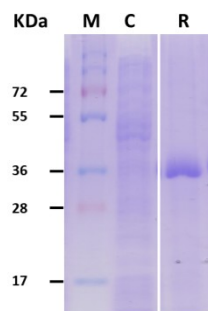


The absorbance of the reaction mixture was recorded at 410 nm every five minutes for two hours. The data was plotted in a time-course curve (Figure 1C). The curve showed good linearity within the first 45 minutes. We employed this reaction to test whether prospective inhibitors (Table 1) can decrease PtpB activity. The inhibition mixture containing PtpB, substrate pNPP, and inhibitor was allowed to react, and the absorbance at 410 nm was recorded after 15 minutes of reaction.

### A. PtpB expression in *E. coli* BL21(DE3)



### B. Resolubilization of PtpB



### C. PtpB activity

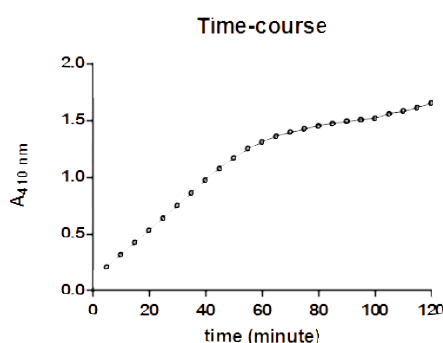


**Figure 1:** Expression of PtpB in *E. coli* BL21(DE3).

A. Expression of PtpB in *E. coli* BL21(DE3) under IPTG induction. M: protein ladder; C: untransformed *E. coli* extract; IB: inclusion body found in the insoluble fraction; S: soluble fraction or supernatant.

B. Solubilization of PtpB with Guanidine hydrochloride and its recovery in refolding buffer. M: protein ladder; C: lysate from untransformed *E. coli*; R: recovered PtpB. Proteins were separated by 12.5% SDS-PAGE.

C. Activity of recombinant PtpB was measured over time. PtpB hydrolyzed pNPP substrate to release the

yellow color of *para*-nitrophenol. The absorbance was measured at 410 nm at 5-minute intervals for 120 minutes.

We tested the inhibitory effect of *cis*-2 and *trans*-2 eicosenoic fatty acids on the activity of PtpB. In this preliminary work, we employed a single dose of inhibitors of 16  $\mu$ M that represent a low dose (26). Figure 2 shows the activity of PtpB is reduced by *cis*-2 and *trans*-2-eicosenoic fatty acids to 36.28% and 25.33, respectively. In other words, *cis*-2 and *trans*-2-eicosenoic fatty acids inhibit PtpB by

63.72% and 74.67%, respectively. The inhibition of PtpB by *trans*-2-eicosenoic fatty acid was in line with the effect of sodium orthovanadate, a general inhibitor for phosphatases (27). In an *in silico* study, Dhanjal and co-workers suggested that the compound DTP is a potential inhibitor for PtpB (22). We also showed for the first time that DTP inhibits PtpB with a slightly less effect than *cis*-2 and *trans*-2-eicosenoic acids. *Trans*-11-eicosenoic fatty acid, a related fatty acid whose double bond lies apart from the carboxyl group, only slightly inhibited PtpB activity (Figure 2). It showed that the double bond position that is close to the carboxy group is crucial for *cis*-2- and *trans*-2-eicosenoic to inhibit PtpB.

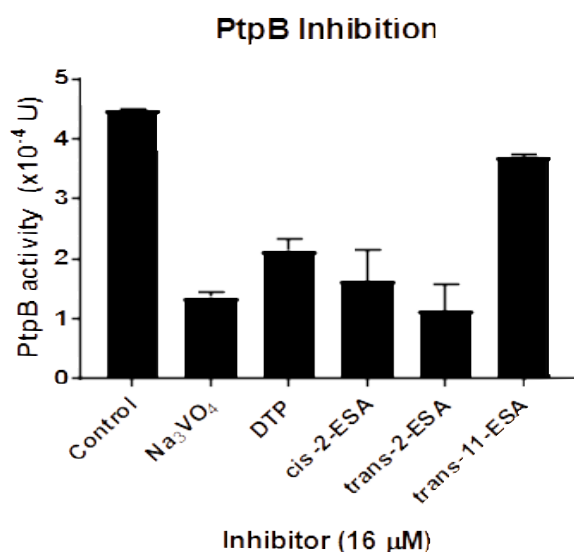
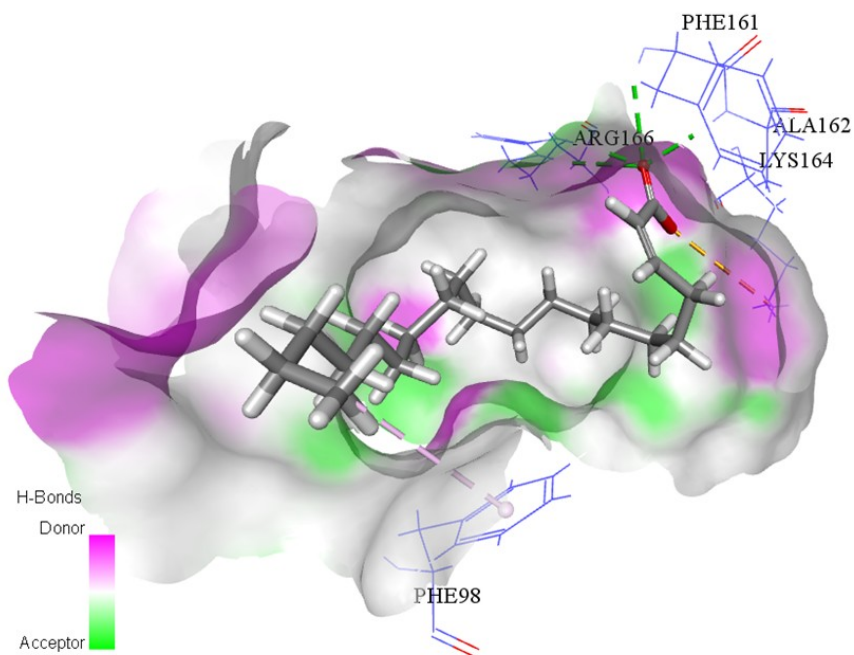


**Figure 2:** The activity of PtpB in the presence of several inhibitors.

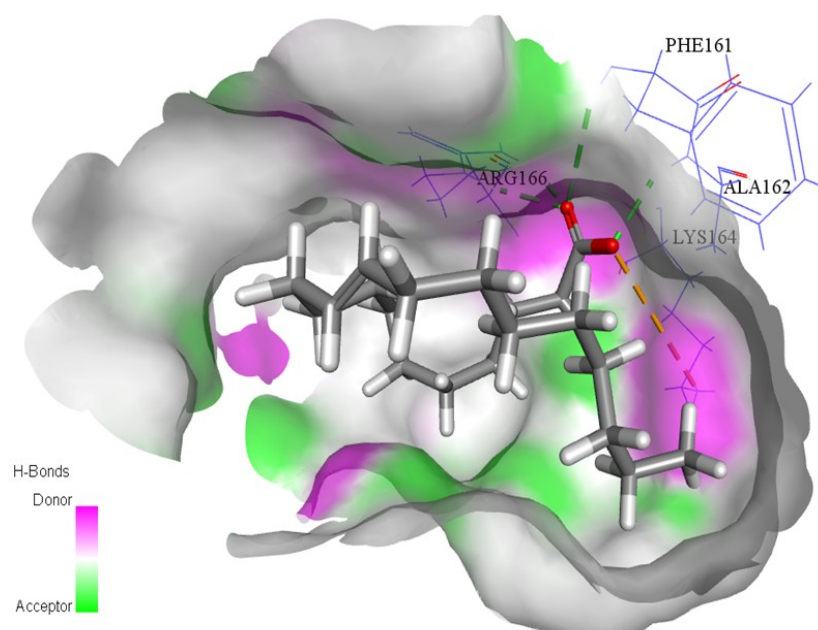
PtpB activity in the presence of several inhibitors at a concentration of 16 μM. Control: PtpB without inhibitor. Inhibition by sodium orthovanadate (Na<sub>3</sub>VO<sub>4</sub>), DTP, *cis*-2-eicosenoic fatty acid, *trans*-2-fatty acid, and *trans*-11-fatty acid correspond to 69.44%, 52.22%, 63.72%, 74.67% and 17.53%, respectively, with regard to control. All data are averages of two measurements. ESA: eicosenoic fatty acid.

To reveal the interaction between those inhibitors with PtpB, we performed a docking experiment. Figure 3A-B shows that both *cis*-2 and *trans*-2-eicosenoic acids fit the active site of the PtpB structure with the binding energy of -60.40 and -61.60 kcal/mol, consecutively. These values are closed to the cDock energy of native phosphate ligand of -81.47 kcal/mol; Table 2). This shows that both *cis*-2 and *trans*-2-eicosenoic fatty acids have stable interaction with PtpB. The strong interactions are supported by the presence of three and four hydrogen bonds between *cis*-2 and *trans*-2-eicosenoic fatty acids, respectively, with critical amino acids of PtpB. Besides, both hydrophobic inhibitors are assumed to have a pi stacking ( $\pi$ - $\pi$  stacking) interaction with the aromatic ring of Phe<sub>98</sub> residue. A weaker interaction of PtpB is observed with *trans*-11-eicosenoic fatty acid. Although *trans*-11-eicosenoic fatty acid forms three hydrogen bonds and an attractive charge interaction with PtpB, the lack of pi stacking interaction seems to be responsible for the weaker interaction (summarized in Table 2). Based on the binding energy and the presence of hydrogen bonds between *cis*-2 and *trans*-2-eicosenoic fatty acids with PtpB, it can be concluded that both fatty acids have high inhibition activity against the virulence factor of Mtb. This finding is also in agreement with the *in vitro* inhibition assay described in Figure 2.

### A. Complex of PtpB and *cis*-2-eicosenoic acid



### C. Complex of PtpB and *trans*-11-eicosenoic acid



## B. Complex of PtpB and *trans*-2-eicosenoic acid

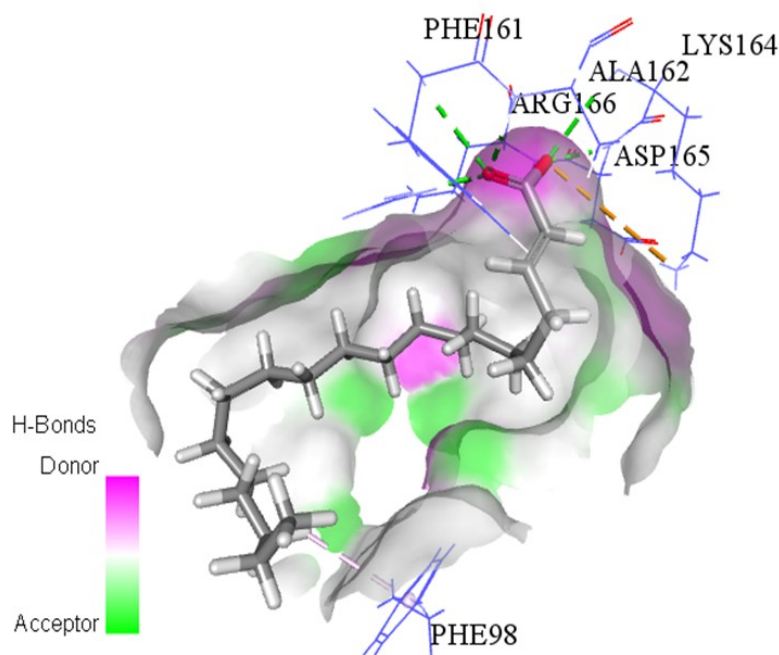


**Figure 3:** Docking of PtpB with selected inhibitors.

The strong interaction of PtpB with *cis*-2 and *trans*-2 eicosenoic fatty acids is supported by three potential hydrogen bonds of the protein through residues Phe<sub>161</sub>, Ala<sub>162</sub>, and Arg<sub>166</sub>. The interaction is also strengthened by the presence of attractive charge interaction with the positively charged residue Lys<sub>164</sub>, which is also observed with *trans*-11-eicosenoic fatty acid (A-C). An additional hydrogen bond between PtpB with *trans*-2-eicosenoic acid via Asp<sub>165</sub> (B) confirmed the more potent inhibitory effect of *trans*-2-eicosenoic acid than its *cis*-2 isomer (A). In contrast to the *cis*-2 and *trans*-2-eicosenoic fatty acids, a Pi stacking ( $\pi$ - $\pi$  stacking) interaction is absent in the docking of PtpB with *trans*-11-eicosenoic fatty acid (C).

**Table 2:** Docking parameters of PtpB with several inhibitors.

Compound	cDocker (kcal/mol)	Energy	Interaction
<i>cis</i> -2-eicosenoic acid	-60,3957		Hydrogen bonds: Phe <sub>161</sub> , Arg <sub>166</sub> , Ala <sub>162</sub> Pi stacking ( $\pi$ - $\pi$ stacking): Phe <sub>98</sub> Attractive Charge: Lys <sub>164</sub>
<i>trans</i> -2-eicosenoic acid	-61,6195		Hydrogen bonds: Phe <sub>161</sub> , Arg <sub>166</sub> , Ala <sub>162</sub> , Asp <sub>165</sub> Pi stacking ( $\pi$ - $\pi$ stacking): Phe <sub>98</sub> Attractive Charge: Lys <sub>164</sub>
<i>trans</i> -11-eicosenoic acid	-55,4227		Hydrogen bonds: Phe <sub>161</sub> , Arg <sub>166</sub> , Ala <sub>162</sub> Attractive Charge: Lys <sub>164</sub>
co-crystallized ligand PO <sub>4</sub> <sup>2-</sup>	-81,4651		Hydrogen bonds: Phe <sub>161</sub> , Ala <sub>162</sub> , Lys <sub>164</sub> , Asp <sub>165</sub> , His <sub>94</sub> , Pro <sub>81</sub> Pi stacking ( $\pi$ - $\pi$ stacking): Phe <sub>98</sub> , Tyr <sub>125</sub> , Leu <sub>227</sub> , Leu <sub>101</sub> , Val <sub>231</sub> Attractive Charge: Met <sub>126</sub>

Although the primary host substrate of PtpB is primarily unknown, accumulated evidence emphasizes the crucial role of PtpB in preventing the host degradative pathway (28). Hence, targeting PtpB to prevent the onset of latent

tuberculosis infection has lead to the screening of many potential inhibitors (29). Various types of compounds, either naturally occurring or modified compounds, have been reported to inhibit PtpB. A series of chalcones derivatives, for example, has

been reported to inhibit PtpB at low micromolar concentration, i.e., with  $IC_{50} < 30 \mu M$  (27). Further development has expanded the inhibition at submicromolar concentration, such as reported by Liu and coworkers who tested polypropionate derivatives isolated from deep-sea fungus to inhibit PtpB. They revealed that the compounds have  $IC_{50}$  in the range of 5.1 to 12  $\mu M$  (30). Here we demonstrated that *cis*-2 and *trans*-2-eicosenoic fatty acids strongly inhibit PtpB. This finding could be helpful for the development of drugs to prevent latent tuberculosis infection. Targeting PtpB offers an advantage since the protein is secreted into the macrophage's cytoplasm. There is no requirement that the inhibitor has to overcome the thick hydrophobic envelope of mycobacteria (14). Moreover, it is also worth considering alternative application strategies; for instance, using the potential inhibitors in combination with first-line TB drugs such as rifampicin and isoniazid as PtpB inhibitors were reported to enhance mycobacterial elimination (11,31). However, before further exploration, the selectivity of inhibition among human phosphatases might also be deemed necessary.

## CONCLUSION

The present study shows that both *cis*-2 and *trans*-2-eicosenoic fatty are able to inhibit Mtb PtpB. This is also the first report that long fatty acids can inhibit PtpB. The inhibitory potential was also supported by docking analysis. Further study can be directed to investigate whether these compounds can also inhibit macrophage cells or animal model infection by Mtb.

## ACKNOWLEDGMENTS

LRTS and JA received research funding through INSINAS research funding from the Ministry of Research, Technology, and Higher Education in the fiscal year of 2018. The authors thank Siti Rosidah from Bioscience and Biotechnology Research Center, the University of Mataram, for technical assistance.

## CONFLICT OF INTEREST

All authors declare no conflict of interest.

## REFERENCES

1. WHO. Global Tuberculosis Report [Internet]. World Health Organization; URL: <https://www.who.int/teams/global-tuberculosis-programme/tb-reports>.
2. Houben RMGJ, Dodd PJ. The Global Burden of Latent Tuberculosis Infection: A Re-estimation Using Mathematical Modelling. Metcalfe JZ, editor. PLoS Med. 2016 Oct 25;13(10):e1002152. DOI: <https://doi.org/10.1371/journal.pmed.1002152>.
3. Desjardins M, Huber L, Parton R, Griffiths G. Biogenesis of phagolysosomes proceeds through a sequential series of interactions with the endocytic apparatus. Journal of Cell Biology. 1994 Mar 1;124(5):677–88. DOI: <https://doi.org/10.1083/jcb.124.5.677>.
4. Upadhyay S, Mittal E, Philips JA. Tuberculosis and the art of macrophage manipulation. Pathogens and Disease [Internet]. 2018 Jun 1 [cited 2021 Jul 28];76(4): fty037. URL: <https://academic.oup.com/femspd/article/doi/10.1093/femspd/fty037/4970761>.
5. Pahari S, Kaur G, Negi S, Aqdas M, Das DK, Bashir H, et al. Reinforcing the Functionality of Mononuclear Phagocyte System to Control Tuberculosis. Front Immunol. 2018 Feb 9;9:193. DOI: <https://doi.org/10.3389/fimmu.2018.00193>.
6. Kansutton C, Jagannath C, Hunterjr R. Trehalose 6,6'-dimycolate on the surface of Mycobacterium tuberculosis modulates surface marker expression for antigen presentation and costimulation in murine macrophages. Microbes and Infection. 2009 Jan;11(1):40–8. DOI: <https://doi.org/10.1016/j.micinf.2008.10.006>.
7. Queval CJ, Brosch R, Simeone R. The Macrophage: A Disputed Fortress in the Battle against Mycobacterium tuberculosis. Front Microbiol. 2017 Nov 23;8:2284. DOI: <https://doi.org/10.3389/fmicb.2017.02284>.
8. Rankine-Wilson LI, Shapira T, Sao Emani C, Av-Gay Y. From infection niche to therapeutic target: the intracellular lifestyle of Mycobacterium tuberculosis. Microbiology [Internet]. 2021 Apr 7 [cited 2021 Jul 28];167(4). URL: <https://www.microbiologyresearch.org/content/journal/micro/10.1099/mic.0.001041>.
9. Stutz MD, Clark MP, Doerflinger M, Pellegrini M. Mycobacterium tuberculosis: Rewiring host cell signaling to promote infection. J Leukoc Biol. 2018 Feb;103(2):259–68. DOI: <https://doi.org/10.1002/JLB.4MR0717-277R>.
10. Salina EG, Mollenkopf HJ, Kaufmann SHE, Kaprelyants AS. M. tuberculosis Gene Expression during Transition to the "Non-Culturable" State. Acta Naturae. 2009 Jul;1(2):73–7. URL: <https://www.ncbi.nlm.nih.gov/pubmed/22649605>.
11. Dutta NK, He R, Pinn ML, He Y, Burrows F, Zhang Z-Y, et al. Mycobacterial Protein Tyrosine Phosphatases A and B Inhibitors Augment the Bactericidal Activity of the Standard Anti-tuberculosis Regimen. ACS Infect Dis. 2016 Mar 11;2(3):231–9. DOI: <https://doi.org/10.1021/acsinfecdis.5b00133>.

12. Cowley SC, Babakaiff R, Av-Gay Y. Expression and localization of the Mycobacterium tuberculosis protein tyrosine phosphatase PtpA. *Research in Microbiology*. 2002 May;153(4):233–41. DOI: [https://doi.org/10.1016/S0923-2508\(02\)01309-8](https://doi.org/10.1016/S0923-2508(02)01309-8).
13. Singh R, Rao V, Shakila H, Gupta R, Khera A, Dhar N, et al. Disruption of mptpB impairs the ability of Mycobacterium tuberculosis to survive in guinea pigs. *Molecular Microbiology*. 2003 Nov;50(3):751–62. DOI: <https://doi.org/10.1046/j.1365-2958.2003.03712.x>.
14. Wong D, Chao JD, Av-Gay Y. Mycobacterium tuberculosis-secreted phosphatases: from pathogenesis to targets for TB drug development. *Trends in Microbiology*. 2013 Feb;21(2):100–9. DOI: <https://doi.org/10.1016/j.tim.2012.09.002>.
15. Forrellad MA, Klepp LI, Gioffré A, Sabio y García J, Morbidoni HR, Santangelo M de la P, et al. Virulence factors of the Mycobacterium tuberculosis complex. *Virulence*. 2013 Jan;4(1):3–66. DOI: <https://doi.org/10.4161/viru.22329>.
16. Wong D, Bach H, Sun J, Hmama Z, Av-Gay Y. Mycobacterium tuberculosis protein tyrosine phosphatase (PtpA) excludes host vacuolar-H<sup>+</sup>-ATPase to inhibit phagosome acidification. *Proceedings of the National Academy of Sciences*. 2011 Nov 29;108(48):19371–6. DOI: <https://doi.org/10.1073/pnas.1109201108>.
17. Zhou B, He Y, Zhang X, Xu J, Luo Y, Wang Y, et al. Targeting mycobacterium protein tyrosine phosphatase B for antituberculosis agents. *Proceedings of the National Academy of Sciences*. 2010 Mar 9;107(10):4573–8. DOI: <https://doi.org/10.1073/pnas.0909133107>.
18. Fan L, Wu X, Jin C, Li F, Xiong S, Dong Y. MptpB Promotes Mycobacteria Survival by Inhibiting the Expression of Inflammatory Mediators and Cell Apoptosis in Macrophages. *Front Cell Infect Microbiol*. 2018 May 25;8:171. DOI: <https://doi.org/10.3389/fcimb.2018.00171>.
19. Savalas LRT, Furqon BRN, Asnawati D, 'Arduha J, Sedijani P, Hadisaputra S, et al. Cis-2 and trans-2-eisocenoic fatty acids are novel inhibitors for Mycobacterium tuberculosis Protein tyrosine phosphatase A. *Acta Biochim Pol* [Internet]. 2020 Jun 18 [cited 2021 Jul 28]; DOI: [https://doi.org/10.18388/abp.2020\\_5201](https://doi.org/10.18388/abp.2020_5201).
20. Mascarello A, Mori M, Chiaradia-Delatorre LD, Menegatti ACO, Monache FD, Ferrari F, et al. Discovery of Mycobacterium tuberculosis Protein Tyrosine Phosphatase B (PtpB) Inhibitors from Natural Products. *Maga G, editor. PLoS ONE*. 2013 Oct 14;8(10):e77081. DOI: <https://doi.org/10.1371/journal.pone.0077081>.
21. Huyer G, Liu S, Kelly J, Moffat J, Payette P, Kennedy B, et al. Mechanism of Inhibition of Protein-tyrosine Phosphatases by Vanadate and Pervanadate. *Journal of Biological Chemistry*. 1997 Jan;272(2):843–51. DOI: <https://doi.org/10.1074/jbc.272.2.843>.
22. Dhanjal JK, Grover S, Sharma S, Singh A, Grover A. Structural insights into mode of actions of novel natural Mycobacterium protein tyrosine phosphatase B inhibitors. *BMC Genomics*. 2014;15(Suppl 1):S3. DOI: <https://doi.org/10.1186/1471-2164-15-S1-S3>.
23. Laemmli UK. Cleavage of Structural Proteins during the Assembly of the Head of Bacteriophage T4. *Nature*. 1970 Aug;227(5259):680–5. DOI: <https://doi.org/10.1038/227680a0>.
24. Savalas LRT, Sedijani P, Hadisaputra S, Arduha J, Lestari CA, Wahidah EN. Expression of Mycobacterium tuberculosis Protein Tyrosine Phosphatase B in Escherichia coli and Its Recovery from Inclusion Body. *J Bio Bio Edu*. 2017 Dec 31;9(3):530. DOI: <https://doi.org/10.15294/biosaintifika.v9i3.12384>.
25. Pace CN, Grimsley GR, Scholtz JM, Shaw KL. Protein Stability. In: John Wiley & Sons Ltd, editor. *Protein Science Encyclopedia* [Internet]. Chichester, UK: John Wiley & Sons, Ltd; 2014 [cited 2021 Jul 28]. p. a0003002.pub3. URL: <https://onlinelibrary.wiley.com/doi/10.1002/9780470015902.a0003002.pub3>.
26. Mascarello A, Chiaradia LD, Vernal J, Villarino A, Guido RVC, Perizzolo P, et al. Inhibition of Mycobacterium tuberculosis tyrosine phosphatase PtpA by synthetic chalcones: Kinetics, molecular modeling, toxicity and effect on growth. *Bioorganic & Medicinal Chemistry*. 2010 Jun 1;18(11):3783–9. DOI: <https://doi.org/10.1016/j.bmc.2010.04.051>.
27. Chiaradia LD, Martins PGA, Cordeiro MNS, Guido RVC, Ecco G, Andricopulo AD, et al. Synthesis, Biological Evaluation, And Molecular Modeling of Chalcone Derivatives As Potent Inhibitors of Mycobacterium tuberculosis Protein Tyrosine Phosphatases (PtpA and PtpB). *J Med Chem*. 2012 Jan 12;55(1):390–402. DOI: <https://doi.org/10.1021/jm2012062>.
28. Chai Q, Wang L, Liu CH, Ge B. New insights into the evasion of host innate immunity by Mycobacterium tuberculosis. *Cell Mol Immunol*. 2020 Sep;17(9):901–13. DOI: <https://doi.org/10.1038/s41423-020-0502-z>.
29. Mascarello A, Mori M, Chiaradia-Delatorre LD, Menegatti ACO, Monache FD, Ferrari F, et al. Discovery of Mycobacterium tuberculosis Protein Tyrosine Phosphatase B (PtpB) Inhibitors from

Natural Products. Maga G, editor. PLoS ONE. 2013 Oct 14;8(10):e77081. DOI: <https://doi.org/10.1371/journal.pone.0077081>.

30. Liu Z, Wang Q, Li S, Cui H, Sun Z, Chen D, et al. Polypropionate Derivatives with Mycobacterium tuberculosis Protein Tyrosine Phosphatase B Inhibitory Activities from the Deep-Sea-Derived Fungus *Aspergillus fischeri* FS452. J Nat Prod. 2019

Dec 27;82(12):3440–9. DOI: <https://doi.org/10.1021/acs.jnatprod.9b00834>.

31. Vickers CF, Silva APG, Chakraborty A, Fernandez P, Kurepina N, Saville C, et al. Structure-Based Design of MtpB Inhibitors That Reduce Multidrug-Resistant Mycobacterium tuberculosis Survival and Infection Burden in Vivo. J Med Chem. 2018 Sep 27;61(18):8337–52. DOI: <https://doi.org/10.1021/acs.jmedchem.8b00832>.



## Turmeric (*Curcuma longa* L.): Chemical Components and Their Effective Clinical Applications

Thi Sinh Vo<sup>1\*</sup>  , Tran Thi Bich Chau Vo<sup>2</sup> , Tran Thi Thu Ngoc Vo<sup>3,4</sup> ,  
and Thi Ngoc Huyen Lai<sup>5</sup>

<sup>1</sup>School of Mechanical Engineering, Sungkyunkwan University, Suwon 16419, Korea.

<sup>2</sup>Department of Industrial Management, Can Tho University, Can Tho, Vietnam.

<sup>3</sup>Department of Acupuncture, Tuina and Moxibustion, Anhui University of Traditional Chinese Medicine, China.

<sup>4</sup>Qui Nhon City Hospital, Binh Dinh, Vietnam.

<sup>5</sup>School of Advance Materials Science & Engineering, Sungkyunkwan University, Suwon 16419, Korea.

**Abstract:** Turmeric (*Curcuma longa* L.) is widely utilized as a spice, food colorant, and preservative in India, China, and South-East Asia. With containing potential turmeric extracts and compounds, it has been utilized in traditional medicine for various diseases counting diabetes, hepatitis, hemorrhoids, hysteria, indigestion, skin disease, inflammation, anorexia, hepatic disorders, cough, and sinusitis, etc. So far, a large number of work has been conducted to find and prove biological activities and pharmacological applications of turmeric and its extracts in both animals and humans. In particular, curcumin (diferuloylmethane), a characteristic component with major yellow bioactive turmeric feature, has been found to possess numerous biological actions. Nonetheless, the polyphenol compound in curcumin has been limited for human disease treatments even though adequate studies are utilized in animal trials. Plenty of ongoing studies are also contributing significantly to this promising molecule that to the forefront of human therapeutics as well as its activities in health benefits. Thus, curcumin and some turmeric extracts are considered as non-toxic and highly promising compounds with a lot of potentially biological functions based on an appropriately used dose. It is expected that curcumin and some turmeric extracts can be explored in novel medical applications in the future to effectively against or treat various diseases. Here, we hope that it is likely a good and right approach for using and encouraging this product, and its chemical components and effective clinical applications will be briefly summarized in disease treatments.

**Keywords:** Turmeric, *Curcuma longa* L., curcumin, curcuminoids, disease.

**Submitted:** April 11, 2021. **Accepted:** July 26, 2021.

**Cite this:** Vo TS, Vo TTBC, Vo TTTN, Lai TNH. Turmeric (*Curcuma longa* L.): Chemical components and Their Effective Clinical Applications. JOTCSA. 2021;8(3):883-98.

**DOI:** <https://doi.org/10.18596/jotcsa.913136>.

**\*Corresponding author. E-mail:** [vtsinh92@skku.edu](mailto:vtsinh92@skku.edu).

### INTRODUCTION

There is a consecutive increase in treating various diseases based on natural products (herbs) in recent years. Primarily, *Curcuma longa* L. (Zingiberaceae – Ginger family) is known to be turmeric that is native to India, as well as which is cultivated and assigned everywhere tropical/subtropical regions and South East Asia (1, 2) (Figure 1). For *Curcuma longa*

plant, it has ovate or oblong leaves with light green and a spicy aroma while its flowers' color are lilac-white (3). Besides, its rhizomes accord flavorful yellow powder after dried and crushed (4), which have been extensively served with a long history in Chinese and Ayurvedic medicines (Indian system of Medicine, as a "cleanser of the body") (5) (Figure 1). It was probably cropped at first as a dye and later on, which was employed as cosmetic (i.e.,

aromatic food product). Similar to other herbal foods, people first utilized it as a food and later explored that it has effective medicinal actions; therefore, *Curcuma longa* L. has also attracted significant attention because of its colorant nature (6). This natural pigment is considered as a food colorant and as a material that enhances health or even healing diseases (7, 8), instead of synthetic dyes that can weaken the hepatic function and induce oxidative stress. There is currently numerous turmeric products marketed with various concentrations of extracted bioactive compounds (9), as well as plenty of studies demonstrated the high performance of bioactive compounds contained in this plant utilizing like anti-bacterial, anti-inflammatory, anti-oxidant and anti-carcinogenic agents. They were employed to be a herbal medicine to prevent premature aging and diseases (10-12). In particular, natural curcuminoids curcumin (i.e., diferuloylmethane, demethoxycurcumin, and bis-demethoxycurcumin) in turmeric are essentially found in rhizomes, natural monoterpenes are often in essential oils from flowers and leaves, and natural sesquiterpenes are essentially contained from roots and rhizomes. The curcuminoid curcumin contents are often different with various conditions (i.e., sources, locations, varieties, and cultivations), resulting in that the quality and quantity of commercial turmeric products can be significantly varied.

Additionally, *Curcuma longa* L. has found several biological and pharmacological activities leading to becoming an engaging nutraceutical for chemoprevention purposes or disease treatments (13), which have been attributed to natural curcuminoids; curcumin-containing phenolic compounds counted mainly of curcumin I, II, and III (i.e., diferuloylmethane, demethoxycurcumin, and bis-demethoxycurcumin) (14) (Figure 2). Nonetheless, in the curcuminoids, curcumin is poorly stable as well as reach low aqueous solubility (15). Actually, curcumin is unstable in basic solutions that break down easily (especially for non-solubility in acidic solutions), yielding mainly feruloylmethane, ferulic acid, and yellow-brown products (16), which induces its invalidation in pharmaceutical actions as well as its limitation in food industries (17, 18). This often confuses the solubility concept of curcumin; besides, curcumin can be changed to free-flowing micro-particles that support improving its solubility in both acidic media and aqueous stability overcome the above-

mentioned problems (19).

In addition to the above, the combination of turmeric extracts and chitosan films [i.e., antimicrobial, biocompatible, biodegradable, and eco-friendly features (20, 21)] was also investigated to evaluate the anti-bacterial and physical properties. Notably, biopolymers-based wound-healing materials have attached a significant consideration that can combine with curcumin or bioactive turmeric extracts for wound-healing applications to enhance their excellent performances (22). Theoretically, wound healing relates to multiple factors (i.e., growth factors and cytokines), such as cell populations, extracellular matrix, and soluble mediators. It can induce chronic wound growth if healing does not evolve a stepwise procedure. Especially, curcumin is one of them, used to treat dermal injury (23, 24) as well as a variety of diseases (i.e., asthma, hepatic disorders, diabetes, respiratory diseases, etc.). From *in vitro* or *in vivo* tests, curcumin prodded fibroblast proliferation, granulation tissue development and collagen deposition in cutaneous wound healing (23-25).

As known, coronavirus disease 2019 (COVID-19) was found first in Wuhan (China) at the end of 2019 like an infectious disease caused by severe acute respiratory syndrome coronavirus 2 (SARS-CoV-2), handwashing (soap and water/lukewarm water-based handwashing, or alcohol-based hand sanitizers) and wearing masks (cloth masks, medical masks, N95 respirators, and surgical masks) are currently one of the ways that can prevent the influenza virus infection (26, 27). Remarkably, turmeric is served as one of functional foods that can strengthen the immune system and treat respiratory diseases. People in the world are now self-isolating at their homes, the use of turmeric products may support enhancing the immune system and prevent SARS-CoV-2 infection through the daily diet, that may reduce the COVID-19 infection risk and a recovery in SARS-CoV-2 infection cases (28). Therefore, it is imperative to clearly understand its available chemical components and activities to can be utilized in bioactive and pharmacological applications after demonstrated its reliability. Herein, we hope that it is likely a good and right approach for using and encouraging this product, and its chemical components and effective clinical applications with appropriately used doses will be briefly summarized in disease treatments.

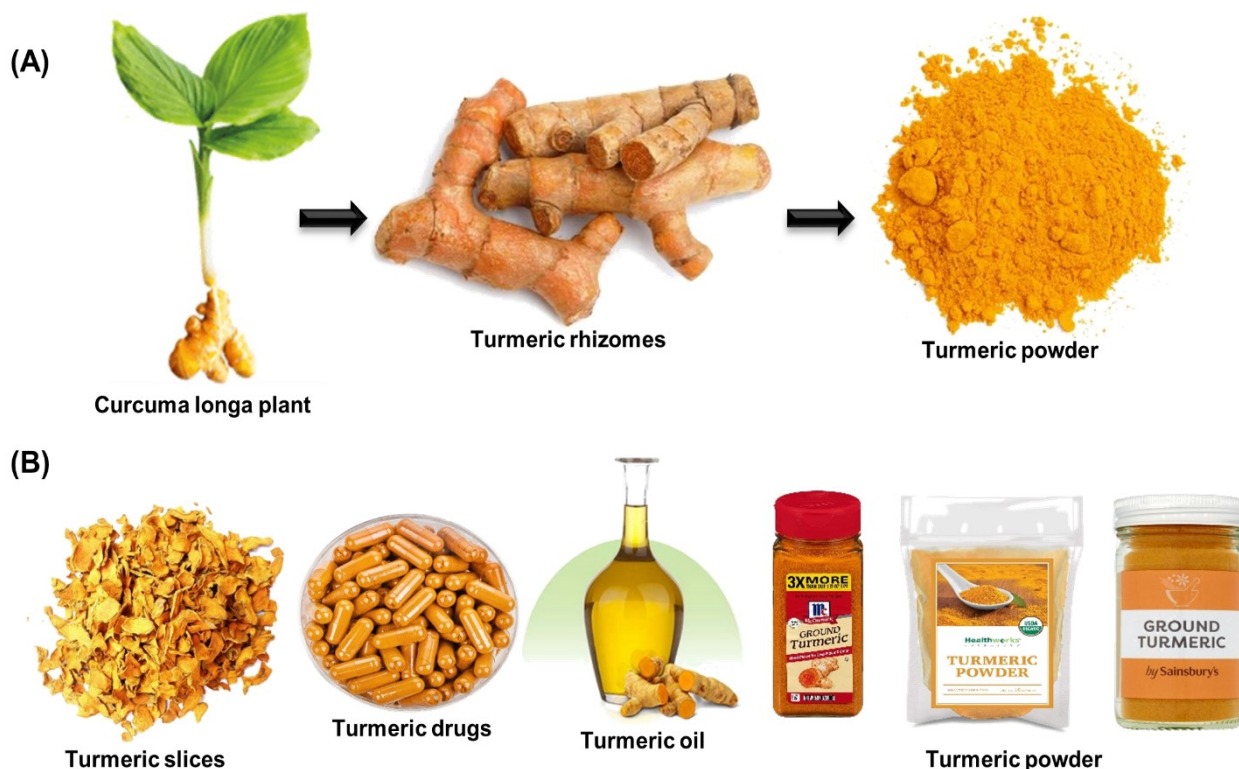


**Figure 1:** *Curcuma longa* L. – turmeric rhizomes and powder (A); and possibly commercial turmeric products (B).

**CHEMICAL COMPONENTS**

*Curcuma longa* L. was known as turmeric that was extensively served as a food colorant; nonetheless, it was considered to be plenty of possible biological and medicinal activities, such as anticancer, antioxidant, anti-inflammatory properties, etc. (Possible biological and medicinal activities of compounds/extracts from turmeric rhizomes are summarized in Table 1). The chemical structures of some available compounds (natural curcuminoids curcumin) are presented in Figure 2.

The quality and quantity of curcuminoids and chemical components of turmeric are significantly noticed to their performance in human disease treatments, for instance, the major bioactive properties in the turmeric rhizome are curcuminoids (14), phenolic acid and flavonoids (29). To maintain the quality of turmeric during storage and usage

processes, dehydration (moisture removal) is suggested as a main method for turmeric preservation (30), such as freeze-drying, low-temperature drying, and microwave-vacuum drying methods (31, 32). Among them, the common hot-air drying method is a good selection, owing to being a simple and easy process; however, if this method is conducted during a long time with high temperatures, it can degrade color, flavor, and bioactive compounds. For the freeze drying method, it is the most effective approach to maintain turmeric quality, but its disadvantages are high cost, long drying time, and high energy consumption. For the sun-drying method, it is known a traditional approach, which takes a long time that can reduce the product quality and bioactive compounds (32). Thereby, a more effective drying method is required to maintain expected quality as well as to preserve the major bioactive compounds in turmeric.

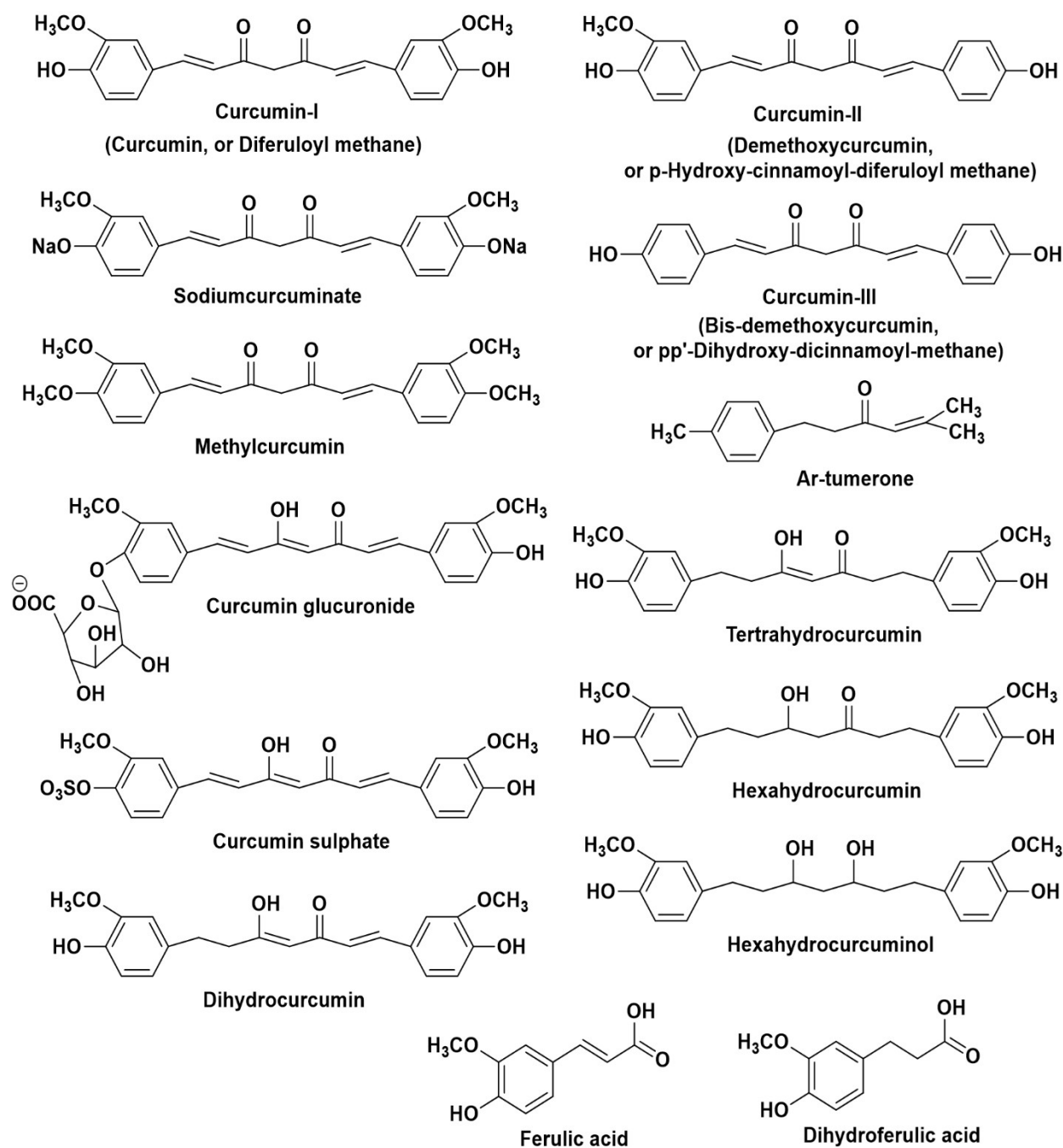


**Figure 2:** Chemical structures of natural curcuminoids and metabolites of curcumin.

Actually, turmeric from *Curcuma longa* L. contained carbohydrates (69.4%), protein (6.3%), fat (5.1%), minerals (3.5%), and moisture (13.1%), as well as its oil, could attain ~5.8% through steam distillation of turmeric rhizomes with borneol (0.5%),  $\alpha$ -phellandrene (1%), zingiberene (25%), sabinene (0.6%), cineole (1%), and sesquiterpenes (53%) (33). In particular, curcumin is a mixture of three curcuminoids [i.e., curcumin I ( $C_{21}H_{20}O_6$ , diferuloylmethane, 94%), curcumin II ( $C_{20}H_{18}O_5$ , demethoxycurcumin, 6%) and curcumin III ( $C_{19}H_{16}O_4$ , bis-demethoxycurcumin, 0.3%)] (14, 34) (Figure 2), which is considered a characteristic for

its yellow color. Besides, curcumin I ( $C_{21}H_{20}O_6$ , curcumin, diferuloylmethane) is a major curcuminoid, as well as phenolic -OH and -CH<sub>2</sub> groups in  $\beta$ -diketone moiety contained in these turmeric compounds, have been revealed to possess anti-inflammatory (35) and antioxidant (36) properties, and other effective bio-activities as shown in Table 1, leading to becoming an engaging nutraceutical for chemopreventive purposes or disease treatments.

Moreover, it is dissolved well in some organic solvents (methanol, ethanol, acetone, and dimethyl

sulfoxide, etc.) that can reach various derivatives/extracts, but they are insoluble in water. The use of solvents in extraction processes is one of important factors to achieve high performance and environment. To attain anti-oxidative extracts in *Curcuma longa* L., it is performed with conventional solvents (methanol, ethanol, and acetonitrile) (37, 38). In recent years, deep eutectic solvents (i.e., solvents based on an incorporation of a hydrogen bond acceptor and a hydrogen bond donor) (39, 40) are considered to be one of new classes of green solvents have emerged that is owing to non-toxic and biocompatible extraction procedures, which can cause less influence to environment and available nature of these bioactive compounds. In fact, the deep eutectic solvents can be prepared from the required purpose, especially for the extraction of bioactive compounds that are known as designer solvents. From solvent characteristics, there are current various hydrogen bond donors and hydrogen bond acceptors used to synthesize these deep eutectic solvents, such as choline chloride (41), menthol, and betaine (42), that for their combination can be sugars, carboxylic acids, alcohols, amines, or other compounds containing hydrogen bonds (41, 42). Other parameters are important in this approach, i.e., solute/solvent ratio, extraction temperature and time (43, 44). Particularly, some studies have conducted the extraction processes to attain bioactive compounds from turmeric based on the use of green solvents (45-47). For example, Oliveira et al. (48) investigated the deep eutectic solvents and various process conditions to extract bioactive compounds from the parts of *Curcuma longa* plant (i.e., leaves, rhizome, and flowers) that could be used as flavonoids, antioxidant, antimicrobial, chelation with Fe<sup>2+</sup>, inhibition of the cholinesterase enzymes,

cytotoxicity, and genotoxicity in *Allium cepa* cells. As a result, these extracts showed non-cytotoxicity, non-genotoxicity, chelation with iron and anti-bacterial features indicating a high potential application in the pharmaceutical industries.

In order to reach highly effective curcumin and some turmeric extracts in biological applications, it depends significantly on suitably used doses. Specifically, dietary use of curcumin/turmeric extracts with appropriate doses has also been indicated to inhibit tumor induction in various organs of mice (49-51) and rats (52). The use of curcumin (53) and turmeric extracts (54) with high doses on mice have not shown an increase in mortality as well; in contrast, those of turmeric oleoresin to pigs has been lowered the food-conversion efficiency (or weight gain) as well as raised the weight of the liver and thyroid leading to having histological changes in their kidney, liver, and urinary bladder (55). Besides, the use of turmeric extracts with high doses on mice has also been impacted strongly to the tissue weights, bodily weight gain, and levels of their red blood cells and white blood cells (54). Thereby, curcumin and some turmeric extracts are served as non-toxic and highly promising compounds with plenty of potentially biological functions based on an appropriately used dose. In addition to above-mentioned biological activities, turmeric has been found in traditional medicine and currently medicinal applications, such as anemia, indigestion, diabetes, hemorrhoids, edema, hepatitis, atherosclerosis, hysteria, wound and bruise healing, urinary disease, psoriasis, rheumatism, anorexia, dermal disease, inflammation, hepatic disorders, cough, sinusitis, etc. (56).

**Table 1:** Biological activities of turmeric compounds and extracts.

Compounds/extracts	Biological activities
<b>Turmeric powder</b>	Wound-healing (57)
<b>Alcoholic extract</b>	Anti-bacterial (58)
<b>Aqueous extract</b>	Anti-fertility (59)
<b>Ar-turmerone</b>	Anti-venom (60)
<b>Bis-demethoxycurcumin or Demethoxycurcumin</b>	Anti-oxidant (61)
<b>Crude etheric or Chloroform extracts</b>	Antifungal (62)
<b>Curcumin</b>	Anti-bacterial (63), anti-protozoan (58), anti-viral (64), hypolipemic (65), hypoglycemic (66), anti-coagulant (67), anti-oxidant (36), anti-tumor (68), anti-carcinogenic (69)
<b>Ethanollic extract</b>	Anti-inflammatory (70), hypolipemic (71), anti-tumor (72), anti-protozoan (73)
<b>Methyl curcumin</b>	Anti-protozoan (74)
<b>Petroleum ether extract</b>	Anti-inflammatory (70), anti-fertility (59)
<b>Sodium curcuminatate</b>	Anti-inflammatory (70), anti-bacterial (58)
<b>Volatile oil</b>	Anti-inflammatory, anti-bacterial (58), anti-fungal (75)

## EFFECTIVE CLINICAL STUDIES

Turmeric has been utilized much in Chinese and Ayurvedic medicines, at same time that various biological and pharmaceutical characterization (i.e., anti-inflammatory, antioxidant, anti-diabetic, anti-carcinogenic, anti-coagulant, anti-bacterial, anti-ulcer, antifungal, anti-fibrotic, hypotensive, antiviral, etc.) of curcumin and some turmeric extracts can contribute to being effective against or treating human diseases. Wherein, crude extracts from turmeric have reached high evaluations in numerous medicinal and clinical applications to can be applied in more extensive studies grounded on their bioactivity, mechanism of action, pharmacological effects, and toxic features. Also, curcumin can exist in a pure compound that shows lots of biological activities, which contribute to developing and expanding novel drugs from this compound based on its mechanism of action and pharmacological effects. Concomitantly, plenty of studies based on animal models have also contributed to building up a solid foundation that can evaluate well the safety and efficacy of curcumin to prevent and treat human diseases (Table 2).

Among them, turmeric extracts and curcumin have revealed possible activities that were utilized for both prevention and treatment of human diseases counting cancer (colorectal cancer, multiple myeloma, prostate cancer, oral cancer, pulmonary cancer, pancreatic cancer, etc.), peptic ulcer, ulcerative proctitis, atherosclerosis, gastric ulcer/inflammation, diabetes, diabetic nephropathy/micro-angiopathy, chronic bacterial prostatitis, etc. (56). As such, turmeric extracts and curcumin have used effectively in the treatment of human diseases, but their bioavailability are poor that can be due to poor absorption, rapid metabolism/systemic elimination inducing some restrictions of their therapeutic efficacies (76). On that basis, there were lots of approaches grounding on combinations of curcumin and several various appropriate components to can be served more effectively in the treatment of human diseases (76-79). Especially, the bioavailability of curcumin has been investigated to be significantly enhanced by considering curcumin and non-curcuminoid compounds of turmeric (80). The polyphenol compound in turmeric also causes several disadvantages in used curcumin doses, and its safety, efficacy, and a non-toxicity at appropriate doses have been suggested through human clinical trials.

In particular, Cheng et al. (81) conducted evaluations of the effectively used curcumin dose (8.0 g/day) in the pharmacokinetics, toxicology, and biological characterization of 25 patients with uterine cervical intraepithelial neoplasm, Bowen

disease of the skin, oral leucoplakia, cancer of the resected urinary bladder, or intestinal metaplasia of the stomach through the oral curcumin for 3 months. Besides, Dhillon *et al.* and Kanai *et al.* (82, 83) also investigated a combination of curcumin (8.0 g/day) and gemcitabine that was safe and effectively applied in >20 patients with pancreatic cancer. Curcumin containing polyphenol lowered the aberrant crypt foci formation (i.e., colorectal polyps' precursor) (84) in 44 smokers through oral curcumin for 30 days (2.0-4.0 g/day), as well as which indicated the effect of curcumin against and prevented an aberrant crypt formation of foci on smokers (84). In addition, 360.0 mg of curcumin in capsules was used for patients with colorectal cancer for 10-30 days (three times a day) (85), suggested that the use of curcumin in the colorectal cancer treatment could improve the patients' health (85). Polasa *et al.* (86) studied the treatment of pulmonary cancer in smokers based on the use of turmeric, resulting in that the urinary excretion of mutagens lowered significantly in these smokers.

Curcumin has not been only used alone, but also combined with other agents. For instance, oral curcumin and piperine have been combined effectively to treat pains and oxidative stress markers (malondialdehyde) in patients with tropical pancreatitis (60), resulting in the plasma malondialdehyde and erythrocyte glutathione levels lowered and increased, respectively; however, the pains were not improved (87). Curcumin also prevented prostate-specific antigen productions in men with high prostate-specific antigens (88); besides, 1.0 g of a curcumin pill for one week could enhance levels of vitamins C/E and reduce the contents of 8-hydroxydeoxyguanosine / malondialdehyde in patients with precancerous lesions (89). Furthermore, curcumin could be used as a maintenance medication for 89 patients with ulcerative colitis (90, 91), indicating that relapse rates in the curcumin-treated group (4.65%) were lower much than that in the placebo group (20.51%) (90, 91). Kedia et al. (92) conducted oral curcumin investigation according to mild-to-moderate level of ulcerative colitis (150 mg/trice/day; 8 weeks), indicating that low dose was ineffective in inducing remission in mild to moderate cases of ulcerative colitis, while oral curcumin (500.0 mg/day) and prednisone have been combined well together to treat a patient with ulcerative colitis by Lahiff et al. (93). Concomitantly, tetrahydrocurcuminoid and narrow-band ultraviolet B have been coupled together to against and treat vitiligo - a skin disorder (94), resulting significant improvements in the overall re-pigmentation degree of the combination group (94). Crohn's disease is a chronic relapsing inflammatory intestinal disease, which influences to the gastrointestinal tract (oral-anal). Holt *et al.* (95) investigated this disease through the use of curcumin, manifesting that there

are significant reduction in symptoms as well as inflammatory indices in all patients. In the case of gallbladder contraction, the use of curcumin could also impact to gallbladder through the studies of Rasyid *et al.* (96, 97). As a result, the gallbladder sizes lowered through an appropriately used curcumin dose (20.0-80.0 mg; 0.5-2 h). Niederau *et al.* (98) showed a faster reduction in dumpy and colicky pain of patients with biliary dyskinesia. For the cases of inflammatory diseases, use of curcumin also achieved effective performances in the recurrent and chronic anterior uveitis treatments. Ocular discomfort reduced after 12-18 months of the recurrent anterior uveitis treatment in more than 80.0% of patients (106 patients) (99), as well as there were not any adverse effect with efficacy and recurrent of disease (100). Besides, oral curcumin was applied for patients with peptic ulcer (101), gastric ulcer (102), and postoperative inflammation (103), resulting in that the ulcer formation reduced significantly (101, 102), as well as the anti-inflammatory property, exhibited superior comparing with phenylbutazone (103). Notably, a standardized preparation of curcuminoids was used in type 2 diabetes treatment of different oxidative stress (malondialdehyde) and inflammatory markers (104), leading to much improving for those markers in these patients. Particularly, the use of curcumin can show a promising and potential treatment for Alzheimer's disease (105, 106). Multiple myeloma (107) was also treated by use of curcumin for 6 months (4.0 g/day), indicating that para-protein load and urinary N-telopeptide of type I collagen in 26 patients decreased much; additionally, theracurmin (i.e., a well absorptive curcumin) dispersed well in colloidal nanoparticles that could inhibit alcoholic intoxication in humans (77).

In general, the use of curcumin has shown beneficial activities that could against or treat human diseases through the above mentions. Nonetheless, there were also several reported restrictions toward the uses of this polyphenol compound. Specifically, it could inhibit the activity of metabolizing enzymes *in vitro/animal* (108-110); in contrast, the use of curcumin to human-like drugs metabolized (i.e., acetaminophen, digoxin, and morphine) by these enzymes could lead to undesired results of them that might induce to toxic features. Curcumin could induce DNA damage in cells (111), leading to a common occurrence in carcinogenesis; concomitantly, it also served as an iron chelator that induced anemia in rats and mice (112). Furthermore, use of curcumin with high doses (0.45-3.6 g/day or 0.9-3.6 g/day) could induce nausea/diarrhea, as well as which raised lactate dehydrogenase and alkaline phosphatase amounts in humans (113, 114); besides, the used doses of curcumin was unallowable at a higher level

of 8.0 g/day in patients with premalignant lesions (81).

Remarkably, curcumin has been also suggested as a COVID-19 disease treatment to prevent the lethal influences of SARS-CoV-2 (115), which may be helpful to be a supportive part for other drugs that can probably prevent or treat the COVID-19 disease (116). A respiratory syncytial virus is recently noticed as a major threatening remark to human with various ages that induces acute respiratory infections. Chen *et al.* (117) demonstrated the influenza virus yield lowering >90.0% in cell culture through the use of curcumin ( $C_0 = 30 \mu\text{M}$ ) that could be due to the influences of viral protein synthesis (i.e., neuraminidase, hemagglutinins, and matrix protein). Likewise, curcumin could also inhibit the budding and replication in the nasal epithelial cells of humans leading to the improvement of the activities of an epithelial barrier to be effective against respiratory syncytial virus (118), as well as the oral curcumin effectively inhibited the inflammatory prostaglandin synthesis and neutrophil functions (119) reducing well desired-inflammation. Simultaneously, several curcumin derivatives have indicated with anti-viral properties; for example, a surveyed-neuraminidase process manifested that curcumin derivatives could reduce influenza A virus subtype H1N1 (H1N1) activation caused neuraminidase in lung cells with infected H1N1 (120). Moreover, turmeric compounds and extracts were also used to be effective against influenza A virus subtype H5N1 (H5N1) virus in Madin-Darby dog renal cells through intervening infectious hem-agglutination activities (*in vitro*) (121), or both the up-regulation of mRNA expressions (IFN- $\beta$  and TNF- $\alpha$ ) (122, 123) to be beneficial for recent disease outbreak cases. The use of curcumin is truly helpful in other viral troubles (i.e., acquired immunodeficiency syndrome, AIDS) (124) that regards to its inhibition activity on both human immunodeficiency virus type 1 (HIV) integrase and protease (125), and which was demonstrated to reduce the influenza virus-infected pulmonary tissue by hampering the NF- $\kappa\text{B}$  signals and preventing the inflammatory cytokines release (126, 127).

For the wound healing, oral administration and topical applications are the most common usages. Actually, the wound healing procedure is known a very complex approach, that regards to substance coagulation, inflammation, accumulation, formation of fibers tissues and collagen proliferation, contraction of wound, and granulation tissue and scar formation (128). In the case of treatment, curcumin has manifested a limitation in pharmaceutical feature, a low absorption in oral bioavailability, quick metabolism, and short half-life (76, 129). Concomitantly, curcumin has a very poor solubility in aqueous solution (nature of a

hydrophobic compound) that leads to be not appropriate for topical applications at wound regions, which can also induce a toxic response from the use of high concentrations (characterization of a polyphenolic compound) (130). Therefore, the therapeutic usefulness of curcumin in topical wound-healing applications has been developed on effective delivery systems, which is based on better curcumin solubilization to build a principle for stable and slow release of the soluble drug form. Curcumin can combine with several biopolymers to enhance the wound healing performance. Zhang et al. (131) conducted a chemical modification for curcumin compounds to apply effectively in the wound healing standardized in streptozotocin-induced diabetic rats, which achieved high performances through daily topical applications ( $C_0 = 1.0\%$  and  $3.0\%$ , over 7-10 days) or administered systemically (oral intubation; 30.0 mg/kg). Nano-formulated curcumin has also well inhibited methicillin-resistant *S. aureus*, and noticeably accelerated the wound healing process on wound mice (7.5 mg/mL, over 7 days) (132). Chereddy *et al.* (133) showed a potential capacity of poly(lactide-co-glycolide) nanoparticles loaded with

curcumin in the wound healing evaluation, as well as improved both the stability and solubility of curcumin. The gel-core hyalurosomes loaded curcumin also indicated a high healing performance for the burn wound on wound rats (134). These proposed that the nano-formulated curcumin can be utilized for preclinical applications in the future. The used curcumin doses have been proved to be similar effects in humans and remain to be explained. Additionally, a large number of studies have indicated in detail the safety and efficacy of this polyphenol in animals (i.e., monkeys, rodents, horses, cats, etc.) to offer a solid foundation for effective surveys in human clinical trials. In other words, this polyphenol's efficacy is needed more investigated before it can be applied for human disease treatment. In summary, the efficacy of curcumin and some turmeric extracts have prevented and treated human diseases that seem promising and potential. It is expected that quantities of ongoing studies can contribute significantly and reveal a detailed and more precise understanding of turmeric efficacy and its action to prevent and treat human diseases.

**Table 2:** Accomplished clinical studies using biological activities of turmeric.

Diseases	Number of patients	Dosages	Durations
<b>Colorectal cancer (84, 85)</b>	44 (84)	2.0-4.0 g/day (84)	1 month (84)
	126 (85)	1.08 g/day (85)	10-30 days (85)
<b>Cancer lesions (81, 89)</b>	25 (81)	8.0 g/day (81)	3 months (81)
	75 (89)	1.0 g/day (89)	7 days (89)
<b>Diabetes (104, 135)</b>	72 (104)	0.6 g/day (104)	8 weeks (104)
	14 (135)	6.0 g (135)	15-120 min (135)
<b>Diabetic micro-angiopathy (136)</b>	25	1.0 g/day	4 weeks
<b>Pancreatic cancer (82, 83, 87)</b>	25 (82)	8.0 g/day (82)	3 months
	21 (83)	8.0 g/day (83)	3 months
	20 (87)	1.5 g/day (87)	6 weeks (87)
<b>Prostatic cancer (88)</b>	85	0.1 g/day	6 months
<b>Pulmonary cancer (86)</b>	16	1.5 g/day	30 days
<b>Ulcerative colitis (90-93)</b>	89 (90, 91)	2.0 g/day (90, 91)	6 months (90, 91)
	1 (93)	0.5 g/day (93)	2-10 months (93)
	29 (92)	150 mg/thrice/day (92)	8 weeks (92)
<b>Vitiligo (94)</b>	10	Twice/day	12 weeks
<b>Alcohol intoxication (77)</b>	7	0.03 g/once	--
<b>Alzheimer's disease (105, 106)</b>	34 (105)	1.0-4.0 g/day (105)	6 months (105)
	33 (106)	2.0-4.0 g/day (106)	24 weeks (106)
<b>Peptic ulcer (101)</b>	45	3.0 g/day	4 weeks
<b>Gastric ulcer (102)</b>	60	1.0 g/day	6-12 weeks
<b>Postoperative inflammation (103)</b>	46	1.2 g/day	6 days
<b>Multiple myeloma (107)</b>	26	4.0 g/day	6 months
<b>Gallbladder contraction (96, 97)</b>	12	20.0-80.0 mg	0.5-2 h
<b>Acquired immunodeficiency syndrome (124)</b>	40	2.5 g/day	8 weeks
<b>Lupus nephritis (137)</b>	24	500.0 mg/day	3 months
<b>Atherosclerosis (138)</b>	10	0.5 g/day	7 days
<b>Acute coronary syndrome (139)</b>	70	0.045-0.18 g/day	2 months
<b>Dejerine-Sottas' disease (140)</b>	1	1.5 g/day	4 months

		2.5 g/day	8 months
<b>Crohn's disease (95, 141)</b>	5 (95) 31 (141)	1.08-1.44 g/day (95) 3.0 g/day (141)	1-2 months (95) 6 months (141)
<b>Ulcerative proctitis (95)</b>	5	1.1 g/day 1.65 g/day	1 month 1 month
<b>Recurrent anterior uveitis (99)</b>	106	1.2 g/day	12-18 months
<b>H. pylori infection (142)</b>	8	1.125 g/day	6-22 months
<b>Chronic anterior uveitis (100)</b>	53	1.125 g/day	12 weeks
<b>Rheumatoid arthritis (143-145)</b>	8 (143) 18 (144) 45 (145)	0.5 g in food (143) 1.2 g/day (144) 0.5 g/day (145)	2 weeks (144) 8 weeks (145)
<b>Osteoarthritis (146, 147)</b>	50 (146) 100 (147)	0.2 g/day (146) 1.0 g/day (147)	3 months (146) 8 months (147)

## CONCLUSION

In summary, turmeric (*Curcuma long L.*) has been directly employed in curries and other spicy dishes from India, China, and South East Asia, which has been proved the correlative bio-activities of curcumin in its possibly pharmaceutical applications that against or treat animal/human diseases. In addition to studies using curcumin in animal trials, it has already been revealed to be safe and effective at appropriately used doses through plenty of clinical trials; however, the polyphenolic compound has also been limited to treat or prevent some human diseases. Numerous studies regarded to absorption, metabolism, distribution, and excretion of curcumin indicated its poor absorption and fast metabolism that gravely restricts its available bioavailability; therefore, plenty of approaches based on a variety of combination between curcumin and several various appropriate components to can be applied in the effective treatment of human diseases. Simultaneously, a large number of ongoing studies can contribute significantly to this promising molecule at the forefront of human therapeutics. Thereby, curcumin and some turmeric extracts are considered as non-toxic and highly promising compounds with a lot of potentially biological functions that based on an appropriately used dose. For further understanding and suitable judgment in medical care, it is expected that curcumin and some turmeric extracts can be explored in novel medical applications in the future to effectively against or treat various human diseases.

## REFERENCES

- Began G, Goto M, Kodama A, Hirose T. Response surfaces of total oil yield of turmeric (*Curcuma longa*) in supercritical carbon dioxide. *Food Research International*. 2000 Jun;33(5):341-5. [<DOI>](#).
- Goel A, Kunnumakkara AB, Aggarwal BB. Curcumin as "Curecumin": From kitchen to clinic. *Biochemical Pharmacology*. 2008 Feb;75(4):787-809. [<DOI>](#).
- Chan EWC, Lim YY, Wong SK, Lim KK, Tan SP, Lianto FS, et al. Effects of different drying methods on the antioxidant properties of leaves and tea of ginger species. *Food Chemistry*. 2009 Mar;113(1):166-72. [<DOI>](#).
- Himesh S, Sharan PS, Mishra K, Govind N, Singhai A. Qualitative and quantitative profile of curcumin from ethanolic extract of *Curcuma longa*. *Int Res J Pharm*. 2011;2(4):180-4.
- Joshi P, Jain S, Sharma V. Turmeric (*Curcuma longa*) a natural source of edible yellow colour. *International Journal of Food Science & Technology*. 2009 Dec;44(12):2402-6. [<DOI>](#).
- Aggarwal BB, Kumar A, Bharti AC. Anticancer potential of curcumin: preclinical and clinical studies. *Anticancer research*. 2003;23(1/A):363-98.
- Amin KA, Abdel Hameid H, Abd Elsttar AH. Effect of food azo dyes tartrazine and carmoisine on biochemical parameters related to renal, hepatic function and oxidative stress biomarkers in young male rats. *Food and Chemical Toxicology*. 2010 Oct;48(10):2994-9. [<DOI>](#).
- Downham A, Collins P. Colouring our foods in the last and next millennium. *International Journal of Food Science & Technology*. 2000 Feb;35(1):5-22. [<DOI>](#).
- Chatzinasiou L, Booker A, MacLennan E, Mackonochie M, Heinrich M. Turmeric (*Curcuma longa L.*) products: What quality differences exist? *Journal of Herbal Medicine*. 2019 Sep;17-18:100281. [<DOI>](#).
- Bavarsad K, Riahi MM, Saadat S, Barreto G, Atkin SL, Sahebkar A. Protective effects of curcumin against ischemia-reperfusion injury in the liver. *Pharmacological Research*. 2019 Mar;141:53-62. [<DOI>](#).
- Grover M, Shah K, Khullar G, Gupta J, Behl T. Investigation of the utility of *Curcuma caesia* in

- the treatment of diabetic neuropathy. *Journal of Pharmacy and Pharmacology*. 2019 Apr 12;71(5):725–32. [<DOI>](#).
12. Kwiecien S, Magierowski M, Majka J, Ptak-Belowska A, Wojcik D, Sliwowski Z, et al. Curcumin: A Potent Protectant against Esophageal and Gastric Disorders. *IJMS*. 2019 Mar 24;20(6):1477. [<DOI>](#).
  13. Gosslau A, Chen KY. Nutraceuticals, apoptosis, and disease prevention. *Nutrition*. 2004 Jan;20(1):95–102. [<DOI>](#).
  14. Maheshwari RK, Singh AK, Gaddipati J, Srimal RC. Multiple biological activities of curcumin: A short review. *Life Sciences*. 2006 Mar;78(18):2081–7. [<DOI>](#).
  15. Araújo RR, Teixeira CCC, Freitas LAP. The Preparation of Ternary Solid Dispersions of an Herbal Drug via Spray Drying of Liquid Feed. *Drying Technology*. 2010 Mar 8;28(3):412–21. [<DOI>](#).
  16. Price LC, Buescher RW. Kinetics of Alkaline Degradation of the Food Pigments Curcumin and Curcuminoids. *J Food Science*. 1997 Mar;62(2):267–9. [<DOI>](#).
  17. Surojanametakul V, Satmalee P, Saengprakai J, Siliwan D, Wattanasiritham L. Preparation of Curcuminoid Powder from Turmeric Root (*Curcuma longa* Linn) for Food Ingredient Use. *Kasetsart J (Nat Sci)*. 2010;44(1):123–30. [<URL>](#).
  18. Wang Y, Lu Z, Wu H, Lv F. Study on the antibiotic activity of microcapsule curcumin against foodborne pathogens. *International Journal of Food Microbiology*. 2009 Nov;136(1):71–4. [<DOI>](#).
  19. Paradkar A, Ambike AA, Jadhav BK, Mahadik KR. Characterization of curcumin–PVP solid dispersion obtained by spray drying. *International Journal of Pharmaceutics*. 2004 Mar;271(1–2):281–6. [<DOI>](#).
  20. Vo TS, Vo TTBC, Suk JW, Kim K. Recycling performance of graphene oxide-chitosan hybrid hydrogels for removal of cationic and anionic dyes. *Nano Convergence*. 2020 Dec;7(1):4. [<DOI>](#).
  21. Vo TS, Hossain MM, Jeong HM, Kim K. Heavy metal removal applications using adsorptive membranes. *Nano Convergence*. 2020 Dec;7(1):36. [<DOI>](#).
  22. Sharma A, Khanna S, Kaur G, Singh I. Medicinal plants and their components for wound healing applications. *Futur J Pharm Sci*. 2021 Dec;7(1):53. [<DOI>](#).
  23. Nachimuthu S, Sundar M, Manikavasagam K, Sadhasivam B, Veerachetty V, Ponnusamy R, et al. In Vivo Wound Healing Study of Chitosan Turmeric Films in Rat Model. *Journal of Chemical and Pharmaceutical Sciences*. 2018;(4):268–73.
  24. Saraswathy N, Rohit R, Shanmugam K, Sozheeswari S, Ramalingam P. A preliminary investigation of Turmeric-Agar composite film as bioactive wound dressing material on excision wound in rat model. *Indian Journal of Natural Products and Resources (IJNPR)*. 2012;3(2):237–41. [<URL>](#).
  25. Gopinath D, Ahmed MR, Gomathi K, Chitra K, Sehgal PK, Jayakumar R. Dermal wound healing processes with curcumin incorporated collagen films. *Biomaterials*. 2004 May;25(10):1911–7. [<DOI>](#).
  26. Vo TS, Vo TTTN, Vo TTBC. Coronavirus Infection Prevention by Wearing Masks. *Eurasian J Med*. 2020 Jun;52(2):197–201. [<DOI>](#).
  27. Vo TS, Vo TTTN, Vo TTBC. Handwashing in against of coronavirus disease 2019 infection. *J Res Clin Med*. 2020 May 18;8(1):19–19. [<DOI>](#).
  28. Yang F, Zhang Y, Tariq A, Jiang X, Ahmed Z, Zhihao Z, et al. Food as medicine: A possible preventive measure against coronavirus disease ( COVID -19). *Phytotherapy Research*. 2020 Dec;34(12):3124–36. [<DOI>](#).
  29. Sarker S, Nahar L. Bioactivity of turmeric. In: Ravindran P, Nirmal Babu K, Sivaraman K, editors. *Turmeric the genus Curcuma*. CRC Press; 2007. p. 257–96. ISBN: 978-1-4200-0632-2.
  30. Flores NC, Davies CS. *Drying Foods* [Internet]. College of Agricultural, Consumer and Environmental Sciences; 2016. (Guide (New Mexico State University. Cooperative Extension Service)). [<URL>](#).
  31. Hirun S, Utama-ang N, Roach PD. Turmeric (*Curcuma longa* L.) drying: an optimization approach using microwave-vacuum drying. *J Food Sci Technol*. 2014 Sep;51(9):2127–33. [<DOI>](#).
  32. Prathapan A, Likhman M, Arumughan C, Sundaresan A, Raghu KG. Effect of heat treatment on curcuminoid, colour value and total polyphenols of fresh turmeric rhizome. *International Journal of Food Science & Technology*. 2009 Jul;44(7):1438–44. [<DOI>](#).
  33. Kapoor LD. *CRC Handbook of Ayurvedic Medicinal Plants* [Internet]. 1st ed. CRC Press; 2018. [<URL>](#). ISBN: 978-1-351-07099-7.
  34. Ruby AJ, Kuttan G, Dinesh Babu K, Rajasekharan KN, Kuttan R. Anti-tumour and

- antioxidant activity of natural curcuminoids. *Cancer Letters*. 1995 Jul;94(1):79–83. [<DOI>](#).
35. Wang X, Jiang Y, Wang Y-W, Huang M-T, Ho C-T, Huang Q. Enhancing anti-inflammation activity of curcumin through O/W nanoemulsions. *Food Chemistry*. 2008 May;108(2):419–24. [<DOI>](#).
36. Jayaprakasha GK, Jaganmohan Rao L, Sakariah KK. Antioxidant activities of curcumin, demethoxycurcumin and bisdemethoxycurcumin. *Food Chemistry*. 2006 Jan;98(4):720–4. [<DOI>](#).
37. Braga MC, Vieira ECS, de Oliveira TF. *Curcuma longa* L. leaves: Characterization (bioactive and antinutritional compounds) for use in human food in Brazil. *Food Chemistry*. 2018 Nov;265:308–15. [<DOI>](#).
38. Pal K, Chowdhury S, Dutta SK, Chakraborty S, Chakraborty M, Pandit GK, et al. Analysis of rhizome colour content, bioactive compound profiling and ex-situ conservation of turmeric genotypes (*Curcuma longa* L.) from sub-Himalayan terai region of India. *Industrial Crops and Products*. 2020 Aug;150:112401. [<DOI>](#).
39. Martins MAR, Pinho SP, Coutinho JAP. Insights into the Nature of Eutectic and Deep Eutectic Mixtures. *J Solution Chem*. 2019 Jul;48(7):962–82. [<DOI>](#).
40. Makoś P, Słupek E, Gębicki J. Hydrophobic deep eutectic solvents in microextraction techniques—A review. *Microchemical Journal*. 2020 Jan;152:104384. [<DOI>](#).
41. Vilková M, Płotka-Wasyłka J, Andruch V. The role of water in deep eutectic solvent-base extraction. *Journal of Molecular Liquids*. 2020 Apr;304:112747. [<DOI>](#).
42. Florindo C, Branco LC, Marrucho IM. Development of hydrophobic deep eutectic solvents for extraction of pesticides from aqueous environments. *Fluid Phase Equilibria*. 2017 Sep;448:135–42. [<DOI>](#).
43. Patil SS, Rathod VK. Synergistic Effect of Ultrasound and Three Phase Partitioning for the Extraction of Curcuminoids from *Curcuma longa* and its Bioactivity Profile. *Process Biochemistry*. 2020 Jun;93:85–93. [<DOI>](#).
44. Shirsath SR, Sable SS, Gaikwad SG, Sonawane SH, Saini DR, Gogate PR. Intensification of extraction of curcumin from *Curcuma amada* using ultrasound assisted approach: Effect of different operating parameters. *Ultrasonics Sonochemistry*. 2017 Sep;38:437–45. [<DOI>](#).
45. Altunay N, Elik A, Gürkan R. Preparation and application of alcohol based deep eutectic solvents for extraction of curcumin in food samples prior to its spectrophotometric determination. *Food Chemistry*. 2020 Apr;310:125933. [<DOI>](#).
46. Aydin F, Yilmaz E, Soylak M. Vortex assisted deep eutectic solvent (DES)-emulsification liquid-liquid microextraction of trace curcumin in food and herbal tea samples. *Food Chemistry*. 2018 Mar;243:442–7. [<DOI>](#).
47. Liu Y, Li J, Fu R, Zhang L, Wang D, Wang S. Enhanced extraction of natural pigments from *Curcuma longa* L. using natural deep eutectic solvents. *Industrial Crops and Products*. 2019 Nov;140:111620. [<DOI>](#).
48. Oliveira G, Marques C, de Oliveira A, de Almeida dos Santos A, do Amaral W, Ineu RP, et al. Extraction of bioactive compounds from *Curcuma longa* L. using deep eutectic solvents: In vitro and in vivo biological activities. *Innovative Food Science & Emerging Technologies*. 2021 Jun;70:102697. [<DOI>](#).
49. Azuine MA, Bhide SV. Chemopreventive effect of turmeric against stomach and skin tumors induced by chemical carcinogens in Swiss mice. *Nutrition and Cancer*. 1992 Jan;17(1):77–83. [<DOI>](#).
50. Huang M-T, You Y-R, Ma W, Newmark H, Reuhl K, Conney A. Inhibitory Effects of Dietary Curcumin on Forestomach, Duodenal, and Colon Carcinogenesis in Mice. *Cancer Research*. 1994;54(22):5841–7. [<URL>](#).
51. Deshpande SS, Ingle AD, Maru GB. Inhibitory effects of curcumin-free aqueous turmeric extract on benzo[a]pyrene-induced forestomach papillomas in mice. *Cancer Letters*. 1997 Sep;118(1):79–85. [<DOI>](#).
52. Rao CV, Rivenson A, Simi B, Reddy BS. Chemoprevention of colon carcinogenesis by dietary curcumin, a naturally occurring plant phenolic compound. *Cancer Research*. 1995 Jan;55(2):259–66.
53. Srimal RC, Dhawan BN. Pharmacology of diferuloyl methane (curcumin), a non-steroidal anti-inflammatory agent. *Journal of pharmacy and pharmacology*. 1973 Jun;25(6):447–52. [<DOI>](#).
54. Qureshi S, Shah AH, Ageel AM. Toxicity studies on *Alpinia galanga* and *Curcuma longa*. *Planta Medica*. 1992 Apr;58(2):124–7. [<DOI>](#).
55. Bille N, Larsen JC, Hansen EV, Würtzen G. Subchronic oral toxicity of turmeric oleoresin in pigs.

- Food and Chemical Toxicology. 1985 Nov;23(11):967-73. [<DOI>](#).
56. Ammon H, Anazodo M, Safayhi H, Dhawan B, Srimal R. Curcumin: A Potent Inhibitor of Leukotriene B 4 Formation in Rat Peritoneal Polymorphonuclear Neutrophils (PMNL). *Planta Medica*. 1992 Apr;58(02):226-226. [<DOI>](#).
57. Barchitta M, Maugeri A, Favara G, Magnano San Lio R, Evola G, Agodi A, et al. Nutrition and Wound Healing: An Overview Focusing on the Beneficial Effects of Curcumin. *International Journal of Molecular Sciences*. 2019 Jan;20(5):1119. [<DOI>](#).
58. Bhavani Shankar TN, Sreenivasa Murthy V. Effect of turmeric (*Curcuma longa*) fractions on the growth of some intestinal & pathogenic bacteria in vitro. *Indian Journal of Experimental Biology*. 1979 Dec;17(12):1363-6.
59. Garg SK. Effect of curcuma longa (rhizomes) on fertility in experimental animals. *Planta Medica*. 1974 Nov;26(7):225-7. [<DOI>](#).
60. Ferreira LAF, Henriques OB, Andreoni AAS, Vital GRF, Campos MMC, Habermehl GG, et al. Antivenom and biological effects of ar-turmerone isolated from *Curcuma longa* (Zingiberaceae). *Toxicon*. 1992 Oct;30(10):1211-8. [<DOI>](#).
61. Unnikrishnan MK, Rao MN. Inhibition of nitrite induced oxidation of hemoglobin by curcuminoids. *Die Pharmazie*. 1995 Jul;50(7):490-2.
62. Misra SK, Sahu KC. Screening of some indigenous plants for antifungal activity against dermatophytes. *Indian Journal of Pharmacology*. 1977 Jan;9(4):269.
63. Lutomski J, Kedzia B, Debska W. Wirkung des äthanolextraktes und aktiver substanzen aus curcuma longa auf bakterien und pilze. *Planta Medica*. 1974 Aug;26(5):9-19. [<DOI>](#).
64. Mazumder A, Raghavan K, Weinstein J, Kohn KW, Pommier Y. Inhibition of human immunodeficiency virus type-1 integrase by curcumin. *Biochemical Pharmacology*. 1995 Apr;49(8):1165-70. [<DOI>](#).
65. Rao DS, Sekhara NC, Satyanarayana MN, Srinivasan M. Effect of Curcumin on Serum and Liver Cholesterol Levels in the Rat. *The Journal of Nutrition*. 1970 Nov;100(11):1307-15. [<DOI>](#).
66. Błasiak J, Trzeciak A, Małecka-Panas E, Drzewoski J, Iwanienko T, Szumiel I, et al. DNA damage and repair in human lymphocytes and gastric mucosa cells exposed to chromium and curcumin. *Teratogenesis, Carcinogenesis, and Mutagenesis*. 1999;19(1):19-31. [<DOI>](#).
67. Srivastava R, Dikshit M, Srimal RC, Dhawan BN. Anti-thrombotic effect of curcumin. *Thrombosis Research*. 1985 Nov;40(3):413-7. [<DOI>](#).
68. Deeb D, Xu YX, Jiang H, Gao X, Janakiraman N, Chapman RA, et al. Curcumin (Diferuloyl-Methane) Enhances Tumor Necrosis Factor-related Apoptosis-inducing Ligand-induced Apoptosis in LNCaP Prostate Cancer Cells1. *Molecular Cancer Therapeutics*. 2003 Jan;2(1):95-103. [<URL>](#).
69. Chen H-W, Huang H-C. Effect of curcumin on cell cycle progression and apoptosis in vascular smooth muscle cells: Curcumin effects on cell cycle and apoptosis. *British Journal of Pharmacology*. 1998 Jul;124(6):1029-40. [<DOI>](#).
70. Yegnanarayan R, Saraf AP, Balwani JH. Comparison of anti-inflammatory activity of various extracts of *Curcuma longa* (Linn). *Indian Journal of Medical Research*. 1976 Apr;64(4):601-8.
71. Dixit VP, Jain P, Joshi SC. Hypolipidaemic effects of *Curcuma longa* L and *Nardostachys jatamansi*, DC in triton-induced hyperlipidaemic rats. *Indian Journal of Physiology and Pharmacology*. 1988 Dec;32(4):299-304.
72. Kuttan R, Bhanumathy P, Nirmala K, George MC. Potential anticancer activity of turmeric (*Curcuma longa*). *Cancer Letters*. 1985 Nov;29(2):197-202. [<DOI>](#).
73. Rastogi RP, Dhawan BN. Anticancer and antiviral activities in indian medicinal plants: A review. *Drug Development Research*. 1990;19(1):1-12. [<DOI>](#).
74. Rasmussen H, Christensen S, Kvist L, Karazmi A. A Simple and Efficient Separation of the Curcumins, the Antiprotozoal Constituents of *Curcuma longa*. *Planta Medica*. 2000 Dec;66(04):396-8. [<DOI>](#).
75. Manzan ACCM, Toniolo FS, Bredow E, Povh NP. Extraction of Essential Oil and Pigments from *Curcuma longa* [L.] by Steam Distillation and Extraction with Volatile Solvents. *Journal of Agricultural and Food Chemistry*. 2003 Nov;51(23):6802-7. [<DOI>](#).
76. Anand P, Kunnumakkara AB, Newman RA, Aggarwal BB. Bioavailability of Curcumin: Problems and Promises. *Molecular Pharmaceutics*. 2007 Dec;4(6):807-18. [<DOI>](#).

77. Sasaki H, Sunagawa Y, Takahashi K, Imaizumi A, Fukuda H, Hashimoto T, et al. Innovative Preparation of Curcumin for Improved Oral Bioavailability. *Biological & Pharmaceutical Bulletin*. 2011;34(5):660-5. [<DOI>](#).
78. Gota VS, Maru GB, Soni TG, Gandhi TR, Kochar N, Agarwal MG. Safety and Pharmacokinetics of a Solid Lipid Curcumin Particle Formulation in Osteosarcoma Patients and Healthy Volunteers. *Journal of Agricultural and Food Chemistry*. 2010 Feb;58(4):2095-9. [<DOI>](#).
79. Cuomo J, Appendino G, Dern AS, Schneider E, McKinnon TP, Brown MJ, et al. Comparative Absorption of a Standardized Curcuminoid Mixture and Its Lecithin Formulation. *Journal of Natural Products*. 2011 Apr;74(4):664-9. [<DOI>](#).
80. Antony B, Merina B, Iyer VS, Judy N, Lennertz K, Joyal S. A Pilot Cross-Over Study to Evaluate Human Oral Bioavailability of BCM-95®CG (Biocurcumin™), A Novel Bioenhanced Preparation of Curcumin. *Indian Journal of Pharmaceutical Sciences*. 2008;70(4):445-9. [<DOI>](#).
81. Cheng AL, Hsu CH, Lin JK, Hsu MM, Ho YF, Shen TS, et al. Phase I clinical trial of curcumin, a chemopreventive agent, in patients with high-risk or pre-malignant lesions. *Anticancer Research*. 2001 Aug;21(4B):2895-900.
82. Dhillon N, Aggarwal BB, Newman RA, Wolff RA, Kunnumakkara AB, Abbruzzese JL, et al. Phase II trial of curcumin in patients with advanced pancreatic cancer. *Clinical Cancer Research*. 2008 Jul;14(14):4491-9. [<DOI>](#).
83. Kanai M, Yoshimura K, Asada M, Imaizumi A, Suzuki C, Matsumoto S, et al. A phase I/II study of gemcitabine-based chemotherapy plus curcumin for patients with gemcitabine-resistant pancreatic cancer. *Cancer Chemotherapy and Pharmacology*. 2011 Jul;68(1):157-64. [<DOI>](#).
84. Carroll RE, Benya RV, Turgeon DK, Vareed S, Neuman M, Rodriguez L, et al. Phase IIa Clinical Trial of Curcumin for the Prevention of Colorectal Neoplasia. *Cancer prevention research (Philadelphia, Pa)*. 2011 Mar;4(3):354-64. [<DOI>](#).
85. He Z-Y, Shi C-B, Wen H, Li F-L, Wang B-L, Wang J. Upregulation of p53 Expression in Patients with Colorectal Cancer by Administration of Curcumin. *Cancer Investigation*. 2011 Feb;29(3):208-13. [<DOI>](#).
86. Polasa K, Raghuram TC, Krishna TP, Krishnaswamy K. Effect of turmeric on urinary mutagens in smokers. *Mutagenesis*. 1992;7(2):107-9. [<DOI>](#).
87. Durgaprasad S, Pai CG, Vasanthkumar null, Alvres JF, Namitha S. A pilot study of the antioxidant effect of curcumin in tropical pancreatitis. *The Indian Journal of Medical Research*. 2005 Oct;122(4):315-8.
88. Ide H, Tokiwa S, Sakamaki K, Nishio K, Isotani S, Muto S, et al. Combined inhibitory effects of soy isoflavones and curcumin on the production of prostate-specific antigen. *The Prostate*. 2010 Jul;70(10):1127-33. [<DOI>](#).
89. Rai B, Kaur J, Jacobs R, Singh J. Possible action mechanism for curcumin in pre-cancerous lesions based on serum and salivary markers of oxidative stress. *Journal of Oral Science*. 2010 Jun;52(2):251-6. [<DOI>](#).
90. Hanai H, Iida T, Takeuchi K, Watanabe F, Maruyama Y, Andoh A, et al. Curcumin Maintenance Therapy for Ulcerative Colitis: Randomized, Multicenter, Double-Blind, Placebo-Controlled Trial. *Clinical Gastroenterology and Hepatology*. 2006 Dec;4(12):1502-6. [<DOI>](#).
91. Hanai H, Iida T, Takeuchi K, Watanabe F, Maruyama Y, Andoh A, et al. Curcumin Maintenance Therapy for Ulcerative Colitis: Randomized, Multicenter, Double-Blind, Placebo-Controlled Trial. *Clinical Gastroenterology and Hepatology*. 2006 Dec;4(12):1502-6. [<DOI>](#).
92. Kedia S, Bhatia V, Thareja S, Garg S, Mouli VP, Bopanna S, et al. Low dose oral curcumin is not effective in induction of remission in mild to moderate ulcerative colitis: Results from a randomized double blind placebo controlled trial. *World Journal of Gastrointestinal Pharmacology and Therapeutics*. 2017 May;8(2):147-54. [<DOI>](#).
93. Lahiff C, Moss AC. Curcumin for clinical and endoscopic remission in ulcerative colitis: *Inflammatory Bowel Diseases*. 2011 Jul;17(7):E66. [<DOI>](#).
94. Asawanonda P, Klahan S-O. Tetrahydrocurcuminoid cream plus targeted narrowband UVB phototherapy for vitiligo: a preliminary randomized controlled study. *Photomedicine and Laser Surgery*. 2010 Oct;28(5):679-84. [<DOI>](#).
95. Holt PR, Katz S, Kirshoff R. Curcumin therapy in inflammatory bowel disease: a pilot study. *Digestive Diseases and Sciences*. 2005 Nov;50(11):2191-3. [<DOI>](#).
96. Rasyid, Lelo. The effect of curcumin and placebo on human gall-bladder function: an ultrasound study: *Curcumin and Gall-Bladder*

Function. *Alimentary Pharmacology & Therapeutics*. 1999 Feb;13(2):245–9. [<DOI>](#).

97. Rasyid A, Rahman ARA, Jaalam K, Lelo A. Effect of different curcumin dosages on human gall bladder. *Asia Pacific Journal of Clinical Nutrition*. 2002;11(4):314–8. [<DOI>](#).

98. Niederau C, Göpfert E. [The effect of chelidonium- and turmeric root extract on upper abdominal pain due to functional disorders of the biliary system. Results from a placebo-controlled double-blind study]. *Medizinische Klinik (Munich, Germany)*: 1983). 1999 Aug;94(8):425–30. [<DOI>](#).

99. Allegri P, Mastromarino A, Neri P. Management of chronic anterior uveitis relapses: efficacy of oral phospholipidic curcumin treatment. Long-term follow-up. *Clinical Ophthalmology (Auckland, N.Z.)* 2010 Oct;4:1201–6. [<DOI>](#).

100. Lal B, Kapoor AK, Asthana OP, Agrawal PK, Prasad R, Kumar P, Srimal RC. Efficacy of curcumin in the management of chronic anterior uveitis. *Phytotherapy research: PTR*. 1999 Jun;13(4):318–22. [<DOI>](#).

101. Prucksunand C, Indrasukhsri B, Leethochawalit M, Nilvises N, Prijavudhi A, Wimolwattanapun S. Effect of The Long Turmeric (*Curcuma Longa* Linn) on Healing of Peptic Ulcer : A Preliminary Report of 10 Cases Study. *Thai journal of pharmacology*. 1986;8:139–151.

102. Kositchaiwat C, Kositchaiwat S, Havanondha J. *Curcuma longa* Linn. in the treatment of gastric ulcer comparison to liquid antacid: a controlled clinical trial. *Journal of the Medical Association of Thailand = Chotmai het thangphaet*. 1993;76(11):601–605.

103. Satoskar RR, Shah SJ, Shenoy SG. Evaluation of anti-inflammatory property of curcumin (diferuloyl methane) in patients with postoperative inflammation. *International journal of clinical pharmacology, therapy, and toxicology*. 1986;24(12):651–654.

104. Usharani P, Mateen AA, Naidu MUR, Raju YSN, Chandra N. Effect of NCB-02, Atorvastatin and Placebo on Endothelial Function, Oxidative Stress and Inflammatory Markers in Patients with Type 2 Diabetes Mellitus. *Drugs in R & D*. 2008;9(4):243–250. [<DOI>](#).

105. Baum L, Lam CWK, Cheung SK-K, Kwok T, Lui V, Tsoh J, et al. Six-Month Randomized, Placebo-Controlled, Double-Blind, Pilot Clinical Trial of Curcumin in Patients With Alzheimer Disease. *Journal of Clinical Psychopharmacology*. 2008;28(1):110–113. [<DOI>](#).

106. Ringman JM, Frautschy SA, Cole GM, Masterman DL, Cummings JL. A potential role of the curry spice curcumin in Alzheimer's disease. *Current Alzheimer research*. 2005;2(2):131–136. [<DOI>](#).

107. Golombick T, Diamond TH, Badmaev V, Manoharan A, Ramakrishna R. The potential role of curcumin in patients with monoclonal gammopathy of undefined significance-its effect on paraproteinemia and the urinary N-telopeptide of type I collagen bone turnover marker. *Clinical cancer research : an official journal of the American Association for Cancer Research*. 2009;15(18):5917–5922. [<DOI>](#).

108. Oetari S, Sudibyo M, Commandeur JN, Samhoedi R, Vermeulen NP. Effects of curcumin on cytochrome P450 and glutathione S-transferase activities in rat liver. *Biochemical pharmacology*. 1996;51(1):39–45. [<DOI>](#).

109. Thapliyal R, Maru GB. Inhibition of cytochrome P450 isozymes by curcumins in vitro and in vivo. *Food and chemical toxicology : an international journal published for the British Industrial Biological Research Association*. 2001;39(6):541–547. [<DOI>](#).

110. Appiah-Opong R, Commandeur JNM, van Vugt-Lussenburg B, Vermeulen NPE. Inhibition of human recombinant cytochrome P450s by curcumin and curcumin decomposition products. *Toxicology*. 2007;235(1–2):83–91. [<DOI>](#).

111. Cao J, Jia L, Zhou H-M, Liu Y, Zhong L-F. Mitochondrial and nuclear DNA damage induced by curcumin in human hepatoma G2 cells. *Toxicological sciences : an official journal of the Society of Toxicology*. 2006;91(2):476–483. [<DOI>](#).

112. Jiao Y, Wilkinson J, Di X, Wang W, Hatcher H, Kock ND, et al. Curcumin, a cancer chemopreventive and chemotherapeutic agent, is a biologically active iron chelator. *Blood*. 2009;113(2):462–469. [<DOI>](#).

113. Sharma RA, Euden SA, Platton SL, Cooke DN, Shafayat A, Hewitt HR, et al. Phase I Clinical Trial of Oral Curcumin. *Clinical Cancer Research*. 2004;10(20):6847–6854. [<DOI>](#).

114. Ilyas S, Naz S. Effect of gamma irradiation on morphological characteristics and isolation of curcuminoids and oleoresins of *Curcuma Longa* L. *Journal of Animal and Plant Sciences*. 2014;24(5):1396–1404.

115. Manoharan Y, Haridas V, Vasanthakumar KC, Muthu S, Thavoorullah FF, Shetty P. Curcumin: A Wonder Drug as a Preventive Measure for

COVID19 Management. Indian journal of clinical biochemistry : IJCB. 2020;35(3):373–375. <DOI>.

116. Pawitan JA. Curcumin as Adjuvant Therapy in COVID-19: Friend or Foe? Journal of International Dental and Medical Research. 2020;13(2):824–829.

117. Chen D-Y, Shien J-H, Tiley L, Chiou S-S, Wang S-Y, Chang T-J, et al. Curcumin inhibits influenza virus infection and haemagglutination activity. Food Chemistry. 2010;119(4):1346–1351. <DOI>.

118. Somasundaram S, Edmund NA, Moore DT, Small GW, Shi YY, Orlowski RZ. Dietary curcumin inhibits chemotherapy-induced apoptosis in models of human breast cancer. Cancer research. 2002;62(13):3868–3875.

119. Cronin JR. Curcumin: Old Spice Is a New Medicine. Alternative and Complementary Therapies. 2003;9(1):34–38. <DOI>.

120. Scannell JW, Blanckley A, Boldon H, Warrington B. Diagnosing the decline in pharmaceutical R&D efficiency. Nature Reviews Drug Discovery. 2012;11(3):191–200. <DOI>.

121. Yu J-J, Pei L-B, Zhang Y, Wen Z-Y, Yang J-L. Chronic Supplementation of Curcumin Enhances the Efficacy of Antidepressants in Major Depressive Disorder: A Randomized, Double-Blind, Placebo-Controlled Pilot Study. Journal of clinical psychopharmacology. 2015;35(4):406–410. <DOI>.

122. Esmaily H, Sahebkar A, Iranshahi M, Ganjali S, Mohammadi A, Ferns G, et al. An investigation of the effects of curcumin on anxiety and depression in obese individuals: A randomized controlled trial. Chinese journal of integrative medicine. 2015;21(5):332–338. <DOI>.

123. Bergman J, Miodownik C, Bersudsky Y, Sokolik S, Lerner PP, Kreinin A, et al. Curcumin as an Add-On to Antidepressive Treatment. Clinical Neuropharmacology. 2013;36(3):73–77. <DOI>.

124. James JS. Curcumin: clinical trial finds no antiviral effect. AIDS treatment news. 1996; (242):1–2.

125. Prasad S, Tyagi AK. Curcumin and its analogues: a potential natural compound against HIV infection and AIDS. Food & Function. 2015;6(11):3412–3419. <DOI>.

126. Gupta H, Gupta M, Bhargava S. Potential use of turmeric in COVID-19. Clinical and experimental dermatology. 2020;45(7):902–903. <DOI>.

127. Lai Y, Yan Y, Liao S, Li Y, Ye Y, Liu N, et al. 3D-quantitative structure-activity relationship and antiviral effects of curcumin derivatives as potent inhibitors of influenza H1N1 neuraminidase. Archives of pharmacal research. 2020;43(5):489–502. <DOI>.

128. Tejada S, Manayi A, Daglia M, F. Nabavi S, Sureda A, Hajheydari Z, et al. Wound Healing Effects of Curcumin: A Short Review. Current Pharmaceutical Biotechnology. 2016;17(11):1002–1007. <DOI>.

129. Mohanty C, Sahoo SK. The in vitro stability and in vivo pharmacokinetics of curcumin prepared as an aqueous nanoparticulate formulation. Biomaterials. 2010;31(25):6597–6611. <DOI>.

130. Gong C, Wu Q, Wang Y, Zhang D, Luo F, Zhao X, et al. A biodegradable hydrogel system containing curcumin encapsulated in micelles for cutaneous wound healing. Biomaterials. 2013;34(27):6377–6387. <DOI>.

131. Zhang Y, McClain SA, Lee H-M, Elburki MS, Yu H, Gu Y, et al. A Novel Chemically Modified Curcumin “Normalizes” Wound-Healing in Rats with Experimentally Induced Type I Diabetes: Initial Studies. Journal of Diabetes Research. 2016;2016:5782904. <DOI>.

132. Krausz AE, Adler BL, Cabral V, Navati M, Doerner J, Charafeddine RA, et al. Curcumin-encapsulated nanoparticles as innovative antimicrobial and wound healing agent. Nanomedicine: Nanotechnology, Biology and Medicine. 2015;11(1):195–206. <DOI>.

133. Chereddy KK, Coco R, Memvanga PB, Ucar B, des Rieux A, Vandermeulen G, et al. Combined effect of PLGA and curcumin on wound healing activity. Journal of controlled release : official journal of the Controlled Release Society. 2013;171(2):208–215. <DOI>.

134. El-Refaei WM, Elnaggar YSR, El-Massik MA, Abdallah OY. Novel curcumin-loaded gel-core hyalurosomes with promising burn-wound healing potential: Development, in-vitro appraisal and in-vivo studies. International journal of pharmaceutics. 2015;486(1–2):88–98. <DOI>.

135. Wickenberg J, Ingemansson SL, Hlebowicz J. Effects of Curcuma longa (turmeric) on postprandial plasma glucose and insulin in healthy subjects. Nutrition Journal. 2010;9(1):43. <DOI>.

136. Appendino G, Belcaro G, Cornelli U, Luzzi R, Togni S, Dugall M, et al. Potential role of curcumin phytosome (Meriva) in controlling the evolution of

- diabetic microangiopathy. A pilot study. *Panminerva medica*. 2011;53(3 Suppl 1):43-49.
137. Khajehdehi P, Zanjanejad B, Aflaki E, Nazarinia M, Azad F, Malekmakan L, et al. Oral supplementation of turmeric decreases proteinuria, hematuria, and systolic blood pressure in patients suffering from relapsing or refractory lupus nephritis: a randomized and placebo-controlled study. *Journal of renal nutrition : the official journal of the Council on Renal Nutrition of the National Kidney Foundation*. 2012;22(1):50-57. [<DOI>](#).
138. Soni KB, Kuttan R. Effect of oral curcumin administration on serum peroxides and cholesterol levels in human volunteers. *Indian journal of physiology and pharmacology*. 1992;36(4):273-275.
139. Alwi I, Santoso T, Suyono S, Sutrisna B, Suyatna FD, Kresno SB, et al. The effect of curcumin on lipid level in patients with acute coronary syndrome. *Acta medica Indonesiana*. 2008;40(4):201-210.
140. Burns J, Joseph PD, Rose KJ, Ryan MM, Ouvrier RA. Effect of oral curcumin on Déjérine-Sottas disease. *Pediatric neurology*. 2009;41(4):305-308. [<DOI>](#).
141. Bommelaer G, Laharie D, Nancey S, Hebuterne X, Roblin X, Nachury M, et al. Oral Curcumin No More Effective Than Placebo in Preventing Recurrence of Crohn's Disease After Surgery in a Randomized Controlled Trial. *Clinical gastroenterology and hepatology : the official clinical practice journal of the American Gastroenterological Association*. 2020;18(7):1553-1560.e1. [<DOI>](#).
142. Lal B, Kapoor AK, Agrawal PK, Asthana OP, Srimal RC. Role of curcumin in idiopathic inflammatory orbital pseudotumours. *Phytotherapy Research*. 2000;14(6):443-447. [<DOI>](#).
143. Shimouchi A, Nose K, Takaoka M, Hayashi H, Kondo T. Effect of dietary turmeric on breath hydrogen. *Digestive diseases and sciences*. 2009;54(8):1725-1729. [<DOI>](#).
144. Deodhar SD, Sethi R, Srimal RC. Preliminary study on antirheumatic activity of curcumin (diferuloyl methane). *The Indian journal of medical research*. 1980;71:632-634.
145. Chandran B, Goel A. A randomized, pilot study to assess the efficacy and safety of curcumin in patients with active rheumatoid arthritis. *Phytotherapy research : PTR*. 2012;26(11):1719-1725. [<DOI>](#).
146. Belcaro G, Cesarone MR, Dugall M, Pellegrini L, Ledda A, Grossi MG, et al. Product-evaluation registry of Meriva®, a curcumin-phosphatidylcholine complex, for the complementary management of osteoarthritis. *Panminerva medica*. 2010;52(2 Suppl 1):55-62.
147. Belcaro G, Cesarone MR, Dugall M, Pellegrini L, Ledda A, Grossi MG, et al. Efficacy and safety of Meriva®, a curcumin-phosphatidylcholine complex, during extended administration in osteoarthritis patients. *Alternative medicine review : a journal of clinical therapeutic*. 2010;15(4):337-344.



## Traditional Medicinal Uses, Phytochemicals, and Pharmacological Activities of Genus *Rhamnus*: A review

Gashaw Nigussie<sup>1,2\*</sup> , Haregua Melak<sup>1</sup> , Milkyas Endale<sup>2</sup> 

<sup>1</sup>Armauer Hansen Research Institute, P.O. Box 1005, Addis Ababa, Ethiopia.

<sup>2</sup>Department of Applied Chemistry, Adama Science and Technology University, P.O. Box 1888, Adama, Ethiopia.

**Abstract:** The genus *Rhamnus* belongs to the Rhamnaceae family, which contains approximately 137 species, traditionally used as folk medicine in East Asia, North and South America, and subtropical regions of Africa. The genus is used traditionally to treat diseases such as cancer, wound, jaundice, hepatitis, gonorrhoea, laxative, hypertension, malaria, stomach ache, snake bite and diarrhea. Anthraquinones and flavonoids are the most cited compounds from the genus of which polyphenols were abundant with tremendous antioxidant, wound healing and anti-inflammatory activities. Pharmacological activity evaluation of the extracts and isolated compounds revealed anti-inflammatory, antioxidant, antimalarial, antibacterial, anti-mutagenic, anti-genotoxic, hepatoprotective, anticancer, and anti-proliferative activity. The genus afforded drug leads such as 6-methoxysorigenin (**12**) and prinoidin (**23**) with anti-tyrosinase and cytotoxicity, respectively, as well as antioxidant drug leads such as Kaempferol-3-O- $\beta$ -rhamninoside (**31**) rhamnetin-3-O- $\beta$ -isorhamninoside (**37**) and isotorachryson (**55**). The present review endeavors to provide a comprehensive and up to date compilation of documented traditional medicinal uses, phytochemicals and pharmacological activities of the genus and provided valuable information in support of its uses as an alternative medicine for future healthcare practice.

**Keywords:** *Rhamnus*, anthraquinones, flavonoids, pharmacological activities.

**Submitted:** April 28, 2021. **Accepted:** July 26, 2021.

**Cite this:** Nigussie G, Melak H, Endale M. Traditional Medicinal Uses, Phytochemicals, and Pharmacological Activities of Genus *Rhamnus*: A review. JOTCSA. 2021;8(3):899–932.

**DOI:** <https://doi.org/10.18596/jotcsa.929188>.

**\*Corresponding author. E-mail:** [gashawnigussie20@gmail.com](mailto:gashawnigussie20@gmail.com).

### INTRODUCTION

Traditional medicine has been in existence even before the advent of modern medicine. It continues to remain as an alternative care available for the majority of the developing countries due to its intrinsic qualities, unique, and holistic approaches as well as its accessibility and affordability (1, 2). The genus *Rhamnus* consists of 137 species (Figure 1) and 19 synonyms (3). The word *Rhamnus* means 'a kind of prickly plant' and 'buckthorn or Christ's thorn' in Greek and Latin languages (4). The genus is distributed in East Asia, North and South America and various parts of

subtropical Africa with a wide spectrum of traditional medicinal uses (5-13).

The chemistry of *Rhamnus* species does not exhibit great diversity. The main groups of secondary metabolites reported from the genus are anthrones, anthraquinones, and flavonoids of which polyphenols were abundant with tremendous antioxidant, wound healing, and anti-inflammatory activities. The present review endeavors to provide a comprehensive and up-to-date compilation of documented biological activities and phytochemistry of the genus and provided valuable information in support of its uses as an alternative medicine for future healthcare practice.



**Figure 1:** Some medicinally important species of the genus *Rhamnus* L. (14, 15).

**Taxonomy of the genus *Rhamnus*:**

**Kingdom:** *Plantae*, **Order:** *Rosales*, **Family:** *Rhamnaceae*, **Genus:** *Rhamnus*. The names redberry, red berry buckthorn, California redberry, evergreen buckthorn, spiny buckthorn, and holly leaf buckthorn have been used for multiple taxa of *Rhamnus* (16).

**Botanical Description and Traditional Uses**

The genus *Rhamnus* comprises 137 species of shrubs and small trees in temperate, sub-tropical and tropical countries (17). It is an evergreen or deciduous plant and resistant to frost. The leaves are either alternate or sub-opposite. The hermaphrodite small flowers are weakly scented (18). Botanical description and traditional uses of various *Rhamnus* species is summarized in Table 1 below.

**Table 1:** Botanical distribution and traditional medicinal uses of the genus *Rhamnus*.

Scientific name	Part	Distribution	Traditional use	Refs
<i>R. alaternus</i> L.	Leaf, Aerial Part,	Algeria	as a digestive, diuretic, laxative, and for the therapeutics of hepatic and dermatological disorders	(19)
	Leaf	Algeria	treatment of gastrointestinal system diseases (hepatitis)	(20)
	Bark	Algeria	Used to treat jaundice	(21)
	Aerial part	Algeria	Hepatic jaundice and chlorosis	(22)
	Root, Aerial Part	Spain, Iberian Peninsula	Used to treat depurative (blood purification)	(23, 24)
	Aerial Part	Spain	therapeutics of hypercholesterolemia	(23)
	Aerial Part	Spain	therapeutics of antihypertensive (lowers blood pressure)	(23)
	Bark, Branch	Italy	to treat hemostatic, wounds, laxative	(25)
	Branch, leaf	Iberian Peninsula	to treat high blood pressure	(24, 26)
	Branch, Leaf	Israel, Algeria	to treat jaundice	(5, 22)
<i>R. alnifolia</i> L'Hér	Root, Bark	USA	to treat gonorrhoea and cathartic	(7)
<i>R. alpina</i> L.	Branch	Italy	to treat cardiac disease, wounds	(27)
<i>R. cathartica</i> L.	Bark	Bosnia and Herzegovina, Turkey	treatments of common buckthorn, diarrhea, diuretic	(28, 29)
	Fruit	Southeast Europe	antiseptic for wounds	(30)
	Fruit	Serbia	to treat laxative	(31)
<i>R. fallax</i> L.	Bark	Bosnia and Herzegovina	to treat and manage dermal diseases	(32, 33)
	Bark	Montenegro/ Serbia	to treat constipation	(34)
<i>R. heterophylla</i> Oliver	Root, Leaf	China	to cease bleeding	(11)
<i>R. ilicifolia</i> Kellogg	Root	USA	laxative, diuretic and to treat gonorrhoea	(16)
	Whole Part	USA	analgesic or antirheumatic	(35)
<i>R. lycioides</i> L.	Leaves, Shoot	Turkey	to treat pulmonary cancer	(36)
<i>R. nepalensis</i> Wall MA Lawson	Root	India	to treat the treatment of pneumonia	(37)
<i>R. nitidus</i> Davis	Bark	Turkey	Used as emetic	(38)
<i>R. persica</i> Boiss.	Leaf	Iran	to treat allergy and itching in children, wound	(39)
<i>R. prinoides</i> L'Hér	Bark, Fruit, Multiple Part	Kenya	to treat sexually transmitted disease (gonorrhoea),	(40)
	Fruit, Stem, Root, and Leaf	Kenya	to treat gonorrhoea, prostate, malaria, brucellosis	(41)
	Root	Kenya	to treat muscular skeleton disorder (Arthritis, backaches, rheumatic)	(42)
	Leaf	Ethiopia	to treat Snakebite	(43)
	Roots, Leaf	South Africa	Used for blood purifiers, pneumonia, emetics, purgative, colic,	(44)

			stimulants	
	Branch	South Africa	Herpes, diabetes, HIV related infections	(45)
	Root, Leaf, and Steam	Kenya	to treat ear, nose, and throat (ENT) diseases	(46)
	Leaf	Ethiopia, Uganda	to treat tonsillitis, wound, eczema, skin infection, fever in children, tuberculosis, dandruff, water-borne disease	(47-56)
	Seed	Ethiopia	to treat ringworm	(57)
	Root	Kenya	to treat sexually transmitted infection	(58)
	Root	Kenya	amoebiasis, bacillary dysentery, tonic, pneumonia	(59)
	Root	Ethiopia	to treat hepatic problems	(60)
<i>R. purpureus</i> Edgew.	Bark, Steam, Fruit, Leaf	Himalayas	to treat digestive disorders	(61, 62)
<i>R. purshiana</i> DC.	Bark	Algeria	to treat respiratory tract diseases (pharyngitis)	(20)
	shell	Mexico	to treat skin rash and stomachache	(63)
<i>R. staddo</i> A.Rich	Tree	Kenya	Used for strength/nutrient supplement, sexually transmitted diseases, flu/cold	(64)
	Multiple Part	Kenya	to treat diarrhea	(40)
	Root, Steam,	Kenya	to treat gonorrhea, diabetes, endometritis	(41)
<i>R. triqueter</i> Wall M. A. Lawson	Leaf, Fruit, Branch	Pakistan	to treat hemorrhagic septicemia	(65)
	Bark, Fruit	Himalaya	used for blood purifier, boils, scabies, skin diseases, tonic	(62)
<i>R. virgatus</i> Roxb.	Bark	Himalaya, India	to treat eczema and ringworms	(61, 66)
	Steam, Fruit, Bark	Himalaya	to treat emetic, purgative, eczema, ringworm, affection of spleen	(62)
	Fruit and Bark	Nepal/Iran	to treat diarrhea and dysentery	(67)
	Fruit, Bark	India	to treat emetic, spleen infection, and purgative, curing white dots of eyes	(61, 68)

### Phytochemicals

Anthraquinones, flavonoids, naphthalene derivatives, terpenoids, alkaloids, steroids, organic acids are secondary metabolites reported from various *Rhamnus* species of which anthraquinones and flavonoids are the most cited ones (Figures 2-4, Table 2).

### Anthraquinones

Several anthraquinones (**1-30**, Table 2) have been isolated from *Rhamnus* species. Of these, compounds, a cytotoxic compound prinoidin (**23**) was reported from the fruits of *R. nepalensis* against KB (human epidermoid carcinoma of the mouth) with  $IC_{50}$  value of 0.045  $\mu$ M, which was four times more potent than the standard doxorubicin having  $IC_{50}$  value of 0.2  $\mu$ M (69). A prominent anti-tyrosinase effect was displayed by 6-methoxysorigenin (**12**) reported from *R. nakaharai* with  $IC_{50}$  value of 42.2  $\mu$ M, which was twofold more potent than kojic acid with  $IC_{50}$  value of 82.1  $\mu$ M (70). In a related study, antioxidant alaternin (**10**) was reported from *R. nakaharai* with  $IC_{50}$  value of 117.7  $\mu$ M compared to ascorbic acid ( $IC_{50}$  value of 63.7  $\mu$ M) using DPPH assay method (70).

### Flavonoids

Flavonoids, which are important secondary metabolites, are widespread in the plant kingdom, either in a free form or in the form of glycosides with wide spectrum of pharmacological application (71). Various flavonoids (**31-52**) and their derivatives have been reported from the genus *Rhamnus*. Of these, flavonoids **31, 33, 36, 37** and **40** exhibited cytotoxic, antioxidant, anti-hyperlipidemia, anti-proliferative, and anti-genotoxic activity (72-75).

### Naphthalene derivatives

To date, 7 naphthalene derivatives (**53-59**) have been reported from different parts of *Rhamnus* species such as *R. prinoides*, *R. cathartica*, *R.*

*wightii*, *R. procumbens*, *R. makaharai*, *R. pallasii* and *R. serrutu*. Of these, musizen (**54**) obtained from whole part of *R. wightii* exhibited antibacterial activities against *S. aureus* and *K. pneumonia* using agar disc diffusion assay with MIC value of 9  $\mu$ g/mL, which was more potent than streptomycin having MIC value of 120  $\mu$ g/mL (76).

### Terpenoids

Up to date, four terpenoids (**60-63**) have been reported from leaves and bark extracts of *R. californica* (77).

### Alkaloids

Alkaloids are a large group of naturally occurring compounds with diverse pharmacological activity (78). To date, four alkaloids (**64-67**) have been reported from leaves and bark extracts of *R. californica* (77).

### Steroids

Previous studies reported limited number of steroids and steroid glycosides such as  $\beta$ -sitosterol (**68**) from roots of *R. formosana*, root bark and leaves of *R. alaternus* and leaves of *R. serrutu* (79-81) whereas stigmasterol- $\beta$ -D-glycoside (**69**) and  $\beta$ -sitosterol-3-O-glycoside (**70**) were reported roots of *R. formosana* (79) and root bark and leaves of *R. alaternus* (80), respectively.

### Organic acids

Organic acids are another important component of the genus *Rhamnus*. Previously studied revealed compounds **71-72** and **73-75** from leaves of *R. alaternus* (82) and leaves of *R. heterophylla* (83), respectively.

### Miscellaneous Compounds

Compounds **76** and **77** were reported from root and bark of *R. serrutu* and *R. davurica*, respectively (81, 84). The later was also reported from heart wood parts of *R. nakaharai* (70).

**Table 2:** Compounds reported from the genus *Rhamnus*.

<b>Compound</b>	<b>Plant species</b>	<b>Part used</b>	<b>Reference</b>	
<b>Anthraquinones</b> Chrysophanol ( <b>1</b> )	<i>R.formosana</i> and <i>R. serrata</i>	Root	(79, 81)	
	<i>R.prinoides</i>	Leaves, Stem	(85)	
	<i>R.alaternus</i>	Stem, bark	(86)	
	<i>R.frangula</i>	Stem bark and branch	(87)	
	<i>R.sphaerosperma</i>	Stem	(88)	
	<i>R.alpinus</i> and <i>R.saxatilis</i>	Bark	(89-91)	
	<i>R.nepalensis</i>	Fruit	(69)	
	<i>R.californica</i>	Leaf and bark	(77)	
	Emodin ( <b>2</b> )	<i>R.formosana</i> and <i>R. serrata</i>	Root	(79, 81)
<i>R.pumila</i>		Stem, bark	(86)	
<i>R.prinoides</i>		Fruit, Leaf	(92, 93)	
<i>R.cathartica</i> , <i>R.pubescens</i> , <i>R. alaternus</i> and <i>R.heterophylla</i>		Leaf	(83, 94-96)	
<i>R.frangula</i>		Stem bark and branch	(87)	
<i>R.sphaerosperma</i>		Stem	(88)	
<i>R.procumbens</i>		Whole part	(97)	
<i>R.alpinus</i> and <i>R.saxatilis</i>		Bark	(89, 90)	
<i>R.nakaharai</i>		heartwood	(70)	
<i>R.nepalensis</i>		Fruit	(69)	
<i>R.californica</i>		Leaf and bark	(77)	
Physcion ( <b>3</b> )		<i>R.formosana</i>	Root	(79)
		<i>R.fallax</i>	Stem, bark	(86)
	<i>R.intermedia</i>	Stem	(86)	
	<i>R.prinoides</i>	Leaf and Stem	(85, 92)	
	<i>R.frangula</i>	Stem bark and branch	(87)	

	<i>R.serrate, R.alaternus</i> and <i>R. alaternus</i>	Root	(81, 98)
	<i>R.sphaerosperma</i>	Stem	(88)
	<i>R.davurica, R.alpinus</i> and <i>R.saxatilis</i>	Bark	(84, 89, 91)
	<i>R.procumbens</i>	Whole part	(97)
	<i>R.nepalensis</i>	Fruit	(69)
	<i>R.californica</i>	Leaf and bark	(77)
Emodinanthrone (4)	<i>R.prinoides</i>	Leaves, Stem	(85, 93)
Emodinbianthrone (5)	<i>R.prinoides</i>	Fruits	(93)
	<i>R.nepalensis</i>	Fruit	(69)
Chrysophanol-emodinbianthrone (6)	<i>R.nepalensis</i>	Fruit	(69)
Chrysophanolbianthrone (7)	<i>R.nepalensis</i>	Fruit	(69)
1,2,6,8-tetrahydroxy-3-methylanthraquinone-8-O- $\beta$ -glucopyranoside (8)	<i>R.nakaharai</i>	heartwood	(70)
emodin-8-O- $\beta$ -glucopyranoside (9)	<i>R.nakaharai</i>	heartwood	(70)
Alaternin (10)	<i>R.nakaharai</i>	heartwood	(70)
6-methoxysorigenin-8-O- $\beta$ -glucopyranoside (11)	<i>R.nakaharai</i>	heartwood	(70)
6-methoxysorigenin (12)	<i>R.nakaharai</i>	heartwood	(70)
Aloe-emodin (13)	<i>R.alaternus</i>	Root	(98)
	<i>R.alpinus</i> and <i>R.saxatilis</i>	Bark	(89-91)
Rhein (14)	<i>R.alaternus</i>	Root	(98)
	<i>R.alpinus</i> and <i>R.saxatilis</i>	Bark	(89-91)
Madagascin (15)	<i>R.saxatilis</i> and <i>R. alpinus</i>	Bark	(90)
	<i>R.cathartica</i> and <i>R. intermedia</i>	Fruit	(99)
3-geranyloxyemodin (16)	<i>R.saxatilis</i> and <i>R. alpinus</i>	Bark	(90)
emodin-6-O-arabinopyranoside-3',4'-diacetate (17)	<i>R.alaternus</i>	Fruit	(100)
emodin-6-O-arabinopyranoside-2',3',4'-triacetate (18)	<i>R.alaternus</i>	Fruit	(100)
Emodin 6-O- $\beta$ -L-rhamnose (19)	<i>R.libanoticus</i>	Bark	(101)
Emodin 8-O- $\beta$ -D-glucoside (20)	<i>R.libanoticus</i>	Bark	(101)

Physcion 8-O- $\beta$ -rutinoside ( <b>21</b> )	<i>R.libanoticus</i>	Bark	(101)
	<i>R.pallasri</i>	Bark	(102)
Emodinanthrone-6-O-rhamnopyranoside-2',3',4'-triacetate ( <b>22</b> )	<i>R.prinoides</i>	Fruit	(93)
Prinoidin ( <b>23</b> )	<i>R.prinoides</i>	Fruit	(85, 93)
Prinoidin-emodinbianthrones ( <b>24</b> )	<i>R. nepalensis</i>	Fruit	(69)
Rhamnepalins ( <b>25</b> )	<i>R. nepalensis</i>	Fruit	(69)
Glucofrangulin ( <b>26</b> )	<i>R.prinoides</i>	Fruit	(103)
	<i>R.cathartica</i>	Leaf	(94)
1,6,8-trihydroxy-3-methylantraquinone 1-O-rhamnosyl (1 $\rightarrow$ 2) glucoside ( <b>27</b> )	<i>R.formosana</i>	Root	(104)
1,8-dihydroxy-6-methoxy-3-methyl anthraquinones 8-O-rhamnosyl-(1 $\rightarrow$ 2)-glucoside ( <b>28</b> )	<i>R.formosana</i>	Root	(79)
1,2,6,8 tetrahydroxy-3 methyl anthraquinone 8-O- $\beta$ -D-glucopyranoside ( <b>29</b> )	<i>R.alaternus</i>	Root bark and Leaf	(80)
1,4,6,8 tetrahydroxy-3 methyl anthraquinones 1-O- $\beta$ -D-glucopyranosyl-4,6-di-O- $\alpha$ -L-rhamnopyranoside ( <b>30</b> )	<i>R.alaternus</i>	Root bark and Leaf	(80)
<b>Flavonoids</b>			
Kaempferol-3-O- $\beta$ -rhamninoside ( <b>31</b> )	<i>R.petiolaris</i>	Fruit	(105)
	<i>R. nakaharai</i>	Heartwood	(70)
	<i>R. alaternus</i>	Leaf	(72, 73)
Luteolin ( <b>32</b> )	<i>R.alaternus</i>	Leaf	(82)
	<i>R.davurica</i>	Bark	(84)
Kaempferol ( <b>33</b> )	<i>R.alaternus</i>	Leaf, Fruit	(96, 106)
	<i>R.lycioides</i>	Aerial parts	(107)
	<i>R.davurica</i>	Bark	(84)
	<i>R.saxatilis, R.catharticus and R.disperma</i>	Fruit	(106)
	<i>R.californica</i>	Leaf and bark	(77)
	<i>R.pallasii</i>	Bark	(108)

	<i>R.heterophylla</i>	Leaf	(83)
Quercetin (34)	<i>R.lycioides</i>	Aerial part	(107)
	<i>R.pallasii</i> and <i>R.davurica</i>	Bark	(84)
	<i>R.saxatilis</i> , <i>R.catharticus</i> , <i>R.alaternus</i> and <i>R.disperma</i>	Fruit	(106)
	<i>R.californica</i>	Leaf and bark	(77)
	<i>R.heterophylla</i>	Leaf	(83)
Rhamnazin-3- isorhamninoside (35)	<i>R.formosana</i>	Root	(104)
Rhamnocitrin 3-O-β-isorhamninoside (36)	<i>R.formosana</i>	Root	(104)
	<i>R.nakaharai</i>	heartwood	(70)
	<i>R. alaternus</i>	Leaf	(72, 73)
Rhamnetin 3-O-isorhamninoside (37)	<i>R. alaternus</i>	Leaf	(72, 73)
Rhamnetin 3-O-(3''''-O-β-coumaroyl)-β – rhamninoside (38)	<i>R.petiolaris</i>	Fruit	(105)
Quercitrin 39)	<i>R.petiolaris</i>	Fruit	(105)
	<i>R.pallnsii</i>	Bark	(108)
Apigenin (40)	<i>R.davurica</i>	Bark	(84)
Rutin (41)	<i>R.alaternus</i>	Leaf	(82)
	<i>R.cathartica</i>	Leaf	(94)
Rhamnazin (42)	<i>R.prinoides</i>	Fruits, Leaf	(93)
	<i>R.lycioides</i>	Arial part	(107)
	<i>R.disperma</i>	Arial part	(109)
	<i>R.heterophylla</i>	Leaf	(83)
Rhamnetin (43)	<i>R.lycioides</i>	Arial Part	(107)
	<i>R.disperma</i>	Fruit	(70)
Aromadendrin (44)	<i>R.lycioides</i>	Arial Part	(110)
	<i>R.pallasii</i>	Bark	(108)
Eriodictyol (45)	<i>R.lycioides</i>	Arial Part	(110)
	<i>R.pallasii</i>	Bark	(108)
Rhamnocitrin (46)	<i>R.prinoides</i>	Leaf and Stem	(93)
	<i>R.lycioides</i>	Arial Part	(107)
	<i>R.davurica</i>	Bark	(84)
	<i>R.saxatilis</i>	Fruit	(106)

	<i>R.catharticus</i>	Fruit	(106)
	<i>R.alaternus</i>	Fruit	(106)
	<i>R.heterophylla</i>	Leaf	(83)
Taxifolin (47)	<i>R.lycioides</i>	Arial Part	(107)
	<i>R.pallnsii</i>	Bark	(108)
	<i>R.davurica</i>	Bark	(84)
	<i>R.pallasii</i>	Bark	(108)
3- methoxy flavone (48)	<i>R.lycioides</i>	Aerial part	(107)
3-O-Methylquercetin (49)	<i>R.prinoides</i>	Leaf and Stem	(93)
Pallasiin (50)	<i>R.pallasii</i>	Bark	(108)
Isorhamnetin (51)	<i>R.pallasii</i>	Bark	(108)
Mearnsetin (52)	<i>R.pallasii</i>	Bark	(108)
<b>Naphthalene Derivatives</b>			
Geshoidin (P-sorigenin-8-O-β-D-glucoside) (53)	<i>R.prinoides</i>	Leaf and stem	(85)
	<i>R. cathartica</i>	Leaf	
Musizin (54)	<i>R.prinoides</i>	Leaf and stem	(85)
	<i>R.wightii</i> and <i>R. procumbens</i>	Whole part	(76, 97)
Isotorachryson (55)	<i>R.nakaharai</i>	Root bark	(111)
β-sorigenin (56)	<i>R.prinoides</i>	Leaf and stem	(85)
	<i>R. cathartica</i>	Leaf	(94)
α-sorinin (57)	<i>R.pallasii</i>	Bark	(102)
Eugenine (58)	<i>R.serrutu</i>	Root	(81)
3-hydroxyeugenine (59)	<i>R.serrutu</i>	Root	(81)
<b>Terpenoids</b>			
Umbellulone (60)	<i>R.californica</i>	Leaf and bark	(77)
1,8-cineole (61)	<i>R.californica</i>	Leaf and bark	(77)
α-terpineol (62)	<i>R.californica</i>	Leaf and bark	(77)
Thymol (63)	<i>R.californica</i>	Leaf and bark	(77)
<b>Alkaloid</b>			
Domesticine (64)	<i>R.californica</i>	Leaf and bark	(77)
Nordomesticine (65)	<i>R.californica</i>	Leaf and bark	(77)

Isoboldine ( <b>66</b> )	<i>R.californica</i>	Leaf and bark	(77)
Bufotenine ( <b>67</b> )	<i>R.californica</i>	Leaf and bark	(77)
<b>Steroids</b>			
Stigmasterol- $\beta$ -D-glycoside ( <b>68</b> )	<i>R.formosana</i>	Root	(79)
$\beta$ -sitosterol ( <b>69</b> )	<i>R.formosana</i>	Root	(79)
	<i>R.alaternus</i>	Root bark and Leaf	(80)
	<i>R.serrutu</i>	Leaf	(81)
$\beta$ -sitosterol-3-O-glycoside ( <b>70</b> )	<i>R.alaternus</i>	Root bark and Leaf	(80)
<b>Organic Acid</b>			
P-coumaric acid ( <b>71</b> )	<i>R.alaternus</i>	Leaf	(82)
Ferulic acid ( <b>72</b> )	<i>R.alaternus</i>	Leaf	(82)
Gallic acid ( <b>73</b> )	<i>R.alaternus</i>	Leaf	(82)
	<i>R.heterophylla</i>	Leaf	(83)
Malic acid ( <b>74</b> )	<i>R.heterophylla</i>	Leaf	(83)
Salicylic acid ( <b>75</b> )	<i>R.heterophylla</i>	Leaf	(83)
<b>Miscellaneous Compounds</b>			
5-hydroxy-7-methoxyptali ( <b>76</b> )	<i>R.serrutu</i>	Root	(81)
	<i>R.davurica</i>	Bark	(84)
p-hydroxybenzaldehyde ( <b>77</b> )	<i>R.nakaharai</i>	Heart wood	(70)

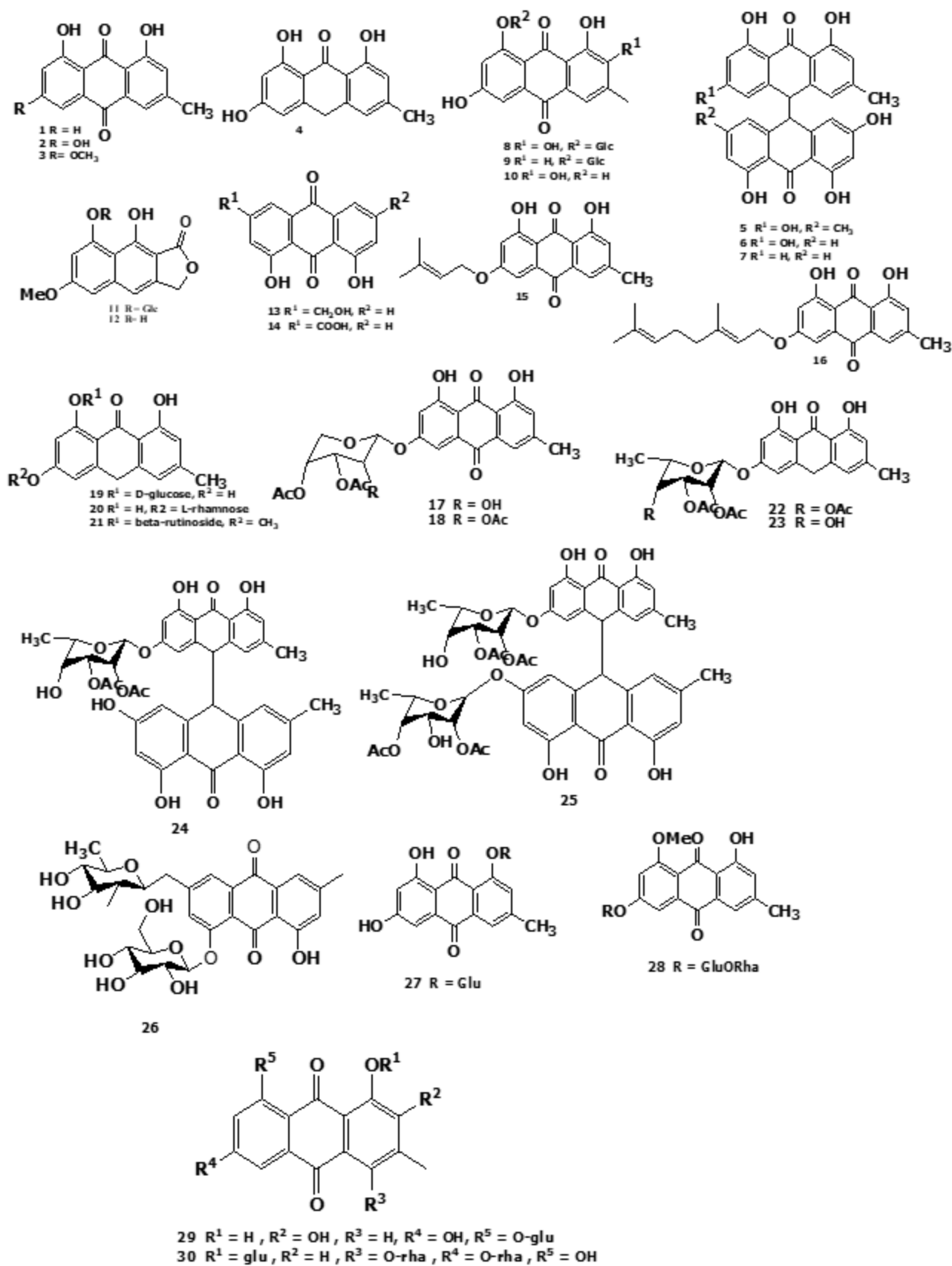


Figure 2: Anthraquinones reported from the genus *Rhamnus*.

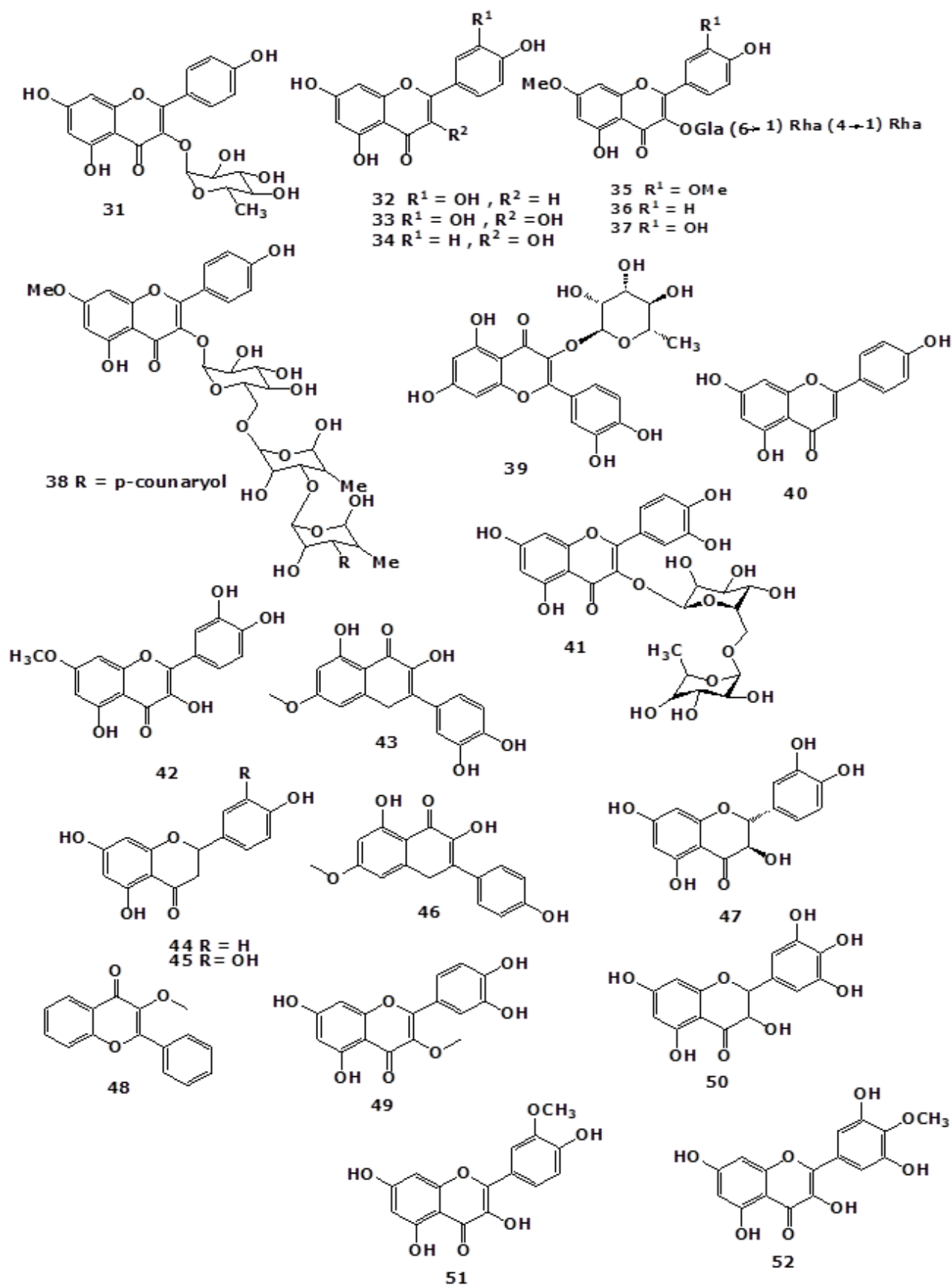
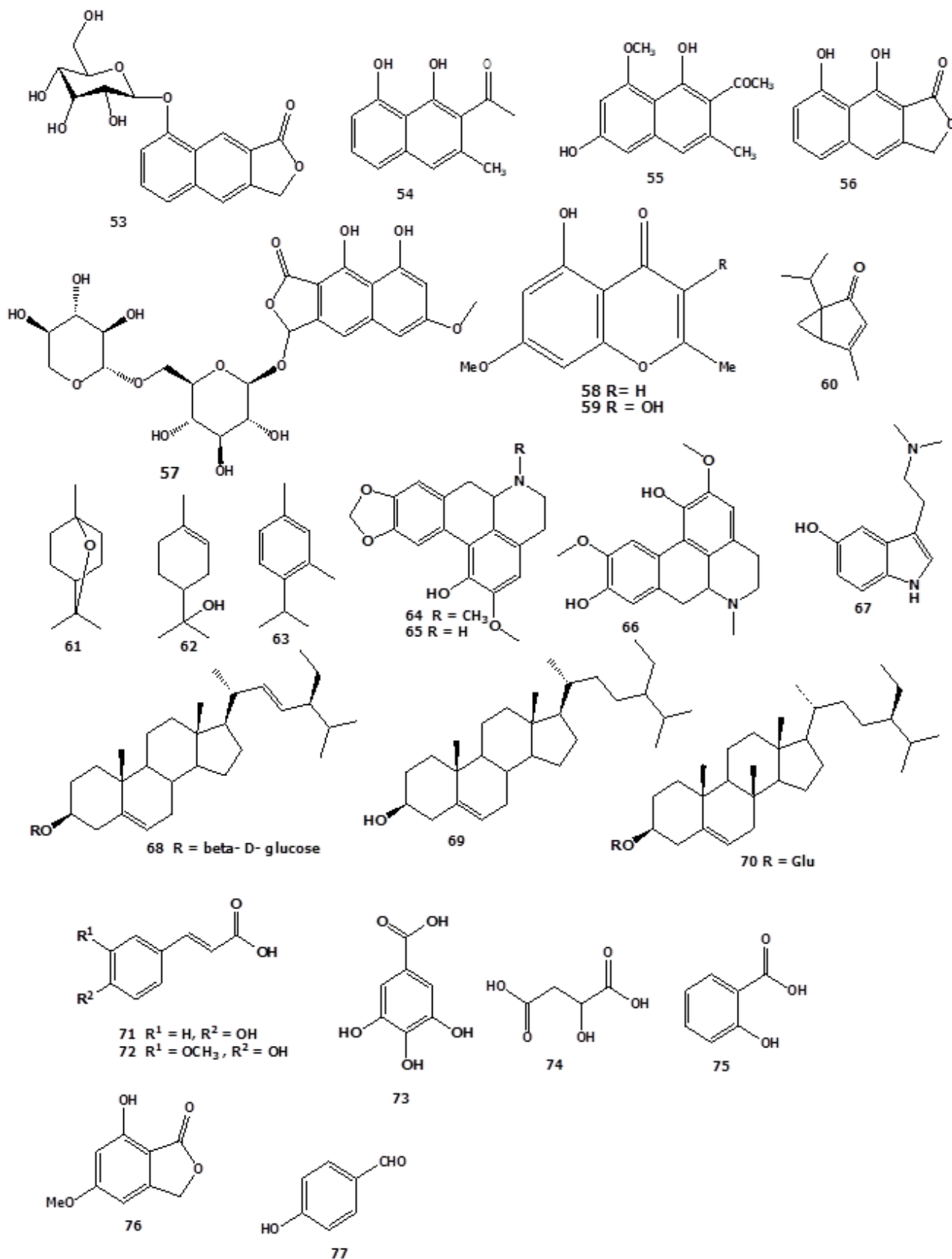


Figure 3: Flavonoids reported from the genus *Rhamnus*.



**Figure 4 :** Naphthalenic derivatives, terpenoids, alkaloids, organic acids and other compounds reported from the *genus Rhamnus*.

## Essential oils

The essential oils from plants are known with various pharmacological activities (112). Campbell et al., (2019) reported essential oils from the leaves of *R. prinoides* of which 4-hydroxy-4-methyl-2-pentanone and ethyl 4-ethoxybenzoate score more than 85% and exhibited significant anti-biofilm activity (113). In a related study, Chouitah et al., (2012) reported essential oils from the leaves of *R. alaternus* (114) of which camphene (17.63 %), linalool (16.13 %), pulegone (15.01 %), naphthalene (14.66 %), mequinol (2.77 %) and borneol (2.13 %) are among the major components.

## Pharmacological activities

### Hepatoprotective activity

Berroukche et al. (2015) evaluated hepatoprotective activity of the macerated *R. alaternus* extract in Wistar rats treated with the toxic carbon tetrachloride (CCl<sub>4</sub>) that causes hepatic damage through evaluation of both the biochemical and histopathological changes in rats. The extracts with bodily weight (250 mg/kg) reduced the elevated levels of alkaline phosphatase (ALP), Glutamic oxaloacetic transaminase (GOT), Glutamic pyruvic transaminase (GPT) and total bilirubin and significantly attenuated the deleterious histopathologic changes in the liver after carbon tetrachloride (CCl<sub>4</sub>)-intoxication (14).

### Anti-inflammatory activity

Thakru and Prasad (2019) evaluated *in vivo* anti-inflammatory activity of ethanolic extract of *R. purpureus* stem bark using the carrageenan-induced rat paw edema assay in adult Swiss albino mice, where 200 mg/kg bodily weight of the extract was administered orally to different groups of mice with indomethacin (10mg/kg) as the positive control. The crude ethanolic extract showed considerable ( $P < 0.05$ ) anti-inflammatory activity with inhibition of 54.50% and 54.77% after 3 h and 4 h of treatment as compared to the standard drug indomethacin (10 mg/kg) showed the inhibition of 50.46%, and 51.78% after 3 h and 4 h of treatment, respectively (115).

Chen et al., (2018) evaluated the anti-inflammatory activity of apigenin (**40**) and Kaempferol (**33**) isolated from 80% methanol bark extract of *R. davurica* Pall using the cyclooxygenase (COX-2) inhibition assay, with aspirin as the positive control. Apigenin (**40**) and Kaempferol (**33**) exhibited anti-inflammatory activity with IC<sub>50</sub> values of 10.14 and 9.27 µg/mL, respectively (74). Chen et al., (2020) evaluated anti-inflammatory activity of 60% ethanol stem and stem bark semi-purified extracts of *R. prinoides* using cyclooxygenase (COX-2) inhibition assay, with

aspirin as the positive control. The semi-purified extract exhibited activity with IC<sub>50</sub> value of 20.6 µg/mL, which was weak activity compared to IC<sub>50</sub> value of 6.33 µg/mL exhibited by ascorbic acid (116).

### Antibacterial activity

Molla et al., (2016) evaluated antibacterial activities of methanol and chloroform solvent fractions of *R. prinoides* crude leaves extract against *S. aureus*, *S. pyogenes*, *S. pneumoniae*, and *S. typhi* using agar well diffusion methods with ampicillin and ciprofloxacin as positive controls. Methanol and chloroform extracts revealed antibacterial activities at different concentrations (78 mg/well, 39 mg/well, and 19.5 mg/well). The average minimum inhibitory concentration of the methanol and chloroform extracts ranged from 8.13-32.5 mg/mL and 8.13-16.25 mg/mL, respectively (117).

Ammar et al., (2007) evaluated the antibacterial activities of petroleum ether, chloroform, ethyl acetate, methanol, and total Oligomers flavonoids (TOF) enriched leaves extracts of *R. alaternus* against *S. aureus*, *E. faecalis*, *E. coli*, *S. enteritidis* and *S. typhimurium* using micro dilution and agar dilution methods. The TOF extracts showed activities against *S. aureus*, *E. faecalis*, *E. coli*, *S. enteritidis* and *S. typhimurium* with MIC values of 120 µg/mL, 175 µg/mL, 1.75 mg/mL, 125 µg/mL and 62.5 µg/mL, respectively, while the ethyl acetate extract exhibited with MIC values of 70 µg/mL, 150 µg/mL, 3.75 mg/mL, 100 µg/mL and 175 µg/mL, respectively (118).

Chouitah et al., (2012) evaluated antibacterial activities of essential oils of *R. alaternus* leaves against *P. aeruginosa*, *E. coli* and *S. typhimurium* using the paper disc diffusion method. The essential oils exhibited activities with zones of inhibition 8, 17 and 15 mm, respectively (114). Carranza et al., (2015) evaluated antibacterial activities of methanol extracts of leaves and bark of *R. californica* against *B. cereus*, *S. pyogenes*, *M. smegmatis*, *S. aureus*, methicillin-resistant *S. aureus* (MRSA), *E. coli*, and *P. aeruginosa* using disc diffusion and minimal inhibitory concentration (MIC) assays. Both extracts inhibited MRSA growth and other Gram-positive bacteria with MICs of 3.3-6.0 mg/mL (77). Raja et al., (2018) evaluated antibacterial activities of ethyl acetate extract of *R. wightii* whole part against *S. aureus*, *B. cereus*, *E. faecalis*, *K. pneumoniae*, *P. aeruginosa* and *E. coli* using agar disc diffusion method with streptomycin and gentamycin as positive controls. The ethyl acetate extract of the whole part of *R. wightii* revealed inhibition zones (in mm) of 15, 16.66, 15, 19, 10.66 and 12, respectively, which is highly comparable with the positive control, streptomycin (25 µg/disc) and gentamycin (50

µg/disc). The isolated compound musizen (**54**) and standard drugs have additionally inhibited *S. aureus* and *K. pneumonia* growth at a concentration (MIC value) of 9 µg/mL and 120 µg/mL, respectively (76).

Kosalec *et al.*, (2013) evaluated antibacterial activities of methanol bark extracts of *R. alaternus*, *R. fallax*, *R. intermedia* and *R. pumila* against *S. aureus*, *P. aeruginosa* and *E. coli* using micro-dilution broth assay. All plant extracts exhibited activities with MIC values of ranging from 1.25 to 2.5 µg/mL (86). Carranza *et al.*, (2015) evaluated antibacterial activities of methanol leaf extracts of *R. californica* against *S. aureus*, Methicillin-resistant *S. aureus*, *B. cereus*, *P. aeruginosa*, *S. pyogenes* and *E. coli* using Kirby-Bauer disc diffusion assay with streptomycin as positive control. The extract exhibited activities with zone of inhibition ranging from 9 mm to 14.3 mm, which was moderate activities compared to the standard with zone of inhibition ranging from 17 mm to 23.8 mm (77).

#### Antifungal Activity

Kosalec *et al.*, (2013) evaluated antibacterial activities of methanol bark extracts of *R. alaternus*, *R. fallax*, *R. intermedia* and *R. pumila* against *C. albicans*, *A. niger* and *M. gypseum* using micro-dilution broth assay. All the plant extracts exhibited activities with MIC values of 0.625 mg/mL and 2.5 mg/mL against *Candida albicans* and *Aspergillus niger*, respectively, whereas extracts of *R. fallax*, *R. intermedia* and *R. pumila* exhibited with MIC value of 0.313 mg/mL against dermatophyte species (*Microsporum gypseum*) (86).

#### Antimalarial activity

Koch *et al.* (2009) evaluated antimalarial activities of chloroform root bark extracts of *R. prinoides* against chloroquine-sensitive *Plasmodium falciparum* strain using ELISA assay with chloroquine as standard drug. The extract exhibit with IC<sub>50</sub> value of 3.53µg/mL, which was weak activities compared to IC<sub>50</sub> value of 0.004 µg/mL exhibited by chloroquine the standard drug (119). Another study evaluated the anti-plasmodia activities of n-hexane, dichloromethane, and methanol root extracts of *R. prinoides* using the radioisotope method. All extracts were found to have *in vitro* antimalarial activity. The highest activity was displayed by n-hexane and dichloromethane extracts with IC<sub>50</sub> values of 19.9 µg/mL and 30.3 µg/mL, respectively (120). The naphthalene derivative geshoidin (**53**) from *R. prinoides* showed an IC<sub>50</sub> value of 4.0 pM and 0.4 pM against the chloroquine-sensitive (D6) and chloroquine-resistant (W2) strains of *Plasmodium falciparum* (121). In a related study, *in vivo* anti-malarial activity of aqueous extracts from leaves

and root barks of *R. staddo*, *R. prinoides* and their chloroquine (CQ) potential effects against a blood-induced CQ-resistant rodent parasite in mice showed high chemo suppression in the range 51% -75% (122). Results of those studies suggest that the extracts of *R. prinoides* have a promising antiplasmodial activity which supports the folkloric use of the plant for treating malaria.

#### Antioxidant activity

Bhouri *et al.*, (2011) evaluated Kaempferol 3-O-β-isorhamninoside (**31**) and rhamnocitrin 3-O-β-isorhamninoside (**36**) isolated from soxhlet methanolic leaves extract of *R. alaternus* using superoxide radical scavenging activity with riboflavin as reference signal. The compounds produced an 80.4% and 85.6% decrease in NBT/riboflavin photo reduction, respectively, at a dose of 150 µg/assay. However K3O-ir was more potent superoxide scavenger with an IC<sub>50</sub> value of 18.75 µg/mL than R3O-ir (IC<sub>50</sub> = 22.5 µg/mL)(73). Rocchetti *et al.*, (2019) determined the antioxidant activities of methanol and aqueous unmatute fruit extracts of *R. petiolaris* using radical scavenging activities (DPPH and ABTS assay) with reported as trolox equivalents (mgTE/g extract) as reference. The methanolic and aqueous unmatute fruit extracts were the most effective 2,2-diphenyl-1-picrylhydrazyl (DPPH) and 2,2'-azino-bis(3-ethylbenzothiazoline-6-sulfonic acid) (ABTS) scavenger (470.96 mg trolox equivalent (TE)/g and 394.96 mg TE/g) respectively (123).

Zeouk *et al.*, (2020) evaluated *in vivo* antioxidant activities of ethanolic extracts of *R. alaternus* leaves using scavenging activities (DPPH assay) with butylated hydroxytoluene (BHT) as a standard. The crude extract showed activities with IC<sub>50</sub> value of 58 µg/mL, which has good antioxidant activities when compared to IC<sub>50</sub> value of 31 µg/mL exhibited by butylated hydroxytoluene (BHT), the positive control. Similarly, ethanolic extracts of *R. alaternus* leaves fraction have exhibited highest antioxidant activity with IC<sub>50</sub> values of 32.76%, 27.01% and 38.87%, respectively(96).

Ammar *et al.*, (2008) evaluated the antioxidant activity of aqueous extract and ethyl acetate fraction leaves of *R. alaternus* using Xanthine Oxidase (XOD) assay with allopurinol as positive control. The aqueous extract and ethyl acetate fraction exhibited high xanthine oxidase inhibiting with respective IC<sub>50</sub> values of 208 and 137 µg/mL and super oxide anion scavenging effects with IC<sub>50</sub> values of 132 and 117 µg/mL (124). Ammar *et al.*, (2009) evaluated the antioxidant activities of methanolic and total oligomer flavonoid enriched extracts from *R. alaternus* leaves using DPPH radical scavenging and xanthine oxidase (XOD) assay with vitamin E and allopurinol as positive control, respectively. Rhamnetin-3-O-

isorhamninoside (**37**) showed DPPH activities with IC<sub>50</sub> value of 1.5 µg/mL which is more antioxidant activity as compared to IC<sub>50</sub> value of 3 µg/mL exhibited by vitamin E the standard drug. Similarly, the isolated compound exhibited xanthine oxidase (XOD) inhibiting with respective IC<sub>50</sub> values of 18, 81 and 40 µg/mL and superoxide anion scavenging effects with IC<sub>50</sub> values of 42, 79 and 35 µg/mL as compared with the positive control allopurinol having IC<sub>50</sub> value of 37 and 4 µg/mL, respectively (72).

Ben Ammar *et al.*, (2008) evaluated antioxidant activities of methanol extracts from *R. alaternus* leaves and root bark using DPPH radical scavenging and xanthine oxidase (XOD) assay with α-tocopherol and allopurinol as positive control, respectively. The root bark extract of *R. alaternus* revealed more effective than the leaves extract with IC<sub>50</sub> values of 7.21 and 18.84 µg/mL, respectively, compared to IC<sub>50</sub> value of 3 µg/mL exhibited by α-tocopherol. Similarly, the leaves and root bark extract exhibited xanthine oxidase (XOD) inhibiting with respective IC<sub>50</sub> values of 103.96 and 83.33 µg/mL and superoxide anion scavenging effects with IC<sub>50</sub> values of 171 and 92 µg/mL compared to allopurinol having IC<sub>50</sub> value of 37.3 and 6 µg/mL, respectively (125).

Bhourri *et al.*, (2012) evaluated antioxidant activities of Kaempferol-3-O-β-isorhamninoside and rhamnocitrin 3-O-β-isorhamninoside (**37**) isolated from leaves of *R. alaternus* using cupric reducing antioxidant capacity (CUPRAC), reducing power assay, and ferric reducing antioxidant power (FRAP) with Trolox (10-1000 µg/mL) as a positive control. The compound K3O-ir and R3O-ir exhibited a significant ability to reduce the Cu<sup>2+</sup> neocuproine complex to Cu<sup>+</sup> neocuproine in a dose dependent manner. The highest values obtained with 1 mg/mL of each compound, were 374 µg/mL and 310 µg/mL equivalent to Trolox, respectively. The reducing power assay evaluates antioxidant capacity of compounds based on their ability to reduce ferric (Fe<sup>3+</sup>) to ferrous (Fe<sup>2+</sup>) ion through the donation of an electron, with the resulting ferrous ion (Fe<sup>2+</sup>) formation monitored spectrophotometrically at 700 nm. The tested compounds exhibited good reducing potential a concentration of 1 mg/mL. R3O-ir exhibited higher reducing power of iron (368 µg/mL equivalent of Trolox) than K3O-ir (330 µg/mL equivalent of Trolox) (126).

Chaouche *et al.*, (2020) evaluated the antioxidant activities of methanol-acetone leaves and stem bark extracts of *R. alaternus* using DPPH radical scavenging and ferric reducing antioxidant potential (FRAP) assay with butylated hydroxyanisole (BHA) as a positive control. The leaves and stem bark extracts exhibited DPPH

activities with IC<sub>50</sub> values of 10.5 and 51.2 µg/mL, respectively, which was weak activity compared to IC<sub>50</sub> value of 5.6 µg/mL exhibited by BHA the positive control. Similarly, the leaves and stem bark extracts exhibited FRAP activities with EC<sub>50</sub> values of 0.4 and 1.8 µg/mL, respectively, which was weak activity compared to EC<sub>50</sub> value of 0.1 µg/mL exhibited by BHA (127).

Hsiao *et al.*, (1996) evaluated antioxidant activities of compound isotorachryson (**55**) isolated from root bark extracts of *R. nakaharai* using iron-induced lipid peroxidation technique in rat brain homogenates with butylated hydroxytoluene (BHT), alpha tocopherol and desferrioxamine as a positive controls. The study revealed that isotorachryson (**55**) exhibited IC<sub>50</sub> value of 1.64 µM, which was comparable to IC<sub>50</sub> value of 1.08 µM exhibited by BHT and was more potent than alpha tocopherol and desferrioxamine with IC<sub>50</sub> values of 3.71 and 97.10 µM as standard drug (111).

Kosalec *et al.*, (2013) evaluated antioxidant activities of bark extracts of *R. alaternus*, *R. fallax*, *R. intermedia* and *R. pumila* using β-carotene-linoleic acid, DPPH radical scavenging, reducing power assay, and chelating activity with BHA, ascorbic acid, quercetin, and EDTA as positive controls. All the plant extracts, *R. alaternus*, *R. fallax*, *R. intermedia* and *R. pumila* exhibited activities using β-carotene-linoleic acid assay with EC<sub>50</sub> values of 250, 289, 38 and 29.5 µg/mL respectively, which was greater activity compared to EC<sub>50</sub> value of 852 µg/mL exhibited by ascorbic acid. Similarly, all the plant extracts, *R. alaternus*, *R. fallax*, *R. intermedia* and *R. pumila* exhibited activities using reducing power assay with EC<sub>50</sub> values of 0.91, 1.99, 0.81 and 0.99 µg/mL respectively, which was comparable and greater activities compared to EC<sub>50</sub> values of 7.53, 1.8 and 7.59 µg/mL, respectively, exhibited by BHA, quercetin and ascorbic acid as standard drugs (86).

Lu *et al.*, (2016) evaluated antioxidant activities of alaternin (**10**) and emodin-8-O-glucoside (**20**) isolated from methanol extracts of *R. nakaharai* heart wood using ABTS, DPPH and Superoxide dismutase (SOD-like) assay with ascorbic acid, 3-t-butyl-4-hydroxyanisole (BHA) as positive control. The compound alaternin (**10**), showed DPPH activity with IC<sub>50</sub> value of 117.7 µM, which was moderate activities compared to IC<sub>50</sub> value of 63.7 µM exhibited by ascorbic acid. Also, alaternin (**10**) and emodin-8-O-glucoside (**20**) exhibited SOD-like activities with IC<sub>50</sub> values of 247 and 232 µM, respectively, which were better activities compared to IC<sub>50</sub> value of 292 µM exhibited by BHA (70). Chen *et al.*, (2020) evaluated antioxidant activities of 60% ethanol stem and stem bark crude and semi purified extracts of *R. prinoides* using DPPH

and ABTS assay with butylated hydroxytoluene (BHT) as positive control. The semi-purified extract exhibit DPPH activities with IC<sub>50</sub> value of 0.2 mg/mL, which was more potent than the standard BHT having IC<sub>50</sub> value of 0.286 mg/mL. Similarly, the crude extracts exhibit ABTS activities with IC<sub>50</sub> value of 0.0596 mg/mL, which was comparable to IC<sub>50</sub> value of BHT (116).

Mazhar *et al.*, (2013) evaluated antioxidant activities of methanol extract and their fractions (ethyl acetate, n-butanol, chloroform and n-hexane) of *R. triquetra* aerial parts using DPPH assay with butylated hydroxytoluene (BHT) as a positive control. The crude extract and their fractions exhibited activities with IC<sub>50</sub> values of 70.26, 7.59, 37.98, 60.09 and 182.99 µg/mL respectively, of which the ethyl acetate fraction showed better activity among the extracts, compared to IC<sub>50</sub> value of 12.1 µg/mL exhibited by BHT (128). Boussahel *et al.*, (2013) evaluated antioxidant activities of methanol and aqueous extract of *R. alaternus* leaves using DPPH and β-carotene-linoleic acid assay with butylated hydroxytoluene (BHT) as a positive control. The methanolic and aqueous extracts exhibited DPPH activities with IC<sub>50</sub> values of 0.082 and 0.398 mg/mL, respectively, of which methanol extract is more active, compared to IC<sub>50</sub> value of 0.032 mg/mL exhibited by BHT. Similarly, the methanol extract exhibited activities using β-carotene-linoleic acid assay with 89% inhibition, which was comparable to 99.2% inhibition displayed by BHT (129). Boussahel *et al.*, (2015) evaluated antioxidant activities of methanol bark extract of *R. alaternus* using oxygen radical absorbance capacity assay (ORAC) with trolox equivalent antioxidant capacity as a standard. The extract exhibited with 6.55 mmol TE/g extract, which was more active as compared to the standard TEAC with 0.75 mmol TE/g extract (130).

#### Antiproliferative Activity

Ben Ammar *et al.*, (2008) evaluated the antiproliferative effect of root bark and leaves extracts obtained from *R. alaternus* against K562 human cell line and L1210 mouse lymphoma cells, at various concentrations comprised between 100 and 800 µg/mL using tetrazolium salt (3-(4,5-dimethylthiazol-2-yl)-2,5-diphenyltetrazolium bromide) (MTT) assay. The leaves and roots extracts from *R. alaternus* showed interesting antiproliferative in a dose-dependent manner. The root extract was more effective than the leaves, on both types of leukemia cells. Indeed, concerning the K562 human cell, the IC<sub>50</sub> values of roots and leaves extracts were determined at 165 and 260.69 µg/mL, respectively. Concerning the L1210 cells, the IC<sub>50</sub> values of roots and leaves extracts were determined at 210.73 and 343.10 µg/mL,

respectively, in the presence of α-tocopherol as positive control (125).

Chen *et al.*, (2016) evaluated the antiproliferative effect of 80% methanol extracts obtained from *R. davurica* using protein-staining sulforhodamine B (SRB) microculture colorimetric assay against human cancer cell lines of HT-29 (intestinal carcinoma) and SGC-7901 (gastric carcinoma). The extract exhibited significant dose-dependent antiproliferative activities against HT-29 and SGC-7901 cells with IC<sub>50</sub> values of 24.96 and 89.53 µg/mL, respectively. Meanwhile, inhibitory activities against both HT-29 and SGC-7901 cells significantly increased by the treatment with *R. davurica* bark extract in a time-dependent manner from 24-96 h at a dose of 150 µg/mL, although there was a decrease on SGC-7901 cells at the time from 72 h-96 h (84).

Chen *et al.*, (2018) evaluated the antiproliferative effect of compounds apigenin (**40**) and kaempferol (**33**) obtained from 80% methanol extracts of *R. davurica* bark using MTT colorimetric assay against three human cancer cell lines of Hep G2 (hepatic cancer), SGC-7901 (gastric carcinoma), and HT-29 (intestinal carcinoma). Kaempferol (**33**) exhibited antiproliferative activities against HT-29, SGC-7901 and Hep G2 cells with IC<sub>50</sub> values of 25.7, 13.43 and 20 µg/mL respectively, while the compound apigenin (**40**) exhibited with IC<sub>50</sub> values 19.79, 17.76 and 10.20 µg/mL, respectively (74).

#### Wound healing Activity

Tessema *et al.*, (2021) evaluated wound healing activities of methanol leaf extracts of *R. prinoides* using excision and incision models in adult Swiss albino mice, with nitrofurazone ointment as a standard. Treatment with 5 % and 10 % (w/w) methanol extract ointment exhibited significant wound recovery activities in both excision and incision models, which has higher activity when compared the standard nitrofurazone ointment (131).

#### Cytotoxicity and Toxicity Activity

Ahmadi *et al.*, (2016) evaluated the cytotoxic activities of hydroalcoholic extracts of *R. frangula* against breast cancer cellline (MCF-7) using 3-(4,5-dimethylthiazol-2-yl)-2,5-diphenyl tetrazolium bromide (MTT) assay. The extract exhibited activities with half maximal cytotoxic concentration (CC<sub>50</sub>) value of 10 mg/mL (132). Ben Ammar *et al.*, (2008) evaluated the cytotoxic activities of petroleum ether, chloroform, ethyl acetate, methanol and total oligomers flavonoids (TOF) enriched leaves extracts of *R. alaternus* against human chronic myelogenous K562 and murine Leukaemia L1210 cells using 3-(4,5-dimethylthiazol-2-yl)-2,5-diphenyltetrazolium bromide (MTT) assay. The TOF extract exhibited

with IC<sub>50</sub> values of 75 µg/mL and 198 µg/mL against K562 and L1210 cells, respectively. Similarly, the ethyl acetate extract showed activities with IC<sub>50</sub> values of 232 µg/mL and 176 µg/mL respectively (125).

Bhourri *et al.*, (2011) evaluated the cytotoxic activities of kaempferol 3-O-β-isorhamninoside and rhamnocitrin 3-O-β-isorhamninoside isolated from methanol leaves extracts of *R.alaternus* using Alamar blue assay against human lymphoblastoid TK6 cells, with cells treated by 0.5% DMSO as a control. The compound neither K30-ir nor R30-ir reached 50% inhibition of TK6 cell proliferation (75). Chen *et al.*, (2016) evaluated *in vitro* toxicity activity of 80% ethanol bark extracts of *R. davurica* against normal human hepatic cells (L-O2) using protein-staining sulforhodamine B (SRB) microculture colorimetric assay. The extract exhibited activities with IC<sub>50</sub> value of 229.19 µg/mL on L-O2, which suggested that *R. davurica* bark extract showed very low or no toxicity on hepatic cell viability (84).

Mai *et al.*, (2001) evaluated cytotoxicity activity of prinoidin (**23**) isolated from methanol extracts of *R.nepalensis* fruit against KB (human epidermoid carcinoma of the mouth) cell using MTT assay with doxorubicin as a positive control. Prinoidin (**23**) exhibited IC<sub>50</sub> value of 0.045 µM, which was four times more potent than the standard, doxorubicin, having IC<sub>50</sub> value of 0.2 µM (69). Boussahel *et al.*, (2015) evaluated cytotoxicity of methanol extract of *R.alaternus* bark against human monocytic leukemia cells (U937) using trypan blue assay with taxol as standard drug. The extract exhibited activities with IC<sub>50</sub> values of 6.39 µg/mL, which was comparable to IC<sub>50</sub> value of 2.47 µg/mL exhibited by taxol the standard drug (130).

#### Anti-tyrosinase Activity

Lu *et al.*, (2016) evaluated the anti-tyrosinase activity of 6-methoxysorigenin (**12**) isolated from methanol extracts of *R.nakaharai* using mushroom tyrosine inhibitory assay with kojic acid as positive control. The study revealed that 6-methoxysorigenin (**12**) exhibited activities with IC<sub>50</sub> value of 42.2 µM, which was twofold inhibitory effect than the positive control kojil acid having IC<sub>50</sub> value of 82.1 µM (70).

#### Antihyperlipidemic Activity

Tacherfiout *et al.*, (2018) evaluated antihyperlipidemic activities of methanol extracts of *R.alaternus* leaf on circulating lipids in rats with Triton WR-1339-induced hyperlipidemia, intracellular lipid accumulation and expression of genes of fatty acid metabolism in human hepatoma HepG2 cells, and adipogenesis in the 3T3-L1 murine adipocyte cell model. The Oral crude extract administration decreased blood levels of

cholesterol and triacylglycerol in hyperlipidemic rats (by 60% and 70%, respectively, at 200 mg extract/kg). In HepG2 cells, the extract exposure dose-dependently decreased intracellular lipids and up-regulated gene expression of carnitine palmitoyl transferase 1 involved in fatty acid oxidation, while in the 3T3-L1 model the extract favored preadipocyte proliferation and adipogenesis, pointing to positive effects on adipose tissue expandability(133).

Ammar *et al.*, (2009) evaluated the anti lipid peroxidation activity of kaempferol 3-O-β-isorhamninoside, rhamnocitrin-3-O-isorhamninoside and rhamnetin-3-O-β-isorhamninoside (**37**) from methanol leaf extracts of *R. alaternus* was estimated by calculating the values of malondialdehyde (MDA) in cultured K562 human chronic myelogenous leukemia cells. In this study, the compounds displayed IC<sub>50</sub> values of 180,320 and 106 µg/mL, respectively, compared to IC<sub>50</sub> value of 15µg/mL exhibited by vitamin C as a reference (72).

#### Antimutagenic activity

Ammar *et al.*, (2008) evaluated the antimutagenic activity of leaves extracts by the Ames assay, using the mutagen Aflatoxin B1 (AFB1) at a concentration of 10 µg/mL. The experiment was carried out with two strains of *Salmonella Typhimurium* (i.e., TA98 and TA100) in the presence of various extracts, and spontaneous revertant was used as control. Petroleum ether, chloroform, methanol, water, and total oligomers flavonoids (TOF) extracts obtained by *R. alaternus* were investigated at various doses (10, 50, and 250 µg/mL) and remarkably reduced the AFB1-induced mutagenicity. The study revealed that ethyl acetate extract to be the most effective at a dose of 250 µg/mL. At such dose, the inhibition percentage of mutagenicity was determined by the Ames assay up to 78% for the TA98 strain (124).

#### Antigenotoxic activity

Bhouriet *al.*, (2011) evaluated the antigenotoxic activity of Kaempferol 3-O-β-isorhamninoside and rhamnocitrin3-O-β-isorhamninoside isolated from methanol extract of leaves of *R. alaternus* on *E. coli* PQ37 using SOS chromo test with two positive control snifuroxazide and aflatoxin B1 used at 10 µg/assay and 5 µg/assay, respectively. The assay carried out in absence of both aflatoxin B1 and extracts constituted the negative control. For the three flavonoid concentrations studied (1, 5, and 10 µg/assay), the antigenotoxic activity of rhamnocitrin 3-O-β-isorhamninoside was higher than the one determined for Kaempferol 3-O-β-isorhamninoside (73).

Bhourri *et al.*, (2012) evaluated antigenotoxic properties of Kaempferol 3-O-β-isorhamninoside

(**31**) and rhamnocitrin 3-O- $\beta$ -isorhamninoside (**36**) isolated from leaves of *R. alaternus* (i.e.,) using comet assay on human lymphoblastoid cells TK6 and NH32. Quantification of the comet data was reported as Total DNA damage (TDD). The compound exhibited no significant difference was detected between the TDD induced by K3O-ir (TDD=212, 151 and 67 at concentrations of respectively of 800, 400 and 200  $\mu\text{g}/\text{mL}$ ) and that induced by R3O-ir (TDD=238, 139 and 110) at the same tested concentrations in TK6 cells and the negative control (non-treated cells; TDD=163) on the other hand. In the opposite, a significant increase of the total DNA damage (TDD=348) was

observed in TK6 cells exposed to 75  $\mu\text{M}$  of  $\text{H}_2\text{O}_2$ , compared to the untreated cells. Likewise, K3O-ir and R3O-ir revealed a non genotoxic effect at the doses of (200 and 400  $\mu\text{g}/\text{ml}$ ) whereas the highest tested concentration (800  $\mu\text{g}/\text{mL}$ ) exhibited a genotoxic effect when tested with NH32 cells. The TDD values were 240 and 226 with respectively K3O-ir and R3O-ir, suggesting inducing of DNA breakage in p53 deficient lymphoblastoid human cells (126).

Summary of pharmacological activity of *Rhamanus* species is presented in Table 3 below.

**Table 3:** Pharmacological activities of extracts and isolated compounds from *Rhamnus* species

Activity	Plant species	Extract	Plant Part	Method	Effect	Refs
Hepatoprotective	<i>R. alaternus</i>	aqueous	leaves	Biochemical and histopathological changes in Wistar rats	Extract reduced levels of alkaline phosphatase (ALP), Glutamic oxaloacetic transaminase (GOT), Glutamic pyruvic transaminase (GPT) and total bilirubin and significantly attenuated deleterious histopathological changes in the liver	(14)
Anti-inflammatory	<i>R. alaternus</i>	ethanol	Stem bark	Carrageenan-induced rat paw edema assay	extract exhibited anti-inflammatory activity with inhibition of 54.50% and 54.77% after 3 hr and 4 hr of treatment as compared the standard drug indomethacin (10 mg/kg) showed the inhibition of 50.46%, and 51.78% after 3hr and 4hr of treatment, respectively	(115)
Anti-inflammatory	<i>R. prinoides</i>	ethanol	Stem and stem bark	Cyclooxygenase (COX-2) assay	extract exhibited activities with IC <sub>50</sub> value of 20.6 µg/mL, which was weak activities compared to IC <sub>50</sub> value of 6.33 µg/mL exhibited by ascorbic acid the standard	(116)
Anti-inflammatory	<i>R. davurica</i>	methanol	bark	Cyclooxygenase (COX-2) assay	The isolated compounds, apigenin ( <b>40</b> ) and Kaempferol ( <b>33</b> ) exhibited activities with IC <sub>50</sub> values of 10.14 and 9.27 µg/mL respectively	(74)
Antibacterial	<i>R. prinoides</i>	Methanol and chloroform	leaves	Agar well diffusion	Extract exhibited activities against <i>S. aureus</i> , <i>S. pyogen</i> , <i>S. pneumoniae</i> , and <i>S. typhi</i> with MIC value of methanol and chloroform fractions ranged from 8.13 mg/mL to 32.5 mg/mL and from 8.13 mg/mL to 16.25 mg/mL, respectively.	(117)
Antibacterial	<i>R. californica</i>	methanol	Leaf and bark	Disc diffusion	Both extracts exhibited activities against <i>B. cereus</i> , <i>S. pyogenes</i> , <i>M. smegmatis</i> , <i>S. aureus</i> , methicillin-resistant <i>S. aureus</i> (MRSA) with MIC value of 3.3-6.0 mg/mL	(77)
Antibacterial	<i>R. alaterus</i>	Ethyl acetate and Total Oligomers flavonoids (TOF)	leaves	Microdilution and agar dilution	The TOF extract exhibited activities against <i>S. aureus</i> , <i>E. faecalis</i> , <i>E. coli</i> , <i>S. enteritidis</i> and <i>S. typhimurium</i> with MIC values of 120 µg/mL, 175 µg/mL, 1.75 mg/mL, 125 µg/mL and 62.5 µg/mL respectively, while the ethyl acetate extract exhibited with MIC values of 70µg/mL, 150µg/mL, 3.75 mg/mL, 100 µg/mL and 175 µg/mL respectively	(118)
Antibacterial	<i>R. wightii</i>	Ethyl acetate	Whole part	Agar disc diffusion	Extract exhibited activities against <i>S. aureus</i> , <i>B. cereus</i> , <i>E. faecalis</i> , <i>K.pneumonia</i> , <i>P. aeruginosa</i> and <i>E. coli</i> with inhibition zones (in mm) of 15, 16.66, 15, 19, 10.66 and 12 respectively	(76)
Antibacterial	<i>R.</i>	methanol	Bark	Micro-dilution	All extract exhibited activities against <i>S. aureus</i> , <i>P.</i>	(86)

	<i>alaternus, R. fallax, R. intermedia</i> and <i>R. pumila</i>			broth assay	<i>aeruginosa</i> and <i>E. coli</i> with MIC value of ranging from 1.25 to 2.5 µg/mL	
Antibacterial	<i>R. californica</i>	methanol	Leaves	Kirby-Bauer disc diffusion	Extract exhibited activities against <i>Staphylococcus aureus</i> , <i>Methicillin-resistant Staphylococcus aureus</i> , <i>Bacillus cereus</i> , <i>Pseudomonas aeruginosa</i> , <i>Streptococcus pyogenes</i> and <i>Escherichia coli</i> with zone of inhibition ranging from 9 mm to 14.3 mm	(77)
Antibacterial	<i>R. wightii</i>	Ethyl acetate	Whole part	Agar disc diffusion	Musizen ( <b>54</b> ) exhibited activities against <i>S. aureus</i> and <i>K. pneumonia</i> with MIC value of 9 µg/mL, which was more potent than the standard drug Streptomycin having MIC value of 120 µg/mL	(76)
Antifungal	<i>R. alaternus, R. fallax, R. intermedia</i> and <i>R. pumila</i>	methanol	Bark	micro-dilution broth assay	All extract exhibited activities against <i>C. albicans</i> , <i>A. niger</i> and <i>M. gypseum</i> with MIC values of 0.625 mg/mL and 2.5 mg/mL against <i>C. albicans</i> and <i>A. niger</i> respectively, while the plant extracts <i>R. fallax, R. intermedia</i> and <i>R. pumila</i> exhibited with MIC value of 0.313 mg/ml against dermatophyte species ( <i>M. gypseum</i> )	(86)
Antimalarial	<i>R. prinoides</i>	Chloroform	Root bark	ELISA assay	extract exhibited activities against chloroquine-sensitive <i>Plasmodium falciparum</i> strain with IC <sub>50</sub> value of 3.53 µg/mL, which was weak activities compared to IC <sub>50</sub> value of 0.004 µg/mL exhibited by chloroquine the standard drug	(119)
Antimalarial	<i>R. prinoides</i>	Hexane & dichloromethane	root	Radioisotope	extracts of hexane and dichloromethane exhibited activities anti-plasmodia with IC <sub>50</sub> values of 19.9 µg/mL and 30.3 µg/mL, respectively	(120)
Antimalarial	<i>R. prinoides</i> and <i>R. staddo</i>	aqueous	Leaves and root bark	blood-induced CQ-resistant rodent parasite in mice	The plant extract and standard drug, chloroquine (CQ) potential effects against a blood-induced CQ-resistant rodent parasite in mice showed high chemo suppression in the range 51% -75%	(122)
Antioxidant	<i>R. alaterus</i>	methanol	Root bark and leaves	DPPH, Xanthine Oxidase (XOD) and Superoxide anion scavenging effects	The root bark and Leaves extract exhibited DPPH activities with IC <sub>50</sub> values of 7.21 and 18.84 µg/mL, respectively, when compared to IC <sub>50</sub> value of 3 µg/mL exhibited by α-tocopherol the positive control. Similarly, the leaves and root bark extract exhibited xanthine oxidase (XOD) inhibiting with respective IC <sub>50</sub> values of 103.96 and 83.33 µg/mL and superoxide anion scavenging effects with IC <sub>50</sub> values of 171 and 92 µg/mL as compared with the positive control allopurinol having	(125)

Antioxidant	<i>R. petiolaris</i>	Methanol and aqueous	fruit	DPPH and ABTS assay	IC50 value of 37.3 and 6 µg/mL respectively Extracts exhibited activities with 470.96 mg trolox equivalent (TE)/g and 394.96 mg TE/g respectively	(123)
Antioxidant	<i>R. alaternus</i>	methanol	leaves	DPPH, Xanthine Oxidase and Superoxide anion scavenging effects	Rhamnetin-3-O-β-isorhamninoside ( <b>38</b> ) exhibited DPPH activities with IC <sub>50</sub> value of 1.5 µg/mL which is more antioxidant activity as compared to IC <sub>50</sub> value of 3 µg/mL exhibited by vitamin E the standard drug. Similarly, kaempferol 3-O-β-isorhamninoside ( <b>31</b> ), rhamnocitrin-3-O-β-isorhamninoside ( <b>36</b> ) and rhamnetin-3-O-isorhamninoside ( <b>37</b> ) exhibited xanthine oxidase (XOD) inhibiting with respective IC <sub>50</sub> values of 18, 81 and 40 µg/mL and superoxide anion scavenging effects with IC <sub>50</sub> values of 42, 79 and 35µg/mL as compared with the positive control allopurinol having IC <sub>50</sub> value of 37 and 4µg/mL respectively	(72)
Antioxidant	<i>R. alaternus</i>	methanol	leaf	Super oxide radical scavenging	Kaempferol 3-O-β-isorhamninoside ( <b>31</b> ) and rhamnocitrin 3-O-β-isorhamninoside exhibited activities with IC <sub>50</sub> values 18.75 and 22.5 µg/mL respectively	(73)
Antioxidant	<i>R. nakaharai</i>	methanol	Heart wood	DPPH assay	The isolated compound, alaternin ( <b>10</b> ) exhibited activities with IC <sub>50</sub> value of 117.7 µM, which was moderate activities compared to IC <sub>50</sub> value of 63.7 µM exhibited by ascorbic acid the standard drug	(70)
Antioxidant	<i>R. nakaharai</i>		Root bark	Iron induced lipid peroxidation	The isolated compound, isotorachryson ( <b>55</b> ) exhibited activities with IC <sub>50</sub> value of 1.64 µM, which was comparable to IC <sub>50</sub> value of 1.08 µM exhibited by the standard butylated hydroxyl toluene (BHT) and was more potent than α-tocopherol and desferrioxamine with IC <sub>50</sub> values of 3.71 and 97.10 µM respectively	(111)
Antioxidant	<i>R. alaternus</i>	ethanol	leaves	DPPH assay	extract exhibited activities with IC <sub>50</sub> value of 58 µg/mL, which has good antioxidant activities when compared to IC <sub>50</sub> value of 31 µg/mL exhibited by butylatedhydroxytoluene (BHT), the positive control	(96)
Antioxidant	<i>R. alaterus</i>	Aqueous and ethyl acetate fraction	leaves	Xanthine Oxidase (XOD) and Super oxide anion scavenging	aqueous extract and ethyl acetate fraction exhibited high xanthine oxidase inhibiting with respective IC <sub>50</sub> values of 208 and 137µg/mL, and super oxide anion scavenging effects with IC <sub>50</sub> values of 132 and 117µg/mL	(124)
Antioxidant	<i>R. alaterus</i>	Methanol-acetone	Leaf and stem bark	DPPH assay and ferric reducing antioxidant potential	leaves and stem bark extracts exhibited DPPH activities with IC <sub>50</sub> values of 10.5 and 51.2µg/mL respectively, which was weak activity compared to IC <sub>50</sub> value of 5.6µg/mL exhibited by BHA the positive control and FRAP	(127)

					activities with EC <sub>50</sub> values of 0.4 and 1.8 µg/mL respectively, which was weak activity compared to EC <sub>50</sub> value of 0.1 µg/mL exhibited by BHA the positive control	
Antioxidant	<i>R. alaternus</i>		leaves	Cupric reducing antioxidant (CUPRAC), reducing power assay and ferric reducing antioxidant power (FRAP)	Kaempferol 3-O-β-isorhamninoside ( <b>31</b> ) and rhamnocitrin 3-O-β-isorhamninoside ( <b>36</b> ) exhibited CUPRAC and reduced power assay activities with IC <sub>50</sub> value of 1 mg/mL, while FRAP activities exhibited at the same concentration 1000 µg/mL reduce a maximum of iron ion by 300 µg/mL and 320 µg/mL equivalent of Trolox respectively	(126)
Antioxidant	<i>R. alaternus</i> , <i>R. Fallax</i> , <i>R. intermedia</i> and <i>R. pumila</i>		Bark	beta-Carotene-linoleic acid, DPPH radical scavenging, reducing power assay and Chelating activity	All exhibited activities using β-Carotene-linoleic acid assay with EC <sub>50</sub> values of 250,289, 38 and 29.5 µg.mL respectively, which was greater activity compared to EC <sub>50</sub> value of 852 µg/mL exhibited by ascorbic acid the positive control. Similarly, all the plant extracts exhibited activities using reducing power assay with EC <sub>50</sub> values of 0.91, 1.99, 0.81 and 0.99 µg/mL respectively, which was comparable and greater activities compared to EC <sub>50</sub> values of 7.53, 1.8 and 7.59 µg/mL respectively exhibited by BHA, quercetin and ascorbic acid as standard drugs	(86)
Antioxidant	<i>R. prinoides</i>	ethanol	Stem and stem bark	DPPH and ABTS assay	The semi purified extract exhibited DPPH activities with IC <sub>50</sub> value of 0.2 mg/mL, which was more potent than the standard BHT having IC <sub>50</sub> value of 0.286 mg/mL. Similarly, the crude extracts exhibit ABTS activities with IC <sub>50</sub> value of 0.0596 mg/mL, which was comparable to IC <sub>50</sub> value of BHT, the positive control	(116)
Antioxidant	<i>R. triquetra</i>	methanol	Aerial part	DPPH assay	crude extract and their fractions (ethyl acetate , n-butanol, chloroform and n-hexane) exhibited activities with IC <sub>50</sub> values of 70.26, 7.59, 37.98, 60.09 and 182.99 µg/mL respectively, which was the ethyl acetate fraction, is more active compared to IC <sub>50</sub> value of 12.1 µg/mL exhibited by the standard (BHT)	(128)
Antioxidant	<i>R. alaternus</i>	Methanol and aqueous	leaves	DPPH and β-carotene-linoleic acid assay	The methanol and aqueous extracts exhibited DPPH activities with IC <sub>50</sub> values of 0.082 and 0.398 mg/mL respectively, which was the methanol extract, is more active compared to IC <sub>50</sub> value of 0.032 mg/mL exhibited by the standard (BHT). Similarly, the methanol extract exhibit activities using β-carotene-linoleic acid assay with 89% inhibition, which was comparable to 99.2% inhibition by BHT the standard	(129)

Antioxidant	<i>R. alaternus</i>	methanol	leaves	Oxygen radical absorbance capacity assay (ORAC)	extract exhibited with 6.55 mmol TE/g extract, which was more active as compared to the standard TEAC with 0.75 mmol TE/g extract	(130)
Anti-hyperlipidemia	<i>R. alaternus</i>	methanol	leaves	Calculating Malondialdehyde in cultured K562 cells	kaempferol 3-O- $\beta$ -isorhamninoside ( <b>31</b> ), rhamnocitrin-3-O- $\beta$ -isorhamninoside ( <b>36</b> ) and rhamnetin-3-O-isorhamninoside ( <b>37</b> ) from methanol leaf extracts exhibited by calculating the values of malondialdehyde (MDA) in cultured K562 human chronic myelogenous leukemia cells with IC <sub>50</sub> values of isolated compound 180,320 and 106 $\mu$ g/mL, respectively	(72)
Anti-hyperlipidemia	<i>R. alaternus</i>	methanol	leaves	Using Hyperlipidemia rats	The Oral crude extract administration decreased blood levels of cholesterol and triacylglycerols in human hepatoma HePG2 and 3T3-L1 murine dipocyte cell hyperlipidemic rats model (by 60% and 70%, respectively, at 200 mg extract/kg)	(133)
Anti-proliferative	<i>R. alaternus</i>	methanol	Root bark and leaf	MTT assay	The root barks and leaf extract exhibited activities against K562 cells with IC <sub>50</sub> value of 165 and 260.69 $\mu$ g/mL. Similarly the extracts exhibited activities against L1210 cells with IC <sub>50</sub> value of 210.73 and 343.10 $\mu$ g/mL, respectively	(125)
Anti-proliferative	<i>R. davurica</i>	methanol	bark	sulforhodamine B (SRB)micro culture colorimetric assay	The extract exhibited activities against human cancer cell lines HT-29 and SGC-7901 with IC <sub>50</sub> values of 24.96 and 89.53 $\mu$ g/mL. respectively	(84)
Anti-proliferative	<i>R. davurica</i>	methanol	bark	MTT colorimetric assay	Kaempferol ( <b>33</b> ) exhibited activities against human cancer cell lines HT-29, SGC-7901 and HePG2 with IC <sub>50</sub> values of 25.7, 13.43 and 20 $\mu$ g/mL respectively, while the compound apigenin ( <b>40</b> ) exhibited with IC <sub>50</sub> values 19.79, 17.76 and 10.20 $\mu$ g/mL respectively	(74)
Wound healing	<i>R. prinoides</i>	methanol	leaves	Excision and incision models in adult Swiss albino mice	Treatment with 5 % and 10 % (w/w) methanol extract ointment exhibited significant wound recovery activities in both excision and incision models	(131)
Cytotoxicity	<i>R. frangula</i>	hydroalcoholic		MTT assay	Extract exhibited activities against breast cancer cell lines (MCF-7) with half maximal cytotoxic concentration (CC <sub>50</sub> ) value of 10 mg/mL.	(132)
Cytotoxicity	<i>R. alaternus</i>	Ethyl acetate and Total Oligomers	leaf	MTT assay	TOF extract exhibited activities against human chronic myelogenous K562 and murine leukemia L1210 with IC <sub>50</sub> values of 75 $\mu$ g/mL and 198 $\mu$ g/mL against K562 and L1210 cells respectively. Similarly, the ethyl acetate	(125)

		flavonoids			extract showed activities with IC <sub>50</sub> values of 232 µg/mL and 176 µg/mL respectively	
Toxicity	<i>R. davurica</i>	ethanol	bark	Sulforhodamine B (SRB) microculture colorimetric assay	Extract exhibited activities against normal human hepatic cells (L-02) with IC <sub>50</sub> value of 229.19 µg/mL .	(84)
Cytotoxicity	<i>R. alaternus</i>	methanol	leaf	Alamar blue assay	kaempferol 3-O-β-isorhamninoside ( <b>31</b> ) and rhamnocitrin 3-O-β-isorhamninoside ( <b>36</b> ) exhibited activities against human lymphoblastoid TK6 cells, the compound neither K30-ir nor R30-ir reached 50% inhibition of TK6 cell proliferation	(75)
Cytotoxicity	<i>R. nepalensis</i>	methanol	fruit	MTT assay	The isolated compound, prinoidin ( <b>23</b> ) exhibited activities against KB ( human epidermoid carcinoma of the mouth) with IC <sub>50</sub> value of 0.045 µM, which was four times more potent than the standard, doxorubicin having IC <sub>50</sub> value of 0.2 µM	(69)
Cytotoxicity	<i>R. alaternus</i>	methanol	bark	Trypan blue assay	extract exhibited activities against human monocytic leukemia cells (U937) with IC <sub>50</sub> values of 6.39 µg/mL, which was comparable to IC <sub>50</sub> value of 2.47 µg/mL exhibited by taxol the standard drug	(130)
Anti-tyrosinase	<i>R. nakaharai</i>	methanol	Heart wood	Mushroom tyrosine inhibitory assay	6-methoxysorigenin ( <b>12</b> ) exhibited activities with IC <sub>50</sub> value of 42.2 µM, which was twofold inhibitory effect than the positive control kojil acid having IC <sub>50</sub> value of 82.1 µM	(70)
Anti-mutagenicity	<i>R. alaternus</i>	aqueous	leaf	Ames assay	The ethyl acetate fraction exhibited against <i>Salmonella Typhimurium</i> (TA98) strains with a dose of 250 µg/mL and 78% inhibition mutagenicity	(124)
Antigenotoxic	<i>R. alaternus</i>	methanol	leaf	SOS chromo test	kaempferol 3-O-β-isorhamninoside ( <b>31</b> ) and rhamnocitrin 3-O-β-isorhamninoside ( <b>36</b> ) on <i>E. coli</i> PQ37 at different concentration (1,5 and 10 µg/mL) showed antigenotoxicity activities	(73)
Antigenotoxic	<i>R. alaternus</i>	methanol	leaf	Comet assay	Kaempferol 3-O-β-isorhamninoside ( <b>31</b> ) and rhamnocitrin 3-O-β-isorhamninoside ( <b>36</b> ) exhibited activities against human lymphoblastoid cells TK6 at the same tested concentration, the total DNA damage induced by K30-ir and R30-ir showed no significant difference was detected	(126)

**CONCLUSION**

Traditional medicine continues as an alternative care available for the majority of the developing countries due to its intrinsic qualities, unique and holistic approaches as well as its accessibility and affordability. The present review endeavors to provide a comprehensive and up to date compilation of documented traditional medicinal uses, phytochemicals and pharmacological activities of the genus and provided valuable information in support of its uses as an alternative medicine for future healthcare practice. Phytochemicals including anthraquinones and flavonoids are the most dominant compounds reported from the genus of which polyphenols were abundant with tremendous antioxidant, wound healing and antiinflammatory activities. The genus afforded exemplary drug leads such as 6-methoxysorigenin (**12**) and prinoidin (**23**) with anti-tyrosinase and cytotoxicity as well as antioxidant drug leads such as Rhamnetin-3-*O*- $\beta$ -isorhamninoside (**37**) and isotorachryson (**55**). Nevertheless, more attention should be paid to the genus considering its wide spectrum of pharmacological properties. Further investigation should be conducted to evaluate promising crude extracts as well as compounds in search for new drug candidates.

**CONFLICT OF INTEREST**

The authors declare that there is no conflict of interest.

**ACKNOWLEDGMENT**

Authors express their gratitude to Adama Science and Technology University for providing access to various journal databases.

**REFERENCES**

1. Nigussie G. A review on traditionally used medicinal plants for scabies therapy in Ethiopia. *ADV TRADIT MED (ADTM)*. 2021 Jun;21(2):199–208. [<DOI>](#).
2. Nigussie G, Ibrahim F, Neway S. A Phytopharmacological Review on a Medicinal Plant: *Cordia africana* Lam. *J Trop Pharm Chem*. 2021 Jan 18;5(3):254–63. [<DOI>](#).
3. Anonymous. Plants of the World online [Internet]. 2021. [<URL>](#).
4. Quattrocchi U. CRC world dictionary of medicinal and poisonous plants [Internet]. CRC Press; 2014 [cited 2021 Jul 29]. [<URL>](#).
5. Dafni A, Yaniv Z, Palevitch D. Ethnobotanical survey of medicinal plants in northern Israel. *Journal of Ethnopharmacology*. 1984 May;10(3):295–310. [<DOI>](#).
6. Watson RR, Preedy VR, editors. Arab herbal medicine. In: Botanical medicine in clinical practice. Wallingford, UK; Cambridge, MA: CABI; 2008. p. 31–9. ISBN: 978-1-84593-413-2.
7. Moerman DE. Native American ethnobotany. Portland, Or: Timber Press; 1998. 927 p. ISBN: 978-0-88192-453-4.
8. Zevin IV, Altman N, Zevin LV. A Russian herbal: traditional remedies for health and healing [Internet]. Rochester, Vt.: Healing Arts Press; 1997 [cited 2021 Jul 29]. ISBN: 978-0-89281-549-4.
9. Watson RR, Preedy VR, editors. Botanical medicine in clinical practice. Wallingford, UK; Cambridge, MA: CABI; 2008. 915 p. ISBN: 978-1-84593-413-2.
10. Page L. Detoxification: all you need to know to recharge, renew and rejuvenate your body, mind and spirit! Carmel Valley, CA: Traditional Wisdom, Inc.; 2002. ISBN: 978-1-884334-54-2.
11. Xutian S. Handbook of traditional chinese medicine. Singapore: World Scientific; 2014. ISBN: 978-981-4571-34-0.
12. Tucakov J. [Ethnophytotherapy of diabetes. Critical view on the use of medicinal plant extracts in our national medicine in the treatment of diabetes mellitus]. *Srp Arh Celok Lek*. 1978 Feb;106(2):159–73.
13. Chhabra S, Uiso F. Antibacterial activity of some Tanzanian plants used in traditional medicine. *Fitoterapia*. 1991;62(6):499–503.
14. Abdelkrim B, Khaled K, Miloud S, Imane D, Kheira A. Hepatoprotective effects of the decoction and macerated leaves of *Rhamnus alaternus* L. on rats exposed to carbon tetrachloride. *J Pharmacognosy Phytother*. 2015 Oct 31;7(10):253–62. [<DOI>](#).
15. Amabye TG. Evaluation of Phytochemical, Chemical Composition, Antioxidant and Antimicrobial Screening Parameters of *Rhamnus prinoides* (Gesho) Available in the Market of Mekelle, Tigray, Ethiopia. *Nat Prod Chem Res* [Internet]. 2016;04(01):1000198, 1-6. [<DOI>](#).
16. Montalvo A, Riordan E, Beyers J. Plant profile for *Rhamnus crocea* and *Rhamnus ilicifolia*. Native

Plant Recommendations for Southern California Ecoregions. 2020;

17. Evans WC, Evans D. Trease and Evans pharmacognosy. Edinburgh; London; New York: Saunders Elsevier; 2009. ISBN: 978-0-7020-2933-2.

18. Kubitzki K. Flowering plants - Dicotyledons: Celastrales, oxalidales, rosales, cornales, ericales [Internet]. 2004 [cited 2021 Jul 29]. ISBN: 978-3-662-07257-8.

19. Boukef K. Rhamnus alaternus. Essaydali. 2001;81:34–5.

20. Benarba B. Medicinal plants used by traditional healers from South-west Algeria: an ethnobotanical study. J Intercult Ethnopharmacol. 2016;5(4):320. [<DOI>.](#)

21. Nazim B, Houari T, Ismail B. Ethnobotanical Survey of Some Plants Used in Tessala Region, Algeria. Current Perspectives on Medicinal and Aromatic Plants (CUPMAP). 2020 Apr 1;3(1):18–24. [<DOI>.](#)

22. Miara MD, Bendif H, Rebbas K, Rabah B, Hammou MA, Maggi F. Medicinal plants and their traditional uses in the highland region of Bordj Bou Arreridj (Northeast Algeria). Journal of Herbal Medicine. 2019 Jun;16:100262. [<DOI>.](#)

23. Calvo MI, Cavero RY. Medicinal plants used for cardiovascular diseases in Navarra and their validation from Official sources. Journal of Ethnopharmacology. 2014 Nov;157:268–73. [<DOI>.](#)

24. Menendez-Baceta G, Aceituno-Mata L, Molina M, Reyes-García V, Tardío J, Pardo-de-Santayana M. Medicinal plants traditionally used in the northwest of the Basque Country (Biscay and Alava), Iberian Peninsula. Journal of Ethnopharmacology. 2014 Feb;152(1):113–34. [<DOI>.](#)

25. Leto C, Tuttolomondo T, La Bella S, Licata M. Ethnobotanical study in the Madonie Regional Park (Central Sicily, Italy)—Medicinal use of wild shrub and herbaceous plant species. Journal of Ethnopharmacology. 2013 Mar;146(1):90–112. [<DOI>.](#)

26. Akerreta S, Cavero RY, López V, Calvo MI. Analyzing factors that influence the folk use and phytonomy of 18 medicinal plants in Navarra. J Ethnobiology Ethnomedicine. 2007 Dec;3(1):16. [<DOI>.](#)

27. Fortini P, Di Marzio P, Guarrera PM, Iorizzi M. Ethnobotanical study on the medicinal plants in the Mainarde Mountains (central-southern Apennine, Italy). Journal of Ethnopharmacology. 2016 May;184:208–18. [<DOI>.](#)

28. Redzic S. Wild medicinal plants and their usage in traditional human therapy (Southern Bosnia and Herzegovina, W. Balkan). Journal of Medicinal Plants Research. 2010;4(11):1003–27. [<URL>.](#)

29. Altundag E, Ozturk M. Ethnomedicinal studies on the plant resources of east Anatolia, Turkey. Procedia - Social and Behavioral Sciences. 2011;19:756–77. [<DOI>.](#)

30. Jarić S, Kostić O, Mataruga Z, Pavlović D, Pavlović M, Mitrović M, et al. Traditional wound-healing plants used in the Balkan region (Southeast Europe). Journal of Ethnopharmacology. 2018 Jan;211:311–28. [<DOI>.](#)

31. Jarić S, Popović Z, Mačukanović-Jocić M, Djurdjević L, Mijatović M, Karadžić B, et al. An ethnobotanical study on the usage of wild medicinal herbs from Kopaonik Mountain (Central Serbia). Journal of Ethnopharmacology. 2007 Apr;111(1):160–75. [<DOI>.](#)

32. Šamec D, Kremer D, Grúz J, Jurišić Grubešić R, Piljac-Žegarac J. Rhamnus intermedia Steud. et Hochst.—a new source of bioactive phytochemicals. Croatica Chemica Acta. 2012;85(2):125–9. [<URL>.](#)

33. Šarić-Kundalić B, Dobeš C, Klatte-Asselmeyer V, Saukel J. Ethnobotanical survey of traditionally used plants in human therapy of east, north and north-east Bosnia and Herzegovina. Journal of Ethnopharmacology. 2011 Feb;133(3):1051–76. [<DOI>.](#)

34. Menković N, Šavikin K, Tasić S, Zdunić G, Stešević D, Milosavljević S, et al. Ethnobotanical study on traditional uses of wild medicinal plants in Prokletije Mountains (Montenegro). Journal of Ethnopharmacology. 2011 Jan;133(1):97–107. [<DOI>.](#)

35. Mohagheghzadeh A, Faridi P, Shams-Ardakani M, Ghasemi Y. Medicinal smokes. Journal of Ethnopharmacology. 2006 Nov;108(2):161–84. [<DOI>.](#)

36. Bozyel ME, Merdamert Bozyel E, Canli K, Altuner EM. Türk Geleneksel Tıbbında Tıbbi Bitkilerin Antikanser Kullanımları. Kahramanmaraş Sütçü İmam Üniversitesi Tarım ve Doğa Dergisi. 2019 Dec 31;22(Suppl2):465–84. [<DOI>.](#)

37. Purkayastha J, Nath SC, Islam M. Ethnobotany of medicinal plants from Dibru-Saikhowa Biosphere Reserve of Northeast India. *Fitoterapia*. 2005 Jan;76(1):121-7. [<DOI>..](#)
38. Fakir H, Korkmaz M, Güller B. Medicinal Plant Diversity of Western Mediterranean Region in Turkey. *Journal of Applied Biological Sciences*. 2019;3(2):33-43. [<URL>..](#)
39. Maleki T, Akhiani H. Ethnobotanical and ethnomedicinal studies in Baluchi tribes: A case study in Mt. Taftan, southeastern Iran. *Journal of Ethnopharmacology*. 2018 May;217:163-77. [<DOI>..](#)
40. Nankaya J, Nampushi J, Petenya S, Balslev H. Ethnomedicinal plants of the Loita Maasai of Kenya. *Environ Dev Sustain*. 2020 Mar;22(3):2569-89. [<DOI>..](#)
41. Muthee JK, Gakuya DW, Mbaria JM, Kareru PG, Mulei CM, Njonge FK. Ethnobotanical study of anthelmintic and other medicinal plants traditionally used in Loitokitok district of Kenya. *Journal of Ethnopharmacology*. 2011 Apr;135(1):15-21. [<DOI>..](#)
42. Nankaya J, Gichuki N, Lukhoba C, Balslev H. Medicinal Plants of the Maasai of Kenya: A Review. *Plants*. 2019 Dec 27;9(1):44. [<DOI>..](#)
43. Mesfin F, Seta T, Assefa A. An ethnobotanical study of medicinal plants in Amaro Woreda, Ethiopia. *Ethnobotany Research and Applications*. 2014;12:341-54.
44. Elgorashi E. Screening of medicinal plants used in South African traditional medicine for genotoxic effects. *Toxicology Letters*. 2003 Jul 20;143(2):195-207. [<DOI>..](#)
45. Seleteng Kose L, Moteetee A, Van Vuuren S. Ethnobotanical survey of medicinal plants used in the Maseru district of Lesotho. *Journal of Ethnopharmacology*. 2015 Jul;170:184-200. [<DOI>..](#)
46. Njoroge GN, Bussmann RW. Traditional management of ear, nose and throat (ENT) diseases in Central Kenya. *J Ethnobiology Ethnomedicine*. 2006 Dec;2(1):54. [<DOI>..](#)
47. Kidane B, van Andel T, van der Maesen L, Asfaw Z. Use and management of traditional medicinal plants by Maale and Ari ethnic communities in southern Ethiopia. *J Ethnobiology Ethnomedicine*. 2014;10(1):46. [<DOI>..](#)
48. Teka A, Asfaw Z, Demissew S, Van Damme P. Traditional uses of medicinal plants practiced by the indigenous communities in Gurage Zone, south central Ethiopia. *Ethnobotany Research and Applications*. 2020;19:1-31.
49. Tamene S. Ethnobotanical study of indigenous knowledge on medicinal plant uses and threatening factors around the Malga District, Southern Ethiopia. *International Journal of Biodiversity and Conservation*. 2020;12(3):215-26.
50. Bitew H, Gebregergs H, Tuem KB, Yeshak MY. Ethiopian medicinal plants traditionally used for wound treatment: a systematic review. *Ethiopian Journal of Health Development*. 2019;33(2).
51. Araya S, Abera B, Giday M. Study of plants traditionally used in public and animal health management in Seharti Samre District, Southern Tigray, Ethiopia. *J Ethnobiology Ethnomedicine*. 2015 Dec;11(1):22. [<DOI>..](#)
52. Teklehaymanot T, Giday M. Ethnobotanical study of medicinal plants used by people in Zegie Peninsula, Northwestern Ethiopia. *J Ethnobiology Ethnomedicine*. 2007 Dec;3(1):12. [<DOI>..](#)
53. Asmare T, Yilkal B, Mekuannint T, Yibeltal A. Traditional medicinal plants used to treat maternal and child health illnesses in Ethiopia: an ethnobotanical approach. *J Tradit Med Clin Natur*. 2018;7(277):2.
54. Tabuti JRS, Kukunda CB, Waako PJ. Medicinal plants used by traditional medicine practitioners in the treatment of tuberculosis and related ailments in Uganda. *Journal of Ethnopharmacology*. 2010 Jan;127(1):130-6. [<DOI>..](#)
55. Mesfin K, Tekle G, Tesfay T. Ethnobotanical study of traditional medicinal plants used by indigenous people of Gemad District, Northern Ethiopia. *Journal of Medicinal Plants Studies*. 2013;1(4):32-7. [<URL>..](#)
56. Siyum D, Woyessa D. Assessment of bacteriological quality and traditional treatment methods of water-borne diseases among well water users in Jimma Town, South West Ethiopia. *ARPN J Ag & Bio Sci*. 2013;8:477-86.
57. Abdeta D, Amante M, Tamiru Y. Survey on Ethno Botany and Medicinal Animals at Sayo and Hawa Gelan Districts of Kelem Wollega Zone, Western Ethiopia. *preventive medicine*. 2020;28(2):21408-20.
58. Kamanja I, Mbaria J, Gathumbi P, Mbaabu M, Lanyasanya A, Gakuya D, et al. Medicinal plants used in the management of sexually transmitted infections by the Samburu Community Kenya. *Int J Pharm Res*. 2015;7:44-52.

59. Amuka O, Mbugua PK, Okemo PO. Ethnobotanical survey of selected medicinal plants used by the Ogiek communities in Kenya against microbial infections. *Ethnobotany Research and Applications*. 2014;12:627-41.
60. Garedeew B, Bizuayehu B. A Review on Ethnobotanical Study of Traditional Medicinal Plants Used for Treatment of Liver Problems in Ethiopia. *EJMP*. 2018 Dec 1;26(1):1-18. [<DOI>..](#)
61. Malik ZA, Bhat JA, Ballabha R, Bussmann RW, Bhatt AB. Ethnomedicinal plants traditionally used in health care practices by inhabitants of Western Himalaya. *Journal of Ethnopharmacology*. 2015 Aug;172:133-44. [<DOI>..](#)
62. Sharma P, Samant S. Diversity, distribution and indigenous uses of medicinal plants in Parbati Valley of Kullu district in Himachal Pradesh, Northwestern Himalaya. *Asian J Adv Basic Sci*. 2014;2:77-98.
63. Josabad Alonso-Castro A, Jose Maldonado-Miranda J, Zarate-Martinez A, Jacobo-Salcedo M del R, Fernández-Galicia C, Alejandro Figueroa-Zuñiga L, et al. Medicinal plants used in the Huasteca Potosina, México. *Journal of Ethnopharmacology*. 2012 Aug;143(1):292-8. [<DOI>..](#)
64. Kiringe JW. A survey of traditional health remedies used by the Maasai of Southern Kaijiado District, Kenya. *Ethnobotany Research and Applications*. 2006;4:061-74. [<URL>..](#)
65. Ajaib M, Khan Z, Khan N, Wahab M. Ethnobotanical studies on useful shrubs of district Kotli, Azad Jammu & Kashmir, Pakistan. *Pak J Bot*. 2010;42(3):1407-15. [<URL>..](#)
66. Phondani P, Maikhuri R, Bisht N. Medicinal plants used in the health care system practiced by traditional Vaidyas in Alaknanda catchment of Uttarakhand, India. *Ethnobotanical Leaflets*. 2009;2009(12):4. [<URL>..](#)
67. Rokaya MB, Münzbergová Z, Timsina B. Ethnobotanical study of medicinal plants from the Humla district of western Nepal. *Journal of Ethnopharmacology*. 2010 Aug;130(3):485-504. [<DOI>..](#)
68. Rana TS, Datt B. E THNOBOTANICAL O BSERVATION AMONG J AUN SARIS OF J AUN SAR -B AWAR , D EHRA D UN (U.P.), I NDIA. *International Journal of Pharmacognosy*. 1997 Jan;35(5):371-4. [<DOI>..](#)
69. Mai LP, Guéritte F, Dumontet V, Tri MV, Hill B, Thoison O, et al. Cytotoxicity of Rhamnosylanthraquinones and Rhamnosylanthrones from *Rhamnus nepalensis*. *J Nat Prod*. 2001 Sep;64(9):1162-8. [<DOI>..](#)
70. Lu T-M, Ko H-H. A new anthraquinone glycoside from *Rhamnus nakaharai* and anti-tyrosinase effect of 6-methoxysorigenin. *Natural Product Research*. 2016 Dec 1;30(23):2655-61. [<DOI>..](#)
71. Liao J-C, Deng J-S, Chiu C-S, Huang S-S, Hou W-C, Lin W-C, et al. Chemical Compositions, Anti-Inflammatory, Antiproliferative and Radical-Scavenging Activities of *Actinidia callosa* var. *ephippioides*. *Am J Chin Med*. 2012 Jan;40(05):1047-62. [<DOI>..](#)
72. Ammar RB, Bhouri W, Sghaier MB, Boubaker J, Skandrani I, Neffati A, et al. Antioxidant and free radical-scavenging properties of three flavonoids isolated from the leaves of *Rhamnus alaternus* L. (Rhamnaceae): A structure-activity relationship study. *Food Chemistry*. 2009 Sep;116(1):258-64. [<DOI>..](#)
73. Bhouri W, Sghaier MB, Kilani S, Bouhlef I, Dijoux-Franca M-G, Ghedira K, et al. Evaluation of antioxidant and antigenotoxic activity of two flavonoids from *Rhamnus alaternus* L. (Rhamnaceae): Kaempferol 3-O- $\beta$ -isorhamnoside and rhamnocitrin 3-O- $\beta$ -isorhamnoside. *Food and Chemical Toxicology*. 2011 May;49(5):1167-73. [<DOI>..](#)
74. Chen G, Wu J, Li N, Guo M. Screening for anti-proliferative and anti-inflammatory components from *Rhamnus davurica* Pall. using bio-affinity ultrafiltration with multiple drug targets. *Anal Bioanal Chem*. 2018 Jun;410(15):3587-95. [<DOI>..](#)
75. Bhouri W, Bouhlef I, Boubaker J, Kilani S, Ghedira K, Ghedira LC. Induction of apoptosis in human lymphoblastoid cells by kaempferol 3-O- $\beta$ -isorhamnoside and rhamnocitrin 3-O- $\beta$ -isorhamnoside from *Rhamnus alaternus* L. (Rhamnaceae): Induction of apoptosis in human lymphoblastoid cells. *Cell Proliferation*. 2011 Jun;44(3):283-90. [<DOI>..](#)
76. Raja WRT, Antony S, Entomology Research Institute, Loyola College, Chennai - 600034, India, Pachaiyappan SK, Entomology Research Institute, Loyola College, Chennai - 600034, India, Amalraj J, et al. Antibacterial Activity study of Musizin isolated from *Rhamnus wightii* Wight & Arn. *Bioinformation*. 2018 Dec 31;14(9):511-20. [<DOI>..](#)

77. Carranza MG, Sevigny MB, Banerjee D, Fox-Cubley L. Antibacterial activity of native California medicinal plant extracts isolated from *Rhamnus californica* and *Umbellularia californica*. *Ann Clin Microbiol Antimicrob*. 2015 Dec;14(1):29. [<DOI>..](#)
78. Brihi N. Pharmacological activity of alkaloids: a review. *Asian Journal of Botany*. 2018;1:1-6.
79. Lin C-N, Chung M-I, Lu C-M. Anthraquinones from *Rhamnus formosana*. *Phytochemistry*. 1990;29(12):3903-5. [<DOI>..](#)
80. Ben Ammar R, Miyamoto T, Chekir-Ghedira L, Ghedira K, Lacaille-Dubois M-A. Isolation and identification of new anthraquinones from *Rhamnus alaternus* L and evaluation of their free radical scavenging activity. *Natural Product Research*. 2019 Jan 17;33(2):280-6. [<DOI>..](#)
81. Hernández-Carlos B, Fernández R, Delgado F, Tamariz J, Zepeda LG, Joseph-nathan P. The Chemical Constituents of *Rhamnus serrata* var. *serrata*. *Natural Product Letters*. 1996 Feb;8(1):39-42. [<DOI>..](#)
82. Moussi K, Nayak B, Perkins LB, Dahmoune F, Madani K, Chibane M. HPLC-DAD profile of phenolic compounds and antioxidant activity of leaves extract of *Rhamnus alaternus* L. *Industrial Crops and Products*. 2015 Nov;74:858-66. [<DOI>..](#)
83. Wang L, Fan S, Wang X, Wang X, Yan X, Shan D, et al. Physicochemical Aspects and Sensory Profiles as Various Potential Factors for Comprehensive Quality Assessment of Nü-Er-Cha Produced from *Rhamnus heterophylla* Oliv. *Molecules*. 2019 Sep 4;24(18):3211. [<DOI>..](#)
84. Chen G, Li X, Saleri F, Guo M. Analysis of Flavonoids in *Rhamnus davurica* and Its Antiproliferative Activities. *Molecules*. 2016 Sep 23;21(10):1275. [<DOI>..](#)
85. Abegaz BM, Kebede T. Geshoidin: A bitter principle of *Rhamnus prinoides* and other constituents of the leaves. *Bulletin of the Chemical Society of Ethiopia*. 1995;9(2):107-14. [<URL>..](#)
86. Kosalec I, Kremer D, Locatelli M, Epifano F, Genovese S, Carlucci G, et al. Anthraquinone profile, antioxidant and antimicrobial activity of bark extracts of *Rhamnus alaternus*, *R. fallax*, *R. intermedia* and *R. pumila*. *Food Chemistry*. 2013 Jan;136(2):335-41. [<DOI>..](#)
87. Gonçalves RS, Silva EL, Hioka N, Nakamura CV, Bruschi ML, Caetano W. An optimized protocol for anthraquinones isolation from *Rhamnus frangula* L. *Natural Product Research*. 2018 Feb 1;32(3):366-9. [<DOI>..](#)
88. Moreira TF, Sorbo JM, Souza F de O, Fernandes BC, Ocampos FMM, de Oliveira DMS, et al. Emodin, Physcion, and Crude Extract of *Rhamnus sphaerosperma* var. *pubescens* Induce Mixed Cell Death, Increase in Oxidative Stress, DNA Damage, and Inhibition of AKT in Cervical and Oral Squamous Carcinoma Cell Lines. *Oxidative Medicine and Cellular Longevity*. 2018 Jul 3;2018:1-18. [<DOI>..](#)
89. Genovese S, Tammara F, Menghini L, Carlucci G, Epifano F, Locatelli M. Comparison of three different extraction methods and HPLC determination of the anthraquinones aloemodine, emodine, rheine, chrysophanol and physcione in the bark of *Rhamnus alpinus* L. (Rhamnaceae): Determination of Anthraquinones in *Rhamnus Alpinus*. *Phytochem Anal*. 2010 May;21(3):261-7. [<DOI>..](#)
90. Locatelli M, Genovese S, Carlucci G, Kremer D, Randic M, Epifano F. Development and application of high-performance liquid chromatography for the study of two new oxyprenylated anthraquinones produced by *Rhamnus* species. *Journal of Chromatography A*. 2012 Feb;1225:113-20. [<DOI>..](#)
91. Locatelli M, Tammara F, Menghini L, Carlucci G, Epifano F, Genovese S. Anthraquinone profile and chemical fingerprint of *Rhamnus saxatilis* L. from Italy. *Phytochemistry Letters*. 2009 Nov;2(4):223-6. [<DOI>..](#)
92. Abegaz B, Dagne E. Anthracene derivatives of *Rhamnus prinoides*. *Bulletin of the Chemical Society of Ethiopia*. 1988;2(1):15-20. [<URL>..](#)
93. Abegaz BM, Peter MG. Emodin and emodinanthrone rhamnoside acetates from fruits of *Rhamnus prinoides*. *Phytochemistry*. 1995 Aug;39(6):1411-4. [<DOI>..](#)
94. Hamed MM, Refahy LA, Abdel-Aziz MS. Evaluation of antimicrobial activity of some compounds isolated from *Rhamnus cathartica* L. *Orient J Chem*. 2015;31(2):1133-40.
95. Sharp H, Latif Z, Bartholomew B, Thomas D, Thomas B, Sarker SD, et al. Emodin and syringaldehyde from *Rhamnus pubescens* (Rhamnaceae). *Biochemical systematics and ecology*. 2001;29(1):113-5.
96. Zeouk I, Ouedrhiri W, Jiménez IA, Lorenzo-Morales J, Bazzocchi IL, Bekhti K. Intra-combined antioxidant activity and chemical characterization of three fractions from *Rhamnus alaternus* extract:

- Mixture design. *Industrial Crops and Products*. 2020 Feb;144:112054. <DOI>..
97. Dwivedi SPD, Pandey VB, Shah AH, Rao YB. Chemical constituents of *Rhamnus procumbens* and pharmacological actions of emodin. *Phytother Res*. 1988 Mar;2(1):51-3. <DOI>..
98. Ben Ghezala H, Chaouali N, Gana I, Snouda S, Nouioui A, Belwaer I, et al. Toxic Effects of *Rhamnus alaternus*: A Rare Case Report. *Case Reports in Emergency Medicine*. 2015;2015:1-5. <DOI>..
99. Epifano F, Genovese S, Kremer D, Randic M, Carlucci G, Locatelli M. Re-investigation of the Anthraquinone Pool of *Rhamnus* spp.: Madagascian from the Fruits of *Rhamnus cathartica* and *R. intermedia*. *Natural Product Communications*. 2012 Aug;7(8):1934578X1200700. <DOI>..
100. Cuoco G, Mathe C, Vieillescazes C. New emodin arabinoside acetates from fruits of *Rhamnus alaternus*. *Current Topics in Phytochemistry*, Volume 10. 2011;61-6.
101. Coskun M, Toshiko S, Hori K, Saiki Y, Tanker M. Anthraquinone glycosides from *Rhamnus libanoticus*☆. *Phytochemistry*. 1990;29(6):2018-20. <DOI>..
102. Coskun M, Tanker N, Sakushima A, Kitagawa S, Nishibe S. An anthraquinone glycoside from *Rhamnus pallasii*. *Phytochemistry*. 1984 Jan;23(7):1485-7. <DOI>..
103. Bezabih M, Abegaz BM. Glucofrangulin A diacetate from the fruits of *Rhamnus prinoides*. *Bulletin of the Chemical Society of Ethiopia*. 1998;12(1):45-8. <URL>..
104. Lin C-N, Chung M-I, Gan K-H, Lu C-M. Flavonol and anthraquinone glycosides from *Rhamnus formosana*. *Phytochemistry*. 1991 Jan;30(9):3103-6. <DOI>..
105. Özipek M, Çaliş İ, Ertan M, Rüedi P. Rhamnetin 3-p-coumaroylrhamnoside from *Rhamnus petiolaris*. *Phytochemistry*. 1994 Jan;37(1):249-53. <DOI>..
106. Cuoco G, Mathe C, Vieillescazes C. Liquid chromatographic analysis of flavonol compounds in green fruits of three *Rhamnus* species used in Stil de grain. *Microchemical Journal*. 2014 Jul;115:130-7. <DOI>..
107. Payá M, Máñez S, Villar A. Flavonoid Constituents of *Rhamnus lycioides* L. *Zeitschrift für Naturforschung C*. 1986 Dec 1;41(11-12):976-8. <DOI>..
108. Sakushima A, Coşkun M, Hisada S, Nishibe S. Flavonoids from *Rhamnus pallasii*. *Phytochemistry*. 1983 Jan;22(7):1677-8. <DOI>..
109. Marzouk MS, El-Toumy SAA, Merfort I, Nawwar MAM. Polyphenolic metabolites of *Rhamnus disperma*. *Phytochemistry*. 1999 Nov;52(5):943-6. <DOI>..
110. Máñez S, Payá M, Terencio C, Villar A. Flavonoids of *Rhamnus lycioides*; Part 2. *Planta Med*. 1988 Apr;54(02):187-8. <DOI>..
111. Hsiao G, Ko F-N, Lin C-N, Teng C-M. Antioxidant properties of isotorachryson isolated from *Rhamnus nakaharai*. *Biochimica et Biophysica Acta (BBA) - Protein Structure and Molecular Enzymology*. 1996 Nov;1298(1):119-30. <DOI>..
112. Sut S, Dall'Acqua S, Ibrahim Sinan K, Bene K, Kumar G, Fawzi Mahomoodally M, et al. *Cola caricifolia* (G.Don) K. Schum and *Crotalaria retusa* L. from Ivory Coast as sources of bioactive constituents. *Industrial Crops and Products*. 2020 May;147:112246. <DOI>..
113. Campbell M, Zhao W, Fathi R, Mihreteab M, Gilbert ES. *Rhamnus prinoides* (gesho): A source of diverse anti-biofilm activity. *Journal of Ethnopharmacology*. 2019 Sep;241:111955. <DOI>..
114. Chouitah O, Meddah B, Aoues A. Analysis of the Chemical Composition and Antimicrobial Activity of the Essential Oil from *Rhamnus alaternus*. *Journal of Biologically Active Products from Nature*. 2012 Jan;2(5):302-6. <DOI>..
115. Thakur C, Prasad B. Antiinflammatory Activity of Stem Bark of *Rhamnus purpureus*. *Int J Adv Microbiol Health Res*. 2019;3(1):21-8.
116. Chen G-L, Munyao Mutie F, Xu Y-B, Saleri FD, Hu G-W, Guo M-Q. Antioxidant, Anti-inflammatory Activities and Polyphenol Profile of *Rhamnus prinoides*. *Pharmaceuticals*. 2020 Mar 26;13(4):55. <DOI>..
117. Molla Y, Nedi T, Tadesse G, Alemayehu H, Shibeshi W. Evaluation of the in vitro antibacterial activity of the solvent fractions of the leaves of *Rhamnus prinoides* L'Herit (*Rhamnaceae*) against pathogenic bacteria. *BMC Complement Altern Med*. 2016 Dec;16(1):287. <DOI>..
118. Ben Ammar R, Kilani S, Bouhlel I, Skandrani I, Naffeti A, Boubaker J, et al. Antibacterial and cytotoxic activities of extracts from (Tunisian) *Rhamnus alaternus* (*Rhamnaceae*). *Ann Microbiol*. 2007 Sep;57(3):453-60. <DOI>..

119. Koch A, Tamez P, Pezzuto J, Soejarto D. Evaluation of plants used for antimalarial treatment by the Maasai of Kenya. *Journal of Ethnopharmacology*. 2005 Oct;101(1-3):95-9. [<DOI>..](#)
120. Bosire K. An investigation of a traditional herbal therapy used to treat malaria in Kisii [Internet] [Master of Science Thesis]. [Nairobi, Kenya]: University of Nairobi; 2003. [<URL>..](#)
121. Gebru M. Phytochemical and antiplasmodial investigation of rhamnus prinoides and kniphofia foliosa [Internet] [Master of Science Thesis]. [Nairobi, Kenya]: University of Nairobi; 2010. [<URL>..](#)
122. Muregi FW, Ishih A, Suzuki T, Kino H, Amano T, Mkoji GM, et al. In Vivo antimalarial activity of aqueous extracts from Kenyan medicinal plants and their Chloroquine (CQ) potentiation effects against a blood-induced CQ-resistant rodent parasite in mice. *Phytother Res*. 2007 Apr;21(4):337-43. [<DOI>..](#)
123. Rocchetti G, Miras-Moreno MB, Zengin G, Senkardes I, Sadeer NB, Mahomoodally MF, et al. UHPLC-QTOF-MS phytochemical profiling and in vitro biological properties of Rhamnus petiolaris (Rhamnaceae). *Industrial Crops and Products*. 2019 Dec;142:111856. [<DOI>..](#)
124. Ammar RB, Sghaier MB, Boubaker J, Bhourri W, Naffeti A, Skandrani I, et al. Antioxidant activity and inhibition of aflatoxin B1-, nifuroxazide-, and sodium azide-induced mutagenicity by extracts from Rhamnus alaternus L. *Chemico-Biological Interactions*. 2008 Jul;174(1):1-10. [<DOI>..](#)
125. Ben Ammar R, Kilani S, Bouhlel I, Ezzi L, Skandrani I, Boubaker J, et al. Antiproliferative, Antioxidant, and Antimutagenic Activities of Flavonoid-Enriched Extracts from (Tunisian) Rhamnus alaternus L.: Combination with the Phytochemical Composition. *Drug and Chemical Toxicology*. 2008 Jan;31(1):61-80. [<DOI>..](#)
126. Bhourri W, Boubaker J, Kilani S, Ghedira K, Chekir-Ghedira L. Flavonoids from Rhamnus alaternus L. (Rhamnaceae): Kaempferol 3-O- $\beta$ -isorhamninoside and rhamnocitrin 3-O- $\beta$ -isorhamninoside protect against DNA damage in human lymphoblastoid cell and enhance antioxidant activity. *South African Journal of Botany*. 2012 May;80:57-62. [<DOI>..](#)
127. Chaouche TM, Haddouchi F, Boudjemai O, Ghellai I. Antioxidant and hemolytic activity of Ziziphus jujuba Mill and Rhamnus alaternus L (Rhamnaceae) extracts from Algeria. *Activité antioxydante et hémolytique des extraits de Ziziphus jujuba Mill et Rhamnus alaternus (Rhamnaceae) d'Algérie*. *Bulletin de la Société Royale des Sciences de Liège [Internet]*. 2020; [<URL>..](#)
128. Mazhar F, Jahangir M, Abbasi MA, Ilyas SA, Khalid F, Khanum R, et al. Rhamnus triquetra: A Valuable Source of Natural Antioxidants to Shield from Oxidative Stress. *Asian Journal of Chemistry*. 2013;25(15):8569-73.
129. Boussahel S, Dahamna S, Ruberto G, Siracusa L, Harzallah D. Phytochemical Study and Antioxidant Activities of Leaves Extracts from Rhamnus alaternus L. *Pharmacognosy Communications*. 2013;3(1):46-53.
130. Speciale A, Ferlazzo G, Harzallah D, Boussahel S, Dahamna S, Amar Y, et al. Flavonoid profile, antioxidant and cytotoxic activity of different extracts from Algerian Rhamnus alaternus L. bark. *Phcog Mag*. 2015;11(42):102. [<DOI>..](#)
131. Tessema Z, Molla Y. Evaluation of the wound healing activity of the crude extract of root bark of Brucea antidysentrica, the leaves of Dodonaea angustifolia and Rhamnus prinoides in mice. *Heliyon*. 2021 Jan;7(1):e05901. [<DOI>..](#)
132. Ahmadi R, Hatami F, Molseghi M. The Effects of Co-administration of Frangula alnus and Rhamnus frangula Extract on Breast Cancer Cells in Cell Culture. In: *BIOES-16 [Internet]*. 2016. p. 78-80. [<URL>..](#)
133. Tacherfiout M, Petrov PD, Mattonai M, Ribechini E, Ribot J, Bonet ML, et al. Antihyperlipidemic effect of a Rhamnus alaternus leaf extract in Triton-induced hyperlipidemic rats and human HepG2 cells. *Biomedicine & Pharmacotherapy*. 2018 May;101:501-9. [<DOI>..](#)





## Drug Repurposing Against SARS-CoV-2: Targeting Nsp16-Nsp10 Interaction

Sefer Baday\*  

Applied Informatics Department, Informatics Institute, Istanbul Technical University, Ayazaga Campus, Maslak, 34469 Istanbul-Turkey

**Abstract:** Drug repurposing studies have played a crucial role in fighting the Covid-19 pandemic. Discovering a new drug molecule for disease takes a very long time. However, repurposing a drug molecule developed for another disease can accelerate new treatments for a disease. Thus, several drug repurposing studies were carried out targeting essential proteins for SARS-CoV-2. Nsp16-Nsp10 interaction was targeted in this work since this interaction is needed for SARS-CoV-2 to evade the human immune system. Therefore, docking calculations of approved 2126 drug molecules obtained from the Drugbank database were performed using the AutoDock Vina program. These docking calculations, drugs Ledipasvir, Elbasvir, Venetoclax, Digitoxin, Irinotecan, Dexamethasone, Acetyldigitoxin, Dactinomycin, Lumacaftor, and Simeprevir, have the highest docking scores. Significant interactions for these drug molecules were presented.

**Keywords:** Covid-19, SARS-CoV-2, Docking, Drug Repurposing, Nsp16.

**Submitted:** April 20, 2021. **Accepted:** August 05, 2021.

**Cite this:** Baday S. Drug Repurposing Against SARS-CoV-2: Targeting Nsp16-Nsp10 Interaction. JOTCSA. 2021;8(3):933-40.

**DOI:** <https://doi.org/10.18596/jotcsa.923455>.

**\*Corresponding author. E-mail:** [badays@itu.edu.tr](mailto:badays@itu.edu.tr).

### INTRODUCTION

Since the outbreak of the Covid-19 pandemic, more than 130 million people have been infected by SARS-CoV-2 as of April 2021 (1). Even though several vaccines have been developed to combat SARS-CoV-2, existing mutations and prospective mutations necessitate alternative therapeutics (2). Since discovering a novel small molecule against a drug target could take a significant amount of time, drug repurposing studies were performed to speed up the process of finding a drug molecule against SARS-CoV-2 (3). In drug repurposing studies, alternative drug targets are needed due to two important reasons: The loss of efficacy resulting from mutations and enhancing efficacy due to combination therapies. Also, some molecules might not show efficacy in clinical trials despite having promising pre-clinical trial results. Thus, the diversity and abundance of available therapies for the treatment of covid-19 patients is important. Many attempts have been made to contribute the

Covid-19 arsenal. As an example, a detailed interaction study was performed and 332 important protein-protein interactions were reported to be potential drug targets (4). Among apparent targets such as spike Receptor Binding Domain (RBD), SARS-CoV-2 main protease, and transmembrane serine protease 2 (TMPRSS2), Non-structural protein 16 is a promising target for drug repurposing studies (5-7).

Non-structural protein 16 (Nsp16) methylates the viral RNA cap so that viral RNA cannot be distinguished from the host RNA. For the enzymatic activity, Nsp16 needs Non-structural protein 10 (Nsp10). Nsp16 and Nsp10 form a heterodimer complex structure (8). The Nsp16/Nsp10 complex transfers a methyl group from S-adenosylmethionine (SAM) cofactor to the 2' hydroxyl of ribose sugar of viral mRNA. Interestingly human homolog of Nsp10, CMTr1 does not need a partner for the methylation activity. Since SAM cofactor is also needed in several human

methyltransferases, targeting SAM binding site for the drug discovery might not be an ideal strategy due to potential off-target side effects (9). Drug molecules targeting SAM binding site of Nsp16 might also bind human CMTr1. An alternative strategy would be preventing the formation of the Nsp16/Nsp10 complex structure. Thus, in this work, drug repurposing is applied on SARS-CoV-2 Nsp16/Nsp10 interaction site.

Molecular docking calculations are one of the fundamental methods to predict the binding of a ligand to a protein (10-12). There have been several drug repurposing studies that target Nsp16 protein. Tazikeh-Lemeski et al. selected 1516 FDA-approved drug molecules based on similarity with SAM and docked these molecules into the SAM binding groove of Nsp16 (13). Quan Yang and co-workers screened 7,173 stereoisomers of 4,574 approved ligands obtained from the MTiOpenScreen database. They carried out docking of these molecules in the SAM binding pocket (14). Vijayan et al. performed docking of 2,100 FDA drugs from ZINC and 400 compounds from Spec database, and 1,600 drugs from DrugBank into the SAM binding site (15). In these drug repurposing studies, docking calculations were performed on the SAM binding site. However, targeting Nsp16-Nsp10 interaction has not been the focus yet. Therefore, in this work, we aim to predict potential drug molecules which might hamper the interaction of Nsp16 with Nsp10. To do so, the Nsp16-Nsp10 interface is selected as the center in the docking calculations.

## MATERIAL AND METHODS

### Protein and Ligand preparation

The structure of the Nsp16-Nsp10 complex was obtained from the protein data bank (PDB ID: 6W4H). All crystallographic water molecules and non-amino acid molecules were removed from the structure. Protonation states of the amino acids of Nsp16 were determined using python implementation of PROPKA3 (16, 17). Hydrogen atoms were added using the AutoDockTools program (18). The docking box was centered on the Nsp16-Nsp10 interface (Figure 1). The center for the grid box was selected to be 76, 25,16 on X, Y and Z axis by manually orienting the center for the grid box. Note that these coordinates are based on the 6W4H.pdb structure. The dimensions of the docking box were set to be 20, 35, and 25 Å in the X, Y, and Z-axis, respectively. Docking calculations were performed using the AutoDock Vina program (19). The exhaustiveness parameter is set to 24 in these calculations. Information of the 2126 drug molecules was downloaded from the DrugBank in the SDF file format as of April 2021 (20). Three-dimensional structures of the ligands were created and converted into the PDBQT file format using the Open Babel software (21). Ligand interaction diagrams were produced using Maestro (academic version) program (22).

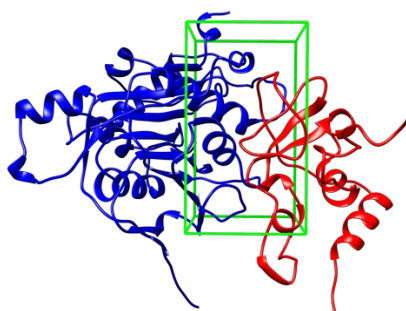


**Figure 1:** Visualization of grid box used in docking calculations. Blue: Nsp16, red: Nsp10, and Green: Docking box.

## RESULTS AND DISCUSSION

Prior to screening of drug molecules, re-docking of SAM molecule was performed to validate the docking protocol. RMSD difference between the binding pose obtained by the docking calculation and the binding pose observed in the crystal

structure was calculated as 0.647 Å (Figure 2). The distribution of the docking scores for tested drug molecules is given in Figure 3. Docking scores were populated around -6.1 kcal/mol. Top-ranked compounds as a result of docking screening are summarized in Table 1.

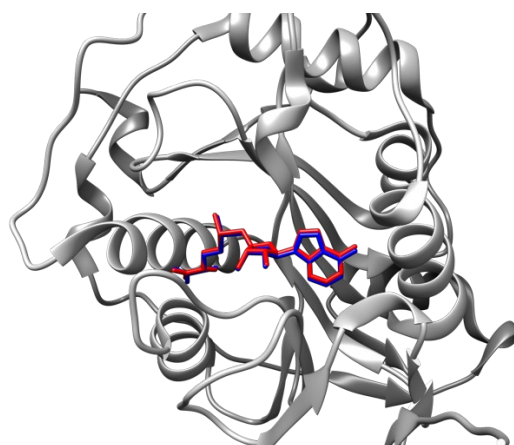


**Figure 2:** Re-docking of SAM molecule. Nsp16 is shown by gray color. Binding pose of SAM obtained by docking calculation is shown by red color. SAM conformation observed in the crystal structure is shown by blue color.

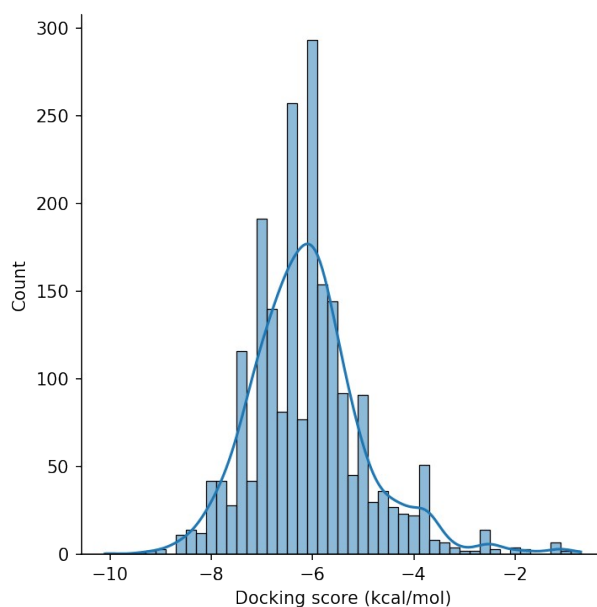


**Figure 3:** Distribution of docking scores.

**Table 1:** Docking scores for the top-ranked drug molecules.

	Drug Name	Docking Score (kcal/mol)	Disease or Condition
1	Ledipasvir	-10.1	Hepatitis C
2	Elbasvir	-9.4	Hepatitis C
3	Venetoclax	-9.2	lymphocytic leukemia
4	Digitoxin	-9.2	Congestive cardiac insufficiency, arrhythmias, and cardiac failure
5	Irinotecan	-9.0	metastatic colorectal cancer
6	Dexamethasone	-9.0	endocrine, rheumatic, collagen, dermatologic, allergic, ophthalmic, gastrointestinal, respiratory, hematologic, neoplastic, edematous
7	Acetyldigitoxin	-8.9	Congestive cardiac failure
8	Dactinomycin	-8.7	Wilms' tumor, childhood rhabdomyosarcoma, Ewing's sarcoma and metastatic, nonseminomatous testicular cancer
9	Lumacaftor	-8.7	cystic fibrosis (CF)
10	Simeprevir	-8.7	hepatitis C

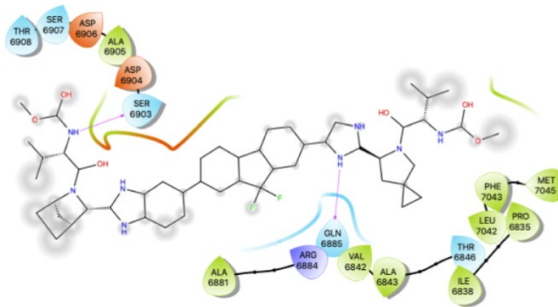
In these docking calculations, the Ledipasvir molecule has the highest absolute docking score of -10.1 kcal/mol. Ledipasvir is used as an antiviral for treating chronic hepatitis C. Important interactions between Ledipasvir and Nsp16 are given in Figure 4. Ledipasvir forms hydrogen bond interactions with Gln6885 and Ser6903 and forms hydrophobic contacts with Val6842, Ala6843, Ala6881, Phe7043, and Leu7042. After Ledipasvir, Elbasvir has the second-highest docking score of -9.4 kcal/mol. Elbasvir is also an antiviral used to treat chronic hepatitis C. Elbasvir makes hydrogen bonds with Ser6903 and Asp6904 and makes hydrophobic contacts with Ala6881, Leu7042, Ala6905, and Pro6835. Venetoclax has the third-highest docking score of -9.2 kcal/mol. Venetoclax is a BCL-2 inhibitor and used for the treatment of chronic lymphocytic leukemia. Venetoclax forms hydrogen bonds with Arg6884 and has hydrophobic contacts with Pro6878, Ala6877, Val6876, and Leu6887. Digitoxin also has a docking score of -9.2 kcal/mol. Digitoxin is a cardiac glycoside used to treat atrial fibrillation, chronic cardiac failure, and arrhythmias. Digitoxin forms hydrophobic contacts with Nsp16 through Pro6888, Leu6887, Val6882, Ala6881, Val6882, Ile6838, Pro6835, Phe7043, and Leu7042 residues. Irinotecan has a docking score of -9.0 kcal/mol. Irinotecan is a topoisomerase-1 inhibitor used for the treatment of colorectal cancer. Irinotecan makes hydrogen bond interaction with Arg6884 and forms hydrophobic contacts with Pro6888, Leu6887, Ala 6877, Val6876, Val6842 and Val6902 residues. Dexamethasone also has -9.0 kcal/mol predicted binding affinity. Dexamethasone is an anti-inflammatory and immunosuppressant molecule used to treat a variety of diseases and conditions such as arthritis, blood/hormone disorders, and allergic reactions. Dexamethasone has hydrophobic contacts with Val6882, Ala6881,

Val6842, Ile6838, and Pro6835. Acetyldigitoxin is an acetyl derivative of digitoxin and has a binding score of -8.9 kcal/mol. Acetyldigitoxin is used for the treatment of congestive cardiac failure. Acetyldigitoxin has hydrophobic interactions with Val6882, Ala6881, Val6842, Ile6838, Pro 6835, Phe7043, and Leu7042. Dactinomycin has -8.9 kcal/mol predicted binding affinity. Dactinomycin is a chemotherapy agent used to treat various cancers such as Wilms' tumor, childhood rhabdomyosarcoma, and Ewing's sarcoma. Dactinomycin has hydrophobic contacts with Ala6881, Val6882, Val6842, Ile6838, and Val6876 amino acids of Nsp16. Lumacaftor also has a binding affinity of -8.7 kcal/mol. Lumacaftor is used for the treatment of cystic fibrosis. Lumacaftor has hydrophobic interaction with Gln6885 and hydrophobic contacts with Pro7049, Leu6887, Pro6888, and Met7045. Simeprevir has a docking score of -8.7 kcal/mol. Simeprevir is an antiviral used to treat hepatitis C. Simeprevir has hydrophobic interactions with Val6876, Ala6877, Pro6878, Ala6881, Leu6887, Ala6905, and Met6839 amino acids. When we compare these top-10 ranked compounds with the predicted compound due to other drug-repurposing studies by Tazikeh-Lemeski et al.; and Vijayan et al., our predictions do not overlap with predictions of these studies (15). This situation is normal since, in those drug repurposing studies against Nsp16, SAM binding site was selected for docking calculations. We also investigated how docked molecules overlap the Nsp16-Nsp10 interface. To do so, we visualized the Nsp16-Nsp10 complex with docked structures of a few drug molecules in Figure 6. It is seen that docked molecules cover the Nsp16-Nsp10 interaction surface well. A summary of the amino acids forming important interactions with drug molecules is presented in Table 2.

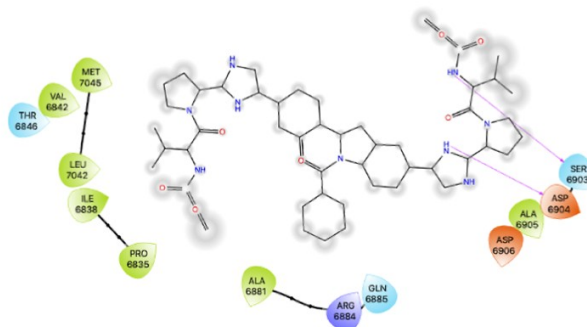
**Table 2:** Summary of important amino acids forming hydrophobic contacts and hydrogen bonds with drug molecules.

Drug Name	Hydrophobic contacts	Hydrogen bonding
Ledipasvir	Val6842, Ala6843, Ala6881, Phe7043	Gln6885, Ser6903
Elbasvir	Ala6881, Leu7042, Ala6905, Pro6835	Ser6903, Asp6904
Venetoclax	Pro6878, Ala6877, Val6876, Leu6887	Arg6884
Digitoxin	Pro6888, Leu6887, Val6882, Ala6881, Val6882, Ile6838, Pro6835, Phe7043, Leu7042	
Irinotecan	Pro6888, Leu6887, Ala 6877, Val6876, Val6842, Val6902	Arg6884
Dexamethasone	Val6882, Ala6881, Val6842, Ile6838, Pro6835	
Acetyldigitoxin	Val6882, Ala6881, Val6842, Ile6838, Pro 6835, Phe7043, Leu7042	
Dactinomycin	Ala6881, Val6882, Val6842, Ile6838, Val6876	
Lumacaftor	Pro7049, Leu6887, Pro6888, and Met704	Gln6885
Simeprevir	Val6876, Ala6877, Pro6878, Ala6881, Leu6887, Ala6905, Met6839	

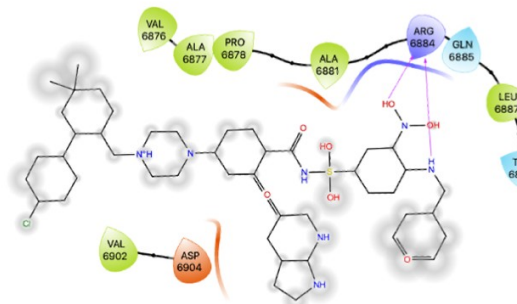
Ledipasvir



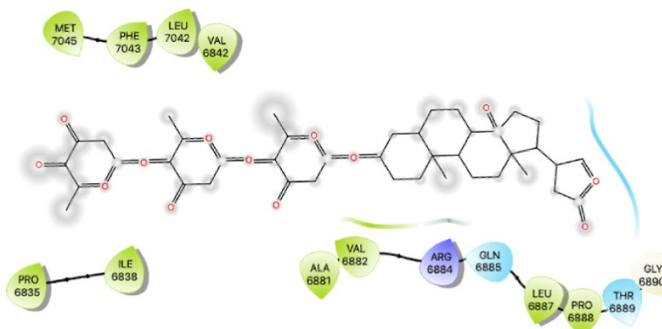
Elbasvir



Venetoclax



Digitoxin



Irinotecan

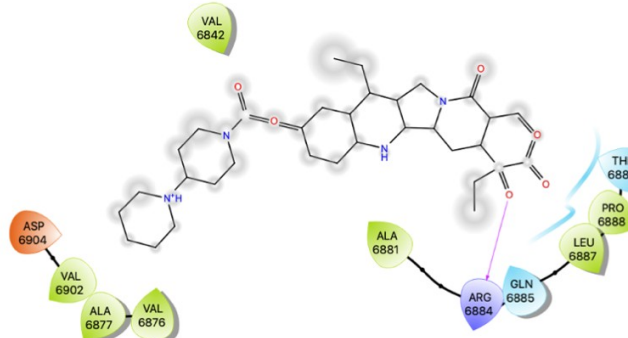
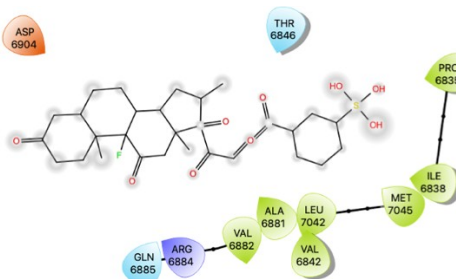
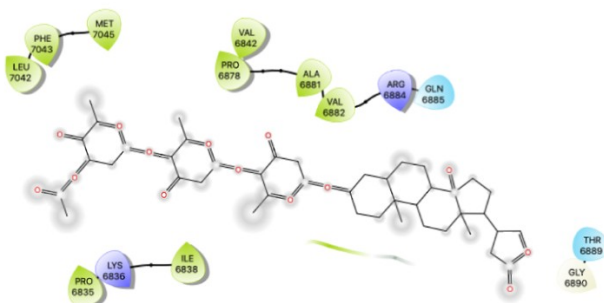


Figure 4: Ligand interaction diagrams using the docked structures of the drug molecules.

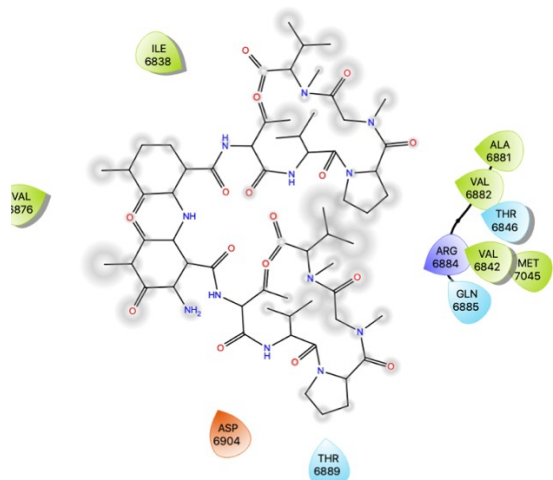
Dexamethasone



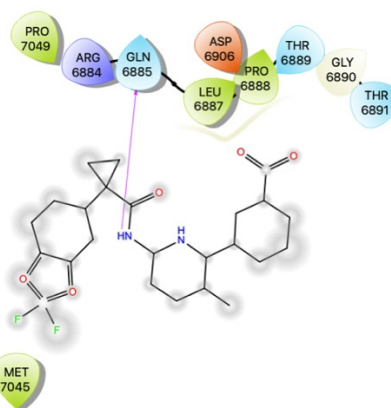
Acetyldigitoxin



Dactinomycin



Lumacaftor



Simeprevir

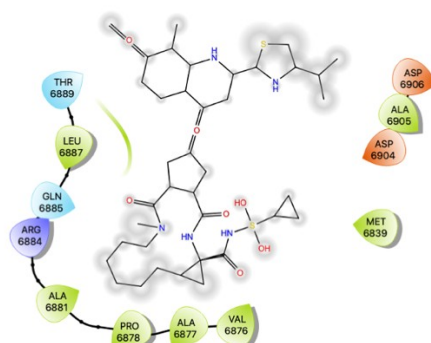
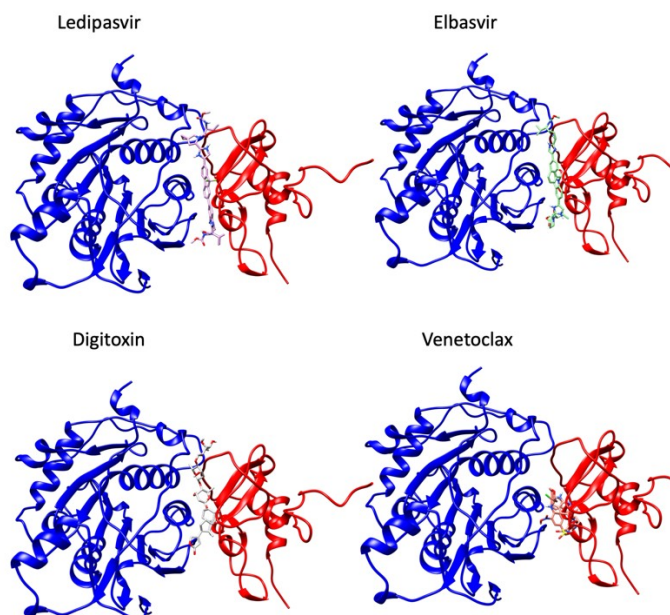


Figure 5: Ligand interaction diagrams using the docked structures of the drug molecules.



**Figure 6:** Visualization of Nsp16-Nsp10 complex with a docked drug molecule. Note that in docking calculations, only Nsp16 is used. Blue color shows Nsp16, and Red color shows Nsp10 proteins.

Current use of the drugs predicted in this work was searched in the literature. Dexamethasone is currently being used for the treatment of hospitalized patients. In randomized clinical trials (RCT) Dexamethasone significantly lowered the mortality rate (23). Ledipasvir/sofosbuvir combination did not exhibit significant efficacy in a very small RCT, yet RCTs with larger sample sizes are needed to assess the efficacy of Ledipasvir (24). Venetoclax is being tested on Covid-19 fit patients with Chronic lymphocytic leukemia (25). There is no RCT study on Digitoxin but there is an experimental evidence on impeding the cytokine storm which eventually could lead to the death of Covid-19 patients (26). Simeprevir has not been tested in an RCT but in combination with remdesivir it can suppress the replication of SARS-CoV-2 in vitro (27). No clinical trial has been performed on Elbasvir, Irinotecan, Acetyldigitoxin, Dactinomycin and Lumacaftor.

## CONCLUSION

The interaction between Nsp16 and Nsp10 is essential for SARS-CoV-2 to escape from the host immune system. In this work, potential drug molecules which could prevent the formation of the Nsp16-Nsp10 complex were predicted using docking calculations. Drugs Ledipasvir, Elbasvir, Venetoclax, Digitoxin, Irinotecan, Dexamethasone, Acetyldigitoxin, Dactinomycin, Lumacaftor, and Simeprevir were ranked in the top-10 by their docking scores. Among other amino acids of Nsp16, Gln6885, Ser6903, Val6842, Ala6881, Phe7043, Leu7042, Asp6904, and Arg6884 were predicted to be essential amino acids for the interaction with drug molecules. Drug molecules predicted in this

study will open new possibilities for the treatment of SARS-CoV-2 infected patients.

## REFERENCES

1. WHO. Coronavirus disease (COVID-19) pandemic [Internet]. World Health Organization; 2021 [cited 2021 Aug 5]. [<URL>](#)
2. Madhi SA, Baillie V, Cutland CL, Voysey M, Koen AL, Fairlie L, et al. Efficacy of the ChAdOx1 nCoV-19 Covid-19 Vaccine against the B.1.351 Variant. *N Engl J Med*. 2021 May 20;384(20):1885-98. [<DOI>](#).
3. Durdagi S. Virtual drug repurposing study against SARS-CoV-2 TMPRSS2 target. *Turkish Journal of Biology*. 2020 Jun 21;44(SI-1):185-91. [<URL>](#).
4. Gordon DE, Jang GM, Bouhaddou M, Xu J, Obernier K, White KM, et al. A SARS-CoV-2 protein interaction map reveals targets for drug repurposing. *Nature*. 2020 Jul 16;583(7816):459-68. [<DOI>](#).
5. Idris MO, Yekeen AA, Alakanse OS, Durojaye OA. Computer-aided screening for potential TMPRSS2 inhibitors: a combination of pharmacophore modeling, molecular docking and molecular dynamics simulation approaches. *Journal of Biomolecular Structure and Dynamics*. 2020 Jul 16;1-19. [<DOI>](#).
6. Choudhary S, Malik YS, Tomar S. Identification of SARS-CoV-2 Cell Entry Inhibitors by Drug Repurposing Using in silico Structure-Based Virtual Screening Approach. *Front Immunol*. 2020 Jul 10;11:1664. [<DOI>](#).
7. Baby K, Maity S, Mehta CH, Suresh A, Nayak UY, Nayak Y. Targeting SARS-CoV-2 Main Protease: A Computational Drug Repurposing Study. *Archives of Medical Research*. 2021 Jan;52(1):38-47. [<DOI>](#).

8. Lin S, Chen H, Ye F, Chen Z, Yang F, Zheng Y, et al. Crystal structure of SARS-CoV-2 nsp10/nsp16 2'-O-methylase and its implication on antiviral drug design. *Sig Transduct Target Ther*. 2020 Dec;5(1):131. [<DOI>](#).
9. Vithani N, Ward MD, Zimmerman MI, Novak B, Borowsky JH, Singh S, et al. SARS-CoV-2 Nsp16 activation mechanism and a cryptic pocket with pan-coronavirus antiviral potential. *Biophysical Journal*. 2021 Jul;120(14):2880-9. [<DOI>](#).
10. El Khatabi K, Aanouz İ, El-MerniSsi R, Khaldan A, Ajana MA, Bouachrine M, et al. Designing of Novel Potential Inhibitors of  $\alpha$ -amylase by 3D-QSAR Modeling and Molecular Docking Studies. *Journal of the Turkish Chemical Society Section A: Chemistry*. 2020 May 10;469-78. [<DOI>](#).
11. Sulaiman M, Hassan Y, Taskin Tok T, Noundou XS. SYNTHESIS, ANTIBACTERIAL ACTIVITY AND DOCKING STUDIES OF BENZYL ALCOHOL DERIVATIVES. *Journal of the Turkish Chemical Society Section A: Chemistry*. 2020 May 11;481-8. [<DOI>](#).
12. Kiliç Kurt Z. Synthesis of Novel Oxadiazole Derivatives, Molecular Properties Prediction and Molecular Docking Studies. *Journal of the Turkish Chemical Society Section A: Chemistry*. 2020 Oct 30;7(3):753-74. [<DOI>](#).
13. Tazikeh-Lemeski E, Moradi S, Raoufi R, Shahlaei M, Janlou MAM, Zolghadri S. Targeting SARS-COV-2 non-structural protein 16: a virtual drug repurposing study. *Journal of Biomolecular Structure and Dynamics*. 2021 Sep 2;39(13):4633-46. [<DOI>](#).
14. Jiang Y, Liu L, Manning M, Bonahoom M, Lotvola A, Yang Z-Q. Repurposing Therapeutics to Identify Novel Inhibitors Targeting 2'-O-Ribose Methyltransferase Nsp16 of SARS-CoV-2 [Internet]. 2020 May [cited 2021 Aug 8]. [<URL>](#). Note: This content is a preprint and has not been peer-reviewed.
15. Vijayan V, Pant P, Vikram N, Kaur P, Singh TP, Sharma S, et al. Identification of promising drug candidates against NSP16 of SARS-CoV-2 through computational drug repurposing study. *Journal of Biomolecular Structure and Dynamics*. 2020 Aug 3;1-15. [<DOI>](#).
16. Olsson M, Søndergard C, Rostkowski M, Jensen J. PROPKA3: Consistent Treatment of Internal and Surface Residues in Empirical pKa predictions. *J Chem Theo Comput*. 2011;(2):525-37.
17. Søndergaard CR, Olsson MHM, Rostkowski M, Jensen JH. Improved Treatment of Ligands and Coupling Effects in Empirical Calculation and Rationalization of pKa Values. *J Chem Theory Comput*. 2011 Jul 12;7(7):2284-95. [<DOI>](#).
18. Morris GM, Huey R, Lindstrom W, Sanner MF, Belew RK, Goodsell DS, et al. AutoDock4 and AutoDockTools4: Automated docking with selective receptor flexibility. *J Comput Chem*. 2009 Dec;30(16):2785-91. [<DOI>](#).
19. Trott O, Olson AJ. AutoDock Vina: Improving the speed and accuracy of docking with a new scoring function, efficient optimization, and multithreading. *J Comput Chem*. 2009;455-61. [<DOI>](#).
20. Wishart DS, Feunang YD, Guo AC, Lo EJ, Marcu A, Grant JR, et al. DrugBank 5.0: a major update to the DrugBank database for 2018. *Nucleic Acids Research*. 2018 Jan 4;46(D1):D1074-82. [<DOI>](#).
21. O'Boyle NM, Banck M, James CA, Morley C, Vandermeersch T, Hutchison GR. Open Babel: An open chemical toolbox. *J Cheminform*. 2011 Dec;3(1):33. [<DOI>](#).
22. Maestro. Schrödinger Release 2016-4 [Internet]. Schrödinger, LLC; 2016 [cited 2021 Aug 5]. [<URL>](#).
23. RECOVERY Collaborative Group, Horby P, Lim WS, Emberson JR, Mafham M, Bell JL, et al. Dexamethasone in Hospitalized Patients with Covid-19. *N Engl J Med*. 2021 Feb 25;384(8):693-704. [<DOI>](#).
24. Khalili H, Nourian A, Ahmadinejad Z, Emadi Kouchak H, Jafari S, Dehghan Manshadi SA, et al. Efficacy and safety of sofosbuvir/ ledipasvir in treatment of patients with COVID-19; A randomized clinical trial. *Acta Biomed*. 2020 Nov 10;91(4):e2020102. [<DOI>](#).
25. Fürstenau M, Langerbeins P, De Silva N, Fink AM, Robrecht S, von Tresckow J, et al. COVID-19 among fit patients with CLL treated with venetoclax-based combinations. *Leukemia*. 2020 Aug;34(8):2225-9. [<DOI>](#).
26. Pollard BS, BLANCOI JC, Pollard JR. Classical Drug Digitoxin Inhibits Influenza Cytokine Storm, With Implications for Covid-19 Therapy. *In Vivo*. 2020;34(6):3723-30. [<DOI>](#).
27. Lo HS, Hui KPY, Lai H-M, He X, Khan KS, Kaur S, et al. Simeprevir Potently Suppresses SARS-CoV-2 Replication and Synergizes with Remdesivir. *ACS Cent Sci*. 2021 May 26;7(5):792-802. [<DOI>](#).



## Adsorption of Nitrogen on Mn(II) Metal-Organic Framework Nanoparticles

Idongesit Justina Mbonu <sup>1\*</sup>  and Olusegun Kehinde Abiola 

<sup>1</sup>Department of Chemistry, Federal University of Petroleum Resources, Effurun, Nigeria

**Abstract:** Adsorption of N<sub>2</sub> on mixed-ligand benzoic acid and 1, 10-phenanthroline ligand of Mn(II) metal-organic framework (MOF)-nanoparticles were demonstrated. The synthesized nanostructures are characterized by techniques such as scanning electron microscopy (SEM), fourier-transform infrared spectroscopy (FT-IR), and UV-visible spectrophotometry (UV-Vis). The pore size distribution and adsorption capacity of the synthesized MOF were investigated experimentally by measuring the N<sub>2</sub> adsorption isotherm at 77.3 K, and the resulting data were fitted to Brunauer-Emmett-Teller (BET), de Boer, Dubinin-Radushkevich (DR), Banet-Joyner-Halenda (BJH), Horvath-Kawazoe (HK), and also applied to Density Functional Theory (DFT) models. Excitation of the Mn-MOF nanostructure resulted in an emission at 400 nm. The DSC study reveals that this molecule has a good chemical stability. The FT-IR measurement shows a variety of functional groups that are highly coordinated. Moreover, the adsorption properties evaluated by several adsorption models compared with current adsorbent materials show Mn-MOF has superior thermal stability, a high surface area, and pore openings. Because of these findings, Mn-MOF appears to be a viable material for storing gases and energy, whether at low or high pressures.

**Keywords:** Metal-organic framework, nanoparticles, Mn complex, adsorption studies.

**Submitted:** March 23, 2021. **Accepted:** August 09, 2021.

**Cite this:** Mbonu IJ, Abiola OK. Adsorption of Nitrogen on Mn(II) Metal-Organic Framework Nanoparticles. JOTCSA. 2021;8(3):941-52.

**DOI:** <https://doi.org/10.18596/jotcsa.901593>.

**\*Corresponding author. E-mail:** [mbonu.idongesit@fupre.edu.ng](mailto:mbonu.idongesit@fupre.edu.ng).

### INTRODUCTION

Self-assembly (1) methodology of synthesis can be a robust (1) tool (2) for the preparation (3) of complex supramolecular (3-4) architectures with fascinating properties. Self-assembly permits greater control (1) in creating two and three-dimensional structures on account of predicting the way metal-ligand coordination sphere (5) and ligand liability direct the reactions (6) to the desired products (7). Nature utilizes different kinds of weak (8), non-covalent (9) interactions (5) like hydrogen (10) bonding, charge-charge (11), donor-acceptor (12),  $\pi$ - $\pi$  (13), van der Waals (14), and hydrophilic and hydrophobic interactions (15), to create self-assembled complex structures with controlled shapes (16), and sizes (17). Self-assembly (3) offers a wealth of understanding processes (4) like natural life fibers (18-19), micelles (20), vesicles (21), ribbons (22), and tubes (23).

Nanoparticles are materials in the size range of 1-100 nm and can be synthesized in a variety of morphologies such as spheres, platelets, disks, rods and tubes. They have large surface area per unit volume and many functions in this small volume.

Research into complex functional organic molecules through dynamic (2) covalent bonding have brought out exploitable chemical and physical properties (24) of these molecules for exciting applications (25) within the fields of energy (4) storage, gas (23) adsorption, gas separation (24), host-guest chemistry (25) and nano-composite preparations (26). The metal ions in coordination polymers (20) are the sources of energy storage, magnetism, luminescence (13), and adsorption within the compound (27). Tailoring functionality to meet required luminescence (28), electronic, mechanical (29), and optical properties need careful control over numerous components for the

formation of self-assembled coordination (21) polymers.

This account focuses on investigating the adsorption (30) capacity of the manganese(II) supramolecular reaction induced by the benzoate ion and 1,10-phenanthroline ligands rearrangement. The two hemilabile ligands possessing different binding sites reacted with manganese metal ions resulting in a heteroligated complex compound with enhanced adsorption capacity for various applications in luminescence and energy storage (4).

In this present work, we established how porous Mn-MOF adsorb nitrogen and can be used for storing energy through comparing theoretical breakthrough curves with the experimentally observed results (11,16). The prepared Mn-MOF builds out as a crystal in all directions, exhibiting a very rigid, uniform, and precise arrangement of atoms with six-coordinate manganese(II) centers as the primary metal node. The carboxylate ligands adopt monodentate and bidentate coordination modes. Because of their affinity for oxygen atoms, they are often used to synthesize functional metal complexes. 1, 10-phenanthroline was in-cooperated to the backbone of the carboxylate ligand to prevent the coordination of more water molecules with the manganese(II) metal ions.

The electronic properties of this six-coordinate Mn(II) center make this MOF reactive towards nitrogen, creating a stronger M-N<sub>2</sub> interaction. The coordination sites saturated with Mn-MOF nanoparticles cannot interact with nitrogen gases (22) easily. The high density of Mn(II) shows a high gas uptake capacity, making Mn-MOF a promising N<sub>2</sub> adsorbent (31) capacity for various applications in the areas of luminescence and energy storage (4). Different adsorption isotherm models (22) were used to evaluate the adsorption (31) capacity of the Mn-MOF and its pore filling towards applications for adsorbent-based chillers, heat pumps, and gas storage (8,32).

## MATERIALS AND METHODS

All the chemicals utilized in this work are of reagent grade (8) and used as obtained. The elemental composition of Mn-MOF was performed on Perkin-Elmer 2400 elemental analyzer. Morphology of the prepared compound was carried out on a Zeiss Supra (32) instrument with a resolution of 5 nm at 30 kV (8). Vibration bands within Mn-MOF were determined using a Nicolet Magna (33) FT-IR spectrometer within the range of 4000–400 cm<sup>-1</sup>.

The surface area, pore size, and pore diameter of the Mn-MOF were evaluated by measuring the N<sub>2</sub> adsorption isotherms (13) at "77.3 K" using an iQMicropore-XR (Quantachrome Instruments, FL, USA). Prior to the experiment, the sample was outgassed (31) under vacuum at 120 °C (33).

A single crystal Mn-MOF (0.05 mm x 0.54 mm x 0.60 mm) was selected and mounted on a cryoloop for structure determination on a Bruker DUO APEX II CCD diffractometer using graphite-monochromatic Moka (λ = 0.71073 Å) Oxford Cryostream-700. The structure was solved by a direct method in SHELXT-2018/3 (34).

### Self-assembly of Mn-MOF nanoparticles

Mn-MOF was prepared as shown in Figure 1. The mixture of MnCl<sub>2</sub>·4H<sub>2</sub>O (0.5 mmol) and benzoic acid (0.1 mmol) in 20 mL aqueous solution was stirred for 5 minutes at 50 °C. NaOH (1 mol/L) solution was used to maintain the hydrogen ion concentration of the reaction mixture. A 5-mL alcoholic solution of 1, 10-phenanthroline (1.5 mmol) was added with stirring for 3 hours at 50 °C. On the fifth day, pale yellow crystals were observed to have separated from the mother liquor in the reaction vessel (31,35). The elemental analysis result shows that the C, H, Mn, and O are 50.50, 4.20, 16.50, and 28.80 (calc.) and 50.48, 4.27, 16.40, and 28.85 (found), respectively.

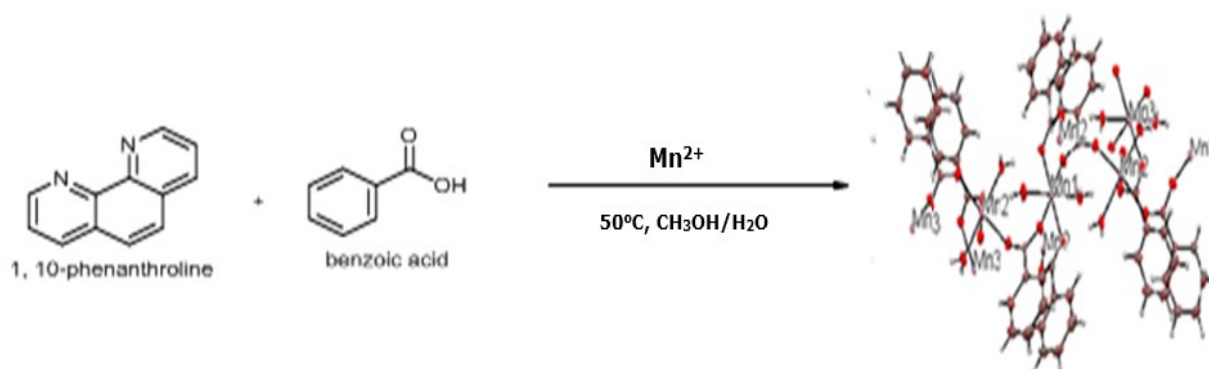


**Figure 1:** Graphical reaction pathway to Mn-MOF nanoparticles.

## RESULTS

The one-pot synthesis of yellow Mn-MOF single crystal analysis in Figure 2a shows a 3D microporous supramolecular network constructed by 2D-layered Mn-MOF with related crystallographic data (8) listed in Table 1. The diffractogram in Figure 2b & 2c shows that the Mn-MOF crystallized in a triclinic space group P-1(31). The asymmetric unit displayed a monodentate

benzoate ligand, two 1, 10-phenanthroline ligands, and a coordinated water molecule. The Mn(II) ion is six coordinated (32) by four nitrogen atoms from two (32) 1,10-phenanthroline ligands, one oxygen atom (15) from the carboxylate group of benzoate ligand, and one oxygen atom (31) from coordinated water molecule resulting in a distorted octahedral shape. Neighboring benzoate and phenyl groups are interlinked through  $\pi$ - $\pi$  stacking interactions (25).

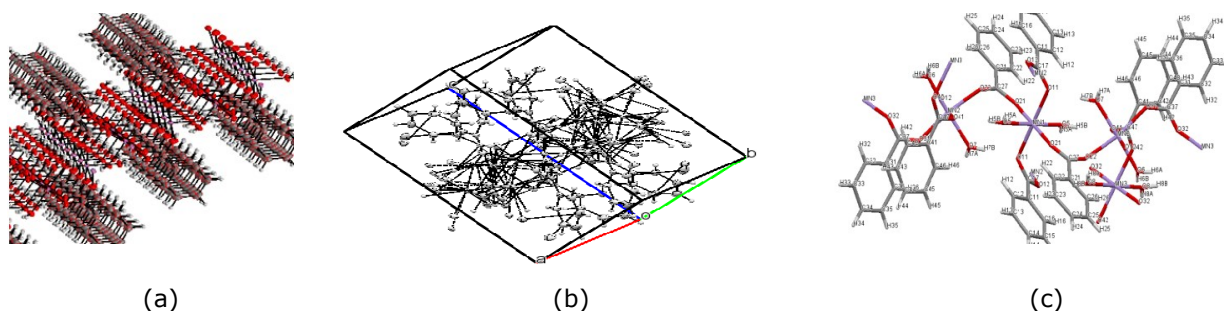


**Figure 2:** a) Projection along 'a' axis of the three-dimensional framework showing the cavities b) Molecular packing along the b axis c) ORTEP drawing of Mn-MOF.

**Table 1:** Crystal data, data collections, and refinement of Mn(II)-MOF at 200 K.

Crystal Data	
Empirical formula	C <sub>28</sub> H <sub>28</sub> Mn <sub>2</sub> O <sub>12</sub>
Formula weight	666.38
Unit Cell Weight	1332.77 [Based on SHELXL2014 Atomic Weights]
Crystal system	Triclinic
Space group	P-1(No.2)
a/Å, a/°	7.4369(3), 88.847(2)
b/Å, β/°	12.9898(6), 82.518(2)
c/Å, γ/°	14.1176(6), 89.975(2)
Volume/Å <sup>3</sup>	1351.93(10)
Z	2
ρ <sub>calc</sub> /g cm <sup>-3</sup>	1.637
μ/mm <sup>-1</sup>	1.001
F(000)	684 [calc. 685.70]
Crystal size/mm <sup>3</sup>	0.05 x 0.54 x 0.60
Wavelength/Å	

Micro-sized structures seen in the SEM image in Figure 3 are plate-like sizes and have porous surface area, implying that Mn-MOF will have high nitrogen adsorption capacity (35). Figure 4 shows

Data Collection	
Temperature/K	200
Theta Min-Max/°	1.6, 28.4
Dataset	-9: 9; -16: 17; -18: 18
/restraints/parameters	
Tot., Uniq. Data, R(int)	49223, 6713, 0.025
Observed Data [I ≥ 2.0σ(I)]	5021
Refinement	
Nref, Npar	6713, 414
R, wR2, S	
w = ∑(FO <sup>2</sup> ) / ∑(wFO <sup>2</sup> )	0.0353, 0.1092, 1.05
+ (0.0551P) <sup>2</sup> + 1.0319	
P] Where	
P = (FO <sup>2</sup> + 2FC <sup>2</sup> ) / 3	
Max. and Av. Shift/Error	0.00, 0.00
Min. and Max. Resd.	-0.56, 1.34
Dens. [e/Å <sup>3</sup> ]	
Radiation/ Å MoKα	0.71073

the fluorescent spectrum, measured within the range of 300-800 nm, shifting to a longer wavelength with an emission maximum of 400 nm (23).

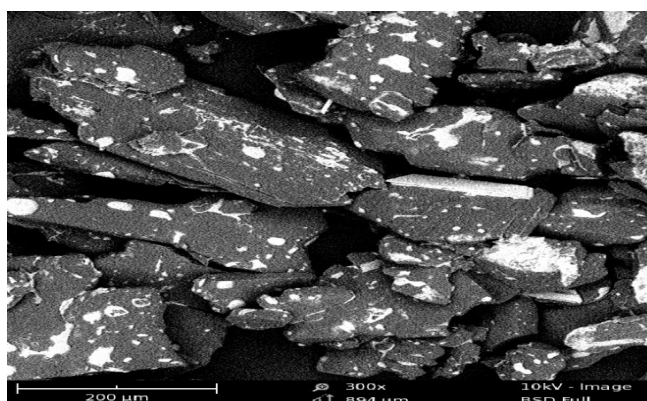


**Figure 3:** SEM micrograph of Mn-MOF.

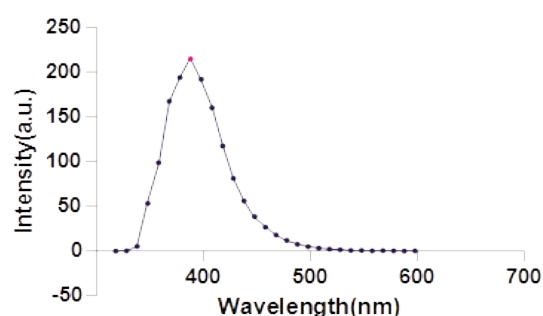


**Figure 4:** Spectrum at  $\lambda_{ex}$  = 308 nm.

The infrared spectrum of Mn-MOF in Figure 5 shows vibration bands within the range (13) of 3100-3753  $\text{cm}^{-1}$  for  $\nu(\text{OH})$  (13) and 842-920  $\text{cm}^{-1}$  for  $\sigma(\text{OH})$  (Kupgan *et al.*, 2019), an indication of coordinated water (13) in Mn-MOF. The complex exhibits N-H stretching within the range of 2753-3373  $\text{cm}^{-1}$ . The asymmetric and symmetric stretching frequencies of carboxylate (29) ions are shown within the range of 1688-1618  $\text{cm}^{-1}$  and

1416-1282  $\text{cm}^{-1}$  (22). The characteristic IR bands of the Mn(II) complex appear at 1688  $\text{cm}^{-1}$  (C=O) (30) and 3373  $\text{cm}^{-1}$  ( $\text{H}_2\text{O}$ ) (23). The N-N stretching frequency (29) of the complex appeared at 779-708  $\text{cm}^{-1}$  (29) is associated with the bidentate bridging nature of neutral ligands. These results are an indication that Mn-MOF was successfully synthesized.

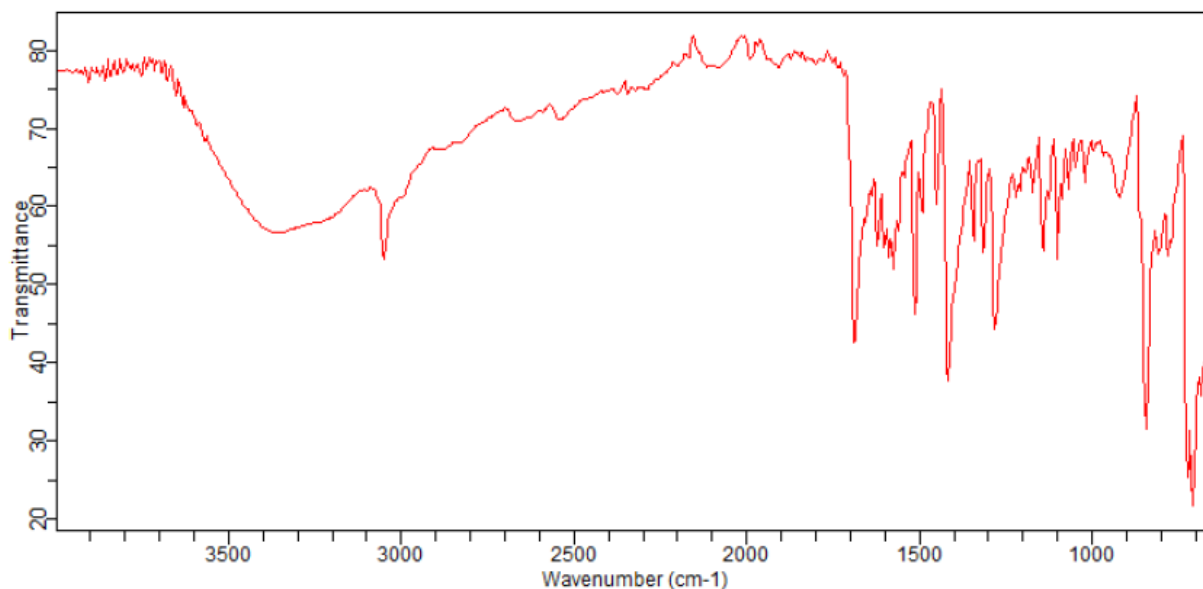


**Figure 5:** FT-IR spectrum of Mn-MOF.

Figure 6 shows the Brunauer-Emmett-Teller (BET) single- multilayer adsorption/desorption isothermal plot of Mn-MOF at 77.3 K (Table 2). The correlation coefficient ( $R^2 = 0.992$ ) and surface area using the BET model was determined by the following linear expression in Equation 1 (22):

$$\frac{1}{W \left[ \left( \frac{P_0}{P} \right) - 1 \right]} = \frac{1}{W_m C} + \frac{C-1}{W_m C} \left( \frac{P_0}{P} \right) \quad (\text{Eq. 1})$$

Where  $W$  = weight of gas adsorbed,  $P/P_0$  = relative pressure,  $W_m$  = weight of adsorbate as a monolayer,  $C$  = BET constant. Slope ( $s$ ), intercept ( $i$ ), and weight ( $W_m$ ) were determined from Equation 2 below:

$$s = \frac{C-1}{W_m C} \quad i = \frac{1}{W_m C} \quad W_m = \frac{1}{s+i} \quad (\text{Eq. 2})$$

Total surface area ( $S_t$ ) was calculated from expression (Equation 3):

$$S_t = \frac{W_m N A_{cs}}{M} \quad (\text{Eq. 3})$$

$N$  = Avogadro's number ( $6.023 \times 10^{23}$ ),  $M$  = Molecular weight of Adsorbate (28.013),  $A_{cs}$  = Adsorbate cross-sectional area ( $16.2 \text{ \AA}^2$  for

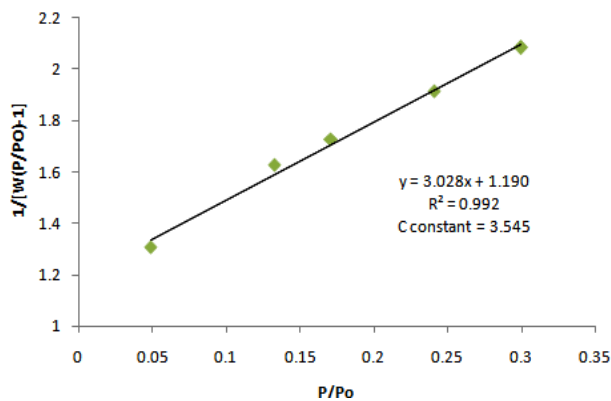
Nitrogen). Specific Surface Area ( $S$ ) (23) is then determined by the total surface area (23) by sample weight in Equation 4:

$$S = \frac{S_t}{W} \quad (\text{Eq. 4})$$

The experimentally determined surface area with the BET model =  $825.465 \text{ m}^2\text{g}^{-1}$  which is large compared to some natural porous (18) materials, such as clay ( $10\text{-}100 \text{ m}^2\text{g}^{-1}$ ) (19), activated graphite ( $119 \text{ m}^2\text{g}^{-1}$ ), and other types of zeolite and porous carbons (18, 23).

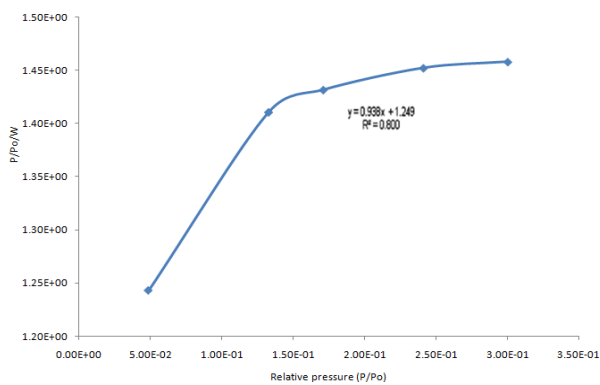
Langmuir's experimental data plot (Figure 7) features a broader plateau region of the loop, which extends up to relatively high  $P/P_0$ . The optimization of relative pressure within the range of  $0.00\text{E}+00$  -  $3.50\text{E}-02$  in Figure 7 shows that adsorption increased with increasing relative pressure, and at 1.71, the adsorption process was maximum with 84.62 % and then slightly decreases and practically constant till relative pressure  $3.00\text{E}-01$ . The lesser adsorption at lower relative pressure could be attributed to lesser surface sites available for sorption (22). This model was used to investigate the sorption capacity of Mn-MOF using the linear expression in Equation 3:

$$\frac{1}{V_d \left[ \frac{P_0}{P} - 1 \right]} = \frac{C-1}{V_m C} \times \frac{P}{P_0} + \frac{1}{V_m C} \quad (\text{Eq. 5})$$



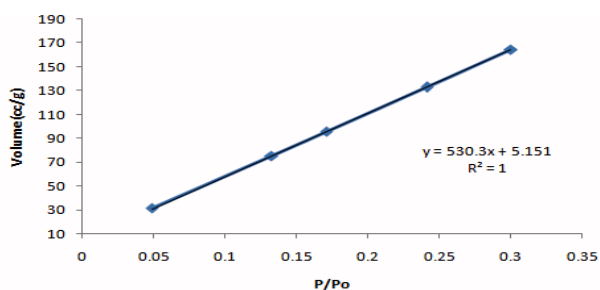
**Figure 6:** BET Single-multilayer nitrogen adsorption isotherm of Mn-MOF.

Where P= partial vapor pressure (33) of adsorbate, P<sub>0</sub> = saturated pressure of adsorbate.



**Figure 7:** Langmuir plot of N<sub>2</sub> on Mn-MOF at 77.3K.

Figure 8 shows the isotherm plot of volume at STP (cc/g) against relative pressure shows a linear fitting result with a strong correlation of +1, indicating a perfect positive linear relationship. The estimated micropore volume of Mn-MOF from this model is found to be 5.151cc/g (14).



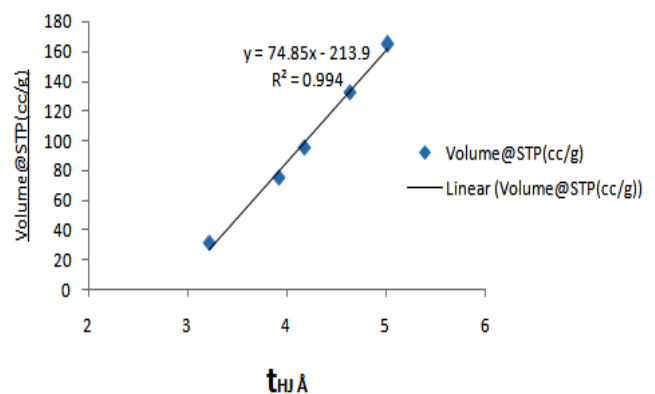
**Figure 8:** A linear form of Langmuir isotherm.

Figure 9 shows a linear correlation between the volumes adsorbed with statistical thickness. The t values were determined using the Halsey equation in Eq.6 &7 (26):

$$t(\text{\AA}) = \left[ \frac{13.99}{0.034 - \log \frac{P}{P_0}} \right]^{0.5} \quad (\text{Eq. 6})$$

$$t = \frac{V_{liq}}{S} \times 10^4(\text{\AA}) \quad (\text{Eq. 7})$$

Where S is the total surface area (26) and V<sub>liq</sub> is the adsorbed liquid volume (27); V<sub>liq</sub> = V<sub>ads</sub> (STP) × 15.47 for nitrogen adsorption at 77.3 K(26). The T- method for external surface area analysis calculated from the slope (Equation 1) gives surface area comparable to BET values (29), showing an agreement between the two methods.



**Figure 9:** Temkin Adsorption isotherm for Mn-MOF.

Dubinin-Radushkevch (DR)-plot by expression (4) gave information on the micropore volume (13). The shape of the experimental Logarithm weight adsorbed plot against Log<sup>2</sup>P/P<sub>0</sub> (Figure 10) results in a linear uniform Gaussian distribution with a negative intercept and negative slope. The adsorption energy, average pore width, micropore volume, and micropore surface area of the Mn-MOF were determined from Equation 8, Table 2 (24):

$$W = W_0 \exp \left[ - \left( \frac{A}{\beta E_0} \right)^2 \right] \quad (\text{Eq. 8})$$

$$A = -\Delta G = RT \ln \left( \frac{P_0}{P} \right), E = \beta E_0 \quad (\text{Eq. 8a})$$

Where, β =affinity coefficient (0.3300), A = adsorption potential, DR exp(n)= 2.000, E = characteristic adsorption energy, W and W<sub>0</sub> are amount adsorbed at P/P<sub>0</sub> and the micropore volume, respectively.

The PSD (Table 3) from the experimental adsorption (20) isotherm  $N_{exp} \left( \frac{P}{P_0} \right)$  were determined from Equation 9 (20). The experimental isotherm (Table 3) is represented in

Figures 11a & b as differential (left) and cumulative (right) distributions. Figure 11b shows pore size distribution (21) calculated by QSDFT and NLDFT (22) methods to overlap generously, indicating that both methods give similar results despite different approaches. Both methods show the three-peak distribution of micropores region with sizes 1.93 and 2.31-2.64 nm. The smallest pore size on QSDFT PSD, as expressed in Equation 9, is 1.68 nm resulting in not fully resolved peak in low pore size range with an L-curve (27).

$$N_{exp}\left(\frac{P}{P_o}\right) = \int_{D_{min.}}^{D_{max.}} N_{QSDFT}\left(\frac{P}{P_o}, D\right) F(D) dD \tag{Eq. 9}$$

Where:  $N\left(\frac{P}{P_o}, W\right)$  = experimental adsorption isotherm data,  $W$  = pore width,  $N_{exp}\left(\frac{P}{P_o}\right)$  = isotherm on a single pore of width  $W$ ,  $f(W)$  = pore size distribution function. Here  $D_{min}$  and  $D_{max}$  are the minimum and maximum pore sizes (31) in the kernel, respectively.

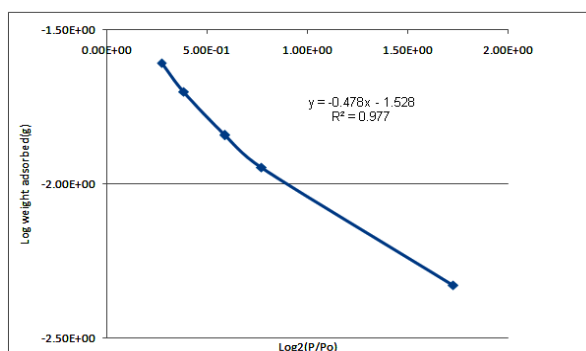


Figure 10: Dubinin-Radushkevich adsorption isotherm for Mn-MOF.

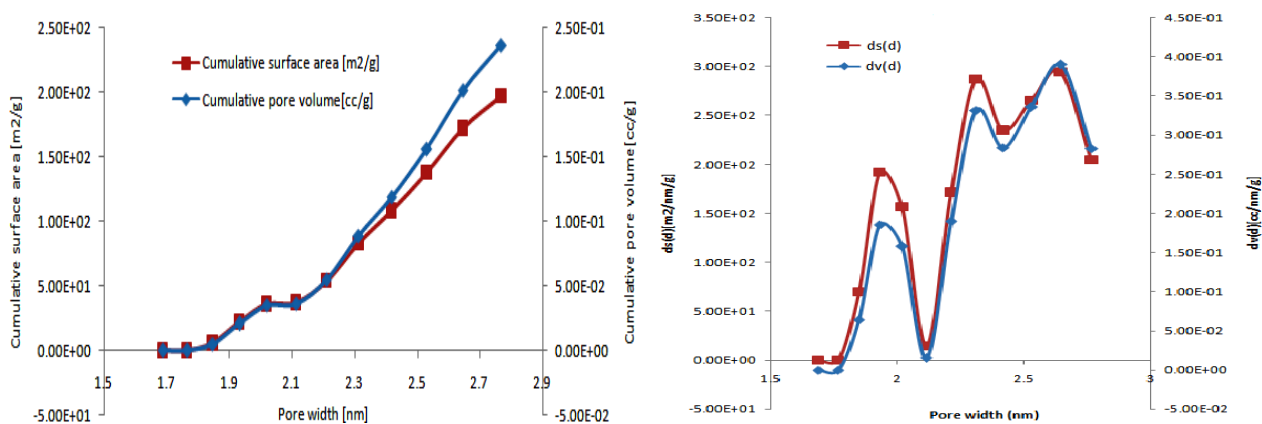


Figure 11.(a) Cumulative (20) and (b) differential cumulative pore volume (19) and cumulative surface area distributions of Mn -MOF on carbon slit pore from N<sub>2</sub> adsorption isotherms at 77.3 K (19) using NLDFT equilibrium mode.

**Table 2: Nitrogen adsorption on Mn-MOF.**

<b>P/Po</b>	<b>Volume at STP (cc/g)</b>	<b>1/[W(Po/P)-1]</b>	<b>P/Po/W</b>	<b>Log<sub>2</sub>(P/Po)</b>	<b>Weight adsorbed [(g)]</b>	<b>Statistical thickness, Å</b>
4.85E-02	31.2535	1.31E+00	1.24E+00	1.73E+00	4.69E-03	3.221736914
1.33E-01	75.3158	1.63E+00	1.41E+00	7.69E-01	1.13E-02	3.919188098
1.71E-01	95.5990	1.73E+00	1.43E+00	5.88E-01	1.43E-02	4.179641641
2.41E-01	132.8608	1.91E+00	1.45E+00	3.82E-01	1.99E-02	4.633363309
3.00E-01	164.7080	2.08E+00	1.46E+00	2.73E-01	2.47E-02	5.013433024

**Table 3: DFT & NDFLT Pore Analysis.**

<b>Pore width [nm]</b>	<b>Cumulative pore volume [cc/g]</b>	<b>Cumulative surface area [m<sup>2</sup>/g]</b>	<b>dv(d) [cc/nm/g]</b>	<b>ds(d) [m<sup>2</sup>/nm/g]</b>
1.6879	0.00E+00	0.00E+00	0.00E+00	0.00E+00
1.7656	0.00E+00	0.00E+00	0.00E+00	0.00E+00
1.8469	5.23E-03	5.66E+00	6.43E-02	6.96E+01
1.9319	2.10E-02	2.20E+01	1.85E-01	1.92E+02
2.0208	3.50E-02	3.59E+01	1.58E-01	1.56E+02
2.1138	3.64E-02	3.72E+01	1.51E-02	1.43E+01
2.2111	5.49E-02	5.39E+01	1.90E-01	1.72E+02
2.3129	8.87E-02	8.31E+01	3.32E-01	2.87E+02
2.4194	1.19E-01	1.08E+02	2.84E-01	2.35E+02
2.5307	1.56E-01	1.38E+02	3.36E-01	2.65E+02
2.6472	2.02E-01	1.72E+02	3.90E-01	2.95E+02
2.7691	2.36E-01	1.97E+02	2.83E-01	2.05E+02

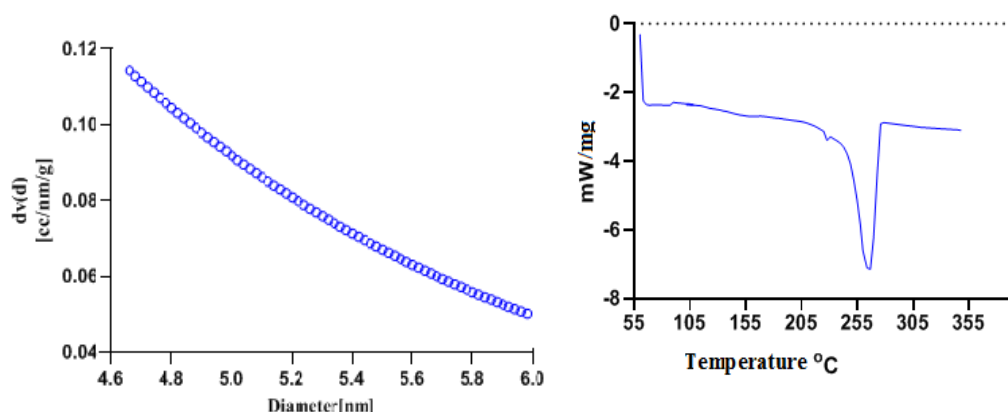


**Figure 12:** (a) shows the pore size distribution and (b) shows the DSC plot with a depression at 264.43 °C (- 7.20 mW) ,  $\Delta H$  +107.00 KJ/mol ( $\Delta H$  +551.00J/g).

Table 4 gives the micropore analysis by Dubinin-Radushkevich (DR), Horvath-Kawazoe (HK), and Dubinin-Astakhov (DA) methods. Dollimore and Heal (DH) (20) were used to estimate the pore size distribution (13). The pore-size distribution (18) is obtained by applying the BJH (Barret, Joyner, and Halenda) technique.

## DISCUSSION

The Langmuir surface area of 4374 m<sup>2</sup>g<sup>-1</sup> after activation shows a high permanent porosity with an octahedrally coordinated environment. FT-IR spectrum results show that Mn-MOF has well-populated functional groups that form a strong coordination network for storage purposes. The Mn-MOF exhibits a pore size of 6.077 nm and pore volume of 2.920 nm displaying a highly porous and high nitrogen uptake capacity.

## CONCLUSION AND RECOMMENDATIONS

These findings are consistent with literature reviews and adsorption experiments published by a number of authors revealing the storing capacity of metal-organic frameworks'. This work describes a novel synthetic method for preparing self-assembled porous metal-organic frameworks with potential energy storage capabilities.

We use several adsorption isotherms to investigate the storage and adsorption capacity of the Mn-MOF produced in this study. We performed DSC, SEM, single-crystal diffraction studies, FTIR,

fluorescence, and UV-visible spectrophotometry to characterize this compound. The strong storing and adsorption capacity of the manganese(II) nanoparticles is revealed by experimental findings and evaluation adsorption capacity of this compound under some adsorption isotherms. The Mn-MOF surface area is currently being optimized for hydrogen and carbon capture.

## CONFLICT OF INTEREST

The authors declare the nonexistence of any conflicts of interest

## AUTHORS' CONTRIBUTION

This work was carried out in collaboration between both authors. IJM designed the study, carried out analyses. IJM and KOA wrote the manuscript for publication

## FUNDING

This work was supported by the Tertiary Education Trust Fund (RE: FUPRE/TO/RESR/2017/01), Nigeria.

## ACKNOWLEDGMENTS

The authors wish to acknowledge single-crystal structure analysis by Summerstrand Campus South, northwest University South Africa..

**Table 4:** Adsorption properties of Mn-MOF given by different Isotherm Models.

Adsorption Models	Surface Area (m <sup>2</sup> g <sup>-1</sup> )	Pore Size (nm)	Pore Volume ccg <sup>-1</sup>	Slope	Adsorption energy KJ/mol	C constant	Average pore width (nm)	Pore Diameter (nm)	Intercept	Best n	R <sup>2</sup>
SinglePoint BET	5.017 E+02			3.029					1.190 E+00		0.9960
MultiPoint BET	8.255 E+02			3.029		3.545			1.190 E+00		
Langmuir	4.374 E+03			0.79612					1.25689		0.8650
Barrett, Joyner, and Halenda Method (BJH)	9.570 E+02	2.093	4.614 E-01						2.093 E+00		
Dollimore and Heal (DH)	1.034 E+03	2.093	4.776 E-01						2.093 E+00		
T-method	8.255 E+02										0.9940
Dubinin Radushkevich method (DR)	8.601E+02	6.077	3.056 E-01	-4.780 E-01	4.279		6.077 E+00		2.964E-02	2.000	0.9770
Density Functional Theory (DFT)	196.913		0.236						2.647		
Dubinin-Astakhov Method (DA)		2.920			0.707		2,92E+00		2.964E-02	1.000	
Horvath-Kawazoe (HK)		1.882	1.326 E-01						1.882 E+00		
SF		3.534	2.708 E-02						3.534 E+00		

## REFERENCES

1. Chakrabarty R, Mukherjee PS, Stang PJ. Supramolecular Coordination: Self-Assembly of Finite Two- and Three-Dimensional Ensembles. *Chem Rev.* 2011 Nov 9;111(11):6810–918. [<DOI>](#).
2. Agthe M, Høydalsvik K, Mayence A, Karvinen P, Liebi M, Bergström L, et al. Controlling Orientational and Translational Order of Iron Oxide Nanocubes by Assembly in Nanofluidic Containers. *Langmuir.* 2015 Nov 17;31(45):12537–43. [<DOI>](#).
3. Sun Y, Zhang F, Jiang S, Wang Z, Ni R, Wang H, et al. Assembly of Metallacages into Soft Suprastructures with Dimensions of up to Micrometers and the Formation of Composite Materials. *J Am Chem Soc.* 2018 Dec 12;140(49):17297–307. [<DOI>](#).
4. Shoji S, Ogawa T, Matsubara S, Tamiaki H. Bioinspired supramolecular nanosheets of zinc chlorophyll assemblies. *Sci Rep.* 2019 Dec;9(1):14006. [<DOI>](#).
5. Jin Y, Wang Q, Taynton P, Zhang W. Dynamic Covalent Chemistry Approaches Toward Macrocycles, Molecular Cages, and Polymers. *Acc Chem Res.* 2014 May 20;47(5):1575–86. [<DOI>](#).
6. Ion AE, Nica S, Madalan AM, Shova S, Vallejo J, Julve M, et al. Two-Dimensional Coordination Polymers Constructed Using, Simultaneously, Linear and Angular Spacers and Cobalt(II) Nodes. New Examples of Networks of Single-Ion Magnets. *Inorg Chem.* 2015 Jan 5;54(1):16–8. [<DOI>](#).
7. Springer MA, Liu T-J, Kuc A, Heine T. Topological two-dimensional polymers. *Chem Soc Rev.* 2020;49(7):2007–19. [<DOI>](#).
8. Bandoz TJ, Petit C. MOF/graphite oxide hybrid materials: exploring the new concept of adsorbents and catalysts. *Adsorption.* 2011 Feb;17(1):5–16. [<DOI>](#).
9. Zhang S. Fabrication of novel biomaterials through molecular self-assembly. *Nat Biotechnol.* 2003 Oct;21(10):1171–8. [<DOI>](#).
10. Guo J, Tardy BL, Christofferson AJ, Dai Y, Richardson JJ, Zhu W, et al. Modular assembly of superstructures from polyphenol-functionalized building blocks. *Nature Nanotech.* 2016 Dec;11(12):1105–11. [<DOI>](#).
11. Piot M, Abécassis B, Brouri D, Troufflard C, Proust A, Izzet G. Control of the hierarchical self-assembly of polyoxometalate-based metallomacrocycles by redox trigger and solvent composition. *Proc Natl Acad Sci USA.* 2018 Sep 4;115(36):8895–900. [<DOI>](#).
12. Bose A, Mal P. Mechanochemistry of supramolecules. *Beilstein J Org Chem.* 2019 Apr 12;15:881–900. [<DOI>](#).
13. Kuppang G, Abbott LJ, Hart KE, Colina CM. Modeling Amorphous Microporous Polymers for CO<sub>2</sub> Capture and Separations. *Chem Rev.* 2018 Jun 13;118(11):5488–538. [<DOI>](#).
14. Jiang H-L, Liu B, Lan Y-Q, Kuratani K, Akita T, Shioyama H, et al. From Metal–Organic Framework to Nanoporous Carbon: Toward a Very High Surface Area and Hydrogen Uptake. *J Am Chem Soc.* 2011 Aug 10;133(31):11854–7. [<DOI>](#).
15. Zhao Y, Song Z, Li X, Sun Q, Cheng N, Lawes S, et al. Metal organic frameworks for energy storage and conversion. *Energy Storage Materials.* 2016 Jan;2:35–62. [<DOI>](#).
16. Wu HB, Lou XW (David). Metal-organic frameworks and their derived materials for electrochemical energy storage and conversion: Promises and challenges. *Sci Adv.* 2017 Dec;3(12):eaap9252. [<DOI>](#).
17. Dey C, Kundu T, Biswal BP, Mallick A, Banerjee R. Crystalline metal-organic frameworks (MOFs): synthesis, structure and function. *Acta Crystallogr B Struct Sci Cryst Eng Mater.* 2014 Feb 1;70(1):3–10. [<DOI>](#).
18. Aizuddin M MA, Yin C-Y, Mikhail Sa R. Analysis of the Textural Characteristics and Pore Size Distribution of a Commercial Zeolite using Various Adsorption Models. *J of Applied Sciences.* 2011 Oct 15;11(21):3650–4. [<DOI>](#).
19. Seredych M, Bandoz TJ. Manganese oxide and graphite oxide/MnO<sub>2</sub> composites as reactive adsorbents of ammonia at ambient conditions. *Microporous and Mesoporous Materials.* 2012 Mar;150:55–63. [<DOI>](#).
20. Landers J, Gor GYu, Neimark AV. Density functional theory methods for characterization of porous materials. *Colloids and Surfaces A: Physicochemical and Engineering Aspects.* 2013 Nov;437:3–32. [<DOI>](#).
21. Ravikovitch PI, Vishnyakov A, Russo R, Neimark AV. Unified Approach to Pore Size

Characterization of Microporous Carbonaceous Materials from N<sub>2</sub>, Ar, and CO<sub>2</sub> Adsorption Isotherms †. *Langmuir*. 2000 Mar;16(5):2311–20. [<DOI>](#).

22. Foo KY, Hameed BH. Insights into the modeling of adsorption isotherm systems. *Chemical Engineering Journal*. 2010 Jan 1;156(1):2–10. [<DOI>](#).

23. Wang LH, Li PF. Synthesis, Structure, and Catalytic Activity of A New Mn(II) Complex with 1,4-Phenylenediacetic Acid and 1,10-Phenanthroline. *Bull Chem React Eng Catal*. 2018 Apr 2;13(1):1. [<DOI>](#).

24. Li L-J, Lau DSP, De Gendt S, Ren F. Properties and Applications of 2-Dimensional Layered Materials. *ECS J Solid State Sci Technol*. 2016;5(11):Y7–Y7. [<DOI>](#).

25. Jiang J, Yaghi OM. Brønsted Acidity in Metal–Organic Frameworks. *Chem Rev*. 2015 Jul 22;115(14):6966–97. [<DOI>](#).

26. Lowell S, Shields J, Thomas M, Thommes M, editors. Characterization of porous solids and powders: surface area, pore size and density. 4. ed., 1. reprint with some corr. Dordrecht: Springer; 2006. 347 p. (Particle technology series). ISBN: 978-1-4020-2303-3 978-1-4020-2302-6.

27. Lv Y, Shi P, Shen W, Chen X, Zhao G. A series of novel Zn(II) and Mn(II) metal-organic frameworks constructed by 2,4-bis-oxyacetate-benzoic acid: syntheses, structures and photoluminescence. *Sci China Chem*. 2015 Mar;58(3):448–56. [<DOI>](#).

28. Gawas UB, Verenkar VMS, Mojumdar SC. Nano-crystalline Mn<sub>0.3</sub>Ni<sub>0.3</sub>Zn<sub>0.4</sub>Fe<sub>2</sub>O<sub>4</sub> obtained by novel fumarato-hydrazinate precursor method: Synthesis, characterization and studies of magnetic and electrical properties. *J Therm Anal Calorim*. 2012 Jun;108(3):865–70. [<DOI>](#).

29. Sasmal HS, Halder A, Kunjattu H S, Dey K, Nadol A, Ajithkumar TG, et al. Covalent Self-Assembly in Two Dimensions: Connecting Covalent Organic Framework Nanospheres into Crystalline and Porous Thin Films. *J Am Chem Soc*. 2019 Dec 26;141(51):20371–9. [<DOI>](#).

30. Mokhatab S, Poe WA, Mak JY. Handbook of natural gas transmission and processing: principles and practices. Fourth edition. Cambridge, MA: Gulf Professional Publishing; 2019. 826 p. ISBN: 978-0-12-815817-3.

31. Li Y-L, Zhao Y, Wang P, Kang Y-S, Liu Q, Zhang X-D, et al. Multifunctional Metal–Organic Frameworks with Fluorescent Sensing and Selective Adsorption Properties. *Inorg Chem*. 2016 Nov 21;55(22):11821–30. [<DOI>](#).

32. Balzer C, Cimino RT, Gor GY, Neimark AV, Reichenauer G. Deformation of Microporous Carbons during N<sub>2</sub>, Ar, and CO<sub>2</sub> Adsorption: Insight from the Density Functional Theory. *Langmuir*. 2016 Aug 16;32(32):8265–74. [<DOI>](#).

33. Mabayoje O, Seredych M, Bandosz TJ. Enhanced adsorption of hydrogen sulfide on mixed zinc/cobalt hydroxides: Effect of morphology and an increased number of surface hydroxyl groups. *Journal of Colloid and Interface Science*. 2013 Sep;405:218–25. [<DOI>](#).

34. Tahier T, Oliver CL. In situ variable-temperature single crystal X-ray diffraction studies of the single-crystal-to-single-crystal dehydration and rehydration of a mixed-ligand 2D zinc metal–organic framework using trimesate and 4,4'-bipyridine- N, N'-dioxide as ligands. *CrystEngComm*. 2015;17(46):8946–56. [<DOI>](#).

35. Justina Mbonu I. Synthesis, Crystal Structure and Photoluminescence Properties of Diaquabis (1,10Phenanthroline, κ,N,N')(Benzoato-κ,O) Manganese(II)Dihydrate. *OMCIJ [Internet]*. 2020 Jul 28 [cited 2021 Aug 10];9(5): 555773. [<DOI>](#).





## Aqueous Extracts of *Aaronsohnia pubescens* subsp. *pubescens* Aerial Parts as Green Corrosion Inhibitor for Mild Steel in Hydrochloric Acid Solution

Mounir Manssouri\*<sup>1</sup>  , Yassir El Ouadi<sup>2</sup> , Anas Chraka<sup>3</sup> , Mohamed Khaddor<sup>4</sup> ,  
Mohamed Znini<sup>1</sup>  and Lhou Majidi<sup>1</sup> 

<sup>1</sup> Moulay Ismail University of Meknes, Laboratory of Natural Substances & Synthesis and Molecular Dynamics, Faculty of Sciences and Techniques, BP 509, 52000, Errachidia, Morocco

<sup>2</sup> University of Mohammed Premier, Laboratory of Analytical Chemistry, Materials, and Environment (LC2AME), Faculty of Sciences, B.P. 717, 60000 Oujda, Morocco

<sup>3</sup> Abdelmalek Essaâdi University, Materials and Interfacial Systems Laboratory, ERESI Team. Department of Chemistry, Faculty of Sciences, Avenue de Sebta, Mhannech II, 93002 Tetouan, Morocco.

<sup>4</sup> University Abdelmalek Essaadi, Laboratory of LAMSE, Faculty of Sciences and Techniques, Tangier, Morocco

**Abstract:** In this study, two aqueous extracts from the aerial parts of *Aaronsohnia pubescens* subsp. *pubescens* (Odorized aqueous extract (OE) and Deodorized aqueous extract (DE)) were used as some novel ecological corrosion inhibitors for mild steel (MS) in 1 M HCl medium. For this reason, the inhibition behavior of the OE and DE were investigated using weight loss measurements, electrochemical assays, kinetics, and thermodynamic parameters, and electrochemical methods, both stationary (Potentiodynamic polarization (PDP)) and transient (Electrochemical impedance spectroscopy (EIS)). The obtained results showed that EO and DE act as effective corrosion inhibitors and the inhibition efficiency of inhibitors increases for the concentration of 1.5 g/L; reaching some high values of 93.11 and 87.88% in 1 M HCl solution at 308 K for OE and DE, respectively. Furthermore, PDP measurements exhibited that the studied of each inhibitor performs as a mixed-type inhibitor. The results of the thermodynamic kinetic parameters indicate the adsorption of OE and DE on the MS surface sites obeying the Langmuir adsorption isotherm.

**Keywords:** *Aaronsohnia pubescens* subsp. *pubescens*; aqueous extracts; mild Steel; ecological corrosion inhibitors; 1 M HCl.

**Submitted:** June 13, 2021. **Accepted:** August 09, 2021.

**Cite this:** Manssouri M, El Ouadi Y, Chraka A, Khaddor M, Znini M, Majidi L. Aqueous Extracts of *Aaronsohnia pubescens* subsp. *pubescens* Aerial Parts as Green Corrosion Inhibitor for Mild Steel in Hydrochloric Acid Solution. JOTCSA. 2021;8(3):953–68.

**DOI:** <https://doi.org/10.18596/jotcsa.951852>.

**\*Corresponding author.** E-mail: [man.mounir@yahoo.fr](mailto:man.mounir@yahoo.fr).

### INTRODUCTION

Mild Steel (MS) is extensively used in many industries such as tanks and water utilities, power production, heat exchangers, oil, chemical, and electrochemical technologies due to good mechanical strength and relatively low price, but it is susceptible to several forms of corrosion in some environments especially in the acidic environment (1, 2). This phenomenon can be minimized or

delayed by various means such as coatings, cathodic protection, and corrosion inhibitors (3). Corrosion inhibitors, classified as inorganic and organic types, are one of the most cost-effective methods for controlling corrosion. The most well-known acid corrosion inhibitors are organic compounds that adsorb on the MS surface and protects it from corrosion by blocking the active sites. These inhibitors are rich in electrons and can share their electrons with unoccupied d-orbitals of

steel (4). Nowadays, the researchers' interests are directed towards environmental-friendly inhibitors (i.e., biodegradable molecules). The essential oils (EOs) and extracts components from a variety of plants origins as eco-friendly sources of sustainable corrosion inhibitors (5-9). These types of inhibitors, which are readily available through a simple extraction process, are able and effective to protect the metal from corrosion (10).

In our laboratory, a great deal of research has been carried out to study inhibitive effect several plant extract on the corrosion of steel in 1 M HCl (11-16). In this context, recently, *Aaronsohnia pubescens subsp. pubescens* essential oil has been established, as an eco-friendly corrosion inhibitor of acid corrosion of MS in 1 M HCl. The inhibition efficiency IE (%) was found to increase with naturally substance content to attain 82.11% at 1.50 g/L (17).

The main objective of current research is to study for the first time the potency of the power of extracts from the aerial parts of *Aaronsohnia pubescens subsp. pubescens* Figure 1 (Odorized aqueous extract (OE) and Deodorized aqueous extract (DE)) to protect mild steel in 1M HCl medium were assessed by WL measurement, PDP, and EIS examinations.

## EXPERIMENTAL PART

### Inhibitors

The experimental phase followed in the current study such as preparations of the aqueous extract

(OE and DE) have been mentioned according to a previously described experimental procedure in our work (18). A portion (100 g) of dried plant material was extracted with 1 L of water under refluxing for 3 h. The liquid retentate was collected, filtered, and centrifuged at 5000 rpm for 30 min. The supernatant was also filtered to eliminate any residues and lyophilized to give finally odorized aqueous extract (OE) in a yield of 11.37 % (w/w). However, the liquid retentate obtained after completion of hydrodistillation of 100 g dried plant material in 1 L of water for 3 h, using a Clevenger-type apparatus to isolate volatile compounds, was collected, filtered, centrifuged and lyophilized to give finally deodorized aqueous extract (DE) in a yield of 10.82 % (w/w) (19).



**Figure 1:** *Aaronsohnia pubescens subsp. pubescens* in its native habitat in south-eastern Morocco.

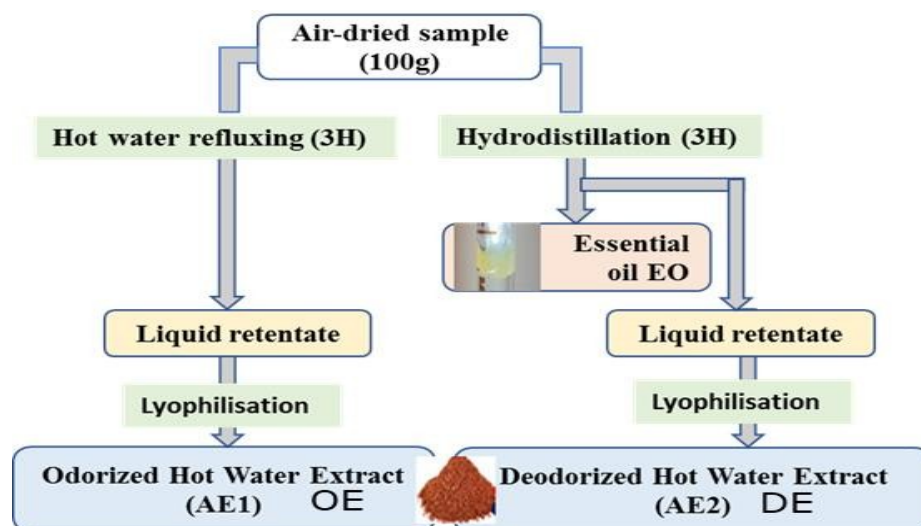


**Figure 2:** Scheme of the extraction methods of aqueous extracts from aerial parts of *Aaronsohnia pubescens subsp. Pubescens*.

### Corrosion test

Corrosion inhibition on MS in 1 M HCl by OE and DE was performed by using WL, PDP and EIS methods according to the methodology described previously in our work (13,17). A very low concentration range (0.25-1.5 g/L) of inhibitors were prepared in 1M HCl media for its corrosion

inhibition potential at different temperatures (308-343 K).

### Preparation of MS segments, corrosive solutions and inhibitors

Corrosion tests were conducted on the MS segments with dimension of 2 cm×2 cm×0.05 cm; the MS metal presents the subsequent composition

with mass percentage (%): P 0.09, Si 0.38, Al 0.01, Mn 0.05, C 0.21, S 0.05 and Fe 99.21. Before each corrosion test, the MS segments were mechanically ground with sequential grades of emery papers (400, 600 and 1200 grit), and ensuing rinsed and degreased with distilled water and acetone, then dried and weighed. The corrosive acid solution was a molar hydrochloric acid (1 M of HCl), was prepared from concentrated commercial acid of HCl (37%) by dilution with distilled water.

### Electrochemical (PDP and EIS) measurements

Before conducting each electrochemical corrosion test, the sample was immersed in the test solution during 30 min at the open circuit potential ( $E_{OC}$ ) to find a steady state. Both PDP and EIS tests were performed from utilizing an assembly of electrochemical cell containing three electrodes: a disc cut from the MS as working electrode ( $1\text{ cm}^2$ ), a saturated calomel electrode as a reference electrode, and a platinum electrode as counter electrode. All electrochemical measurements were carried out using a potentiostat/galvanostat (Model PAR 263A) and the electrochemical parameter values were determined using the Volta Master 4 software. We note that all potentials measurement in this study were obtained with respect to the potential value of the reference electrode.

## RESULTS AND DISCUSSION

### Effect of both concentration and temperature

The effect of different concentrations of OE and DE on MS corrosion in 1 M HCl at 308 K was investigated using the gravimetric method. The inhibition efficiency (IEW (%)) was calculated on the basis of the Equation 1:

$$IE \% = \frac{W_{corr} - W_{corr(inh)}}{W_{corr}} \times 100 \quad (\text{Eq. 1})$$

where  $W_{corr}$  and  $W_{corr(inh)}$  are the values of corrosion rate of MS in 1 M HCl medium without and with the addition of the aqueous extracts tested.

The obtained results of the study are summarized in Table 1. It shows that the corrosion rate reduces and the IE (%) increase with concentrations and reach a maximum value of 93.46 and 80.48 % at 1.5 g/L of OE and DE, respectively. These results suggesting that the aqueous extracts inhibited the corrosion of MS in a dose-dependent manner. This behavior can be attributed to the strong interaction

of the compounds forming these extracts with the metal surface. In other words, we observed that the inhibition efficiency of OE is slightly increased when the temperature media increases, which results probably to the chemisorption behavior of OE onto MS surface.

### PDP investigation

The effect of EO and DE at 308 K on anodic and cathodic reactions was demonstrated by PDP plots in 1 M HCl medium and the embodiments obtained are displayed in Figures 3 and 4. The outputted parameters of PDP analysis including the potential of corrosion ( $E_{corr}$ ), the current density of corrosion ( $I_{corr}$ ) and cathodic and anodic Tafel slopes ( $\beta_a$  and  $\beta_c$ ) are given in Table 2. The corrosion inhibition efficiency  $IE_{PDP}$  (%) was derived as given below:

$$IE_{PDP} \% = \left( \frac{I_{corr} - I_{corr,inh}}{I_{corr}} \right) \times 100 \quad (\text{Eq. 2})$$

Where  $I_{corr}$  and  $I_{corr,inh}$  are the corrosion current densities in the absence and the presence of inhibitor, respectively.

According to Figures 3 and 4, we have noticed that the use of OE and DE at 308 K are suppressed both the cathodic hydrogen development and anodic metal dissolution reactions. Moreover, the PDP curves in the inhibited solutions were translated into lower current densities. The polarization diagrams noted that the addition of different concentrations of the two aqueous extracts that both the cathodic and anodic reactions did not affect, as well as the corresponding  $E_{corr}$  appeared to be approximately constant significant. Therefore, EO and DE can be classified as mixed-type inhibitors (20). In addition, the results of Table 2 indicate that the rate of the  $I_{corr}$  values of MS is decreased with an increase in the concentrations of the two inhibitors; reaching some high values of 517 and 862  $\mu\text{A}/\text{cm}^2$  in 1 M HCl solution at 308 K for OE and DE, respectively at 1.5 g/L. These results suggest that the addition of EO and DE loading more compounds of both adsorbed on the MS surface, and thus the corrosion-resistant film can be generated on the metal surface (21). As shown in Table 2, the  $IE_{PDP}$  (%) of EO and DE in the 1 M HCl solution is about 91.02% and 85.05% respectively. It can be concluded from these findings that both aqueous extracts provided the good anti-corrosion performance, with a clear preference for OE.

**Table 1:** Weight loss results for MS in 1 M HCl with and without different concentrations of aqueous extracts (OE and DE) at different temperatures.

C (g/L)	308 K		313 K		323 K		333 K		343 K	
	W (mg/cm <sup>2</sup> .h)	IE% (%)	W (mg/cm <sup>2</sup> .h)	IE% (%)	W (mg/cm <sup>2</sup> .h)	IE% (%)	W (mg/cm <sup>2</sup> .h)	IE% (%)	W (mg/cm <sup>2</sup> .h)	IE% (%)
<b>OE 1M HCl</b>	<b>0.942</b>	.....	<b>1.751</b>	.....	<b>2.836</b>	.....	<b>3.641</b>	.....	<b>6.301</b>	.....
0.25	0.186	80.25	0.344	80.37	0.532	81.24	0.682	81.28	1.115	82.30
0.50	0.116	87.66	0.214	87.78	0.320	88.70	0.409	88.78	0.638	89.88
1.00	0.108	88.58	0.197	88.74	0.315	88.88	0.404	88.90	0.633	89.96
1.50	0.065	93.11	0.119	93.22	0.189	93.33	0.241	93.39	0.412	93.46
<b>DE</b>	0.224	76.21	0.470	73.15	0.824	70.95	1.064	70.77	1.872	70.29
0.50	0.193	79.50	0.378	78.44	0.622	78.08	0.822	77.42	1.426	77.37
1.00	0.152	83.89	0.309	82.38	0.507	82.12	0.667	81.68	1.170	81.43
1.50	0.114	87.88	0.276	84.23	0.473	83.33	0.621	82.95	1.230	80.48

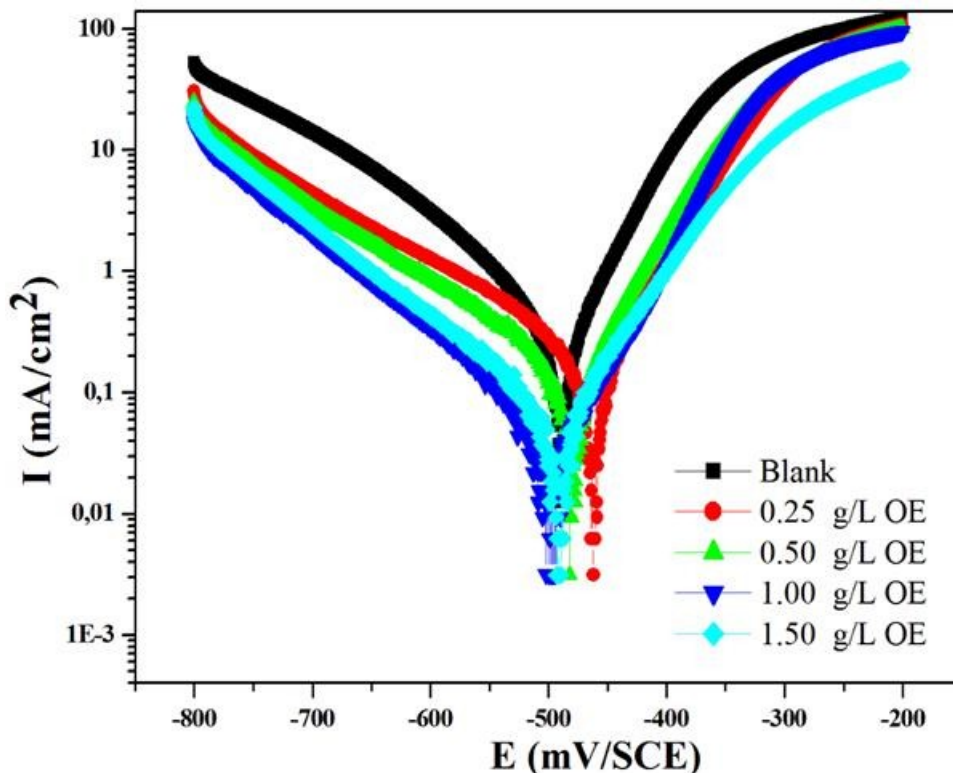


Figure 3: Anodic and cathodic polarization curves of MS in solutions of 1 M HCl without and with different concentrations of odorized extract.

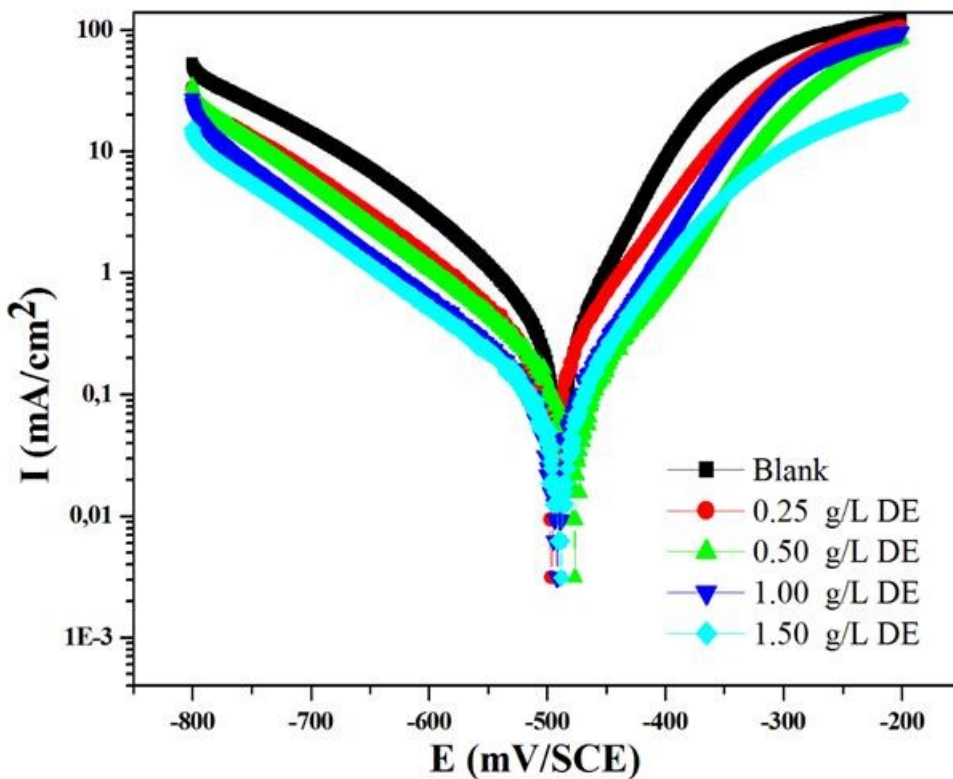


Figure 4: Anodic and cathodic polarization curves of MS in solutions of 1 M HCl without and with different concentrations of deodorized extract.

**Table 2:** Electrochemical parameters for the MS in 1 M HCl with and without various concentrations of aqueous extracts from *Aaronsohnia pubescens* aerial parts (OE and DE) at 308 K.

	C (g/L)	- E <sub>corr</sub> (mV/SCE)	I <sub>corr</sub> (mA cm <sup>-2</sup> )	-β <sub>c</sub> (mV dec <sup>-1</sup> )	β <sub>a</sub> (mV dec <sup>-1</sup> )	IE <sub>PDP</sub> (%)
<b>1 M HCl</b>		490.0	0.5779	147.4	74.8	.....
<b>OE</b>	0.25	462.9	0.1145	110.2	60.8	80.18
	0.50	460.1	0.0857	100.1	67.1	85.17
	1.00	498.9	0.0701	109.2	62.9	87.86
	1.50	497.0	0.0517	100.7	65.0	<b>91.02</b>
<b>DE</b>	0.25	497.8	0.1651	110.6	74.3	71.43
	0.50	480.8	0.0997	104.8	73.5	82.74
	1.00	495.3	0.0897	110.7	72.1	84.47
	1.50	494.0	0.0862	106.5	74.4	85.05

**EIS investigation**

The EIS is a convenient and rapid approach for examining the protective properties of inhibitors onto metal surfaces in different corrosive environments (22). Thus, it was used to evaluate

the effectiveness of the two aqueous extracts tested. The EIS measurements of the immersed MS in 1 M HCl medium protected with various concentrations of EO and DE at 308 K are depicted in Figures 5 and 6 sequentially.

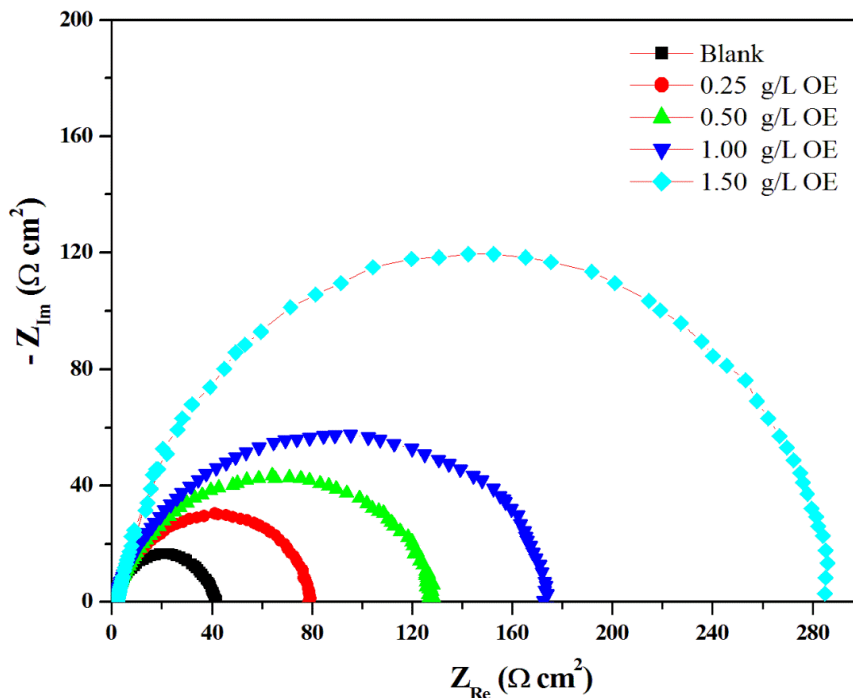


**Figure 5:** The Nyquist plots of the immersed MS in 1 M HCl without and with different concentrations of OE at 308 K.

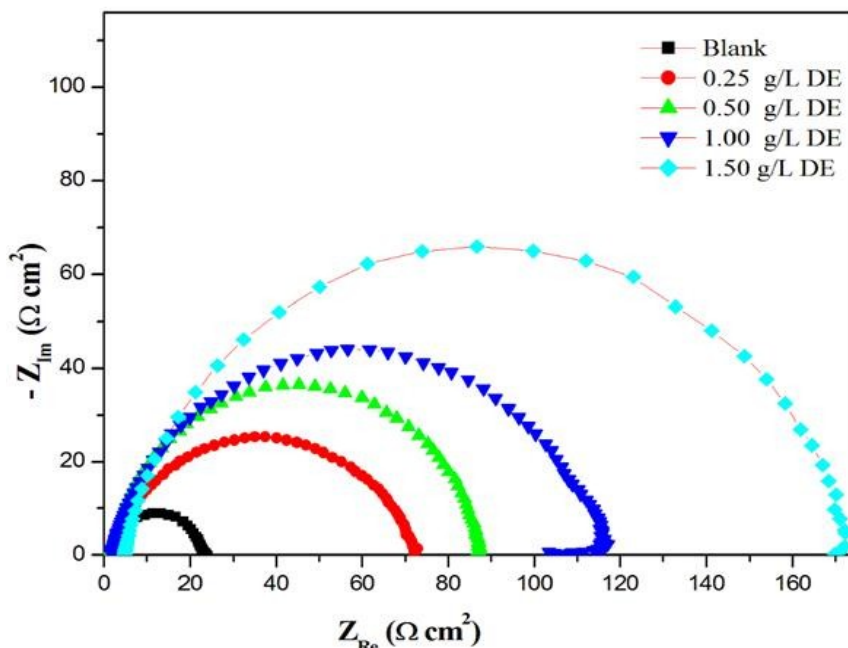


**Figure 6:** The Nyquist plots of the immersed MS in 1 M HCl without and with different concentrations of DE at 308 K.

In the present investigation, the Nyquist plots of EO and DE (Figures 5 and 6) showed a single capacitive loop whose size increases with increased concentrations of both aqueous extracts employed (23,24). However, these capacitive loops are not the perfect semicircles because of a frequent

dispersion effect attributing to roughness because of heterogeneous solid surface (25-27). In addition, the diameter of the Nyquist plots increases as a function of the concentration of each inhibitor, which affirms the adsorption of the EO and DE molecules on the MS surface.

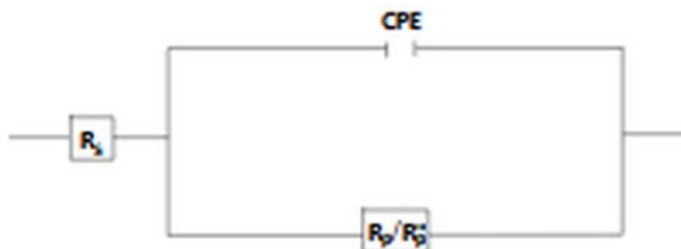


**Figure 7:** Equivalent circuit used to fit the experimental EIS data of the immersed MS in 1 M HCl without and with different concentrations of OE and DE.

Furthermore, the impedance curves were fitted by using EC-LAB software, and an equivalent electrical circuits (EEC) diagram corresponds to the metal/solution interface (the double layer between the MS / EO / HCl and MS / DE / HCl) was proposed in Figure 7 (28-30). As reported in Figure 7, the equivalent circuit elements consisting of solution resistance ( $R_s$ ) connected in ( $CPE_{dl}$ ) represent the constant phase element coupled with the polarization resistance ( $R_p$ ). In this circuit,  $R_p$  corresponds to the sum of charge transfer resistance ( $R_{ct}$ ) and diffuse layer resistance ( $R_d$ ) at the metal/solution interface in the absence of OE and DE ( $R_p = R_{ct} + R_d$ ). While that ( $R''_p$ ) corresponds to the sum of  $R_p$ ,  $R_a$  (accumulated species) and  $R_f$  (film resistance) in the presence of

the two studied extracts ( $R''_p = R_p + R_a + R_f$ ) (31,32). The  $CPE_{dl}$  is defined as follows:

$$Z_{CPE} = \frac{1}{Y_2(j\omega)^2} \tag{Eq. 3}$$

Where  $Y_0$  benefits from the possibility of a non-ideal capacitance of ( $CPE_{dl}$ ), ( $\omega$ ) is the angular frequency and ( $j$ ) is the imaginary unit, and  $n$  is the phase shift, which gives details about the degree of surface inhomogeneity for whole numbers ( $0 < n < 1$ ) (29,33).

The inhibition efficiency  $E_{EIS}$  (%) is designed according to (Equation 4), where  $R''_p$  and  $R_p$  are the

polarization resistance in the presence and absence of inhibitors, respectively.

$$IE_{EIS}(\%) = \left( R_{p_{inh}} - \frac{R_p}{R} \right) \times 100 \quad (\text{Eq. 4})$$

The impedance data that were fitted according to the equivalent circuit and inhibition efficiency ( $IE_{EIS}$  %) are listed in Table 3. According to the fitted results, that the double layer capacitance ( $C_{dl}$ ) values were reduced for the inhibited samples, evidencing the enhancement of the OE and DE molecules adsorption onto the surface. The reduction of the ( $CPE_{dl}$ ) values for the protected samples is attributed to the replacement of water molecules adsorbed on the metal surface with the

compounds of OE and DE at the metal /solution interface (34). In addition, we noticed that the values of  $R_p$  increases with the increase of different concentrations of two aqueous extracts to reaches its maximum values 288.10 and 174.05 ( $\Omega.cm^2$ ) at 1.5 g/L for the OE and DE respectively. Consequently, the inhibition efficiencies ( $IE_{EIS}$ %) of OE and DE showed the maximum  $IE_{EIS}$  is approximate 92.09% and 86.91% respectively. Thus, it reveals that the OE and DE molecules have considered as a useful green inhibitors to protect MS against corrosion and to reduce the reactive sites which could be created during corrosion phenomenon (35). These results are in good agreement with the results obtained by PDP investigation and show that OE has the best inhibitory performance compared to DE.

**Table 3:** The electrochemical data obtained from the fitting of EIS curves for MS immersed in 1 M HCl without and with various concentrations of OE and DE at 308 K.

C (g/L)	$R_s$ ( $\Omega.cm^2$ )	$R_p$ ( $\Omega.cm^2$ )	$CPE_{dl}$ $Y_o$ ( $\times 10^6 S^n \Omega^{-1}cm^{-2}$ )	n	$C_{dl}$ ( $\times 10^6 S \Omega^{-1}cm^{-2}$ )	$IE_{EIS}$ (%)
Blank						
0.00	1.699	22.78	327.88	0.902	92.88	-
<b>EO</b>						
0.25	1.731	80.08	223.09	0.891	58.27	71.55
0.50	1.772	133.02	118.18	0.866	45.72	82.87
1.00	1.821	174.72	94.08	0.925	42.02	86.96
1.50	1.891	288.10	84.80	0.851	37.88	<b>92.09</b>
<b>DE</b>						
0.25	1.701	76.08	258.01	0.888	64.07	70.05
0.50	1.752	87.98	175.11	0.849	54.00	74.10
1.00	1.791	117.67	107.18	0.981	42.52	80.64
1.50	1.823	174.05	93.22	0.893	39.75	<b>86.91</b>

**Kinetics/Activation parameters**

Inhibitory performance as a function of temperature (T) has been discussed in this part. It is understood that the variation of the corrosion rate as a function of temperature gives results that make it possible to thermodynamically demonstrate the mechanism of OE and DE adsorption onto an MS surface. According to the Arrhenius plot  $\ln(W/T)$  versus  $10^3/T$ , we calculated the enthalpy  $\Delta H^{\circ}_a$  and entropy  $\Delta S^{\circ}_a$  energies; then the standard activation  $E^{\circ}_a$  was calculated from the plot of  $\ln(W)$  against  $10^3/T$ . These parameters are associated for MS without and with inhibitors basing on the following equations: Equation 5 for  $\Delta H^{\circ}_a$  and  $\Delta S^{\circ}_a$  energies (36) and Equation 6 for  $E^{\circ}_a$  energy (37).

$$\ln \left[ \frac{W}{T} \right] = \ln \left[ \left( \frac{R}{N_a h} \right) + \frac{\Delta S^{\circ}_a}{R} \right] + \left[ \frac{-\Delta H^{\circ}_a}{R T} \right] \quad (\text{Eq. 5})$$

The outputted parameters from the Arrhenius plot (Figures 8 and 9) are listed in Table 4.

$$\ln W = \ln A + \left[ \frac{-E^{\circ}_a}{R T} \right] \quad (\text{Eq. 6})$$

Where W, R, T, h and  $N_a$  signify the corrosion rate, the universal constant of the ideal gas, the absolute temperature, the Planck’s constant and universal Avogadro number, respectively.

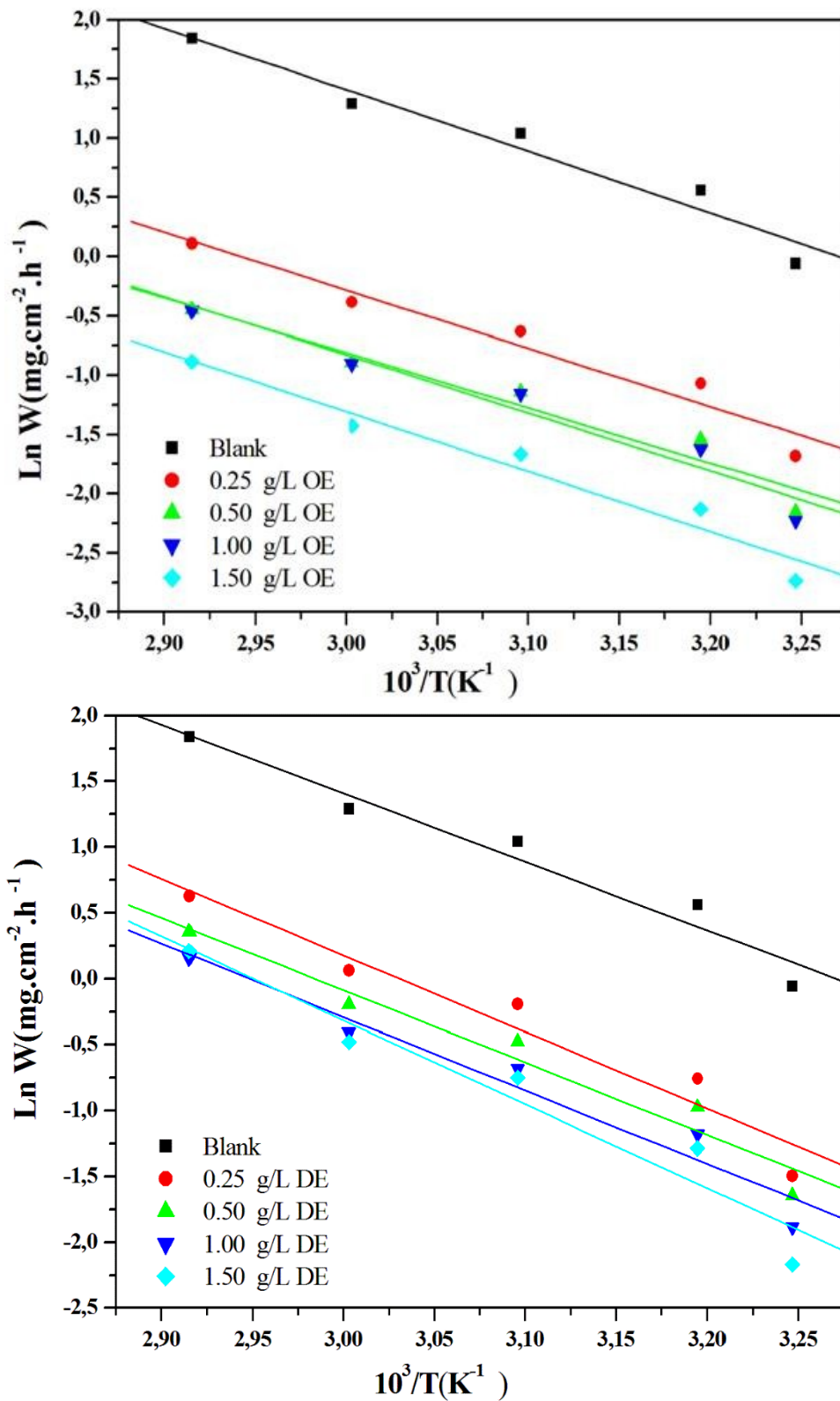


**Figure 8:** Arrhenius plots for MS corrosion rates (W) in 1 M HCl in the absence and presence of different concentrations of each inhibitor.

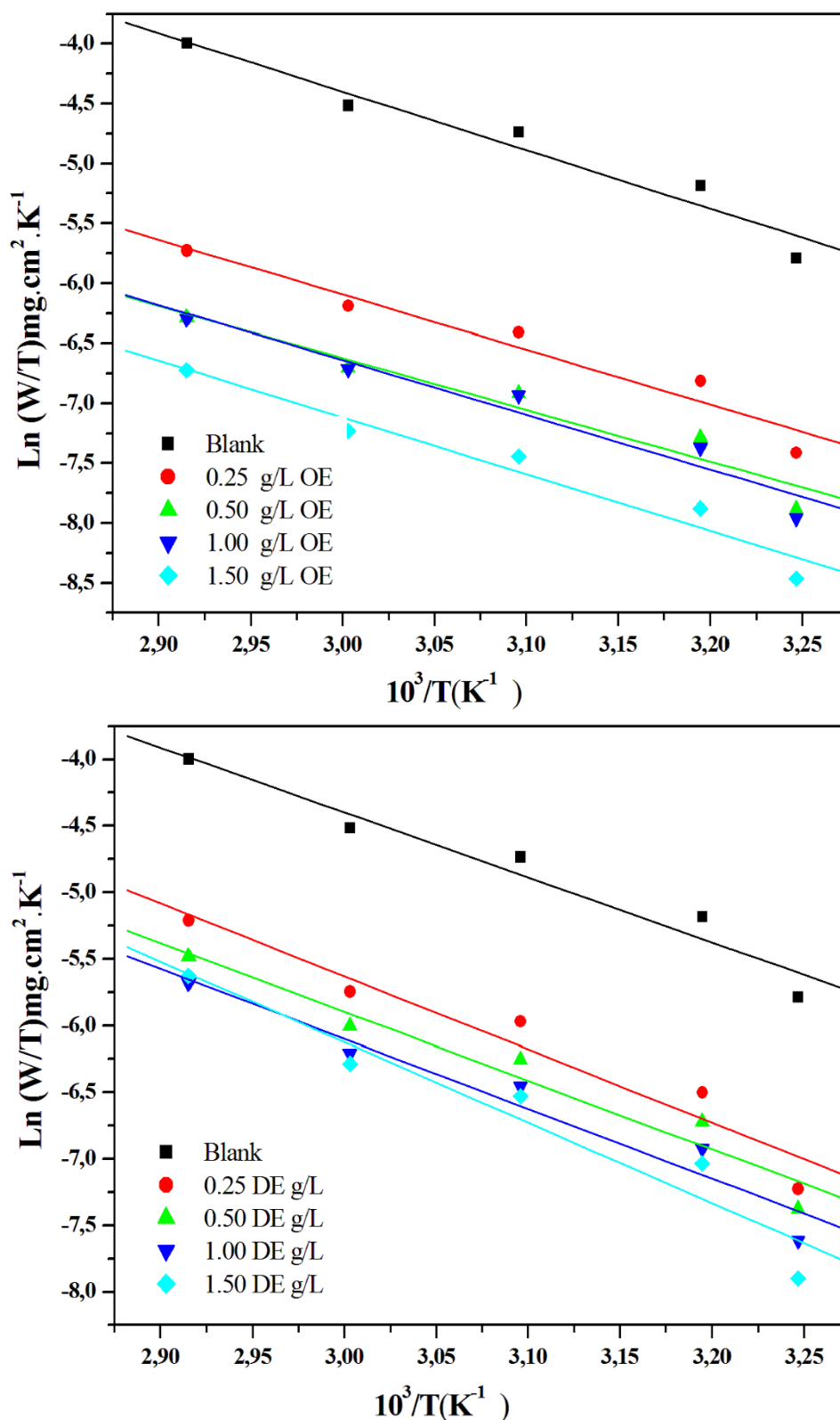


**Figure 9:** Transition-state plots for MS corrosion rates (W) in 1 M HCl in the absence and presence of various concentrations of each inhibitor.

**Table 4:** Enthalpy  $\Delta H^\circ_a$  and entropy  $\Delta S^\circ_a$  energies for MS without and with various concentrations of OE and DE.

	C (g/L)	$E^\circ_a$ (kJ. mol <sup>-1</sup> )	$\Delta H^\circ_a$ (kJ. mol <sup>-1</sup> )	$E_a - \Delta H^\circ_a$ (kJ. mol <sup>-1</sup> )	$\Delta S^\circ_a$ (J. mol <sup>-1</sup> . K <sup>-1</sup> )
OE	1 M HCl	43.35	40.65	2.70	-112.32
	0.25	40.74	38.04	2.70	-134.24
	0.50	38.62	35.92	2.70	-145.00
	1.00	40.69	38.00	2.70	-138.91
	1.50	42.11	39.42	2.70	-138.61
DE	0.25	48.29	45.59	2.71	-122.13
	0.50	45.66	42.96	2.70	-117.86
	1.00	46.35	43.65	2.70	-117.45
	1.50	52.96	50.26	2.71	-97.82

It is crystal clear from the data in Table 4 that the increase of  $E_w$  (%) with temperature and the lower value of  $E^\circ_a$  are in favor of chemisorption for OE, but are in favor of physical electrostatic nature for DE.

Additionally, the positive value of standard activation enthalpy reveals the endothermic process of corrosion phenomenon of MS (38). However, in other words, the positive value of the standard activation entropy showed a high disorder of the inhibitors molecules during adsorption. (39).

**Adsorption isotherm and thermodynamic parameters**

To get information more about the adsorption and the surface behavior of OE and DE molecules, different models of adsorption isotherms including Langmuir, Temkin and Frumkin were considered with the range of temperature of 308 to 348 K at the different concentrations of OE and DE. The equations related to these isotherms are use these formulas (40):

$$\text{Langmuir : } \frac{C}{\theta} = \frac{1}{K_{ads}} + C \quad (\text{Eq. 7})$$

$$\text{Temkin : } \ln \left[ \frac{C}{\theta} \right] = \ln K_{ads} - g \cdot \theta \quad (\text{Eq. 8})$$

$$\text{Frumkin : } \ln \left[ C \cdot \left( \frac{\theta}{1-\theta} \right) \right] = \ln K_{ads} + g \cdot \theta \quad (\text{Eq. 9})$$

where  $K_{ads}$  is adsorption coefficient,  $\theta$  is the surface coverage and  $C_{inh}$  is the concentrations of the OE and DE.

The  $K_{ads}$  values can be calculated from the intercept lines on the  $C_{inh}/\theta$  axis. As shown in the results Figures 10 and 11 and Table 5, the linear regression factor of this isotherm model appears close to 1 for the both aqueous extracts. it is understood that the OE and DE adsorption onto the metal followed the Langmuir isotherm. Using the following equation (Eq. 10) the standard free energy of adsorption  $\Delta G^\circ_{ads}$  for OE and DE was calculated:

$$K_{ads} = \frac{1}{55.5} \exp \left( \frac{-\Delta G^\circ_{ads}}{RT} \right) \quad (\text{Eq. 10})$$

where R, T, 55.5 are gas constant, absolute temperature of experiment the molar concentration of water in solution in respectively.

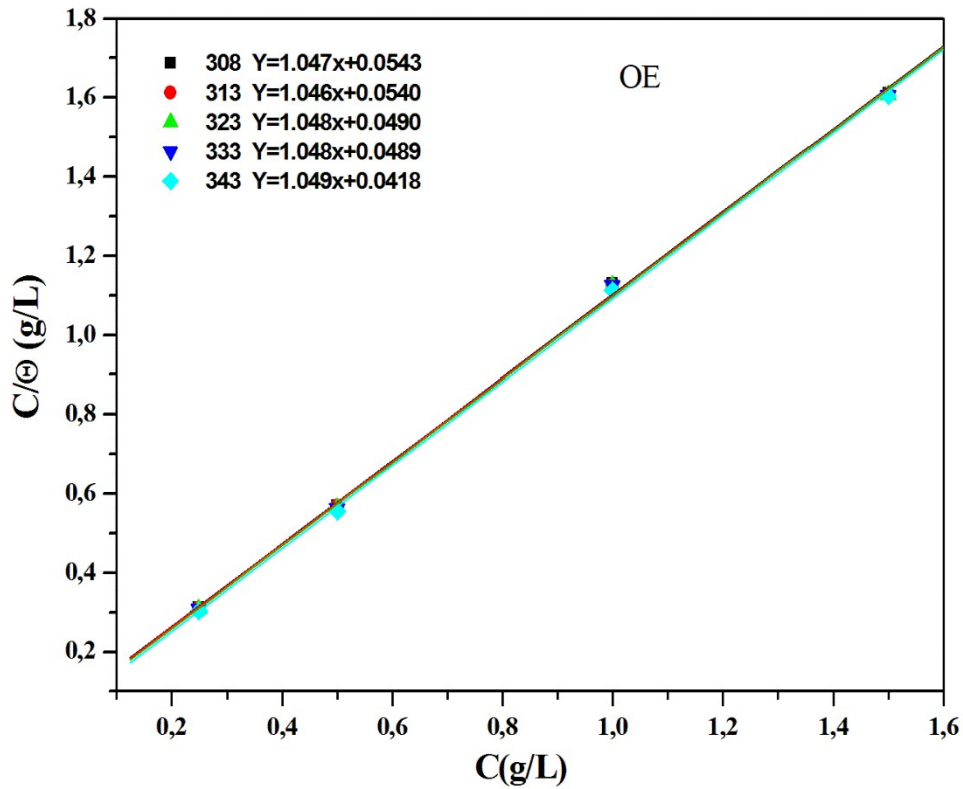


**Figure 10:** The Langmuir adsorption isotherm of OE on the MS surface in 1 M HCl at different temperatures.

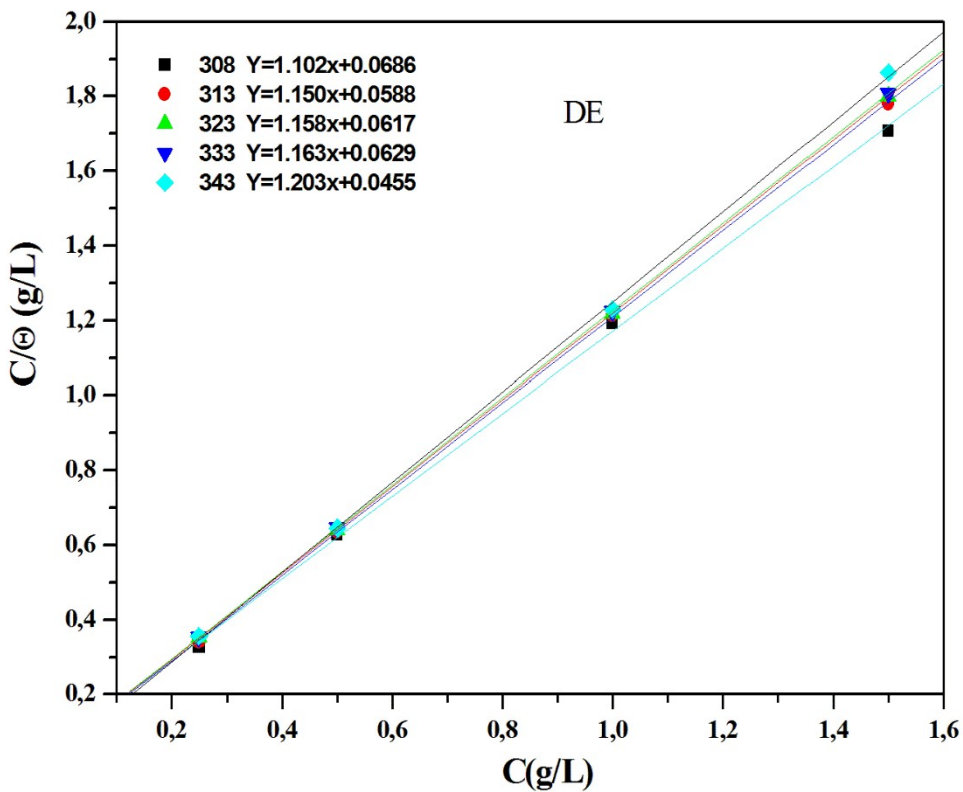


**Figure 11:** The Langmuir adsorption isotherm of DE on the MS surface in 1 M HCl at different temperatures.

**Table 5:** Langmuir isotherm adsorption parameters for 1 M HCl/OE and DE/MS interface at various temperatures.

	T(K)	R <sup>2</sup>	K <sub>ads</sub> (L. g <sup>-1</sup> )	ΔG° <sub>ads</sub> (KJ. mol <sup>-1</sup> )
OE	308	0.999	18.41	-25.66
	313	0.999	18.51	-25.58
	323	0.999	20.40	-26.66
	333	0.999	20.49	-27.50
	343	0.999	24.39	-28.82
DE	308	0.999	14.70	-24.58
	313	0.999	17.24	-25.40
	323	0.998	16.39	-26.07
	333	0.999	16.12	-26.84
	343	0.999	22.02	-28.56

We can conclude from Table 5, OE has a greater value indicating its ability to be absorbed easily and strongly (41). Also, it is clear that, the negative values of ΔG°<sub>ads</sub> suggest that the adsorption of inhibitor molecules onto MS surface is a spontaneous phenomenon. The predominant adsorption mode of OE and DE depends upon factors such as the nature of the extract molecules, type of acid anion, as well as chemical changes in the extracts. Molecular adsorption of the OE and DE at the metal surface can be attributed to the presence of electronegative elements such as oxygen and nitrogen atoms and also to the presence of n-electrons. The high inhibitive performance of OE is due probably to the synergic effect of their volatile especially, E-anethole (15.4%), (E)-heptadeca-10,16-dien-7-one (11.1 %), and Z-β-ocimene (8.6%) were identified as major constituents of the essential oil from *Aaronsohnia pubescens subsp. pubescens* and non-volatile compounds. These results are coherent those of the studies previously reported in our group (12).

## CONCLUSION

The experimental results showed that the odorized aqueous extract (OE) and deodorized aqueous extract (DE) of *Aaronsohnia pubescens subsp. pubescens* proved significant corrosion inhibition activity. PDP curves demonstrate that inhibitors acts as a mixed type inhibitor in 1 M HCl. The inhibition is accomplished by a mixture physical and chemical adsorption of the extract components on the MS surface. The aqueous extracts obeys a Langmuir adsorption isotherm. The Nyquist diagram showed that adsorption mechanism of OE and DE are governed by a charge transfer process. The high protective efficiency of OE is due to the synergic effect of their volatile and non-volatile molecules.

## REFERENCES

1. Al-Azawi KF, Mohammed IM, Al-Baghdadi SB, Salman TA, Issa HA, Al-Amiery AA, et al. Experimental and quantum chemical simulations on the corrosion inhibition of mild steel by 3-((5-(3,5-dinitrophenyl)-1,3,4-thiadiazol-2-yl)imino)indolin-2-one. Results in Physics. 2018 Jun;9:278–83. [<DOI>](#).
2. Dehghani A, Bahlakeh G, Ramezanzadeh B, Ramezanzadeh M. Potential of Borage flower aqueous extract as an environmentally sustainable corrosion inhibitor for acid corrosion of mild steel: Electrochemical and theoretical studies. Journal of Molecular Liquids. 2019 Mar;277:895–911. [<DOI>](#).
3. Ghames A, Douadi T, Issaadi S, Sibous L, Alaoui K. Theoretical and Experimental Studies of Adsorption Characteristics of Newly Synthesized Schiff Bases and their Evaluation as Corrosion Inhibitors for Mild Steel in 1 M HCl. Int J Electrochem Sci. 2017 Jun;12:4867–97. [<DOI>](#).
4. Kumar A, Trivedi M, Bhaskaran B, Kishore Sharma R, Singh G. Synthetic, spectral and structural studies of a Schiff base and its anticorrosive activity on mild steel in H<sub>2</sub>SO<sub>4</sub>. New J Chem. 2017;41(16):8459–68. [<DOI>](#).
5. Chraka A, Raissouni I, Seddik NB, Khayar S, Mansour AI, Tazi S, et al. Identification of Potential Green Inhibitors Extracted from *Thymbra capitata* (L.) Cav. for the Corrosion of Brass in 3% NaCl Solution: Experimental, SEM-EDX Analysis, DFT Computation and Monte Carlo Simulation Studies. J Bio Tribo Corros. 2020 Sep;6(3):80. [<DOI>](#).
6. El Ouadi Y, Bouyanzer A, Majidi L, Paolini J, Desjoberg J-M, Costa J, et al. Evaluation of

- Pelargonium extract and oil as eco-friendly corrosion inhibitor for steel in acidic chloride solutions and pharmacological properties. *Res Chem Intermed.* 2015 Oct;41(10):7125-49. [<DOI>](#).
7. Manssouri M, Znini M, El Ouadi Y, Laghchimi A, Ouakki M, Majidi L. Effect of Aaronsohnia Pubescens Extracts to Prevent Against the Corrosion of Mild Steel in 1.0 M HCl. *Analytical and Bioanalytical Electrochemistry.* 2020;12(7):944-58.
8. Benabbouha T, Siniti M, El Attari H, Chefira K, Chibi F, Nmila R, et al. Red Algae Halopitys Incurvus Extract as a Green Corrosion Inhibitor of Carbon Steel in Hydrochloric Acid. *J Bio Tribo Corros.* 2018 Sep;4(3):39. [<DOI>](#).
9. Anupama KK, Joseph A. Experimental and Theoretical Studies on Cinnamomum verum Leaf Extract and One of Its Major Components, Eugenol as Environmentally Benign Corrosion Inhibitors for Mild Steel in Acid Media. *J Bio Tribo Corros.* 2018 Jun;4(2):30. [<DOI>](#).
10. Gonzalez-Rodriguez JG, Gomez-Guzman NB, Porcayo-Calderon J. Corrosion Inhibition of X70 Pipeline Steel Under Hydrodynamic Conditions of CO<sub>2</sub> with Amide Extraction from Coffee Bagasse. *J Bio Tribo Corros.* 2021 Sep;7(3):86. [<DOI>](#).
11. Manssouri M, El Ouadi Y, Znini M, Costa J, Bouyanzer A, Desjobert J, et al. Adsorption properties and inhibition of mild steel corrosion in HCl solution by the essential oil from fruit of Moroccan Ammodaucus leucotrichus. *J Mater Environ Sci.* 2015;6(3):631-46.
12. Manssouri M, Znini M, Ansari A, Bouyanzer A, Faska Z, Majidi L. Odorized and deodorized aqueous extracts of Ammodaucus leucotrichus fruits as green inhibitor for C38 steel in hydrochloric acid solution. *Der Pharma Chemica.* 2014;6(6):331-45.
13. Manssouri M, Znini M, Lakbaibi Z, Ansari A, El Ouadi Y. Experimental and computational studies of perillaldehyde isolated from Ammodaucus leucotrichus essential oil as a green corrosion inhibitor for mild steel in 1.0 M HCl. *Chem Pap.* 2021 Mar;75(3):1103-14. [<DOI>](#).
14. Manssouri M, Laghchimi A, Ansari A, Znini M, Lakbaibi Z, El Ouadi Y, et al. Effect of Santolina pectinata (Lag.) Essential Oil to protect against the corrosion of Mild steel in 1.0 M HCl: Experimental and quantum chemical studies. *MediterrJChem.* 2020 Mar 17;10(3):253-68. [<DOI>](#).
15. Manssouri M, Znini M, El Ouadi Y, Ansari A, Costa J, Majidi L. Essential Oil of Aaronsohnia Pubescens Subsp. Pubescens as Novel Eco-Friendly Inhibitor for Mild Steel in 1.0 M HCl. *Analytical and Bioanalytical Electrochemistry.* 2020;12(6):841-56.
16. Manssouri M, Znini M, Lakbaibi Z, El Ouadi Y, Majidi L. Aqueous extracts of Santolina pectinata lag., aerial parts as green corrosion inhibitor for mild steel in 1.0 M HCl. *Analytical and Bioanalytical Electrochemistry.* 2020;12(5):607-24.
17. Manssouri M, Lakbaibi Z, Znini M, Ouadi YEL, Jaafar A, Majidi L. Impact of Aaronsohnia pubescens Essential Oil to Prevent Against the Corrosion of Mild Steel in 1.0 M HCl: Experimental and Computational Modeling Studies. *J Fail Anal and Preven.* 2020 Dec;20(6):1939-53. [<DOI>](#).
18. Manssouri M, Znini M, Majidi L. Studies on the antioxidant activity of essential oil and various extracts of Ammodaucus leucotrichus Coss. & Dur. Fruits from Morocco. *Journal of Taibah University for Science.* 2020 Jan 1;14(1):124-30. [<DOI>](#).
19. Dapkevicius A, Venskutonis R, van Beek TA, Linsen JP. Antioxidant activity of extracts obtained by different isolation procedures from some aromatic herbs grown in Lithuania. *Journal of the Science of Food and Agriculture.* 1998;77(1):140-6.
20. Satapathy AK, Gunasekaran G, Sahoo SC, Amit K, Rodrigues PV. Corrosion inhibition by Justicia gendarussa plant extract in hydrochloric acid solution. *Corrosion Science.* 2009 Dec;51(12):2848-56. [<DOI>](#).
21. Ezuber H, Alshater A, Nisar S, Gonsalvez A, Aslam S. Effect of surface finish on the pitting corrosion behavior of sensitized AISI 304 austenitic stainless steel alloys in 3.5% NaCl solutions. *Surface Engineering and Applied Electrochemistry.* 2018;54(1):73-80.
22. Khalili Dermani A, Kowsari E, Ramezanzadeh B, Amini R. Utilizing imidazole based ionic liquid as an environmentally friendly process for enhancement of the epoxy coating/graphene oxide composite corrosion resistance. *Journal of Industrial and Engineering Chemistry.* 2019 Nov;79:353-63. [<DOI>](#).
23. Jamil HE, Montemor MF, Boulif R, Shrii A, Ferreira MGS. An electrochemical and analytical approach to the inhibition mechanism of an amino-alcohol-based corrosion inhibitor for reinforced concrete. *Electrochimica Acta.* 2003 Oct;48(23):3509-18. [<DOI>](#).
24. Sathiya Priya AR, Muralidharan VS, Subramania A. Development of Novel Acidizing Inhibitors for Carbon Steel Corrosion in 15% Boiling Hydrochloric Acid. *CORROSION.* 2008 Jun;64(6):541-52. [<DOI>](#).
25. Hsissou R, Benhiba F, About S, Dagdag O, Benkhaya S, Berisha A, et al. Trifunctional epoxy

- polymer as corrosion inhibition material for carbon steel in 1.0 M HCl: MD simulations, DFT and complexation computations. *Inorganic Chemistry Communications*. 2020 May;115:107858. [<DOI>](#).
26. Yanardağ T, Bayraktar N, Yanardağ YK, Özgen Y, Aksut AA. THE INHIBITOR EFFECTS OF CANNABIS SATIVA L. EXTRACTS ON THE CORROSION OF ALUMINIUM IN H<sub>2</sub>SO<sub>4</sub> SOLUTIONS. *Communications Faculty of Sciences University of Ankara Series B Chemistry and Chemical Engineering*. 2020 Jun 30;62(1):12–22. [<URL>](#).
27. Arrousse N, Salim R, Abdellaoui A, Hajjaji FE, Hammouti B, Mabrouk EH, et al. Synthesis, characterization, and evaluation of xanthene derivative as highly effective, nontoxic corrosion inhibitor for mild steel immersed in 1 M HCl solution. *Journal of the Taiwan Institute of Chemical Engineers*. 2021 Mar;120:344–59. [<DOI>](#).
28. Benali O, Benmehdi H, Hasnaoui O, Selles C, Salghi R. Green corrosion inhibitor: inhibitive action of tannin extract of *Chamaerops humilis* plant for the corrosion of mild steel in 0.5 M H<sub>2</sub>SO<sub>4</sub>. *J Mater Environ Sci*. 2013;4(1):127–38.
29. Hsu CH, Mansfeld F. Technical Note: Concerning the Conversion of the Constant Phase Element Parameter Y<sub>0</sub> into a Capacitance. *Corrosion*. 2001 Sep 1;57(09).
30. Yıldız R. An electrochemical and theoretical evaluation of 4,6-diamino-2-pyrimidinethiol as a corrosion inhibitor for mild steel in HCl solutions. *Corrosion Science*. 2015 Jan;90:544–53. [<DOI>](#).
31. Solmaz R, Kardaş G, Çulha M, Yazıcı B, Erbil M. Investigation of adsorption and inhibitive effect of 2-mercaptothiazoline on corrosion of mild steel in hydrochloric acid media. *Electrochimica Acta*. 2008 Aug;53(20):5941–52. [<DOI>](#).
32. Erbil M. The determination of corrosion rates by analysis of AC impedance diagrams. *Chimica Acta Turcica*. 1988;1:59–70.
33. Özcan M, Dehri İ. Determination of impedance parameters for mild steel/HCl interface using integration method. *Corrosion Science*. 2012 Jan;54:201–4. [<DOI>](#).
34. Chai C, Xu Y, Li D, Zhao X, Xu Y, Zhang L, et al. Cysteamine modified polyaspartic acid as a new class of green corrosion inhibitor for mild steel in sulfuric acid medium: Synthesis, electrochemical, surface study and theoretical calculation. *Progress in Organic Coatings*. 2019 Apr;129:159–70. [<DOI>](#).
35. Jüttner K. Electrochemical impedance spectroscopy (EIS) of corrosion processes on inhomogeneous surfaces. *Electrochimica Acta*. 1990 Oct;35(10):1501–8. [<DOI>](#).
36. Benali O, Cherkaoui O, Lallam A. Adsorption and corrosion inhibition of new synthesized Pyridazinium-Based Ionic Liquid on Carbon steel in 0.5 M H<sub>2</sub>SO<sub>4</sub>. *J Mater Environ Sci*. 2015;6:598–606.
37. Badiea AM, Mohana KN. Effect of temperature and fluid velocity on corrosion mechanism of low carbon steel in presence of 2-hydrazino-4,7-dimethylbenzothiazole in industrial water medium. *Corrosion Science*. 2009 Sep;51(9):2231–41. [<DOI>](#).
38. Khamis E, Bellucci F, Latanision R, El-Ashry E. Acid corrosion inhibition of nickel by 2-(triphenylphosphoranylidene) succinic anhydride. *Corrosion*. 1991;47(9):677–86.
39. Bentiss F, Lebrini M, Vezin H, Chai F, Traisnel M, Lagrené M. Enhanced corrosion resistance of carbon steel in normal sulfuric acid medium by some macrocyclic polyether compounds containing a 1,3,4-thiadiazole moiety: AC impedance and computational studies. *Corrosion Science*. 2009 Sep;51(9):2165–73. [<DOI>](#).
40. Bourazmi H, Tabyaoui M, Hattabi L, El Aoufir Y, Ebenso E, Ansari A. Camphor as an effective corrosion inhibitor for carbon steel in 1M HCl solution: electrochemical and quantum chemical investigation. *Journal of Materials and Environmental Science*. 2018;9:1058–74.
41. Tang L, Mu G, Liu G. The effect of neutral red on the corrosion inhibition of cold rolled steel in 1.0 M hydrochloric acid. *Corrosion Science*. 2003 Oct;45(10):2251–62. [<DOI>](#).





## Effect of Nitrogen Precursor on Optical Properties of Hexagonal Boron Nitride Quantum Dots

Esranur Budak<sup>1</sup>  and Caner Ünlü<sup>1,2,3\*</sup>  

<sup>1</sup>Istanbul Technical University, Department of Nanoscience and Nanoengineering, Maslak, 34469 Istanbul, Turkey

<sup>2</sup>Istanbul Technical University, Faculty of Science and Letters, Department of Chemistry, 34469, Maslak, Istanbul, Turkey

<sup>3</sup>Istanbul Technical University Nanotechnology Research and Application Center (ITUNano), 34469, Maslak, Istanbul, Turkey

**Abstract:** Boron nitride quantum dots (BNQDs) are of high interest with their excellent photophysical and structural characteristics. BNQDs can be synthesized through hydrothermal synthesis methods with different nitrogen precursors; however, until now, the optical properties of BNQDs synthesized with different nitrogen precursors have not been compared in details yet. In this study, BNQDs were synthesized through hydrothermal synthesis methods by using urea, melamine, and thiourea as nitrogen precursors and optical properties of BNQDs were compared by comparing emission and excitation characteristics of each BNQD synthesized by different nitrogen precursor. Structural properties of BNQDs were compared through infrared spectrum of each BNQDs. Our results revealed that the change in nitrogen precursor causes significant differences in photophysical and structural properties of BNQDs.

**Keywords:** Quantum dots, boron nitride, fluorescence.

**Submitted:** June 29, 2021. **Accepted:** August 17, 2021.

**Cite this:** Budak E, Ünlü C. Effect of Nitrogen Precursor on Optical Properties of Hexagonal Boron Nitride Quantum Dots. JOTCSA. 2021;8(3):969-76.

**DOI:** <https://doi.org/10.18596/jotcsa.959577>.

**\*Corresponding author. E-mail:** [canerunlu@itu.edu.tr](mailto:canerunlu@itu.edu.tr).

### INTRODUCTION

Quantum dots made of 2-dimensional materials, in other words graphene like materials, are called 2D quantum dots and have become the center of attention with their excellent photophysical and structural properties (1-4). 2D quantum dots have a lateral size in the range of 2 - 6 nm with thickness less than 1 nm and display graphene-like geometry (1-4). These nanomaterials are simply nanometer-sized blocks of well-known 2D materials such as graphene, graphitic carbon nitride, hexagonal boron nitride, molybdenum sulfide, molybdenum selenide, tungsten sulfide, etc (1-4). 2D quantum dots have been considered as versatile materials since their discovery and have been used in many different application and research areas such as optoelectronics, supercapacitors, batteries, cell imaging, and sensors (1-7).

Amongst all, BNQDs have been studied widely with their unique features such as low toxicity and high biocompatibility (1-4). BNQDs were discovered in 2014 by Lin et al. and firstly synthesized through reducing the size of bulk hexagonal boron nitride (top-down approach) (8). After their discovery, BNQDs have been synthesized through top-down synthesis methods (8-16) and bottom-up synthesis methods (15,17-19) in many different studies. In most of studies in which bottom-up synthesis methods were used, boric acid was used as the boron precursor; however, the nitrogen precursor was different (15,17-19). The most common used nitrogen precursors were ammonia, urea, and melamine (15,17-19). Each study claimed the final product that they obtained were BNQDs, and also the spectral outcomes were pointing out the quantum dots were indeed similar in structure, however, no detailed comparison on optical

properties of BNQDs synthesized with different nitrogen precursor was conducted until now.

In this study, we synthesized BNQDs through hydrothermal bottom-up synthetic methods by using boric acid as the boron precursor and 3 different nitrogen precursors; urea, melamine, and thiourea. The photophysical properties of BNQDs were analyzed in details by collecting emission and excitation spectrum of each quantum dot type. Detailed structural analysis was conducted by using Fourier transform infrared spectroscopy. Our results showed that each BNQD type had its unique optical and structural properties and therefore they should be considered as different quantum dot type.

## MATERIALS AND METHODS

All chemicals that were used in this work were of the highest purity and were purchased from Sigma-Aldrich Co. They were used without further purification.

### Synthesis of Boron Nitride Quantum Dots

Boron nitride (BN) quantum dots were synthesized through a modified hydrothermal synthesis method (17). To synthesize BN quantum dots, boric acid was used as a boron precursor and three different nitrogen precursors (urea, thiourea, and melamine) were selected to accompany boric acid. Firstly, 300 mg of boric acid and 100 mg of nitrogen precursor were completely dissolved in 5 mL of distilled water. Then, the clear solution was transferred into a Teflon-lined stainless steel reaction chamber, sealed, and placed in a furnace oven (brand: Isolab). The reaction chamber was heated until 200 °C and kept at that temperature for 24 hours. After 24 hours, the reaction chamber was taken out and cooled down to room temperature. A colorless clear solution was obtained as the crude product, which was purified by filtering with 0.22 micrometer syringe and centrifuging at 14,000 rpm for 30 minutes. The purified solution was kept at 4 °C for further use.

### Optical and Structural Characterization of C-BN and BCN QDs

Optical properties of BN QDs were characterized by Scinco Neosys-2000 single - beam ultraviolet-visible (UV-Vis) spectrophotometer and Varian Cary Eclipse fluorescence spectrofluorimeter. Each sample was dissolved in 10 mL of ultrapure water after purification and diluted until optical density was under 0.1 in order to prevent errors resulting from self-absorption, then the absorption spectrum of each sample was collected by a UV-Vis spectrophotometer. The further optical properties were determined through aqueous solutions of

quantum dots. Emission spectrum of each sample was collected by using different excitation wavelengths ( $\lambda_{exc}$ ) in the range of 250 - 400 nm. The emission color of each sample was observed under 366 nm UV-light. Photoluminescent excitation (PLE) spectrum of each sample was collected at 440 nm. Quantum yields of the BN QDs were measured by using coumarin 102 in ethanol as a standard (the reference quantum yield was 0.93) (20,21).

Structural analysis of BN quantum dots was performed through Fourier transform infrared spectroscopy (FTIR) and Transmission electron microscopy (TEM). Bonding characteristics of BN quantum dots were determined by attenuated total reflectance FTIR spectroscopy. FTIR spectrum of each quantum dot was carried out in the range of 3750–800  $cm^{-1}$  by using a Perkin Elmer Spectrum One ATR-FTIR spectrometer.

The shape and size of quantum dots were determined by using TEM. TEM measurements were conducted with JEOL JEM 1220 at an acceleration voltage of 100 kV.

## RESULTS AND DISCUSSION

### Synthesis of BN quantum dots

Bottom-up synthesis of BN QDs are generally carried out by using various boron and nitrogen precursors (15,17–19). In most of the studies, even though the precursors for boron and nitrogen differ, the synthesis conditions are similar to synthesize BN quantum dots (15,17–19). In this study, boric acid was chosen to be the sole boron precursor (Figure 1). As nitrogen precursor, melamine, urea, or thiourea were used with boric acid separately to synthesize BN QDs in order to check the effect of nitrogen precursor on structural and optical properties of BN QDs. The duration for synthesis and synthesis temperature were chosen to be 24 hours and 200 °C, respectively, as these conditions were frequently used to synthesize BN QDs (Figure 1) (15,17–19).

As the molecular structure of nitrogen precursors were compared, it was seen that in fact all these precursors can also act as precursor of additional elements, such as sulfur, oxygen, and carbon (Figure 2). Urea and melamine are frequently used in synthesis of BN QDs, however, thiourea has not been preferred widely (15,17–19). In the literature, it was suggested that BN QDs can be synthesized through using either melamine or urea, however, it should be considered that different molecular structures of urea and melamine most likely cause a distinct difference in the structure of QDs, therefore in the optical properties of QDs.

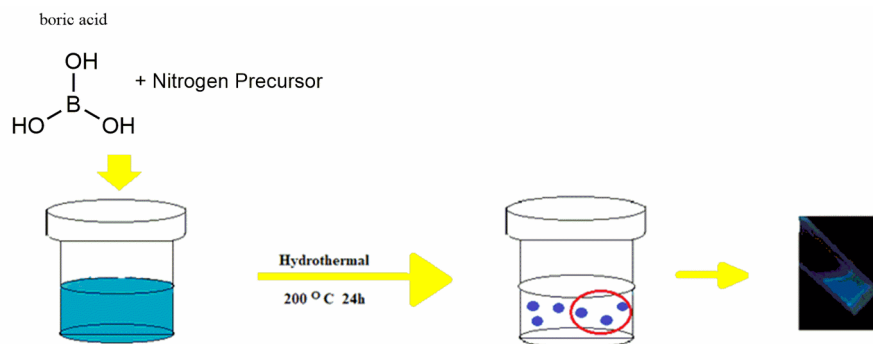


**Figure 1.** Schematic representation of synthesis of Boron Nitride quantum dots.

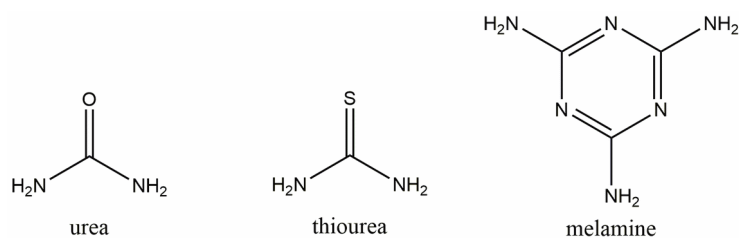


**Figure 2.** Structures of nitrogen precursors.

### Structural characterization of BN QDs

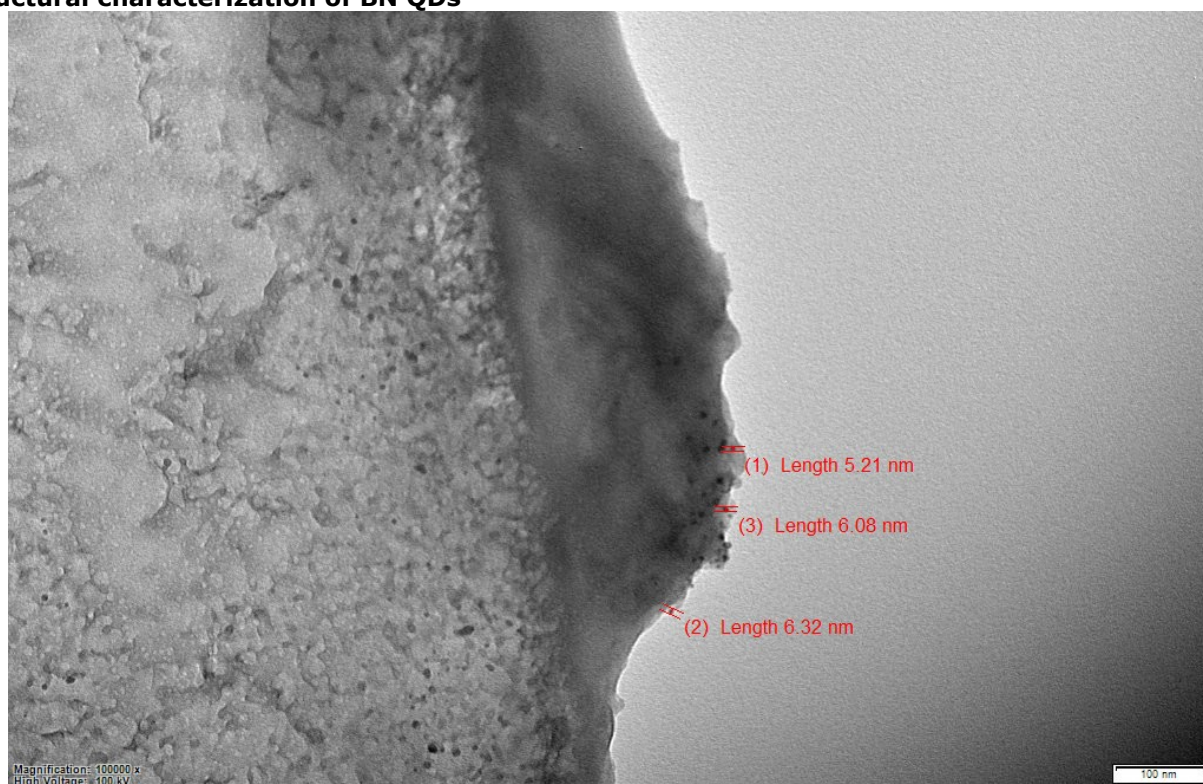


**Figure 3.** TEM image of BNQDs.

The size characterization was performed on U-BNQDs by TEM and it was found out that BN QDs had a size around 2 – 5 nm, which is the typical size range for BNQDs (Figure 3). The structural differences in BN QDs synthesized by different nitrogen precursors displayed themselves in FTIR spectrum of each QD (Figure 4). The most

observable difference was explained as follows; BN QDs derived from thiourea (T-BNQDs) had a very sharp and intense peak at  $2550\text{ cm}^{-1}$  which corresponded to S-H bonding where neither BN QDs derived from urea (U-BNQDs) nor BN QDs derived from melamine (M-BNQDs) had (Figure 4) (15,17–19). This peak showed that S=C double bond in

thiourea was broken during synthesis of BN QDs and thiol groups were formed in the structure of T-BNQDs. FTIR spectrum of U-BNQDs and M-BNQDs had typical -BOH bonding peaks around  $1180\text{ cm}^{-1}$ , however, this peak shifted to  $1210\text{ cm}^{-1}$  in FTIR spectrum of T-BNQDs due to existence of -SH groups on the surface of T-BNQDs (Figure 4) (15,17-19). Each BN QD had typical B-N bonding peak around  $780 - 800\text{ cm}^{-1}$  and  $1380 - 1420\text{ cm}^{-1}$  (Figure 4). As the structures of U-BNQDs and M-BNQDs were compared, the main difference

between the FTIR spectra of U-BNQDs and M-BNQDs was the peak around  $920\text{ cm}^{-1}$ , the -N-B-O edge peak, which was the clear evidence of structural difference between U-BNQDs and M-BNQDs (Figure 4). Adjacent to the peak at  $880\text{ cm}^{-1}$ , attributed to stretching vibration bands of C-O, the U-BNQDs possessed a peak at  $920\text{ cm}^{-1}$  which showed that U-BNQDs had N-B-O groups on the surface (Figure 4). These clear differences showed that depending on nature of nitrogen precursor, BN QDs had different structural characteristics.

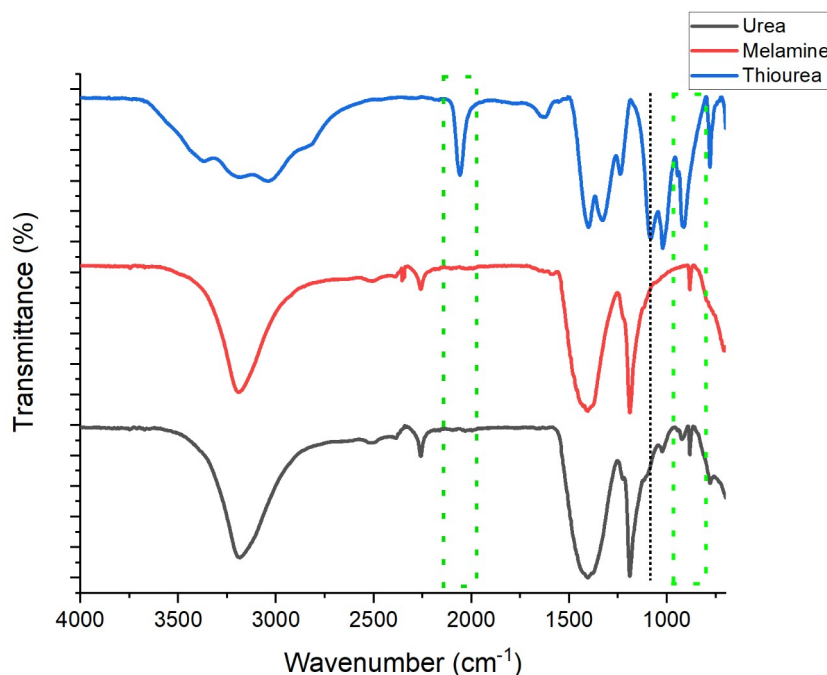


**Figure 4.** FTIR spectra of BNQDs synthesized with urea (black), melamine (red) and thiourea (blue).

### Optical characterization of BN QDs

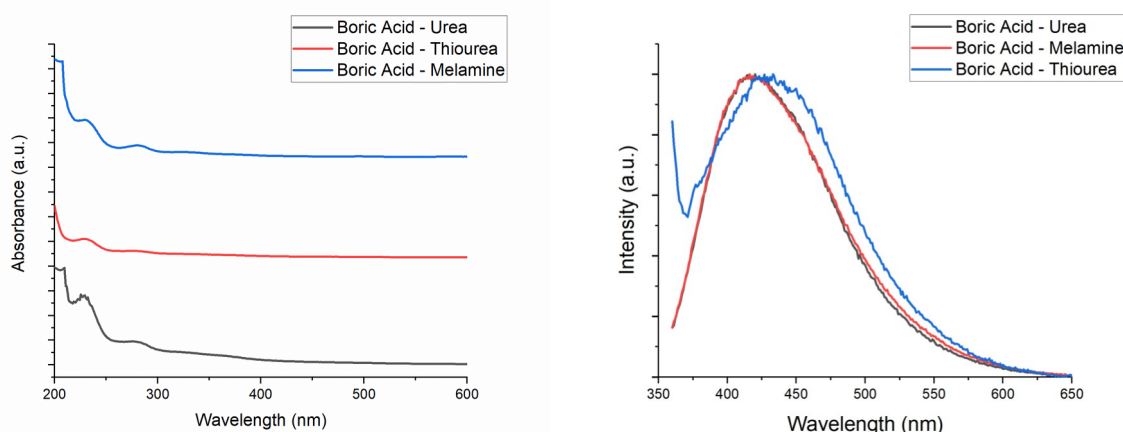


**Figure 5.** Absorption (left) and Fluorescent spectrum (right) of BNQDs synthesized with urea (black), melamine (blue), and thiourea (red). For fluorescent spectrum, each BNQDs were excited by 350 nm light.

Absorption spectrum and emission (PL) spectrum of a quantum dot are the two main indicators that let us characterize optical properties of all types of quantum dots (15,17-19). The comparison of

absorbance spectrum of each BN QDs revealed that the absorption characteristics of M-BNQDs and U-BNQDs were similar, where absorbance spectrum of T-BNQDs was different from those of U-BNQDs and

M-BNQDs (Figure 5). Absorbance spectra of U-BNQDs and M-BNQDs possessed an intense peak around 230 nm, due to C=C peak in the structure of BN QDs and a relatively mild peak around 280 nm, due to band-edge transition in BN QDs (Figure 5) (15,17–19). Both of these peaks also appeared in T-BNQDs, but with a dramatically low intensity, which showed that the structure of T-BNQDs was considerably different from structure of M-BNQDs and U-BNQDs, as was also indicated through FTIR spectrum of each BN QDs. The emission spectrum of each BN QDs revealed the same story; emission spectrum of M-BNQDs upon  $\lambda_{exc} = 350$  nm and emission spectrum of U-BNQDs upon  $\lambda_{exc} = 350$  nm were almost identical, a single peak around 416 nm,

where the emission peak of T-BNQDs red-shifted almost 15 nm, a single peak around 432 nm (Figure 5). The incorporation of S into BN QD structure caused a considerable red-shift in emission peak of BN QDs, and also caused a significant decrease in quantum yield of BN QDs; the U-BNQDs and M-BNQDs had quantum yield of 24% and 21%, respectively, where T-BNQDs had quantum yield of 6%. Although the FTIR spectrum of M-BNQDs and U-BNQDs were different, the absorption and emission spectrum were quite similar. Yet, the further analysis on optical properties of BN QDs showed that M-BNQDs and U-BNQDs had different excitation properties (Figures 6, 7, and 8).

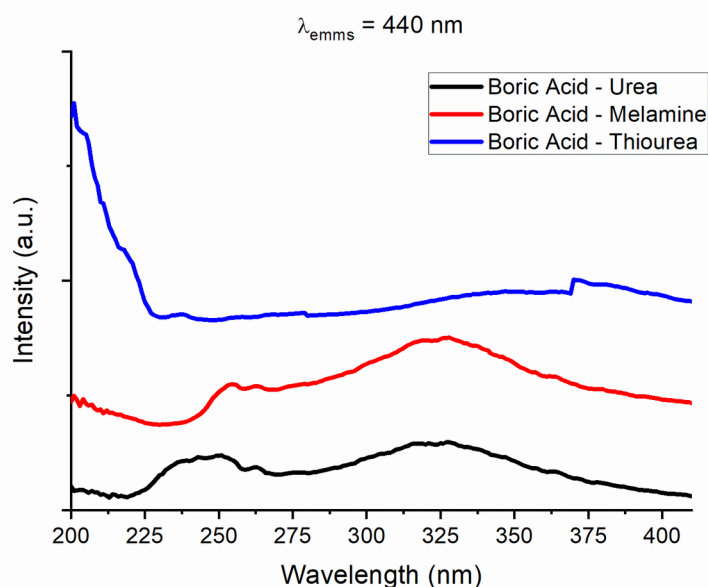


**Figure 6.** PLE spectrum of BNQDs synthesized with urea (black), melamine (red), and thiourea (blue).

U-BNQD and M-BNQD had similar photoluminescence excitation (PLE) spectra; however, there was one significant difference that U-BNQD had broadened the excitation peak in 225 – 250 nm region while M-BNQD did not (Figure 6). T-BNQD had an entirely different PLE spectrum with

an intense peak between 200 - 225 nm (Figure 6). The difference in the PLE spectrum of U-BNQD and M-BNQD resulted in an observable difference in emission spectrum of these quantum dots with  $\lambda_{exc} = 250$  nm.

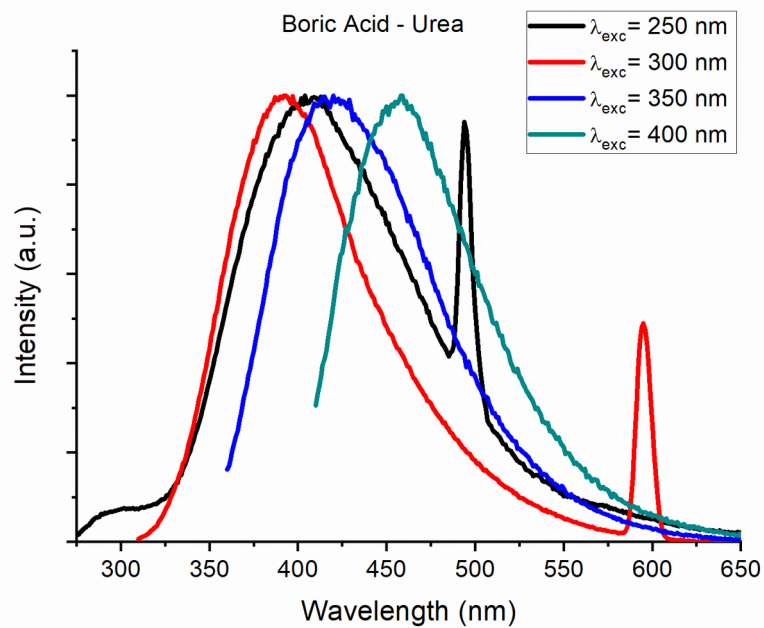


**Figure 7.** Fluorescent spectra of BNQDS synthesized with melamine with different excitation wavelengths.

The emission spectrum of M-BNQD had a single peak at 415 nm with  $\lambda_{exc} = 250$  nm (Figure 7) where the emission spectrum of U-BNQD had a single peak at 395 nm with  $\lambda_{exc} = 250$  nm (Figure 8). This difference is most likely due to existence of different groups on the surface of M-BNQD and U-

BNQD, the existence N-B-O groups on the surface of U-BNQDs. It should be noted that U-BNQD and M-BNQD had very similar emissive properties with  $\lambda_{exc} = 300$  nm,  $\lambda_{exc} = 350$  nm and  $\lambda_{exc} = 400$  nm (Figures 7 and 8).

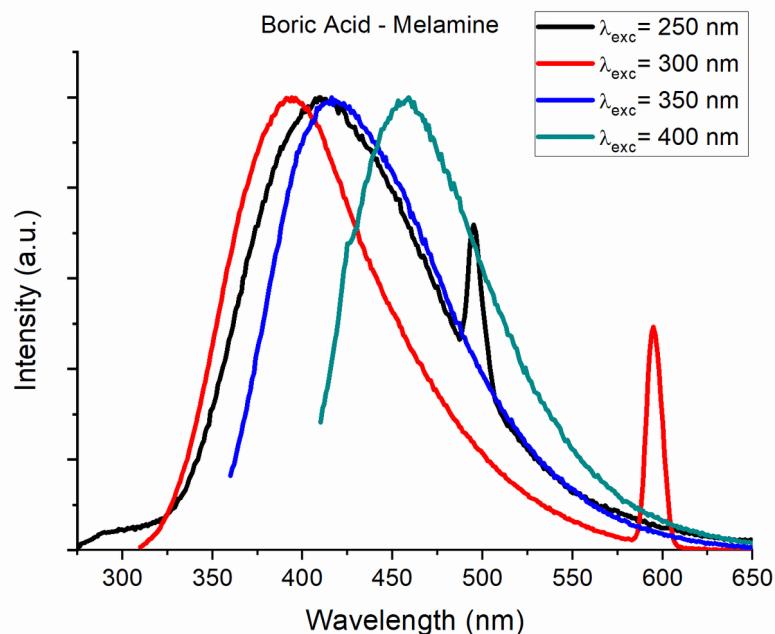


**Figure 8.** Fluorescent spectrum of BNQDS synthesized with urea with different excitation wavelengths.

These observations showed that, despite the differences on the surface of U-BNQD and M-BNQD, these quantum dots had similar inner crystal structure and the crystal structure can be excited

through lower energy possessing light (300 – 400 nm), where surface of BN QDs could be excited through higher energy possessing light (250 nm).

**CONCLUSION**

Boron nitride quantum dots are generally synthesized through hydrothermal methods by using boric acid as a boron precursor and various chemicals such as urea, melamine, and thiourea as nitrogen precursors. The BN quantum dots synthesized with different nitrogen groups had significant optical and structural differences. When thiourea was used as nitrogen precursor, it was observed that sulfur was incorporated with crystal structure and incorporation of sulfur to nanocrystal structure caused significant changes in optical properties of quantum dots, such as decrease in quantum yield and shift in emission peak wavelength. The BN quantum dots synthesized by using urea and melamine as nitrogen precursors had similar emission properties upon excitation through 300, 350, and 400 nm light, however, the U-BNQD had a broadened PLE spectrum compared to M-BNQD and had different emission properties upon excitation through 250 nm, which was a consequence of existence of N-B-O bonding on the surface of U-BNQD that was observed in FTIR spectrum of U-BNQD.

**ACKNOWLEDGEMENT**

We would like to thank Dr. Bünyamin Karagöz for letting use of fluorescent spectrophotometer. Also, we thank Dr. Ahmet Gül for helpful discussion, support, and letting use of UV-Vis spectrophotometer. This work was supported by TUBITAK (The Scientific and Technological Research Council of Turkey) under Career Development Programme for Young Researchers (Career Programme) (Programme No: 3501) [Grant number: 118Z259].

**REFERENCES**

1. Wang X, Sun G, Li N, Chen P. Quantum dots derived from two-dimensional materials and their applications for catalysis and energy. *Chem Soc Rev.* 2016;45(8):2239–62. [<DOI>](#).
2. Xu Y, Wang X, Zhang WL, Lv F, Guo S. Recent progress in two-dimensional inorganic quantum dots. *Chem Soc Rev.* 2018;47(2):586–625. [<DOI>](#).
3. Xu Q, Cai W, Li W, Sreepasad TS, He Z, Ong W-J, et al. Two-dimensional quantum dots: Fundamentals, photoluminescence mechanism and their energy and environmental applications. *Materials Today Energy.* 2018 Dec;10:222–40. [<DOI>](#).
4. Manikandan A, Chen Y-Z, Shen C-C, Sher C-W, Kuo H-C, Chueh Y-L. A critical review on two-dimensional quantum dots (2D QDs): From synthesis toward applications in energy and optoelectronics. *Progress in Quantum Electronics.* 2019 Nov;68:100226. [<DOI>](#).
5. Budak E, Ünlü C. Boron regulated dual emission in B, N doped graphene quantum dots. *Optical Materials.* 2021 Jan;111:110577. [<DOI>](#).
6. Budak E, Aykut S, Paşaoğlu ME, Ünlü C. Microwave assisted synthesis of boron and nitrogen rich graphitic quantum dots to enhance fluorescence of photosynthetic pigments. *Materials Today Communications.* 2020 Sep;24:100975. [<DOI>](#).
7. Budak E, Erdoğan D, Ünlü C. Enhanced fluorescence of photosynthetic pigments through conjugation with carbon quantum dots. *Photosynth Res.* 2021 Jan;147(1):1–10. [<DOI>](#).
8. Lin L, Xu Y, Zhang S, Ross IM, Ong ACM, Allwood DA. Fabrication and Luminescence of Monolayered Boron Nitride Quantum Dots. *Small.* 2014 Jan 15;10(1):60–5. [<DOI>](#).
9. Pan C, Long M, He J. Enhanced thermoelectric properties in boron nitride quantum-dot. *Results in Physics.* 2017;7:1487–91. [<DOI>](#).
10. Fan L, Zhou Y, He M, Tong Y, Zhong X, Fang J, et al. Facile microwave approach to controllable boron nitride quantum dots. *J Mater Sci.* 2017 Dec;52(23):13522–32. [<DOI>](#).
11. Matsoso BJ, Ranganathan K, Mutuma BK, Leretholi T, Jones G, Coville NJ. Single-step synthesis of crystalline h-BN quantum- and nanodots embedded in boron carbon nitride films. *Nanotechnology.* 2017;28(10):105602. [<DOI>](#).
12. Thangasamy P, Santhanam M, Sathish M. Supercritical Fluid Facilitated Disintegration of Hexagonal Boron Nitride Nanosheets to Quantum Dots and Its Application in Cells Imaging. *ACS Appl Mater Interfaces.* 2016 Jul;8(29):18647–51. [<DOI>](#).
13. Bandyopadhyay A, Yamijala SSRKC, Pati SK. Tuning the electronic and optical properties of graphene and boron-nitride quantum dots by molecular charge-transfer interactions: a theoretical study. *Phys Chem Chem Phys.* 2013;15(33):13881. [<DOI>](#).
14. Li H, Tay RY, Tsang SH, Zhen X, Teo EHT. Controllable Synthesis of Highly Luminescent Boron Nitride Quantum Dots. *Small.* 2015 Dec;11(48):6491–9. [<DOI>](#).
15. Yang Y, Zhang C, Huang D, Zeng G, Huang J, Lai C, et al. Boron nitride quantum dots decorated ultrathin porous g-C<sub>3</sub>N<sub>4</sub>: Intensified exciton dissociation and charge transfer for promoting visible-light-driven molecular oxygen activation.

Applied Catalysis B: Environmental. 2019 May;245:87-99. [<DOI>](#).

16. Stampfl J, Tasch S, Leising G, Scherf U. Quantum efficiencies of electroluminescent poly(para-phenylenes). Synthetic Metals. 1995 Apr;71(1-3):2125-8. [<DOI>](#).

17. Yao Q, Feng Y, Rong M, He S, Chen X. Determination of nickel(II) via quenching of the fluorescence of boron nitride quantum dots. Microchim Acta. 2017 Oct;184(10):4217-23. [<DOI>](#).

18. Huo B, Liu B, Chen T, Cui L, Xu G, Liu M, et al. One-Step Synthesis of Fluorescent Boron Nitride Quantum Dots via a Hydrothermal Strategy Using Melamine as Nitrogen Source for the Detection of

Ferric Ions. Langmuir. 2017 Oct 10;33(40):10673-8. [<DOI>](#).

19. Liu M, Xu Y, Wang Y, Chen X, Ji X, Niu F, et al. Boron Nitride Quantum Dots with Solvent-Regulated Blue/Green Photoluminescence and Electrochemiluminescent Behavior for Versatile Applications. Advanced Optical Materials. 2017 Feb;5(3):1600661. [<DOI>](#).

20. Liu B, Yan S, Song Z, Liu M, Ji X, Yang W, et al. One-Step Synthesis of Boron Nitride Quantum Dots: Simple Chemistry Meets Delicate Nanotechnology. Chem Eur J. 2016 Dec 23;22(52):18899-907. [<DOI>](#).

21. Fletcher AN, Bliss DE. Effects of chemical substituents of bicyclic dyes upon photodegradation parameters. Appl Phys. 1978;16:289.